REPORT DOCUMENTATION PAGE

1. AGENCY USE ONLY (Leave Blank)	2. REPORT DATE May, 2005	3. REPORT TYPE AND DATES COVERED Final Report for the period 02/19/2002 thru 2/28/2005

4. TITLE AND SUBTITLE Mathematical Fluid Dynamics of Store and Stage Separation	5. FUNDING NUMBERS AFOSR Contract F49620-02-C-0024

6. AUTHOR(S) N. Malmuth, V. Shalaev, and A. Fedorov

7. PERFORMING ORGANIZATION NAME(S) AND ADDRESS(ES) Rockwell Scientific Company, 1049 Camino Dos Rios, Thousand Oaks, California 91360	8. PERFORMING ORGANIZATION REPORT NUMBER SC71193.RFRFTV

9. SPONSORING / MONITORING AGENCY NAME(S) AND ADDRESS(ES) The Air Force Office of Scientific Research-NM, 875 North Randolph Street, Arlington, VA 22203	10. SPONSORING / MONITORING AGENCY REPORT NUMBER

11. SUPPLEMENTARY NOTES

The views, opinions and/or findings contained in this report are those of the author(s) and should not be construed as an official Department of the Army position, policy or decision, unless so designated by other documentation.

12 a. DISTRIBUTION / AVAILABILITY STATEMENT Approved for public release; distribution unlimited.	12 b. DISTRIBUTION CODE

13. ABSTRACT (Maximum 200 words)

Multi-body aerodynamics relevant to store and stage separation as well as modeling of hypersonic laminar flow control related problems was studied in the research. New progress in simulating interaction of stores and stages escaping from wing-like surfaces and cavities in transonic and supersonic flows is discussed. Treatment of the interaction involves the solution of singular perturbation problems in which the near field solves a challenging mixed unsteady boundary value problem.. The supersonic regime leads to a wave train interaction with the surface from which the body is launched. If the surface is the underside of a wing, a staircase downstream increasing pressure distribution is obtained, whereas for shear layers such as above weapons bay cavities alternating step function behavior is obtained. Parametric computational studies reveal strong sensitivities of safe body release to the initial launch conditions. In the laminar flow research, thermal protection system microstructure acoustic properties are related to incident wave admittance and the ability to damp second mode instabilities that lead to hypersonic laminar-turbulent boundary layer transition. Linearized Navier Stokes models are used to characterize the interaction of the waves with the microstructure and the results are validated against experiment.

14. SUBJECT TERMS boundary layer transition, transonic flow, supersonic flow, asymptotic expansions, flow control, wavetrains, shock diffraction, mixed boundary value problems, partial differential equations	15. NUMBER OF PAGES 20
	16. PRICE CODE

17. SECURITY CLASSIFICATION OR REPORT unclassified	18. SECURITY CLASSIFICATION ON THIS PAGE	19. SECURITY CLASSIFICATION OF ABSTRACT	20. LIMITATION OF ABSTRACT

Mathematical Fluid Dynamics of Store and Stage Separation

Final Report
on AFOSR Contract F49620-02-C-0024
for the period 02/19/2002 thru 2/28/2005

Prepared by:

Dr. Norman D. Malmuth
Rockwell Scientific Company
Thousand Oaks, CA 91360

May 2005

Table of Contents

List of Illustrations

Background

Air-launched weapons are an essential military technology that can provide strategic and tactical supremacy. Emphasis on safe, high-accuracy, reliable store separation will be critical for weapon system upgrades to cost-effectively meet threats in a financially austere environment for new aircraft development for the foreseeable future. Although the problem of weapons release from an aircraft platform has received much attention as exemplified by Refs. r1-r3, more effort is needed to understand the underlying basic physics and essential parameters.

In a larger sense, this technology is a subset of the problem of the interactions between moving bodies in all speed ranges. Multi-body interaction applications include separation and carriage of various staged vehicles for space missions and flight-testing as well as crew escape. For this group, hypersonic multistage vehicle concepts of interest to the U.S. Air Force frequently utilize the launch of a small rocket-powered stage from a large subsonic or transonic aircraft such as the B-52. Other examples are the PEGASUS series and the Shuttle. Currently, multistage launch scenarios are envisioned for future hypersonic and space applications. A new thrust involves the use of air breathing (scramjet or turbo-scramjet) rather than rocket-powered stages. These can be associated with recoverable launch vehicles such as the RLV series (second and third generation) being studied in the Boeing CRI program. Other applications include the Boeing Delta IV series.

Recent experience with unsuccessful staging such as with the X-43 (Hyper-X) vehicle before the successful mission indicates the criticality of the problem. In a larger sense, the payload mass fraction can be drastically affected by sizing of the separation motors. Overly conservative estimates requiring extra thrust will give a larger weight penalty associated with more motor thrust for stage separation. A smaller (optimistic) separation motor design solution will increase payload with the risk of re-contact and reduced safety. The correctness of these decisions depends on our understanding of the interaction of the fluid dynamics with the dynamics of the motion. The effort described in this report is a continuation of a program emphasizing this understanding. Rather than emphasizing speed, efficiency and accuracy of production CFD codes, numerics and algorithms such as for electromagnetic scattering for application for complex geometries, we stress computationally non-intense PC application to understand and harness (through new flow control concepts) the important physical mechanisms that pervade a wide class of store and stage separation phenomena. This emphasis applies to the other research effort besides store and stage separation discussed herein. Emphasis is on the first order physics and representative unit problems from dissection of more complicated situations that combine these. Another emphasis is to identify new interesting mathematical techniques to solve the unit problems and combine with them current large-scale numerical techniques to improve them. On the other hand, more realism is being introduced as our effort progresses. For example, as compared to previous phases of the effort, increasing emphasis is being placed on high speeds and nonlinear phenomena.

In this report, results from of our program over the last three years will be summarized in which mathematical techniques were further developed to provide desktop models to quickly illuminate the physics of store and stage separation and provide useful tools for conceptual and preliminary design of flight vehicles that use stores and staged components.

Besides the new research thrust of stage separation embodied in the effort discussed herein, another tie-in has been made with current efforts regarding optimizing weapons-bay acoustic

ROCKWELL
SCIENTIFIC

mitigation measures with stage trajectory characteristics, (see r4). Current control measures include jet blowing and actuators to reduce the amplitudes of the noise power from weapons-bay cavities. Flight and ground tests are underway to investigate the effects on store trajectories. The physics and time scales of the mitigation measures and their possible coupling with the dynamic characteristics of the separation bodies needs to be better understood. Our models will be further developed to provide useful insight into this interaction. Examples of our work are in r5-r12 and our publications in the Appendix.

Physics and Modeling Issues for Multibody Flows

In this phase of the research, we have continued our effort in both formulating and solving unit problems to improve our understanding of the physics of multi-body interactions associated with store and stage separation especially at supersonic speeds. Along with solving the unit problems, we are developing a PC-oriented capability for prediction of store and stage separation characteristics with an ultimate relationship to control. There is a strong need for ground tests that will help us to understand cavity flows and the relationship to weapons-bay store separation leading ultimately to control of this process. The PI is participating with Boeing in such tests. The problems selected for study are central to building our models to account for unsteady effects, interaction with acoustic mitigation measures, supersonic separation dynamics, interaction of the body with the cavity flow and an assessment of the time averaging used in our models for characterizing the interaction of the body with the weapons-bay shear layer. The role of time scales is important in justifying the applicability of pseudo-steady approximations assumed in Captive Trajectory System (CTS) testing and understanding of measures to reduce acoustic radiation, vibration in weapons bay cavities and doors while insuring safe escape.

Modeling of Hypersonic Flow Control Processes

Porous materials of fine structure (such as fiber ceramics and felt metals) are widely used for absorption of acoustic disturbances such as what we have developed for hypersonic laminar flow control and reported in r12-r15. State-of-the-art theoretical models r16-r19 predicting acoustic characteristics of these materials ignore effects associated with gas rarefaction. In these models, the linearized Navier-Stokes equations with no slip and no temperature jump conditions on pore walls govern the problem, which is analyzed using combinations of analytical solutions for isolated pore and statistical methods to treat random structures. However, the continuum approximation is not valid in many practical applications. The following issues can arise:

- Gas filling pores may be of low density. This occurs in high altitude flight.

- The porous material may have ultra-fine structure. This is typical for fiber-ceramic materials and micro-fluid systems.

In both cases, the Knudsen layers formed on the pore walls may have a thickness of the order of the pore size; *i.e.*, gas rarefaction may significantly affect acoustic characteristics of porous materials. As just indicated, our interest to this problem is motivated by our current theoretical and experimental studies of ultrasonically absorptive coatings (UAC) for hypersonic laminar flow control. We have discovered that UAC can stabilize the dominant unstable mode by extracting the disturbance energy and thereby increasing the laminar run as theoretically demonstrated in r12, r13. This concept was confirmed by experiments r14 in the Caltech high

enthalpy Mach=5-6 T5 shock tunnel. It was shown that a thin porous coating, which comprises equally spaced blind micro holes (*regular* porosity), doubles the transition Reynolds number and completely laminarized the tested cone! Furthermore, our stability experiments r15 in the ITAM (Novosibirsk) Mach 6 wind tunnel showed that a *random* porosity microstructure (felt metal™) coating dramatically reduces the second-mode growth rate. Performing parametric studies of UAC performance, we recognized that the flow density relevant to hypersonic, high-altitude flight is so small that gas rarefaction becomes significant.

Objectives

To address the foregoing needs, the part of our research dealing with multi-body interactions we performed research to study store interaction with cavity bay shear layers relevant to separation and delivery with emphasis on the following tasks:

1. Continue combined asymptotic and numerical modeling of store separation and multibody flow processes

2. Investigate shock interactions relevant to stage separation

3. Develop combined dynamics and aerodynamic models for analysis of store and stage separation

4. Calculate examples of a slender body separation from a wing into a supersonic freestream

Added to this scope of effort our objective was to develop the ultrasonic absorption coating technology so that ultimately it can be deployed on hypersonic flight vehicles for passive laminar flow control. A major objective was to mathematically simulate the energetics related to admittance of typical thermal protection system microstructures to tailor them to absorb energy of second mode instabilities leading to delay of laminar turbulent boundary layer transition.

Major Technical Accomplishments

Multi-body Store and Stage Separation Effort

In FY 1999, the phases of store separation above, below and crossing cavity shear layers bounding subsonic streams were treated with our combined asymptotic and numerical methods. Good agreement of our predictions with IIT experiments was demonstrated. (*cf.*r5 -r10).

A major thrust in FY 2000 was extension of the model and its coupling with 3-DOF dynamics from *subsonic* to *transonic* flow. This involved a multitude of subtasks, including a study of the asymptotic matching of the near and far field flows. External separation from a solid flat wall boundary was modeled as a forerunner of treatment of interaction with the shear layer over a cavity. It was shown that our theoretical model is able to capture such complex phenomena as store re-contact with the parent body. A tremendous sensitivity of the initial launch conditions was discovered, a property later verified by the PI's experimental work with Boeing. Our results for this model problem are also directly applicable to stage separation of space vehicles.

In FY 2001, the FY 2000 transonic theoretical and computer models were generalized for treatment of *transonic* store separation from a flat body surface simulating external carriage as well as launch from a rectangular cavity of finite span (*cf.* r21-r22).

SC71193.RFRFTV

ROCKWELL SCIENTIFIC

In FY 2002-2005, our major effort has been focused on external store separations into a *supersonic* outer flow (*cf.*r23) with emphasis on:

- Analysis of store interaction with a stratified external flow field induced by the parent body

- Scattering of a plane shock wave by a slender body within the framework of geometric acoustics

- Parametric studies of 3-DOF trajectories of a slender body of revolution separating from a thin wing in a supersonic free stream

Modeling of store interaction with *external non-uniform flows* is discussed in r23. As previously indicated, parent body elements such as a wing and fuselage induce external interference flow fields around the store. The external flow field contributes to the forces acting on the body. Our effort has been to assess the importance of this effect in relation to the flow modifications analyzed in our previous studies for store separation in a uniform stream. We used slender body theory with an assumption that the store is small and does not affect the external field, *i.e.*, the external flow field is a *passive scalar*. Considering the leading terms in the expansions, we identified different cases, defined lumped parameters for the external-field effect and indicated regimes when this approximation captures the primary physics.

In subsonic (elliptic) flows, the external flow perturbations are distributed in space. Their contributions to forces and moments acting on the store are reduced to a superimposed, induced angle of attack due to the external flow inclination as well an external pressure field representing the effect of the background airplane flow. *In supersonic (hyperbolic) flows*, new effects are due to scattering and reflection of weak shocks. At the initial stage of separation, these phenomena lead to formation of the shock-wave system (called a wave train) between the parent body and the store. Unit problems associated with the wave train formation are shown in Figure 1.
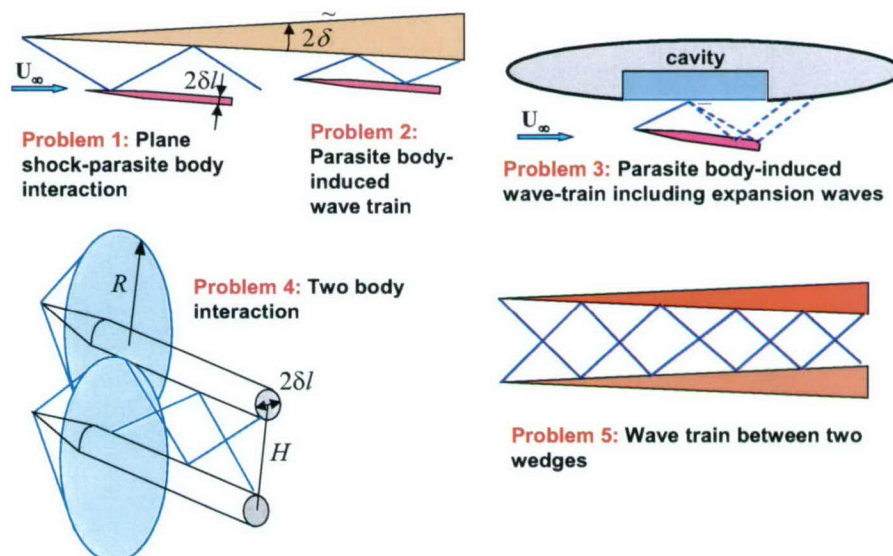

Figure 1. Unit problems associated with scattering/scattering of body-induced shocks.

Since the shock waves are weakly attenuated, their diffraction and re-reflection needs to be analyzed in accord with the previous discussion. Moreover, the shock-body interaction leads to important changes of the pressure distribution on the store surface that, in turn, causes appreciable changes of aerodynamic forces and moments acting on the store.

Starting in FY 2003, we have performed first-cut modeling of the plane shock wave scattering by a slender body of revolution (Problem 1 in Figure 1.) The problem was analyzed within the framework of geometric acoustics. Figure 2 shows an incident ray containing the unit vector **I**, and the reflected ray containing the unit vector **R**. These vectors and the normal vector **N** to the body surface lie in the same plane. The vector **S** is tangent to the body surface in this plane. The vectors **I**, **R** are inclined to **N** at the reflection angle γ that is expressed in terms of the polar angle θ and the Mach number as $\gamma=\cos^{-1}(\sin\theta/M)$. With these findings, the pressure on the body surface behind the shock reflection is expressed as a function of the incident ray angle in a simple analytical form

$$p'' = p' + \Delta p = \frac{\varepsilon}{\beta}[1 + sin\theta(s)], \tag{1}$$

where $\beta = \sqrt{M^2 - 1}$. In the shadow region $\theta < 0$, the pressure is assumed constant, *i.e.* $p'' = \varepsilon/\beta$.
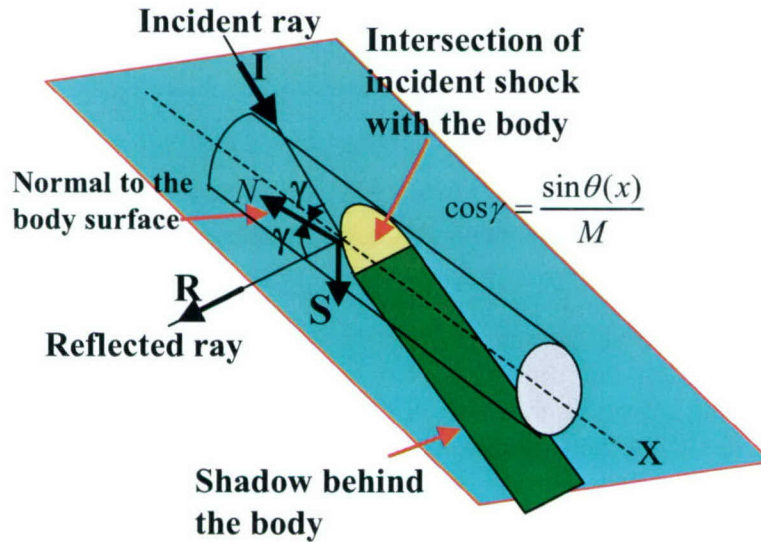

Figure 2. Geometric acoustics of the plane shock-body interaction.

SC71193.RFRFTV

ROCKWELL
SCIENTIFIC

The aforementioned solution is valid for Mach numbers $M > \sqrt{2}$. This restriction results from the condition of supersonic flow in the scattering direction **S**. The solution has been incorporated into our computational code predicting store trajectories. Numerical examples, one of which is shown in Figure 3, indicate that the parasite body-shock interaction crucially affects the parasite body trajectory: compare the red line (the shock interaction is included in the trajectory calculations) with the black line (the shock interaction is not taken into account). This example clearly indicates that accurate modeling of the parasite body-shock interaction is very important. This motivates us to perform further theoretical, CFD and experimental studies of this phenomenon.
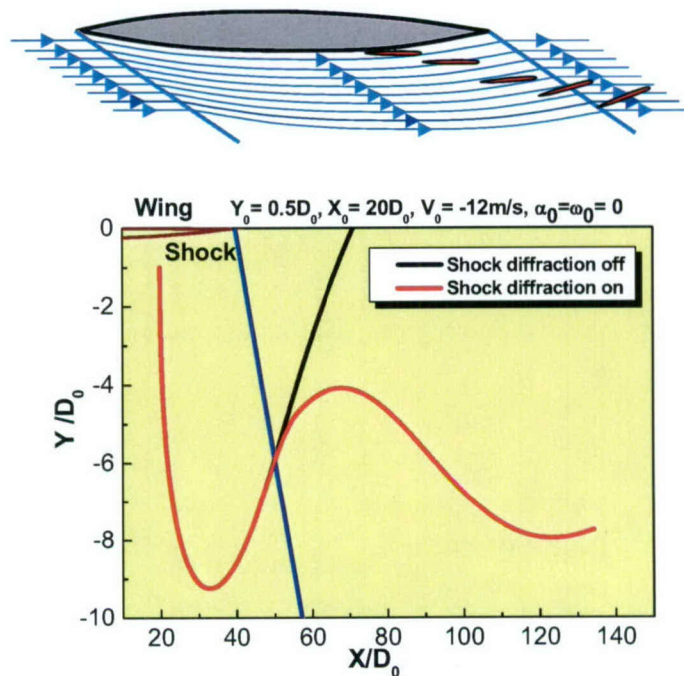

Figure 3. Parent body induced shock substantially affects parasite body trajectory.

In early FY 2004, the near field diffraction effect on the forces on two interfering slender bodies of revolution was studied. A key unit problem for multi-body separation at supersonic speeds (see Problem 5 in Figure 1) was treated. The far field flow was analyzed by linearized supersonic slender body theory based on the Prandtl-Glauert Equation (PGE) equation for the perturbation velocity potential. This led to a solution that was used to obtain the interference flow between two arbitrary bodies. This interference occurs because of the reflected waves necessary to maintain inviscid tangency boundary conditions on each body of the pair. The transient PGE initial boundary value problem is solved using the transform calculus. The wave train structure consisting of sequence of conical wave fronts has been obtained by term-by-term inversion of the expansion in exponentials of the transforms for large values of the transform parameter, according to a Tauberian theorem. Conical fronts as compared to the two-dimensional case of

6

plane waves were obtained. Space damping of the disturbances in the three-dimensional case considered here is related to energy spreading implying three-dimensional "disturbance relief." and in accord with Huygens' principle. Although significant interference pressure (Figure 4 and drag (Figure 5) are obtained to dominant order, lift and moment are higher order (Figure 6) that we are discovering are controlled by the intricate and subtle details of the wave diffraction near field and its matching to the far field.

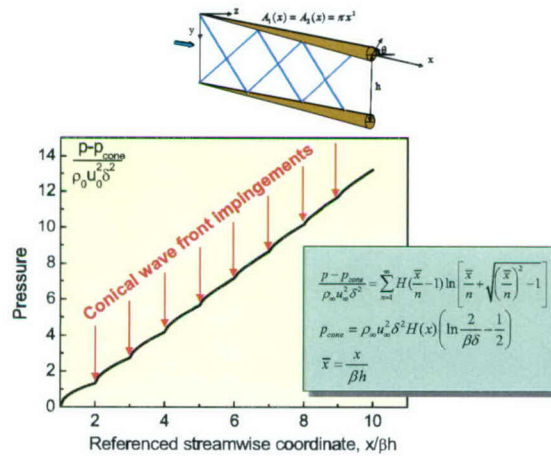Figure 4. Pressure on the surface of one cone induced by another cone.
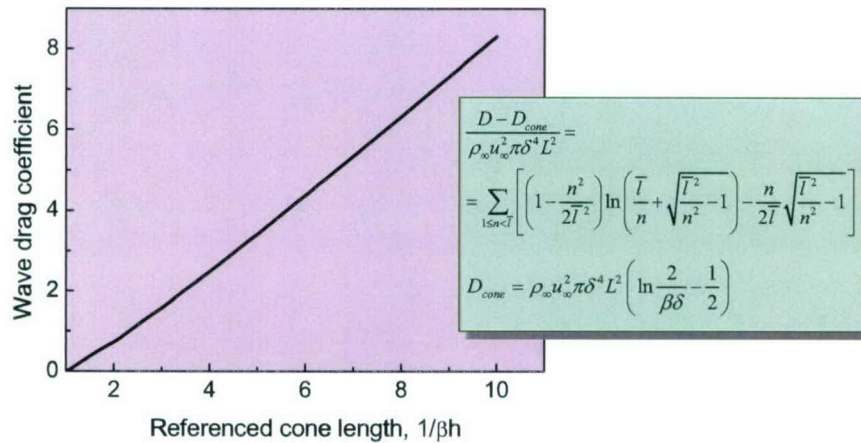

Figure 5. Wave drag of one cone induced by another cone.

The higher order pressure integrals for the lift and moment include Heaviside functions with azimuthal angular dependence that appear to roughly model the scattering/diffraction of the conical fronts from the wave systems of one body on the other. The scattering scheme and

analytical expressions for the lift and pitching moment are shown in Figure 7. These solutions indicate rapid increase of aerodynamic loads with the number N of wave-front reflections.
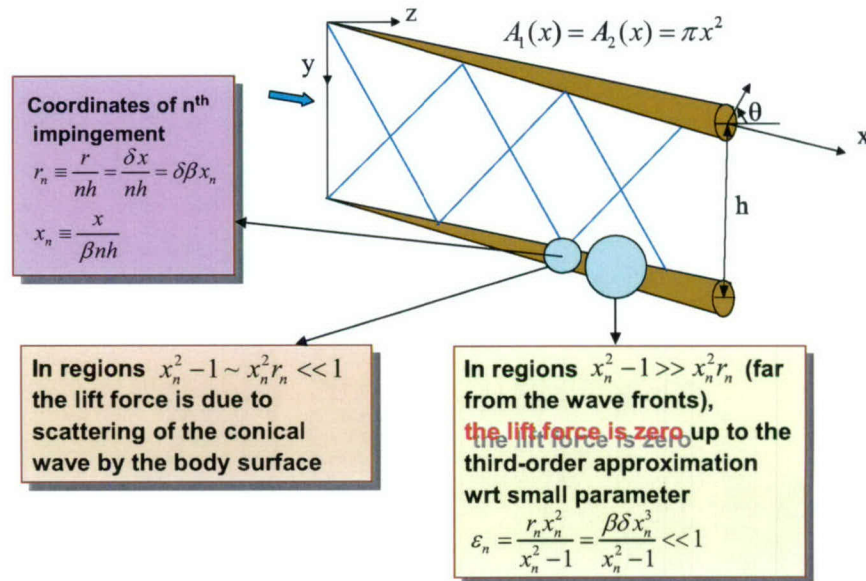

Coordinates of nth impingement

$$r_n \equiv \frac{r}{nh} = \frac{\delta x}{nh} = \delta \beta^2 x_n$$

$$x_n \equiv \frac{x}{\beta nh}$$

$$A_1(x) = A_2(x) = \pi x^2$$

In regions $x_n^2 - 1 \sim x_n^2 r_n \ll 1$ the lift force is due to scattering of the conical wave by the body surface

In regions $x_n^2 - 1 \gg x_n^2 r_n$ (far from the wave fronts), the lift force is zero up to the third-order approximation wrt small parameter

$$\varepsilon_n = \frac{r_n x_n^2}{x_n^2 - 1} = \frac{\beta \delta x_n^3}{x_n^2 - 1} \ll 1$$

Figure 6. Lift force is generated in the local regions of conical shock-wave scattering.

Front of incident wave

Front of reflected wave

$r \to 0$, local coordinate $u_n \equiv \dfrac{x_n^2 - 1}{2 r_n x_n^2} = O(1)$

Lift force

$$L = -\int_{-\pi}^{\pi} \sin\theta \, d\theta \int_0^l p_n(x,\theta) \delta x \, dx = -\frac{1}{6} \rho_\infty u_\infty^2 h^2 \beta^{\frac{7}{2}} \delta^{\frac{9}{2}} \left[\frac{4\Gamma^2\left(\frac{3}{4}\right)}{5\sqrt{\pi}} - \frac{1}{3}\sqrt{\beta\delta} \right] N(N+1)(2N+1)$$

Pitch moment

$$M = -\frac{1}{4} \rho_\infty u_\infty^2 h^3 \beta^{\frac{9}{2}} \delta^{\frac{9}{2}} \left[\frac{4\Gamma^2\left(\frac{3}{4}\right)}{5\sqrt{\pi}} - \frac{1}{3}\sqrt{\beta\delta} \right] N^2(N+1)^2$$

N – number of impingements
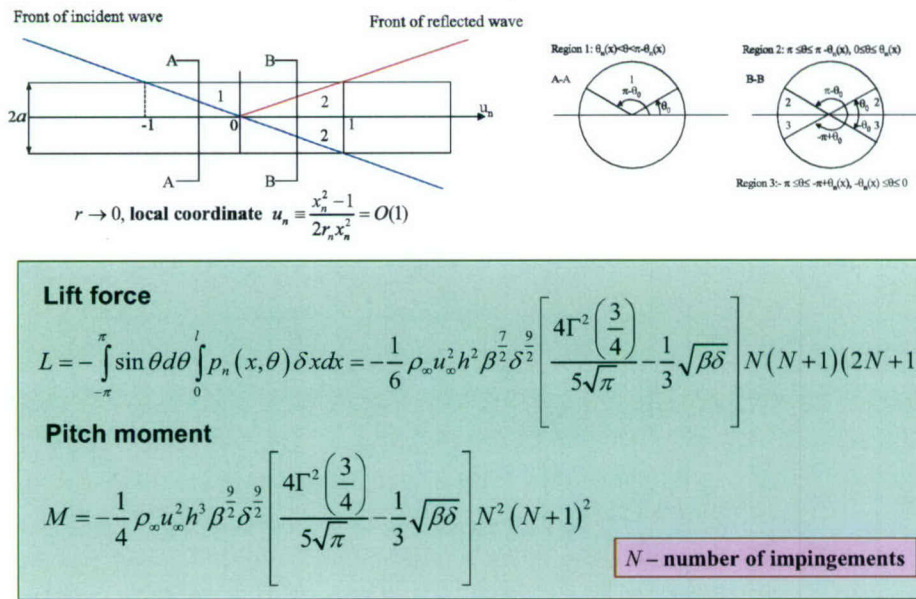
Figure 7. Approximate scheme of local scattering and corresponding analytical solutions for the lift force and pitching moment.

SC71193.RFRFTV

ROCKWELL
SCIENTIFIC

In summary, the aforementioned analysis provides for the first time an approximate but coherent picture of the wave train structure occurring in multi-body interference problems such as supersonic stage separation and flight crew escape. This is particularly important for internal carriage and cocoon release where shear layers bounding cavities exist. Moreover, this work provides a launching pad for future effort to obtain more understanding of the near field as well as increased prediction accuracy. This will strongly impact ejection system design and safe separation flow control.

Our complementary effort under Boeing sponsorship to obtain databases for this research phase is in progress. This involves highly cost-effective testing in high Mach number facilities of ITAM in Siberia as well as CFD studies (see Figure 8). Stage separation is a critically important aspect of high-speed flight vehicles such as that the Hyper-X (X-43), the FALCON DARPA program. FALCON includes trans-atmospheric vehicle concepts that will skip outside and inside the earth's atmospheric layers to obtain global cross-range capability. Besides L/D, *fuel weight fraction* is a metric that needs to be optimized to meet this requirement. Overly conservative sizing of stage separation rocket motors adversely influences this weight fraction and can reduce payload. Accurate and rapid estimation of stage dynamics and aerodynamic interference tools such as those emerging from our research are important in a satisfying these needs.
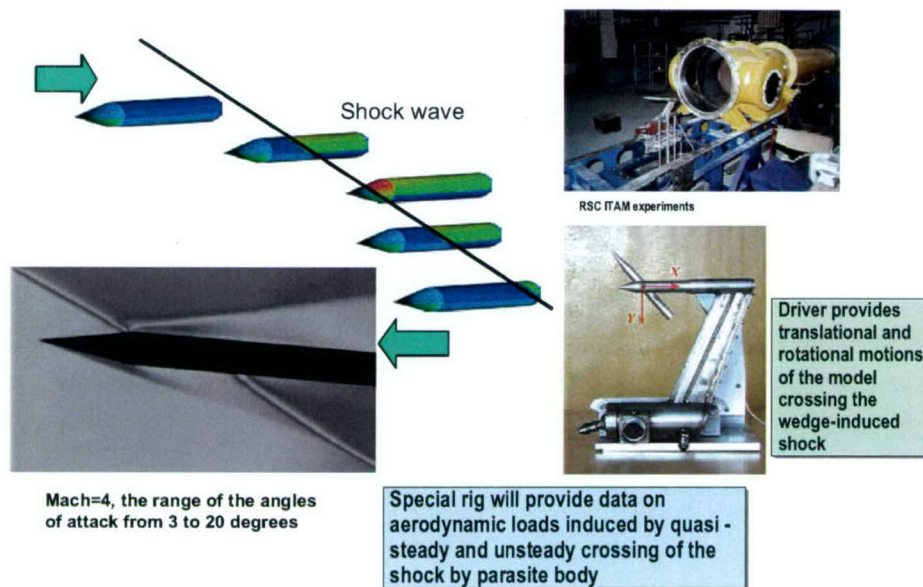

Figure 8. ITAM experiments from r31 on steady and unsteady shock-body interactions are complemented by CFD studies.

9

A unit problem occurring in supersonic and hypersonic store and stage separation is the impingement of shock waves on escaping bodies. Strong evidence exists that such waves can drastically affect store and stage separation trajectories. This however can be exploited for trajectory control schemes that avoid re-contact. Our experiments at ITAM in Novosibirsk and our current supersonic store and stage separation analyses that we developed under previous phases of this program have shown that the proper control laws are needed. These are required to design a system to avoid end-over-end tumbling or flat spins that can result with over control. At high speeds, complex shock interference heating results from high-speed jet shear layers. These convect downstream from shock limbs as well as lead to interactions such as those of Edney IV type and Mach reflections. An exciting innovation for which we have just made a patent disclosure is to use lightweight, simple, low current plasma discharges that do not have the fluidic jet on-board stored air requirements or the drag penalties of spoilers for control of cavity flows. At low supersonic speeds, the problem has some features in common with classical electromagnetic scattering (EMS). One of these is that its Prandtl-Glauert perturbation potential Laplace transform obeys the Helmholtz equation, as does the EMS field space factor. It however has many critically different aspects, especially for strong shocks, for which nonlinearities are decisive. Even the linear supersonic problem is different since the flow tangency boundary conditions are on the *near field* wedge shock wave generator as contrasted to *far field* asymptotic compatibility with an incident wave coming from infinity in the electromagnetic problem. In the shock diffraction/scattering problem, the wave is an oblique front rather than one that is normal or parallel to the scatterer for which eigenfunction expansion solutions are documented in the classical texts. For the nonlinear case, Rankine-Hugoniot shock relations have to be satisfied on the shock and shock-shocks as well as caustics that form from secondary wavelet envelopes as in Huygens' construction. Early literature on this topic is mainly *inductive* (using wave geometry ideas) and needs to be made part of a *deductive* scheme from first principles to be applicable to more complex stage and store separation physics. As contrasted to the development of fast, accurate high-order EMS solvers such as numerical schemes based on short wavelength expansion solutions of the EM integral equation for three-dimensional airplane geometries, our main focus is to model the connection of the near field scattering process with far field wave trains for weapons emerging from cavities. These decisively affect lift, drag, and moment as well as pressure distributions. We intend to make this connection by matched asymptotics. This new approach will provide considerable physical insight. Another differentiator of our shock interaction work from EMS algorithm development is the role of shock refraction in transonic, thick shear layers that separate the cavity flow from the external flow. This issue emerges continually in our discussions with Boeing, WPAFB-VA and AFSEO who are concerned with acoustic mitigation and safe separation.

Figure 9 shows key features of the aforementioned linear problem which we have formulated in the effort under this contract. This unit problem models interaction of a wing-like surface with an ogive cylinder body in a supersonic flow. An incident Mach wave from a wedge generator is reflected by the cylinder surface to satisfy the boundary conditions of flow tangency. The trace of intersection is an ellipse in the plane of the incident wave. The reflected wave is the envelope of ray cones a typical one of which is shown in Figure 9. In accord with the previous remarks, this interaction is quite different from the scattering of a plane wave over a cylinder in the sense that the plane wave is in the near field rather than the far field in the classical problem, *i.e.*,

$h < \infty$. As indicated previously, this problem leads to a boundary value one for the Helmholtz equation. Techniques to solve such problems but with different boundary conditions are discussed in r24- r29. However, in significant contrast to our application, r29 uses the 3-D Helmholtz *fundamental solution* as contrasted to a *Green's function* for the kernel for the Fredholm integral equation of the second kind that we plan to treat. We intend to exploit the advantage that this Green's function satisfies the boundary conditions on the scatterer for our specific problem. Moreover, and as previously indicated, we stress that the Helmholtz operator applies to the Laplace transform of the perturbation potential rather than the space part of the electromagnetic field as in much of the just-cited EMS work. Because of this and the near field boundary conditions, the interpretation of the short wavelength approximation will be different than that for the EMS problem. In addition, we will be considering other approximations besides the short wavelength asymptotic series that is very useful in obtaining accurate numerical solutions as described in recent EMS literature. Strong indications are that they will have limited relevance to our goal of obtaining forces and moments controlling weapons separation from weapons bays. Returning to our formulation, a side view of the wedge scatterer in relation to cylinder is shown in Figure 10.

In a supersonic flow with a freestream of Mach number M_∞, the plane wave emanating from a wedge apex A experiences multiple scattering. The primary wave is ABD and the first reflected wave of the downstream wave train is BC. If the wedge angle is small, $\delta \ll 1$, supersonic small perturbation (Prandtl-Glauert) theory applies. Denoting the perturbation potential as ϕ, the initial boundary-value problem is
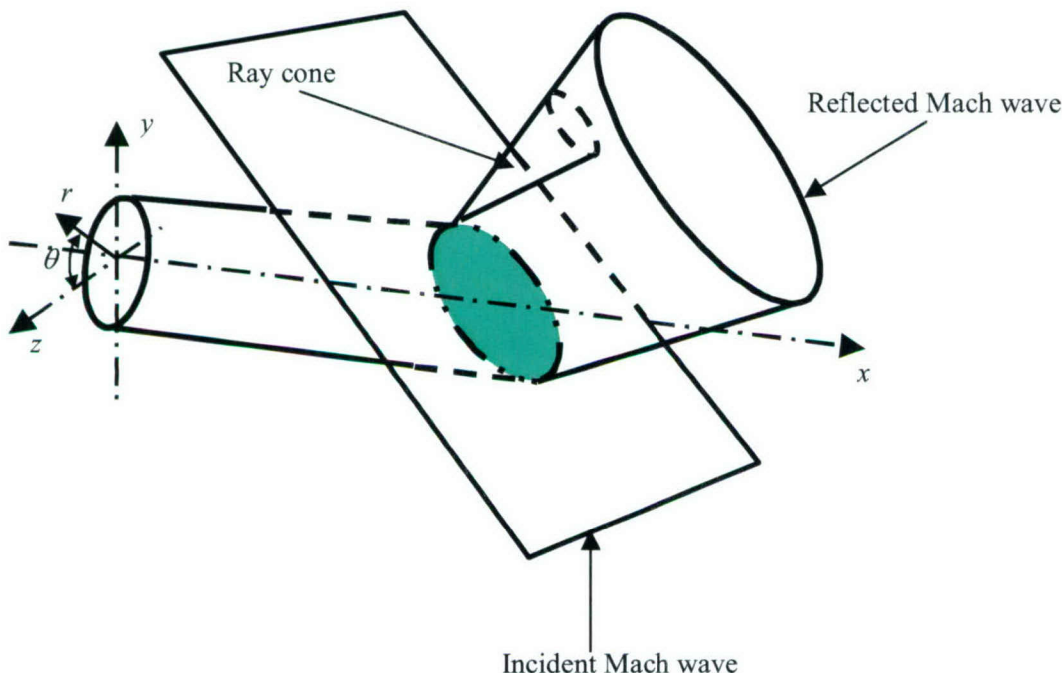

Figure 9.Shock diffraction geometry.

$$\beta^2\phi_{xx} - \left(\phi_{yy} + \phi_{zz}\right) = 0, \Rightarrow \left[\beta^2\frac{\partial^2}{\partial x^2} - \left(\frac{1}{r}\frac{\partial}{\partial r}\left(r\frac{\partial}{\partial r}\right) + \frac{1}{r^2}\frac{\partial}{\partial \theta^2}\right)\right]\phi = 0 \qquad (2a)$$

$$\left.\frac{\partial\phi}{\partial r}\right|_{r=a} = 0 \qquad (2b)$$

$$\left.\frac{\partial\phi}{\partial y}\right|_{y=h} = 1 \qquad (2c)$$

The multiple reflection shock train is a basic feature of the problem. It has been analyzed for the supersonic interaction of two bodies of revolution in r30, assuming their spacing is large compared to their thicknesses. *The purpose to treat more closely spaced bodies where such an approximation may be invalid. This is relevant to critical aerodynamic loads occurring in the initial phases of stage and store separation. This can be evaluated by matched asymptotics for which an outer limit of the solution of the problem to be now discussed will be used.* Note that for narrow spacing $\frac{h}{\delta} = o(1)$, there may be a special one-dimensional regime in which the cross flow derivatives are small providing that the $\frac{h}{\rho} = o(1)$ as well, where ρ is the minimum characteristic radius of curvature between both bodies in the cross flow plane. This contrasts with the usual slender body theory approximations used for $\frac{h}{\rho} = O(1)$, where the dominant orders in the slender body near field expansions where the cross flow derivatives are more important than the streamwise ones. Our preliminary assessment indicates that this will be applicable to the case to where $\frac{h}{\rho}$ will be assumed to be $O(1)$.

Returning to the diffraction problem, we use the Laplace transform of the perturbation potential

$$\bar{\phi} = \int_0^\infty \phi e^{-px}dx.$$

Applying this to the problem defined by (2) we obtain the subsidiary boundary value problem (P1) for the reduced wave (Helmholtz) equation (see also Figure 11).

$$L[\bar{\phi}] = 0, \quad L \equiv \Delta_T - \lambda^2,$$

$$\Delta_T \equiv \frac{1}{r}\frac{\partial}{\partial r}\left(r\frac{\partial}{\partial r}\right) + \frac{1}{r^2}\frac{\partial^2}{\partial \theta^2} = \frac{\partial^2}{\partial y^2} + \frac{\partial^2}{\partial z^2},$$

$$\lambda^2 \equiv \beta^2 p^2$$

$$\left.\frac{\partial \bar\phi}{\partial y}\right|_{y=h} = \frac{1}{p},$$

$$\left.\frac{\partial \bar\phi}{\partial r}\right|_{r=a} = 0,$$

Using separation of variables, and a generic notation for $\bar\phi \equiv u$, accordingly $u = R(r)T(\theta)$ is assumed. Equation (4.1a) implies

$$r^2\left[\frac{d^2}{dr^2} + \frac{1}{r}\frac{d}{dr} - \lambda^2\right]R = \Lambda^2 = -\frac{T''(\theta)}{T}, \tag{3}$$

where Λ is the eigenvalue. Since $T(\theta)$ is to be continuous at $\theta = 2n\pi$, it must be a periodic function and n is an integer $0,1,2,\ldots$. Thus R satisfies the modified Bessel equation
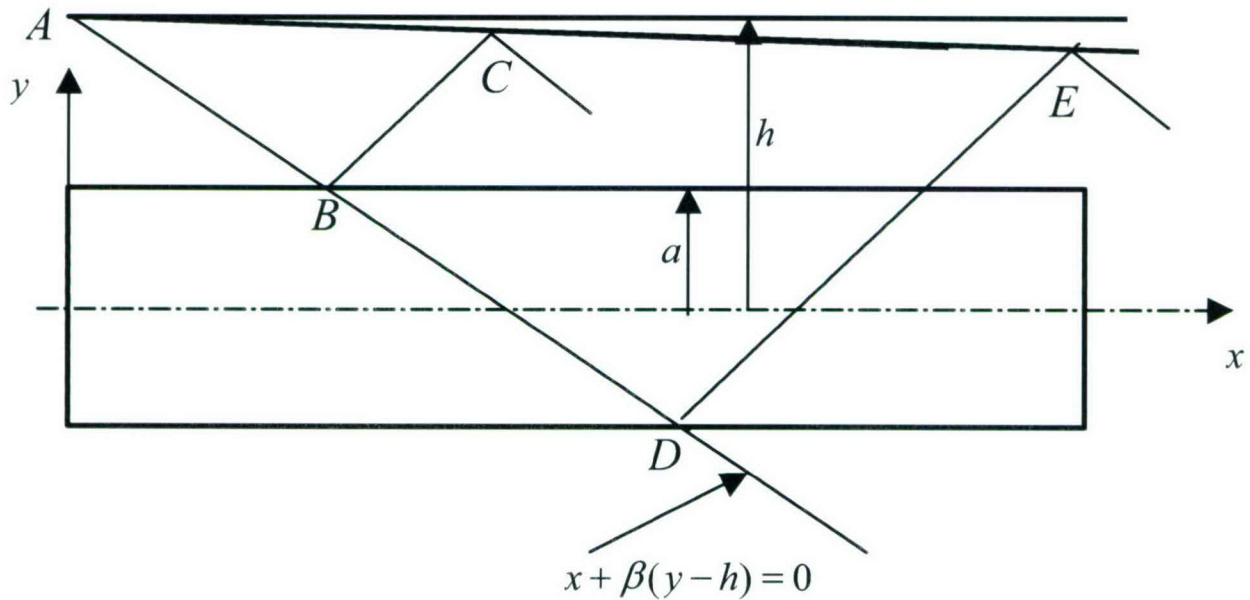

Figure 10 Side view of Mach wave interaction.

$$\frac{d^2R}{dr^2} + \frac{1}{r}\frac{dR}{dr} - \left(\frac{\Lambda^2}{r^2} + \lambda^2\right)R = 0 \tag{4}$$

.

The eigensolutions of (3) and (4) are

$$T_n(\theta) = \begin{cases} \cos n\theta \\ \sin n\theta \end{cases}, \tag{5}$$

,

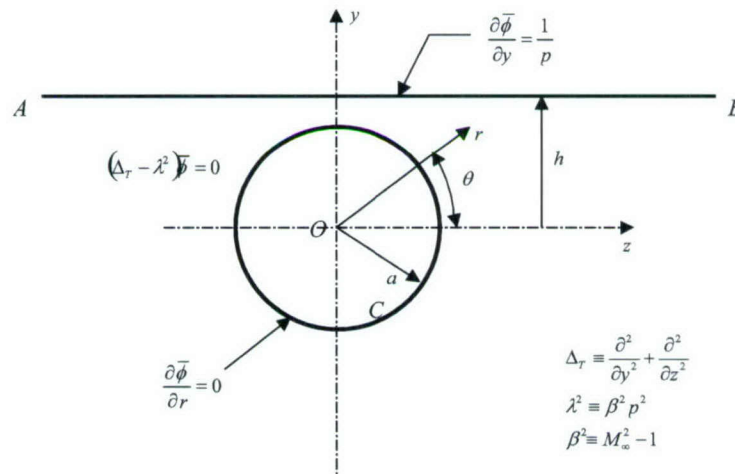$$R_n(r) = \begin{cases} K_n(\lambda r) \\ I_n(\lambda r) \end{cases} \tag{6}$$

.

Figure 11 Laplace transform reduced Helmholtz boundary value problem (Problem P1).

The method of variation of parameters or projection in space of the homogeneous problem eigenfunctions (5), (6) solving the usual Sturm-Liouville problems for $T(\theta)$ in (3) and $R(r)$ in (5) is used to obtain the Green's function $G(r,\theta;r',\theta')$ which is governed by

$$L[G] = \frac{\delta(r - r')}{r} \delta(\theta - \theta'), \qquad (7a)$$

$$\left. \frac{\partial G}{\partial r} \right|_{r=a} = 0, \qquad (7b)$$

$$G(\infty, \theta) < \infty \qquad (7c)$$

where $\delta(x)$ signifies the delta function of x. Further analysis will be focused on an integral equation resulting from Green's formula to solve the boundary value (multiple scattering) problem defined by Eqs. (2). As previously indicated our approach has very limited commonality with EMS analyses illustrated by r29. Yet, we believe that this may permit application of some of the tools developed in our applications to impact the EMS procedures. Since the integral equation will be for the Laplace transform and we are interested in many questions that involve parametric and spatial dependencies, we will be focusing on low order analytical asymptotic closed form representations in contrast to the important quest for high fidelity numerical solutions that pervades much current EMS effort.

With asymptotic methods, we will analyze different limits such as short and long wavelength approximations as well as small and large spacing between interacting bodies, in order to clarify basic features of multiple scattering. Our approach will be to emphasize alternating procedures such as continued fractions and recursive methods such as Schwarz alternating sequences and obtaining functional analysis-based-fixed-point maps to insure convergence of the iterative sequences. For problems involving boundary data on two disconnected arcs, the alternating sequence is a form of imaging such as that used in potential theory in which the sequence involves an added correction iterate to repair the spoiling of the boundary conditions on one arc by a previous iterate that was designed to satisfy those on the other arc. A major hurdle is to make the developments analytically tractable and un-messy to facilitate the inversion of the transforms. We envision that this can be addressed with "elastic" low-order asymptotics, particularly of the large and small h spacing parameter variety. Our preliminary studies indicate that by concentrating on the trajectory-determining aerodynamic forces, rather than pressure fields, it is feasible to obtain compact analytical solutions for the shock-induced lift force and pitching moment. We will study integral theorems in this connection. These solutions will be compared with experimental data and CFD of ITAM (Novosibirsk). This allows us to evaluate elasticity of the first-order asymptotic approximations. As in previous phases of the effort, the theoretical results will be incorporated into our codes predicting store or stage escape trajectories.

15

Cavity Flows Relevant to Store Separation

At present, qualitative studies are underway regarding the flow physics of normal injection of jets ahead and behind supersonic cavities. The PI is collaborating with Caltech's Professor Hans Hornung in this connection through the former's faculty position at Caltech. Figure 12 shows snapshots taken from computational schlieren movies developed by Hornung. The left panel shows cavity flow without normal injection in front of it. An unsteady Euler code, Amrita, developed by James Quirk was used for these simulations. The free-stream Mach number of the two flows is 1.5, and the jet Mach number is 1.1. Pressure and density in the free-stream and the jet are the same. The graphs give pressure, temperature (normalized by free-stream values) and x-Mach number (blue, red and green respectively) along the top of the cavity. The scale for pressure and temperature is the one given on the left, and Mach number range is from 0 to 2. The right panel shows the effect of the injection. In connection with the previous remarks, the jet alleviates the strong disturbances and quenches the Kelvin–Helmholtz instability near the cavity lip. We are starting to look at the time-average flow pattern, which is vitally significant on the Froude or ejection time scale. The latter is at least an order of magnitude longer than the convection times for acoustic disturbances. This is why temporal averaging is important in understanding the mechanisms to be exploited by weapons-bay cavity flow control.
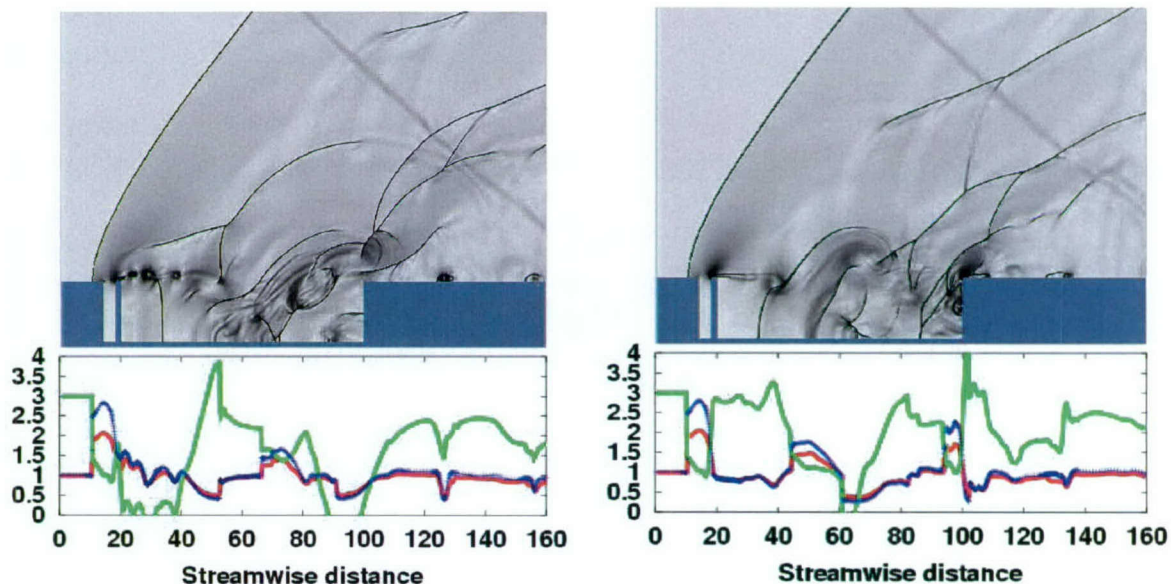

Figure 12 Computational schlieren snapshots of instantaneous cavity flow fields with and without jet control,

Physics and Modeling for Passive Hypersonic Boundary Layer Flow Control

A semi-empirical first-cut model of gas rarefaction effects on acoustic disturbances in porous media was given in r15. Exact solutions describing propagation of acoustic disturbances in cylindrical long pores of various cross-sectional shapes were obtained in r20 with the assumption that the Knudsen number Kn is small. In this case, the gas rarefaction leads to slip and temperature jump conditions on the pore walls whereas the disturbance fluid dynamics is governed by the linearized Navier-Stokes equations for a continuum. It was shown that these

solutions agree well with experimental data in the low frequency band, which is of most practical interest. In a wide range of Knudsen number ($0 < Kn < 5$); i.e., the small Kn approximation is quite elastic. This leads to the hypothesis that the isolated-pore solutions r20 may be used as key elements for theoretical analyses of acoustics in porous materials at low ambient densities as well as in materials of ultra-fine microstructures. Examples of our analyses are given in the Appendix.

However, the solutions r20 for straight cylindrical pores do not account for effects associated with tortuousity and cross-sectional non-uniformity of actual pores. To fill this gap, we will generalize solutions for tortuous and non-uniform isolated pores and incorporate them into our methodology providing acoustic characteristics of porous materials. This will allow us to replace empirical parameters such as a shape factor and turtuousity coefficient by relations based on self-consistent analyses.

For materials of high porosity and anisotropy, the aforementioned concept of equivalent cylindrical pore is not valid. These practically important configurations will be treated using kinetic theory. We believe that this is a novel approach to the problem and should provide important new insights.

Cumulative Lists of Personnel and Publications
Personnel Supported

N. Malmuth, V. Shalaev, A. Fedorov

Publications

Published and Accepted
1. Malmuth, N.D., Fedorov, A.V., Shalaev, V., Cole, J., Khokhlov, A., Hites, M., and Williams, D., "Problems in High Speed Flow Prediction Relevant to Control," AIAA Paper No. 98-2695, 2nd AIAA Theoretical Fluid Dynamics Meeting, June 15-18, 1998, Albuquerque, NM.

2. Malmuth, N., Fedorov, A., Shalaev, V., Cole, J., Hites, M., and Williams, D. "Desktop Aerodynamic Models for Store Separation from Weapons Bay Cavities and Related Vortical Processes," Vortex Flow at High Angle Attack, AVT Symposium, Paper 37, Loen, Norway, May 7-11, 2001.

3. Malmuth, N. D., Shalaev, V. I., Fedorov, A. V. "Combined Asymptotics and Numerical Methods for Store Interactions," Technical Report of Contract CF49620-96-C-0004, AFOSR/NM, October 1998 (available in Defense Technical Information Center, stient.dtic.mil).

4. Malmuth, N., Hites, M., and Williams , D., "Photographic Investigation of the Dynamics of an Ogive Model near a Cavity at Subsonic Mach Numbers," Final Report. Fluid Dynamics Research Center Illinois Institute of Technology, January 18, 1998.

5. Shalaev, V.I., Fedorov, A.V., and Malmuth, N.D., "Dynamics of Slender Bodies Separating from Rectangular Cavities," AIAA Paper No. 2001-2996, 31 AIAA Fluid Dynamics Conference and Exhibit, 11-14 June 2001.

6. Shalaev, V., Fedorov, A. and Malmuth. N., "Dynamics of Slender Bodies Separating from Rectangular Cavities," AIAA J. 40 3, pp.517-525, March 2002.

7. Malmuth, N.D. Shalaev, V. and Fedorov, A, "Theoretical Analysis of Flow Between Two Supersonic Slender Bodies," Rockwell Scientific Company, Report NM03-24892, December 2003.

8. Malmuth, N.D., Fedorov, A.V., Shalaev, V., Cole, J., and Khokhlov, A., "Problems in High Speed Flow Prediction Relevant to Control," AIAA Paper No. 98-2995, 2nd AIAA Theoretical Fluid Mechanics Meeting, June 15-18, 1998/Albuquerque, NM.

9. Fedorov, A.V., Malmuth, N.D., Rasheed, A., and Hornung, H.G., "Stabilization of Hypersonic Boundary Layers by Porous Coatings," *AIAA J.*, Vol. 39, No. 4, April 2001, pp. 605-610.

10. Rasheed, A., Hornung, H.G., Fedorov, A.V. & Malmuth, N.D. Experiments on passive hypervelocity boundary layer control using an ultrasonically absorptive surface, *AIAA J.* 40, No.3, March 2002, pp. 481-489.

11. Fedorov, A., Shiplyuk, A., Maslov, A., Burov, E., and Malmuth, N., "Stabilization of a Hypersonic Boundary Layer Using an Ultrasonically Absorptive Coating," *Journal of Fluid Mechanics*, Vol. 479, 2003, pp. 99-124.

12. Shalaev, V. Malmuth, N. and Fedorov. A. "Analytical Modeling of Transonic Store Separation from a Cavity," AIAA Paper AIAA 2003-0004, 2003.

13. Malmuth, N., Shalaev, V. and Fedorov, A. "A PC-Oriented Method to Estimate Store Trajectories," presented at Aircraft-Stores Compatibility Symposium XIII, Eglin AFB, February 2003.

14. N. Malmuth, V. Shalaev, "Theoretical Modeling of Slender Bodies Interaction in Supersonic Flows," AIAA Paper AIAA-2004-1127 AIAA 42st Aerospace Sciences Meeting and Exhibit, Reno, Nevada, January 6, 2004.

15. Cole, J. and Malmuth, N., "Wave Drag of Transonic Airplanes," *Proc. Roy. Soc. A*, Vol. 2054, Feb. 2005, pp. 541-560.

16. Malmuth, N. and Fedorov, A., "Thin Layer Model for a Jet in a Hypersonic Cross Flow, AIAA Paper 2005-0893.

17. Malmuth, N., "Theoretical Aerodynamics in Today's Real World," Opportunities and Challenges," Julian D. Cole Lecture, 4th AIAA Theoretical Fluid Dynamics Meeting, June 6-9, Toronto, Canada, AIAA Paper 2005-5059.

18. Malmuth, N., Shalaev, V. and Fedorov, A., "Separation of a Slender Body from a Flat Wall and a Shear Layer," Rockwell Scientific Report SCNM-2004-05.

19. Kozlov, V., Fedorov, A., and Malmuth, N., "Acoustic Properties of Rarified Gases Inside Pores of Simple Geometry," *J. Acoust. Soc. Am.*, Vol. 117 in press.

References

r1 Goodwin, F.K., Dillenius, M.F.E., Nielsen, J.N., "Prediction of six-degree-of-freedom store separation trajectories at speeds up to the critical speed. V.1. Theoretical methods and comparison with experiment". AFFDL-TR-72-83.

r2 Wood, M.E., "Application of Experimental Techniques to Store Release Problems". Proceedings of NEAR Conference on Missile Aerodynamics, Monterey, California, 1988.

r3 Nielsen, J. N. Missile Aerodynamics. McGraw-Hill Company, Inc., New York, 1960.

r4 Bower, W. Kibens, V., Cary, A., Alvi, F., Annaswamy, A. and Malmuth, N., "High-Frequency Active Control for High-Speed Weapon Release (HIFEX) , AIAA 2004-2513. June 2004.

r5 Malmuth, N.D., Fedorov, A.V., Shalaev, V., Cole, J., Khokhlov, A., Hites, M., and Williams, D., "Problems in High Speed Flow Prediction Relevant to Control," AIAA Paper No. 98-2695, 2nd AIAA Theoretical Fluid Dynamics Meeting, June 15-18, 1998, Albuquerque, NM

r6 Malmuth, N., Fedorov, A., Shalaev, V., Cole, J., Hites, M., and Williams, D. "Desktop Aerodynamic Models for Store Separation from Weapons Bay Cavities and Related Vortical Processes," Vortex Flow at High Angle Attack, AVT Symposium, Paper 37, Loen, Norway, May 7-11, 2001

r7 Malmuth, N. D., Shalaev, V. I., Fedorov, A. V. "Combined Asymptotics and Numerical Methods for Store Interactions," Technical Report of Contract CF49620-96-C-0004, AFOSR/NM, October 1998 (available in Defense Technical Information Center, stient.dtic.mil).

r8 Malmuth, N., Hites, M., and Williams , D., "Photographic Investigation of the Dynamics of an Ogive Model near a Cavity at Subsonic Mach Numbers," Final Report. Fluid Dynamics Research Center Illinois Institute of Technology, January 18, 1998.

r9 Shalaev, V.I., Fedorov, A.V., and Malmuth, N.D., "Dynamics of Slender Bodies Separating from Rectangular Cavities," AIAA Paper No. 2001-2996, 31 AIAA Fluid Dynamics Conference and Exhibit, 11-14 June 2001.

r10 Shalaev, V., Fedorov, A. and Malmuth. N., "Dynamics of Slender Bodies Separating from Rectangular Cavities," *AIAA J.* 40 3, pp.517-525, March 2002.

r11 Malmuth, N.D. Shalaev, V. and Fedorov, A, "Theoretical Analysis of Flow Between Two Supersonic Slender Bodies," Rockwell Scientific Company, Report NM03-24892, December 2003.

r12 Malmuth, N.D., Fedorov, A.V., Shalaev, V., Cole, J., and Khokhlov, A., "Problems in High Speed Flow Prediction Relevant to Control," AIAA Paper No. 98-2995, 2nd AIAA Theoretical Fluid Mechanics Meeting, June 15-18, 1998/Albuquerque, NM.

r13 Fedorov, A.V., Malmuth, N.D., Rasheed, A., and Hornung, H.G., "Stabilization of Hypersonic Boundary Layers by Porous Coatings," *AIAA J.*, 39, No. 4, April 2001, pp. 605-610.

r14 Rasheed, A., Hornung, H.G., Fedorov, A.V. & Malmuth, N.D. 2002 Experiments on passive hypervelocity boundary layer control using an ultrasonically absorptive surface, *AIAA J.* 40, No.3, pp. 481-489.

ROCKWELL
SCIENTIFIC

r15 Fedorov, A., Shiplyuk, A., Maslov, A., Burov, E., and Malmuth, N., "Stabilization of a Hypersonic Boundary Layer Using an Ultrasonically Absorptive Coating," *Journal of Fluid Mechanics*, 479, 2003, pp. 99-124.

r16 Delany, M.E., and Bazley, E.N., "Acoustic Properties of Fibrous Absorbent Materials," *Appl. Acoust.*, 3, 105-116 (1970).

r17 Attenborough, K., "On the acoustic slow wave in air-filled granular media," *J. Acoust. Soc. Am.*, 81, 93-102 (1987).

r18 Johnson, D.L., Koplik, J., and Dashen R., "Theory of dynamic permeability and tortuosity in fluid saturated porous media," *J. Fluid Mech.* 176 379-402 (1987).

r19 Allard J.-F., and Champoux Y., "Empirical equations for sound propagation in rigid frame porous materials," *J. Acoust. Soc. Am.* 91 3346-3353 (1992).

r20 Kozlov, V.F., Fedorov, A.V., and Malmuth, N.D., "Acoustic Properties of Rarefied Gases Inside Pores of Simple Geometries," submitted to *J. Acoust. Soc. Am.*, 2004.

r21 Shalaev, V. Malmuth, N. and Fedorov. A. "Analytical Modeling of Transonic Store Separation from a Cavity," AIAA Paper AIAA 2003-0004, 2003.

r22 Malmuth, N., Shalaev, V. and Fedorov, A. "A PC-Oriented Method to Estimate Store Trajectories," presented at Aircraft-Stores Compatibility Symposium XIII, Eglin AFB, February 2003.

r23 N Malmuth, V. Shalaev, "Theoretical Modeling of Slender Bodies Interaction in Supersonic Flows," AIAA Paper AIAA-2004-1127 AIAA 42st Aerospace Sciences Meeting and Exhibit, Reno, Nevada, January 6, 2004.

r24 Morse, P. and Feshbach, H., *Methods of Theoretical Physics*, Vol. II, P. 1380, McGraw Hill, New York, 1953.

r 25 Jaswon And Symm, *Integral Equation Methods in Potential Theory and Elastostatics*, Academic Press, 1977.

r26 Meecham, W.C. , "On the Use of the Kirchoff Approximation for the Solution of Reflection Problems," *J. Rational Mech. Anal.* 5 pp.323-334, 195 6.

r27 Friedlander, F.G. and Keller, J.B., "Asymptotic Expansion of Solution of the Helmholtz Equation," *Commun. Pure appl. Math*, 8, pp. 387-394, 1955.

r28 Bouche, D Molinet, F. and Mittra, R., *Asymptotic Methods in Electromagnetics*, Springer-Verlag, New York, 1997.

r29 Bruno, O.P., "High-Order High-Frequency Solutions of Rough Surface Scattering Problems," *Radio Science* 37 No. 4, pp. 2-1 – 2-13, 2002.

r30 Malmuth, N., Shalaev, V. Fedorov, A. "Theoretical Analysis of Flow Between Two Supersonic Slender Bodies," Rockwell Scientific Company, Report NM03-24892, 2003.

r31 Fomin, V., Maslov, A., Pikalov, V., Korotaeva, T., Shashkin, A., Zvegintsev, "Investigation of Moving Body Interaction with Oblique Shock Wave During Separation Process," Final Report ITAM_Separ_2003.

ROCKWELL
SCIENTIFIC

Appendix-Selected Publications and Reports

Theoretical Aerodynamics in Today's Real World, Opportunities and Challenges

Norman D. Malmuth[*][†]
Rockwell Scientific Company, Thousand Oaks, California, 91360
California Institute of Technology, Pasadena, California 91125

In spite of the CFD revolution, significant challenges still face aerodynamicists in predicting and controlling various classes of flows. These include three-dimensional separation, boundary layer transition, interaction of separation and transition such as on re-entry capsules, multi-element airfoils and wings, UAV low Reynolds number flows and high angle of attack applications. Others include multi-body flows such as those occurring in store and stage separation, "stiff" combustion reacting and unsteady flows as well as plasma aerodynamics and turbulence, to name a few. In many cases, diverse multiple scales are involved and the proper identification and treatment of associated disparate length and time scales is critical in obtaining accurate prediction and effective control. The solution of such multi-scale problems can be a hurdle to effective domain decomposition, even overset, unstructured adaptive gridding and ultimately, solution accuracy. Theoretical insights can help make proper decisions on numerical pre-processing, solution, post-processing and interpretation. Opportunities for a combined theoretical, computational and experimental approach will be discussed. These will be illustrated by examples from the author's experience. As compared to the limited "pen and paper" theoretical methods of the 50's, illustrations will be given of the effectiveness of combined asymptotics, similitude, group invariance, approximate physics-based modeling and numerical methods for conceptual vehicle design, flow control innovation, identification of key parameters, leveraging of computational solutions, reducing the parameter space as well as providing added insight into the basic physical processes. These will be related to tradeoffs between accuracy and response speed in typical aerospace environments.

Nomenclature

AR	=	aspect ratio
A	=	admittance coefficient
α	=	angle of attack, freestream to jet momentum flux or dynamic pressure ratio, wave number
b	=	wing semispan
$B(x, y, z)$	=	body surface
c	=	wing root chord, phase speed
C_{D_w}	=	wave drag coefficient
C_P	=	pressure coefficient
d^*	=	jet exit width
δ	=	characteristic flow deflection parameter, or body thickness ratio
D_w	=	wave drag
D_{w_1}	=	wave drag first approximation
$\varepsilon_i(\delta)$	=	gauge function
$f(x)$	=	wing shape function in constant span plane, jet shape function

---

[*] Program Manager and Senior Scientist, Fluid Mechanics, 1049 Camino Dos Rios/A-3, Fellow AIAA, APS
[†] Visiting Associate, California Institute of Technology, Pasadena, California

ϕ_i = i^{th} approximation to perturbation potential

Φ = velocity potential

$G_1(x)$ = second term in inner expansion for perturbation potential

γ = specific heat ratio

h = jet penetration ratio

H = Hypersonic Similarity Parameter

H_0 = total enthalpy

K = Transonic Similarity Parameter

J = α = freestream to jet momentum flux or dynamic pressure ratio

λ = $(\gamma - 1)/(\gamma + 1)$

L = characteristic length scale

$l_1(x)$ = cumulative lift up to the station x

M_∞ = M = freestream Mach number

$m(x)$ = wing camber function

μ, τ = coordinate stretching factors

μ = leading edge shape exponent

N = Newtonian Similarity Parameter

ρ_∞ = freestream density

p = pressure, pressure disturbance

q = dynamic pressure

r, θ, x = polar coordinates

$\tilde{r}$ = stretched inner radius

$S_1(x)$ = effective source strength

Re_{tr} = transition Reynolds number

t = time

τ = reflection coefficient

T = temperature

θ_j = jet inclination angle

θ_S = local shock angle

U = freestream speed

U, V, ω = horizontal, vertical and pitch displacements

ω = complex disturbance frequency ($\mathrm{Im}\,\omega$ = growth rate)

x, y, z = Cartesian coordinates, (overbars imply dimensional quantities)

X, Y, Z = Cartesian coordinates

$z_{LE}(x)$ = leading edge shape function

Subscripts

ad = adiabatic wall

C = jet cavity

∞ = freestream quantity

j = jet

S = quantity at shock

w = wall

Superscripts

i = iteration counter

Special Symbols

O = large order of magnitude

o = small order of magnitude

I.   Introduction – Technical Landscape

IN the 1970's, a revolution occurred in computing nonlinear transonic and other high-speed flows with computational algorithms and computers. From this pioneering effort, computational fluid dynamics (CFD) has been an asset and workhorse for the aerospace engineer and designer in obtaining aerodynamic characteristics of complex realistic shapes in nonlinear transonic, hypersonic regimes when the flow is essentially attached to the vehicle. Yet, in spite of CFD's power, challenges still exist to predict drag and other quantities such as pitching and hinge moments rapidly enough for the initial phase of aircraft development known as conceptual design. Typical CFD calculations require significant amounts of pre-processing, a large portion of which involves grid generation. Conceptual design optimization also requires the study of hundreds to thousands of airplane geometry and related parametric variations as well as the interplay of physical intuition and compromises based on aerodynamic reasoning and systems impacts. Conflicting demands exist between quick response and pre-processing. Because the latter cannot yet be universally adapted to quickly restructure the grid for rapidly changing large parameter sets and moderate reshaping, CFD's role is emphasized in later phases of preliminary and advanced design more than the conceptual one. Alternatively, it is used to anchor a selected small subset of the conceptual (basepoint) design aerodynamic predictions using other methods.

Recent reviews, assessments and surveys of CFD approaches currently used in industry to estimate drag as well as other forces and moments are typified by Refs. 1 and 2 and other papers in this conference. As a rapid response alternate to CFD, empirical methods have been employed in conceptual design. One such application is the use of algebraic fairings to estimate zero-lift transonic drag rise of fighters or near the fuel consumption pinch point of hypersonic airbreathers, a salient performance obstacle. Such fairings are of limited value because their validity is restricted to the supporting datasets and they do not apply physical ideas in a self-consistent way based on first principles. At the other extreme, large scale Reynolds averaged closure Navier Stokes (RANS) CFD and other closures such as DES, with careful application and study are capable of providing excellent, high-accuracy results for nearly attached flows over a family of shapes for which there are wind tunnel and flight tests to benchmark and even in some cases, calibrate them. However, they provide limited design direction based on gasdynamic ideas for rapid-response, optimal aerodynamic shaping. Mathematical shaping guidance is possible from modern optimization techniques such as adjoint methods, stimulated annealing and control theory but is implicitly restricted to small perturbations around an initial iterate. Such methods currently require high-end workstations, which with the exception of computer-aided design platforms are atypical in today's conceptual design environment but perhaps not in the future. Accordingly, the question of global optimality is a challenge to such techniques. New approaches such as continuation may be a possibility in this connection.

Other nonlinear regimes that pose challenges are high angle attack and hypersonic flows. Although continuing outstanding success occurs in CFD modeling of attached steady flows, three-dimensional separation can be a considerable challenge. Even greater stumbling blocks are environments in which boundary layer transition strongly interacts with separation. Examples are multi-element airfoils such as those occurring on flapped and slatted wings and spoilers. Others are hypersonic elevons, scramjet inlet ramps, weapons bay, flame holder, aero-optic cavities, turbine blades and flows over the lee side of reentry body/capsules, to mention only a few. These are a challenge to common turbulence closures, even those intended to empirically and numerically characterize transition in highly non-parallel separation bubbles such as in trapped vortex applications and wing leading edges at high angle of attack or in low Reynolds number UAV or UCAV high altitude, long endurance applications.

To assess the current state of the art in the prediction and control of transitional separated flows, the author organized a NATO Specialist Meeting in Prague in October 2004 that was sponsored by six NATO nations under the Research and Technology Organization Air Vehicle Technology panel (RTO/AVT).[3] A general theme was that a *unified triad of theory, computation and experiment* is needed to deal with challenges of this class of commonly occurring flows. It was clear from the papers presented that Direct Numerical Simulation (DNS) is now emerging as a fertile opportunity for characterizing the complex physics of transitional separation. Notwithstanding Moore's Law and nanotechnology, it is evident that substantial advancements in the next five to twenty years will be required in computer power and algorithms to make DNS a practical tool for the accurate prediction and control of flow over flight vehicles. Formidable obstacles exist even in DNS such as the need to specify physically meaningful and accurate boundary conditions on the computational boundaries.

Limitations of theory and experiment are well known and were a strong motivation of the CFD revolution. Accordingly, they will not be emphasized here. What is important is that new opportunities exist to have both disciplines couple with numerical modeling to predict and control the first order flow physics. On the experimental

American Institute of Aeronautics and Astronautics

side, although test facilities are rapidly and sadly vanishing, new instrumentation techniques including non-invasive optical diagnostics such as PLIF and PIV are attractive tools to allow us to understand flow physics in many applications.

II. Theoretical Approaches

A major drawback of theoretical tools that stimulated CFD development was the latter's inability to model the flow over complex, realistic, three-dimensional practical airplane shapes as well as other bodies. At the same time, a popular misconception is that theory is strictly limited to linear flows. Counterexamples are its ability to model and give useful information regarding transonic and hypersonic flows. When aligned, asymptotics and similarity/group invariance are powerful tools to treat situations that can be difficult to treat purely computationally.

In this paper, a few examples will be discussed that illustrate application of theory in the CFD age. These provide varying interplays of theory computation and experiment. Because of space restrictions, other potent illustrations of the triad idea will be relegated to the references. It has been the author's continuing belief that the combination of elements of the aforementioned triad can provide substantial insight not possible by any single element of the trio alone. Other benefits of a combined asymptotic[4] and numerical (CAN) approach is the identification of high gradient regions such as boundary layer and shear layer zones that provide insight and even requirements for the gridding and zonal decompositions. Frequently, reduced order equations (besides Euler and other approximations) are identified with the CAN approach that when solved numerically give the first order physics such as nonlinear effects. Similitude arising from theoretical considerations, e.g., Reynolds number, blast wave scaling, often reduces the dimensionality of the independent variable and parameter space to describe the flow field and economize the design of experiments or even make them possible. Some have proposed that theory can facilitate interpolation between computational solutions. For three-dimensional separation such as those determining cavity flows, theory gives guidance on expected flow topologies, e.g., saddle points, higher order nodes and other singularities as well as vortical "lift-off" singularities on bodies at angles of attack. The latter play a decisive role in vortical fractals, bifurcations and interaction of feeding sheets with large-scale vortex dynamics. These determine how lee-side separations on slender bodies evolve. In fact, understanding the role of these singularities in determining the global flow pattern can augment our grasp of three-dimensional separation and help us properly interpret CFD solutions. Another benefit of theory is that it identifies the relevant time and space scales. This is especially valuable in multi-scale problems. Examples are numerically "stiff", singular perturbation reacting flow problems such as in combustion where diverse disparate ranges of chemical rate constants occur.

Identification of the various scales allows us to naturally decompose and downwardly cascade the problem at hand into much simpler "unit" sub problem building blocks that besides helping to understand component physical mechanisms that can be upwardly integrated to give the solution of the original problem. This is the basis of all analysis. Classical examples of this approach are Prandtl's wing and boundary layer theories. Others are transonic and hypersonic small disturbance approximations and Newtonian theory for slender bodies developed by Julian Cole as well as thin shock layer, snowplow and thin shock layer theories by the same author.

An underlying concept in the decomposition idea is the use of parameter limits in which various speed ranges can be accurately approximated in a self–consistent way using asymptotic series or expansions that become increasingly more accurate as the limits are approached. As compared to classical Taylor and other series, these "limit-process expansions" frequently diverge and there is an optimum number of terms to retain to get the best approximation to the flow for a fixed value of the relevant parameter(s). In many cases, the optimum number of terms is one! Examples of limits are freestream Mach number M_∞ tending to zero (such as the Janzen-Rayleigh, Karman-Tsien approximations discussed in Ref. 5), unity or infinity. Freestream Reynolds Re_∞ number tending to zero (Stokes and Oseen flows) and infinity (boundary layer theory), aspect ratio (AR) $\to \infty$ (lifting line theory), characteristic flow deflection (δ) $\to 0$ (small disturbance theory) are other examples. Many of the aforementioned pure Mach number limits do not lead to systematic approximations (capable of successive accuracy refinements.) Ones that do are called "distinguished limits" (DL).[4] Frequently these are obtained by more subtle "double" limits involving two or possibly even more parameters. Common examples are M_∞ fixed as $\delta \to 0$ (Prandtl-Glauert Theory (PGT)[5], linearized theory[5], and acoustics), $K \equiv \left(1 - M_\infty^2\right)/\delta^{2/3} \equiv$ Transonic Similarity Parameter, fixed as $\delta \to 0$, (2-D Transonic Small Disturbance Theory[5-7] (TSDT), $H = 1/\left(M_\infty^2 \delta^2\right) \equiv$ Hypersonic Similarity Parameter fixed as $\delta \to 0$ (Hypersonic Small Disturbance Theory (HSDT)[5,8]), if $\gamma \equiv$ specific heat ratio, $\lambda \equiv (\gamma - 1)/(\gamma + 1)$, $N \equiv H/\lambda \equiv$ Newtonian Similarity Parameter fixed as $\lambda \to 0$, (Newtonian thin body theory[8]), $AR \to 0$, $\delta \to 0$

slender wing or body theory[9]). Actually, Newtonian and slender body theories are respectively within HSDT and PGT respectively.

Once these limits are defined, approximate limit-process series/sequence/asymptotic expansions using "gauge" functions to measure the size of the various terms in the series can be determined. These gauge functions depend on the small or large limiting parameter. As an example, the velocity potential in TSDT for flow over symmetric zero incidence 2-D airfoils, the expansion in the generic form

$$\Phi(\bar{x}, \bar{y}; M_{\infty}, \delta) = Ux + \varepsilon_1(\delta)\phi_1(x, y; K) + \varepsilon_2(\delta)\phi_2(x, y; K) + \cdots$$
$$x = \bar{x}/(\mu(\delta)L), \ y = \bar{y}/(\tau(\delta)L), \ K \text{ fixed as } \delta \to 0 \tag{1}$$

is valid, where, $\bar{x}, \bar{y}$ are coordinates aligned and normal to the freestream velocity U, L = a characteristic length scale such as the airfoil chord, the $\phi_i \ i = 1, 2, 3, \cdots$ are $O(1)$, (i.e., bounded) in the TSDT limit and the semicolon represents parametric rather than functional dependence. Here the $\varepsilon_i(\delta), \mu(\delta), \tau(\delta)$ are the gauge functions. Reference 6 details the procedures to determine these functions. These will not be repeated here. Suffice to say that the coordinate scaling gauge functions $\mu(\delta)$ and $\tau(\delta)$ are determined by a physical feature of the flow. For transonic flows, the wave system gets steeper for $M_{\infty} \to 1$ or equivalently, the TSDT limit in (1). In order to keep the flow structures scaled to these waves in view in the transonic limit (such as the supersonic bubble[*], for slightly subsonic freestreams), the coordinate system is stretched by that steepened scale[4]. The latter is related to the increasing Mach angle (tending to 90° in the TSDT limit). A similar idea holds for boundary layer theory where a stretching is introduced for points in the boundary layer based on the boundary layer thickness, which scales with the Reynolds number Re_{∞}.[10] At the same time, the scaling keeps the relative position of a selected observation point to the flow features invariant in the limit. Returning to TSDT, in contrast to 2-D flows, axisymmetric flows and 3-D flows in TSDT represent "singular" perturbation problems of boundary layer type rather than "regular" perturbation ones. (For example, see Refs. 4 and 10 for more details.)[†] Namely, expansions such as (1) are not uniformly valid over the entire space of the flow considered. Accordingly, local expansions are needed for various zones in singular perturbation approximations to various flows. For slender asymmetric transonic bodies, the axis of symmetry is singular and the asymmetric generalization of (1) (the outer expansion based on the outer limit in (1)) breaks down. Therein, a different (inner expansion) is needed that is based on an inner limit and suitable coordinate rescalings (changes in the gauge functions $\mu(\delta)$ and $\tau(\delta)$ are required). This scale is related to the body transverse dimension rather the Mach wave scale. Both inner and outer expansions are mutually valid in an "overlap" domain. An intermediate expansion and limit is developed and both inner and outer representations are equated in this overlap intermediate region. This "matching" procedure plays a pivotal role in determining the gauge functions and other unknown elements of both inner and outer expansions. The boundary conditions including far field behaviors determine others. Often, additional terms have to be added to initial trial representations to achieve this matching. These are called switchbacks.

There are some "theory" appellations such as Shock Expansion Theory[5] (SET) that are not systematic approximation schemes of the foregoing type. Although these are useful engineering methods they do not belong to the class of distinguished limits or can be embedded in limit process asymptotic expansions based on DL's such as those in the previous paragraph. What is important is that these approaches are not capable of systematic refinement. Frequently, ad hoc approximations are attempted based on parameters that are not really parameters, namely those that are unknown in advance and are based on the solution being sought.

Paco Lagerstrom[10], Saul Kaplun and Julian Cole's[4] limit-process. matched asymptotics methodology uses *deductive* schemes as contrasted to *inductive* schemes. For the former, a given asymptotic framework is set up and a *deterministic* "drill" ("turn the crank" procedure) is executed to obtain the solution. Inductive methods such as local

---

[*] Actually, special features such as the freezing of the flow pattern occur as the Mach number approaches unity and the bubble opens up into a bow and tail shock. This is called the "Stabilization Law". Besides Ref. 6, detailed analyses of the flow field have been carried out. See for example, V. Diesperov, Y. Lifshitz and O. Ryzhov, *Archives of Mechanics*, Vol. 26, No.3, Warsaw 1974, pp. 511-521, and *Symposium Transsonicum*, 1976.
[†] Another interesting problem is the breakdown of transonic small disturbance theory near a blunt nose. For an excellent treatment of the singular perturbation problem and correction of TSDT near the nose see Z. Rusak in *J. Fl. Mech.* Vol. 248, pp.1-26, 1993 and *Europ. J. of Appl. Mech.* Vol. 5, pp. 283-311, 1994.

similarity (widely used in nevertheless valuable engineering predictive schemes based on physical intuition and reasoning) belong to less systematic approximation methods since the bookkeeping in assessing the size of the approximations is frequently not clear. Local similarity for boundary layers subject to pressure gradients exemplifies one such inductive method. Nevertheless, many of these approaches still have our respect as responsible for remarkable innovations. Often, the inductive schemes provide the groundwork for the deductive ones.

Although previous workers such as Lax[11], Magnus and Yoshihara[12] and others had laid much of the groundwork, the "Wright Flyer" of modern nonlinear CFD was the seminal paper by Murman and Cole.[13] in the author's opinion. This is an excellent example of a combination of theory and modern computational methods. Although, the latter have progressed considerably since the SLOR scheme used, Ref. 13 illustrates CAN. Up to this achievement, theoretical solutions of the nonlinear transonic problem were limited to hodograph solutions such as those using hypergeometric functions. Many theoretical studies evolved for mixed unit problems for the Tricomi equation that is hodograph map of the transonic small disturbance Karman Guderley equation.[5-7] Transonic problems that could be solved by intricate analytical "pen and pencil" methods include transonic wedge dividers and jets as well as sonic flows.[5] A non-asymptotic approximate approach was the local linearization and other related integral equation methods by John Spreiter.[14] With the CAN approach of Ref. 13, arbitrarily shaped symmetric thin 2-D airfoils could be computed to obtain a systematic approximation of the first order physics from the asymptotically derived transonic small disturbance Karman-Guderley (KG) equation

$$\left(K - (\gamma+1)\phi_x\right)\phi_{xx} + \phi_{yy} = 0. \tag{2}$$

where ϕ is a perturbation potential related to terms shown in (1). A critical feature was that the realistic *curved* shocks formed by the envelope building process in the recompression part of the supersonic bubble could be *captured* as part of the numerical scheme rather than assumed ones iteratively *fitted* into the solution as in Spreiter's methods. Application of the latter was challenging for all but the simplest shapes. Of course, a continuing issue is capturing these as sharp discontinuities with the proper Rankine-Hugoniot jumps. Much progress has been made in this direction and will not be cited or documented here since it is well known. Still, wave trains that interact with boundary layers and shear layers that occur in inlets, ducts, supersonic weapons bay store separation as well as Edney IV structures in shock interference heating can provide a challenge, even for current RANS methods, especially for non-expert code users.

In addition to inductive and other work preceding Refs. 6 and 13, the derivation of (2) is accomplished by substituting (1) into the Euler equations and retaining like order terms. Asymptotics were used to derive the far field computational boundary conditions for (2) and the formulation provided a close to asymptotically consistent approximation. Of course, application of the far field boundary conditions on a finite boundary still requires some discussion of its effect on solution accuracy. This element has received only limited theoretical analysis in spite of the preference of some to map the point at infinity into a finite boundary as a workaround. The author is not clear how this can be done in general as a practical workable procedure for three dimensions with even single bodies to say nothing of multiple bodies and boundaries. As previously indicated, the question of how to apply asymptotic far fields on finite computational boundaries is of renewed importance in connection with DNS simulations. Current RANS approaches use Riemann conditions and non-reflecting boundaries. This interface between near and far field approximations and its effect on solution accuracy also arises in current sonic boom simulations that *patch* rather than *asymptotically match* ray-traced acoustics far fields with CFD mid and near fields.

To illustrate the continuing power of theoretical methods in the CFD age in relation to the foregoing remarks, a formal matched asymptotic example is given in what follows as well as others that although are not purely formal asymptotic procedures that are approximate physics-based models created from asymptotic ideas. One of the latter provides and engineering method for understanding jets in hypersonic cross flows and another is the basis for a new passive laminar flow control scheme at hypersonic speeds. The first example is provided in considerably greater mathematical detail than the others to show how the CAN approach can be applied. Space limitations relegate details of the analyses for the others to be given in the references.

III. Transonic Wave Drag Due to Lift

A. Background
An important issue in high-speed vehicle performance is transonic wave drag rise. Wing-body blending and area ruling are well-known tools that have been applied to deal with this issue. Before modern computational optimization methods, the widely publicized area ruling philosophy was mostly based on the linear supersonic area

rule specialized to $M_\infty = 1$. This approach usually neglects drag due to lift as well as nonlinear effects. As previously indicated, computational optimization usually addresses small perturbations about some baseline configuration. A more global approach is needed to account for the nonlinearities, and develop a design philosophy from first physical principles. The nonlinear area and Oswatitisch[15] equivalence rules from TSDT and nonlinear slender body theory provide valuable tools to approach these goals. As an illustration of CAN and the concepts, optimum wing planform shaping to minimize transonic wave drag due to lift will be discussed. Full details are given in Ref. 16.

Figure 1 indicates a typical configuration that we have studied in connection with wing planforms that minimize transonic wave drag due to lift. This quantity can significantly affect range and other vehicle performance metrics. We consider the lift-dominated DL in which $A \equiv \alpha/\delta \to \infty$ in the TSDT body limit $\delta \to 0$. To make the approximations more transparent, two-dimensionally cambered, untwisted lifting wings of zero thickness with aspect ratio of order unity were treated in this study. An inner expansion, which starts as Jones' theory, was matched to a nonlinear outer transonic theory as in Cheng, Barnwell and Cramer's excellent earlier work in Refs. 17-19.

To clarify issues, minimize ad hoc assumptions existing in earlier studies, as well as provide a systematic expansion scheme, the aforementioned deductive approach was used with the aid of intermediate limits and matching not documented for this problem in previous literature. A new expression for the dominant approximation of the wave drag due to lift was derived. The main result is that although wave drag due to lift integral has the same form as that due to thickness, the source strength of the equivalent body depends on streamwise derivatives of the lift up to a streamwise station rather than the streamwise derivative of cross sectional area. Some examples of numerical calculations and optimization studies for different configurations are given that provide new insight on how to carry the lift with planform shaping (as one option) so that wave drag can be minimized.
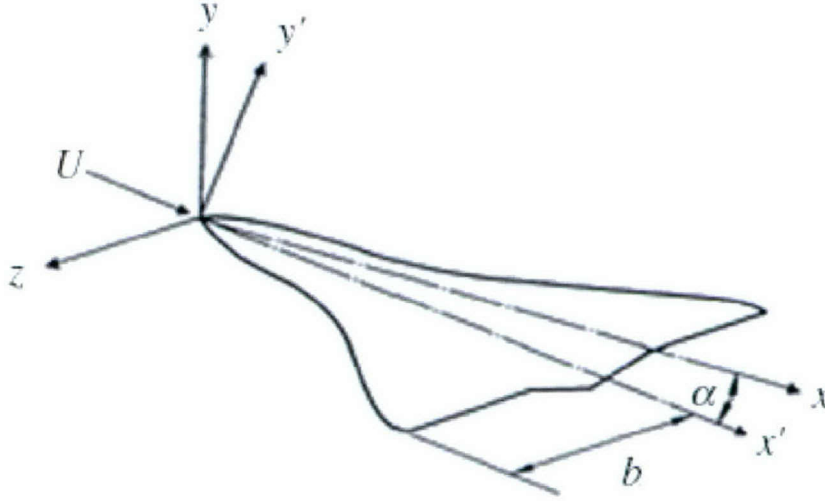
Fig.1 Wing planform for drag rise studies.

B. Theoretical Analysis

As in (1) we allow the velocity potential Φ that satisfies the full potential equation, to be expanded into the asymptotic expansion:

$$\Phi(x,y,z;M_\infty,\alpha) = U\left\{x + \varepsilon_1(\alpha)\phi_1(x,\tilde{y},\tilde{z};K) + \varepsilon_2(\alpha)\phi_2(x,\tilde{y},\tilde{z};K) + \varepsilon_3(\alpha)\phi_3(x,\tilde{y},\tilde{z};K)\cdots\right\} \quad (3a)$$

in the TSDT limit

$$K = \frac{1-M_\infty^2}{\varepsilon_1(\alpha)}, \tilde{y},\tilde{z} \text{ fixed as } \varepsilon_1 \to 0 \quad (3b)$$

where K is the Transonic Small Disturbance parameter and $\varepsilon_1(a) \rightarrow 0$ as the angle of attack $\alpha \rightarrow 0$, (x, y, z) are a nondimensionalized Cartesian frame with respect to c, the body length, and the tilded coordinates are strained in accord with the previous discussion, i.e., $\sqrt{\varepsilon_1}(y, z) \equiv \tilde{y}, \tilde{z}$.

The steady inviscid boundary condition of flow tangency to the surface can be written

$$\nabla \Phi \cdot \nabla B = 0 \tag{4}$$

which holds on $B(x, y, z) = 0$ which defines the surface. We consider an untwisted wing of zero thickness specified by the angle of attack α and the camber function $m(x)^*$. The maximum chord of $c = 1$ and the maximum span $2b$ is $O(1)$. Thus

$$B(x, y, z) = 0 = y - \alpha f(x) + O(\alpha^3) \begin{pmatrix} 0 < x < 1 \\ -z_{LE} < z < z_{LE} \end{pmatrix} \tag{5}$$

where $f(x) = m(x) - x$ and $m(1) = 1$. For a straight trailing edge at $y = 0$, the trailing vortex sheet lies in the plane $y = 0, x > 1$. The planform is specified by $\pm z_{LE}(x)$ where $z_{LE}(1) = b$.

Substituting (3a) into the full potential or Euler equations and carrying out the analysis outlined in the previous discussion, the dominant approximation for the perturbation potential is governed by the axisymmetric form of the Karman-Guderley (KG) transonic small disturbance equation (1). Namely,

$$\left(K - (\gamma + 1)\phi_{1_x}\right)\phi_{1_{xx}} + \phi_{1_{\tilde{r}\tilde{r}}} + \frac{1}{\tilde{r}}\phi_{1_{\tilde{r}}} = 0 . \tag{6}$$

where $\tilde{r}^2 \equiv \tilde{y}^2 + \tilde{z}^2$. This constitutes a deductive proof of the *nonlinear* transonic area rule and in accord with the previous discussion, *is an important reduction from three to two dimensions* of the original problem. It therefore provides a drastic simplification of the gridding pre-processing problem. Matching reveals that the ε_i are subject to the following recursive relations

$$\frac{\varepsilon_2}{\sqrt{\varepsilon_1}} = \alpha$$
$$\varepsilon_3 = \alpha^2 \qquad . \tag{7}$$
$$\varepsilon_3 \log \frac{1}{\sqrt{\varepsilon_1}} = \varepsilon_1$$

In addition to far field boundary conditions, (6) is subject to the singular boundary condition

$$\lim_{\tilde{r} \rightarrow 0} \tilde{r}\phi_{\tilde{r}} = S_1'(x) \tag{8}$$

which is a consequence of the inner expansion that is

$$\phi_1(x, \tilde{r}) = S_1(x)\log \tilde{r} + G_1(x) + O(\tilde{r}^2 \log^2 \tilde{r}) \quad \text{as } \tilde{r} \rightarrow 0 \tag{9}$$

---

* A body is added to the wing in the parametric studies to be discussed later.

Part of this result is from the solution of the cross flow harmonic inner problem that drives the whole matching procedure. In contrast to a body of revolution in which the source strength $S_1(x)$ is proportional to the x rate of change of cross sectional area, the source strength depends on the streamwise lift distribution $l_1(x)$. Namely,

$$S_1(x) = \frac{(\gamma+1)}{2} \frac{l_1' l_1''}{(2\pi)^2} = \frac{(\gamma+1)}{8} \left(z_{LE}^2(x)\right)' \left(z_{LE}^2(x)\right)'', \tag{10}$$

where

$$l_1(x) = -\pi f'(x) z_{LE}^2(x). \tag{11}$$

The main result is the wave drag due to lift is given by

$$\tilde{D}_{w_1} = -2\pi \int_0^1 S_1(x) \, G_1'(x) \, dx = 2\pi \int_0^1 S_1'(x) \, G_1(x) \, dx \tag{12}$$

where $G_1(x)$ and $S_1(x)$ are given by (9) and (10) respectively.

C. Computational Approach and Results

The solution of the TSDT boundary value problem for the axisymmetric KG equation subject to the far field boundary conditions and the singular axis condition, (8) would have been impossible to carry out in the pre-CFD age. Empowered by this reduced formulation and even dated SLOR numerics, the TSD boundary value problem is solved by lagging $G_1(x)$ in an iterative numerical procedure. It is updated from (9) after each SLOR sweep for the solution $\phi_1(x, \tilde{r})$ on a small cylinder $\tilde{r} = \sigma$, $\sigma \ll 1$. Namely,

$$G_1^{i+1}(x) = \phi_1^i(x) - S_1(x) \log \tilde{r} \tag{13}$$

where i signifies the old global iterate over the computational domain, $i+1$ the new one and $\phi_1(x) \equiv \phi_1(x, \sigma)$. Converged results with even the old SLOR method could be obtained on a typical Windows modern PC in less than a minute. Results from the executing code NLWAVE are plotted as C_{Dw} vs. M_∞ for two different angles of attack in Fig. 2. Substantial drag due to lift is evident. The planform shape and the distribution of $l_1(x)$ which is typical appears in Fig. 3.
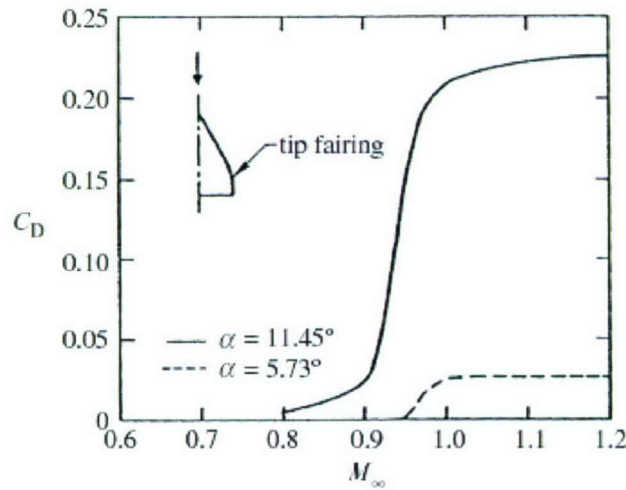
Fig. 2 Transonic wave drag rise due to lift for typical planform

Another set of calculations incorporates a parabolic body of revolution (thickness ratio 0.057) and adds the source strength of this body to $S_1(x)$. A series of planforms with semispan $z_{LE}(x)$ given by

$$z_{LE}(x) = \frac{x\left(\mu - x^{\mu-1}\right)}{\mu - 1} \tag{13}$$

and shown in Fig. 4 was considered for various μ, $M_\infty = .995$, $\alpha = 0.2$ rad. The idea is to optimize the L/D figure of merit C_{Dw}/AR, (AR =aspect ratio) by a choice of planform. Here,

$$C_{Dw} = \frac{D_w}{\dfrac{\rho_\infty U^2}{2}S}, \quad AR = \frac{b^2}{S}$$
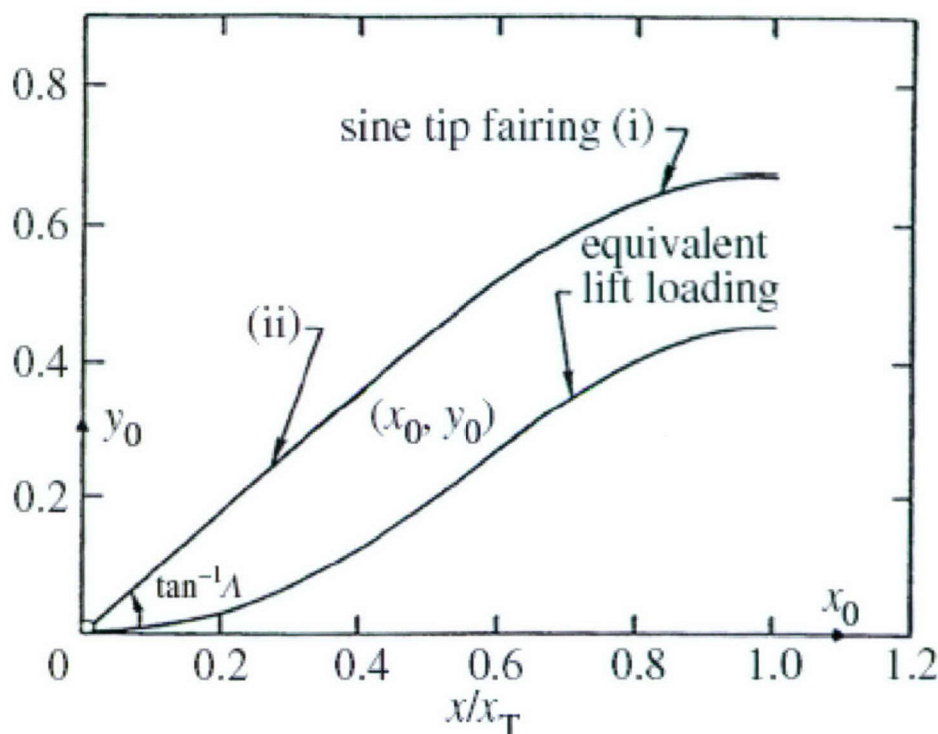
Fig. 3. Lift loading of model wing with sine tip fairing

(i) $y - y_0 = (2\Lambda(x - x_0)/\pi)\sin(\pi(x - x_0)/2(x_T - x_0))$;(ii) $y_0/x_0 = \Lambda$

where S is the planform area and b is the semispan.

A minimum drag occurs for $\mu = 2.5$. The planform shape and curve of C_{Dw} vs. μ appears in Fig. 5. Also shown in Figs. (6a - 6c) for $\mu = 1.2, 2.0, 10.0$ are isobars which make evident the shock wave which occurs. As a qualitative substantiation of the minimum, the isobars and shock envelope forming process appear more intense for (6a) and (6c) compared to (6b). The wave drag for small μ is large because of the small sweep and for large μ because of rapid changes of $l_1(x)$ near the wing tip. These studies show the relative effectiveness of various planforms and the utility of CAN to select them in a computationally non-intense, rapid-response, desktop PC environment. This approach can be readily extended to study more realistic wing-bodies as well as twist and thickness effects.
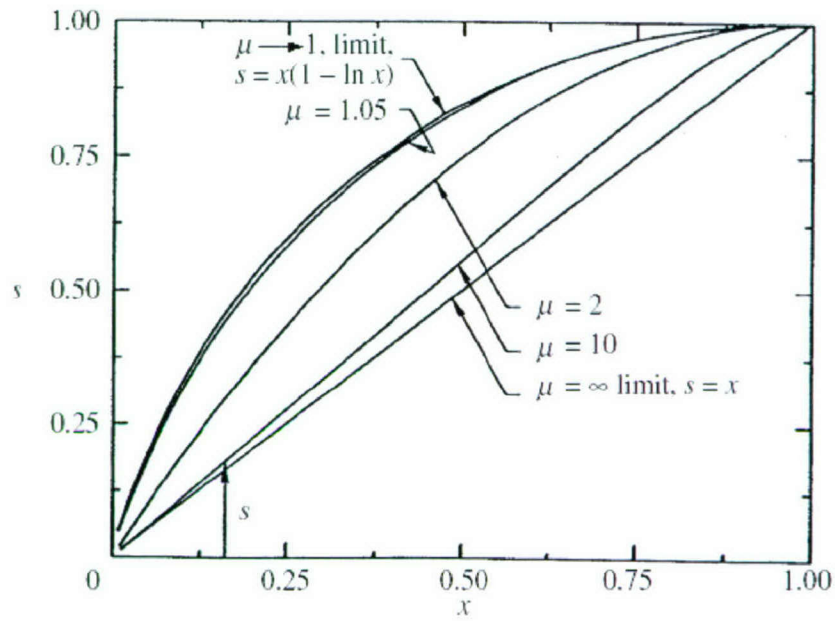
Fig. 4. μ family of wing bodies in which semi-span equals $x(\mu - x^{\mu-1}/(\mu-1))$.
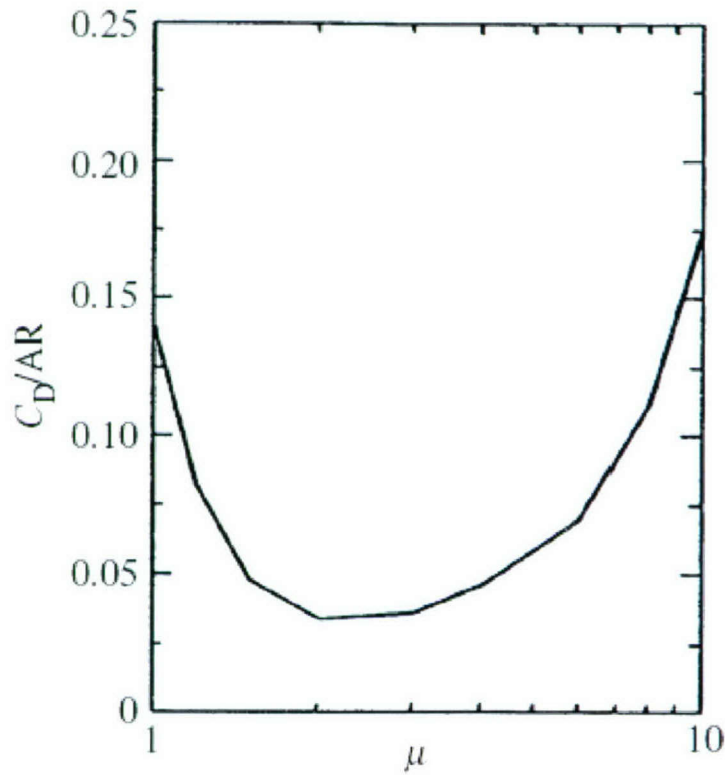
Fig. 5. Wave drag/aspect ratio figure of merit for μ wing-body family, M_∞ =0.9951, α =.2 rad
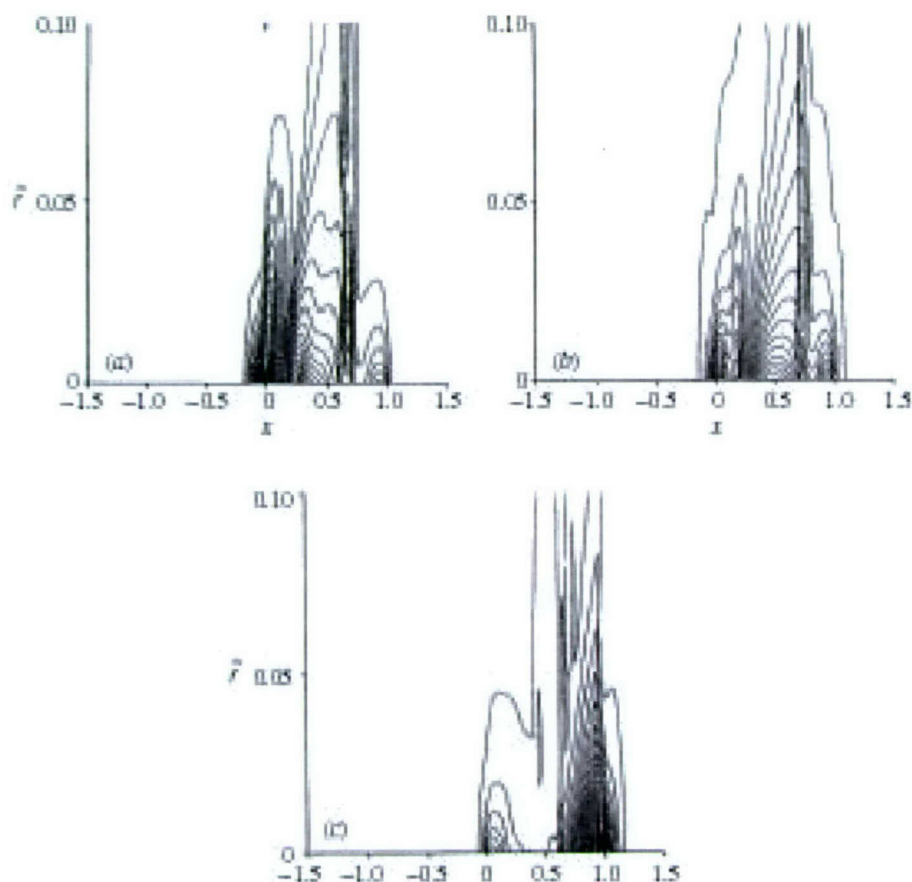
Fig. 6. Isomachs of (a) $\mu = 1.2$ (b) $\mu = 2.0$ and $\mu = 10.0$ wing-body $M_\infty = 0.995$, $\alpha = 0.2$ rad, $\Delta M = 0.1$.

IV. Multi-body Problems

A. Background

A challenging area for modern computational methods, theory and experiment is the treatment of multi-body problems such as store and stage separation. Typical applications are illustrated in Fig. 7, which shows transonic bomb release from the B-1, weapons bay arrangements on the F-22 and stage arrangements on an early Boeing Space Launch Initiative vehicle concept. For the latter there is an important design trade between separation rocket motor weight and safety that is impacted by accurate prediction of stage separation aerodynamics.

(a)   (b)   (c)
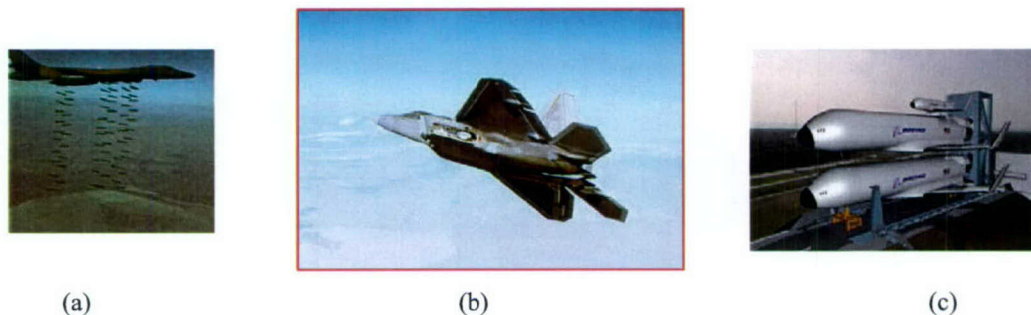
Fig. 7. Typical multi-body problems. (a) B-1 internal transonic store carriage and release, (b) F-22 supersonic internal bay configuration, (c) Hypersonic Space Launch Initiative (SLI) stages.

Impressive progress is being made with new supercomputers and algorithms, particularly for biological flows and other applications. Major centers such as AEDC, NASA, AFSEO and the PET project are performing research to apply evolving techniques to store and stage separation problems. Experimentally, the CTS approach in which the fluid dynamics is used as an input to a six-degree of freedom dynamics code to advance the body position in a two sting wind tunnel support system has been extensively applied to treat a class of motions where pseudo-steady assumptions hold and sting interference can be accurately estimated. There are others where the validity of the pseudo-steady assumptions needs to be carefully investigated. The major issue is the possibility of a difference between the time it takes for the flow to fully evolve or relax and the body motion time scale. Vortex and vorticity diffusion and convective shocks are good examples in which flow transients are disparate relative to the body motion time scales such as Froude and ejection times. Alternates to this approach are the grid method and the free drop and ejection methods with sacrificial test articles. Each of these test methods has its advantages and disadvantages. For the free drop and ejection method, a problem is the ability to relate the subscale test results to the full scale, because of the lack of affordable, non-toxic (not gold, lead or uranium!) high-density materials for correct scaling of the sacrificial subscale models. Another problem is not destroying the wind tunnel components or the cars or people in the parking lot outside of a blow-down facility! Some of this is achieved by the use of sometimes "conservative" "light scaling" rather than realistic heavy scaling in connection with the choice of Froude of convective times in building the scaling parameters and the use of rigid sacrificial but not structurally tough models. An advantage is that it avoids sting interference and gives insight into unsteady effects, especially for internal weapons bay separations. In the author's opinion, a combination of all three approaches is needed as a crosscheck of any one of them. This is similar to the situation with the analytical methods.

In spite of the considerable CFD and experimental progress, major gaps exist in our ability to simulate a variety of situations. Although the trajectory of a moving body (e.g. submarine) in a fluid has received much classical attention in incompressible perfect fluid *hydrodynamics* (see for example Ref. 20 using apparent mass, flow kinetic energy, Hamilton's theorem and generalized coordinates) with emphasis on coupling of the dynamics and aerodynamics, our understanding of the basic coupling physics in compressible *gasdynamics*, especially involving shocks, is limited, in spite of current CFD modeling capabilities.

The store separation problem has important practical applications and its different aspects were investigated extensively using experimental and computational methods such as in Refs. 21-31. Substantial advances are being made with overset, solution-adaptive, unstructured and moving grid approaches as indicated in these citations. Most of the studies have been concerned with *external* separation at subsonic or supersonic speeds. Relatively less attention has been given to *internal* separation from weapons bay cavities, especially at transonic speeds and the challenging supersonic and hypersonic speed ranges. A major focus at high speed is acoustic properties of the cavity. High amplitude noise arises due to feedback loops associated with stagnation of the shear layer (bounding the cavity and external flow) on the downstream cavity bulkhead. These excite structural vibrations that can cause catastrophic flight interruption from damage to the airplane. It can also destroy weapon components, including delicate guidance electronics, affecting targeting and pilot safety. This problem is very complicated due to the large number of parameters governing the flow structure and a broad variety of physical phenomena involved in the separation process. Much fundamental research has been done on empty cavities with a major focus on understanding and controlling coupling of the shear layer with the acoustic processes. Cavities filled with bodies have received only limited basic study. Computationally intense modeling RANS, DES and even DNS to understand the acoustic excitation and the basic physics is exemplified by Refs. 32-34, among many others. A notable worthwhile exception to the empty cavity experimental emphasis is Ref. 35, which necessarily uses an invasive sting in the cavity to study the cavity shear layer interaction in the presence of a body. Nevertheless, the results are quite illuminating, particularly when the body crosses the shear layer.

Besides the flow-induced noise and vibration problem, the cavity shear layer is an obstacle to safe separation, particularly at supersonic speeds. Our objectives are to identify first-order physical effects, simplify the key aerodynamic problems, and develop fast and reliable models for predicting store trajectories. These are intended to favorably interact with large-scale computational approaches and provide additional tools for conceptual design. An important perspective that the singular perturbation method brings to the problem is to deal with its multi-scale aspects. Such a viewpoint needs to be exploited in the large-scale numerics as well. An obvious decomposition is to regard the cavity flow as a near field coupled to the global airplane midfield. Since they are over a much shorter length scale, gradients near the cavity are expected to be large compared to those over the complete airplane. In fact, the latter can be regarded as a passive scalar. We have formalized this idea with inner and outer expansions and regarded the global airplane flow field as a weak stratification of the cavity flow that is on a much longer length scale. Both in CFD and theory, the iteration process can be envisioned in which the flow over the airplane without

the cavity provides an initial iterate of boundary conditions for the local cavity inner flow field on some computational boundary. The cavity flow is solved and then used to update the airplane flow field. The iteration is continued until convergence. In accord with this idea and the same motivations of all the empty cavity research, we focus on this inner problem in what follows. Understanding it is critical to studies that we are conducting with Boeing on simultaneously suppressing cavity noise and achieving safe separation.[36]

Another idea that needs exploitation is the fact that with all the uncertainties prediction of the translational trajectories can be reasonably accurate in validations with experiment. A conjecture that would support this outcome is that for "heavy" bodies in which the aerodynamic forces are small compared to inertial or ejection ones, the flow is controlled by the latter. This is another opportunity for large-scale computational modeling in which an iteration process could be developed in which the trajectory is obtained with a sequence of iterations starting with vacuum dynamics and introducing subsequent small aerodynamic corrections in which even coarse grid CFD details of the near field cavity flow are emphasized. Asymptotic methods may be able to provide specific elements of such an iteration process or sequence although the execution will be dominantly computational. Here, the emphasis would not be high fidelity of the fluid dynamics, but accurate prediction of the trajectory, since the fluid dynamics is only a small part of the answer for heavy bodies. "Heaviness" in this context needs to be specified in terms of the non-dimensional ballistic parameters that compare aerodynamic forces and moments with analogous inertial quantities.
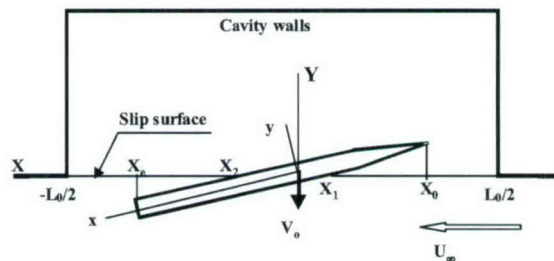
Fig. 8. Inner cavity problem.

B. Summary of Theoretical Approach

Figure 8 represents the framework we used to study the near field cavity problem. We generalized many of the ideas in the first example discussed to treat this flow. Shown in the figure is a slender body escaping from the cavity. This problem itself can be decomposed into another singular perturbation problem. Near the slender body, it is still dominated by its cross flow. Away from the body, it looks like a line source except that the latter interacts with the walls. We neglect the finite span effects and focus on the interaction of the body with the shear layer. Since the near field is cross flow dominated, various cross flow problems occur along the body. Essentially there are three cases 1) the body is on the cavity side of the shear layer, 2) it is crossing the shear layer, and 3) it is above it. Figure 9 outlines the formulation of the problem. If (X,Y,Z) denote the normalized Cartesian wind axes, the problem obeys Laplace equation (1) in the crossflow plane (Y,Z) (1). Here, the velocity potential is denoted by $\Phi(X,Y,Z,t)$. Boundary conditions are specified on the slip surface or shear layer, $Y_f = F(X,Z,t)$. Since the flow is unsteady in the crossflow plane, the unsteady from of the Bernoulli equation (2) is used for the pressure p This is needed because the boundary conditions are time-dependent due the body motion and in spite of time not appearing explicitly in the cross flow equation of motion (1). Therefore, time is a *parameter* rather than an *independent variable* in the solution of the cross flow Laplace equation of motion. This situation is related to an assumed limit involving an unsteadiness parameter related to body motion speed in units of the flow convection speed that is characterized by a Strouhal number. In addition, the slip surface or vortex sheet boundary conditions, the tangency boundary conditions (4) and (5) respectively, on the body and cavity walls apply. Typical boundary value problems associated with these conditions are shown in Fig. 10. for Cases 2) and 3). Note that in the near field (inner flow), streamwise stations are independent of each other. In addition, it is possible to have different cross sections of the body that represent Cases 1)-3).

The upper right hand panel of Fig. 9 shows the coupled set of aerodynamic and three-degree of freedom (3-DOF) equations. Here, (U,V,ω) respectively represent the horizontal, vertical and pitch displacements; (D,L,M) respectively represent drag, lift and pitching moment. Initial conditions for the displacements are shown.

Coupling of the aerodynamics with the dynamics is evident in these equations since the D, L, ω are computed from the pressure field as shown in the panel. For transonic freestreams, the drag D has a wave drag portion in addition to friction. The former is obtained by solving boundary value problem for the far field axisymmetric KG equation shown in the bottom left hand panel in Fig. 9. This equation was discussed in the previous example. As in the previous example, the singular boundary condition involving the source strength $S(x) = \dfrac{\partial A_{eff}}{\partial x}$, where $A_{eff}(x)$ is the effective cross sectional area and x is an alternate notation for X. $A_{eff}(x)$ is determined from the outer expansion for solutions of the cross flow boundary value problems shown in Fig. 10. Determining this quantity is more involved than in the previous example because of the more complicated near field boundary value problem. These solutions were worked out as generalizations of the more simple flow over a log discussed in Ref. 20. It involves the use of conformal mapping, elliptic functions and singular integral equations in the complex plane for Riemann-Hilbert problems. The main point is that the crossing of the shear layer physics is systematically included in the problem and it influences the shock dynamics in the far field. Details of the analyses for subsonic, transonic and supersonic freestreams are given in Refs. 37-39.

C. Physical Mechanisms Relative to the Noise Reduction and Safe Separation of Supersonic Stores from Weapons Bay Cavities

For supersonic store separation, the formation of a bow shock over the nose of the body as it crosses the supersonic part of the shear layer is responsible for the loadings shown in Ref. 35. It can be a major reason why supersonic store ejection is so difficult, as compared to subsonic ejections. The nose loading creates a nose-toward-cavity pitching moment attracting the body to the cavity. This moment is unstable for the nose; namely, a pitch towards the cavity increases that tendency since the compression on the upper part of the body (that first crossed the shear layer) will be increased and that on the lower side (that subsequently crosses the shear layer) will be decreased.

As indicated in Ref. 36, jets upstream of supersonic weapons cavities helped safe separation in tests at the Boeing Polysonic Wind Tunnel. One mechanism that enters into this method of flow control is that a jet upstream of the cavity lip creates its own shear layer that air-curtain-wise shields/screens the high velocity shear layer interface from the supersonic freestream that was there before the jet was. It produces an upwash-induced, increased, angle-of-attack, favorable flow turning induced normal force and moment away from the cavity on the weapon like that from the "ski slope" turning vane or spoiler that the author developed with Boeing personnel that counteracts the download from the shock that is present without the jet. It even might create a subsonic flow behind itself that could avoid the shock in the supersonic part of the shear layer or above it. Another possible bonus, besides the upwash that produces a normal force away from the cavity on the weapon is the "fire hose" effect that gives a pressure footprint on the forward part of the weapon further forcing it away from the cavity. To determine the relative effectiveness of the fire hose effect, loads on the store from shock pressures need to be compared to loads from those from the jet momentum flux. This comparison could give appropriate non-dimensional scaling parameters to size the jets and design their pneumatic supply systems. Anecdotal evidence is that although this mechanism would act for stores near the rear of the cavity, safe separation is usually obtained. It is conjectured that this might be explained by the flow toward the fins into the cavity produced by the cavity eddy circulation for deep cavities, e.g. 5:1. This load could favorably compete with the unfavorable shock loads.

An additional mechanism of course comes from the jet bow shocks that can compound the favorable flow turning upwash. The jet shear layer in some sense replaces the cavity shear layer, (there will still be a small vestigial remnant of this layer as can be seen by the PLIF and schlierens of Hanson and Ben Yakar conducted at Stanford and described in more detail later in this paper). Euler calculations with adaptive mesh refinement run by Hans Hornung of Caltech under collaboration with the author using James Quirk's Amrita software system described in Ref. 40 also show this behavior.

The new jet shear layer is an interface with the freestream and its loft will avoid the noise spectra feedback loop (and its effects on the weapon) produced by stagnation of the uncontrolled shear layer on the downstream cavity bulkhead. This is because the new jet shear layer is elevated enough to reattach on the downstream horizontal surface behind and not on the cavity downstream bulkhead. This is critical in avoiding the associated feedback loop and weapon flow induced structural vibrations from shear layer cavity downstream bulkhead stagnation. This is offset by a static stability contribution of any tail fins. In addition, the lumped parameters shown in the right upper panel of Fig. 9 collapse the test matrix and are helpful for implementing control for safe internal bay separation.

The loft of the shear layers under jet control is important in controlling the broadband and discrete fluctuations that act on the weapon when the doors open or even without doors during release. Even though the impulse time is

15

American Institute of Aeronautics and Astronautics

short, fatigue can occur on an s-n curve because of the amplitude of these pressure load cycles. These are transmitted to the weapon as pressure oscillations. They are probably on too short a time scale to influence the trajectory in the later stages of launch but certainly affect the electronics, fins, arming mechanisms etc. They may also affect the initial launch conditions depending on the time of release and what is going on in the cavity at that instant.

D. Parametric Studies

Figure 11 exemplifies some parametric studies that we have conducted with the theory just outlined. In these figures and to avoid clutter and illuminate the trajectory details in the motion sequences, only the centerline of the body is shown, in contrast to its actual cone-cylinder shape. The top two panels show incredibly marked difference between vertical initial translation V_0 imparted to the body for nearly Mach 1 freestream conditions. An approximately 30% difference in velocities makes the difference between safe escape and re-contact in this example with a nose toward cavity initial pitch angle $\alpha_0 = 6°$. Even for transonic as contrast to supersonic ejection the nose-toward cavity initial pitch provides a greater pressure on the lower than upper side of the nose for a conical forebody with the greater compressive flow turning tending to push the store toward the cavity. For $V_0 = 20$ fps, the pitch induced lift is not sufficiently countered by the plunge imparted to the body. Whereas for $V_0 = 30$ fps there is enough plunge momentum to allow it to escape the normal suction force toward the cavity due to the fluid mechanics. As previously mentioned, other factors that enter this equation are the phase lag between pitch and plunge as well as static stability afforded by fins.

Fluid dynamics problem

- **Inner asymptotic region**

  Laplace equation for cross-flow potential $\Phi_{ZZ} + \Phi_{YY} = 0$ (1)

  Bernoulli equation $\quad p = -\left\{ \Phi_t + u + \frac{1}{2}\left[w^2 + v^2\right] \right\}$ (2)

  B.c. on slip surface $Y_f = F(X, Z, t)$

  $v_f = \dfrac{\partial \Phi}{\partial Y} = \varepsilon F_t + F_X + w_f F_Z \quad v_f^+ = \dfrac{\partial \Phi^+}{\partial Y} = F_t + w_f^+ F_Z$

  $\Phi_t + u + \dfrac{1}{2}\left(w^2 + v^2\right) = \Phi_t^+ + \dfrac{1}{2}\left(w^{+2} + v^{+2}\right)$ (3)

  B.c. on body surface $r = a(x)$

  $v_n = \dfrac{\partial \Phi}{\partial r} = a_X + V_e \sin\theta, \quad V_e = V - \omega X - \alpha$

  $v_n^+ = \dfrac{\partial \Phi^+}{\partial r} = V_e^+ \sin\theta, \quad V_e^+ = V - \omega X$ (4)

  B.c. on cavity walls: $v_{nw} = \dfrac{\partial \Phi_w^+}{\partial n_w} = 0$ (5)

- **Outer asymptotic region**

  Karman-Guderley equation: $\left[K - (\gamma+1)\varphi_X\right]\varphi_{XX} + \dfrac{1}{R}(R\varphi_R)_R = 0$

  Linear Cauchy equation: $p = -\varphi_X$

  Matched condition: $\lim_{R \to 0}(R\varphi_R) = \partial A_{eff}/\partial X$

3-DOF body dynamics problem

$\dfrac{dV}{dt} = c_l L - c_g, \quad L = -\displaystyle\int_{X_0}^{X_e}\int_0^{2\pi} P(x,\theta,t)a(x)\sin\theta\,dxd\theta$

$\dfrac{d\omega}{dt} = c_m M, \quad M = -\displaystyle\int_{X_0}^{X_e}\int_0^{2\pi} P(x,\theta,t)xa(x)\sin\theta\,dxd\theta$

$\dfrac{dU}{dt} = c_l D(t), \quad D = D_{wave} + D_{base} + D_f + D_{cf}$

$V(0) = V_0, \quad \omega(0) = \omega_0, \quad U(0) = U_0$

$c_g = \dfrac{gl_0}{\delta U_\infty^2}, \quad c_l = \dfrac{\rho_0 l_0^3 \delta^2}{m}, \quad c_m = \dfrac{\rho_0 l_0^5 \delta^2}{I}, \quad P = \begin{cases} p^+, & Y_b > F \\ p, & Y_b < F \end{cases}$

- **Fluid dynamics is governed by nonlinear integral-differential problem with free boundary**

- **Body dynamics problem is governed by nonlinear ODE**

- **Fluid dynamics and body dynamics are strongly coupled**

Fig. 9. Coupled dynamics and aerodynamics problem of store separation from cavity.
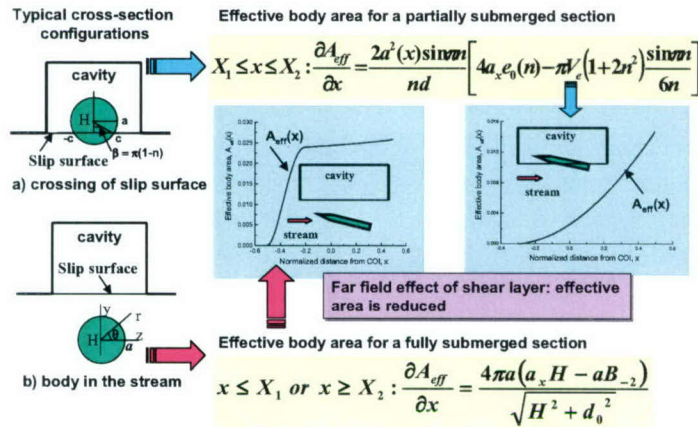
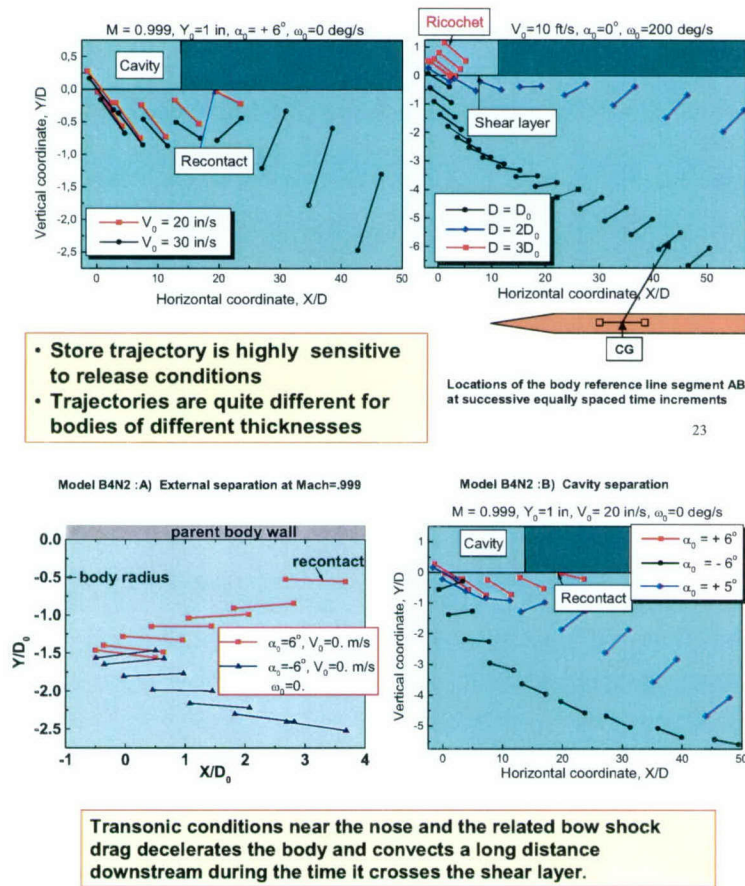Fig. 10 Crossflow boundary value problems for body in relation to shear layer.

Fig. 11. Parametric studies of store escape from a cavity to a transonic flow.

Note that despite the missing fins, the body in this example was statically stable because it had a CG forward of the aerodynamic center. This is because the example parameters coincided with a body tested by at Hites and Williams et al[41] at the Illinois of Technology low speed tunnel for a low speed verification of our theory in Ref. 37. The forward CG position was because the nose of that body was solid and its cylindrical afterbody was hollow. Other factors that need to be further studied in this interpretation is dynamic stability and the coupling of plunge induced unsteady flow field as well as the influence of the changing boundary conditions as the body is quickly

projected downstream because of the significant transonic drag, which is augmented by a base drag component. In this streamwise motion, the boundary conditions change from those from the slip surface to the solid wall. The right upper panel shows a dramatic influence of body thickness ratio in which the thicker bodies tend to re-contact the wall for the same release conditions as the thinner ones. This is most likely due to greater nose loading due to increased slope of the forebody with increasing thickness ratio. Evidence however exists that the effect of this change may damp out quite quickly above the parent body.

The bottom two panels show the effect of an initial angle of attack on store plunge and pitch trajectory. In the left upper panel for "external" ejection without a cavity, with pitch into the surface (positive α_0 represents pitch to the parent body of parasite store body.) It is evident that $\alpha_0 > 0$ with zero initial pitch velocity ω_0 leads to re-contact for external carriage. In contrast, $\alpha_0 < 0$ gives safe escape. The trends shown for external release carry over the thicker body in the presence of the cavity shown in the bottom left of Fig. 11.

V. Jets in Hypersonic Cross Flows

A. Background

Performance of hypersonic air breathing propulsion systems strongly depends on efficiencies of fuel injection and mixing in the supersonic combustion chamber. Mixing and flame stabilization may be achieved in recirculation regions and coherent structures containing unmixed fuel and air. Transverse injection, which is commonly used in the design of supersonic combustors, involves these mechanisms. This example that is discussed in more detail in Ref. 42 shows how some of the ideas of asymptotics can be used to create a practical engineering method to estimate jet penetration in hypersonic crossflows.
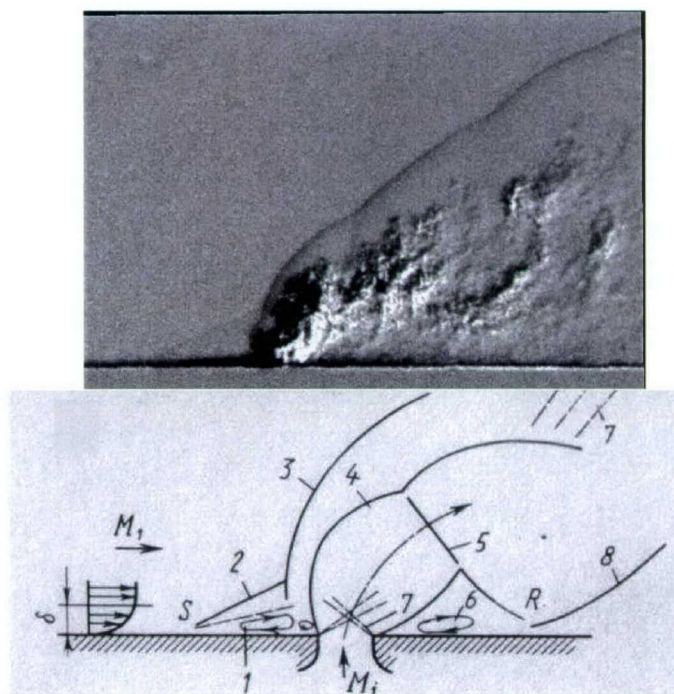
Fig. 12. Upper panel: Schlieren image of the normal under-expanded hydrogen injection into supersonic cross-flow from Ref. 43; Lower panel: schematic of the flow pattern (from Ref. 44): 1 – separation bubble upstream the jet exit; 2 – shock due to upstream separation at the point S; 3 – bow shock induced by the jet; 5 – Mach disc; 6 – separation bubble downstream from the slot; 7 – expansion waves; 8 – shock induced by the jet reattachment R; M_1 - freestream Mach number; M_j - Mach number of the out-flowing jet.

These ideas and analysis are extremely relevant to store separation from weapons bay cavities discussed in the previous section and by use controlling it by blowing upstream of the cavity as discussed in Ref. 36. They provide

actual quantitative measures for jet penetration and scaling useful for the design of jet control of weapons bay cavities and the design of relevant experiments. Although the application to store separation is in the low supersonic regime, the elasticity of Newtonian theory to lower Mach numbers than hypersonic provides a useful tool for the assessment of the jet effects on the cavity flow, specifically those related to jet penetration.

As shown in Fig. 12, the flow pattern induced by under-expanded transverse injection is rather complicated as further indicated in Ref. 45. Referring again to the lower panel of Fig. 12, the fuel jet displaces the supersonic crossflow as if a bluff body was inserted into the flow. A bow shock (3) upstream of the injector exit is formed causing the upstream boundary layer to separate at the point S. In the separation region (1), the boundary layer and jet mix subsonically. The jet turns to the freestream direction and reattaches to the wall at the point R forming another recirculation region (6) downstream from the jet exit. This process is accompanied by formation of shocks (2, 8) and expansion waves (7). Nevertheless, in the near-field region, the time-averaged jet-penetration profile mimics the bow shock shape and looks smooth. In the far-field region (downstream from the point A), the jet thickness continues to grow. However, this growth, which is due to the turbulent mixing rather than the pressure gradient, is much slower than that in the near-field region.

The near-field mixing is driven by large-scale jet-shear layer vortices generated by the jet-freestream interaction as shown in Refs. 43 and 45. These vortices are formed along the jet-freestream interface starting near the injector exit. They periodically entrain large quantities of free-stream air and draw them into the jet shear layer. In the far field, the eddies travel with velocities close to the freestream velocity. These coherent structures, where the fuel and air are mixed by slow molecular diffusion, also travel at high speeds. Consequently the combustion process is mixing (vorticity diffusion)-controlled.

Experiments discussed in Refs. 43, 45-49 show that ignition is likely to occur in the recirculation region ahead of the jet exit. The flame is convected downstream along with the large eddies and observed near the outer edge of the jet plume. To estimate flame-holding capability of the transverse injection and stagnation pressure losses due to the jet-induced shock, it is necessary to predict the bow-shock shape and the average penetration profile of the jet plume. This could be done empirically using correlations of experimental data.[44] The average penetration profile is commonly approximated by a power law fit as in Refs. 43,44,46,48 that couples the jet outer edge with the downstream distance from the jet exit. However, this correlation varies widely between experimental studies.

Although CFD approaches such as RANS and DES are nominally capable of handling jets in a crossflow, depending on turbulence modeling and use of implicit algorithms, they are time-consuming in engineering practice. Quicker response, analytical models are required to shed light on the physics of jet penetration and interpolate between large-scale CFD solutions. These are also useful for conceptual and preliminary design phases associated with turn-around parametric studies. This motivated us to analyze the transverse injection into supersonic cross flow using asymptotics-related methods. We believe that such a model can shed light on previous experiments and recent large simulations. An excellent example of the latter is Ref. 50.

Here, the cross-flow jet problem is formulated for a hypersonic freestream in the Newtonian limit[8] of the Euler equations in natural streamline coordinates[51]. Although, some sort of blast wave theory[52-54] seems appropriate associated with hypersonic blunt bodies, basic ideas of the thin layer Newtonian theory[8] are also appropriate. It is shown that a shape of the thin shock-jet filament is governed by an ordinary differential equation, which is solved analytically here. In addition, the analytical solution is compared with the experiments in Refs. 43, 45 and 49 on combustion and mixing of the transverse hydrogen jet injected into supersonic cross flows.

B. Basic Formulation

Consider normal injection of a fuel jet into a supersonic cross-flow shown in Fig. 12. The jet displaces the supersonic flow, qualitatively as if a blunt body was inserted into the flow. In this situation, the characteristic flow deflection slope is $\delta \equiv U_j^* / U_\infty^* = O(1)$, where U_j^* is speed at the jet exit, U_∞^* is the freestream speed, and asterisks denote dimensional quantities. Assuming that the freestream Mach number $M \to \infty$ and the specific heat ratio $\gamma \to 1$, consider the Newtonian limit[8] of the Euler equations: $H \equiv (M\delta)^{-2} \to 0$ and $\lambda \equiv (\gamma - 1)/(\gamma + 1) \to 0$ so that $N = H / \lambda$ is fixed. Neglecting viscous shear-layer processes, we assume that U_j is constant along the jet, and the jet thickness approximately equals to the jet exit width d^*. With these assumptions, the flow pattern is schematically shown in Fig. 13. The bow shock and the outer edge of the fuel jet form a thin shock-jet filament, which is approximated by a single line $y = f(x)$ with $x = x^* / d^*$ and $y = y^* / d^*$.

Following results of the Newtonian and blunt body theory,[8,55,56] an approximate model is based on the balance of pressure with centrifugal force inside the jet-shock filament. It is assumed that the pressure p_c^* behind the

downstream boundary of the jet is of the order of the pressure in the downstream recirculation region (see the dead-water cavity eddy (6) in Fig. 12). This pressure is small compared to the static pressure p_S^* inside of the shock-jet filament shown in Fig. 13. The latter approximately equals the pressure directly behind the shock, which is determined by the 2-D shock relations for a blunt body Newtonian limit. The pressure coefficient $C_{P_S} \equiv (p_S^* - p_\infty^*)/q_\infty^*$ is estimated as,

$$C_{P_S} \cong 2\sin^2\theta_S = 2\frac{f'^2}{1+f'^2}, \tag{14}$$
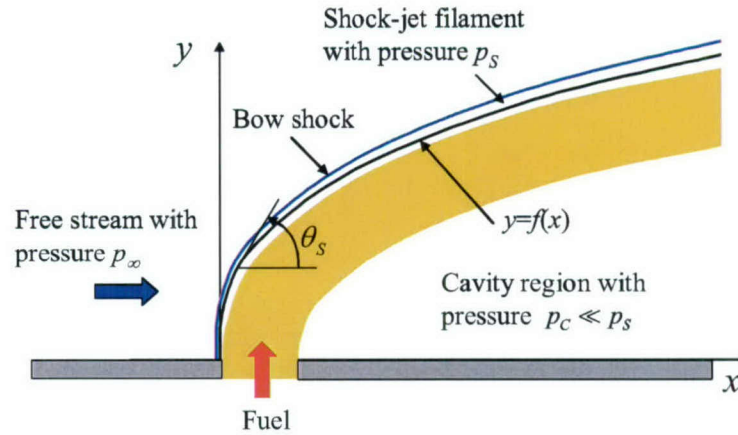
Fig. 13. Approximate flow pattern in the inviscid Newtonian limit.

where $\tan\theta_S = f'$ specifies the local slope of the shock-jet filament (Fig. 13). This equation leads to the relation

$$p_S^* \cong 2q_\infty^* \frac{f'^2}{1+f'^2}.$$

Along the jet-shock filament, the centrifugal force is balanced by the pressure gradient across the filament that gives[51]

$$\frac{\partial p^*}{\partial n^*} \cong \frac{\Delta p^*}{d^*} = \frac{p_S^* - p_C^*}{d^*} \cong \frac{\rho_j^* U_j^{*2}}{R^*(x)}, \tag{15}$$

where n signifies the direction normal to the jet-shock filament; ρ_j is jet density, which is approximately constant along the jet length; $d^*/R^*(x) = |f''(1+f'^2)^{-3/2}|$ is the normalized curvature of the shock-jet filament. The absolute value sign is important since for the normal injection $f'' < 0$, and imaginary limiting solutions for small x can arise if this is not taken into account.

Using the approximation $\Delta p^* \cong p_S^*$ and (1) we obtain the nonlinear ordinary differential equation

$$f'^2 = \alpha \left| f''(1+f'^2)^{-1/2} \right|, \tag{16}$$

where $\alpha \equiv q_j^* / q_\infty^*$ is the jet-to-freestream momentum flux ratio, $q_j^* = \rho_j^* U_j^{*2} / 2$. The appropriate initial conditions for (16) are

$$f(0) = 0, \, f'(0) \to \infty \, . \tag{17}$$

C. Solution

The problem (16)-(17) gives a one-parameter family of solutions with α as the parameter. This parameter may be scaled out of Eq. (16) by the transformations

$$F(X) = f(x) / \alpha, \, X = x / \alpha \, . \tag{18}$$

Substitution of (18) into (16) and (17) gives the initial-value problem

$$
\begin{aligned}
F'' &= -F'^2 \sqrt{1 + F'^2} \\
F(0) &= 0, \, F'(0) = \infty
\end{aligned}
, \tag{19}
$$

where the primes signify differentiation with respect to X. An exact solution of (19) is

$$F(X) = \log \left| (1 + X) + \sqrt{(1 + X)^2 - 1} \right| = \cosh^{-1} \left| (1 + X) \right| \, . \tag{20}$$

For small X relevant to the near field, the solution (20) is approximated as

$$F(X) = \log \left| 1 + \sqrt{2X} + X + ... \right| \cong \sqrt{2X} \, , X \to 0 \, . \tag{21}$$

Note in contrast to the blast wave theory[52-54] the exponent in (21) should be 2/3 rather than 1/2 for this 2-D flow. This appears appropriate since the equations are not embedded in the blast wave similitude. Note that the 1/2 exponent applies for an axisymmetric body in the blast wave theory.

For large X, we obtain

$$F(X) \cong \log X, \, X \to \infty \tag{22}$$

Equation (22) shows that the shock does not become asymptotic to a Mach line, as it should. This is associated with a breakdown of thin shock layer approximations in the far-field region, where the strong shock and hypersonic approximations are inappropriate and some form of the Prandtl-Glauert linearized theory approximations is more valid. In some form of an outer limit and asymptotic matching that has yet to be discovered, (although unified supersonic-hypersonic similarity has been proposed), the body appears as a supersonic source generating a Mach wave in the far field. The yet-to-be-determined unified theory would systematically match thin shock layer, blast wave and linearized regions as well as provide a uniformly valid description of the flow. Nevertheless, the physics-based "engineering" approximation used here provides a useful estimate for the jet penetration as will be shown in the next section.

D. Comparison with Experiment

In the empirical model of Ref. 44 the jet penetration depth h^* is defined as a distance from the point A to the wall (see Fig. 12). The experimental data discussed in Ref. 43 are correlated as

$$h \equiv \frac{h^*}{d^*} = \frac{1.51}{(1 + \cos \theta_j)} \sqrt{\alpha} \, , \tag{23}$$

where θ_j is the jet injection angle. For the normal injection, $\theta_j = 90°$, the relation (23) gives $h = 1.51\sqrt{\alpha}$. Using the near-field asymptotic form (21) and assuming that the point A corresponds to $x \approx 1$, we obtain $h = \sqrt{2\alpha} \approx 1.41\sqrt{\alpha}$, which is close to the correlation (23). More importantly, the square-root singularity near the jet origin $x = 0$ predicted by the theory agrees with the empirical fit. This indicates that the analytical solution (20) resulting from the inviscid approximate thin shock layer model captures basic features of the near-field flow. As previously mentioned, the approximation is not strictly embedded in blast wave similitude and therefore gives a different singular behavior near the origin than that from the blast wave theory.

Ben-Yakar and Hanson[43,45,49] performed experimental studies of combustion and mixing in high total enthalpy supersonic flows. The experiments, conducted in an expansion tube facility of Stanford University, were designed to investigate the near-field mixing and auto ignition of a three-dimensional under-expanded transverse hydrogen jet injected through a cylindrical hole. Simultaneous OH-PLIF and schlieren imaging were performed at the jet centerline to obtain information on the location of shock waves, the jet penetration, and the region of combustion. These data are used hereinafter for testing our theoretical model.

Figure 14 compares the theoretical solution (20) with the instantaneous schlieren images[43,49] of hydrogen and OH injection into the cross flow at $M \approx 3.5$, static temperature $T^* = 1300$ K, static pressure $p^* = 0.32$ psi and freestream velocity $U_\infty^* = 2420$ m/s. The jet-to-freestream momentum flux ratios are $\alpha = 1.4$. Large-scale coherent vortical structures generated by the jet-stream interaction are clearly observed along the jet-freestream interface. These structures cause local fluctuations of the bow shock as documented in Ref. 42. Nevertheless, the time-averaged shock position is smooth rather than a bumpy instantaneous shape. In the near-field region $x < 3$, the jet outer edge is located close to the bow shock forming a thin shock-jet filament that confirms our theoretical concept. In this region, the solution (20) agrees well with the average position of the jet outer edge as shown in Fig. 15.

Some of this agreement needs to be explained in view of the two-dimensional nature of the model, which is applicable to slot injection and the three-dimensional nature of the flow out of a round hole in the experiments. As shown in Refs. 57 and 58, round jets in cross flows flatten out due to vortical kinematics as soon as one jet exit diameter along their length. The flattening process can legitimize the approximation that the curvature of the jet axis is more important than the circumferential one in determining the pressure jump across the jet.
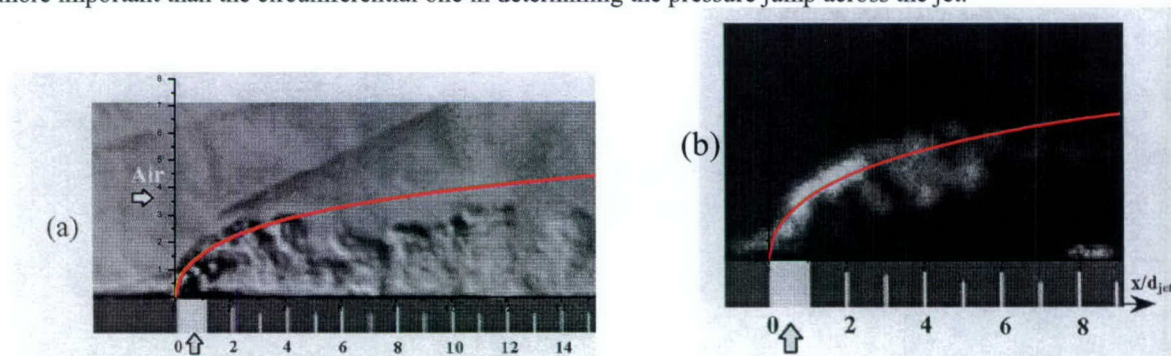
Fig. 14. Comparison of the theoretical solution (20) (red line) with simultaneous schlieren (a) and OH-PLIF (b) images of hydrogen injection into supersonic cross-flow;[8] $M = 3.46$, $T^* = 1300$ K, $p^* = 0.32$ psi, $U_\infty^* = 2420$ m/s; the jet-to-freestream momentum flux ratio $\alpha = 1.4$.

In Fig. 14b and Fig. 16, the theoretical prediction is compared with instantaneous OH-PLIF images, which indicate the presence of the OH radicals formed by the auto ignition of jet hydrogen. The OH radicals are primarily produced in the hot separation region upstream of the jet exit (see region (1) in Fig. 12) and directly behind the bow shock and convected downstream with the shear-layer vortices. The OH-mole fraction decreases as the gases expand around the jet and the local mixture temperature falls.[43] In the near-field region, the solution (20) mimics the shape of a thin filament along the outer edge of the plume. Additional comparisons with experiment are given in Ref. 42. The theory breaks down and does not give the jet shock as a Mach line in the far-field region. This is because the jet interface is no longer close to the shock. In addition, the shock is attenuated and becomes weak. Accordingly, the thin-layer Newtonian assumptions are no longer applicable and a linearized model involving the jet flow appearing as a Prandtl-Glauert supersonic source-like singularity in the far field may be applicable. Asymptotic modeling of this region and its matching with the near-field solution needs attention. Although the present model is not a formal asymptotic solution, it is a good starting point for such a systematic approximation scheme, using the Newtonian

distinguished limit. In spite of the aforementioned limitations, comparison of the theory in this paper and experiment reveals that it gives a good account of the physics important for fuel penetration estimation.

The scaling arising in terms of the jet to freestream momentum ratio parameter α (sometimes denoted as J in the literature) provides a means of collapsing normalized penetration data in units of jet exit width on to a universal curve shown by Srnivesan and Bowersox as well as others arises naturally in our analysis. Indications are that the ideas of the present model with some modification apply to oblique injection. An important aspect of this work is that it can be used for a good first quantitative, non-empirical estimate of penetration of fuel into a hypersonic stream. The associated time and distance scales may be decisive in determining the fraction of fuel burned and other scramjet combustion metrics. This is being used in connection with our plasma jet ignition studies involving plasma chemistry modules and large-scale parallel computations to study the mixing processes in Ref. 59.
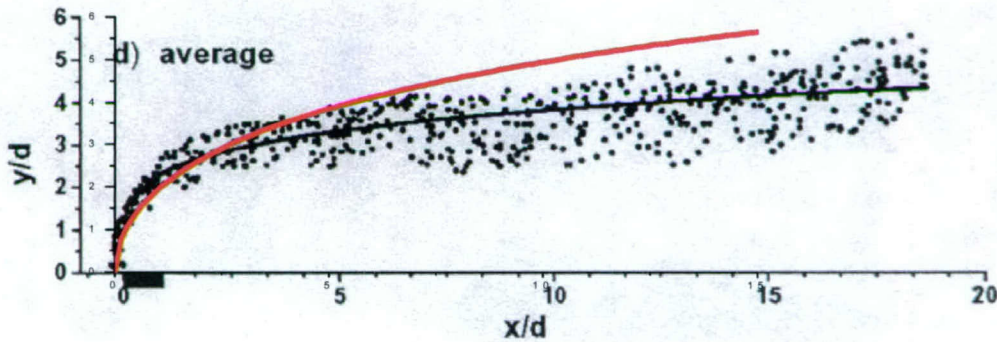
Fig. 15. Comparison of the theoretical solution (7) (red lines) with jet penetration measured from 8 consecutive schlieren images of hydrogen injection into supersonic cross-flow; **Error! Reference source not found.**[2] $M = 3.5$, $T^* = 1300$ K, $p^* = 0.32$ psi, $U_\infty^* = 2420$ m/s; the jet-to-freestream momentum flux ratio $\alpha = 2$.
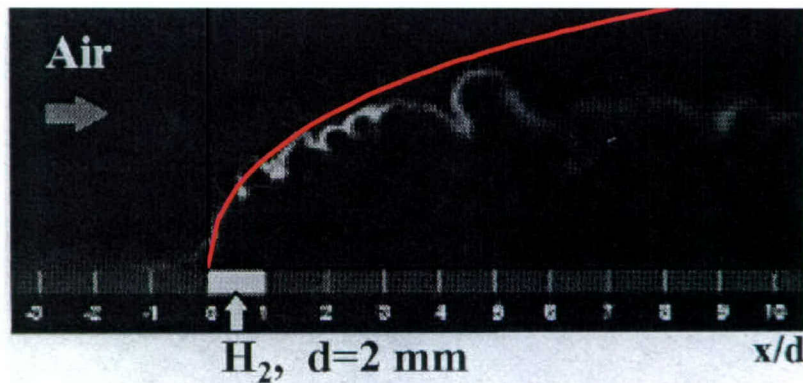
Fig. 16. Comparison of the theoretical solution (7) (red line) with simultaneous OH-PLIF image of hydrogen injection into supersonic cross-flow;[2] $M = 3.5$, $T^* = 1300$ K, $p^* = 0.32$ psi, $U_\infty^* = 2420$ m/s; the jet-to-freestream momentum flux ratio $\alpha = 2$.

VI.   Hypersonic Laminar Flow Control

A. Background
The ability to stabilize hypersonic boundary layer and increase its laminar run is of critical importance in hypersonic vehicle design.[60] Early transition causes significant increases in heat transfer and skin friction. Higher heating requires a higher-performance thermal protection system (TPS), active cooling, or trajectory modification. This

American Institute of Aeronautics and Astronautics

translates to higher cost and weight of hypersonic vehicles due to increased TPS weight. Moreover, with the low payload mass fraction, even a small savings in TPS weight can provide a significant payload increase.

Vehicle maintainability and operability are also affected by transition. Robust metallic TPS have temperature limits lower than ceramic TPS. Laminar flow control (LFC) can help to meet these more severe constraints. For a streamlined vehicle with large wetted area, viscous drag becomes important. It can be 10% (fully laminar) to 30% (fully turbulent) of the overall drag.[61] For optimized hypersonic wave-riders, viscous drag may represent up to 50% of the total drag.[62] Vehicle aerodynamics is another area impacted by laminar-turbulent transition. Asymmetry of the transition locus can produce significant yawing moments. Aerodynamic control surfaces and reaction control systems are also affected due to sensitivity of boundary-layer separation to the flow state (laminar or turbulent).

Since severe environmental conditions make it difficult to use active and reactive LFC concepts for hypersonic vehicles, passive LFC techniques are of great interest. As another example of a multi-scale problem that is a challenge to conventional RANS approaches alone but accessible to a combination of theory, computation and experiment, Fedorov and Malmuth[63] developed a new passive method for stabilization of second and higher modes (Mack's acoustic modes). Without control and at hypersonic speeds, and although there others such as crossflow, roughness, Görtler types, the second mode instability provides a route to laminar-turbulent boundary layer transition that is important to scramjet inlets and large acreage surfaces on hypersonic airbeathing cruise vehicles such as the X-43 Hyper-X. Although recent strategy has been to excite turbulence to promote scramjet ignition, it is well known that range and other performance metrics can benefit from laminarization of the inlets and other surfaces. The author believes that future vehicles will incorporate such improvements.

B. Control Concept

Fedorov and Malmuth exploited the fact that the hypersonic boundary layer behaves as an acoustic waveguide schematically shown in Fig. 17. Therein, acoustic rays are reflected by the wall and turn around near the sonic line: $y = y_a$, $U(y_a) = \text{Re}(c) - a(y_a)$, where c is disturbance phase speed, U is mean flow speed and a is local sound speed. The second, third and higher boundary-layer modes correspond to the waveguide normal modes. Malmuth and Fedorov[63] assumed that the absorption of acoustic energy by an ultrasonically absorptive coating stabilizes these disturbances. This assumption was examined using stability theory for inviscid disturbances. It was found that an ultrasonically semi-transparent wall provides substantial reduction of the second-mode growth rate.
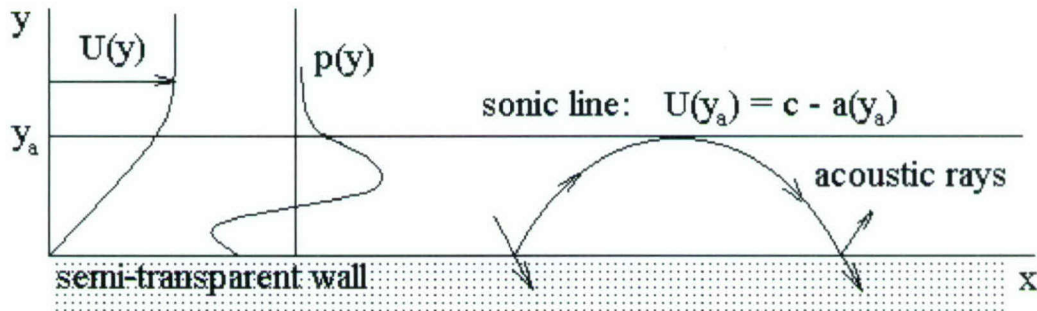
Fig. 17. Acoustic mode in a supersonic boundary layer on semi-transparent wall.

To include viscous effects of the boundary layer, a second-mode stability analysis was performed for hypersonic boundary layers over walls covered by porous coatings with equally spaced blind micro-holes in Ref. 64. A schematic of the arrangement is shown in Fig. 18. Fourier decomposition was made in a linear stability characterization of the spatial and temporal parts of velocity, pressure and temperature disturbances as shown in Eq. (1) of Fig. 19. This leads to the stability equation for the pressure amplitude (2) and (3), subject to Darcy law-like boundary conditions (4) and (5) on the ultrasonically absorbing wall (UAC). Absorption of the disturbance energy by porous layers was modeled using the theory of sound wave propagation in thin and long tubes to give the Darcy constant, admittance or absorption coefficient A as shown in (6). The latter coefficient coupling the pressure disturbance with the vertical velocity disturbance on the porous surface is expressed as an explicit function of porosity characteristics. Stability calculations showed that the dissipative absorption of disturbance energy by the porous coating provides massive reduction of the second mode growth rate in a wide range of disturbance

frequencies and Reynolds numbers as indicated with the variations with the reflection coefficient r in the plot in Fig. 19. This conclusion is consistent with the results of Malmuth and Fedorov[63] obtained from their inviscid stability analysis. The most profound effect is observed on a cool wall that is typical for hypersonic vehicle TPS surfaces. A relatively thin porous coating (of thickness about half of the laminar boundary-layer displacement thickness) provides a strong stabilization effect. Such porous coatings can be designed for passive laminar flow control in hypersonic vehicle surfaces. Note that the disturbance absorption should be produced at the initial phase of transition process where the unstable disturbance amplitude is about 0.01-0.1% of its level in transitional and turbulent boundary layers. In this phase, additional heating of the porous coating associated with partial absorption of the disturbance energy is negligibly small compared to the turbulent heating. Rasheed and Hornung[65] verified that the stabilization predicted by the theory actually delayed transition in experiments in the GALCIT T-5 wind tunnel and in later work by ITAM. Shown in Panel (a) of Fig. 20 is a right circular cone that was tested in the tunnel. One half of its surface consisted of the fine porous layer. The other half was an ordinary metal finish as shown in Panel (b). Panel (c) shows that dramatic increase in transition Reynolds number Re_{tr} at different enthalpy levels in the T-5 runs. In fact with the porosity, no transition was noted on the model and the laminar run was doubled. Panels ((d) and (e) confirm this finding. New work in Ref. 66 shows excellent applicability of this concept for random porosity providing a symbiotic relationship between natural TPS materials that are engineered to provide the UAC effect and a magnification of the aeroheating protection by laminarization. We intend to scale up this proof of concept to larger wind tunnels and ultimately deploy it on flight vehicles as schematically indicated for the X-43 configuration in Fig. 21.

VII.   Other Examples

The foregoing four examples illustrate only a small subset of the tremendous benefit in using a triad of theory, computation and experiment. In this connection, it is hoped that the value of the old pencil and pen analytical methods can be seen in the modern context described here. In addition to the illustrations given, we have used the triad on modeling counterflow and crossflow jets to simulate nose-tip plasma-jet aerospike drag reduction and plasma jet enhanced scramjet ignition in Refs. 59 and 67. In addition, a gridless technique was developed to treat the problem of shock manipulation by MHD Lorentz forces in Ref. 68 that has been validated by large scale CFD and experiments with the new MHD rig at ITAM. Additional use of the theoretical modeling showing the potential for forebody plasma streamers in reducing wave drag was described in Ref. 69. Modeling and experiment for use of plasma discharges for UAV and UCAV tailless and agile fighter nose-tip symmetry breaking control is given in Refs. 70 and 71.
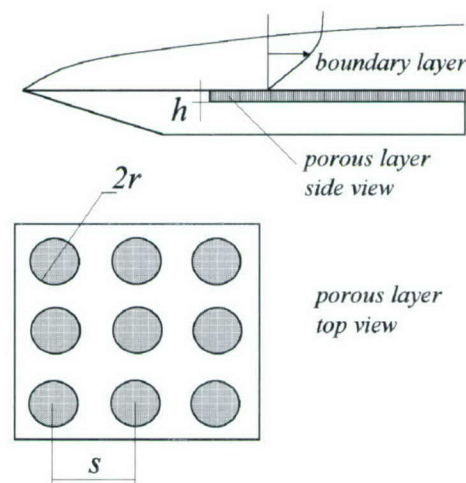
Fig. 18. Schematic of a wall covered by porous layer.

Velocity and pressure disturbances in traveling wave form:

$$[\tilde{u}, \tilde{v}, \tilde{p}, \tilde{\theta}]^T(x,y,t) = [u,v,p,\theta]^T(y)\exp[i(\alpha x - \omega t)] \quad (1)$$

Stability equation for pressure amplitude:

$$p'' - \left(\frac{2U'}{U-c} - \frac{T'}{T}\right)p' + \lambda^2 p = 0 \quad (2)$$

$$\lambda^2 = \alpha^2\left[\frac{M^2(U-c)^2}{T} - 1\right] \quad (3)$$

B.C. on UAC

$$p'(0) = A \cdot \frac{i\alpha c}{T(0)}p(0) \quad (4)$$

$$p(\infty) = 0 \quad (5)$$

Ultrasonically absorptive wall causes massive reduction of disturbance growth rate

Absorption coefficient can be expressed as a function of the UAC reflection coefficient τ

$\tau =$ (reflected wave amplitude)/(incident wave amplitude)

$$A = -\frac{T_w}{c}\sqrt{\frac{M^2 c^2}{T_w} - 1}\frac{1-\tau}{1+\tau}, \quad \mathrm{Re}(A) < 0 \quad (6)$$

M=6
$T_w/T_{ad} = 0.2$

$\tau = 1$
$\tau = 0.8$
$\tau = 0.6$

Increasing transparency
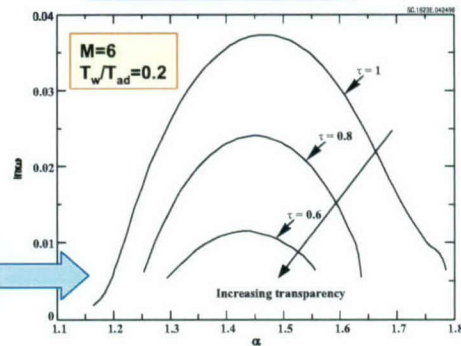
Fig. 19. Second mode instability control with ultrasonically absorbing walls.

(a)

(b)

(c)

Sharp cone model with porous surface

black squares - solid wall
open circles - porous wall
arrowed circles - flow is totally laminar

Summary of Caltech data (H_0 is total enthalpy) (N_2)

*A. Rasheed and H. Hornung, 1999

(d)

Transitional flow on solid surface

Flow direction

Laminar flow on porous surface

(e)
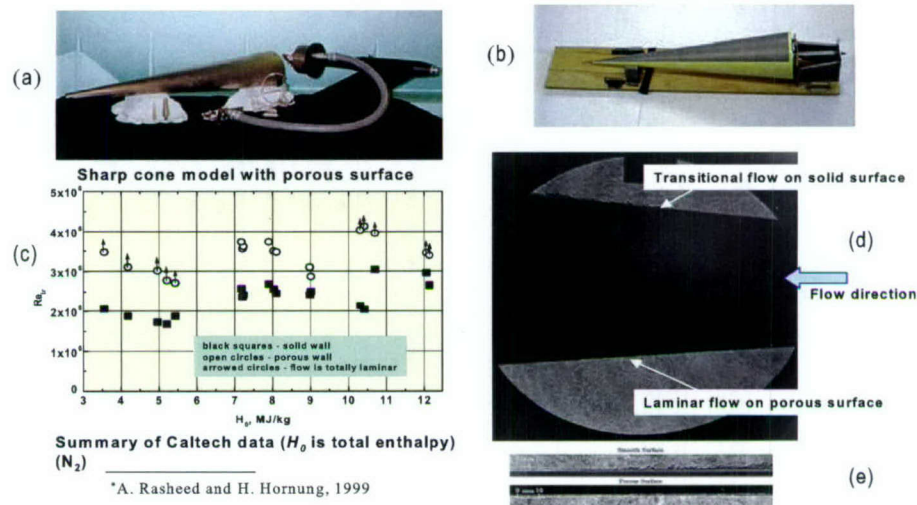
Fig. 20. Caltech and ITAM experiments showing that UAC substantially delays transition.

HYPER-X RESEARCH VEHICLE CONFIGURATION

UAC

TPS
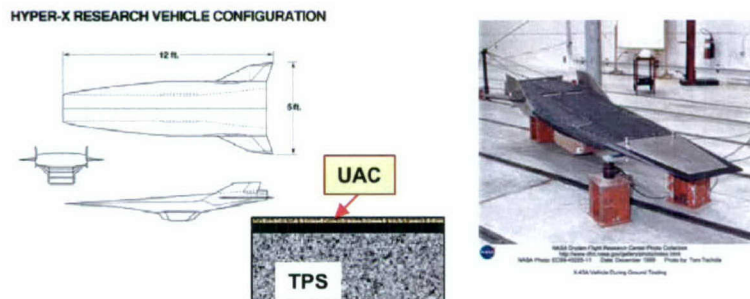
Fig. 21. Application of the UAC concept for a realistic airbreather.

VIII. Conclusion

This paper reviewed the state of theory with the present CFD emphasis in industry. Besides the many roles that were discussed, it is important that the educational system reinvigorate the concept that theoretical modeling is an indispensable tool to the engineer and scientist in addition to current emphasis on familiarity and use of legacy codes as well as development of new ones. It still is a very important skill to know how to set up problems from first principles and make approximations for theoretical physics-based models as well as combine this capability with modern computational methods. In the author's opinion, suitable curricula need to be retained and student interest developed to foster these skills. These are very important even in the CFD environment when interpretation of the results is critical.

Acknowledgements

References

[1]Cosner, R., "Assessment of Vehicle Performance Predictions Using CFD," AIAA Paper 2000-0384, 2000.

[2]Lee-Rausch, E.M., Buning, P.G., Mavriplis, D., Morrison, J.H., Park, M.A. Rivers, S.M. and Rumsey, C.L., "CFD Sensitivity Analysis of a Drag Prediction Workshop Wing/Body Transport Configuration," AIAA Paper 2003-3400, 2003.

[3]Malmuth, N. et al., NATO RTO-AVT Specialist Meeting, "Management of Transitional Separation for Flow Control of Military Flight Vehicles," AVT-111, Prague, CZ, October 2004, (CD proceedings in preparation).

[4]Kevorkian, J. and Cole, J., *Perturbation Methods in Applied Mathematics*, Springer-Verlag, New York, 1981.

[5]Sears, W., ed., *General Theory of High Speed Aerodynamics, Vol. VI, High Speed Aerodynamics and Jet Propulsion*, Princeton University Press, Princeton, New Jersey, 1954.

[6]Cole, J. and Cook, L., *Transonic Aerodynamics*, North Holland, New York, 1986.

[7]Guderley, K., *Theory of Transonic Flow*, Addison Wesley, 1962.

[8]Cole, J.D., "Newtonian Flow Theory for Slender Bodies," *J. Aero, Sci*, Vol. 24, 1957, pp. 448-455.

[9]Jones, R. T., "Properties of Low-Aspect - Ratio Pointed Wings at Speeds Below and Above the Speed of Sound," NACA Rep. 835, 1946.

[10]Lagerstrom, P., "Laminar Flow Theory," Section B. *Theory of Laminar Flows, High Speed Aerodynamics and Jet Propulsion, Vol. IV*, Moore, F. ed., Princeton University Press, Princeton, N.J., 1964, pp. 20-150., also see, *Matched Asymptotic Expansions, Ideas and Techniques*, Springer-Verlag, 1988.

[11]Lax, P., "Weak Solutions of Nonlinear Hyperbolic Equations and Their Numerical Computation," *Comm, Pure Appl. Math*, 7, Vol.7, 1954, pp. 159-193.

[12]Magnus, R. and Yoshihara, H., "Inviscid Transonic Flow Over Airfoils," *AIAA J.* Vol. 8, No. 12, 1970, pp.2157-2162.

[13]Murman, E. and Cole, J. "Calculation of Plane Transonic Flows," *AIAA J.*, Vol. 9, 1971, pp. 114-121.

[14]Spreiter, J., "The Local Linearization Method in Transonic Flow Theory," *Symposium Transsonicum*, Springer-Verlag, Berlin, 1964, pp. 152-183

[15]Oswatitsch, K. and Keune, F., "Ein Äquivalenzsatz für Nichtangestellet Flügel Kleiner Spannweite in Schallnaher Strömung," *S. Flugwiss.* 3 2, 1955, pp.29-46.

[16]Cole, J. and Malmuth, N., "Wave Drag of Transonic Airplanes," *Proc. Roy, Soc. A.*, Vol. 461, No. 2054, Feb. 2005, pp.541-560.

[17]Cheng, H. K. and Hafez, M. M., "Equivalence rule and Transonic Flow Theory Involving Lift," *AIAA J.* v. 11, No. 8, Aug. 1973, pp 1210-1212.

[18]Barnwell, R. W, "Analysis of Transonic Flow about Lifting Wing-Body Configurations," NASA TR R-440, June 1975.

[19]Cramer, M. S., "Lifting Three-Dimensional Wings in Transonic Flow, " *J. Fluid Mechanics*, (1979) **95** pp. 223-240. See also: A Note on 'Lifting Three-Dimensional Wings in Transonic Flow', *J. Fluid Mechanics*, Vol. 109, 1981, pp. 257-258.

[20]Milne Thomson, L., *Theoretical Hydrodynamics*, 3rd ed. Macmillan, New York, 1955.

[21]Schindel, L.H., "Store Separation," AGARD-AG-202, June, 1975.

[22]Goodwin, F.K., Dillenius, M.F.E., Nielsen, J.N., "Prediction of Six-degree-of-Freedom Store Separation Trajectories at Speeds Up to the Critical Speed. V.1. Theoretical Methods and Comparison with Experiment." AFFDL-TR-72-83, 1972.

[23]Wood, M.E., "Application of Experimental Techniques to Store Release Problems." Proceedings of NEAR Conference on Missile Aerodynamics, Monterey, California, 1988.

[24]Prewitt, N.C., Belk, D.M., Maple, R.C., "Multiple Body Trajectory Calculations Using the Beggar Code", *J. Aircraft*, **36**, No. 5, pp. 802-808, 1999.

[25]Lijewski, L. and Suhs, N.E., "Time-Accurate Computational Fluid Dynamics to Transonic Store Separation Trajectory Prediction, *J. Aircraft*, Vol. 31, No.4, 1994, 1004, pp. 886-891.

[26]Sickles, W., Denny, A. and Nichols, R., "Time-Accurate CFD Predictions of the JDAM Separation from an F-18C Aircraft, AIAA 00-0796, January 2000.

[27]Rizk, M., Ellison, S. and Prewitt, N., "Beggar"—A Store Separation Predictive Tools," AIAA 2002-3190, June 2002.

[28]Murphy, K., Buning, P., Pamadi, B. Scallion, W., and Jones, K., "Overview of Transonic to Hypersonic Stage Separation Tool Development to Multi-Stage-to-Orbit Concepts," AIAA 2004-2595, June 2004.

[29]Murman, S., Aftosmis, M. and Berger, M., "Simulations of 6-DOF Motion with a Cartesian Method," AIAA-2003-1246, Jan 2003.

[30]Murman, S., Aftosmis, M. and Berger, M., "Implicit Approaches for Moving Boundaries in a 3-D Cartesian Method, AIAA 2003-1119, Jan 2003.

[31]Liever, P., and Habchi, S., "Separation Analysis of Launch Vehicle Crew Escape Systems, AIAA 2004-4726, 2004.

[32]Aradag, S. and Knight, D., "Simulation of Supersonic Cavity Flow Using 3D RANS Equations, AIAA 2004-4966, August 2004.

[33]Rizzeta, D. and Visbal, M., Large-Eddy Simulation of Supersonic Flowfields Including Flow Control," Vol. 41, No. 8, *AIAA J.*, August 2003.

[34]Colonius, T., Basu, A. and Rowley, C. "Numerical Investigation of the Flow Past a Cavity, AIAA 99-1912, 1999.

[35]Bjorge, S., Reeder, M., Subramanian, C., Crafton, J., "Flow Around an Object Projected from a Cavity into a Freestream, AIAA 2004-1253, 2004.

[36]Bower, W. Kibens, V., Cary, A., Alvi, F., Annaswamy, A. and Malmuth, N., "High-Frequency Active Control for High-Speed Weapon Release (HIFEX) , AIAA 2004-2513. June 2004.

[37]Shalaev, V. Fedorov, A. and Malmuth, N. "Dynamics of Slender Bodies Separating from Rectangular Cavities," *AIAA J.*, Vol. 40 3, March 2002, pp.517-525.

[38]Shalaev, V. Malmuth, N. Fedorov, A."Analytical Modeling of Transonic Store Separation from a Cavity," AIAA Paper 2003-0004 at AIAA 41st Aerospace Sciences Meeting, Reno, Nevada, January 6, 2003.

[39] Malmuth, N., Shalaev,V., "Theoretical Modeling of Slender Bodies Interaction in Supersonic Flows," AIAA Paper AIAA-2004-1127, Nevada, January 6, 2004.

[40]Quirk, J., "Amrita—A Computational Facility (for CFD modeling)." VKI 29th CFD Lecture Series, ISSN-0377-8312, 1988.

[41]Malmuth, N., Hites, M., and Williams , D., "Photographic Investigation of the Dynamics of an Ogive Model near a Cavity at Subsonic Mach Numbers," Final Report. Fluid Dynamics Research Center Illinois Institute of Technology, January 18, 1998.

[42]Malmuth, N. and Fedorov, A., "Thin Shock Layer Model for a Jet in a Hypersonic Cross Flow," AIAA 2005-0893.

[43]Ben-Yakar, A., and Hanson, R.K., "Supersonic Combustion of Cross-Flow Jets and the Influence of Cavity Flame-Holders," AIAA Paper No. 99-0484, 1999.

[44]Krasnov, N.F., Koshevoy, V.N., and Kalugin, V.T., *Aerodynamics of Separated Flows*, Moscow, Vysshaya Shkola, 1988 (in Russian).

[45]Ben-Yakar, A., and Hanson, R.K., "Experimental Investigation of Flame-Holding Capability of Hydrogen Transverse Jet in Supersonic Cross-Flow," 27th Symposium on Combustion, The Combustion Institute, 1998, pp. 2173-2180.

[46]McDaniel, J.C., and Graves, J., "Laser Induced Fluorescence Visualization of Transverse Gaseous Injection in a Nonreacting Supersonic Combustor," *Journal of Propulsion and Power*, Vol. 4, No. 6, 1988, pp. 591-597.

[47]Gruber, M.R., Nejad, A.S., Chen, T.H., and Dutton, J.C., "Mixing and Penetration Studies of Sonic Jets in a Mach 2 Freestream," *Journal of Propulsion and Power*, Vol. 11, No. 2, 1995, pp. 315-323.

[48]Rothstein, A.D., and Wantuck, P.J., "A Study of the Normal Injection of Hydrogen into a Heated Supersonic Flow Using Planar Laser-Induced Fluorescence," AIAA Paper No. 92-3423, 1992.

[49]Ben-Yakar, A., Kamel, M.R., Morris, C.I., and Hanson, R.K., "Experimental Investigation of H_2 Transverse Jet Combustion in Hypervelocity Flows," AIAA Paper No. 97-3019, 1997.

[50]Srnivesan, R. and Bowersox, R., "Detached Eddy Simulation of Gaseous into a Mach 5.0 Freestream," AIAA 2005-0893, 43rd AIAA, 10-13 January 2005.

[51]Liepmann, H. and Roshko, A. *Gasydnamics*, 1957.

28

[52]Chernyi, G. G, *Introduction to Hypersonic Flow*, translated by Ronald F. Probstein, Academic Press, New York and London, 1961, pp. 209, 215.

[53]Sedov, L.I., *Similarity and Dimensional Methods in Mechanics*, English translation, (M. Holt ed.) Academic Press, New York and London, 1959.

[54]Taylor, G.I., "The Formation of Blast Wave by a Very Intense Explosion," *Proc. Roy. Soc., London, Ser. A*. Vol. 201, 159 – 186, 1950.

[55]Hayes, W, and Probstein, R., *Hypersonic Flow Theory*, Academic Press, New York, 1959.

[56]Cheng, H.K., "Inviscid Leading Edge Effect in Hypersonic Flow," *J. Aero. Sci.*, Vol. 23, pp. 898-900, 1956.

[57]Abramovich, G., *The Theory of Turbulent Jets*, English Translation by Scripta Technica, MIT Press, 1963, pp. 541-556.

[58]Shandorov, G., "Flow from a Channel into Stationary and Moving Media," *Zh. Tekn. Fiz*, Vol. 37, 1, 1957.

[59]Ardelyan, N., Bytchkov, V. Kosmachevskii, K. Malmuth, N. and I. Timofeev, "Plasma Generators with Divergent Channel for Aerodynamic Applications," AIAA Paper 2004-0179, January 6, 2004.

[60]Malik, M.R., Zang, T.A., and Bushnell, D.M., "Boundary Layer Transition in Hypersonic Flows," AIAA Paper No. 90-5232, 1990.

[61]Reed, H.L., Kimmel, R., Schneider, S., and Arnal, D., "Drag Prediction and Transition in Hypersonic Flow," AIAA Paper No. 97-1818, June 1997.

[62]Bowcutt, K.G., Anderson, J.D., and Capriotti, "Viscous Optimized Hypersonic Waveriders," AIAA Paper No. 87-0272, 1987.

[63]Malmuth, N.., Fedorov, A., Shalaev, V., Cole, J., and Khokhlov, A., "Problems in High Speed Flow Prediction Relevant to Control," AIAA Paper No. 98-2995, 2nd AIAA Theoretical Fluid Mechanics Meeting, June 15-18, 1998/Albuquerque, NM.

[64]Fedorov, A. and Malmuth, N., Rasheed, A. and Hornung, H., "Stabilization of Hypersonic Boundary Layers by Porous Coatings," *AIAA J.*, Vol. 39 April 2002, pp. 605-610.

[65]Rasheed, A., Hornung, H., Fedorov, A. and Malmuth, N. "Experiments on Passive Hypersonic Boundary Layer Control Using a Porous Surface," *AIAA J.*, Vol. 40 3, March 2002, pp. 481-489.

[66]Fedorov, A., Shiplyuk, A., Maslov, A., Burov, E. and Malmuth, N., "Stabilization of a Hypersonic Boundary Layer Using an Ultrasonically Absorptive Coating," *J. Fluid Mechanics*, Vol. 479, 2003, pp. 99-124, 2003.

[67]Fomin, V. Maslov, A., Malmuth, N., Fomichev, V., Shashkin, A. Korotaeva, T., Shipyuk, A. and. Pozdnyakov, G., "Influence of Counterflow Plasma Jet on Supersonic Blunt-Body Pressures, *AIAA J.*, Vol. 40 No.6, June 2002, pp. 1170-1177.

[68]Malmuth, N., Krivstov, V. and Soloviev, V., "Quick Gridless Estimation of MHD Effects on Hypersonic Inlet Ramp Shocks, AIAA 2004-0862, 2004.

[69]Soloviev, V., Kristov, K., Konchakov, A., and Malmuth, N., "Drag Reduction by Plasma Filaments Over Supersonic Forebodies," AIAA J., Vol. 41, No. 12, December 2003, pp. 2403-2409.

[70]Maslov, A., Zanin, B., Sidorenko, A., Fomichev, V., Postnikov, B., and Malmuth, N., "Plasma Control of Separated Flow Asymmetry on a Cone at High Angle of Attack," AIAA Paper 2004-0843, January 6, 2004.

[71]Shalaev, V., Fedorov, A., Malmuth, N., and Shalaev, I. "Mechanism of Forebody Nose Vortex Symmetry Breaking Relevant Plasma Flow Control," January 6, 2004.

Dynamics of Slender Bodies Separating from Rectangular Cavities

V. I. Shalaev, A. V. Fedorov, N. D. Malmuth

Dynamics of Slender Bodies Separating from Rectangular Cavities

V. I. Shalaev* and A. V. Fedorov†
Moscow Institute of Physics and Technology, Zhukovski, 14080, Russia
and
N. D. Malmuth‡
Rockwell Scientific Company, Thousand Oaks, California 91630

Vertical and pitching motions (two degrees of freedom) of a thin body of revolution separating from a rectangular cavity in a subsonic stream are investigated using combined asymptotic and numerical methods. The analysis is based on explicit analytical solutions for the lift force and pitching moment obtained in our previous studies. Body trajectory dependencies on initial conditions, body parameters, and freestream velocity are studied. The problem is divided into three phases of the motion. In phase 1, the body is inside the cavity. In phase 2, the body crosses the shear layer, and in phase 3, the body is outside the cavity. For phases 1 and 3, analytical solutions of the body dynamics are obtained for typical cases. This analysis provides insight into the separation process and identifies governing lumped nondimensional parameters relevant to the body dynamics as well providing a model that can provide quick, computationally non-intensive estimates of store separation with a personal computer. The role of the nondimensional parameters in the dynamic stability eigenvalues is identified and found particularly useful in this connection. These parameters implicitly contain the effect of the shear layer. Numerical calculations for all three phases are in good agreement with a major portion of the free-drop experimental data obtained in a subsonic wind tunnel. However, there are cases when the agreement is only satisfactory. The discrepancy is associated with a pitching bifurcation when the body crosses the shear layer. It is shown that small variation of the initial conditions can trigger quick transition from one pitch angle trajectory to another and cause dramatic changes of the body trajectory outside the cavity.

Nomenclature

$a(x)$	=	local body radius
a_0	=	maximum body radius
b_i	=	coefficient defined after Eqs. (4), $i = 1, 2$
b_{ij}	=	coefficient defined after Eqs. (4), $i, j = 1, 2$
c_g	=	gravity force coefficient (Froude number); Eq. (2c)
c_l	=	lift force apparent mass; Eq. (2c)
c_m	=	apparent pitch inertia; Eq. (2c)
G_1, G_2, G_3	=	coefficients defined in Eq. (3d)
g	=	gravity acceleration
g_0, g_1, g_2	=	body shape factors; Eq. (3c)
$H(X, t)$	=	vertical distance from body axis to slip surface
H_0	=	cavity depth
I	=	moment of inertia
L	=	lift force
l_0	=	body length
M	=	pitch moment
m	=	body mass
p	=	pressure
t	=	time
u, v, w	=	flow velocity components
V_a	=	defined in Eq. (2b)
V_r	=	characteristic vertical speed

V_0	=	body initial vertical speed; see Eq. (2d)
X, Y, Z	=	Cartesian laboratory frame with origin shown in Fig. 1a
X_c, Y_c, Z_c	=	Cartesian moving body axes with origin at body c.g.
x, y, z	=	Cartesian moving body axes at general location in body
α	=	pitch angle or angle of attack
$\alpha_{11}, \alpha_{12}, \alpha_{22}$	=	coefficients defined after Eq. (3)
γ	=	angular velocity stability parameter, $\mathrm{Re}(\lambda)$
$\Delta_1, \Delta_2, \Delta_3$	=	coefficients defined after Eqs. (4)
δ	=	body half-thickness ratio, $\hat{a}_0/\hat{l}_0$
θ	=	azimuth angle
λ	=	eigenvalue
ρ	=	density
Φ	=	near-field flow potential
Ω	=	angular frequency of body oscillations, $-\mathrm{Im}(\lambda)$
ω	=	pitch angular velocity
ω_a	=	defined in Eq. (2b)

Subscripts

a	=	body cross section of radius a
b	=	body surface
c	=	c.g.
e	=	body base
0	=	initial value
∞	=	freestream

Superscripts

$\wedge$	=	dimensional value
$+$	=	inside the cavity

*Associate Professor, Department of Aeromechanics and Flight Engineering.
†Associate Professor, Department of Aeromechanics and Flight Engineering. Member AIAA.
‡Senior Scientist, Department of Material Sciences. Fellow AIAA.

Introduction

MODELING of store separation from a cavity, even into a subsonic external stream is a very difficult problem that is the subject of the intensive application of current computational fluid

dynamics. The motivation of the work described herein is the need for quick methods for certification and assessment of the physics of store separation from cavities. Similar rapid evaluation methods are needed for stage and cargo separations. A variety of computational methods have been developed.[1-3] As contrasted to pure computational modeling, this paper discusses a combined asymptotic and numerical approach. It will be applied to solve aerodynamic problems relevant to separation of a thin body of revolution from rectangular cavities into subsonic or transonic flows.[4,5] The separation process can be divided into three phases. In phase 1, the body is inside the cavity. In phase 2, the body crosses the shear layer that separates the cavity flow from the external flow. In phase 3, the body is outside the cavity. In many practical cases, viscous effects can be approximated with inviscid models. As an example, a vortex sheet representing an infinitesimally thin slip surface can be used to approximate the shear layer over a cavity. This approach is consistent with simulating the cavity shear layer interaction as a rational outer solution that is associated with viscous–inviscid interaction theory. This is an extension of the concept of transpiration velocities (outer limit of inner solution for asymptotic matching) that arises in boundary-layer viscous–inviscid interactions. It leads to a self-consistent simulation of the shear layer as an inviscid vortex sheet. Also, we time average the unsteady motions of the shear layer, because these are on a timescale that is at least three orders faster than the Froude scale of the dropping body. This is a self-consistent approximation that should be realistic for the practical case of high Reynolds number of the approaching boundary layer.

Also, the flow over the separating body can be modeled using slender body theory.[6] In Refs. 4 and 5, effects of the side cavity walls were shown to be negligible in all phases of the separation process. In the analysis of this paper, the near-field flow associated with the body aerodynamics is governed by a system of nonlinear integro–differential equations. In Refs. 4 and 5, this problem was analyzed using asymptotic methods giving explicit analytical expressions for the lift force and pitching moment acting on the body in all three phases of the separation process. In the analysis, the slip-surface displacement is neglected. A more general case is when the slip surface is a free boundary supporting nonlinear boundary conditions and interacting with the solution. For the practically important case of small deflections, the boundary conditions can be linearized on the slip surface, on the length scale of the cavity. Local flow scales have larger deflections in which an iterative scheme needs to be used. The nondeflected slip surface corresponds to the initial iterate in such a small-perturbation scheme.

Problem Formulation

In this paper, we couple our previous results on the body aerodynamics with the body dynamics and analyze two-degree-of-freedom (DOF) vertical and pitching motions induced by aerodynamic and gravity forces during the separation process. The coordinate systems XYZ (attached to the cavity) and $oxyz$ (attached to the body center of gravity) are shown in Fig. 1. The oxy frame is inclined with respect to the XY frame at an angle of attack $\alpha(t)$. This frame can rotate around the oz axis with the angular speed $\omega(t) = d\alpha/dt$. The c.g. coordinates are expressed as $X_c = Z_c = 0$ and $Y_c(t)$; $H(X, t) = Y_c - \alpha X$ is the vertical coordinate of the body axis. Using scaling of the slender body theory,[6] we introduce the nondimensional variables

$$X = \widehat{X}/\widehat{l}_0, \quad Y = \widehat{Y}/\widehat{a}_0, \quad Z = \widehat{Z}/\widehat{a}_0, \quad x = \widehat{x}/\widehat{l}_0$$

$$y = \widehat{y}/\widehat{a}_0, \quad z = \widehat{z}/\widehat{a}_0, \quad t = U_\infty \widehat{t}/\widehat{l}_0$$

$$\alpha = \widehat{\alpha}/\delta, \quad V_c = \widehat{V}_c/\widehat{V}_r, \quad \omega = \delta U_\infty \widehat{\omega}/\widehat{l}_0 \quad (1)$$

where the body half-thickness ratio δ is treated as a small parameter. Crossflow velocities and coordinates are normalized by δU_∞ and $\widehat{a}_0$, respectively. The streamwise and axial coordinates are scaled using $\widehat{l}_0$, and the pressure perturbation p is normalized with respect to $\rho_\infty U_\infty^2 \delta^2 \widehat{l}_0^2$.
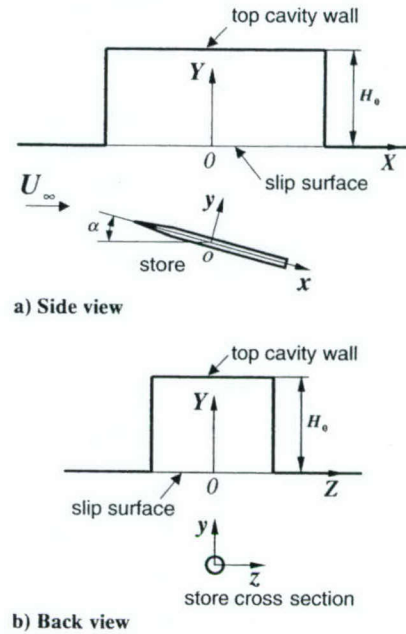

a) Side view

b) Back view

Fig. 1 Scheme of store separation.

As shown in Ref. 5, the equations for vertical and pitching body motions can be expressed in the form

$$\frac{d(V_c + c_l V_a)}{dt} = c_l L_1(t) - c_g, \qquad \frac{dY_c}{dt} = V_c(t)$$

$$\frac{d(\omega + c_m \omega_a)}{dt} = c_m M_1(t), \qquad \frac{d\alpha}{dt} = \omega(t) \qquad (2a)$$

$$V_a(t) = \int_{x_0}^{x_e} \int_0^{2\pi} \Phi(x, \theta, t) a(x) \, d\theta \, dx$$

$$\omega_a(t) = \int_{x_0}^{x_e} \int_0^{2\pi} \Phi(x, \theta, t) a(x) x \, d\theta \, dx \qquad (2b)$$

$$c_g = \frac{g \widehat{l}_0}{\delta U_\infty^2}, \qquad c_l = \frac{\pi \rho_\infty \widehat{l}_0^3 \delta^2}{m}, \qquad c_m = \frac{\pi \rho_\infty \widehat{l}_0^5 \delta^2}{I} \qquad (2c)$$

where x_0 and x_e are coordinates of the body nose and base, respectively, and Φ is the near field with respect to the body (inner) flow potential. We consider the Cauchy initial-value problem for Eqs. (2a) assuming that the body speeds, c.g. coordinate, and angle of attack are prescribed at the initial time $t = 0$ as

$$V_c(0) = V_0, \qquad \omega(0) = \omega_0, \qquad Y_c(0) = Y_0, \qquad \alpha(0) = \alpha_0 \qquad (2d)$$

Note that dV_a/dt and $d\omega_a/dt$ in Eq. (2a) represent the time derivative of the crossflow potential (incompressible harmonic inner solution) needed for the pressure in the crossflow plane from the unsteady Bernoulli equation. The terms L_1 and M_1 are integrals involving the square of the crossflow speed that also appear in the Bernoulli law for the pressure in the crossflow inner problem. These are determined from the square of the crossflow gradient of Φ.

In this paper, analytical solutions of the problem (2a–2d) for phase 1 are obtained for small lift forces compared to the weight. Slip-surface deflections are neglected, and Eqs. (2a–2d) are transformed into two decoupled ordinary differential equations with constant coefficients. A stability analysis of their solutions is performed, and behaviors of the pitch angle $\alpha(t)$ and the vertical coordinate $Y_c(t)$ are discussed for typical cases. In addition, the theoretical model for all three phases [in Eqs. (2) (without the stability linearizations)] is evaluated by comparison of the predicted trajectories with the experimental data of Ref. 7. The paper concludes with some parametric trajectory studies.

Phase 1: Body Inside Cavity

The lift force $L(t)$ and the pitching moment $M(t)$ acting on the body moving inside the cavity are derived in Ref. 5. They are expressed as integrals along the body axis with the integrands being a power series with respect to the parameters $q_1(x, t) = 0.5a/(H_0 - H)$ and $q = 0.5a/H$, where H_0 is cavity depth shown in Figs. 1a and 1b. If the body is far from the top cavity wall and the slip surface, then q_1 and q can be treated as small parameters. When terms of the order of $\mathcal{O}(q^3, q_1^3)$ are neglected, the body cross section vertical velocity $V_a^+(t)$ and angular velocity $\omega_a^+(t)$ are expressed in the form

$$V_a^+(t) \equiv \alpha_{11}(t)V_c(t) - \alpha_{12}(t)\omega(t)$$

$$\omega_a(t) \equiv \alpha_{12}(t)V_c(t) - \alpha_{22}(t)\omega(t) \qquad (3a)$$

$$\alpha_{11}(t) \equiv \pi[g_0 + G_0(t)], \qquad \alpha_{12}(t) = \pi[g_1 + G_1(t)]$$

$$\alpha_{22}(t) \equiv \pi[g_2 + G_2(t)] \qquad (3b)$$

$$g_0 \equiv \int_{x_0}^{x_e} a^2(x)\,dx, \qquad g_1 \equiv \int_{x_0}^{x_e} a^2(x)x\,dx$$

$$g_2 \equiv \int_{x_0}^{x_e} a^2(x)x^2\,dx \qquad (3c)$$

$$G_0(t) \equiv 2\int_{x_0}^{x_e} \left[q_1^2(x, t) - q^2(x, t)\right]a^2(x)\,dx \qquad (3d)$$

$$G_1(t) \equiv 2\int_{x_0}^{x_e} \left[q_1^2(x, t) - q^2(x, t)\right]a^2(x)x\,dx$$

$$G_2(t) \equiv 2\int_{x_0}^{x_e} \left[q_1^2(x, t) - q^2(x, t)\right]a^2(x)x^2\,dx \qquad (3e)$$

This transformation helps to express the dynamic equations in a form convenient for further discussion of the body trajectory features. When Eqs. (3a–3e) are used, the trajectory equations (2a) can be integrated once and expressed in the form

$$\frac{dY_c}{dt} = -\frac{b_{22}(t)}{\Delta(t)}c_g t + \frac{\Delta_1(t)}{\Delta(t)}V_0 + c_l\pi\omega_0 b_1(t) \qquad (4a)$$

$$\frac{d\alpha}{dt} = \frac{b_{21}(t)}{\Delta(t)}c_g t + \frac{\Delta_2(t)}{\Delta(t)}\omega_0 + c_m\pi V_0 b_2(t) \qquad (4b)$$

where the coefficients are defined as

$$b_{11}(t) \equiv 1 + c_l\alpha_{11}(t), \qquad b_{12}(t) \equiv c_l\alpha_{12}(t)$$

$$b_{21}(t) \equiv c_m\alpha_{12}(t), \qquad b_{22}(t) \equiv 1 - c_m\alpha_{22}(t)$$

$$\Delta \equiv b_{11}(t)b_{22}(t) + b_{12}(t)b_{21}(t)$$

$$\Delta_1 \equiv b_{11}(0)b_{22}(t) + b_{12}(t)b_{21}(0)$$

$$\Delta_2 \equiv b_{11}(t)b_{22}(0) + b_{12}(0)b_{21}(t)$$

$$b_1 \equiv (1/\Delta)\{(1 - c_m\pi g_2)[G_1(t) - G_1(0)] + c_m\pi g_1[G_2(t) - G_2(0)]$$
$$+ c_m\pi[G_1(0)G_2(t) - G_1(t)G_2(0)]\}$$

$$b_2 \equiv (1/\Delta)\{(1 + c_l\pi g_0)[G_1(0) - G_1(t)] + c_l\pi g_1[G_0(t) - G_0(0)]$$
$$+ c_l\pi[G_1(0)G_0(t) - G_1(t)G_0(0)]\}$$

The first term of Eqs. (4a–4b) models the gravity effect, the second term comes from the initial conditions, and the third term arises from the boundary and initial conditions. The angular acceleration is proportional to the product of the pitching moment coefficient c_m, the gravity force coefficient c_g, and the value $g_1 + G_1(t)$ characterizing the displacement of the center of pressure from the c.g.[8] Equations (4) can be solved numerically using, for example, the Runge–Kutta method. Note that the slip-surface effect and the top-wall effect rapidly decrease as the body moves away from these boundaries. Neglecting terms of the order of $\mathcal{O}(q^2 + q_1^2)$, which are associated with the boundary effects, the solution of Eqs. (4) can be expressed in explicit analytical form:

$$Y_c(t) = Y_0 + V_0 t - \frac{1 - \pi c_m g_2}{2\Delta_0}c_g t^2$$

$$\alpha(t) = \alpha_0 + \omega_0 t + \frac{\pi g_1 c_m c_g}{2\Delta_0}t^2 \qquad (5a)$$

$$\Delta_0 = (1 + c_l\pi g_0)(1 - c_m\pi g_2) + c_l c_m\pi^2 g_1^2 \qquad (5b)$$

Equations (5) show that the c.g. coordinate $Y_c(t)$ and the pitch angle $\alpha(t)$ are parabolic functions of time when the body moves in an unbounded fluid at rest.

It is also possible to obtain analytical solutions of Eqs. (4), when the lift and moment are small compared to the body weight. This is typical for many practical cases because the coefficients c_l and c_m are proportional to the air density to body density ratio, $\rho_\infty/\rho_b \ll 1$. For a body of uniform density, nondimensional ballistic parameters may be defined as

$$c_l = \frac{\rho_\infty}{\rho_b\pi g_0}, \qquad c_m = \frac{\rho_\infty}{\rho_b\pi g_2}, \qquad \frac{c_l}{c_m} = \frac{g_2}{g_0} \qquad (6)$$

For the experimental conditions,[7] the coefficients c_l and c_m as well as other basic parameters are shown in Tables 1 and 2, where the gravity force coefficient is calculated at the freestream speed $U_\infty = 77.1$ m/s.

If terms linear in c_l and c_m are retained in Eqs. (4), the approximate linear and angular trajectories are

$$Y_c = Y_0 + V_0 t - 0.5(1 - \pi c_l g_0)c_g t^2$$

$$\bar{\alpha} = \alpha_0 + \omega_0 t + 0.5\pi g_1 c_m c_g t^2 \qquad (7)$$

The c.g. coordinate and the pitch angle are parabolic functions of time. In the first-order approximation, the vertical motion corresponds to a pure gravity drop. The lift force gives a small negative correction of the c.g. acceleration similar to the case of a plunging cylinder in the presence of a shear layer considered in Ref. 4. As will be shown, the analytical expressions (7) are consistent with trends of numerical solutions and experimental data.

Table 1   Nondimensional parameters of models[7]

Model	δ	X_e	g_0	g_1	g_2
B1N1	$0.31250E-01$	$0.51333E+00$	$0.86206E+00$	$0.68807E-01$	$0.66707E-01$
B4N2	$0.31250E-01$	$0.49500E+00$	$0.86206E+00$	$0.53002E-01$	$0.57596E-01$
B5N5	$0.32609E-01$	$0.62261E+00$	$0.85606E+00$	$0.16423E+00$	$0.12753E+00$

Table 2   Aerodynamic and gravity acceleration coefficients for models[7]

Model	c_l	c_m	$c_g U_\infty^2$, m²/s²	c_g
B1N1	$0.29915E-03$	$0.22204E-02$	$0.95585E+02$	$0.16080E-01$
B4N2	$0.72519E-03$	$0.38857E-02$	$0.95585E+02$	$0.16080E-01$
B5N5	$0.36773E-02$	$0.24684E-01$	$0.87786E+02$	$0.14768E-01$

Phase 3: Body Outside Cavity

If the body is totally outside the cavity and moves into an external freestream, the lift force and pitching moment are again expressed as integrals along the body axis with the integrands being a power series with respect to the parameter $q = 0.5a/H$ (see Ref. 5). When these analytical solutions are analyzed, the slip-surface effect on the body trajectory is found to be proportional to the quantity

$$\int_{x_0}^{x_e} q a^2 a_x \, dx + \int_{x_0}^{x_e} q^2 a^2 \, dx \sim \frac{\bar{q}}{3} + \overline{q^2} g_0 + \mathcal{O}(\overline{q^3} g_0) \quad (8)$$

where the over bars denote averaging along the body axis. For typical cases, the body shape factor is given by Eq. (3c), $g_0 = \mathcal{O}(1)$. The average distance parameter is $\bar{q} \le 0.5$. Its maximum value $\bar{q} = 0.5$ corresponds to contact of the body surface with the slip surface. The maximum values of the first and second terms in Eq. (8) are $\frac{1}{6}$ and $\frac{1}{4}$, respectively. As the body drops, both terms decrease quickly, and the slip-surface effect vanishes. Thus, dominant terms are associated with the body drop in an unbounded uniform stream. In this case, the equations for the lift force and pitch moment can be reduced to

$$L = \pi \left[-g_0 \frac{dV_c}{dt} + g_1 \frac{d\omega}{dt} - (V_c - \alpha)a_e^2 + \omega \left(g_0 + x_e a_e^2 \right) \right] \quad (9a)$$

$$M = \pi \left[-g_1 \frac{dV_c}{dt} + g_2 \frac{d\omega}{dt} + (V_c - \alpha)\left(g_0 - x_e a_e^2 \right) + \omega x_e^2 a_e^2 \right] \quad (9b)$$

where $a_e = a(x_e)$ is the base radius ($a_e = 1$ for a cylindrical afterbody). These expressions were derived for bodies with a sharp nose, $a(x_0) = 0$. Substitution of Eqs. (9a) and (9b) into the trajectory equations (2a) and integration once give the linear ordinary differential equation (ODE) system (with constant coefficients)

$$\frac{dV_c}{dt} = c_{11}(V_c - \alpha) + c_{12}\omega - c_{10}$$

$$\frac{d\omega}{dt} = c_{21}(V_c - \alpha) + c_{22}\omega + c_{20} \quad (10a)$$

$$c_{10} = \frac{1 - c_m \pi g_2}{\Delta_0} c_g, \qquad c_{20} = \frac{c_m c_g \pi g_1}{\Delta_0}$$

$$c_{11} = \frac{c_l \pi}{\Delta_0} \left[c_m \pi g_1 \left(g_0 - x_e a_e^2 \right) - (1 - c_m \pi g_2)a_e^2 \right] \quad (10b)$$

$$c_{12} = \frac{c_l \pi}{\Delta_0} \left[(1 - c_m \pi g_2)\left(g_0 + x_e a_e^2 \right) + c_m \pi g_1 x_e^2 a_e^2 \right] \quad (10c)$$

$$c_{21} = \frac{c_m \pi}{\Delta_0} \left[(1 + c_l \pi g_0)\left(g_0 - x_e a_e^2 \right) + c_l \pi g_1 a_e^2 \right] \quad (10d)$$

$$c_{22} = \frac{c_m \pi}{\Delta_0} \left[(1 + c_l \pi g_0)x_e^2 a_e^2 - c_l \pi g_1 \left(g_0 + x_e a_e^2 \right) \right] \quad (10e)$$

where Δ_0 is given by Eq. (5b).

We consider the Cauchy problem for Eqs. (10a) assuming that the body is totally outside the cavity for $t \ge t_0$, and its initial speeds, coordinate, and pitch angle are

$$V_c(t_0) = V_0', \qquad \omega(t_0) = \omega_0', \qquad Y_c(t_0) = Y_0', \qquad \alpha(t_0) = \alpha_0' \quad (11)$$

From Eqs. (10a), the angular velocity ω and the function $W(t) = V_c(t) - \alpha(t)$ are solutions of the decoupled equations

$$\frac{d^2 W}{dt^2} - 2\gamma \frac{dW}{dt} + \kappa W + c_1 = 0, \qquad \frac{d^2 \omega}{dt^2} - 2\gamma \frac{d\omega}{dt} + \kappa \omega + c_2 = 0 \quad (12)$$

where the constant coefficients are

$$\gamma = \frac{c_m \pi a_e^2}{2\Delta_0} \left[x_e^2 - \frac{c_l}{c_m} + \pi c_l \left(x_e^2 g_0 - 2x_e g_1 + g_2 \right) \right]$$

$$\kappa = \frac{c_m \pi}{\Delta_0} \left[g_0 - a_e^2 x_e - c_l \pi a_e^2 (g_0 x_e - g_1) \right] \quad (13a)$$

$$c_1 = \frac{c_m c_g \pi}{\Delta_0} \left(g_1 - x_e^2 a_e^2 \right), \qquad c_2 = \frac{c_m c_g \pi}{\Delta_0} \left(g_0 - x_e a_e^2 \right) \quad (13b)$$

The characteristic (secular) equation for the eigenvalues of ODE system (10a) and its solutions are

$$\lambda^2 - 2\gamma\lambda + \kappa = 0, \qquad \lambda_1 = \gamma + i\Omega$$

$$\lambda_2 = \gamma - i\Omega, \qquad \Omega = \sqrt{\kappa - \gamma^2} \quad (14)$$

Various cases significant for the trajectory stability will now be discussed.

Eigenvalues λ_1 and λ_2 Are Complex

If λ_1 and λ_2 are complex, then the trajectory parameters are expressed in the form

$$V_c(t) = V_0' + (d - c_2\tau)/\kappa + e^{\gamma\tau}(A_1 \cos \Omega\tau + A_2 \sin \Omega\tau)$$

$$\omega = -(c_2/\kappa) + e^{\gamma\tau}(B_1 \cos \Omega\tau + B_2 \sin \Omega\tau) \quad (15a)$$

$$Y_c(t) = Y_0' + (V_0' + d/\kappa)\tau - (c_2/2\kappa)\tau^2 + (e^{t\gamma}/\kappa)$$
$$\times [(\gamma A_1 - \Omega A_2) \cos \Omega\tau + (\Omega A_1 + \gamma A_2) \sin \Omega\tau] \quad (15b)$$

$$\alpha(t) = \alpha_0' - (1/\kappa)\{c_2\tau + \gamma B_1 - \Omega B_2 - e^{\gamma\tau}[(\gamma B_1 - \Omega B_2) \cos \Omega\tau$$
$$+ (\Omega B_1 + \gamma B_2) \sin \Omega\tau]\} \quad (15c)$$

where $\tau = t - t_0$ and $d = -\kappa(V_0' - \alpha_0') - c_1 - \gamma B_1 + \Omega B_2$. The coefficients A_1, A_2, B_1, and B_2 are determined from the initial conditions (11) and Eqs. (10a). They are expressed as

$$A_1 = -\frac{d}{\kappa}, \qquad A_2 = \frac{c_2}{\Omega\kappa} + \frac{\dot{V}_0 - \gamma A_1}{\Omega}$$

$$\dot{V}_0 = \frac{dV(0)}{dt} = c_{11}(V_0' - \alpha_0') + c_{12}\omega_0' - c_{10} \quad (16a)$$

$$B_1 = \omega_0' + \frac{c_2}{\kappa}, \qquad B_2 = \frac{\dot{\omega}_0 - \gamma B_1}{\Omega}$$

$$\dot{\omega}_0 = \frac{d\omega(0)}{dt} = c_{21}(V_0' - \alpha_0') + c_{22}\omega_0' + c_{20} \quad (16b)$$

Equations (15) indicate that the body motion includes two components. The first terms of Eqs. (15a) and (15b) correspond to body rotation with the constant angular speed $-c_2/\kappa$ and a vertical translation with uniform acceleration $-c_2/\kappa$. Also present is a drift with constant velocity $\alpha_0' - (c_1 + 2\gamma B_1 - \dot{\omega}_0)/\kappa$ that depends on the initial angle of attack and angular velocity. These terms are associated with a nonoscillatory motion, which is called the mean state. The second component corresponds to periodic modulations of the mean state. These oscillations are neutral for $\gamma = 0$, unstable for positive γ, and stable for negative γ. For zero base radius $a_e = 0$, Eq. (13) specializes to

$$\gamma = 0, \qquad \kappa = \Omega^2 = (c_m \pi / \Delta_0)g_0, \qquad c_1 = (c_m c_g \pi / \Delta_0)g_1$$

$$c_2 = (c_m c_g \pi / \Delta_0)g_0$$

This case corresponds to neutral oscillations. For heavy bodies with base radius $a_e = 1$ and small ballistic coefficients $c_l \ll 1$ and $c_m \ll 1$, we can linearize about c_l and c_m. Equations (13) yield

$$\gamma = \pi c_m \left(x_e^2 - c_l/c_m \right), \qquad \kappa = \Omega^2 = c_m \pi (g_0 - x_e) \quad (17a)$$

$$c_1 = \pi c_m c_g \left(g_1 - x_e^2 \right), \qquad c_2 = \pi c_m c_g (g_0 - x_e)$$

$$d = \pi c_l (\omega_0 + c_g) \quad (17b)$$

Equations (17) show that oscillations are unstable for $x_e^2 > c_l/c_m$. This case fits the experimental conditions of Ref. 7. For $x_e^2 \leq c_l/c_m$, oscillations are stable or neutral. In all cases the increment is small, $\gamma \sim c_m \sim \Omega^2 \ll 1$. The expressions for the vertical speed and angular velocity are

$$V_c = V_0' - c_g\tau + A_1(e^{\gamma\tau}\cos\Omega\tau - 1) + A_2 e^{\gamma\tau}\sin\Omega\tau$$

$$\omega = -c_g + e^{\gamma\tau}(B_1\cos\Omega\tau + B_2\sin\Omega\tau)$$

The first equation indicates that the c.g. oscillates near its mean state associated with free drop. If the body dynamics is stable, $\gamma < 0$, then the oscillations vanish as $\tau \to \infty$. Nevertheless, they induce the constant vertical velocity $-A_1 = c_l\pi(\omega_0' + c_g)/\Omega^2$. The second equation shows that the angular velocity oscillates near its mean level, $\bar{\omega} = -c_g$, associated with free drop.

Eigenvalues λ_1 and λ_2 Are Real

If $\lambda_1 = \gamma + \nu$ and $\lambda_2 = \gamma - \nu$ [$\nu = \sqrt{(\gamma^2 - \kappa)}$] are real, then the solution of Eqs. (10a) or Eqs. (12) is

$$V_c(t) = V_0' + (d - c_2\tau)/\kappa + e^{\gamma\tau}(A_1 ch\nu\tau + A_2 sh\nu\tau)$$

$$\omega = -(c_2/\kappa) + e^{\gamma\tau}(B_1 ch\nu\tau + B_2 sh\nu\tau) \tag{18a}$$

$$Y_c(t) = Y_0' + (V_0' + d/\kappa)\tau - (c_2/2\kappa)\tau^2$$

$$+ (e^{t\gamma}/\kappa)[(\gamma A_1 - \nu A_2)ch\nu\tau + (\gamma A_2 - \nu A_1)sh\nu\tau] \tag{18b}$$

$$\alpha(t) = \alpha_0' - (1/\kappa)\{c_2\tau + \gamma B_1 - \nu B_2 - e^{\gamma\tau}[(\gamma B_1 - \nu B_2)ch\nu\tau$$

$$+ (\gamma B_2 - \nu B_1)sh\nu\tau]\} \tag{18c}$$

where $d = -\kappa(V_0' - \alpha_0') - c_1 - \gamma B_1 + \nu B_2$ and the coefficients are

$$A_1 = -(d/\kappa), \qquad A_2 = c_2/\nu\kappa + (\dot{V}_0 - \gamma A_1)/\nu$$

$$B_1 = \omega_0' + c_2/\kappa, \qquad B_2 = (\dot{\omega}_0 - \gamma B_1)/\nu \tag{19}$$

Again the body motion has two components. The first component is similar to that of the earlier case. It is associated with a pure gravity drop and can be treated as a basic state. The second component is relevant to an exponential drift from or toward the basic state depending on the signs of the eigenvalues. If $\lambda_1 < 0$ and $\lambda_2 < 0$, then the exponents decay as $\tau \to \infty$, and the body motion evolves from the initial conditions to the basic state, which includes rotation with constant angular velocity and translation with constant acceleration. If λ_1 and/or λ_2 are positive, then the exponential terms grow with time, and the body departs from its basic state (aperiodic divergence). If $\nu = 0$, then the second component of the body motion is governed by the sign of γ.

The aforementioned analytical solutions and stability characteristics of the body dynamics can be used for fast qualitative estimations of the body trajectory outside the cavity. To our knowledge, these results are new.

Results and Discussion

To calculate the body trajectory including all phases of the separation process Eqs. (2a) are numerically integrated using a sixth-order Runge–Kutta scheme (see Ref. 9). Our computational code includes a module that calculates the lift force and pitching moment for phases 1–3 using the analytical results of Ref. 5. The accuracy of the predictions can be related to the size of the perturbation parameters and uncertainties in the experimental launch conditions. (Because these data are referenced, their accuracy can be obtained from the authors.) In the best cases, the accuracy can be as good as a few percent when the aerodynamic forces are small compared to the weight and the characteristic pitch inertia with experimental initial conditions that matched those assumed in the theory. Large excursions can result if large-scale shear layer motions occur and other disturbances evolve in the external flow.

The combined asymptotic and numerical method described provides a means to calculate rapidly body trajectories. One trajectory is normally predicted in less than 0.5 min using a personal computer Pentium 166. This quick-turnaround personal-computer-
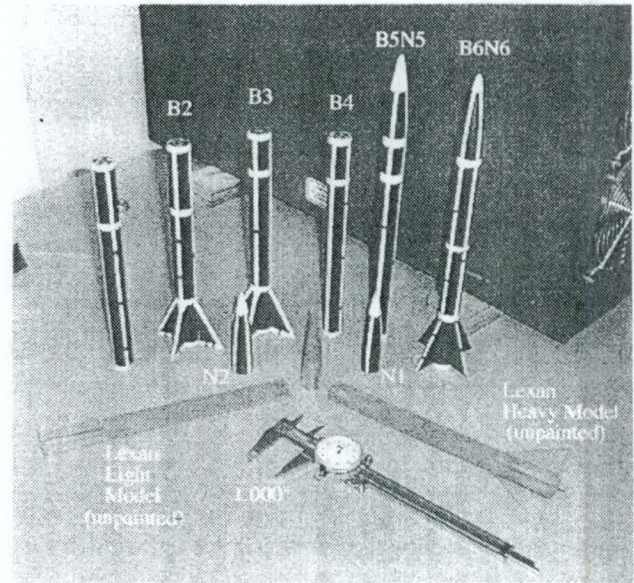

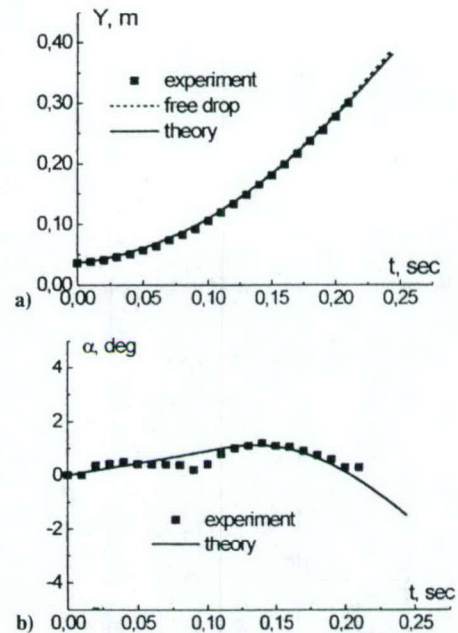Fig. 2 Models for free-drop tests in the IIT wind tunnel.

Fig. 3 Model B4N2, $U_\infty = 62.3$ m/s, $Y_0 = 1.42$ in. (0.0361 m), $\alpha_0 = 0$ deg, $V_0 = 8$ in./s (0.2032 m/s), and $\omega_0 = 9$ deg/s.

oriented tool will be compared to the subsonic experimental data[7] in what follows.

Experimental Data

Drop tests[7] were conducted in the National Diagnostic Wind Tunnel of the Illinois Institute of Technology (IIT) Fluid Dynamics Research Center at the Mach number range $0.12 < M < 0.23$. The rectangular cavity of 20 in. (0.508 m) length, 41 in. (1.0414 m) width, and 4 in. (0.1016 m) height was mounted on the top wall of the wind-tunnel test section. The test articles were bodies of revolution of radius $\hat{a}_0 = \frac{3}{8}$ in. (0.009525 m) and nose length $\hat{x}_n = 3.56$ in. (0.090424 m) (Fig. 2). Two models (B1N1 and B4N2) were ogive cylinders 12 in. (0.3048 m) length. The third model (B5N5) had an elliptic nose and a total length of 11.5 in. (0.2921 m). The heaviest model, B1N1, had mass $m = 111.85$ g, moment of inertia $I = 0.0014$ kg·m², and c.g. location $\hat{x}_0 = 6.16$ in. (0.1565 m). For model B4N2, $m = 46.14$ g, $I = 0.0008$ kg·m², and $\hat{x}_0 = 5.94$ in. (0.1509 m). The lightest model, B5N5, had $m = 8.72$ g and $I = 0.000015$ kg·m². In these experiments, bodies were dropped from a cavity in the IIT wind tunnel.
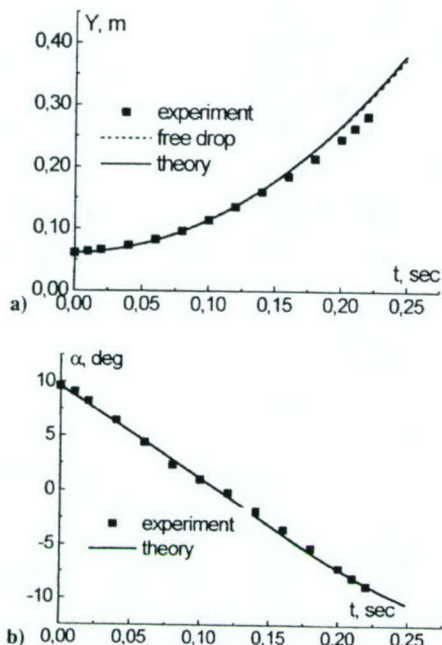
Fig. 4   Model B4N2, $U_\infty = 41.3$ m/s, $Y_0 = 2.4$ in. (0.061 m), $\alpha_0 = 9.6$ deg, $V_0 = 2$ in./s (0.0508 m/s), and $\omega_0 = -80$ deg/s.
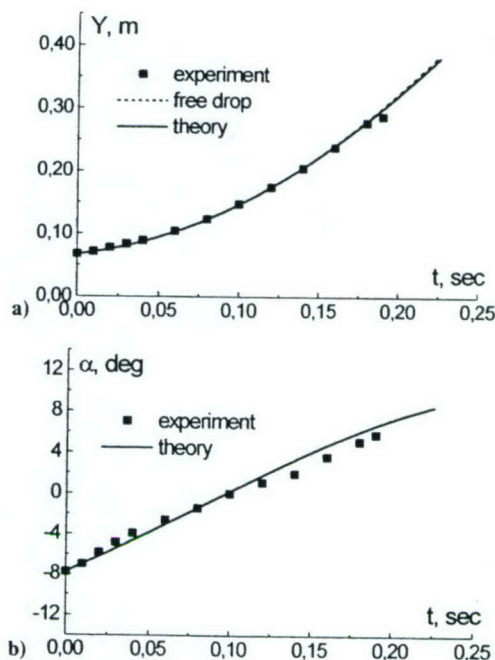

Fig. 6   Model B1N1, $U_\infty = 40.8$ m/s, $Y_0 = 2.65$ in. (0.0673 m), $\alpha_0 = -7.8$ deg, $V_0 = 15$ in./s (0.381 m/s), and $\omega_0 = 80$ deg/s.
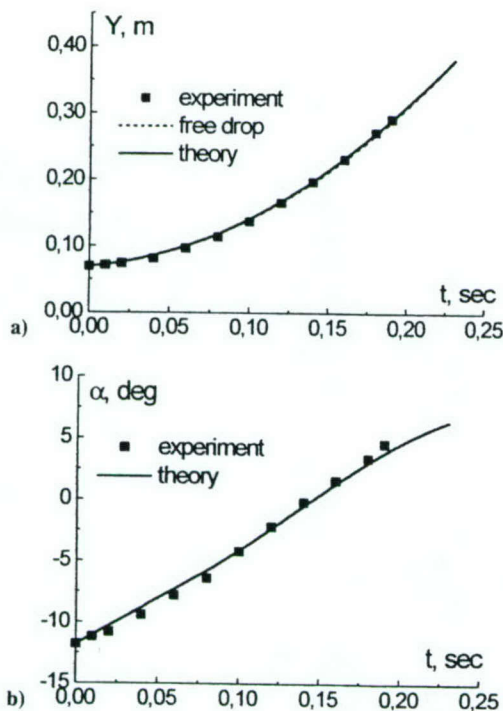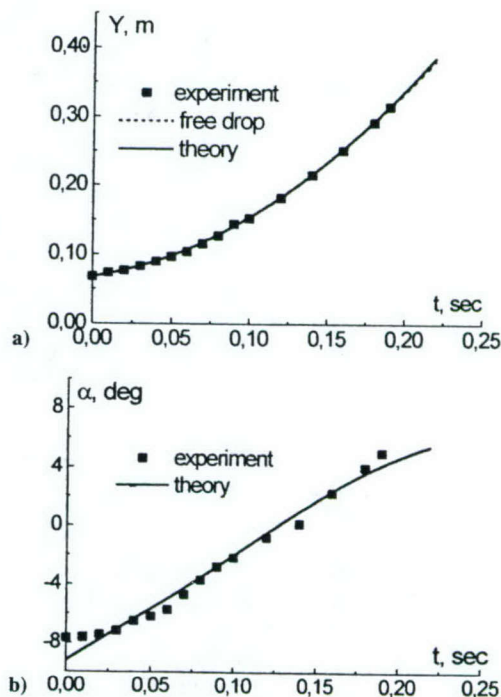

Fig. 5   Model B1N1, $U_\infty = 62.7$ m/s, $Y_0 = 2.72$ in./s (0.0691 m), $\alpha_0 = -11.8$ deg, $V_0 = 9$ in./s (0.2286 m/s), and $\omega_0 = 75$ deg/s.

Fig. 7   Model B4N2, $U_\infty = 40.6$ m/s, $Y_0 = 2.65$ in. (0.0673 m), $\alpha_0 = -9.2$ deg, $V_0 = 15$ in./s (0.381 m/s), and $\omega_0 = 70.8$ deg/s.

The models were released by withdrawing pins holding them at their noses and tails.

Comparison with Experiment

Preliminary analysis of the experimental data shows that during the release time $t_r \approx 0.03$ s, the initial angular and vertical velocities can be essentially affected by uncontrolled disturbances that may be induced by the release mechanism. During the release time, the gravity force may increase the pitch rate, if the model ends are not released simultaneously. This motivated identification of the actual initial angular speed $\widehat{\omega}_0$ and vertical velocity $\widehat{V}_0$ by differentiating the experimental distributions of the pitch angle $\widehat{\alpha}(t)$ and the c.g. vertical coordinate $\widehat{Y}_c(t)$.

Figures 3a–10a show comparisons between predicted (solid lines) and experimental (symbols) c.g. trajectories for all three models. Dashed lines indicate the free-drop trajectories under the gravity force only. As already noted, the lift is small compared to the body weight. The free drop in a vacuum is very close to the computational results and the experimental data for moderate angles of attack, especially for the heavier model, B1N1. However, the vacuum curve diverges from the experimental data if the body enters into the external stream at relatively large $\widehat{\alpha}$. This is clearly seen in Figs. 4a, 8a, and 10a. In these cases, the theoretical prediction accounting for aerodynamic loads is in a good agreement with the experiment. Moreover, the theoretical model is capable of capturing trajectory nuances shown in Fig. 8a.
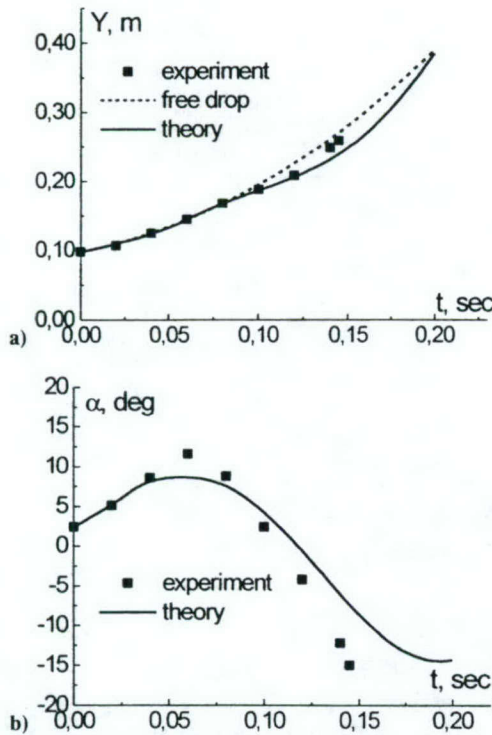
Fig. 8   Model B5N5, $U_\infty = 62.5$ m/s, $Y_0 = 3.85$ in. (0.978 m), $\alpha_0 = 2.4$ deg, $V_0 = 19$ in./s (0.4826 m/s), and $\omega_0 = 140$ deg/s.
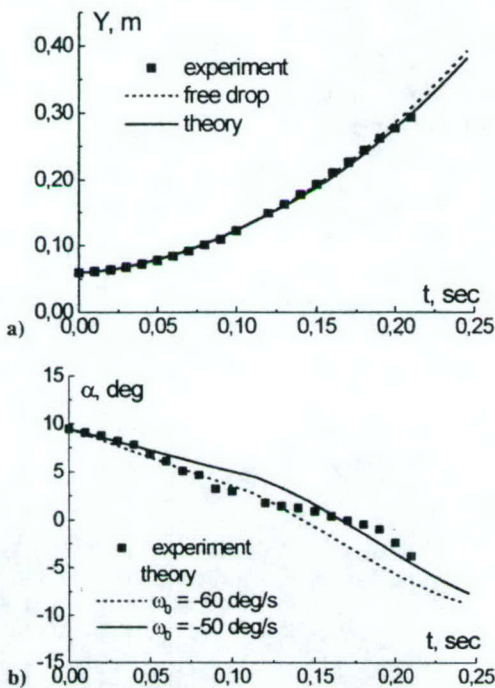
Fig. 9   Model B4N2, $U_\infty = 62.3$ m/s, $Y_0 = 2.33$ in. (0.592 m), $\alpha_0 = 9.5$ deg, and $V_0 = 6$ in./s (0.1524 m/s).
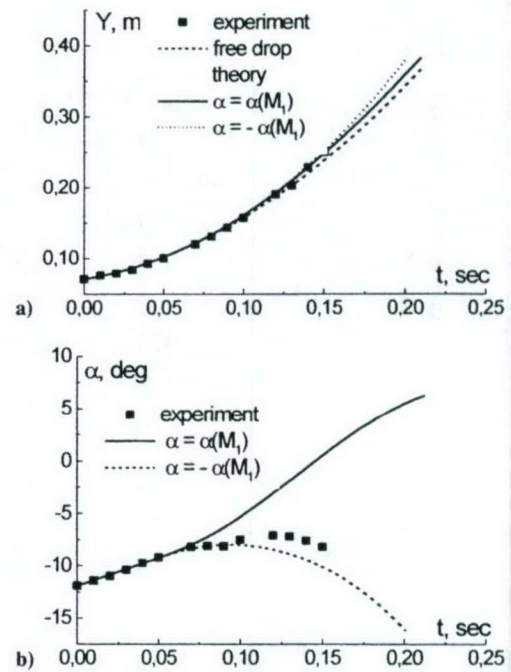

Fig. 10   Model B4N2, $U_\infty = 62.1$ m/s, $Y_0 = 2.8$ in. (0.0711 m), $\alpha_0 = -11.9$ deg, $V_0 = 15$ in./s (0.381 m/s), and $\omega_0 = 52.86$ deg/s.
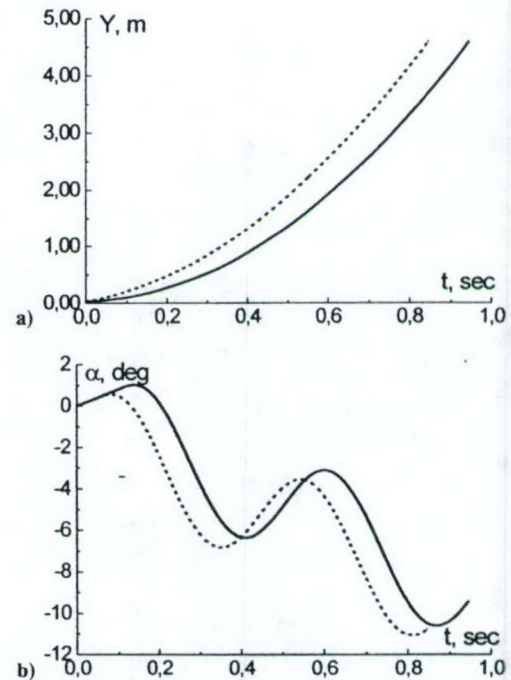

Fig. 11   Effects of initial vertical velocity: model B4N2, $U_\infty = 62.3$ m/s; $Y_0 = 1.42$ in. (0.0361 m); $\alpha_0 = 0$ deg; $\omega_0 = 8$ deg/s; —— , $V_0 = 8$ in./s (0.2032 m/s); – – –, $V_0 = 50$ in./s (1.27 m/s).

Figures 3b–10b show a comparison between predicted (lines) and experimental (symbols) histories of the angle of attack $\hat{\alpha}(t)$. Figures 3b–6b show good agreement between the theory and the experiment. The agreement is only satisfactory for the cases shown in Figs. 7b–9b. Rough estimates indicate that the initial growth of $\hat{\alpha}$ (Fig. 7b) may be associated with an initial pitch impulse generated by the release mechanism under a gravitational couple from the pins. In this case, both the initial angle of attack and angular speed were estimated from the experimental data. These were used as the initial conditions for the calculations. For the lightest model, B5N5 (Fig. 8b), the discrepancy seems to be due to the difference between the actual nose shape (elliptic) and the shape used in our

calculations (parabolic ogive). Unfortunately, calculations were not possible for the actual nose because its geometry was not available. Note that the nose shape becomes more important at large pitch angles. The divergence of the predicted and experimental curves in Fig. 9b seems to be due to the flow inside the cavity, which is presently not included in our modeling. Namely, the nonuniform upwash field due to the recirculatory flow in the cavity has not been included. Such an upwash field will change the crossflow angle of attack from that due solely to the vertical speed of the body, which has been accounted for in the approximate model described here. This can be thought of as a first estimate of the flow physics. The effect of the upwash field can be considered a refinement of this
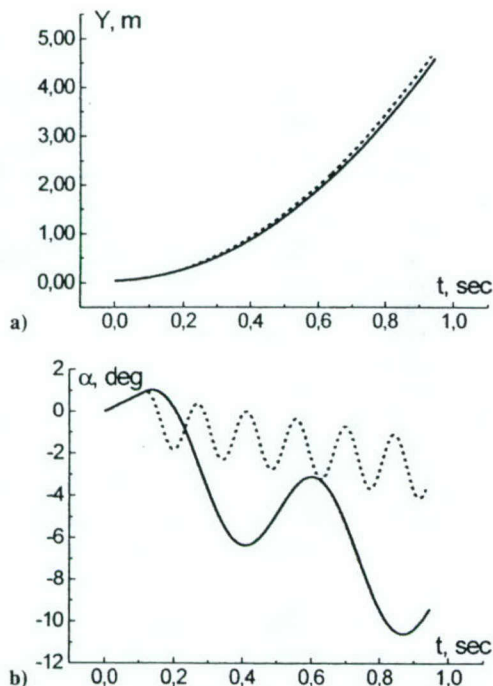
Fig. 12   Effect of freestream velocity on the body trajectory: model B4N2, $Y_0 = 1.42$ in. (0.0361 m); $\alpha_0 = 0$ deg; $V_0 = 8$ in./s; $\omega_0 = 8$ deg/s; ——, $U_\infty = 62.3$ m/s; ———, $U_\infty = 200$ m/s.
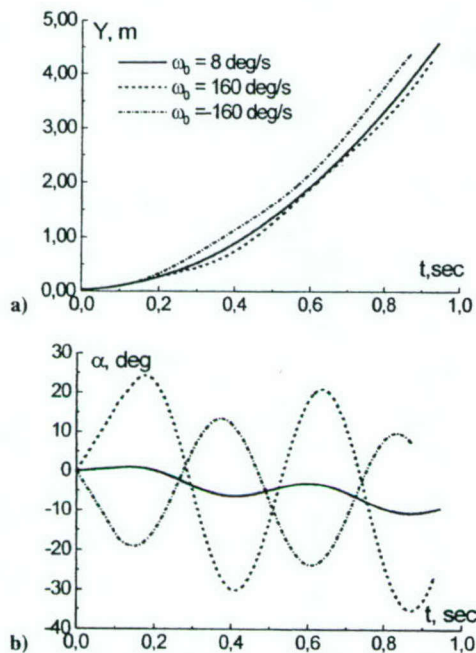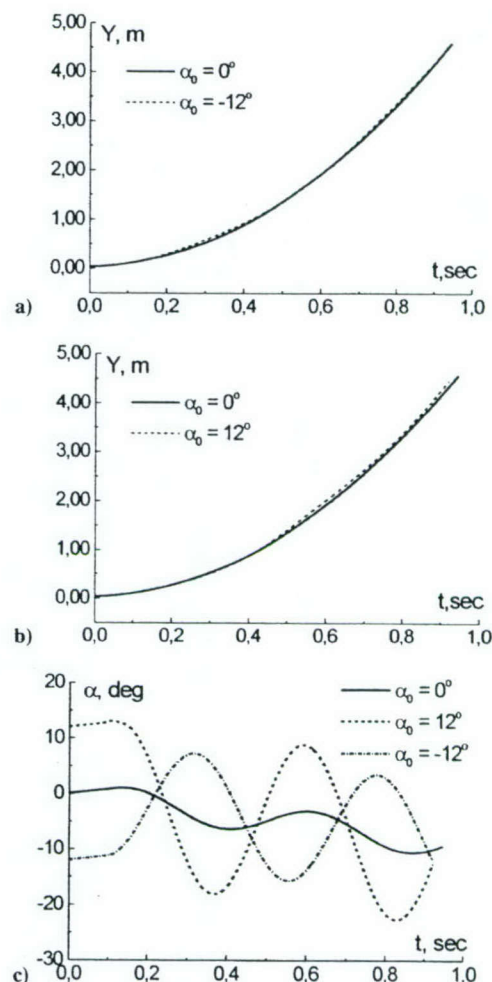

Fig. 13   Influence of the initial angular speed on the body trajectory: model B4N2, $U_\infty = 62.3$ m/s, $Y_0 = 1.42$ in. (0.0361 m), $\alpha_0 = 0$ deg, and $V_0 = 8$ in./s (0.2032 m/s).

Fig. 14   Influence of the initial pitch angle on the body trajectory: model B4N2, $U_\infty = 62.3$ m/s, $Y_0 = 1.42$ in. (0.0361 m), $V_0 = 8$ in./s (0.2032 m/s), and $\omega_0 = 8$ deg/s.

model in which this recirculatory flow can be estimated from the empty cavity flow. An inviscid approximation for the latter is given in Ref. 4 for deep cavities. (Deep cavities are almost bridged at their top end by the shear layer in contrast to shallow cavities for which the shear layer will collide with their bottom.) Further refinements would include the interaction of the moving body with this nonuniform flow for both deep and shallow cavities. Pitch oscillations observed in phase 1 (body is totally inside the cavity) clearly indicate the presence of this effect, which may also explain the substantial difference between the theory and the experiment shown in Fig. 10b.

As indicated earlier, the pitch behavior in phase 3 (body is outside the cavity) strongly depends on the entry condition, which is a function of the angular velocity, vertical speed, and their derivatives. For the case shown in Fig. 10b, the shear layer displacement from its basic state into the cavity may cause a phase jump of the right-hand-side term in Eq. (2a) from 0 to 180 deg. Such a jump affects the pitch history outside the cavity. This is illustrated in Fig. 10b by the dotted line that was calculated with the opposite sign of the pitching moment. It is seen that this curve is in a good agreement with the experimental data. On the other hand, experimental curves, shown in Figs. 5b, 6b, and 7b for approximately the same initial conditions, have a regular behavior, that is, they are in a good agreement with the computations performed without changes of the sign of pitching moment. These findings suggest that there is a bifurcation in the pitch history $\alpha(t)$ when the body enters into the external stream. The trajectory equations allow such a bifurcation because the aerodynamic forcing terms of Eqs. (2a) are nonlinear (quadratic) functions of speeds V and ω. One of two possible trajectories is selected when the body crosses the shear layer. Therefore, phase 2 serves as a trigger of the pitch bifurcation. Accurate modeling of this mechanism is important for prediction of the pitch history and store trajectory in the next phase, when the store is outside the cavity. To verify this hypothesis additional theoretical, numerical, and experimental studies are needed.

Parametric Studies

Parametric studies of the body trajectory were conducted for different initial conditions, body parameters, and freestream speeds. The results are shown in Figs. 11–15. Variations of the initial vertical velocity cause not only c.g. acceleration but phase shift of the pitch angle (Fig. 11). In accord with the analytical solution discussed earlier, an increase of the freestream velocity leads to a substantial increase of the mean pitching angle and the pitch oscillation
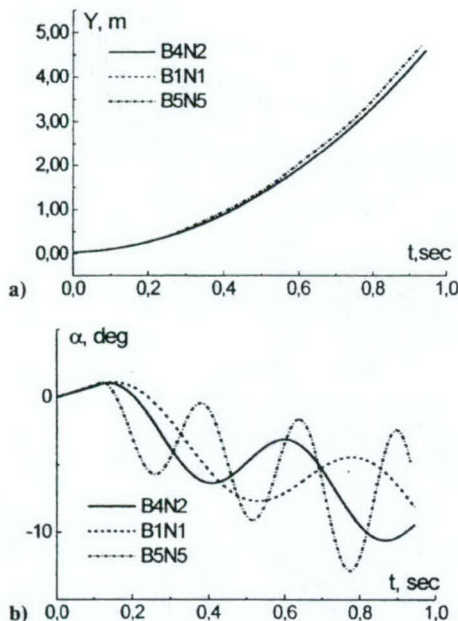
Fig. 15   Trajectories of different models: $U_\infty = 62.3$ m/s, $Y_0 = 1.42$ in. (0.0361 m), $\alpha_0 = 0$ deg, $V_0 = 8$ in./s (0.2032 m/s), and $\omega_0 = 8$ deg/s.

frequency (Fig. 12), while the c.g. trajectory is changed slightly. Figure 13 shows that the pitch oscillation amplitude increases and the phase shift occurs as the initial angular speed increases. Amplification of the pitch oscillations is stronger in the case of positive ω_0 with the c.g. trajectory also noticeably affected. The effect of the initial pitch angle is similar to the effect of ω_0 (compare Figs. 14 and 15). However, the variation of the c.g. trajectory in this case is smaller.

Trajectory dependencies on the body shape are shown in Fig. 15. The calculations were performed for three experimental models of Ref. 7 under the same initial conditions. As expected, the highest amplitude and frequency of the body oscillations correspond to the lightest model, B5N5. It is also seen that the body trajectories outside the cavity are consistent with the analytical solution discussed earlier.

Conclusions

This paper discussed modeling of two-DOF vertical and pitching motions of thin bodies of revolution separating from a rectangular cavity into an external freestream. The problem is analyzed using combined asymptotic and numerical methods. The body dynamic equations include aerodynamic forces and moments, which are predicted using approximate analytical solutions obtained in our previous studies within the framework of the slender body theory. Different phases of the separation process were analyzed using small perturbation theories. This leads to simplifications of the trajectory equations and their integration in closed form for different typical cases associated with phase 1 (body is inside the cavity) and phase 3 (body is outside the cavity). These analytical solutions provide explicit dependencies of the body trajectory on the flow and body characteristics, which allows identification of the critical parameters and insight gained into the physics of the separation process.

The numerical code predicting the trajectories for all three phases of store separation was validated by comparison with the experiment. For a major portion of the data, the calculations are in a good

agreement with experiment. Moreover, the theory is able to capture nuances of the body pitching observed experimentally. These results confirm our theoretical model. However, there are cases when the agreement is only satisfactory. The body separation is affected by more complex flow phenomena, which are not captured by our model. One discrepancy seems to be due to the slip-surface displacement induced by the shear layer instability and/or self-excited oscillations of the cavity flow. These effects can lead to the pitching moment phase jump from 0 to 180 deg during phase 2, when the body crosses the shear layer. The jump may trigger quick transition from one pitch angle trajectory to another for phase 3, when the body is outside the cavity. Our calculations showed that this interpretation is consistent with the experimental data indicating the existence of two substantially different pitching trajectories for approximately the same initial conditions. Because nonlinear dynamic equations are involved, the body trajectory may have a bifurcation point associated with phase 2. Although this transitional phase is relatively short, its aerodynamics may determine the selection between possible trajectories outside the cavity. Further theoretical and experimental studies are needed to establish and clarify the bifurcation mechanism. Our future work will extend this model to transonic speeds.

References

[1]Goodwin, F. K., Dillenius, M. F. E., and Nielsen, J. N., "Prediction of Six-Degree-of-Freedom Store Separation Trajectories at Speeds up to the Critical Speed. V.1. Theoretical Methods and Comparison with Experiment," U.S. Air Force Flight Dynamics Lab., Dayton, OH, AFFDL-TR-72-83, Oct. 1972.

[2]Wood, M. E., "Application of Experimental Techniques to Store Release Problems," *Proceedings of Nielsen Engineering and Research Inc., Conference on Missile Aerodynamics*, Monterey, CA, 1988.

[3]Stanek, M. J., Sinha, N., Ahuja, V., and Birkbeck, R. M., "Acoustic-Compatible Active Flow Control for Optimal Weapon Separation," AIAA Paper 99-1911, 1999.

[4]Malmuth, N. D., Fedorov, A. V., Shalaev, V., Cole, J., Khokhlov, A., Hites, M., and Williams, D., "Problems in High Speed Flow Prediction Relevant to Control," AIAA Paper 98-2695, June 1998.

[5]Malmuth, N. D., Shalaev, V. I., and Fedorov, A. V., "Combined Asymptotics and Numerical Methods for Store Interactions," Final Rept., Contract F49620-96-C-0004, Air Force Office of Scientific Research/NM, Oct. 1998; available from Defense Technical Information Center [online database], URL: http//stient.dtic.mil.

[6]Cole, J. D., *Perturbation Methods in Applied Mathematics*, Waltham, MA, 1968.

[7]Hites, M., Williams, D., and Malmuth, N., "Photographic Investigation of the Dynamics of an Ogive Model Near a Cavity at Subsonic Mach Numbers," Final Rept., Fluid Dynamics Research Center, Illinois Inst. of Technology, Chicago, IL, Jan. 1998.

[8]Nielsen, J. N., *Missile Aerodynamics*, McGraw–Hill, New York, 1960.

[9]Korn, G. A., and Korn, T. M., *Mathematical Handbook*, McGraw–Hill, New York, 1968.

P. Givi
Associate Editor

ANALYTICAL MODELING OF TRANSONIC STORE SEPARATION FROM A CAVITY

Vladimir Shalaev[*], Norman Malmuth[†] and Alexander Fedorov[*]

[*] Department of Aeromechanics and Flight Engineering, Moscow Institute of
Physics and Technology, Zhukovski 140182, Russia

[†] Rockwell Scientific Company, Thousand Oaks, California 91360

E-mail: **nmalmuth@rwsc.com**

Abstract

Aerodynamic and dynamic problems relevant to separation of a thin body of revolution from rectangular cavities into subsonic and transonic flows are considered. In the dominant approximation, the shear layer separating cavity flow from outer flow is approximated by a plane slip surface of zero potential and the flow is described by slender body theory. Asymptotic models for inner (near field) and outer (far field) asymptotic regions are provided. Analytical solutions of the inner asymptotic problem as a basis for systematic approximation desktop PC prediction schemes are obtained for all phases of the body motion. This allows extraction of the basic physical parameters governing the separation process, illumination of the basic physics and dramatic simplification of the trajectory determination. Simple analytical and empirical models are presented for cross-flow drag, friction drag and base drag. The theoretical results are used to analyze 3DOF body dynamics for separation from a cavity into a transonic freestream. Numerical examples including critical cases of recontact and ricochet for ultimate application of trajectory control of light and other bodies are discussed. Strong sensitivities and trajectory bifurcations from small changes in initial conditions are discussed and the role of wave drag in connection with such applications is discussed.

Nomenclature

$\hat{a}_0$ = maximum body radius

a = local body radius

A = cross-sectional area of actual body

A_{eq} = equivalent body area

C_D = total drag coefficient

C_{DF} = friction drag coefficient

C_{DB} = base drag coefficient

C_{DW} = wave drag coefficient

C_{DP} = cross-flow drag coefficient

D_d = dipole intensity

d_0 = cavity half span

g = gravity acceleration

H = vertical distance

H_0 = cavity depth

I = moment of inertia

$\hat{l}_0$ = body length

L = lift force

M = pitching moment

p = $\dfrac{\hat{p} - p_\infty}{\delta^2 \rho_\infty U_\infty^2}$, pressure coefficient

r = polar radius in the inner region

$\tilde{r}$ = $r\delta^2$, polar radius in the outer region

t = time

u, v, w = flow velocity components

W = $w - iv$, complex conjugate velocity

V_e = effective cross-section speed

V_o = speed of center of gravity

X, Y, Z = coordinates attached to cavity

x, y, z = coordinates attached to body

Y_o = vertical coordinate of the center of gravity

x_0 = body nose coordinate

x_e = body base coordinate

α = $\dfrac{\hat{\alpha}}{\delta}$, pitch angle

▓ = angle between the body cross-section and OZ-axis

δ = $\hat{a}_0 / \hat{l}_0$, half of body thickness ratio

ε = ratio of the body radius to the cavity half span

ω = pitch angular speed

Π = $\Phi + i\Psi$, complex flow potential

Φ = flow potential

θ = polar angle

ζ = $= Z + iY$

ρ = density

Subscripts

∞ = free stream

o = center of gravity

f = slip surface

b = body surface

Superscripts

$\wedge$ = dimensional values

$+$ = values above shear-layer

$\sim$ = dimensionless functions in outer region

1. Introduction

Diverse aspects of the store separation problem have been intensively investigated. Engineering, semi-empirical, computational and experimental approaches are illustrated in Refs. [1-3]. Most studies have been concerned with external separation at subsonic or supersonic speeds. Relatively less attention has been given to separation from cavities, especially at transonic speeds. This is because the problem is very complicated due to a large number of parameters governing the flow structure and the vast variety of physical phenomena involved in the separation process.

Our objectives are to fill this gap by identifying the first-order physics, solve unit problems related to modeling the basic mechanisms and develop fast and robust methods for predicting store trajectories. Key thrusts are to divide the separation process into component phases, formulate unit problems for each phase and solve these problems using a combination of asymptotic and numerical methods. In contrast to ad-hoc approaches, these give systematic

approximation schemes modeling store separation processes that easily couple with rigid-body dynamics for desktop PC "design" codes that rapidly predict store trajectories They also improve our understanding of the physics, parametric limits and trends. Another ultimate objective with these methods is to provide convenient tools to obtain control laws for trajectory manipulation systems. An additional theme is to assess the impact of noise control measures such as those with cavity blowing on separation trajectories.

Matched asymptotics suggest that a component of the global problem of interaction of the separating with the entire airplane flow field is the local problem of separation of a body of revolution from a rectangular cavity into an external subsonic or transonic flow of uniform freestream speed. In this physical system we divide the separation process into three phases, which will hereinafter be denoted Phases 1-3. In Phase 1, the body moves inside the cavity, whereas in Phase 2 the body crosses the shear layer separating the cavity flow from external stream. In Phase 3 the body is totally outside the cavity and moves in the external flow.

To simplify the problem and obtain analytical solutions it is assumed that the body is slender, the vertical flow velocity and angles of attack $\hat{\alpha}$, the ratio of shear-layer thickness $\hat{\delta}_s$ to body radius $\hat{a}_0$ and flow velocities inside the empty cavity are small. Also, the cavity height $\hat{H}_0$ and half-width $\hat{D}_0$ are much larger than the body radius. Deep cavities of the length-to-height ratio $\hat{L}_0 / \hat{H}_0 < 6$ are considered and this assumes that the outer flow weakly penetrates into the cavity. Due to these simplifications viscous effects are neglected and the flow over the body can be described by slender body theory.[4-6] The shear layer is treated as a free slip vortex sheet surface with a tangential velocity jump and continuous normal velocity, pressure and the density across itself; the flow in the empty cavity is neglected the cavity wall effect is considered as a small perturbation. From this approximation, it is possible to isolate the wall-body and slip surface-body interactions and treat them as separate component sub-problems whose solutions can be superimposed to provide the complete flow. Intrinsic to this approximation is the assumption that the highly active slip surface can be treated as its temporal mean since the time fluctuations are short on the Froude time scale of dropping of the store. Even with the temporal average approximation the coupling of the free boundary shape

with the solution represents a difficult component problem. This is because the shape of the free boundary is not known *a priori* and should be determined as a part of the solution since it strongly and nonlinearly interacts with it. This is a challenging problem even for current CFD modeling, even with unstructured adaptive grids and many methods are in development to solve it. A new approach to slip surface-body interactions is discussed in Ref. [7]. To develop a transparent model of the physics as well as rapid turnaround prediction method, the slip surface is assumed to be a plane of zero potential. This simplification of the boundary-valued problem corresponds to a first step of a global iteration procedure.[7] A similar technique was used for analyses of subsonic store separation and gave satisfactory agreement with experiments.[8]

In Section 2, the inner asymptotic problem is formulated. In Section 3, analytical expressions for the flow potential in Phases 1 and 3 are obtained in in the form of rapidly converging series. In Section 4, a conformal mapping is applied to obtain the solution for Phase 2. These solutions differ from known results such as[13] by new terms related with three-dimensional flow effects. In Section 5, the outer asymptotic problem is analyzed. An equivalence rule similar to [14-19] is formulated. Matching conditions and a general form of the outer solution are determined. Different drag components including the wave drag, cross-flow drag, viscous drag and base drag are discussed. The analytical results are incorporated into a numerical algorithm solving the 3-DOF trajectory equations. In Sections 6, numerical examples of store separations from cavities are presented and discussed. It is demonstrated that the theoretical model can simulate such complex phenomena as the re-contact and ricocheting.

2. Inner asymptotic problem

Consider a slender body of revolution released from the top wall of a rectangular cavity at an initial instant $\hat{t} = 0$. The initial angle of attack $\hat{\alpha}_0$, vertical speed $\hat{V}_0$ and angular speed $\hat{\omega}_0$ are assumed to be small,

Neglecting terms $O(\hat{\alpha}^2)$ and assuming that the transverse coordinates of the CG are constant, in particular, $Z_o(t) = 0$, we obtain the relations

$$X = X_o(t) + x, \ Y = Y_o(t) + y - x\alpha, \ Z = z, \quad (3)$$

of the order of $O(\delta)$. The body drops under gravity along the cavity symmetry plane and separates from the cavity into the external flow. At the initial instant, the flow within the cavity is neglected. The cavity interior is separated from external stream by the slip surface bridging the cavity edges. The flow scheme for Phase 2 and the coordinate systems are shown in Figures 1 and 2. The coordinate system $O\widehat{XYZ}$ is attached to the unperturbed slip surface, as shown in Fig.1. Therein, the $O\hat{X}$-axis is directed along the freestream velocity and $O\hat{Y}$ as well as $O\hat{Z}$ are respectively vertical and spanwise coordinates. The coordinate system $o\widehat{xyz}$ is attached to the body center of gravity (CG) that moves vertically with the velocity $\hat{V}_o(\hat{t})$. The $o\hat{x}$-axis is directed along the body symmetry axis and the $o\hat{y}$ and $o\hat{z}$ axes lie in the cross-sectional plane. The direction of $o\hat{z}$-axis coincides with the direction of $O\hat{Z}$ - axis. The axes $o\hat{x}$ and $o\hat{y}$ are inclined with respect to the axes $O\hat{X}$ and $O\hat{Y}$ at the angle $\hat{\alpha}(\hat{t})$; they rotate around $o\hat{z}$-axis with the angular speed $\hat{\omega}(\hat{t})$. Along with the Cartesian coordinates we use the polar coordinates, $\hat{r}$ and θ, specified as

$$\hat{z} = \hat{r}\cos\theta, \ \hat{y} = \hat{r}\sin\theta. \quad (1)$$

The dimensionless variables for the inner asymptotic region are determined as

$$X = \frac{\hat{X}}{l_0}; Y = \frac{\hat{Y}}{a_0}; Z = \frac{\hat{Z}}{a_0}; \ x = \frac{\hat{x}}{l_0}; y = \frac{\hat{y}}{a_0},$$

$$z = \frac{\hat{z}}{a_0}; d_0 = \frac{\hat{D}_0}{a_0}; L_0 = \frac{\hat{L}_0}{a_0}; H_0 = \frac{\hat{H}_0}{a_0};$$

$$t = \frac{U_\infty \hat{t}}{l_0}; \alpha = \frac{\hat{\alpha}}{\delta}; V_o = \frac{\hat{V}_o}{V_r}; \omega = \frac{\delta U_\infty \hat{\omega}}{l_0}. \quad (2)$$

where $X_o(t)$ and $Y_o(t)$ are streamwise and vertical coordinates of CG.

The flow space consists of the cavity region (above the slip surface) and the external stream region (below the slip surface). In the cavity region, the potential, $\hat{\Phi}^+$, and flow velocities are defined as

3

$$\hat{\Phi}^+ = \hat{a}_0 \hat{V}_r \Phi^+ = \delta^2 U_\infty \hat{l}_0 \Phi, \ \hat{\Phi}_t^+ = \delta^2 U_\infty^2 \Phi_t^+ ,$$

$$\hat{\Phi}_{\hat{X}}^+ = \delta^2 U_\infty u^+, \ \hat{\Phi}_{\hat{Y}}^+ = \delta U_\infty v^+, \ \hat{\Phi}_{\hat{Z}}^+ = \delta U_\infty w^+ ,$$

$$u^+ = \Phi_X^+, \ v^+ = \Phi_Y^+, \ w^+ = \Phi_Z^+. \tag{4}$$

Hereinafter, the superscript "+" denotes flow quantities inside the cavity. The parameters in the external stream region are expressed as

$$\hat{\Phi} = \hat{l}_0 U_\infty \left[1 + \delta^2 (A_0 + \Phi) \right], \ \hat{\Phi}_t = \delta^2 U_\infty^2 \Phi_t ,$$

$$\hat{\Phi}_{\hat{X}} = U_\infty \left[1 + \delta^2 (A_{0X} + u) \right], \ \hat{\Phi}_{\hat{Y}} = \delta U_\infty v ,$$

$$\hat{\Phi}_{\hat{Z}} = \delta U_\infty w, \ u = \Phi_X, \ v = \Phi_Y, \ w = \Phi_Z , \tag{5}$$

where the function $A_0(X,t)$ is determined from matching conditions with outer asymptotic solution. The pressures $\hat{p}$ and $\hat{p}^+$ are determined from the unsteady form of Bernoulli's equation

$$p^+ = \frac{\hat{p}^+ - p_\infty}{\delta^2 \rho_\infty U_\infty^2} = -\varepsilon \left[\Phi_t^+ + \frac{\varepsilon}{2} \left(w^{+2} + v^{+2} \right) \right] ,$$

$$p = \frac{\hat{p} - p_\infty}{\delta^2 \rho_\infty U_\infty^2} =$$

$$= -\left[(A_0 + \Phi)_t + (A_0 + \Phi)_X + \frac{1}{2} \left(w^2 + v^2 \right) \right]. \tag{6}$$

To $O(\delta^2)$, both potentials are harmonic functions in the cross-sectional planes. Accordingly, we can introduce the complex variable ζ, the complex potential $\Pi(\zeta; X,t)$, and the complex conjugate velocity $W(\zeta; X,t)$ as

$$\Pi(\zeta; X,t)) = \Phi + i\Psi ,$$

$$W(\zeta, X,t) = \frac{d\Pi}{d\zeta} = w - iv, \ \zeta = Z + iY$$

where $\Psi(X,Y,Z,t)$ is the nondimensional stream function. The boundary conditions on the body surface $Y = Y_b$ are expressed in the form

$$Y_b(X,Z,t) = H + a\sin\theta , \tag{7a}$$

$$r = a, \ Y_b > Y_f : \ v_n^+ = \frac{\partial \Phi^+}{\partial r} = V_e^+ \sin\theta , \tag{7b}$$

$$r = a, \ Y_b < Y_f : \ v_n = \frac{\partial \Phi}{\partial r} = a_X + V_e \sin\theta , \tag{7c}$$

$$H(X,t) = Y_o(t) - \alpha(t) X ,$$

$$V_e^+(X,t) = \frac{\partial H}{\partial t} = V_o(t) - \omega(t) X ,$$

$$V_e(X,t) = \varepsilon V_e^+(X,t) - \alpha(t) ,$$

where v_n is flow velocity normal to the body surface and $H(X,t)$ is the distance from the body axis to the plane $Y = 0$. Equations (7b) and (7c) correspond to the body surface inside and outside the cavity, respectively; and $V_e^+(X,t)$ and $V_e(X,t)$ are effective velocities of the body cross-section. The slip surface is approximated as a plane of zero potential. In the inner asymptotic region, the side cavity-wall effect has the order $\varepsilon^2 = (\hat{a}_0 / \bar{D}_0)^2$ and can be neglected. In the first step, the problem is decomposed into the following unit problems.

1. Thin body of revolution drops from a flat rigid wall: a) to fluid at rest; b) to a stream.

2. Thin body of revolution drops: a) in fluid at rest toward a flat slip surface of zero potential; b) away a flat slip surface of zero potential in the free stream.

3. Thin body of revolution crosses a flat slip surface of zero potential.

Problems 1a and 2a allow us to find solutions for Phases 1; Problem 3 corresponds to Phase 2; Problem 2b gives the solution for Phase 3; Problem 1b is relevant to external store separation. Using the multipole expansion technique,[10] we solve Problems 1, 2 in the form of Laurent series and obtain coefficients up to the fifth term. This allows for explicit calculations of the flow characteristics with appropriate accuracy. To solve Problem 3 we use conformal mapping.[9,11,13] Some terms of the solutions of Problems 1-3 are known, and we use them for cross checking. The other terms, relevant to three-dimensional effects have not been determined elsewhere.

3. Solutions for Phases 1 and 3

Within the framework of slender body theory,[4-6] the complex conjugate velocity $W(X,\zeta,t)$ is harmonic

4

function in the cross-section planes. The body cross-section profile is a circle of radius $a(X)$ centered at the point $\zeta = iH(X,t)$. This circle moves with the vertical velocity $V_e(x,t)$ in a uniform stream or with the velocity $V_e^+(x,t)$ within cavity. Let the wall or slip surface coincide with the plane $Y = 0$. For half planes containing the body, we have the following problem:

- Find an analytical function $W(X,\zeta,t)$ that satisfies Eqs. (7) for a specified normal velocity on the circle and has zero real (imaginary) part on the slip surface (wall).

The analytical continuation through the wall and the slip surface gives $W(\overline{\zeta}) = \overline{W}(\zeta)$ and $W(\overline{\zeta}) = -\overline{W}(\zeta)$ respectively. Here, the overbar denotes complex conjugation. From these conditions we reduce the half plane problem containing the circle to the problems for full space containing two identical circles located symmetrically with respect to the plane $Y = 0$. The flow scheme in the cross-section plane is shown in Fig. 3. The method of multipole expansions[10] is more appropriate for the analysis. It allows us to express the solutions in the form of Laurent series and obtain relatively simple analytical expressions for aerodynamic forces and moments. As contrasted to the problem analyzed in Ref. [10], problems treated herein are three-dimensional. This leads to new effects, which has not been previously studied and motivates us to represent details of our analysis as well as discuss the new results.

Using the Cauchy formula we obtain the integral equation for the function $W(X,\zeta,t)$ [10]

$$W(X,\zeta,t) = \frac{1}{2i\pi} \int_{|s|=a} \frac{W(X,iH+s,t)ds}{\zeta - iH - s} +$$
$$+ \frac{1}{2i\pi} \int_{|\overline{s}|=a} \frac{W(-iH+\overline{s})d\overline{s}}{\zeta + iH - \overline{s}} \quad (8)$$

Expanding the kernels into Taylor series, using the analytical continuation and flow symmetry we obtain the solution of this equation and the complex potential in the form of the series

$$W = \sum_{n=0}^{\infty} a^{n+1} \left\{ \frac{C_{-n-1}}{(\zeta - iH)^{n+1}} \pm \frac{\overline{C}_{-n-1}}{(\zeta + iH)^{n+1}} \right\},$$
$$\Pi = aA_{-1}\left[\ln(\zeta - iH) \pm \ln(\zeta + iH)\right] -$$
$$- \sum_{n=1}^{\infty} \frac{a^{n+1}}{n} \left[\frac{C_{-n-1}}{(\zeta - iH)^n} \pm \frac{\overline{C}_{-n-1}}{(\zeta + iH)^n} \right], \quad (9)$$
$$C_{-n-1} = A_{-n-1} + iB_{-n-1},\, A_{-2n} = 0,\, B_{-2n-1} = 0.$$

Here the upper (lower) sign corresponds to the body motion near the wall (slip surface). Functions $C_{-n-1}(X,t)$ are coefficients in the Laurent series of the complex conjugate velocity at the points $\zeta = iH(X,t)$; $A_{-n-1}(X,t)$ and $B_{-n-1}(X,t)$ are their real and imaginary parts. They are found from the boundary condition on the body surface. For a body dropping into the stream from the wall or slip surface, this condition leads to the infinite system of the linear algebraic equations

$$A_{-1} = a_x,\, B = B_{-2} = V_e \pm$$
$$\pm q \sum_{m=0}^{\infty} (-1)^m q^{2m} (A_{-2m-1} + qB_{-2m-2}), \quad (10a)$$
$$A_{-2n-1} = \pm \frac{(-1)^n q^{2n}}{(2n-1)!} \sum_{m=0}^{\infty} \frac{(2m+2n-1)!}{2m!} (-1)^m \times$$
$$\times q^{2m} \left(A_{-2m-1} + \frac{2m+2n}{2m+1} qB_{-2m-2} \right), \quad (10b)$$
$$B_{-2n-2} = \pm \frac{(-1)^n q^{2n+1}}{(2n)!} \sum_{m=0}^{\infty} \frac{(2m+2n)!}{2m!} (-1)^m \times$$
$$\times q^{2m} \left(A_{-2m-1} + \frac{2m+2n+1}{2m+1} qB_{-2m-2} \right), \quad (10c)$$

Here, $q(X,t) = 0.5a(X)/|H(X,t)| \leq 0.5$. If the body is a cylinder or it drops in fluid at rest (inside the cavity), then $A_{-1} = a_x = 0$ and the other coefficients are determined from a system of algebraic equations similar to (10). In this case, these equations coincide with the system formulated in Ref. [9]. In a particular case for a store near a wall at zero angle of attack the obtained solution (10) coincides with the explicit solution.[22]

To accuracy $O(q^8)$ (where $q^8 \leq 1/256$) the solution of Problem 1b (for the circle dropping into a stream from a rigid wall) has the coefficients

5

$$B = V_e\left[1 + q^2 S_1(q)\right] + qa_x S_2(q), \qquad (11a)$$

$$A_{-3} = -q^2\left[a_x\left(1 + 2q^2 + 5q^4 + 14q^6\right) + \right.$$
$$\left. + 2V_e q\left(1 + q^2 + 4q^4\right)\right], \qquad (11b)$$

$$S_1(q) = 1 + q^2 + 3q^4 + 8q^6, \qquad (11c)$$

$$S_2(q) = 1 + q^2 + 2q^4 + 5q^6. \qquad (11d)$$

For a fluid at rest (Problem 1a), the coefficients are given by Eqs. (11) with $a_x = 0$ and V_e replaced by V_e^+. For a circle dropping in a stream from the free surface (Problem 2b) we obtain

$$B = V_e\left[1 - q^2 S_3(q)\right] - qa_x S_4(q), \qquad (12a)$$

$$A_{-3} = q^2\left[a_x\left(1 - 2q^2 - q^4 - 4q^6\right) + \right.$$
$$\left. + 2qV_e\left(1 - q^2 + q^4\right)\right], \qquad (12b)$$

$$B_{-4} = q^3\left[a_x\left(1 - 3q^2 - 3q^4\right) + \right.$$
$$\left. + 3qV_e\left(1 - q^2 - 3q^4\right)\right], \qquad (12c)$$

$$A_{-5} = -q^4\left[a_x\left(1 - 4q^2 - 6q^4\right) + \right.$$
$$\left. + 4qV_e\left(1 - q^2\right)\right], \qquad (12d)$$

$$S_3 = 1 - q^2 - q^4 - 2q^6, \qquad (12e)$$

$$S_4(q) = 1 - q^2 - 3q^6. \qquad (12e)$$

When the body drops to the slip surface in an immovable fluid (Problem 2a), these expressions reduce to

$$B = V_e^+\left[1 - q^2 S_5(q)\right], \ S_5(q) = 1 - q^2 - q^4, (13a)$$

$$A_{-3} = -2V_e^+ q^3\left(1 - q^2 - 2q^4\right), \qquad (13b)$$

$$B_{-4} = 3V_e^+ q^4\left(1 - q^2 - 4q^4\right). \qquad (13c)$$

It is seen that the shear-layer effect is proportional to first power of q for body motion in the stream; *i.e.*, it is stronger than for the body motion inside the cavity. This is due to the three-dimensional effect associated with the axial variation of the body shape ($a_x \neq 0$). In Phase 1 (body drops in the cavity), the complete solution is expressed as a superposition of the two solutions: $W_1^+(X,\zeta,t)$ (corresponding to the body which drops from the top wall) and ($W_2^+(X,\zeta,t)$ corresponding to the body which drops toward the slip surface. This composite solution is

$$W^+ = W_1^+ + W_2^+ - W_0^+,$$

where W_0^+ is the common part of the both solutions corresponding to the circle motion in the unbounded flow.

In the coordinate system $oxyz$ attached to the body CG, the potential and pressure on the body surface relevant to Phases 1 and 3 are represented as

$$\Phi = -\left(2B - V_e\right)a\sin(\theta) + \phi, \qquad (14a)$$

$$\phi = -2a\sum_{n=1}^{\infty}\left\{\frac{A_{-2n-1}}{2n}\cos(2n\theta) + \right.$$
$$\left. + \frac{B_{-2n-2}}{2n+1}\sin\left[(2n+1)\theta\right]\right\}, \ u_1 = \frac{1}{a}\frac{\partial\phi}{\partial\theta}, \ (14b)$$

$$p = \left\{a\left(2B - V_e\right)_t + \left[\left(2B - V_e\right)a^2\right]_x / a - \right.$$
$$- 2\left(B - V_e\right)a_x\right\}\sin\theta + 2Bu_1\cos\theta - \frac{u_1^2}{2} - $$
$$- \phi_t - \phi_x + \frac{V_e^2 - a_x^2}{2} - 2B^2\cos^2\theta - $$
$$- A_{0t} - A_{0x}, \qquad (14d)$$

$$p^+ = a\left(2B - V_e^+\right)_t\sin\theta + 2Bu_1\cos\theta - $$
$$- \frac{u_1^2 - V_e^{+2}}{2} - \phi_t - 2B^2 u_1\cos^2\theta. \qquad (14e)$$

The dimensional forms of the local, $L_x(x,t)$, and total, $L(t)$, lift forces as well as the pitching moment, $M(t)$, are

$$L_x(x,t) = -a\int_0^{2\pi} p\sin\theta d\theta, \ L(t) = \int_{x_0}^{x_e} L_x(x,t)dx$$

$$M(t) = \int_{x_0}^{x_e} L_x(x,t)xdx$$

Evaluating the pressure from Eqs. (14) we obtain the following expressions for the cross-sectional lift force (in the case of the body dropping inside the stream and in the cavity)

$$L_x = -\pi\left\{\frac{\partial\left[\left(2B - V_e\right)a^2\right]}{\partial x} + a^2\frac{\partial\left(2B - V_e\right)}{\partial t} - \right.$$

$$-2(B - V_e)aa_x + 2BA_{-3}a -$$

$$-2a\sum_{n=1}^{\infty}(A_{-2n-1} - A_{-2n-3})B_{-2n-2}\Bigg\}, \quad (15a)$$

$$L_x^+ = -\pi a\left[a\frac{\partial(2B^+ - V_e^+)}{\partial t} + 2B^+ A_{-3} - \right.$$

$$\left. -2\sum_{n=1}^{\infty}(A_{-2n-1} - A_{-2n-3})B_{-2n-2}\right]. \quad (15b)$$

Integrating these equations along the body axis we derive formulas for the lift force and pitching moment. If the body is inside the cavity, then

$$L^+(t) = -\frac{dV_a^+(t)}{dt} + L_1^+(t)$$

$$M^+(t) = -\frac{d\omega_a^+(t)}{dt} + M_1^+(t), \quad (16a)$$

$$L_1^+(t) = -2\pi\int_{x_0}^{x_e}\left[B^+ A_{-3} - \right.$$

$$\left. -\sum_{n=1}^{\infty}(A_{-2n-1} - A_{-2n-1})B_{-2n-2}\right]a(x)dx, \quad (16b)$$

$$M_1^+(t) = -2\pi\int_{x_0}^{x_e}\left[B^+ A_{-3} - \right.$$

$$\left. -\sum_{n=1}^{\infty}(A_{-2n-1} - A_{-2n-1})B_{-2n-2}\right]a(x)xdx, \quad (16c)$$

$$V_a^+ = \pi\int_{x_0}^{x_e}\left[2B^+(x,t) - V_e^+(x,t)\right]a^2(x)dx, \quad (16d)$$

$$\omega_a^+ = \pi\int_{x_0}^{x_e}\left[2B^+(x,t) - V_e^+(x,t)\right]a^2(x)xdx. \quad 16e)$$

If the body drops inside the stream, then we obtain

$$L^-(t) = -\frac{dV_a^-(t)}{dt} + L_1^-(t)$$

$$M^-(t) = -\frac{d\omega_a^-(t)}{dt} + M_1^-(t), \quad (17a)$$

$$L_1^-(t) = -\pi a^2(x_e)\left[2B(x_e,t) - V_e(x_e,t)\right] +$$

$$+ 2\pi\int_{x_0}^{x_e}\left[(B - V_e)a_x - BA_{-3} + \right.$$

$$\left. + \sum_{n=1}^{\infty}(A_{-2n-1} - A_{-2n-3})B_{-2n-2}\right]a(x)dx, \quad (17b)$$

$$M_1^-(t) = V_a^- - \pi a^2(x_e)x_e\left[2B(x_e,t) - V_e(x_e,t)\right] +$$

$$+ 2\pi\int_{x_0}^{x_e}\left[(B - V_e)a_x - BA_{-3} + \right.$$

$$\left. + \sum_{n=1}^{\infty}(A_{-2n-1} - A_{-2n-3})B_{-2n-2}\right]a(x)xdx, \quad (17c)$$

$$V_a^-(t) = \pi\int_{x_0}^{x_e}\left[2B(x,t) - V_e(x,t)\right]a^2(x)dx,$$

$$\omega_a^-(t) = \pi\int_{x_0}^{x_e}\left[2B(x,t) - V_e(x,t)\right]a^2(x)xdx.$$

The first terms of (16a) and (17a) for the force and moment are due to the fluid inertia. The first terms of (17b) and (17c) are associated with the pressure gradient in the stream along the body axis. The integral terms represent the effect of the flow boundary, which vanish at great distances from it. Explicit dependencies of the force and moment on the trajectory parameters are found by substituting into (16)-(17) the coefficients $B(x,t)$, $A_{-2n-1}(x,t)$ and $B_{-2n-2}(x,t)$ given by (11)-(13). These expressions give the explicit dependencies of the lift force and pitching moment on the trajectory parameters, CG speed $V_o(t)$, angular speed $\omega(t)$, angle of attack $\alpha(t)$, and CG vertical coordinate $Y_o(t)$ and allow us to develop a fast numerical algorithm for solving the trajectory equations.

4. Solutions of flow equations for Phase 2 (body crosses the slip surface)

In Phase 2, the slip surface $Y = 0$ divides the body surface into three portions; typical configurations are shown in Fig. 4. Depending on the angle of attack and the submerging depth, the nose ($X_0 < X < X_1$) or/and the base portion ($X_2 < X < X_e$) is located in the cavity or/and in the stream; the solutions for these portions are presented in Section 2.2. The third portion ($X_1 < X < X_2$) is partially submerged into the stream.

The flow schemes in the cross-section planes are shown in Fig. 2. The body surface intersects the slip surface at the line $Z = \pm c(X,t) = \pm a \sin\beta$, where $\beta(X,t) = \arccos(H/a)$ is the angle between the body and slip-surface cross-section contours. The upper portion of the circle moves with the vertical speed $V_e^+(X,t)$ in the fluid at rest; the normal velocity on its boundary is $v_n = V_e^+ \sin\theta$. The lower portion moves with the vertical speed $V_e^-(X,t)$ in the stream so that the normal velocity on its boundary is $v_n = a_x + V_e^- \sin\theta$. Thus, in each half plane separately we can formulate the problem:

- Find the complex conjugate velocity $W(X,\zeta,t)$, which provides a specified normal velocity on the corresponding circular arc and has zero real part on $Y = 0, |Z| > c$.

Solutions are obtained separately in the cavity ($Y > 0$) and stream ($Y < 0$) using conformal mapping of these regions to the flat plate exterior in the complex plane $\sigma = \xi + i\eta$ (see Fig. 5). The mapping of the stream region has the form

$$\zeta = f^-(\sigma, X, t) = c\frac{R^n(\sigma, X, t) + 1}{R^n(\sigma, X, t) - 1},$$

$$n(X,t) = \frac{\pi - \beta}{\pi}, \quad R = \frac{\sigma + b}{\sigma - b},$$

$$b(X,t) = \frac{c}{n}, \quad \frac{\partial\sigma}{\partial\zeta} = \frac{(\sigma^2 - b^2)(R^n - 1)^2}{4c^2 R^n},$$

$$l(\xi) = \left|\frac{\partial\sigma}{\partial\zeta}\right|_{\eta=0, \xi<b} = \frac{(b^2 - \xi^2)D(\xi,n)}{4c^2 Q^n(\xi,b)},$$

$$Z(\xi)_{\eta=0} = c\frac{Q^{2n} - 1}{D},$$

$$Y(\xi)_{\eta=0} = -2c\frac{Q^n}{D}\sin\pi n,$$

$$D = Q^{2n} - 2Q^n \cos\pi n + 1, \quad Q = \frac{\xi + b}{\xi - b}. \quad (18)$$

In the σ-plane, the submerged circle portion is transformed to the lower side of the interval $[-b,b]$. The mapping $\zeta = f^+(\sigma, X, t)$ of the cavity region

to the upper half plane (as well as the upper body portion to the upper side of the interval $[-b^+, b^+]$) is obtained by replacing $m = 1 - n$ by n in (18).

In the transformed space, the explicit solution is found using Keldysh-Sedov formula.[9] After integration, the complex conjugate velocity and potential in the stream region are represented as

$$W(\sigma, X, t) = -iV_e\left(1 - \frac{\sigma}{\sqrt{\sigma^2 - b^2}}\frac{\partial\sigma}{\partial\zeta}\right) +$$

$$+ \frac{a_x}{i\pi\sqrt{\sigma^2 - b^2}}\frac{\partial\sigma}{\partial\zeta}\int_{-b}^{b}\frac{\sqrt{b^2 - s^2}\,ds}{(s-\sigma)l(s)}, \quad (19a)$$

$$\Pi(\sigma, X, t) = -iV_e\left[\zeta(\sigma) - \sqrt{\sigma^2 - b^2}\right]$$

$$- \frac{2iaa_x\sqrt{\sigma^2 - b^2}}{\pi}\int_{-b}^{b}\frac{\psi(s)ds}{\sqrt{b^2 - s^2}(s-\sigma)}, \quad (19b)$$

$$\psi(s,n) = arctg\left(\frac{Q^n(s) - 1}{Q^n(s) + 1}ctg\frac{\pi n}{2}\right).$$

The first terms of Eqs. (19a), (19b) are due to the body motion and angle of attack. They are a modification for the flow over a log given in Ref. [13] for slip line boundaries instead of walls obtained by Malmuth[23] for the flow over a portion of a circle. The second terms arise due to the body shape variation in the streamwise direction. For $n > 1/2$, the flow velocities have a singularity of the type $(\zeta^2 - c^2)^{\frac{1}{2n} - 1}$ or $(\sigma^2 - b^2)^{\frac{1}{2} - n}$ at the points where the free surface intersects the body. Since this singularity is integrable, the lift force and pitching moment are not singular. However, local asymptotic analysis near these points is needed for the next-order approximations.

On the body surface, $\eta = -0, |\xi| < b$, the flow potential and pressure are expressed as

$$\Phi(x, \lambda, t) = \Phi_1 + \Phi_2$$

$$\Phi_1 = V_e\frac{\sin\pi n}{n}\left(\sqrt{1 - \lambda^2} - \frac{2nQ^n(\lambda)}{D(\lambda, n)}\sin\pi n\right)$$

$$\Phi_2 = -\frac{2aa_x}{\pi}\sqrt{1 - \lambda^2}E(\lambda, n), \quad (20a)$$

$$p(x, \lambda, t) = -A_{0t} - A_{0x} - \Phi_t - \Phi_x +$$

8

$$+\frac{V_e^2}{2}\left[1-\frac{\lambda^2(1-\lambda^2)D^2(\lambda,n)}{16n^4Q^{2n}(\lambda)}\right]-$$

$$-\frac{a_x^2}{2}\left[1+\frac{(1-\lambda^2)D^2(\lambda,n)}{\pi^2Q^{2n}(\lambda)}I^2(\lambda,n)\right]+$$

$$+V_e a_x\frac{\lambda(1-\lambda^2)D^2(\lambda,n)}{4n^2\pi Q^{2n}(\lambda)}I(\lambda,n). \qquad (20b)$$

$$\lambda=\frac{\xi}{b},\ E(\lambda,n)=\int_{-1}^{1}\frac{\psi(s)ds}{\sqrt{1-s^2}(s-\lambda)},$$

$$I(\lambda,n)=\int_{-1}^{1}\frac{Q^n(s)ds}{D(s,n)\sqrt{1-s^2}(s-\lambda)}, \qquad (20c)$$

where $E(\lambda,n)$ and $I(\lambda,n)$ are the principal values of the integrals and the potential $\Phi_1(x,\lambda,t)$ and $\Phi_2(x,\lambda,t)$ are induced by the circle vertical motion and axial body radius variation, respectively. The flow potential and pressure on the body portion inside the cavity are obtain from Eqs. (20) by omitting the terms proportional to a_x and replacing n by $m=1-n$. As shown below, the singularities in (20)-(21) at $n\to0$, $n\to1$ and $\lambda\to\pm1$ are integrable.

The local lift force $L_x(x,t)$ acting on a cross-section of the partially submerged body portion, $X_1\le X\le X_2$, is determined as

$$L_x(x,t)=\int_{-c}^{c}p(x,z,t)dz-\int_{-c}^{c}p^+(x,z,t)dz=$$

$$-\frac{\partial(\Phi-\Phi^+)}{\partial t}-\frac{\partial\Phi}{\partial x}+P(x,t), \qquad (21a)$$

$$P(x,t)=aV_e^2P_1(x,t)-aa_x^2P_2(x,t)+$$

$$+aa_xV_eP_{12}(x,t)-V_e^{+2}P^+(x,t). \qquad (21b)$$

Using results of Appendix A, the mean values of potentials,

$$\overline{\Phi}(x,t)=\int_{-c}^{c}\Phi(x,z,t)dz=$$

$$=a^2\left[V_e\Phi_1(n)+a_x\Phi_2(n)\right] \qquad (22)$$

and $\overline{\Phi}^+(x,t)$, are expressed as

$$\Phi_1=\frac{1}{a^2}\left[\int_{-c}^{c}Y_b(z)dz+\int_{-b}^{b}\sqrt{b^2-\xi^2}Z_\zeta d\xi\right]=$$

$$=-\left[\pi(1-n)+\frac{1}{2}\sin2\pi n-\right.$$

$$\left.-\frac{\pi(2n^2+1)\sin^2\pi n}{6n^2}\right], \qquad (23a)$$

$$n\to1:\Phi_1(n)\approx-2\pi(1-n)$$

$$\Phi_1(0)\approx-\pi\left(1-\frac{\pi^2}{6}\right). \qquad (23b)$$

$$\Phi^+(x,t)=-V_e^+a^2\left[\pi(1-m)+\frac{1}{2}\sin2\pi m-\right.$$

$$\left.-\frac{\pi(2m^2+1)\sin^2\pi m}{6m^2}\right], \qquad (23c)$$

$$m\to1:\Phi^+(x,t)\approx-2V_e^+a^2\pi(1-m)$$

$$m\to0:\Phi^+(x,t)\approx-V_e^+a^2\pi\left(1-\frac{\pi^2}{6}\right). \qquad (23d)$$

The second term of the mean potential is

$$\Phi_2=-4\frac{\sin\pi n}{n}\times$$

$$\times\left\{e_0(n)-\frac{n}{2}[1+\pi(1-n)ctg\pi n]\right\}, \qquad (24a)$$

$$\Phi_2(1)=0;\ \Phi_2(0)=-2(2\ln2-1)\pi. \qquad (24a)$$

The function $e_0(n)$ is analyzed in Appendix B and shown in Fig. 6; it can be written as

$$e_0(n)=n\sin(\pi n)\int_{-1}^{1}\frac{Q^n(s)ds}{D(s)\sqrt{1-s^2}},$$

$$n \to 1: \quad e_0 = \frac{\pi^2(1-n)}{8},$$

$$n \to 0: \quad e_0 = \ln 2 - \frac{\pi^2 n^2}{12}.$$

The first nonlinear term of (21b), $P_1(n)$, is determined by the expression

$$P_1 = \sin \pi n \left[1 - \frac{1}{8n^5} \int_{-1}^{1} \frac{\lambda^2(1-\lambda^2)D^2}{Q^{2n}} \frac{\partial z}{\partial \xi} d\lambda \right] =$$

$$= \sin \pi n \left[1 - \frac{1 - \pi n(1+2n^2)ctg\pi n}{6n^3} \right], \quad (25a)$$

$$P_1(1) \approx -\frac{1}{2}\pi \quad P_1(0) \approx -\frac{\pi(\pi^2-6)}{18}. \quad (25b)$$

The second nonlinear term of (21b), $P_2(n)$, is expressed as

$$P_2 = \sin \pi n \left[1 + \frac{1}{\pi^2 n} \int_{-1}^{1} \frac{(1-\lambda^2)D^2}{Q^{2n}(\lambda)} I^2 \frac{\partial Z}{\partial \xi} d\lambda \right] =$$

$$= 2\sin \pi n \left\{ 1 + 2\frac{ctg^2\pi n}{n} \left[e_0(n) - \right. \right.$$

$$\left. \left. -\frac{n}{2}(1+\pi(1-n)ctg\pi n) \right] - 4\frac{e_{10}(n)}{\pi^2 n^3} \right\}, \quad (26a)$$

$$P_2(1) \approx \frac{\pi}{2}, \quad P_2(0) \approx \frac{3}{2}\pi(3 - 4\ln 2). \quad (26b)$$

The function

$$e_{10}(n) = n^4 \int_{-1}^{1}\int_{-1}^{1} \frac{Q^n(s)Q^n(t)\ln Q(t)dsdt}{D(s)D(t)\sqrt{1-s^2}\sqrt{1-t^2}(t-s)},$$

$$n \to 1: e_{10} = \frac{\pi^2}{48},$$

$$n \to 0: e_{10} = \frac{1}{4}\left[2\ln 2 - 1 - \frac{\pi^2 n^2}{6}(3 - 4\ln 2) \right]$$

is given in Appendix B; its plot is shown in Fig. 6. The third nonlinear term of Eq. (21b), $P_{12}(n)$, is

$$P_{12} = \frac{\sin \pi n}{4n^3 \pi} \int_{-1}^{1} \frac{\lambda(1-\lambda^2)D^2(\lambda,n)}{Q^{2n}(\lambda)} I(\lambda,n)\frac{\partial Z}{\partial \xi} d\lambda =$$

$$= -\frac{1}{\pi n^2}\left\{ 4[1 - \pi n ctg(\pi n)]e_0(n) - 2e_2(n) + \right.$$

$$\left. + \frac{2n^2+1}{6}\pi^2 \cos^2(\pi n) \right\}, \quad (27a)$$

$$P_{12}(1) = -\pi,$$

$$P_{12}(0) = -\frac{\pi}{3}\left(4\ln 2 + 2 - \frac{\pi^2}{2} \right). \quad (27b)$$

The function

$$e_2(n) = n\sin(\pi n)\int_{-1}^{1}\frac{Q^n(s)\ln Q(s)sds}{D(s)\sqrt{1-s^2}},$$

$$n \to 1: e_2 = \frac{\pi^2(1-n)}{12},$$

$$n \to 0: e_2 = \frac{\pi^2}{12}\left[1 - 2n^2 \right].$$

is given in Appendix B; its plot is shown in Fig. 6. The last term of (21b), $P^+(n)$, which corresponds to the nonlinear pressure component on the body surface inside the cavity, has the form

$$P^+ = \sin \pi n \left\{ 1 - \frac{1 + \pi n(1+2m^2)ctg\pi n}{6m^3} \right\},$$

$$P^+(1) \approx -\frac{1}{2}\pi,, \quad P^+(0) \approx -\frac{\pi(\pi^2-6)}{18}. \quad (28)$$

Due to the first linear terms of Eq. (21a) the local lift force is singular at a small submerging depth, when $n \to 1$,

$$L_x(n \to 1) \sim -\frac{\partial \Phi_1}{\partial t} - \frac{\partial \Phi_1}{\partial x} \sim$$

$$\sim 2V_e a^2 \pi \left(\frac{\partial n}{\partial t} + \frac{\partial n}{\partial x} \right) \sim 2a\frac{V_e(V_e - a_x)}{\pi(1-n)}.$$

This result is consistent with the two-dimensional theory.[24] However, there is the additional term, which is due to the axial variation of body shape. This singularity leads to impulsive loads at the beginning of the body submergence process. Nevertheless, the body momentum is continuous; it is proportional to the potential $\overline{\Phi}_1 \sim 1 - n$.

The foregoing relations allow us to evaluate the lift force and pitching moment acting on the body in the transitional phase 2, when the body passes through the slip surface. In this phase, the total lift force and pitching moment can be expressed as the three terms superposition, namely,

$$L(t) = L^+(t) + L^\pm(t) + L^-(t),$$
$$M(t) = M^+(t) + M^\pm(t) + M^-(t).$$

The terms $L^\pm$ and $M^\pm$ correspond to integration of the local lift (21) over the interval $[x_1, x_2]$. We can express them as

$$L^\pm(t) = -\frac{dV_a^\pm(t)}{dt} + L_1^\pm(t),$$

$$M^\pm(t) = -\frac{d\omega_a^\pm(t)}{dt} + M_1^\pm(t),$$

$$L_1^\pm = \int_{x_1}^{x_2} P(x,t)dx + x_{1t}\left[\Phi^+(x_1,t) - \Phi(x_1,t)\right] +,$$

$$+ \Phi(x_1,t) - (1 - x_{2t})\Phi(x_2,t) - x_{2t}\Phi^+(x_2,t),$$

$$M_1^\pm = \int_{x_1}^{x_2} P(x,t)x\,dx + \int_{x_1}^{x_2}\Phi(x,t)dx +$$

$$+ x_1\left[(1 - x_{1t})\Phi(x_1,t) + x_{1t}\Phi^+(x_1,t)\right] -,$$

$$- x_2\left[(1 - x_{2t})\Phi(x_2,t) + x_{2t}\Phi^+(x_2,t)\right],$$

$$V_a^\pm(t) = \int_{x_1}^{x_2}\left[\Phi(x,t) - \Phi^+(x,t)\right]dx,$$

$$\omega_a^\pm(t) = \int_{x_1}^{x_2}\left[\Phi(x,t) - \Phi^+(x,t)\right]x\,dx.$$

The critical points $x_1(t)$, $x_2(t)$ and their speeds are solutions of the equations

$$\alpha x_k \pm a(x_k) = Y_o(t), \quad x_{kt}(t) \equiv \frac{dx_k(t)}{dt} =$$

$$= \frac{V_o - \omega x_k}{\alpha \pm a_x(x_k)}, \quad k = 1, 2.$$

Note that this representation of the lift force and pitching moment allows us to avoid the singularity in the critical points on the lowest body generator corresponding to $n = 1$. On the other hand, this singularity is integrable since $1 - n \sim \sqrt{x_k - x}$.

The lift force $L^+(t)$ is determined by integrating the local lift force over the body portion totally inside the cavity. This term is similar to that given by (16) plus the additional sum accounting for the critical point motion. The lift force $L^-(t)$ acts on the body portion being totally in the external stream. Its expression is similar to (17) plus additional terms due to the critical point motion.

Extracting the inertia term, we express the total lift force and pitching moment acting on the body in Phase 2 as

$$L(t) = -\frac{dV_a(t)}{dt} + L_1(t),$$

$$M(t) = -\frac{d\omega_a(t)}{dt} + M_1(t), \tag{29a}$$

$$L_1(t) = L_1^+(t) + L_1^\pm(t) + L_1^-(t),$$
$$M_1(t) = M_1^+(t) + M_1^\pm(t) + M_1^-(t), \tag{29b}$$
$$V_a(t) = V_a^+(t) + V_a^\pm(t) + V_a^-(t),$$
$$\omega_a(t) = \omega_a^+(t) + \omega_a^\pm(t) + \omega_a^-(t). \tag{29c}$$

This form is convenient for numerical solution of the trajectory equations. Similar equations are used to analyze subsonic store separations.[8]

5. Outer asymptotic solution and drag components

The form of outer asymptotic solution is defined by the form of outer limit of inner solution.[4,5] The outer limits of the solutions (9) and (19) for infinite span cavity corresponds to the dipole distributions on the body axis

$$\Phi_0 = -\frac{D_d(X,t)}{r}\sin\theta .$$

For Phase 2 $D_d = -\dfrac{1}{\pi}\displaystyle\int_{-b}^{b}\dfrac{\sqrt{b^2-s^2}\,v_{nb}(s)}{l(s)}\,ds$; for

Phase 3 $D_d(X,t) = 2a\big(a_x H + B_{-2}\big)$. This situation is similar to the flow over a thin wing[14-19] and higher order approximations will be considered to find correct outer solutions and wave drag. Analysis shows that the dominant terms in this limit contain unsteady and finite cavity span effects.[7] The objective of this paper is to calculate the drag components rather than to describe a successive procedure of asymptotic expansions. Although unsteady terms give significant contributions to the outer asymptotic expansion their contributions to drag components relevant to fast time scales are small.[7] Therefore, the dominant wave-drag component is due to the quasi-steady term related to the flow over the equivalent body of revolution with the cross-section area $A_{eq}(x,t)$. This corresponds to the source distribution on the body axis $Q_{eq}(x,t) = \partial A_{eq}/\partial x$. For Phase 2, we obtain[7]

$$Q_{eq} = 2\varepsilon\,\frac{d_0 \sin \pi n}{nd}\left[\frac{2A'(x)}{\pi}e_0(n) - \right.$$

$$\left. - A(x)V_e\big(1+2n^2\big)\frac{\sin \pi n}{6n}\right], \qquad (30a)$$

and for Phase 3

$$Q_{eq} = 2\varepsilon\big[H(x,t)A'(x) - A(x)B_{-2}(x,t)\big], \qquad (30b)$$

where $A(x)$ is body cross-sectional area and $A' = dA/dx$.

For analysis of the outer asymptotic region, we introduce the scaling

$$X = \frac{\bar{X}}{l_0};\quad \bar{Y} = \frac{\bar{Y}\delta}{l_0};\quad \bar{Z} = \frac{\bar{Z}\delta}{l_0};\quad \tilde{r} = \frac{\tilde{r}\delta}{l_0}, \qquad (31a)$$

$$\tilde{p} = \frac{\bar{p}-p_\infty}{\rho_\infty U_\infty^2 \delta^2} = -\varphi_X, \qquad (31b)$$

$$\Phi = l_0 U_\infty\big\{X + \delta^2\varphi(X,\bar{Y},\bar{Z},t;K)\big\}, \qquad (31b)$$

where $K = \big(M^2-1\big)\delta^2$ is transonic similarity parameter. The outer potential φ is a solution of the

Karman-Guderley (KG) transonic small disturbance axisymmetric flow boundary-value problem[4,16,17]

$$\left[K-(\gamma+1)\frac{\partial\varphi}{\partial X}\right]\frac{\partial^2\varphi}{\partial X^2} + \frac{1}{\tilde{r}}\frac{\partial}{\partial\tilde{r}}\tilde{r}\frac{\partial\varphi}{\partial\tilde{r}} = 0,$$

$$\tilde{r}\to\infty:\varphi\to 0;\ \tilde{r}\to 0:\ \tilde{r}\frac{\partial\varphi}{\partial\tilde{r}}\to\frac{Q_{eq}}{2\pi}. \qquad (32)$$

The arbitrary function of integration in the inner solutions (9) and (19) $A_0(X,t)$, which is needed to compute surface pressures wave drag, is determined from solving the KG equation in (32) and imposing the matching condition

$$A_0(X,t) = \lim_{\tilde{r}\to 0}\left[\varphi(X,\tilde{r},t) - \frac{Q_{eq}}{2\pi}\ln\tilde{r}\right]. \qquad (33)$$

Now, the wave drag can be calculated by integrating the pressure over the body surface. In Phase 2, the drag force coefficient is represented as the sum of four terms

$$C_D(t) = \frac{\bar{D}}{\rho_\infty U_\infty^2 \pi\delta^2 l_0^2} =$$
$$= C_{DF}(t) + C_{DB}(t) + C_{DW}(t) + C_{DP}(t). \qquad (34)$$

Here the friction drag coefficient, $C_{DF}(t)$, is found by integrating the local friction coefficient $c_f(X,\mathrm{Re}_x)$ over the body surface; i.e.

$$C_{DF}(t) = \frac{\bar{D}_f}{\rho_\infty U_\infty^2 \pi\delta^2 l_0^2} =$$
$$= \frac{1}{\delta}\int_0^1 kc_f(\bar{X},\mathrm{Re}_x)d\bar{X}, \qquad (35a)$$

$$\bar{X} = X - X_0,\quad \mathrm{Re}_x = \mathrm{Re}\,\bar{X}\big[1-U(t)\big], \qquad (35b)$$

$$\mathrm{Re} = \frac{\rho_\infty U_\infty l_0}{\mu_\infty}, \qquad (35c)$$

where $U(t)$ is horizontal body speed. The coefficient k is indicative of the friction drag being appreciable only on the body portion submerged in the flow external to the cavity. For a partially submerged body portion, $(X_1 \le X \le X_2)$ $k = \beta/\pi$; for the totally submerged portion $k = 1$; for the body portion totally inside the cavity $k = 0$.

Because c_f is a weak function of the Mach number at transonic speeds, we use the Schultz-Grunow correlation for the incompressible axisymmetric turbulent boundary layers.[25] Accordingly,

$$c_f(X, \mathrm{Re}_x) = c_f(\mathrm{Re}_x)\left[\int_0^X a^{7/6}(x)dx\right]^{6/7},$$

$$c_f(\mathrm{Re}_x) = 0.37\left(\lg \mathrm{Re}_x\right)^{-2.584}. \qquad (35d)$$

The base drag coefficient $C_{DB}(t)$ is found by integrating the pressure difference, $\bar{p}_b - p_\infty$, over the body base. It is expressed as a function of the Mach number[26]

$$C_{DB}(M) = \frac{\bar{D}_b}{\rho_\infty U_\infty^2 \pi \delta^2 l_0^2} =$$

$$= \frac{a_e^2}{\gamma M^2}\left[1 - p_b(M)\right], \qquad (36)$$

where $M = M_\infty\left[1 - U(t)\right]$; a_e is base radius, and $p_b(M) = \bar{p}_b / p_\infty$ is non-dimensional base pressure. The function $p_b(M)$ is shown in Fig. 7.

In Phase 2, the slip surface leads to new physical effects. If the body base is not fully submerged into the external flow, then the base pressure $p_b(M) = 1$ due to the boundary condition on the slip surface. Accordingly, the base drag coefficient is $C_{DB} = 0$.

The wave drag coefficient $C_{DW}(t, M)$ is expressed in terms of the function $A_0(X, t)$ as

$$C_{DW}(t) = -2\delta^2 \int_{x_0}^{x_e}\left[\frac{\partial A_0}{\partial t} + \frac{\partial A_0}{\partial x}\right]A'\beta dx. \qquad (37)$$

The numerical code of N. D. Malmuth is used to solve the KG equation and calculate the function $A_0(X, t)$ at each time instant in a pseudo-steady approximation.

The cross-flow drag coefficient $C_{DP}(t)$ results from integrating the pressure component without terms including $A_0(X, t)$. The body is subdivided into the three parts: the first is inside the cavity; the second is partially submerged into the outer stream; the third is totally submerged. Accordingly, the cross-flow drag coefficient can be expressed as

$$C_{DP}(t) = \frac{\bar{D}_p}{\rho_\infty U_\infty^2 \pi \delta^2 l_0^2} =$$

$$= \delta^2\left(C_{DP1} + C_{DP2} + C_{DP3}\right), \qquad (38a)$$

$$C_{DP1}(t) = \int_{x_0, x_2}^{x_1, x_e} c_{x1}(x, t)A'(x)dx,$$

$$C_{DP2}(t) = \int_{x_1}^{x_2} c_{x2}(x, t)A'(x)dx,$$

$$C_{DP3}(t) = \int_{x_0, x_2}^{x_1, x_e} c_{x3}(x, t)A'(x)dx, \qquad (38b)$$

$$c_{x1}(t) = -\delta^2\left\{\frac{\partial}{\partial t}\int_0^{2\pi}\Phi^+ d\vartheta + \right.$$

$$\left. + \int_0^{2\pi}\left[w^{+2} + v^{+2}\right]d\vartheta\right\}, \qquad (38c)$$

$$c_{x2}(t) = -\delta^2\left\{\int_{-\beta}^{\beta}\left[\frac{\partial(\Phi - \Phi^+)}{\partial t} + \frac{\partial \Phi}{\partial x}\right]d\vartheta + \right.$$

$$\left. + \int_{-\beta}^{\beta}\left[w^2 + v^2 - w^{+2} - v^{+2}\right]d\vartheta\right\}. \qquad (38d)$$

$$c_{x3}(t) = -\delta^2\left\{\left(\frac{\partial}{\partial t} + \frac{\partial}{\partial X}\right)\int_0^{2\pi}\Phi d\vartheta + \right.$$

$$\left. + \int_0^{2\pi}\left[w^2 + v^2\right]d\vartheta\right\}. \qquad (38e)$$

The first term, $c_{x1}(x, t)$, corresponds to the body portion being inside the cavity. The second term, $c_{x2}(x, t)$, corresponds to the partially submerged body portion and the third component is the cross-flow local drag of the fully submerged body portion. These drag components can be represented in an analytical form.

Consider the partially submerged body part. In this case, the local cross-flow drag coefficient relevant to the partially submerged body cross section is expressed as

$$c_{x2} = -\left(\frac{\partial}{\partial t} + \frac{\partial}{\partial x}\right)a\Phi(x,t) + V_e^2 N_1(n) +$$
$$+ a_x^2 N_2(n) + V_e a_x N_{12}(n). \tag{39}$$

The average value of the potential over the cross-sectional body contour, $\widetilde{\Phi}(x,t)$, is expressed in the form

$$\widetilde{\Phi} = \int_{-b}^{b} \Phi(X,\xi,t)\frac{\partial Z}{\partial \xi}d\xi =$$
$$= a_x \Phi_2(n) - V_e \Phi_1(n), \tag{40a}$$

$$\Phi_1 = 4\frac{\sin \pi n}{n}\left\{e_0 - \frac{n}{2}\left[1 + \pi(1-n)ctg\,\pi n\right]\right\},$$

$$\Phi_1(0) = 4\pi\left(\ln 2 - \frac{1}{2}\right);\ \Phi_1(1) = 0\,, \tag{40b}$$

$$\Phi_2(n) = 4\frac{\sin \pi n}{n}e_{20}(n),$$

$$\Phi_2(0) = 4\pi e_{20}(0);\ \Phi_2(1) = 0\,. \tag{40c}$$

The special function $e_{20}(n)$ is given by the double improper Cauchy-type integral (see Appendix B); its plot is shown in Fig. 6. The function $N_1(n)$ is expressed as

$$N_1 = -\frac{1}{2a}\int_{-b}^{b}\left[1 - \frac{\lambda^2(1-\lambda^2)D^2}{16n^4 Q^{2n}}\right]\frac{\partial Z}{\partial \xi}d\xi =$$
$$= \frac{\pi}{6n^2}\left(1 + 2n^2 - \frac{\sin 2\pi n}{2\pi n}\right) - \pi(1-n)\,,$$

$$N_1(1) = \frac{\pi}{2};\ N_1(0) = \frac{\pi}{3}\left(\frac{\pi^2}{3} - 2\right). \tag{41}$$

The function $N_2(n)$ is

$$N_2 = \frac{1}{2a}\int_{-b}^{b}\left[1 + \frac{(1-\lambda^2)D^2}{\pi^2 Q^{2n}}I^2(\lambda,n)\right]\frac{\partial Z}{\partial \xi}d\xi =$$
$$= \pi(2-n) + \frac{4\cos \pi n}{n\sin \pi n}\left\{e_0 - 2\left(\frac{\sin \pi n}{\pi n}\right)^2 e_{10} -\right.$$
$$\left.- \frac{n}{2}\left[1 + \pi(1-n)ctg\,\pi n\right]\right\},$$

$$N_2(1) = \frac{\pi}{2};\ N_2(0) = \frac{8\pi}{3}\,. \tag{42}$$

The function $e_{10}(n)$ is given in Appendix B; its plot is shown in Fig. 6. The function $N_{12}(n)$ is

$$N_{12} = -\frac{1}{a}\int_{-b}^{b}\frac{\lambda(1-\lambda^2)D^2}{4n^2\pi Q^{2n}}I(\lambda,n)\frac{\partial Z}{\partial \xi}d\xi =$$
$$= 4\left(1 - \cos \pi n\frac{\sin \pi n}{\pi n}\right)\frac{e_0(n)}{n\sin \pi n} +$$
$$+ \frac{\cos \pi n}{\pi n^2}\left[2e_2(n) - \frac{\pi^2(1+2n^2)}{6}\right],$$

$$N_{12}(1) = \pi;\ N_{12}(0) = \frac{2\pi}{3}(4\ln 2 - 1)\,. \tag{43}$$

The functions $\Phi_0(n)$, $\Phi_1(n)$, $N_1(n)$, $N_2(n)$, and $N_{12}(n)$ are shown in Fig. 8.

Using the results of Section 3, we express the local cross-flow drag coefficient relevant to the submerged body portions in the form

$$c_{x2} = a_x^2 + 2B^2 - V_e^2 +$$
$$+ 2\sum_{n=1}^{\infty}\left(A_{-2n-1}^2 + B_{-2n-2}^2\right). \tag{44}$$

This expression is also valid for Phase 3. A similar relation was obtained for the cross-flow drag associated with the body portion located inside the cavity.

6. 3-DOF trajectory analyses for a store separation from a cavity

The 3-DOF trajectory equations for a store separating from a cavity are written as

$$\frac{dV}{dt} = c_l L(t) - c_g,\ \frac{d\omega}{dt} = c_m M_p(t),$$
$$\frac{dU}{dt} = c_l C_D(t)\,, \tag{45}$$

14

$$c_g = \frac{\hat{g}\hat{l}_0}{\delta U_\infty^2}, \quad c_l = \frac{\pi \rho_\infty \hat{l}_0^3 \delta^2}{\hat{m}}, \quad c_m = \frac{\pi \rho_\infty \hat{l}_0^5 \delta^2}{\hat{I}} \ .$$

where $\hat{m}$ and $\hat{I}$ are body mass and moment of inertia, respectively; the lift force $L(t)$ and the pitching moment $M_p(t)$ are determined in Sections 3 and 4; the drag force coefficient is determined in Section 5. To integrate the two first equations of (45) the sixth-order Runge-Kutta scheme[28] was used. *These relations provide important lumped parameters that can be used to correlate and interpolate CFD solutions as well as design experiments.* The most expensive computations are associated with the wave drag, which requires solution of the KG equation. To reduce the run time, the Adams fourth-order explicit method[28] was used for solving the third equation of (45). The analytical results herein allow us to simplify dramatically the numerical procedure of integrating trajectory equations. Since for bodies of considered shapes the numerical solution of the Karman-Guderley equation converged rapidly, with a total run time for calculating one trajectory being about one hour on a Pentium-166. Without wave drag calculations this time collapses to about one minute. In future computational implementations we intend to improve the KG SLOR solver and use fits to accelerate this part of our prediction process.

In what follows, we analyze effects of the initial conditions and the body thickness effect on the store trajectory to illustrate the predictive method. In our calculations, we use the ogive-cylinder body B4N2 tested in the subsonic wind-tunnel experiments.[8] Physical properties of this body are reported in Ref. [8]. Calculations were performed for the freestream Mach number $M_\infty = 0.999$ and the Reynolds number $Re = 6.4782755 \cdot 10^6$. The initial location and horizontal velocity of the body CG are $X_0 = U_0 = 0$. We selected this slightly subsonic Mach number to maximize the wave drag effect to better understand its impact on the horizontal separation trajectory.

Figures 9-12 demonstrate the body thickness effect on the trajectory characteristics. Three bodies of diameters $D = D_0 = 0.953$ cm, $D = 2D_0$, and $D = 3D_0$ are considered. The initial (release) conditions are $V_0 = 120$ m/s, $\omega_0 = 200$ deg/s and $\alpha_0 = 0°$, $Y_0 = 2.54$ cm. In these calculations, we varied the body diameter at fixed body length. The dimensionless cavity width d_0 is also varied inversely proportional to D.

Figure 9a illustrates the body thickness effect on time histories of the vertical CG coordinate. In Fig. 9b, the CG trajectories are shown in X-Y space. The pitch angle and the vertical speed temporal variations are represented in Figs. 10, 11. It is seen that the body dynamics strongly depend on the thickness ratio. For $D=D_0$, the body separates from the cavity in a relatively short time period. For $D=2D_0$, the body is almost stopped near the parent body for a relatively long time (until the pitch angle is negative). The total vertical displacement is only about $4D$. During this phase, the body drifts downstream and departs in the horizontal direction from the initial state at $X \sim 70D_0$ which is larger than four body lengths. The average pitch angle and the pitch oscillation frequency also strongly depend on the body thickness ratio. The frequency increases approximately proportional to the thickness ratio. For $D=3D_0$, ricochet occurs. The body returns to the cavity with a relatively small downstream displacement. The pitch angle monotonically grows with small oscillations since the pitching moment is too small to overcome pitching due to the initial angular speed.

Figure 12 illustrates centerline trajectories for bodies of different diameters. The body of $D=3D_0$ returns to the cavity. The body of $D=2D_0$ stays near the parent body for a relatively long time. During this time, it is projected downward from the cavity, with pitch angle decreasing. The body of $D=D_0$ enters the external stream almost immediately, and its trajectory weakly depends on the parent body.

The second series of calculations are shown in Figs. 13-17 to illustrate the initial vertical speed effect on the body trajectories. Calculations were made at $\alpha_0 = 6°$, $\omega_0 = 0$ deg/s $Y_0 = 2.54$ cm and the two near-critical values of the initial vertical speed: $V_0 = 0.508$ m/s and 0.762 m/s. The plots of CG histories (Fig. 13), CG trajectories (Fig. 14), and centerline time histories (Fig. 17) at $V_0 = 0.508$ m/s indicate that the body ricochets from the freestream and re-contacts the parent body back of the cavity. When the body enters into the shear layer, the pitch angle grows slightly (see Fig. 15) due to body inertia. Due to a negative pitching moment, then α decreases with a small angular speed. This trend is too weak to decrease the pitch angle to its critical value (at which

the separation becomes possible). For $V_0 = 0.762$ m/s, the body stays near the shear layer for a long time period and penetrates downward a long distance. In this case, the negative angular speed is high enough to decrease the pitch angle below its critical value, and the body separates from the cavity. Figure 16 shows that in both cases the vertical CG speed grows to a positive value. For $V_0 = 0.762$ m/s, the gravity force is strong enough to cause a store departure from the cavity, whereas for $V_0 = 0.508$ m/s this force is too small for separation.

Figures 18-21 illustrate the initial pitch angle effect on the trajectory behavior. The calculations were performed at Y_0 - 2.54 cm, $V_0 = 0.508$ m/s, $\omega_0 = 0$ deg/s. The trajectory characteristics are very sensitive to the angle α_0. The latter may be induced by the release mechanism and/or aircraft maneuvering at the release instant. The variation $\Delta\alpha_0 = 1°$ leads to a substantial perturbation of the body trajectory: at $\alpha_0 = 5°$ the body separates from the cavity, whereas at $\alpha_0 = 6°$ re-contact is observed (see Figs. 18 and 19). Near the critical angle, $\alpha_0 = 5°$, the trajectory behavior is similar to that shown in Figs. 14-15 for the initial speed $V_0 = 0.762$ m/s. However, the vertical CG speed in this case does not become positive (see Fig. 20). The body base enters to the external flow and then returns to the shear layer again when the angle of attack becomes negative. Then, the body exits to the external flow and drops downward from the shear layer. The case $\alpha_0 = -6°$ is also shown for comparison. Here, the body quickly crosses the shear layer and separates from the cavity to a large distance. An interesting feature of this regime is observed for vertical oscillations of the CG speed in Phase 3 (the body outside the cavity). This behavior is consistent with our analysis for the body dropping in an unbounded stream.

7. Summary discussion

Aerodynamic and dynamic problems associated with separation of slender bodies of revolution from rectangular cavities into a transonic stream are considered herein using slender body theory. The inner and outer asymptotic flow regions are treated using combined analytical and numerical methods. Asymptotic analyses allowed us to highlight lumped parameters controlling the separation process and to split the problem into a series of simpler unit problems that were solved analytically for practically significant cases. The analytical results substantially simplify solving the store dynamic equations. They were used to develop fast and robust numerical codes to predict 2-DOF and 3-DOF store trajectories. The computational package was verified by comparisons with IIT subsonic wind tunnel experiments. An important aspect was the similarity of the near fields for the subsonic and transonic cases. Parametric studies of store separation into a transonic freestream emphasized critical regimes relevant to store re-contact and ricochet.

The body separation process was treated as a sequence of the three phases: in Phase 1, body is inside the cavity; in Phase 2, body crosses the shear layer; in Phase 3, body is outside the cavity in the outer stream. We showed that for inner asymptotic solution the cavity side-wall effects could be neglected. This allowed us to decompose the inner problem into simplified unit problems, which was solved analytically for the slip surface treated as a flat plane of zero potential. Analytical solutions of the dominant approximation problems relevant to separation of a thin body of revolution from a rectangular cavity adjacent to a uniform flow were obtained. For Phases 1 and 3, we used multipole expansions that allowed us to derive compact expressions for the pressure on the body surface and the cross-sectional lift. For Phase 2, the solution was obtained using conformal mapping and Keldysh-Sedov integral representations. The local lift force was also expressed in an explicit form with the introduction of new special functions. As contrasted to the two-dimensional problem, the solutions for Phases 2 and 3 include new terms relevant to the body shape variation in the axial direction. These terms lead to qualitatively new features of the slip surface and rigid wall effects. For example, in Phase 3 the slip-surface effect is essentially stronger than in Phase 1 because the influence of this boundary decreases inversely with distance from the body. In Phase 2, the flow velocities of the dominant approximation are singular at the line of intersection between the slip surface and the body surface. However, these singularities are integrable. This allowed us to calculate the lift force and pitching moment without a detailed analysis of the singular regions. Nevertheless, these singularities should be analyzed in future to treat the higher-order approximations.

Using the asymptotic theory we formulated the matching conditions for the inner and outer solutions in the case of a body of revolution separating from a cavity into the outer transonic freestream. We believe that for many practical problems, the transonic wave

16

drag can be predicted in the framework of quasi-steady flow. Short-time effects are averaged out over a long time scale relevant to the outer transonic region, and their contribution to the wave drag seems to be small. Our analysis showed that the wave drag increases from $O(\varepsilon\delta^4)$ (in Phase 2) to $O(\delta^4)$ (in Phase 3) as the body moves away from the slip surface. The quasi-steady outer flow corresponds to transonic flow over an equivalent body of revolution. We obtained explicit forms of the equivalent body as functions of time and the dimensionless cross-section area. The latter continuously grows with time from a small value of the order of ε in Phase 2 to $O(1)$ in Phase 3. We derived formulas for the base and friction drags using known theoretical results and empirical correlations. For Phases 2 and 3, different components of the pressure drag were calculated and analyzed. the wave drag was calculated using the code of N. Malmuth to provide solutions of the Karman-Guderley equation.

Our results formed a foundation for the development of computationally non-intensive algorithms that predict body trajectories through all separation phases. The numerical code predicting the store trajectory for all three phases separation was developed and verified by comparisons with the experimental data.[8] For a majority of the data, the calculations are in good agreement with experiment. Moreover, the theory is able to capture nuances of the trajectory behavior observed experimentally. A bifurcation of the pitch-angle history for Phase 3 for almost identical initial conditions was obtained that is consistent with the experimental data and indicates the existence of two substantially different pitching trajectories. Despite the fact that the transitional phase 2 is relatively short; its aerodynamics is crucial in identifying one of the two possible trajectories outside the cavity. Further theoretical and experimental studies are needed to establish and clarify the bifurcation mechanism. Our future work will extend this model to transonic speeds. The use of the code to establish when this bifurcation occurs will be important in trajectory control.

Numerical results illustrating 3-DOF body dynamics for separations from a wing and cavity in the transonic freestream show that this dynamics could be rather complicated. It includes such phenomena as store ricochet or/and re-contact. The body trajectory is very sensitive to initial "launch" vertical speed or pitch angle. Critical values of these parameters exist. In particular, ricochet/re-contact occurs when the initial pitch angle is larger or the vertical speed is smaller than these critical values. The body dynamics

is very complicated in the case of the separation from a cavity. Above an initial critical pitch angle or below a critical initial vertical speed, the body does not cross the slip surface and returns to the cavity. With pitch angle increasing or horizontal displacement, contact with the upper or back walls is possible. Near the critical conditions, the body can stay at small heights from the shear layer for a long time period and may partially return to the cavity interior. If the horizontal displacement during this time period is larger than the cavity length, contact with the back cavity wall is possible; otherwise, the store slowly separates.

Our parametric studies showed that trajectory parameters, such as the mean state characteristic, oscillation amplitude, frequency and amplification rate depend critically on the body mass, CG location and freestream speed. The trajectory is very sensitive to the initial conditions induced by the release mechanism. Our investigations lead to the conclusion that a satisfactory agreement between theory and experiments is difficult without detailed and accurate release conditions. The latter need to be extracted from analysis of experimental trajectories. Our estimations show that the initial conditions are also influenced by difficult-to-control disturbances such as wind tunnel flow oscillations or/and capture of the model ends by the release mechanism. On the other hand, the store separation can be effectively controlled by the release mechanism. Our modeling can help with the design of ejection units and thrust motors for stage separation. It allows for evaluation of thrust and weight required for these units, and indicates how to avoid an adverse re-contact situation with a relatively small impulse.

Acknowledgments

References

[1]Goodwin, F.K., Dillenius, M.F.E., Nielsen, J.N., "Prediction of Six-Degree-of-Freedom Store Separation Trajectories at Speeds up to the Critical

Speed. V.1. Theoretical Methods and Comparison with Experiment," AFFDL-TR-72-83, 1972.

[2]Wood, M.E., "Application of Experimental Techniques to Store Release Problems," Proceedings of NEAR Conference on Missile Aerodynamics, Monterey, California, 1988.

[3]Prewitt, N. C., Belk, D. M, Maple, R. C., "Multiple Body Trajectory Calculations Using the Beggar Code," *J. Aircraft*, 1999, v. 36, No. 5, pp. 802-808.

[4]Cole, J.D. *Perturbation Methods in Applied Mathematics.* Waltham, Massachusetts, 1968.

[5]Cole, J.D., Cook, L.P. *Transonic Aerodynamics.* Elsevier Science Publisher B.V., 1986.

[6]Nielsen, J.N. *Missile Aerodynamics.* McGraw-Hill Company, Inc., New York, 1960.

[7]Malmuth, N.D., Shalaev, V.I., Fedorov, A.V. "Combined Asymptotics and Numerical Methods in Transonic Store Interactions," Final Technical Report of Contract F49620-99-0005, AFOSR/NM, February 2002 (available in Defense Technical Information Center, stient.dtic.mil).

[8]Shalaev, V.I, Fedorov, A.V., and Malmuth, N.D. "Dynamics of Slender Bodies Separating from Rectangular Cavities," *AIAA J.*, v. 40, No. 3, 2002.

[9]Sedov, L.I. *Two-dimensional Problems of Hydrodynamics and Aerodynamics.* Moscow, Nauka, 1966.

[10]Kochin, N.E. "The Influence of the Lattice Step on its Hydrodynamic Characteristics," *J. Appl. Mathematics and Mechanics*, vol. 5, No. 2, 1941.

[11]Lavrentiev, M.A, Shabat, B.V. *Methods of the Theory of Complex Variable Functions.* Moscow, Nauka, 1973.

[12]Whittaker, E.T., and Watson, G.N. *A Course of Modern Analysis.* Cambridge University Press, 1927.

[13]Milne-Thomson, L.M. *Theoretical Hydrodynamics.* London, Macmillan and Co., LTD, 1960.

[14]Cheng, H.K., Hafez, M.M., "Transonic Equivalence Rule: a Nonlinear Problem Involving Lift," *J. of Fluid Mechanics*, v. 72, No. 1, 1975.

[15]Barnwell, R.W., "Analysis of Transonic Flow about Lifting Wing-Body Configurations," NASA TR, R-440, 1975.

[16]Cole, J. and Malmuth, N., "Wave Drag Due to the Lift for Slender Airplanes," NASA Conference Publication 3020, v. 1, p. 293, 1988.

[17]Cole, J.D., and Cook, L.P., "Some Problems of Transonic Flow Theory," Symposium Transsonicum III, Eds. Zierep, J., and Oertel, H., IUTAM Symp., Gottingen, May 24-27, 1988; Springer Verlag, Berlin, Heldelrberg, 1989, pp. 157-169

[18]Lighthill, M.J., "Higher Order Approximations," In: *General Theory of High Speed Aerodynamics*. Ed. by W.R. Sears. Princeton University Press, Sec. E, 1960.

[19]Hayes, W.D., "La Seconde Approximation pour les Ècoulements Transsonique non Visqueux," *Journal de Mècanique*, v. 5, No. 2, 1966.

[20]Schlichting, G., *Boundary Layer Theory*, McGraw-Hill, New York, 1968.

[21]Chow, W.L., "Base Pressure of a Projectile Within the Transonic Flight Regime," *AIAA J.*, v. 23, No. 3, pp. 388-395, 1985.

[22]Yaroshevskii, V.A. "Calculation of Aerodynamic Interference Forces between Two Bodies of Revolution," *Engineering Journal*, 1963, v. 3, No. 3, p. 546 (In Russian). Translation is in *Fluid Dynamics. Soviet Researches*.

[23]Malmuth, N.D., Fedorov, A.V., Shalaev, V., Cole, J., Khokhlov, A., Hites, M., and Williams, D., "Problems in High Speed Flow Prediction Relevant to Control," AIAA Paper No. 98-2695, 1998, also unpublished notes and memoranda 1999-2001.

[24]Wagner, H. "Uber Stoss- und Gleitfog, H. Uber Stoss- und Gleitfogange an der Oberflache von Flussigkeiten," ZAMM, 1932, N 4, pp. 193-215.

[25]Schlichting, G., *Boundary Layer Theory*, McGrow-Hill, New York, 1968.

[26]Chow, W.L., "Base Pressure of a Projectile Within the Transonic Flight Regime," *AIAA J.*, v. 23, No. 3, pp. 388-395, 1985.

[27]Gradshtein, I.S., and Ryzhik, I. M., *Tables of Integrals, Series, Sums and Products.* Moscow, Nauka, 1970.

[28]Korn, G.A., Korn, T.M. *Mathematical Handbook.* McGraw-Hill Book Company, 1968.
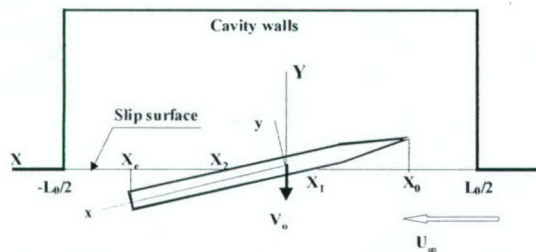
Fig. 1 Flow scheme and coordinate systems: side view.
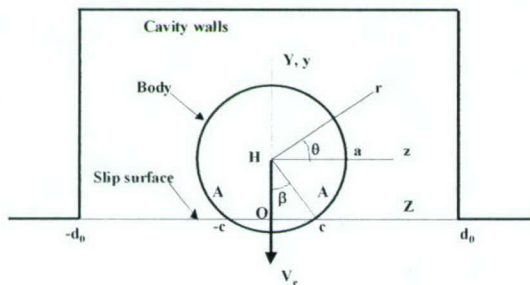
Fig. 2 Flow scheme and coordinate systems: back view.
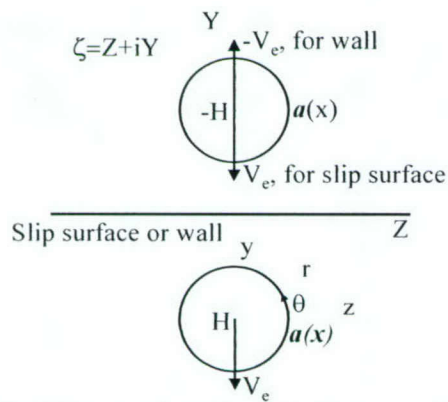
Fig. 3 Cross-section scheme for Phases 1 and 3.
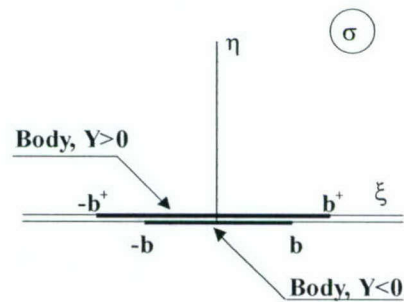

a)   b)

c)   d)

e)   f)
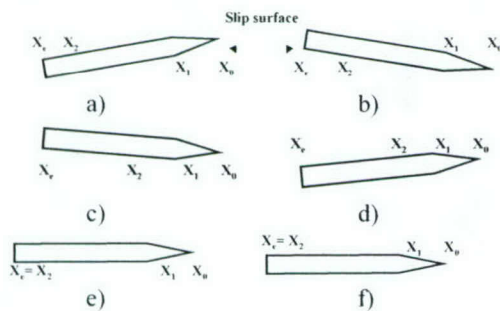
Fig. 4 Different body disposition in Phase 2.
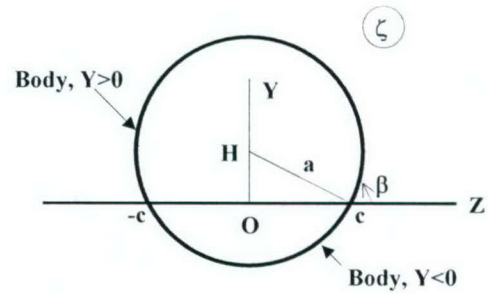
a) Physical plane;

b) Transformed plane;
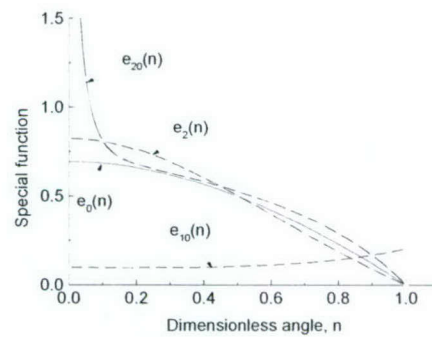
Fig. 5 Cross-section flow scheme for Phase 2.

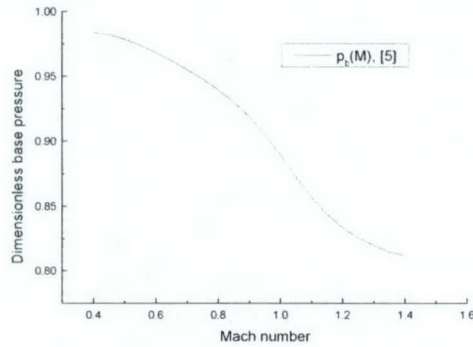
Fig. 6 Plots of special functions.

19

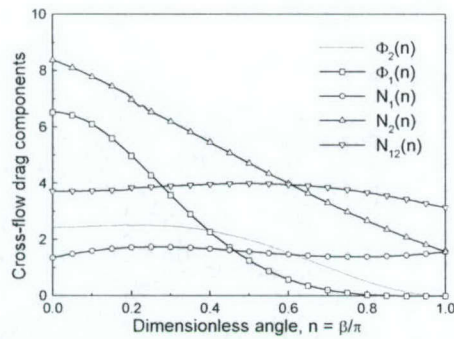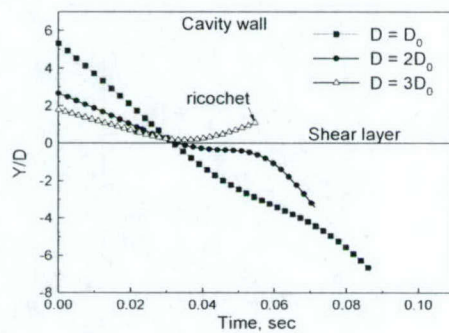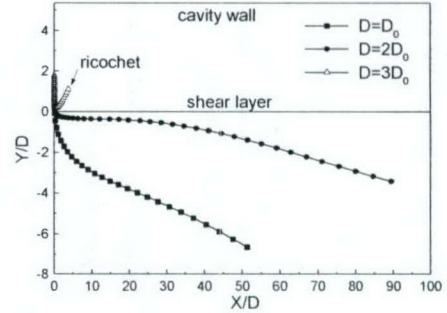Fig. 7 Ogive-cylinder base pressure as a function of Mach number.

b) Trajectories of CG

Fig. 9 CG trajectory parameters for the bodies of various thickness.

Fig. 8 Components of the cross-flow drag.
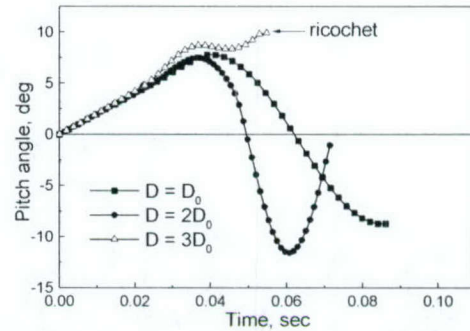
Fig. 10 Pitch angle histories for bodies of various thickness.

a) Time histories of the vertical CG coordinate
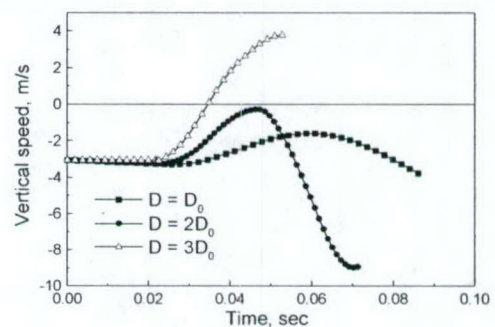
Fig. 11 Vertical speed for bodies of various thickness.

20
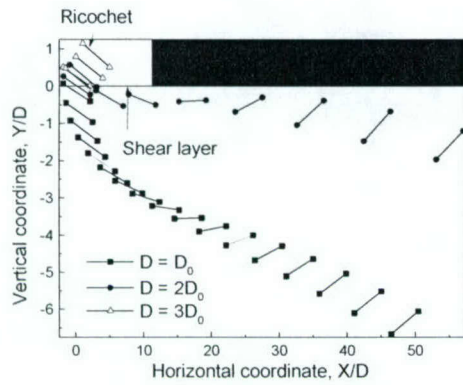
Fig. 12 Centerline positions for bodies of various thickness.

Fig. 13 Time histories of vertical CG coordinate for various initial speeds.

Fig. 14 CG trajectories for various initial speeds.

Fig. 15 Pitch angle evolution for various initial speeds.

Fig. 16 Evolution of CG vertical speed for various initial speeds.
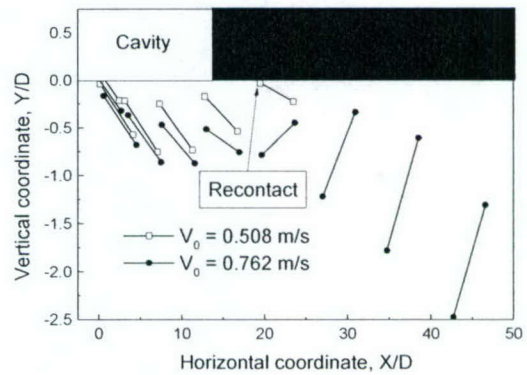
Fig. 17 Centerline trajectories for various initial speeds.

Fig. 20 Pitch angle histories at various initial angles of attack.

Fig. 18 CG vertical coordinate histories at various initial angles of attack.
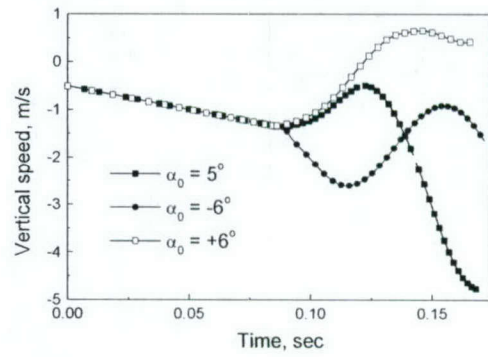
Fig. 21 CG vertical speed histories at various initial angles of attack.

Fig. 19 CG trajectories at various initial angles of attack.

Appendix A. Analytical evaluation of improper integrals

Analyze the integral

$$I_{10}(n) = \int_{-1}^{1} \frac{\left[Q^{2n}(s)-1\right]sds}{D(s)\sqrt{1-s^2}} =$$

$$= 2\int_{-\infty}^{\infty} \frac{\left(e^{4nx}-1\right)\left(e^{2x}-1\right)e^x dx}{D(x)\left(1+e^{2x}\right)^2}, \quad \text{(A1.1a)}$$

$$Q = \frac{1+s}{1-s} = e^{2x}, \quad s = \frac{e^{2x}-1}{e^{2x}+1}$$

$$ds = \frac{4e^{2x}dx}{\left(e^{2x}+1\right)^2}, \quad 1-s^2 = \frac{4e^{2x}}{\left(e^{2x}+1\right)^2},$$

$$D(x) = e^{4nx} - 2e^{2nx}\cos(\pi n) + 1. \quad \text{(A1.1b)}$$

Let's consider the following integral along the closed rectangular contour C_1 in the complex plane $z = x + iy$ (see Fig. A1)

$$I = \int_C f(z)dz = 2\pi i\, resf(0),$$

$$f(z) = \frac{\left(e^{2nz}+1\right)\left(e^{2z}+1\right)e^z}{\left(e^{2nz}-1\right)\left(e^{2z}-1\right)^2}.$$

Calculating the residue and accounting for that the integrals along the vertical lines vanish as $A \to \infty$ we obtain the function $I_{10}(n)$ as

$$I_{10}(n) = \frac{2n^2+1}{6n}\pi. \quad \text{(A1.2)}$$

Using the substitution (A1.1b) analyze the integral

$$I_{12}(n) = \int_{-1}^{1} \frac{Q^{2n}(s)ds}{D^2(s)\left(1-s^2\right)} = \frac{1}{2}\int_{-\infty}^{\infty} \frac{e^{2nx}dx}{D^2(x)} =$$

$$= \frac{1}{4n}\int_0^{\infty} \frac{dt}{\left[ch(t)-\cos(\pi n)\right]^2}. \quad \text{(A2.1)}$$

Using the table integral[27] the function $I_{12}(n)$ is expressed as

$$I_{12}(n) = \frac{1+\pi(1-n)ctg(\pi n)}{4n\sin^2(\pi n)}. \quad \text{(A2.2)}$$

Consider the integral

$$I_{11}(n) = \int_{-1}^{1}\left[Q^n(s)+Q^{-n}(s)\right]s^2 ds =$$

$$= \int_{-1}^{1}\left[\left(\frac{1+s}{1-s}\right)^n + \left(\frac{1+s}{1-s}\right)^{-n} - \right.$$

$$\left. - \frac{(1+s)^{1+n}}{(1+s)^{1-n}} - \frac{(1+s)^{1-n}}{(1+s)^{1+n}}\right]ds. \quad \text{(A3.1)}$$

Using the table of integrals[27] and accounting for properties of the Euler gamma-function, we obtain

$$I_{11}(n) = \tfrac{4}{3}n(1+2n^2)\Gamma(n)\Gamma(1-n) =$$

$$= \frac{4\pi n\left(1+2n^2\right)}{3\sin(\pi n)}. \quad \text{(A3.2)}$$

Using the substitution (A1.1b) we analyze the Cauchy type integral

$$I_1(s,n) = \int_{-1}^{1} \frac{\left[Q^{2n}(\lambda)-1\right]d\lambda}{D(\lambda)\sqrt{1-\lambda^2}\,(\lambda-s)} =$$

$$= \frac{2}{1-s}\int_{-1}^{1} \frac{\left(e^{4nx}-1\right)e^x dx}{D(x)\left[e^{2x}-Q(s)\right]}. \quad \text{(A4.1)}$$

Consider the following integral along the closed contour C_2 in the complex plane $z = x + iy$ (see Fig.A2)

$$I = \int_C f(z)dz = 2\pi i\, resf(0).$$

$$f(z) = \frac{(e^{2nz}+1)e^z}{(e^{2nz}-1)\left[e^{2z}+Q(s)\right]},$$

The contour is similar to that shown in Fig.B1, while the singular points

$$z_1 = \frac{\ln Q(s)+i\pi}{2}, \quad z_2 = \frac{\ln Q(s)-i\pi}{2},$$

23

are bypassed along the half-circles of radii $r \to 0$. Calculating the residue and the integrals along the half-circles around the singular point, we express the function $I_1(s,n)$ in the form

$$I_4 = \int_{-1}^{1} \frac{\left\{2 - \left[Q^n + Q^{-n}\right]\cos(\pi n)\right\}\lambda d\lambda}{\lambda - s} \quad (A5.1)$$

Using the table of integrals[27] and Eq. (A3.2), we get

$$\int_{-1}^{1} \frac{Q^n(\lambda)d\lambda}{\lambda - s} = \int_{-1}^{1} \frac{(1+\lambda)^n(1-\lambda)^{-n}d\lambda}{\lambda - s} =$$

$$= \frac{\pi}{\sin(\pi n)}\left[1 - Q^n(s)\cos(\pi n)\right], \quad (A5.2a)$$

$$\int_{-1}^{1} \frac{d\lambda}{\lambda - s} = -\ln Q(s),$$

$$\int_{-1}^{1}\left[Q^n(\lambda) + Q^{-n}(\lambda)\right]d\lambda = \frac{4\pi n}{\sin(\pi n)}, \quad (A5.2b)$$

$$\int_{-1}^{1} \frac{\left[Q^n(\lambda) + Q^{-n}(\lambda)\right]d\lambda}{\lambda - s} =$$

$$= -\pi ctg(\pi n)\left[Q^n(s) - Q^{-n}(s)\right], \quad (A5.2c)$$

Then, the function $I_4(s,n)$ is represented as

$$I_4(s,n) = 4\left[1 - \pi n ctg(\pi n)\right] +$$

$$+ s\frac{\pi \cos^2(\pi n)}{\sin(\pi n)}\left[Q^n(s) - Q^{-n}(s)\right] -$$

$$- 2s \ln Q(s). \quad (A5.3)$$
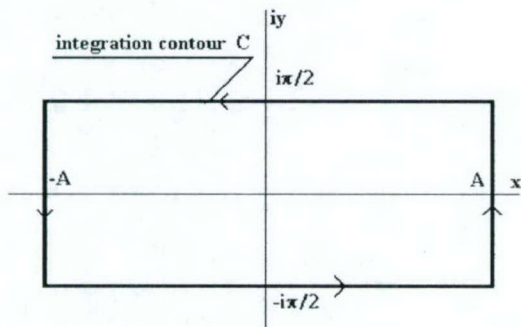
Fig. A1 Integration contour C_1.

$$I_1(s,n) = \frac{\pi}{n}\left[1 - \frac{2n\sin(\pi n)Q^n(s)}{D(s)\sqrt{1-s^2}}\right]. \quad (A4.2)$$

Consider a principal value of the Cauchy-type integral
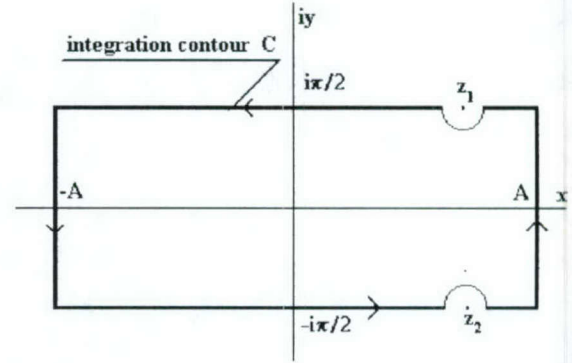
Fig. A2 Integration contour C_2.

Appendix B. Analytical and numerical investigations of integrals

Consider the integral

$$I_0(n) = \int_{-1}^{1} \frac{Q^n(s)ds}{D(s)\sqrt{1-s^2}} =$$

$$= \frac{1}{n\sin \pi n}\int_{0}^{1} \frac{\psi(s)sds}{\sqrt{1-s^2}} = \frac{e_0(n)}{n\sin \pi n}. \quad (B1.1)$$

Using the table of integrals[27] we get the following asymptotic expression at $n \to 1$

$$e_0 \approx \frac{\pi^2(1-n)}{8} \approx 1.2337(1-n). \quad (B1.2)$$

Expanding the integrand to Taylor series versus n we find in the limit $n \to 0$

$$I_0(n) = n^{-2}\left[i_0 + \frac{\pi n^2}{12}\left(2\pi i_0 - 1\right)\right].$$

Using the substitution $Q(s) = \exp(\pi x)$ and the table integral[27] we obtain

24

$$i_0 = \int_{-1}^{1} \frac{ds}{\left[\pi^2 + \ln^2 Q(s)\right]\sqrt{1-s^2}} =$$

$$= \frac{1}{\pi}\int_0^{\infty} \frac{dx}{\left(1+x^2\right)ch(\pi x/2)} = \frac{\ln 2}{\pi}. \quad \text{(B1.3)}$$

Then, we obtain the asymptotic expression

$$e_0(n) = \ln 2 - \frac{n^2\pi^2}{12}. \quad \text{(B1.4)}$$

To calculate the integral $e_0(n)$ in the range $0 < n < 1$, using the substitution $1-s = x^2$ we remove the singularity at the upper integration limit and transform the integral to the form

$$e_0(n) = 2\int_0^{1} \frac{\psi(x)\left(1-x^2\right)dx}{\sqrt{2-x^2}}$$

that is calculated by the method of trapezoids.

Similarly we analyze the integral

$$e_2(n) = n\sin \pi n I_2(n) =$$

$$= -\int_0^{1} \psi \frac{\partial}{\partial s}\left[s\sqrt{1-s^2}\ln Q\right]ds, \quad \text{(B2.1)}$$

In the limit $n \to 1$, we obtain

$$e_2(1) = \frac{\pi^2(1-n)}{12} \approx 0.8225(1-n). \quad \text{(B2.2)}$$

At $n \to 0$, we find

$$i_2(n) = \lim_{n\to 0} n^2 I_2(n) =$$

$$= i_{20} + \frac{n^2}{12}\left[2\pi^2 i_{20} - i_{21}\right].$$

The integral i_{20} is evaluated similar to the case of $I_{10}(n)$ (see Eq. A1.1), and the integral i_{21} is integrated by parts

$$i_{21} = \int_{-1}^{1} \frac{\ln Q(s)s\,ds}{\sqrt{1-s^2}} = 2\pi,$$

$$i_{20} = \int_{-1}^{1} \frac{\ln Q(s)s\,ds}{\left[\pi^2 + \ln^2 Q(s)\right]\sqrt{1-s^2}} = \frac{\pi}{12}.$$

Then, we obtain

$$e_2(n) = \pi\left(1 - \frac{n^2\pi^2}{6}\right)i_2(n) =$$

$$= \frac{\pi^2}{12}\left(1-2n^2\right). \quad \text{(B2.3)}$$

Consider the integral

$$E_1(n) = \int_{-1}^{1} f(\lambda,n)I^2(\lambda,n)d\lambda$$

$$f(\lambda,n) = \left[2 - \left(Q^n + Q^{-n}\right)\cos(\pi n)\right], \quad \text{(B3.1)}$$

where $I(s,n)$ is expressed in the form of successive integral

$$I^2(\lambda,n) = \left[\int_{-1}^{1}\frac{\phi(s,n)ds}{s-\lambda}\right]^2 =$$

$$= \int_{-1}^{1}\frac{\phi(s_1,n)ds_1}{s_1-\lambda}\int_{-1}^{1}\frac{\phi(s_2,n)ds_2}{s_2-\lambda},$$

$$\phi(s,n) = \frac{Q^n(s)ds}{D(s)\sqrt{1-s^2}}.$$

Then, the integral $E_1(n)$ is transformed into the triple integral. Using the Poincare-Bertrand rule we change the integration sequence and express (B3.1) as

$$E_1(n) = \int_{-1}^{1}\phi(s_2)ds_2\int_{-1}^{1}\phi(s_1)E_{11}ds_1 + \frac{\pi^2}{2n},$$

$$E_{11} = \frac{1}{s_2 - s_1}\int_{-1}^{1}\left\{\left(\frac{1}{\lambda-s_2} - \frac{1}{\lambda-s_1}\right)\times\right.$$

$$\left.\times\left[2 - \left(Q^n(\lambda) + Q^{-n}(\lambda)\right)\cos \pi n\right]\right\}d\lambda.$$

Using Eqs. (A3.2) and (A5.2) of Appendix A the function $E_{11}(s_1,s_2,n)$ is expressed in the form

$$E_{11} = \frac{1}{s_2 - s_1} \left\{ 2\left[\ln Q(s_1) - \ln Q(s_2)\right] + \right.$$

$$+ \frac{\pi \cos^2(\pi n)}{\sin(\pi n)} \left[Q''(s_1) - Q^{-n}(s_1) - \right.$$

$$\left. \left. - Q''(s_2) + Q^{-n}(s_2) \right] \right\}.$$

Then, the integral $E_1(n)$ is

$$E_1(n) = \frac{\pi^2}{2n} - 4 \int_{-1}^{1} \phi(s)ds \int_{-1}^{1} \frac{\phi(t)\ln Q(t)dt}{t - s}$$

$$+ \frac{2\pi \cos^2(\pi n)}{\sin(\pi n)} \int_{-1}^{1} \phi(s) I_1(s,n)ds =$$

$$= \frac{\pi^2}{2n} - 4E_{10}(n) + \frac{2\pi \cos^2(\pi n)}{\sin(\pi n)} E_{12}(n).$$

Using Eqs. (A4.2), (B1.1) and (A2.2), the function $E_{12}(n)$ is evaluated as

$$E_{12}(n) = \frac{\pi}{n} \left[I_0(n) - 2n\sin(\pi n) I_{12}(n) \right] =$$

$$= \frac{\pi}{n^2 \sin \pi n} \left\{ e_0 - \frac{n}{2} \left[1 + \pi(1-n)ctg\pi n \right] \right\}.$$

Then, the function $E_1(n)$ is expressed as

$$E_1(n) = \frac{\pi^2}{2n} - 4E_{10}(n) + \frac{2\pi^2}{n^2} ctg^2(\pi n) \times$$

$$\times \left\{ e_0(n) - \frac{n}{2} \left[1 + \pi(1-n)ctg(\pi n) \right] \right\}. \quad \text{(B3.2)}$$

Now, we analyze the double integral

$$e_{10}(n) = n^4 E_{10}(n) =$$

$$= -n^4 \int_{-1}^{1} \frac{Q''(s)\ln Q(s)ds}{D(s,n)\sqrt{1-s^2}} \times$$

$$\times \int_{-1}^{1} \frac{Q''(t)\ln Q(t)dt}{D(t,n)\sqrt{1-t^2}(t-s)}. \quad \text{(B4.1)}$$

Its asymptotic value at $n = 1$ is calculated as

$$e_{10} = \frac{\pi}{16} \int_{-1}^{1} \ln\left(\frac{1+t}{1-t}\right)\sqrt{1-t^2}\, tdt = \frac{\pi^2}{48} \quad \text{(B4.2)}$$

At $n = 0$ we have

$$e_{10}(0) = \int_{-1}^{1} \frac{i_{14}(t)dt}{\left[\pi^2 + \ln^2 Q(t)\right]\sqrt{1-t^2}} =$$

$$= \frac{\pi}{2} (i_0 - 2\pi i_1) = \frac{2\ln 2 - 1}{4}.$$

In the limit $n \to 0$, the integral (B4.1) is reduced to the form

$$e_{10}(n) = e_{10}(0) + \frac{n^2}{12} \left\{ 4\pi^2 e_{10}(0) - \right.$$

$$\left. - \int_{-1}^{1} \frac{i_{14}(s)ds}{1-s^2} - \int_{-1}^{1} \frac{i_{15}(t)ds}{\left[\ln^2 Q(s) + \pi^2\right]\sqrt{1-s^2}} \right\}.$$

The integrals $i_{14}(t)$ and $i_{15}(t)$ are calculated using Eqs. A4.1-A4.2

$$i_{14}(t) = \int_{-1}^{1} \frac{\ln Q(s)ds}{\left[\pi^2 + \ln^2 Q(s)\right]\sqrt{1-s^2}(s-t)} =$$

$$= \frac{\pi}{2} \left[1 - \frac{2\pi}{\sqrt{1-t^2}\left[\ln Q^2(t) + \pi^2\right]} \right].$$

$$i_{15}(t) = \int_{-1}^{1} \frac{\ln Q(s)ds}{\sqrt{1-s^2}(s-t)} = \frac{\pi^2}{\sqrt{1-t^2}}.$$

Then, at $n \to 0$ we find

$$e_{10}(n) = e_{10}(0) + \frac{n^2\pi^2(4\ln 2 - 3)}{24}. \quad \text{(B4.3)}$$

For $0 < n < 1$, the function $e_{10}(n)$ is evaluated numerically using the substitutions

$$x = (1-s)^{(n+1)/2}, \tau = (1-t)^n,$$

$$v = \frac{2}{n+1}, k = \frac{1}{n}.$$

With these variables the above integrals are transformed into the proper integral

Consider the integral

$$E_2(n) = \int_{-1}^{1} f(\lambda,n) I(\lambda,n)\lambda d\lambda =$$

$$= \int_{-1}^{1} \phi(t,n) I_4(t,n)dt \ . \qquad (B5.1)$$

The inner integral $I_4(n)$ is given by Eq. (A5.3). The function $E_2(n)$ is expressed as

$$E_2(n) = 4[1 - \pi n ctg\pi n] I_0(n) - 2I_2(n) +$$

$$+ \pi \frac{\cos^2 \pi n}{\sin \pi n} I_{10}(n) =$$

$$= \frac{1}{n \sin \pi n} \Big[4(1 - \pi n ctg\pi n) e_0(n) - 2e_2(n) +$$

$$+ \frac{(2n^2 + 1)}{6} \pi^2 \cos^2 \pi n \Big]. \qquad (B5.2)$$

Its asymptotic behavior is

$$n \to 1: \ E_2(n) = \frac{\pi}{2(1-n)} \ ,$$

$$E_2(0) = -\frac{\pi}{3}\left(\frac{\pi^2}{2} - 4\ln 2 - 2 \right). \qquad (B5.3)$$

A PC-Oriented Method to Estimate Store Trajectories

N. Malmuth
Rockwell Scientific Company, Thousand Oaks, California
nmalmuth@rwsc.com

V. Shalaev, and A. Fedorov
Moscow Institute of Physics and Technology
Zhukovski, Moscow Region , Russia

Abstract

A PC-oriented method to estimate 3-DOF store trajectories for separation from cavities and external surfaces into subsonic or transonic freestreams was developed. Combined analytical, semi-empirical and numerical approaches were used to calculate the lift force, pitching moment and drag. The asymptotic theory based on slender body theory was developed to evaluate inviscid aerodynamic characteristics. Within this framework, the flow was assumed to be potential and the shear layer dividing the cavity from the freestream was approximated by a slip surface of zero potential. Explicit inner asymptotic solutions derived gave analytical expressions for the lift force, pitching moment and one drag component in all phases of the store motion, including dropping in the cavity, crossing the shear layer and motion in the freestream. Different regimes in the outer asymptotic region relevant to time scales intrinsic to store separation were studied. Short duration processes associated with freestream and body oscillations averaged over a long time scale characterize the outer flow and give a negligibly small contribution to the wave drag. Accordingly, the quasi-steady outer solution was considered, which is induced by sources along the body axis giving the first-order physics in a finite-span cavity. Wave drag modeling was reduced to solving the Karman-Guderley equation over an equivalent body of revolution simulating the store. Friction drag was calculated using a modification of the Schultz-Grunow correlation for axisymmetric flows. The base drag was predicted using the theory of Chow. This information was used to develop a compact and rapid PC-oriented code to predict store trajectories. It was tested using subsonic experimental data. In the majority of cases, the trajectory predictions from it are in good agreement with experiments. Analysis of the experimental data and computations revealed a bifurcation of the pitch angle history. Our parametric studies identify re-contact and ricochet phenomena in the transonic regime. The theoretical model developed herein can be generalized to 6-DOF trajectories, including yawing and rolling motions.

1. *Introduction*

The store separation problem has important practical applications and its different aspects were investigated extensively using experimental and computational methods [1-4]. Most of the studies have been concerned with external separation at subsonic or supersonic speeds. Relatively less attention has been given to separation from cavities, especially at transonic speeds. This problem is very complicated due to the large number of parameters governing the flow structure and broad variety of physical phenomena involved into the separation process. Our objectives are to identify first-order physical effects, simplify the key aerodynamic problems, and develop fast and reliable models for predicting store trajectories.

Separation of a body from a cavity into a subsonic or transonic flow is subdivided into three phases: in Phase 1 the body drops inside the cavity; in Phase 2 the body crosses the shear layer separating

1

the cavity flow from the external stream; and in Phase 3 the body moves in the external stream. For many practical applications, the following relations are fulfilled

$$\delta = \frac{\hat{a}_0}{\hat{l}_0} << 1, \quad \frac{\hat{V}_r}{\delta U_\infty} = \varepsilon \le O(1), \quad \alpha = \frac{\hat{\alpha}}{\delta} = O(1), \quad \frac{\hat{\delta}_s}{\hat{a}_0} << 1, \tag{1.1a}$$

$$\delta^2 \, Re >> 1, \frac{\hat{\delta}_s U_\infty}{\hat{L}_0 \hat{V}_r} << 1, d_0 = \frac{\hat{D}_0}{\hat{a}_0} >> 1, H_0 = \frac{\hat{H}_0}{\hat{a}_0} >> 1. \tag{1.1b}$$

Here $\hat{l}_0$ and $\hat{a}_0$ are respectively the body length and its maximum radius, $\hat{V}_r$ is a characteristic vertical body speed, $\hat{\alpha}$ is the angle of attack, U_∞ is freestream velocity; $\hat{L}_0, \hat{H}_0$ and $\hat{D}_0$ are respectively cavity length, height and half-width; $\hat{\delta}_s$ is the shear-layer thickness, $Re = \rho_\infty U_\infty \hat{l}_0 / \mu_\infty$ is the Reynolds number. Due to the inequalities in (1.1a), the flow over the body can be described with slender body theory [5]. According to the inequalities (1.1b), the shear layer can be approximated as a free slip surface by neglecting the flow inside the cavity and considering the cavity wall effect as a small perturbation. The solution is found separately in the inner and outer asymptotic regions using small perturbation theory.

The slip surface-body interaction of the inner asymptotic expansion presents a great challenge because the shape of the free boundary is free, *i.e.*, not known *a priori* and need to be determined in the solution process. Indeed, many methods are being developed to solve this problem. In this connection, the inner asymptotic problem including the slip-surface effect has been reduced to a system of integral-differential equations, which can be solved by simple iterations a shown in [6] In the first iteration, the slip surface is treated as a plane of zero potential, and analytical solutions are found for all three phases of the separation process. Explicit expressions for the lift force, pressure drag and pitching moment obtained from this solution allow us to identify lumped parameters associated with the center of inertia trajectory and pitch angle history. From these results the 2-DOF trajectory equations were analyzed in [7]. Their approximate analytical solutions permit direct parametric analyses of the store trajectory in the cavity and outer stream. This shows that the body motion outside the cavity consists of two components one of which is an average drift under gravity and aerodynamic forces, and the oscillations/modulations about a temporal mean state. Different time scales of these components were identified. The analytical results can be used for correlations of experimental data and assessments of CFD methods.

The form of the outer asymptotic expansion depends on the time scale. Various outer flow regimes relevant to different time scales are presented in [8]. It is shown that the short time scales are averaged out during the outer long-time period. Accordingly, the outer flow can be treated as quasi-steady in calculations of the wave drag. This flow is described by the Karman-Guderley equation with an asymptotic boundary condition obtained from matching of the inner and outer solutions. For proper matching, the second-order approximation of the inner expansion is analyzed. Our analysis also reveals the effect of finite cavity width gives the main contribution to the boundary condition. Other components need to be approximated empirically. In this regard, the base-drag theory [9] and empirical correlation [10] for the friction drag are used to calculate the other drag force components.

These analytical results allow us to develop a fast and robust PC-oriented method to predict 2-DOF and 3-DOF body motion. The method is based on a sixth order Runge-Kutta finite-difference

scheme. During the few first integration steps, the Adams method is used to initiate the calculations. It is essential for computers of small speed and memory that the forces and moments are calculated using explicit expressions. The wave drag is the more time-consuming element. For external separation, the wave-drag coefficient can be predetermined for affinely-similar bodies as a universal function of the Karman-Guderley transonic similarity parameter. This function is used to accelerate the calculations. For separations from a cavity, a numerical procedure developed by the first author [11] is used to solve the Karman-Guderley equation. This algorithm ensures good convergence after a only few hundred iterations, which is fast enough for trajectory calculations. The codes incorporating this methodology for PC application were developed and validated by comparison with subsonic experimental data in [12]. Parametric runs from these codes for external separation cavity separations into transonic and subsonic streams showed that the theory is capable of predicting such complex physical phenomena as re-contact, body ricochet from the stream and trajectory bifurcation. At near-sonic speeds, the store trajectory is very sensitive to initial conditions; this leads to strong restrictions on the release conditions. Most of the theoretical results described in what follows are new. They give new insight into the physics of store separation and unsteady transonic flows with free boundaries.

Hereinafter, the problem formulation for the inner asymptotic region and the inner solutions for Phases 1, 2 and 3 are presented in Section 2. The outer asymptotic problem is formulated in Section 3. Section 4 briefly describes the numerical method for solving the trajectory equations. A discussion of interesting numerical examples and conclusions is given in Section 5.

2. Inner asymptotic problems

2.1. Problem formulation for inner asymptotic region

Consider a slender body of revolution released from the top wall of a rectangular cavity at the initial time $\hat{t} = 0$. The initial angle of attack $\hat{\alpha}_0$, vertical speed $\hat{V}_0$ and angular speed $\hat{\omega}_0$ are assumed small, $O(\delta)$, where the O symbol is a short hand signifying "the order of". The body drops under gravity in the cavity symmetry plane and separates from the cavity into the external flow. At the initial instant, the flow within the cavity is neglected. The cavity interior is separated from the external stream by a slip surface bridging the cavity edges. The flow scheme for Phase 2 and the coordinate systems are shown in Figs 1a and 1b. The coordinate system $O\hat{X}\hat{Y}\hat{Z}$ is attached to the unperturbed slip surface. Therein, the $O\hat{X}$-axis is directed along the freestream velocity and $O\hat{Y}$ as well as $O\hat{Z}$ are respectively vertical and spanwise coordinates. The coordinate system $o\hat{x}\hat{y}\hat{z}$ is attached to the body center of gravity (CG) that moves vertically with the velocity $\hat{V}_o(\hat{t})$. The $o\hat{x}$-axis is directed along the body symmetry axis; the $o\hat{y}$- and $o\hat{z}$-axes lie in the cross-sectional plane. The direction of $o\hat{z}$-axis coincides with the direction of $O\hat{Z}$- axis. The axes $o\hat{x}$ and $o\hat{y}$ are inclined with respect to the axes $O\hat{X}$ and $O\hat{Y}$ at the angle $\hat{\alpha}(\hat{t})$; they rotate around $o\hat{z}$-axis with the angular speed $\hat{\omega}(\hat{t})$. Along with the Cartesian coordinates, we use the polar coordinates, $\hat{r}$ and θ, specified as $\hat{z} = \hat{r}\cos\theta$, $\hat{y} = \hat{r}\sin\theta$. Slender body theory [5] is used to solve this problem. The following dimensionless variables are introduced for the inner asymptotic region

$$X = \frac{\hat{X}}{\hat{l}_0}, Y = \frac{\hat{Y}}{\hat{a}_0}, Z = \frac{\hat{Z}}{\hat{a}_0}, x = \frac{\hat{x}}{\hat{l}_0}, y = \frac{\hat{y}}{\hat{a}_0}, z = \frac{\hat{z}}{\hat{a}_0}, d_0 = \frac{\hat{D}_0}{\hat{a}_0}, \qquad (2.1a)$$

3

$$L_0 = \frac{\bar{L}_0}{\hat{a}_0}, \; H_0 = \frac{\bar{H}_0}{\hat{a}_0}, \; t = \frac{U_\infty \hat{t}}{\bar{l}_0}, \; \alpha = \frac{\bar{\alpha}}{\delta}, \; \omega = \frac{\delta U_\infty \bar{\omega}}{\bar{l}_0}. \tag{2.1b}$$

$$\bar{\Phi}^+ = \delta^2 U_\infty \bar{l}_0 \Phi(X,Y,Z,t) \; \bar{\Phi} = \bar{l}_0 U_\infty \left\{ 1 + \delta^2 \left[g_0(X,t) + \Phi(X,Y,Z,t) \right] \right\}. \tag{2.1c}$$
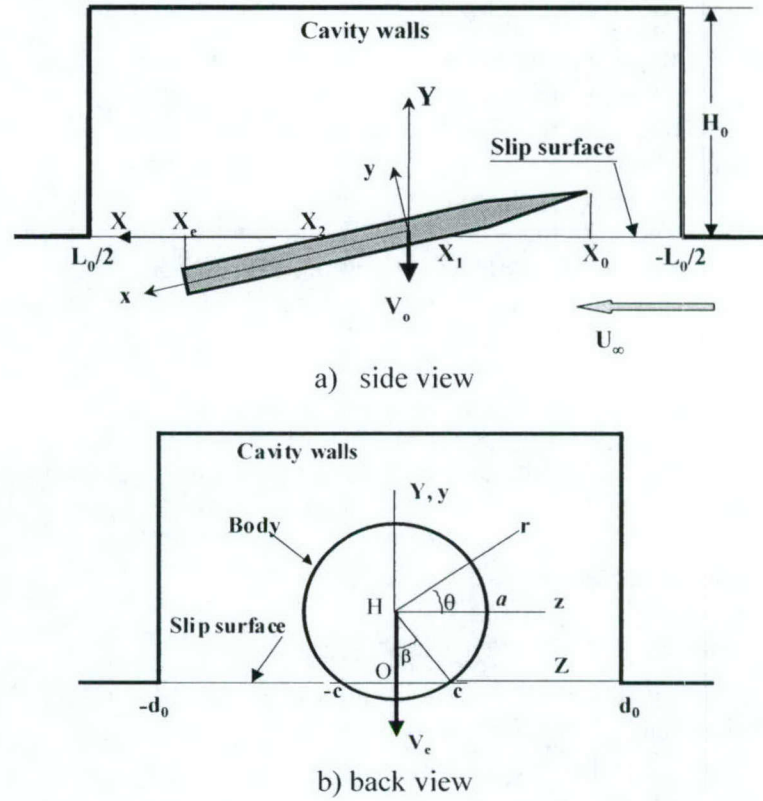

a) side view

b) back view

Fig. 1. Flow scheme and notations.

Neglecting the terms $O(\bar{\alpha}^2)$ and assuming that the transverse coordinates of the CG are constant, in particular, $Z_o(t) = 0$, we obtain the relations between the coordinate systems $OXYZ$ and $oxyz$ $X = X_o(t) + x, \; Y = Y_o(t) + y - x\alpha, \; Z = z$.

In the first order approximation, the near-filed flow potentials in the cavity and in the stream, $\Phi(X,Y,Z,t)$ and $\Phi^+(X,Y,Z,t)$, are solutions of the two-dimensional Laplace equation in cross-section/crossflow planes. The function $g_0(X,t)$ in (2.1c) is determined from matching with the outer solution as described in Section 3. On the body surface, $Y = Y_b(X,\theta,t) = H(X,t) + a(x)\sin\theta$, the boundary conditions are

$$Y > 0: \quad v_n^+ = V_e^+ \sin\theta; \quad V_e^+(X,t) = V_o(t) - \omega(t)X, \tag{2.2a}$$

$$Y < 0: \quad v_n = a_X + V_e \sin\theta, \quad V_e(X,t) = \varepsilon V_e^+(X,t) - \alpha(t), \tag{2.2b}$$

4

where $H = Y_o(t) - \alpha(t)X$ is the distance from the plane $Y = 0$ to the body axis; $Y_o(t)$ and $V_o(t)$ are the CG coordinate and its vertical speed, respectively. The slip surface is assumed to be the plane $Y = 0$ of zero potential, $\Phi_f = \Phi_f^+ = 0$. This approximation corresponds to the first iteration of the more general inner problem accounting for the slip-surface displacement induced by the body motion [6]. In this approximation, the inner problem is simplified enough to make analytical solutions possible. These will be indicated in what follows.

Pressures above and below the slip surface, p and p^+, are defined by the unsteady Bernoulli equations

$$p^+ = \frac{\bar{p}^+ - p_\infty}{\delta^2 \rho_\infty U_\infty^2} = -\varepsilon \left[\Phi_t^+ + \frac{\varepsilon}{2} \left(w^{+2} + v^{+2} \right) \right], \tag{2.3b}$$

$$p = \frac{\bar{p} - p_\infty}{\delta^2 \rho_\infty U_\infty^2} = -\left[\Phi_t + u + \frac{1}{2} \left(w^2 + v^2 \right) \right]. \tag{2.3b}$$

On the cavity walls, the usual boundary conditions of zero normal velocity are fulfilled. Since the cavity depth is assumed large with respect to the body radius, the top wall and slip surface effects on the body motion are treated as small perturbations. In Phase 1, they are calculated separately and represented in a composite form; in Phases 2 and 3 the top wall effect is also neglected. A detailed analysis of the inner problem shows that the side cavity wall effect is $O\left[(2d_0)^{-1} \right]$ and can be neglected in the dominant approximation. Nevertheless, this effect gives the main contribution to the outer asymptotic representation and will be considered in Section 3.

2.2. Solution of the inner problem for Phases 1 and 3

Within the framework of slender body theory [5], the complex conjugate velocity $W(X, \zeta, t)$ is harmonic in the cross-section planes. The body cross-section profile is a circle of radius $a(X)$ centered at the point $\zeta = iH(X, t)$. This circle moves with the vertical velocity $V_e(x, t)$ in the outer uniform stream or with the velocity $V_e^+(x, t)$ within cavity. The cross-flow scheme for Phase 3 is shown in Fig. 2. Let the wall or the slip surface coincide with the plane $Y = 0$. For half planes containing the body, we have the following problem:

- Find an analytical function $W(X, \zeta, t)$ that satisfies Eqs. (2.2) for a specified normal velocity on the circle that has zero real (imaginary) part on the slip surface (wall).

Analytical continuation through the wall and the slip surface gives $W(\bar{\zeta}) = \overline{W}(\zeta)$ and $W(\bar{\zeta}) = -\overline{W}(\zeta)$ respectively. Here, the overbar denotes complex conjugation. From these conditions, we reduce the half-plane problem containing the circle to a problem for the full plane containing two identical circles located symmetrically with respect to the plane $Y = 0$ (see Fig. 2). A multipole expansion [13] is one method to treat this problem. As contrasted to the problem analyzed in Ref. [13], the problems under consideration here are three-dimensional. They lead to new effects that have not been studied previously. Some details of this analysis will now be summarized.
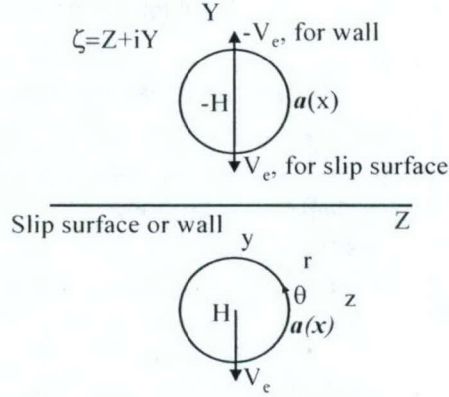
Fig. 2. Cross-flow scheme for Phases 1 and 3.

Using the Cauchy formula we obtain the integral equation for the function $W(X,\zeta,t)$

$$W(X,\zeta,t) = \frac{1}{2i\pi} \int\limits_{s=a} \frac{W(X,iH+s,t)ds}{\zeta-iH-s} + + \frac{1}{2i\pi} \int\limits_{s=a} \frac{W(-iH+\bar{s})d\bar{s}}{\zeta+iH-\bar{s}}$$

Expanding the kernels into Taylor series and using the analytical continuation and flow symmetry we obtain the solution of this equation in the series form

$$W = \sum_{n=0}^{\infty} a^{n+1} \left\{ \frac{C_{-n-1}}{(\zeta-iH)^{n+1}} \pm \frac{\bar{C}_{-n-1}}{(\zeta+iH)^{n+1}} \right\}. \tag{2.4}$$

Here the upper (lower) sign corresponds to the body motion near the wall (slip surface). Functions $C_{-n-1}(X,t) = A_{-n-1}(X,t) + iB_{-n-1}(X,t)$ are coefficients in the Laurent series of the complex conjugate velocity at the points $\zeta = iH(X,t)$. It follows from flow symmetry that $A_{-2n} = B_{-2n-1} = 0$. Other coefficients are found from the boundary condition on the body surface. This leads to the infinite system of linear algebraic equations

$$A_{-1} = a_x, B = B_{-2} = V_e \pm q \sum_{m=0}^{\infty} (-1)^m q^{2m} \left(A_{-2m-1} + qB_{-2m-2}\right), \tag{2.5a}$$

$$A_{-2n-1} = \pm \frac{(-1)^n q^{2n}}{(2n-1)!} \sum_{m=0}^{\infty} \frac{(2m+2n-1)!}{2m!} (-1)^m q^{2m} \left(A_{-2m-1} + \frac{2m+2n}{2m+1} qB_{-2m-2}\right), \tag{2.5b}$$

$$B_{-2n-2} = \pm \frac{(-1)^n q^{2n+1}}{(2n)!} \sum_{m=0}^{\infty} \frac{(2m+2n)!}{2m!} (-1)^m q^{2m} \left(A_{-2m-1} + \frac{2m+2n+1}{2m+1} qB_{-2m-2}\right). \tag{2.5c}$$

These series are convergent since the parameter $q(X,t) = 0.5a(X)/|H(X,t)| \leq 0.5$. If the body is a cylinder or it drops in fluid at rest (inside the cavity), then $A_{-1} = a_x = 0$. In this case, the equations (2.5) coincide with the system formulated in Ref. [13]. When the store is located near the wall at zero angle of attack, the solution (2.5) coincides with the explicit solution [14]. For practical calculations, we can suitably truncate the series in Eqs. (2.5) to provide required accuracy. To

6

accuracy $O(q^8)$ ($q^8 \leq 1/256$), the solution for the circle dropping into uniform stream from a rigid wall is

$$B = V_e \left[1 + q^2 S_1(q) \right] + q a_x S_2(q), \tag{2.6a}$$

$$A_{-3} = -q^2 \left[a_x \left(1 + 2q^2 + 5q^4 + 14q^6 \right) + + 2V_e q \left(1 + q^2 + 4q^4 \right) \right], \tag{2.6b}$$

$$S_1(q) = 1 + q^2 + 3q^4 + 8q^6, \quad S_2(q) = 1 + q^2 + 2q^4 + 5q^6. \tag{2.6c}$$

For a body dropping into a fluid at rest, $a_x = 0$ and V_e are replaced by V_e^+ in Eqs. (2.6). For a circle dropping in a stream from the free/slip surface, the coefficients are approximated as

$$B = V_e \left[1 - q^2 S_3(q) \right] - q a_x S_4(q), \tag{2.7a}$$

$$A_{-3} = q^2 \left[a_x \left(1 - 2q^2 - q^4 - 4q^6 \right) + 2q V_e \left(1 - q^2 + q^4 \right) \right], \tag{2.7b}$$

$$B_{-4} = q^3 \left[a_x \left(1 - 3q^2 - 3q^4 \right) + 3q V_e \left(1 - q^2 - 3q^4 \right) \right], \tag{2.7c}$$

$$A_{-5} = -q^4 \left[a_x \left(1 - 4q^2 - 6q^4 \right) + 4q V_e \left(1 - q^2 \right) \right], \tag{2.7d}$$

$$S_3 = 1 - q^2 - q^4 - 2q^6, \quad S_4(q) = 1 - q^2 - 3q^6. \tag{2.7e}$$

When the body drops to the slip surface in a quiescent fluid that approximates the cavity flow mean state, these expressions reduce to

$$B = V_e^+ \left[1 - q^2 S_5(q) \right], \quad A_{-3} = -2V_e^+ q^3 \left(1 - q^2 - 2q^4 \right), \tag{2.8a}$$

$$B_{-4} = 3V_e^+ q^4 \left(1 - q^2 - 4q^4 \right), \quad S_5(q) = 1 - q^2 - q^4. \tag{2.8b}$$

In Phase 1 (body drops in the cavity), the full solution is expressed as a superposition of the two solutions: $W_1^+(X,\zeta,t)$ corresponding to the body dropping from the top wall and $W_2^+(X,\zeta,t)$ corresponding to the body dropping toward the slip surface. This "composite" solution is

$$W^+ = W_1^+ + W_2^+ - W_0^+ ,$$

where W_0^+ is the common part of both solutions corresponding to the circle motion in the unbounded quiescent/(motionless) fluid.

In the *oxyz* coordinate system attached to the body CG, the pressures on the body surface relevant to Phases 1 and 3 are represented as

$$p = \left\{ a(2B - V_e)_t + \frac{\left[(2B - V_e)a^2 \right]_x}{a} - 2(B - V_e)a_x \right\} \sin\theta + 2Bu_1 \cos\theta - \frac{u_1^2}{2} - $$

$$- \phi_t - \phi_x + \frac{V_e^2 - a_x^2}{2} - 2B^2 \cos^2\theta - g_{0t} - g_{0x}, \tag{2.9a}$$

$$p^+ = a(2B - V_e^+)_t \sin\theta + 2Bu_1 \cos\theta - \frac{u_1^2 - V_e^{+2}}{2} - \phi_t - 2B^2 u_1 \cos^2\theta. \tag{2.9c}$$

$$u_1 = -2\sum_{n=1}^{\infty}\left\{A_{-2n-1}\cos(2n\theta) + B_{-2n-2}\sin[(2n+1)\theta]\right\}, \tag{2.9c}$$

The dimensional forms of the local, $L_x(x,t)$, and total, $L(t)$, lift forces as well as the pitching moment, $M(t)$, are expressed as

$$L_x(x,t) = -a\int_0^{2\pi} p\sin\theta d\theta, \; L(t) = \int_{x_0}^{x_e} L_x(x,t)dx, \; M(t) = \int_{x_0}^{x_e} L_x(x,t)xdx$$

Evaluating the pressure from Eqs. (2.9) we obtain the following expressions for the cross-sectional lift force

$$L_x = -\pi\left\{\frac{\partial\left[(2B-V_e)a^2\right]}{\partial x} + a^2\frac{\partial(2B-V_e)}{\partial t} - 2(B-V_e)aa_x + 2BA_{-3}a -\right.$$
$$\left. -2a\sum_{n=1}^{\infty}(A_{-2n-1}-A_{-2n-3})B_{-2n-2}\right\}, \tag{2.10a}$$

$$L_x^+ = -\pi a\left[a\frac{\partial(2B^+ - V_e^+)}{\partial t} + 2B^+ A_{-3} - 2\sum_{n=1}^{\infty}(A_{-2n-1}-A_{-2n-3})B_{-2n-2}\right]. \tag{2.10b}$$

Integrating these equations along the body axis we derive formulas for the lift force and pitching moment. If the body is inside the cavity, then

$$L^+(t) = -\frac{dV_a^+(t)}{dt} + L_1^+(t), \; M^+(t) = -\frac{d\omega_a^+(t)}{dt} + M_1^+(t), \tag{2.11a}$$

$$L_1^+(t) = -2\pi\int_{x_0}^{x_e}\left[B^+ A_{-3} - \sum_{n=1}^{\infty}(A_{-2n-1}-A_{-2n-1})B_{-2n-2}\right]a(x)dx, \tag{2.11b}$$

$$M_1^+(t) = -2\pi\int_{x_0}^{x_e}\left[B^+ A_{-3} - \sum_{n=1}^{\infty}(A_{-2n-1}-A_{-2n-1})B_{-2n-2}\right]a(x)xdx, \tag{2.11c}$$

$$V_a^+(t) = \pi\int_{x_0}^{x_e}\left[2B^+(x,t)-V_e^+(x,t)\right]a^2(x)dx, \; \omega_a^+ = \pi\int_{x_0}^{x_e}\left[2B^+(x,t)-V_e^+(x,t)\right]a^2(x)xdx.$$

If the body drops into the external stream, then

$$L^-(t) = -\frac{dV_a^-(t)}{dt} + L_1^-(t), \; M^-(t) = -\frac{d\omega_a^-(t)}{dt} + M_1^-(t), \tag{2.12a}$$

$$L_1^-(t) = -\pi a^2(x_e)\left[2B(x_e,t)-V_e(x_e,t)\right] + 2\pi\int_{x_0}^{x_e}\left[(B-V_e)a_x - BA_{-3} +\right.$$
$$\left. +2\pi\int_{x_0}^{x_e}\left[(B-V_e)a_x - BA_{-3} + \sum_{n=1}^{\infty}(A_{-2n-1}-A_{-2n-3})B_{-2n-2}\right]a(x)dx, \tag{2.11b}$$

8

$$M_1^-(t) = V_a^- - \pi a^2(x_e)x_e\left[2B(x_e,t) - V_e(x_e,t)\right] +$$

$$+ 2\pi \int_{x_0}^{x_e}\left[(B-V_e)a_x - BA_{-3} + \sum_{n=1}^{\infty}(A_{-2n-1} - A_{-2n-3})B_{-2n-2}\right]a(x)xdx, \qquad (2.11c)$$

$$V_a^-(t) = \pi \int_{x_0}^{x_e}\left[2B(x,t) - V_e(x,t)\right]a^2(x)dx, \quad \omega_a^-(t) = \pi \int_{x_0}^{x_e}\left[2B(x,t) - V_e(x,t)\right]a^2(x)xdx.$$

The first terms of (2.10a) and (2.11a) for the force and moment are due to the fluid inertia. The first terms of (2.11b) and (2.11c) are associated with the pressure gradient in the stream along the body axis. The integral terms represent effects of the flow boundary and vanish at large distances from it. Explicit dependencies of the force and moment on the trajectory parameters are found by substituting into (2.10)-(2.11) the coefficients $B(x,t)$, $A_{-2n-1}(x,t)$ and $B_{-2n-2}(x,t)$ given by (2.5)-(2.8). The explicit expressions of the lift force and pitching moment in terms of the trajectory parameters, CG speed $V_o(t)$, angular speed $\omega(t)$, angle of attack $\alpha(t)$, and CG vertical coordinate $Y_o(t)$ allow us to develop a fast numerical algorithm for solving the trajectory equations.

The inner solution is also used to predict the cross-flow drag, $\tilde{D}_{CF}^-$, by integrating the inner pressure without the function $g_0(x,t)$. For Phase 3, the cross-flow drag coefficient is expressed as

$$C_{CF}^-(t) = \frac{\tilde{D}_{CF}^-}{\rho_\infty U_\infty^2 \pi \delta^2 l_0^2} = \delta^2 \pi \int_{x_0}^{x_e}c_x^-(x,t)a(x)a'(x)dx, \qquad (2.12a)$$

$$c_x^- = a_x^2 + 2B^2 - V_e^2 + 2\sum_{n=1}^{\infty}\left(A_{-2n-1}^2 + B_{-2n-2}^2\right). \qquad (2.12a)$$

A similar relation was obtained for the cross-flow drag associated with the body portion located inside the cavity.

2.3. Solution for Phase 2

In Phase 2, the body crosses the shear layer (Fig. 1). For the body portions being fully inside the cavity and inside the stream (the regions $X_0 < X < X_1$ and $X_2 < X < X_e$ in Fig. 1a), we can use the solutions obtained in Section 2.2. The body surface intersects the slip surface at the line $Z = \pm c(X,t) = \pm a\sin\beta$, where $\beta(X,t) = \arccos(H/a)$ is the angle between the body and slip-surface cross-section contours. For the partially submerged body portion (the region $X_1 < X < X_2$ in Fig. 1a) the problem is formulated as

- Find the complex conjugate velocity $W(X,\zeta,t)$, which provides a specified normal velocity on the corresponding circular arc and has zero real part at $Y = 0$, $|Z| > c$.

Solutions are obtained separately in the cavity region ($Y > 0$) and the stream region ($Y < 0$) using conformal mapping of these regions to the flat plate exterior in the complex plane $\sigma = \xi + i\eta$ (see Fig. 3). The mapping of the stream region has the form

9

$$\zeta = f^-(\sigma, X, t) = c\frac{R^n(\sigma, X, t)+1}{R^n(\sigma, X, t)-1}, \quad n(X, t) = \frac{\pi - \beta}{\pi}, \quad R = \frac{\sigma + b}{\sigma - b},$$

$$b(X, t) = \frac{c}{n}, \quad \frac{\partial \sigma}{\partial \zeta} = \frac{(\sigma^2 - b^2)(R^n - 1)^2}{4c^2 R^n}, \quad l(\xi) = \frac{\partial \sigma}{\partial \zeta}\bigg|_{\eta=0, \ \xi < b}$$
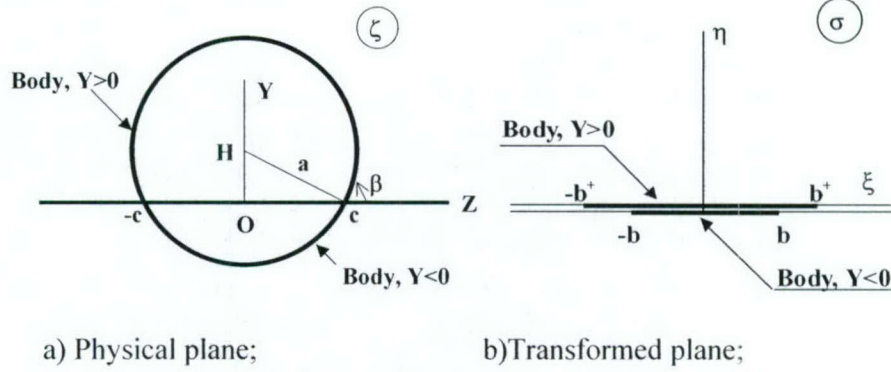

a) Physical plane; b) Transformed plane;

Fig. 5 Cross-section flow scheme for Phase 2.

In the σ-plane, the submerged circle portion is transformed to the lower side of the interval $[-b, b]$. The mapping $\zeta = f^+(\sigma, X, t)$ of the cavity region to the upper half plane (as well as the upper body portion to the upper side of the interval $[-b^+, b^+]$) is obtained with the replacement of $m = 1 - n$ by n.

In the transformed space, the explicit solution is represented by Keldysh-Sedov formula [15]. The complex conjugate velocities in the cavity and stream regions are

$$W^+(\sigma, X, t) = -iV_e^+\left(1 - \frac{\sigma}{\sqrt{\sigma^2 - b^{+2}}}\frac{\partial \sigma}{\partial \zeta}\right), \tag{2.13a}$$

$$W(\sigma, X, t) = -iV_e\left(1 - \frac{\sigma}{\sqrt{\sigma^2 - b^2}}\frac{\partial \sigma}{\partial \zeta}\right) + \frac{a_x}{i\pi}\frac{\partial \sigma}{\sigma^2 - b^2}\frac{\partial \sigma}{\partial \zeta}\int_{-b}^{b}\frac{\sqrt{b^2 - s^2}\,ds}{(s - \sigma)l(s)}. \tag{2.13b}$$

The velocity (2.13a) and the first term of (2.13b) describe the flow fields over cylinders formed by reflection of the upper and lower circle parts [16]. The second terms arise due to the body shape variation in the streamwise direction. For $n > 1/2$, the flow velocities have a singularity of the type $(\zeta^2 - c^2)^{\frac{1}{2n}-1}$ at the points where the free surface intersects the body. Since this singularity is integrable, the lift force and pitching moment are not singular. However, a local asymptotic analysis near these points is needed to treat the higher-order approximations.

On the body surface, $\eta = \pm 0$, $\xi < b$, the pressure is expressed as

$$p^+(x, \lambda, t) = -\Phi_t^+ + \frac{V_e^{+2}}{2}\left[1 - \frac{\lambda^2(1 - \lambda^2)D^2(\lambda, m)}{16m^4 Q^{2m}(\lambda)}\right], \quad \lambda = \frac{\xi}{b^+}$$

10

$$p(x,\lambda,t) = -g_{0t} - g_{0x} - \Phi_t - \Phi_x + \frac{V_e^2}{2}\left[1 - \frac{\lambda^2(1-\lambda^2)D^2(\lambda,n)}{16n^4Q^{2n}(\lambda)}\right] -$$

$$-\frac{a_x^2}{2}\left[1 + \frac{(1-\lambda^2)D^2(\lambda,n)}{\pi^2 Q^{2n}(\lambda)}I^2(\lambda,n)\right] + V_e a_x \frac{\lambda(1-\lambda^2)D^2(\lambda,n)}{4n^2\pi Q^{2n}(\lambda)}I(\lambda,n), \qquad (2.14a)$$

$$\lambda = \frac{\xi}{b}, \quad I(\lambda,n) = \int_{-1}^{1}\frac{Q^n(s)ds}{D(s,n)\sqrt{1-s^2}(s-\lambda)}, \quad D(s,n) = Q^{2n}(s) - 2Q^n(s)\cos\pi n + 1. \quad (2.14b)$$

As shown below, the singularities in (2.14) (at $n \to 0$, $n \to 1$ and $\lambda \to \pm 1$) are integrable.

The local lift force $L_x(x,t)$ acting on cross sections of the partially submerged body portion, $X_1 \le X \le X_2$, is determined as

$$L_x(x,t) = P(x,t) - \frac{\partial(\Phi - \Phi^+)}{\partial t} - \frac{\partial\Phi}{\partial x}, \qquad (2.15a)$$

$$P(x,t) = aV_e^2 P_1(n) - aa_x^2 P_2(n) + aa_x V_e P_{12}(n) - V_e^{+2}P_1(m). \qquad (2.15b)$$

$$\Phi(x,t) = a^2[V_e\Phi_1(n) + a_x\Phi_2(n)], \quad \Phi^+ = a^2 V_e^+\Phi_1(m). \qquad (2.15c)$$

In Ref. [8], the functions of Eqs (2.15) are expressed analytically as

$$\overline{\Phi}_1(n) = -\left[\pi(1-n) + \frac{1}{2}\sin 2\pi n - \frac{\pi(2n^2+1)\sin^2\pi n}{6n^2}\right],$$

$$\Phi_2(n) = -4\frac{\sin\pi n}{n}\left\{e_0(n) - \frac{n}{2}[1 + \pi(1-n)ctg\pi n]\right\},$$

$$P_1(n) = \sin\pi n\left[1 - \frac{1-\pi n(1+2n^2)ctg\pi n}{6n^3}\right],$$

$$P_2(n) = 2\sin\pi n\left\{1 + 2\frac{ctg^2\pi n}{n}\left[e_0(n) - \frac{n}{2}(1 + \pi(1-n)ctg\pi n)\right] - 4\frac{e_{10}(n)}{\pi^2 n^3}\right\},$$

$$P_{12}(n) = -\frac{1}{\pi n^2}\left\{4[1 - \pi n ctg(\pi n)]e_0(n) - 2e_2(n) + \frac{2n^2+1}{6}\pi^2\cos^2(\pi n)\right\},$$

The special functions $e_0(n)$, $e_2(n)$ and $e_2(n)$ are analyzed in Ref. [8]. Due to the first linear terms of Eq. (2.15a) the local lift force is singular for small submerging depth, when $n \to 1$,

$$L_x(n \to 1) \sim -\frac{\partial\Phi_1}{\partial t} - \frac{\partial\Phi_1}{\partial x} \sim$$

$$\sim 2V_e a^2\pi\left(\frac{\partial n}{\partial t} + \frac{\partial n}{\partial x}\right) \sim 2a\frac{V_e(V_e - a_x)}{\pi(1-n)}.$$

11

This is consistent with extensions of the two-dimensional theory [16] by the first author. In the case considered herein, there is the additional term, which is due to axial variations of the body shape. This singularity leads to impulsive loads at the beginning of body submergence. Nevertheless, the body momentum is continuous and is proportional to the potential $\overline{\Phi}_1 \sim 1 - n$.

The foregoing relations allow us to evaluate the lift force and pitching moment acting on the body in the transitional phase 2, when the body passes through the slip surface. In this phase, the total lift force and pitching moment can be expressed as a superposition of three terms, namely,

$$L(t) = L^+(t) + L^\pm(t) + L^-(t) = -\frac{dV_a(t)}{dt} + L_1(t), \tag{2.16a}$$

$$M(t) = M^+(t) + M^\pm(t) + M^-(t) = -\frac{d\omega_a(t)}{dt} + M_1(t) \tag{2.16b}$$

$$V_a(t) = V_a^+(t) + V_a^\pm(t) + V_a^-(t), \quad \omega_a(t) = \omega_a^+(t) + \omega_a^\pm(t) + \omega_a^-(t). \tag{2.16c}$$

The lift force $L^+(t)$ is determined by integrating the local lift force over the body portion totally inside the cavity. This term is similar to that given by (2.10). The lift force $L^-(t)$ acts on the body portion being totally in the external stream. Its expression is similar to (2.11). The terms $L^\pm$ and $M^\pm$ correspond to integration of the local lift (2.15) over the interval $[x_1, x_2]$. They are given by the formulas

$$L_1^\pm = \int_{x_1}^{x_2} P(x,t)dx + x_{1t}\left[\Phi^+(x_1,t) - \Phi(x_1,t)\right] + \Phi(x_1,t) - (1 - x_{2t})\Phi(x_2,t) - x_{2t}\Phi^+(x_2,t),$$

$$M_1^\pm = \int_{x_1}^{x_2} P(x,t)x dx + \int_{x_1}^{x_2} \Phi(x,t)dx + x_1\left[(1 - x_{1t})\Phi(x_1,t) + x_{1t}\Phi^+(x_1,t)\right] -$$
$$- x_2\left[(1 - x_{2t})\Phi(x_2,t) + x_{2t}\Phi^+(x_2,t)\right],$$

$$V_a^\pm(t) = \int_{x_1}^{x_2}\left[\Phi(x,t) - \overline{\Phi}^+(x,t)\right]dx, \quad \omega_a^\pm(t) = \int_{x_1}^{x_2}\left[\Phi(x,t) - \Phi^+(x,t)\right]x dx,$$

where the critical points $x_1(t)$, $x_2(t)$ and their speeds are solutions of the equations

$$\alpha x_k \pm a(x_k) = Y_o(t), \quad x_{kt}(t) \equiv \frac{dx_k(t)}{dt} = \frac{V_o - \omega x_k}{\alpha \pm a_x(x_k)}, \quad k = 1, 2.$$

Note that these representations of the lift force and pitching moment allow us to avoid the singularity at the critical points on the lowest body generator corresponding to $n = 1$. On the other hand, this singularity is integrable since $1 - n \sim \sqrt{x_k - x}$.

The local cross-flow drag coefficient relevant to the partially submerged body cross-sections is expressed as

$$C_{CF}^{\pm}(t) = \int_{x_1}^{x_2} c_x^{\pm}(x,t)a(x)a'(x)dx, \tag{2.17}$$

$$c_x^{\pm} = -\left(\frac{\partial}{\partial t} + \frac{\partial}{\partial x}\right)a\left[a_x\tilde{\Phi}_2(n) - V_e\tilde{\Phi}_1(n)\right] + V_e^2 N_1(n) + a_x^2 N_2(n) + V_e a_x N_{12}(n)$$

The functions $\Phi_{1,2}$, $N_{1,2}$ and N_{12} are investigated in Ref. [8]. They are expressed as

$$\tilde{\Phi}_1(n) = 4\frac{\sin \pi n}{n}\left\{e_0 - \frac{n}{2}[1 + \pi(1-n)ctg\pi n]\right\}, \quad \tilde{\Phi}_2(n) = 4\frac{\sin \pi n}{n}e_{20}(n),$$

$$N_1(n) = \frac{\pi}{6n^2}\left(1 + 2n^2 - \frac{\sin 2\pi n}{2\pi n}\right) - \pi(1-n),$$

$$N_2(n) = \pi(2-n) + \frac{4\cos \pi n}{n\sin \pi n}\left\{e_0 - 2\left(\frac{\sin \pi n}{\pi n}\right)^2 e_{10} - \frac{n}{2}[1 + \pi(1-n)ctg\pi n]\right\},$$

$$N_{12}(n) = 4\left(1 - \cos \pi n \frac{\sin \pi n}{\pi n}\right)\frac{e_0(n)}{n\sin \pi n} + \frac{\cos \pi n}{\pi n^2}\left[2e_2(n) - \frac{\pi^2(1 + 2n^2)}{6}\right].$$

The special function $e_{20}(n)$ is presented in Ref. [8]. In Phase 2, the full crossflow plane drag consists of three parts similar to the lift force (2.16).

3. Outer asymptotic solution and drag components

The outer limit of inner solution dictates the form of outer asymptotic solution. For cavities of infinite span, the outer limits of the solutions (2.4) and (2.13) correspond to dipole distributions on the body axis. This situation is similar to the flow over a thin wing. The latter was analyzed in Refs. [17-20], which showed that higher order approximations are needed to find correct outer solutions and to evaluate the wave drag. As shown in [8] unsteady effects and the finite cavity span effect determine dominant terms of this limit. Although the unsteady terms are present in the outer asymptotic expansion, their contribution to the drag components relevant to short-time scales is small [8]. The dominant wave drag component is due to the quasi-steady term related to the flow over the equivalent body of revolution of the cross-section area $A_{eq}(x,t)$. This corresponds to the source distribution along the body axis $Q_{eq}(x,t) = \partial A_{eq}/\partial x$. For Phases 2 and 3, these source distributions are respectively expressed as [8]

$$Q_{eq} = 2\varepsilon\frac{d_0 \sin \pi n}{nd}\left[\frac{2A'(x)}{\pi}e_0(n) - A(x)V_e\left(1 + 2n^2\right)\frac{\sin \pi n}{6n}\right], \tag{3.1a}$$

$$Q_{eq} = 2\varepsilon\left[H(x,t)A'(x) - A(x)B_{-2}(x,t)\right], \tag{3.1b}$$

where $A(x)$ is body cross-sectional area, and $A' = dA/dx$.

For analysis of the outer asymptotic region, we introduce the scaling

$$X = \frac{\tilde{X}}{\bar{l}_0}; \quad \tilde{Y} = \frac{\tilde{Y}\delta}{\bar{l}_0}; \quad \tilde{Z} = \frac{\tilde{Z}\delta}{\bar{l}_0}; \quad \tilde{r} = \frac{\tilde{r}\delta}{\bar{l}_0}, \tag{3.2a}$$

$$\tilde{p} = \frac{\tilde{p} - p_\infty}{\rho_\infty U_\infty^2 \delta^2} = -\varphi_X \quad \tilde{\Phi} = l_0 U_\infty \{X + \delta^2 \varphi(X, \tilde{Y}, \tilde{Z}, t; K)\}, \tag{3.2b}$$

where $K = (M^2 - 1)/\delta^2$ is transonic similarity parameter. The outer potential φ is a solution of the Karman-Guderley (KG) transonic small disturbance axisymmetric flow boundary-value problem [5,12,19]

$$\left[K - (\gamma + 1)\frac{\partial \varphi}{\partial X}\right]\frac{\partial^2 \varphi}{\partial X^2} + \frac{1}{\tilde{r}}\frac{\partial}{\partial \tilde{r}}\tilde{r}\frac{\partial \varphi}{\partial \tilde{r}} = 0, \tag{3.3b}$$

$$\tilde{r} \to \infty: \varphi \to 0; \tilde{r} \to 0: \tilde{r}\frac{\partial \varphi}{\partial \tilde{r}} \to \frac{Q_{eq}}{2\pi}. \tag{3.3b}$$

The integration function $g_0(X,t)$ of the inner solutions (2.4) and (2.13), which is needed for calculations of the wave drag that results from solving the KG equation (3.3b) and imposing the matching condition

$$g_0(X,t) = \lim_{\tilde{r} \to 0}\left[\varphi(X,\tilde{r},t) - \frac{Q_{eq}}{2\pi}\ln \tilde{r}\right]. \tag{3.4}$$

Now the wave drag can be calculated by integrating the pressure over the body surface. In Phase 2, the drag force coefficient is represented as the sum of four terms

$$C_D(t) = \frac{\hat{D}}{\rho_\infty U_\infty^2 \pi \delta^2 l_0^2} = C_{DF}(t) + C_{DB}(t) + C_{DW}(t) + C_{CF}(t). \tag{3.5}$$

Here the friction drag coefficient, $C_{DF}(t)$, is resulted from integration of the local friction coefficient $c_f(\bar{X}, \text{Re}_x)$ over the body surface

$$C_{DF}(t) = \frac{\hat{D}_f}{\rho_\infty U_\infty^2 \pi \delta^2 l_0^2} = \frac{1}{\delta}\int_0^1 kc_f(\bar{X}, \text{Re}_x)d\bar{X}, \tag{3.6a}$$

$$\bar{X} = X - X_0, \quad \text{Re}_x = \text{Re}\,\bar{X}[1 - U(t)], \quad \text{Re} = \frac{\rho_\infty U_\infty l_0}{\mu_\infty}, \tag{3.6b}$$

where $U(t)$ is horizontal body speed. The coefficient k is indicative of the friction drag being appreciable only on the body portion submerged into the flow external to the cavity. For a partially submerged body portion ($X_1 \le X \le X_2$), this coefficient is $k = \beta/\pi$; for the totally submerged portion, $k = 1$; for the body portion totally inside the cavity, $k = 0$. Because the local friction coefficient c_f is a weak function of the Mach number at transonic speeds, we use the Schultz-Grunow correlation [10] developed for incompressible axisymmetric turbulent boundary layers

$$c_f(X, \text{Re}_x) = \bar{c}_f(\text{Re}_x) \left[\int_0^X a^{7/6}(x) dx \right]^{6/7}, \bar{c}_f(\text{Re}_x) = 0.37 (\lg \text{Re}_x)^{-2.584}. \qquad (3.6c)$$

The base drag coefficient, $C_{DB}(t)$, is obtained from integration of the pressure difference, $\bar{p}_b - p_\infty$, over the body base. It is expressed as a function of the Mach number [11]

$$C_{DB}(M) = \frac{\hat{D}_b}{\rho_\infty U_\infty^2 \pi \delta^2 l_0^2} = \frac{a_e^2}{\gamma M^2} [1 - p_b(M)], \qquad (3.7)$$

where $M = M_\infty [1 - U(t)]$, a_e is base radius, and $p_b(M) = \hat{p}_b / p_\infty$ is a non-dimensional base pressure. For ogive-cylinder bodies, the function $p_b(M)$ is given in Ref. [8].

In Phase 2, the slip surface leads to new physical effects. If the body base is not fully submerged into the external flow, then the base pressure is $p_b(M) = 1$ due to the boundary condition on the slip surface. Accordingly, the base drag coefficient is $C_{DB} = 0$.

The wave drag coefficient, $C_{DW}(t, M)$, is expressed in terms of the function $A_0(X, t)$ as

$$C_{DW}(t) = -2\delta^2 \int_{x_0}^{x_e} \left[\frac{\partial g_0}{\partial t} + \frac{\partial g_0}{\partial x} \right] A' \beta dx. \qquad (3.8)$$

The numerical code of the first author was used to solve the KG equation and calculate the function $g_0(X, t)$ at each time instant of the trajectory in the pseudo-steady approximation.

4. Analysis of trajectory equation

The 3-DOF trajectory equations are expressed in the form

$$\frac{dV}{dt} = c_l L(t) - c_g, \quad \frac{d\omega}{dt} = c_m M_p(t), \quad \frac{dU}{dt} = c_l C_D(t), \qquad (4.1a)$$

$$c_g = \frac{\hat{g} \hat{l}_0}{\delta U_\infty^2}, c_l = \frac{\pi \rho_\infty \hat{l}_0^3 \delta^2}{\hat{m}}, c_m = \frac{\pi \rho_\infty \hat{l}_0^5 \delta^2}{\hat{I}}, \qquad (4.1b)$$

where $\hat{m}$ and $\hat{I}$ are respectively body mass and moment of inertia. The system (4.1) is supplemented by initial conditions at $t = t_0$. In Phases 1 and 3, the equations for V and ω are integrated approximately.

In Phase 1, for small aerodynamic forces the approximate integrals have the form

$$Y_o(t) = Y_0 + V_0 t - \frac{1}{2} (1 - \pi c_m g_2) c_g t^2, \quad \alpha(t) = \alpha_0 + \omega_0 t + \frac{1}{2} \pi g_1 c_m c_g t^2. \qquad (4.2)$$

15

These relations describe the parabolic evolution of the CG vertical coordinate and the angle of attack.

In Phase 3, the explicit integrals can be obtained if the slip surface effect is neglected, $q = 0$ in Eqs. (2.5). In this case, the two first equations in (4.1a) are reduced to the decoupled equations for the angular velocity $\omega(t)$ and the function $W(t) = V_o(t) - \alpha(t)$

$$\frac{d^2W}{dt^2} - 2\gamma\frac{dW}{dt} + \kappa W + c_1 = 0, \quad \frac{d^2\omega}{dt^2} - 2\gamma\frac{d\omega}{dt} + \kappa\omega + c_2 = 0, \tag{4.3}$$

$$\gamma = \frac{c_m A_e}{2\Delta_0}\left[x_e^2 - \frac{c_l}{c_m} + c_l\left(x_e^2 s_0 - 2x_e s_1 + s_2\right)\right], \quad c_1 = \frac{c_m c_g}{\Delta_0}\left(s_1 - x_e^2 A_e\right),$$

$$\kappa = \frac{c_m}{\Delta_0}\left[s_0 - A_e x_e - c_l A_e\left(s_0 x_e - s_1\right)\right], \quad c_2 = \frac{c_m c_g}{\Delta_0}\left(s_0 - x_e A_e\right),$$

$$\Delta_0 = \left(1 + c_l\pi g_0\right)\left(1 - c_m\pi g_2\right) + c_l c_m \pi^2 g_1^2.$$

$$s_0 \equiv \pi\int_{x_0}^{x_e} a^2(x)dx, \; s_1 \equiv \pi\int_{x_0}^{x_e} a^2(x)x\,dx, \; s_2 \equiv \pi\int_{x_0}^{x_e} a^2(x)x^2\,dx.$$

The form of solution depends on roots of the characteristic equation

$$\lambda^2 - 2\gamma\lambda + \kappa = 0; \quad \lambda_1 = \gamma + i\Omega; \quad \lambda_2 = \gamma - i\Omega, \quad \Omega = \sqrt{\kappa - \gamma^2}. \tag{4.4}$$

If the roots λ_1 and λ_2 are complex, the solution is oscillatory

$$V_o(t) = C_0 - C_2\tau + \left(A_1\cos\Omega\tau + A_2\sin\Omega\tau\right)\exp(\gamma\tau), \tag{4.5a}$$
$$\omega = -C_2 + \left(B_1\cos\Omega\tau + B_2\sin\Omega\tau\right)\exp(\gamma\tau), \tag{4.5b}$$

where $\tau = t - t_0$ is the time measured from the beginning of Phase 3, t_0. The coefficients A_1, A_2, B_1, B_2, C_0 and C_2 are determined from the initial conditions at $\tau = 0$ [7]. Equations (4.5) indicate that the body motion includes two components. The first component corresponds to a CG translation with constant acceleration C_2 and the body rotation with the constant angular speed $-C_2$. These terms are associated with a non-oscillatory motion, which is called "mean state." The second component corresponds to periodic modulations of the mean state. These oscillations are neutral for $\gamma = 0$, unstable for positive γ, and stable for negative γ.

If the roots λ_1 and λ_2 are real, we obtain the exponentially growing or decaying solution

$$V_o(t) = C_0 - C_2\tau + \left(A_1\cosh\nu\tau + A_2\sinh\nu\tau\right)\exp(\gamma\tau), \tag{4.6a}$$
$$\omega = -C_2 + \left(B_1\cosh\nu\tau + B_2\sinh\nu\tau\right)\exp(\gamma\tau), \tag{4.6b}$$

where $\nu = i\Omega$. In this case, the motion also consists of two components. The mean state of body motion is the same as in the foregoing case. The second component describes an exponential

approach to the mean state for negative λ_1 and λ_2, and an exponential growth of the vertical and angular speeds for positive λ_1 or/and λ_2. Relations (4.5) and (4.6) can be used for correlation of experiments, in which the body is ejected into the freestream with given initial parameters. Note that the oscillation frequency observed in the experiments [21] is in satisfactory agreement with the relation (4.4) although the experimental models are not slender bodies.

The 3-DOF trajectory equations (4.1) are solved numerically for all three phases of the separation process. An explicit fourth-order Adams procedure is used for few initial time steps. Then, an implicit sixth-order Runge-Kutta scheme is applied. The code allows for rapid solution of Eqs. (4.1a), with the initial conditions being determined by the store release mechanism. Using a PC-166 type computer, a complete 3-DOF trajectory is predicted in a few minutes. In Ref. [7], the code was validated by comparison with the subsonic experimental data [12]. In the majority of cases, the predicted trajectories are in good agreement with the experiment. This proves that the theoretical model correctly simulates basic physical effects of the separation process in all three phases.

Our parametric studies reveal interesting body motion features that are illustrated below for the ogive-cylinder body B4N2 tested in the subsonic wind-tunnel experiments [12]. There, the model has radius $\bar{a}_0 = 0.9525$ cm, nose length $\bar{x}_n = 9.04$ cm, and total length 30.48 cm. The distance from the nose to the CG is $\bar{x}_0 = 15.09$ cm, mass m = 46.14 g, moment of inertia $I = 0.0008$ kg×m^2. The initial location and horizontal velocity of the body CG are $X_0 = U_0 = 0$.

Parametric calculations discovered a bifurcation of pitch angle time history for subsonic separation. In Fig. 6, two quite different curves (solid and dotted lines) correspond to the same initial conditions but opposite signs of the pitching moment in Phase 3. One of the theoretical curves agrees with the experimental data [12] (symbols). Analysis of the full database reported in [12] indicates that such bifurcations are present in the experiments; *i.e.*, two divergent trajectories at about the same initial conditions are observed. This bifurcation is of the special kind for which the different curves are tangent at the bifurcation point [22]. The trajectory equations allow for such a bifurcation, since the aerodynamic forcing terms in Eqs. (4.1a) are nonlinear (quadratic) functions of the speeds V and ω. One of the two possible trajectories is selected when the body crosses the shear layer. Therefore, Phase 2 serves as a trigger of the pitch bifurcation. Although this phase is relatively short, its accurate modeling is important for prediction of the pitch history and store trajectory in the next phase when the store is outside the cavity.

To estimate the Mach number effect, calculations were performed for the transonic flow with $M_\infty = 0.999$ and the Reynolds number Re = 6.4782755×10^6. The freestream Mach number was selected to be very close to unity to maximize the wave drag and investigate its impact on the horizontal component of the body trajectory. Figure 7 demonstrates the body thickness effect on the trajectory parameters. Figure 7a shows time histories of the vertical CG coordinate. In Fig. 7b, the CG trajectories are shown in the *X-Y* plane. The temporal variations of the pitch angle and the vertical speed depend strongly on the body thickness ratio as shown in Figs. 7c and 7d. For $D=D_0$, the body separates from the cavity in a relatively short time period. For $D=2D_0$, the body moves almost horizontally near the parent body for a relatively long time period (until the pitch angle is negative). The total vertical displacement is about $4D$ only. During this phase, the body drifts downstream to the distance $X \sim 70D_0$ from its initial state. This distance is larger than four body lengths. The average pitch angle and the pitch oscillation frequency are also strong functions of the body

thickness ratio. For $D=3D_0$, a ricochet phenomenon is observed. The body returns to the cavity with a relatively small downstream displacement. The pitch angle grows monotonically with small oscillations since the pitching moment is too small to overcome pitching due to the initial angular speed.

Figure 8 illustrates the initial vertical speed effect on the body trajectories. Calculations were made at $\alpha_0 = 6°$, $\omega_0 = 0$ deg/s $Y_0 = 2.54$ cm and the two near-critical values of the initial vertical speed $V_0 = 0.508$ m/s and 0.762 m/s. The plots of CG histories (Fig. 8a) and CG trajectories (Fig. 8b) at $V_0 = 0.508$ m/s indicate that the body ricochets from the slip surface and re-contacts the parent body. When the body enters into the shear layer, the pitch angle grows slightly (see Fig. 8c) due to body inertia. Because of a negative pitching moment, the angle α decreases with small angular speed. This trend is too weak to reduce the pitch angle to its critical value (at which the separation becomes possible). For $V_0 = 0.762$ m/s, the body stays near the shear layer for a long time and moves downstream a long distance. In this case, the negative angular speed is high enough to decrease the pitch angle below its critical value, and the body separates from the cavity. Figure 8d shows that in both cases, the vertical CG speed grows to a positive value. For $V_0 = 0.762$ m/s, the gravity force is strong enough to cause the body departure from the cavity, whereas for $V_0 = 0.508$ m/s this force is too small for separation.

Figure 9 illustrates the initial pitch angle effect on the trajectory behavior. The calculations were performed at $Y_0 = 2.54$ cm, $V_0 = 0.508$ m/s, $\omega_0 = 0$ deg/s. The trajectory characteristics are very sensitive to variations of the initial pitch angle α_0. The latter may be induced by the release mechanism and/or aircraft maneuvering at the release instant. The variation $\Delta\alpha_0 = 1°$ leads to substantial perturbations of the body trajectory; i.e., the body separates from the cavity at $\alpha_0 = 5$ and re-contacts the parent body at $\alpha_0 = 6$ (see Figs. 9a and 9b). Near the critical angle, $\alpha_0 = 5$, the trajectory behavior is similar to that shown in Figs. 8a and 8b for the initial speed $V_0 = 0.762$ m/s. However, the vertical CG speed in this case does not become positive (see Fig. 9d). The body base enters the external flow and then returns to the shear layer when the angle of attack becomes negative. Then, the body exits to the external flow and drops downward from the shear layer. The case, $\alpha_0 = -6$, is also shown for comparison. Here the body quickly crosses the shear layer and separates from the cavity to a large distance. An interesting feature of this regime is associated with vertical oscillations of the CG speed in Phase 3 (see Fig. 9d). This behavior is consistent with the expression (4.5) for the body speed in an unbounded stream.

5. Summary discussion

Aerodynamic and dynamic problems associated with separation of slender bodies of revolution from rectangular cavities into transonic stream are considered herein using slender body theory. The inner and outer asymptotic flow regions are treated with the help of combined analytical and numerical methods. Asymptotic analyses allow us to highlight lumped parameters governing the separation process and decompose the problem into a series of simpler unit problems, which are solved analytically for practical cases. The analytical results substantially simplify the solution of the store dynamic equations, which are used to develop fast and robust numerical codes to predict 2-DOF and 3-DOF store trajectories. The computational package is validated by comparisons with the subsonic wind tunnel experiments of IIT. An important aspect was the similarity of near fields for the

subsonic and transonic cases. Parametric studies of the store separation into transonic free stream indicate critical regimes relevant to store re-contact and ricochet.

The body separation process was treated as a sequence of three phases: in Phase 1, the body is inside the cavity; in Phase 2, the body crosses the shear layer; in Phase 3, the body is outside the cavity in the outer stream. For the inner asymptotic solution, the cavity sidewall effects can be neglected. This allows us to decompose the inner problem into simpler unit problems, which are solved analytically with the slip surface treated as a flat plane of zero potential. Analytical solutions of the dominant approximation problems relevant to separation of a thin body of revolution from a rectangular cavity adjacent to a uniform flow are obtained. For Phases 1 and 3, we use multipole expansions leading to compact expressions for the pressure on the body surface and the cross-sectional lift. For Phase 2, the solution is obtained using conformal mapping and Keldysh-Sedov integral representations. The local lift force is also expressed explicitly using new special functions. As contrasted to the two-dimensional problem, the solutions for Phases 2 and 3 include new terms relevant to the axial variation of the body shape. These terms lead to qualitatively new features of the slip surface and rigid wall effects. For example, in Phase 3 the slip-surface effect is essentially stronger than in Phase 1 because the influence of this boundary decreases inversely with distance from the body. In Phase 2, the flow velocities of the dominant approximation are singular at the line of intersection between the slip surface and the body surface. However, these singularities are integrable. This allows us to calculate the lift force and pitching moment without detailed analyses of the singular regions. Nevertheless, these singularities should be considered in the future to treat the higher-order approximations.

Using the asymptotic theory, we formulated the matching conditions for the inner and outer solutions for a body of revolution separating from a cavity into an outer transonic freestream. We believe that for many practical problems, the transonic wave drag can be predicted within the framework of quasi-steady flow. Short-time effects which may include cavity shear layer oscilliations are averaged out over a long time scale relevant to the outer transonic region, and their contribution to the wave drag seems to be small. The quasi-steady outer flow corresponds to transonic flow over an equivalent body of revolution. Explicit forms of the equivalent body are obtained as functions of time and the dimensionless cross-section area. Formulas for the base and friction drags are derived using known theoretical results and empirical correlations. For Phases 2 and 3, different components of the cross-flow drag were calculated and analyzed. The wave drag, which was one of these, was calculated using the first author's code that provided solutions of the Karman-Guderley equation.

Our results form a foundation for the development of computationally non-intensive algorithms that predict body trajectories during the separation process. The numerical code predicting the store trajectory for all three phases was developed and verified by comparisons with the experimental data of IIT. Parametric studies revealed a bifurcation of the pitch-angle history in Phase 3. This is consistent with the experimental data indicating the presence of two substantially different pitching trajectories at almost identical initial conditions. Although the transitional Phase 2 is relatively short, its aerodynamics is crucial in identifying one of the two possible trajectories in Phase 3 when the body is outside the cavity. Further theoretical and experimental efforts are needed to investigate the bifurcation mechanism. Using the code it is feasible to predict regimes of the bifurcation occurrence, which is important for store separation control.

Numerical results illustrating 3-DOF body dynamics for separations from a cavity in the transonic freestream show that this dynamics could be rather complicated. It includes such phenomena as store ricochet or/and re-contact. The body trajectory is very sensitive to the initial "launch" vertical speed or pitch angle. Ricochet/recontact occurs when the initial pitch angle is larger or the vertical speed is smaller than certain critical values. Above the critical angle or below the critical vertical speed, the body does not cross the slip surface and returns to the cavity (ricochet). With increase of pitch angle and horizontal displacement, contact with the upper or back cavity walls becomes possible. Near the critical conditions, the body can stay at small heights from the shear layer for a long time period and may partially return to the cavity interior. If the horizontal displacement during this time period is larger than the cavity length, contact with the back cavity wall is possible; otherwise, the store slowly separates.

The parametric studies showed that trajectory parameters, such as the mean state characteristic, oscillation amplitude, frequency and amplification rate depend critically on the body mass, CG location and freestream speed. Moreover, the trajectory is very sensitive to the initial conditions induced by the release mechanism. Satisfactory agreement between theory and experiments is difficult without detailed and accurate simulation of the release conditions. These conditions can be established using direct measurements or post-processing of the experimental trajectories. The initial conditions may also be influenced by difficult-to-control disturbances such as wind-tunnel flow oscillations or/and capture of the model ends by the release mechanism. On the other hand, the store separation can be controlled effectively by the release mechanism. Our modeling can help with the design of ejection units and thrust motors for stage separation. The PC-oriented code allows for fast evaluations of thrust and weight required for these units. Quick turnaround calculations also help to understand how to avoid an adverse re-contact situation with a relatively small impulse.

Acknowledgments

References

1. Schindel, L.H., "Store Separation," AGARD-AG-202, June, 1975.

2. Goodwin, F.K., Dillenius, M.F.E., Nielsen, J.N., "Prediction of six-degree-of-freedom store separation trajectories at speeds up to the critical speed. V.1. Theoretical methods and comparison with experiment." AFFDL-TR-72-83.

3. Wood, M.E., "Application of Experimental Techniques to Store Release Problems." Proceedings of NEAR Conference on Missile Aerodynamics, Monterey, California, 1988.

4. Prewitt, N.C., Belk, D.M., Maple, R.C., "Multiple Body Trajectory Calculations Using the Beggar Code", *J. Aircraft*, **36**, No. 5, pp. 802-808, 1999.

5. Cole, J.D., and Cook, L.P., *Transonic Aerodynamics.* Pergamon Press, 1987.

6. Malmuth, N.D., Shalaev, V.I., Fedorov, A.V. 1998 "Combined Asymptotics and Numerical Methods in Transonic Store Interactions", Technical Report of Contract F49620-99-0005, AFOSR/NM. (available in Defense Technical Information Center, stient.dtic.mil).

7. V. Shalaev, A. Fedorov and N. Malmuth. "Dynamics of Slender Bodies Separating from Rectangular Cavities", *AIAA J.*, **40**, No. 3, March 2002, pp.517-525.

8. V. Shalaev, N. Malmuth, A. Fedorov, "Analytical Modeling of Transonic Store Separation from a Cavity," to be presented as AIAA Paper 2003-0004 AIAA 41st Aerospace Sciences Meeting, Reno, Nevada, January 6, 2003.

9. Chow, W.L., "Base Pressure of a Projectile Within the Transonic Flight Regime", *AIAA J.*, **23**, No. 3, pp. 388-395, 1985.

10. Schlichtimg, G., *Boundary Layer Theory,* McGraw-Hill, New York, 1968.

11. Cole, J. and Malmuth, N., "Wave Drag Due to the Lift for Slender Airplanes", NASA Conference Publication 3020, v. 1, p. 293, 1988.

12. Malmuth, N., Hites, M., and Williams, D., "Photographic Investigation of the Dynamics of an Ogive Model near a Cavity at Subsonic Mach Numbers", Final Report. Fluid Dynamics Research Center Illinois Institute of Technology, January 18, 1998.

13. Kochin, N.E. "The Influence of the Lattice Step on its Hydrodynamic Characteristics", *J. Appl. Mathematics and Mechanics*, vol. 5, No. 2, 1941.

14. Yaroshevskii, V.A. "Calculation of Aerodynamic Interference Forces between Two Bodies of Revolution", *Engineering Journal,* 1963, v. 3, No. 3, p. 546 (In Russian). Translation is in *Fluid Dynamics. Soviet Researches.*

15. Sedov, L.I., *Two-dimensional Problems of Hydrodynamics and Aerodynamics,* Nauka, Moscow, 1966.

16. Milne-Thomson, L.M. *Theoretical Hydrodynamics.* London, Macmillan and Co., LTD, 1960.

17. Cheng, H.K., Hafez, M.M., "Transonic Equivalence Rule: a Nonlinear Problem Involving Lift", *J. of Fluid Mechanics*, v. 72, No. 1, 1975.

18. Barnwell, R.W., "Analysis of Transonic Flow about Lifting Wing-Body Configurations", NASA TR, R-440, 1975.

19. Cole, J. and Malmuth, N., "Wave Drag Due to the Lift for Slender Airplanes", NASA Conference Publication 3020, v. 1, p. 293, 1988.

20. Cole, J.D., and Cook, L.P., "Some Problems of Transonic Flow Theory", *Symposium Transsonicum III*, Eds. Zierep, J., and Oertel, H., IUTAM Symp., Gottingen, May 24-27, 1988; Springer Verlag, Berlin, Heidelberg, 1989, pp. 157-169.

21. Carter, H.S. and Lee, J.B. "Investigation of the Injection Release of Several Dynamically Scaled Bluff Internal Stores at Mach Numbers of 0.8, 1.39, and 1.98", NACA RM L56H28.

22. Bautin, N.N., Leonovich, E.A. *Methods and Ways of the Qualitative Analysis of Dynamical Systems in a Plane.* Moscow, Nauka, 1990.
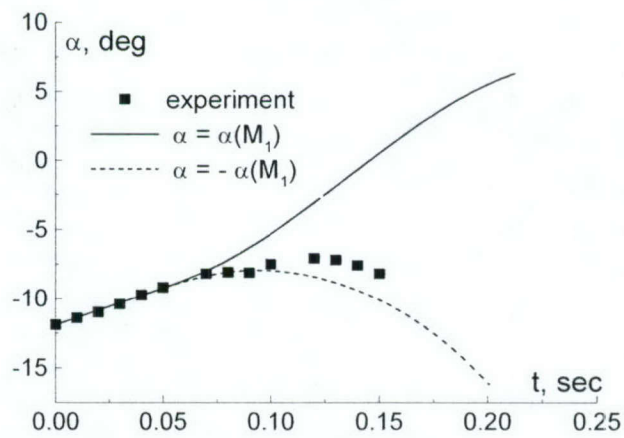
Fig. 6. Bifurcation of the pitch history.
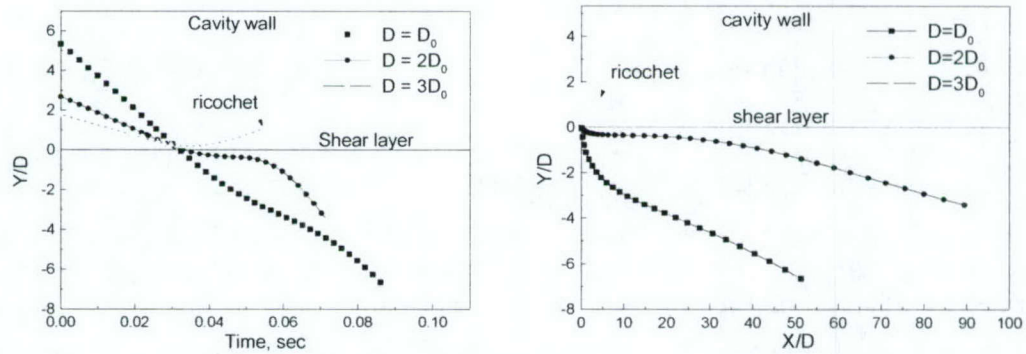
a) Time histories of the vertical CG coordinate;   b) Trajectories of CG
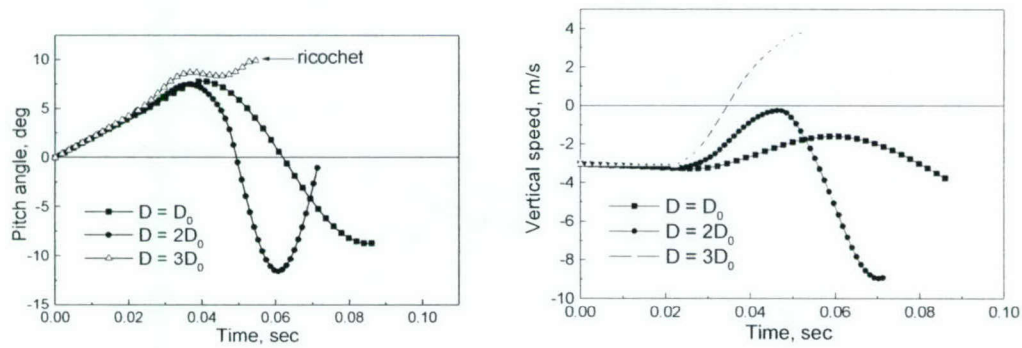
c) Pitch angle histories.

d) Evolution of CG vertical speed;

Fig. 7 Trajectory parameters for the bodies of various thickness.
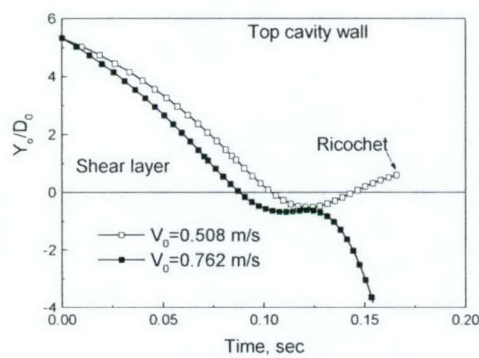
a) Time histories of vertical CG coordinate;   b) CG trajectories
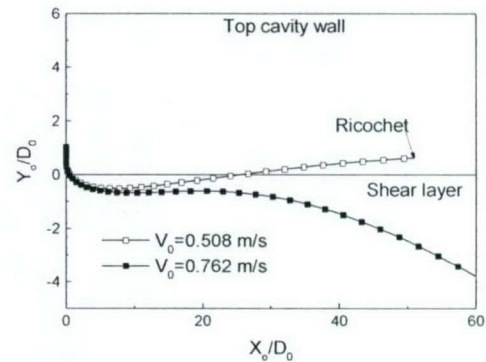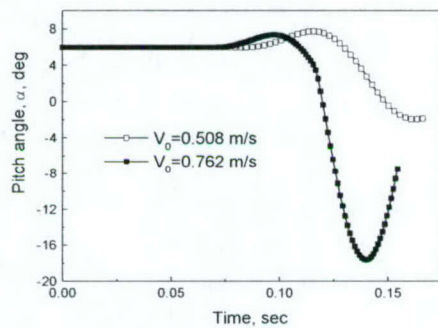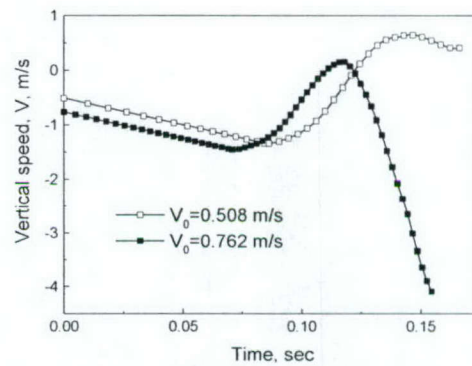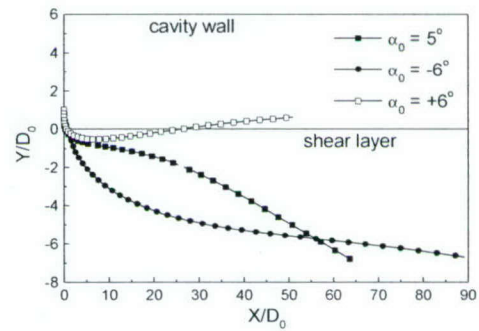

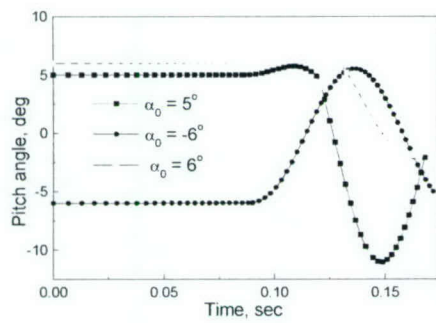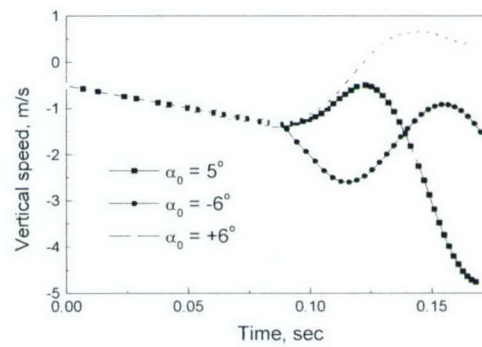c) Pitch angle histories;   d) Evolution of CG vertical speed;

Fig. 8 Trajectory parameters for various initial speeds.
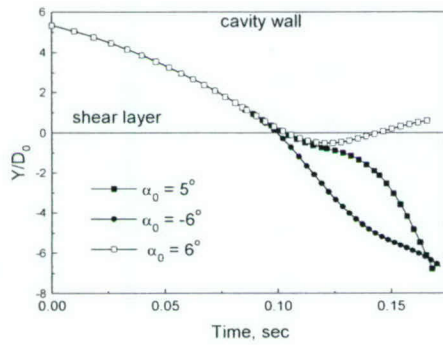
a) CG vertical coordinate histories;   b) CG trajectories;

c) Pitch angle histories;   d) Evolution of CG vertical speed;

Fig. 9 Trajectory parameters at various initial angles of attack.

THEORETICAL MODELING OF SLENDER BODIES INTERACTION IN SUPERSONIC FLOWS

Norman Malmuth[†] and Vladimir Shalaev[††]

[†] Rockwell Scientific, Thousand Oaks, California 91360
nmalmuth@rwsc.com

[††] Department of Aeromechanics and Flight Engineering, Moscow Institute of
Physics and Technology, Zhukovski 140182, Russia

Abstract

Interaction of two slender bodies in supersonic free stream is analyzed using perturbation theory. Four effects of interaction are identified: external flow inclination, additional boundary conditions on the parent body surface, additional forces and moments due to external flow stratification and interaction with external shocks. The latter effect is considered using an approximated model allowing for a simple formula for perturbed pressure. Numerical examples are presented to illustrate the shock-store interaction effects.

Nomenclature

$\tilde{X}, \tilde{Y}, \tilde{Z}$	Cartesian coordinates attached to the parent body	
$\tilde{u}, \tilde{v}, \tilde{w}, \tilde{p}$	flow velocity and pressure perturbations induced by the parent body	
x, y, z	coordinates attached to the store CG	
r, θ	polar radius and angle	
u, v, w, p	flow velocity and pressure perturbations induced by the store	
p', p''	pressures behind the incident and reflected shocks	
t	time	
X, Y	streamwise and vertical store CG coordinates	
U, V	streamwise and vertical store CG speeds	
$\tilde{l}$	parent body length	
l	store length	
$a(x)$	store radius	
D	store diameter	
$\tilde{D}, \tilde{L}, \tilde{M}$	drag, lift forces and pitching moment due to external flow perturbations	

D_s, L_s, M_s	drag, lift forces and pitching moment due to shock-store interaction	
$\mathbf{I}$	unit vector collinear to incident shock	
$\mathbf{N}$	unit vector normal to the store surface	
$\mathbf{R}$	unit vector collinear reflected characteristic	
M	freestream Mach number	
$\tilde{\delta}$	thickness to length ratio of the parent body	
δ	thickness to length ratio of the store	
α	angle of attack	
Δ	length of interaction region	
$\mu = l/\tilde{l}$		
ε	external flow perturbation level	
$\beta = \sqrt{M^2 - 1}$		
$\phi = \arcsin\dfrac{1}{M}$	Mach angle	
γ	angle between normal to the store surface and the incident characteristic	
$\tilde{\Phi}$	external flow potential	
Φ	store induced flow potential	

1. Introduction

The unsteady interaction between bodies moving in free stream is a difficult aerodynamic problem, which has important practical applications, such as body separation from a cavity or external supports and multiple body separation.[1,2] Common engineering approaches to predict the aerodynamic interactions are based on steady experiments and computations.[1,3] However, effects of the external flow nonuniformity and unsteady effects may be dominant, and the traditional methods may lead to essential losses of accuracy in body trajectory calculations.[1,2,4] In this connection, a variety of advanced numerical procedures were developed to predict unsteady aerodynamic loads.[6-9] However, time consuming calculations obstruct to use of CFD solutions for practical applications.

In this paper, an asymptotic theory is used to simplify the solution procedure and identify basic parameters governing the slender bodies interaction in supersonic free stream. Interactions of two slender bodies associated with store separation from a parent body of revolution or from a slender wing are basic unit problems to be addressed hereafter. In the first-order approximation, the parent-body effect on the store can be considered as if the latter moves in the external inhomogeneous flow induced by the former. Similar approaches have been used to account for the aircraft flow-field effect on a store separating to subsonic[10,11] and supersonic[13] streams. From this point of view the theory developed hereafter complements our previous studies of store separations from a rectangular cavity and a flat wall.[5,13-16] This allows for coupling of the global aircraft flow field with the local flow near the store. Note that the developed approach may be applied to other problems such as an interaction of the store with vortices induced inside a cavity, the body motion in a vortical wake, multiple bodies interactions in free stream, etc.

In subsonic flows, the external flow perturbations are distributed in space. Their contributions to forces and moments acting on the store are reduced to the additional angle of attack due to the external flow inclination as well as the inhomogeneous external pressure integrals. In supersonic flows, new effects are due to scattering and reflection of weak shocks. At the initial stage of separation, these phenomena lead to formation of the shock-wave system (called as a wave train) between the parent body and the store. Since shocks are weakly attenuated, the problem of their diffraction and re-reflection needs to be analyzed. Moreover, the shock-body interaction leads to essential changes of the pressure distribution on the store surface that, in turn, causes appreciable changes of aerodynamic forces and moments acting

on the store. In this paper, the problem of shock-wave diffraction by a slender body is analyzed using asymptotic methods It was shown that, in the first-order approximation, the flow field in the local scattering region is described by the linear acoustic equation. In the framework of geometrical acoustics, an analytical solution for shock diffraction is obtained. This solution is useful for understanding of basic features of such flows and allows us to develop a quick and compact code for estimating the trajectory of a store separating from a thin wing to supersonic free stream. Numerical examples are presented to illustrate shock-body interaction effects.

2. Slender-body interaction with weakly inhomogeneous external flow-field

Consider two slender bodies in supersonic free stream: one is a parent body of large size and another is a relatively small store. To analyze the parent body-store interaction, we introduce the coordinate systems: $OX^*Y^*Z^*$ is attached to the parent body; $ox^*y^*z^*$ is attached to the store CG (see Fig.1). The store moves in the vertical plane with the CG horizontal speed $U^*(t^*)$, vertical speed $V^*(t^*)$ and angular speed $\omega^*(t^*)$ at small angle of attack $\alpha^*(t^*)$. To analyze the flow we introduce the nondimensional variables

$$\tilde{X} = \frac{X^*}{\tilde{l}}, \quad \tilde{Y} = \frac{Y^*}{\delta_a \tilde{l}}, \quad \tilde{Z} = \frac{Z^*}{\tilde{l}}, \tag{1}$$

$$X = \frac{X^*}{l}, \quad Y = \frac{Y^*}{\delta l}, \quad Z = \frac{Z^*}{l}, ,$$

$$x = \frac{x^*}{l}, y = \frac{y^*}{\delta l} = r\sin\theta, \quad z = \frac{z^*}{\delta l} = r\cos\theta,$$

$$t = \frac{t^* u_\infty}{l}, \quad \tilde{X} = \tilde{X}_o(t) + \mu x, \quad \tilde{Y} = \tilde{Y}_o(t) + \delta_y (y - \alpha x).$$

Here $\tilde{l}$ and l is length of the parent body and the store respectively; $\tilde{\delta}\tilde{l}$ is the parent body thickness, δl is the store thickness. The parameter δ_a characterizes the external flow-field inhomogeneity induced by the parent body: for a slender body $\delta_a = \tilde{\delta}$, for a thin wing $\delta_a = 1$. The angle of attack, $\alpha(t)$, is referenced to δ ; r and θ are polar radius and angle on the store cross-section plane, t^* is time, u_∞ is freestream velocity; $\tilde{X}_o(t)$, $\tilde{Y}_o(t)$ are coordinates of the body CG. The both bodies are slender

$$\delta \ll 1, \tilde{\delta} \ll 1. \tag{2}$$

The nondimensional parameters

$$\mu = \frac{l}{\tilde{l}} \le O(1), \delta_y = \frac{\mu\delta}{\delta_a} \ll 1, \tag{3}$$

2

are assumed to be small. The store shape is given by the equations

$$\tilde{Y}_b = \tilde{H}(x,t) + \delta_y a(x)\sin\theta \ , \quad r_b = a(x) \ . \tag{4}$$

where $\tilde{H}(x,t) = \tilde{Y}_o(t) - \delta_y \alpha x$ is distance from the plane $\tilde{Y} = 0$ to ox-axis. The parent body shape is

$$\tilde{Y} = \delta\, h(\tilde{X}, \tilde{Z}) \tag{5}$$

The external flow field is assumed to be steady. Then the flow velocities (u^*, v^*, w^*) and the pressure p^* are expressed in the form of asymptotic expansions

$$p^*(X^*, Y^*, Z^*, t^*) = p_\infty + $$
$$+ \rho_\infty U_\infty^2 \left[\varepsilon\, \tilde{p}\left(\tilde{X}, \tilde{Y}, \tilde{Z}\right) + \delta^2 p(x, y, z, t) + \dots \right]$$
$$u^*(X^*, Y^*, Z^*, t^*) = U_\infty + $$
$$+ U_\infty \left[\varepsilon\, \tilde{u}\left(\tilde{X}, \tilde{Y}, \tilde{Z}\right) + \delta^2 u(x, y, z, t) + \dots \right]$$
$$v^*(X^*, Y^*, Z^*, t^*) = $$
$$= U_\infty \left[\delta\, \tilde{v}\left(\tilde{X}, \tilde{Y}, \tilde{Z}\right) + \delta v(x, y, z, t) + \dots \right],$$
$$w^*(X^*, Y^*, Z^*, t^*) = $$
$$= U_\infty \left[\delta\, \tilde{w}\left(\tilde{X}, \tilde{Y}, \tilde{Z}\right) + \delta w(x, y, z, t) + \dots \right], \tag{6}$$

where p_∞ and ρ_∞ are freestream pressure and density; the small parameter ε ($\varepsilon = \delta$ for a wing and $\varepsilon = \tilde{\delta}^2 \ln(1/\tilde{\delta})$ for a slender body) characterizes the level of external pressure perturbations. The first terms in the square brackets of (6) describe an inhomogeneous external flow field induced by the parent body. This field can be vortical, for example in the wake past an aircraft. The second terms of (6) correspond to the free-stream perturbations induced by the store. In the case of nonvortical flow, the potential is expressed as

$$\Phi^*(X^*, Y^*, Z^*, t^*) = X^* + ,$$
$$+ U_\infty \left[\tilde{l}\varepsilon\tilde{\Phi}\left(\tilde{X}, \tilde{Y}, \tilde{Z}\right) + l\delta^2 \Phi(x, y, z, t) + \dots \right],$$
$$\tilde{u} = \frac{\partial \tilde{\Phi}}{\partial \tilde{X}}, \quad \tilde{v} = \frac{\partial \tilde{\Phi}}{\partial \tilde{Y}}, \quad \tilde{w} = \frac{\partial \tilde{\Phi}}{\partial \tilde{Z}}$$
$$u = \frac{\partial \Phi}{\partial x}, \quad v = \frac{\partial \Phi}{\partial y}, \quad w = \frac{\partial \Phi}{\partial z}. \tag{7}$$

The parent-body potential, $\tilde{\Phi}$, corresponds to the asymptotic limit $\tilde{\delta} \to 0$, $\delta = 0$ indicating that in the first order approximation the store does not affect this potential. We consider the two parent bodies: a thin wing and a slender body of revolution. For a thin

wing in supersonic flow, the external potential and pressure are governed by the linear equations with the boundary condition in the plane $\tilde{Y} = 0$

$$\beta^2 \frac{\partial^2 \tilde{\Phi}}{\partial \tilde{X}^2} - \frac{\partial^2 \tilde{\Phi}}{\partial \tilde{Y}^2} = 0 \ , \quad \tilde{p} = -\tilde{u} \ ,$$
$$\tilde{v}\big|_{\tilde{Y}=0} = h'(\tilde{X}) \ , \tag{8}$$

where $\beta^2 = M^2 - 1$ and M is free-stream Mach number. The solution of (8) describes plane waves propagating in the upper (upper sign) and lower half-planes[18]

$$\tilde{\Phi} = \frac{1}{\beta} h(\tilde{X} \mp \beta \tilde{Y}) \ . \tag{9a}$$

This formula describes the distributed flow inhomogeneity between two weak shocks generated at the leading and trailing wing edges (see Fig.1). The pressure jump through the leading (Δp_l) and trailing (Δp_t) shocks are[18]

$$\Delta \tilde{p}_l = \frac{\delta}{\beta} \left| h'(\tilde{X}_l) \right| , \quad \Delta \tilde{p}_t = \frac{\delta}{\beta} \left| h'(\tilde{X}_t) \right| . \tag{9b}$$

where $\tilde{X}_l$ and $\tilde{X}_t$ are coordinates of leading and trailing edges.

For a axisymmetric body, $\tilde{R} = \sqrt{\tilde{Z}^2 + \tilde{Y}^2} = h(\tilde{X})$, the external potential satisfies to 3-D wave equation with the boundary condition being imposed on the body surface. The pressure is determined by the nonlinear Cauchy equation

$$\beta^2 \frac{\partial^2 \tilde{\Phi}}{\partial \tilde{X}^2} - \frac{1}{\tilde{R}} \frac{\partial}{\partial \tilde{R}} \tilde{R} \frac{\partial \tilde{\Phi}}{\partial \tilde{R}} = 0 ,$$
$$\frac{\partial \tilde{\Phi}}{\partial \tilde{R}}\bigg|_{\tilde{R}=h(\tilde{X})} = h'(\tilde{X}) ,$$
$$\tilde{p} = -\left[\tilde{u} + \frac{1}{2}\left(\frac{\partial \tilde{\Phi}}{\partial \tilde{R}}\right)^2 \right] . \tag{10}$$

The solution of (10) is expressed in the integral form[18]

$$\tilde{\Phi} = -\frac{1}{2\pi} \int_0^{\tilde{X}-\beta\tilde{R}} \frac{\tilde{S}'(s)ds}{\sqrt{\left(\tilde{X}-s\right)^2 - \beta^2 \tilde{R}^2}} , \tag{11}$$

where axial coordinate $\tilde{X}$ is measured from the nose and $\tilde{S}(\tilde{X}) = \pi h^2(\tilde{X})$ is cross-section area. Near the body, far from the wave front, $\tilde{X} - \beta\tilde{R} = 0$, Eq. (11) is reduced to the solution of the 2-D Laplace equation

$$\tilde{\Phi} = \frac{\tilde{S}'(\tilde{X})}{2\pi} \ln \frac{\beta \tilde{R}}{2} - \frac{1}{2\pi} \int_0^{\tilde{X}} \tilde{S}'(s) \ln(\tilde{X}-s) ds . \quad (12)$$

There is an essential difference between the solutions (9) for a wing and (11) for a slender body: there is no pressure jump across the wave front, $\tilde{X} - \beta \tilde{R} = 0$, in the case of a slender body, while Eq. (11) describes the distributed pressure wave that transforms to N-wave far from the body.[19] The shock wave arises in the theory of the second order,[19] the pressure jump and the shock are determined by the formulas

$$\Delta p = \frac{3}{2} \frac{(\gamma+1) M^4}{2\beta^2} \tilde{\delta}^4 h'^4(0) .$$

$$\tilde{X} = \left(\beta - \frac{3}{4} \frac{(\gamma+1)^2 M^8}{2\beta^3} \tilde{\delta}^4 h'^4(0) \right) \tilde{R} . \quad (13)$$

The store-induced potential, Φ, corresponds to the limit $\delta \to 0$, $\tilde{\delta} = 0$. Near the body, without effects of shock-body interaction, the potential satisfies 2-D Laplace equation and the boundary conditions

$$\frac{\partial^2 \Phi}{\partial y^2} + \frac{\partial^2 \Phi}{\partial z^2} = 0 ,$$

$$p = -\left[\frac{\partial \Phi}{\partial t} + u + \frac{1}{2}(v^2 + w^2) \right] ,$$

$$v_n \big|_{r=a(x)} = a_x - V_e \sin\theta ,$$

$$V_e = V - \omega x - \alpha - \frac{\tilde{\delta}}{\delta} \tilde{v}(x,t) . \quad (14)$$

Here v_n is the velocity normal to the store surface, $\tilde{v}(x,t) = \tilde{v}(\tilde{H}(x,t))$ is vertical velocity of the external flow on the store axis. The problems (8) and (10) for the parent body are decoupled from the problem (14) for the store. The store problem (14) can be solved using the method developed in Refs. [5,15].

The three external-flow effects on the store motion are distinguished as:

1. The vertical velocity, $\tilde{v}(x,t)$, of the external velocity on the store axis affects the effective cross-section vertical speed $V_e(x,t)$ that leads to additional angle of attack. The correspondent term is of the order of other terms in Eq. (10c) or it is dominant in the case of $\tilde{\delta} \geq O(\delta)$. This effect is important, for example, in store separation from a cavity schematically shown in Fig. 2. In this case, the pressure inside the cavity

and in its vicinity is approximately constant. Nevertheless, the flow inclination may essentially affect the store motion in the phase of shear-layer crossing. Also, the flow inclination effect may be dominant when a slender body moves in the aircraft wake.

2. The presence of the additional boundary (the wing or body) that is the parent body surface dictates the additional boundary condition for Eq. (14a): the normal velocity in this surface is zero on a wall or the pressure jump across the shear layer is zero. This effect is very important. It was analyzes in Refs. [5,15] for separations from a wing or cavity.

3. The external inhomogeneous pressure contributes to aerodynamic forces and moments. If the store moves in inhomogeneous pressure field, then the drag D^*, lift L^* and pitch moment M^* include additional terms: $\tilde{D}^*$, $\tilde{L}^*$ and $\tilde{M}^*$. These terms are external pressure integrals over the store surface

$$\frac{\tilde{D}^*(t^*)}{\rho_\infty U_\infty^2 l^2 \delta^2} = \varepsilon \tilde{D}(t) = -\frac{\varepsilon}{2\pi} \int_{x_0}^{x_e} \int_0^{2\pi} \tilde{p}\left(\tilde{X}_o + \mu x, \tilde{Y}_b\right) S'(x) d\theta\, dx ,$$

$$\frac{\tilde{L}^*(t^*)}{\rho_\infty U_\infty^2 l^2 \delta} = \varepsilon \tilde{L}(t) = -\varepsilon \int_{x_0}^{x_e} \int_0^{2\pi} \tilde{p}\left(\tilde{X}_o + \mu x, \tilde{Y}_b\right) a(x) \sin\theta\, d\theta\, dx ,$$

$$\frac{\tilde{M}^*(t^*)}{\rho_\infty U_\infty^2 l^3 \delta} = \varepsilon \tilde{M}(t) = -\varepsilon \int_{x_0}^{x_e} \int_0^{2\pi} \tilde{p}\left(\tilde{X}_o + \mu x, \tilde{Y}_b\right) xa \sin\theta\, d\theta\, dx$$

$$(15)$$

where $S(x)$ is the body cross-section area, the prime denotes differentiation with respect to x, x_n and x_e are coordinates of the body nose and base, respectively. With the help of the inequalities (2) and (3), the expressions (15) can be simplified for different cases.

For $\delta_y \ll 1$ the external pressure on the body surface can be expanded to the series

$$\tilde{p}(\tilde{X}_o + \mu x, \tilde{Y}_b) = \tilde{p}(\tilde{X}_o + \mu x, \tilde{H}(x,t)) +$$

$$+\delta_y \frac{\partial \tilde{p}(\tilde{X}_o + \mu x, \tilde{H}(x,t))}{\partial \tilde{Y}} a \sin\theta + \dots .$$

The implicit dependence of the function $\tilde{H}(x,t)$ on the angle of attack is retained here to account for the practical case $\alpha\delta \gg 1$. Substituting this expansion to (14) we obtain for the forces and moments the expressions

$$\tilde{D}(t) = -\frac{1}{\pi} \int_{x_n}^{x_e} \tilde{p}\left(\tilde{X}_o + \mu x, \tilde{H}(x,t)\right) S'(x) dx ,$$

$$\tilde{L}(t) = -\delta_y \int_{x_n}^{x_e} \frac{\partial \tilde{p}\left(\tilde{X}_o + \mu x, \tilde{H}(x,t)\right)}{\partial \tilde{Y}} S(x) dx ,$$

4

$$\tilde{M}_z = -\delta_y \int_{x_n}^{x_e} \frac{\partial \tilde{p}\left(\tilde{X}_o + \mu x, \tilde{H}\right)}{\partial \tilde{Y}} Sx\,dx,$$

(16)

These expressions are rather simple since the external pressure distributions on the store axis is only needed to calculate the forces. Further simplification is possible if $\mu \ll 1$. In this case, the integrals (16) are calculated in explicit form and the external pressure derivatives at the store CG location are only needed to estimate the inhomogeneity effect.

3. Diffraction of a weak shock by a slender body

At supersonic speeds, the new problem of shock-store interaction is added to the effects discussed in the previous section. This problem arises at different practical situation, for example, when the separated store intersects one of shocks induced by the wing (see Fig. 1) or the shock generated by other slender body at multiple store separation (see Fig.3). In the latter case, it is reasonable to assume that the wave front radius R shown in Fig. 3 is much larger than the store radius δl. Then the incident shock can be treated as a plane shock for the diffraction problem. Therefore, the interaction of a plane shock with a slender body is a key unit problem.

Consider a weak plane incident shock with unit vector $\mathbf{I} = (\cos\phi, -\sin\phi, 0)$ inclined to the free stream at the Mach angle $\phi = \arcsin(1/M)$. Behind the incident shock, the flow is two-dimensional and inclined to the free-stream direction at the small angle $\varepsilon \ll 1$. This angle may be associated with the wing leading-edge angle, if the incident shock is generated by the edge. In the linear approximation with respect to ε, the nondimensional velocity vector and the pressure rise behind the incident wave are

$$\mathbf{u}' = \left(1, -\varepsilon\varepsilon, 0\right), \quad p' = \frac{\varepsilon}{\beta}.$$

Accordingly, the correspondent entropy rise can be neglected and the potential flow approximation can be used. Let the incident wave collides with the body surface at the station $x^* = x_S^*$. The scheme shown in Fig. 4 indicates that the length size of the scattering region is Δl, where the nondimensional parameter is $\Delta = \delta a_0 \sqrt{M^2 - 1} \sim \delta$ if the Mach number is not so large. Then we introduce the variables in the scattering region

$$x = \frac{x^*}{l}, \quad x = \frac{x^* - x_S^*}{\delta l}, \quad y = \frac{Y^*}{\delta l},$$

$$z = \frac{z^*}{\delta l}, \quad r^2 = y^2 + z^2.$$

In this region, the flow potential is given by the asymptotic expansion

$$\tilde{\Phi} = lU_\infty \left\{ x_S + \delta s + \delta^2 \ln\delta\, g(x_S) + \right.$$
$$\left. + \delta^2 \Phi_1\left(x_S, y, z\right) + \varepsilon\delta\Phi\left(s, y, z\right) + \ldots \right\}.$$

(17a)

The potential $\Phi(x, y, z)$ corresponds to the flow perturbations due to wave scattering. The correspondent pressure rise across the shocks is expressed as

$$P = -\varepsilon\Phi_s.$$

(17b)

In the scattering region, the problem is reduced to the problem of wave diffraction by a cylinder of radius $a_S = a(x_S)$ (see Figs. 4 and 5). The potential is a solution of 3-D wave equation with the boundary condition

$$\beta^2 \frac{\partial^2 \Phi}{\partial s^2} - \frac{\partial^2 \Phi}{\partial z^2} - \frac{\partial^2 \Phi}{\partial y^2} = 0,$$

$$\left.\frac{\partial\Phi}{\partial r}\right|_{r=a_S} = 0.$$

(18)

This problem can be solved using Fourier and Laplace transforms. However, in this paper we obtain a simple solution using geometrical acoustics and weak shock theory.[18, 19] From geometrical consideration (see Fig.5) it is followed that the line of the shock intersection with the body is given by the equation

$$s = a_S \beta \left(1 - \sin\theta\right).$$

(19)

In approximation of geometric acoustics, every incident shock ray, which is collinear to vector $\mathbf{I}$ and collides with the body at a certain point, lies in the plane Q, which is generated by the normal $\mathbf{N}$ to the body surface and the reflected ray $\mathbf{R}$ at this point (see Fig. 6). Since the shock is weak, the incident and reflected rays are inclined to the normal $\mathbf{N}$ at the same angle γ, which is determined as

$$\cos\gamma = -\frac{\sin\theta(s)}{M}.$$

In the considered approximation, the normal $\mathbf{N}$ and the unit vector $\mathbf{R}$ along the reflected ray are expressed as

$$\mathbf{R} = \left(\cos\phi,\ \sin\phi,\ -\frac{\tan\theta(s)}{M}\right),$$

$$\mathbf{N} = \left(0,\ \sin\theta,\ \cos\theta\right).$$

The unit vector $\mathbf{S}$ tangent to the body surface in the plane Q is

$$\mathbf{S}\sin\gamma = \mathbf{I} - \mathbf{N}\cos\gamma = \left(\cos\phi, \; -\frac{\cos^2\theta(s)}{M}, \; \frac{\cos\theta(s)\sin\theta(s)}{M}\right)$$

Behind the incident shock, the velocity normal and tangent to the cylinder surface are

$$v_N = -\varepsilon\sin\theta(s)$$

$$v_S = \frac{1}{\sin\gamma}\left(\cos\phi + \varepsilon\frac{\cos^2\theta(s)}{M}\right)$$

Due to the boundary condition (18), the normal velocity is zero behind the reflected shock. Hence, the flow in the plane Q will be turned to the angle $\varepsilon\sin\theta$. In accordance with the theory of weak shocks,[18] this change of the flow direction corresponds to the pressure rise

$$\Delta p = \frac{\varepsilon\sin\theta(s)}{\beta}$$

Therefore, the pressure behind the incident and reflected shocks is determined as

$$p'' = p' + \Delta p = \frac{\varepsilon}{\beta}[1 + \sin\theta(s)]. \qquad (20)$$

In the shadow region $\theta < 0$, the pressure is constant $p'' = \varepsilon/\beta$.

This solution is restricted by the inequality $M > \sqrt{2}$ resulted from the condition of supersonic flow in the scattering direction. Note that actual diffraction regions have more complicated structures including Mach reflection and a system of shocks. Simulation of such structures is rather difficult problem even for the state-of-the-art CFD methods. In our theoretical model, these effects are neglected.

Additional forces due to the shock-body interaction are calculated as integrals of the pressure (20) over the body surface portion being in the perturbed region. This region lies in the sector $0 \le \theta \le \pi$ of the scattering region $x_S \le x \le x_1 = x_S + \Delta$. It is assumed that downstream from the scattering region the perturbed region is $x > x_1$, $\theta_1(x) \le \theta \le \pi - \theta_1(x)$, where $\theta_1(x)$ is estimated as

$$\theta_1(x) = \arccos\frac{a_1}{a(x)}, \quad a_1 = a(x_1). \qquad (21)$$

Actually, the perturbation region (behind the reflected shock) is restricted by the diverging characteristics and expanded downstream. Due to this expansion the pressure on the store surface decreases downstream. However, for preliminary calculations, this effect is not taken into account. Therefore, the coefficients of the drag force, lift force and pitching moment due to shock diffraction are expressed as

$$D_S = \frac{D_S^*}{\rho_\infty u_\infty^2 (1 - \delta U)^2 l^2 \delta^2} = \frac{1}{2\pi}\int_{X_0}^{X_e} S'(s)\,ds \int_{\theta_1}^{\pi - \theta_1} p''(s,\theta)\,d\theta =$$

$$= \frac{\varepsilon}{\pi\beta}\int_{X_0}^{X_e}\left[\frac{\pi}{2} - \theta_1(s) + \cos\theta_1(s)\right]S'(s)\,ds\,,$$

$$L_S = \frac{L_S^*}{\rho_\infty u_\infty^2 (1 - \delta U)^2 l^2 \delta^2} = \int_{X_0}^{X_e} a(s)\,ds \int_{\theta_1}^{\pi - \theta_1} p''(s,\theta)\sin\theta\,d\theta =$$

$$= -\frac{\varepsilon}{\delta\beta}\int_{X_0}^{X_e}\left[\frac{\pi}{2} - \theta_1(s) + 2\cos\theta_1(s) + \frac{1}{2}\sin 2\theta_1(s)\right]a(s)\,ds\,,$$

$$M_S = \frac{M_S^*}{\rho_\infty u_\infty^2 (1 - \delta U)^2 l^3 \delta^2} =$$

$$= -\frac{\varepsilon}{\delta\beta}\int_{X_0}^{X_e}\left[\frac{\pi}{2} - \theta_1(s) + 2\cos\theta_1(s) + \frac{1}{2}\sin 2\theta_1(s)\right]a(s)s\,ds\,,$$

$$(22)$$

where $U(t)$ is CG streamwise velocity referenced to δu_∞. The integration domain is subdivided into the scattering region ($x_S \le x \le x_1$, $\theta_1 = 0$) and the downstream region $x > x_1$, with $\theta_1(x)$ given by (21). Then, the forces (22) are subdivided into two terms

$$D_S = D_S' + D_S'', \; L_S = L_S' + L_S'',$$
$$M_S = M_S' + M_S''.$$

The first terms of these sums are forces acting in the scattering region, where

$$\cos\theta_1 = \sqrt{\frac{2s}{\bar{\Delta}}\left(1 - \frac{2s}{\bar{\Delta}}\right)}, \quad \bar{\Delta} = \beta a_S,$$

$$\sin\theta_1 = 2\left(1 - \frac{s}{\bar{\Delta}}\right)\sqrt{\frac{2s}{\bar{\Delta}}\left(1 - \frac{2s}{\bar{\Delta}}\right)}.$$

Then, these terms are expressed as

$$D_S' = \frac{\varepsilon\delta}{\pi}a_S S_S'\left(1 + \frac{\pi}{4}\right),$$

$$L_S' = -\frac{5}{4\pi}\varepsilon a_S S_S\left(1 + \frac{\pi}{2}\right),$$

$$M_S' = -\frac{5}{4\pi}\varepsilon a_S S_S x_S\left(1 + \frac{\pi}{2}\right). \qquad (23)$$

The second terms of shock-induced forces are due to the pressure integrals behind the scattering region. These terms have the form

$$D_S'' = \frac{\varepsilon}{\beta} \left\{ (a_e - a_1) \left[\frac{\pi}{2} a_e + \left(2 + \frac{\pi}{2} \right) a_1 \right] - \frac{S_e}{\pi} \arccos \frac{a_1}{a_e} - \frac{S_e}{\pi} \ln \left[\frac{a_1}{a_e} + \sqrt{1 - \left(\frac{a_1}{a_e} \right)^2} \right] \right\}$$

$$L_S'' = -\frac{\varepsilon}{\beta \delta} \int_{x_1}^{x_e} \left[\arcsin \frac{a_1}{a} + 2 \frac{a_1}{a} + \frac{a_1}{a} \sqrt{1 - \left(\frac{a_1}{a} \right)^2} \right] a(x) dx$$

$$L_S'' = -\frac{\varepsilon}{\beta \delta} \int_{x_1}^{x_e} \left[\arcsin \frac{a_1}{a} + 2 \frac{a_1}{a} + \frac{a_1}{a} \sqrt{1 - \left(\frac{a_1}{a} \right)^2} \right] a(x) x dx$$

$$(24)$$

These formulas are suitable for fast calculations of the shock-body interaction.

4. Examples of store trajectories

The discussed above theoretical model was incorporated into the code predicting store separations from external supports to supersonic free streams. Parametric studies are conducted for separation from a thin parabolic wing of the shape

$$h(x) = 4 \left(\tilde{X}^2 - \frac{1}{4} \right).$$

The leading-edge and trailing-edge shocks shown in Fig. 1 are induced by the wing. The base tested body is an ogive-cylinder body B4N2, which has been used in IIT subsonic experiments.[4] Its length is $l = 0.3048$ m, the relative thickness and diameter are $\delta = 0.03125$ and $D_0 = 0.01905$ m, the mass $m = 0.004614$ kg, the moment of inertia $I = 8 \cdot 10^{-2}$ kg·m^2. The wing length is $\tilde{l} = 5l$, its relative thickness $\tilde{\delta} = 6.25 \cdot 10^{-3}$. The free-stream parameters correspond to flight at the altitude $H = 25.5$ km with Mach number $M = 3.9$. In the parametric studies, at the initial time moment $\alpha_0 = \omega_0 = U_0 = 0$; other initial parameters are varied. Effects of the initial vertical speed V_0, body mass, the initial vertical (Y_0) and streamwise (X_0) CG location on the body trajectories are studied. The store CG translates with the speeds $U(t)$, $V(t)$ and rotates with the angular speed $\omega(t)$. The body position and its orientation in the space are determined by the streamwise and vertical CG coordinates, $X(t)$ and $Y(t)$ referenced to $2l/\delta$ and the angle of attack $\alpha(t)$ referenced to δ.

Figures 6 and 7 show CG trajectories and angle of attack histories for different initial vertical velocities in the case of separation from the front wing portion. Interaction with the leading-edge shock crucially changes the trajectory and the angle of attack

behavior. At $V_0 \geq 1$ m/s, the body quickly rotates counterclockwise (pitches down) during crossing the shock. With increasing of the pitch angle the lift and drag increase also, and the body translates downstream with acceleration. The angle of attack quickly grows up 50° and calculations are stopped since such large angles of attack are beyond the scope of slender body theory. At $|V_0| < 1$ m/s the body does not cross the leading-edge shock. In this case the angle of attack and CG slightly oscillate near a certain mean state. As V_0 decreases the trajectory becomes more slant. This "quiet" behavior is observed until the body collides with the trailing-edge shock. Then, the angle of attack quickly increases and the body drops rapidly. This behavior resembles reflection of the body from the trailing-edge shock.

Figures 8-11 illustrate the effect of the body mass for two initial vertical speeds in the case of separation from the front wing portion. Trajectories are shown for three bodies of identical geometry but different mass and moment of inertia: $M_b = 0.5m$, m and $2m$. At $V_0 = -5$ m/s the body interacts with the leading-edge shock only (see Fig. 8). Apparently, the interaction region decreases as the body mass increases (it is easier to accelerate a lighter body). On the other hand, the lightest body ($M_b = 0.5m$) has the largest angular acceleration and its angle of attack grows more rapidly (see Fig. 9). As shown in Fig. 10, at $V_0 = 0$ m/s even the heaviest body ($M_b = 2m$) does not collide with the leading shock.. The CG trajectory becomes more slant as the body mass decreases. The angle-of-attack oscillation period is inversely proportional to the body mass that is consistent with the theoretical model.[5] Trajectory parameters slightly oscillate until the body crosses the trailing-edge shock. This occurs for the bodies of $M_b = 0.5m$, m. Then the angle of attack quickly increases and the body drops rapidly (Fig. 11).

Figures 12 and 13 illustrate the effect of initial vertical locus $Y(0) = Y_0$ on trajectory parameters at the front separation. For $V_0 = -5$ m/s, this effect is slightly visible: the trajectories at different Y_0 are almost identical. For $V_0 = 0$ m/s, the trajectories are significantly different as shown in Fig. 12. They are approximately parallel to each other. The increase of Y_0 leads to the later body collision with the trailing shock. The angle of attack is almost independent on the Y_0 when the body moves between the shocks.

To estimate the effect of the initial streamwise CG location X_0, we calculate body trajectories at $Y_0 = D$ and $X_0 = 0$, $20D$ for different initial velocities $V_0 = 0$, -1, -2.5, -5 m/s (see Figs. 14-17). At $X_0 = 0$ (Figs. 14, 15) the body crosses the leading-edge shock when the initial

American Institute of Aeronautics and Astronautics

speeds are $V_0 = 5$ and 2.5 m/s. At smaller V_0 the body moves between shocks for a long time period. A contact with the trailing-edge shock occurs at the initial vertical speeds close to zero. At $X_0 = 20D$ (see Figs. 16, 17) the body does not cross the leading-edge shock besides the case of $V_0 = 0$. In both cases, the angle of attack oscillates with small amplitude.

5. Summary and conclusions

A theory of multi-body aerodynamic interaction in supersonic flows is developed using asymptotic methods. In this framework it is feasible to analyze different practical problems including store separation from a cavity or external supports. In this connection, the interaction of two slender bodies is a key unit problem. The theoretical model based on asymptotic theory is developed to treat this interaction in the first order approximation. The analysis of this model leads to the following conclusions:

1. The external-flow inclination with respect to the free stream changes the local angle of attack. This effect is dominant when the pressure is approximately constant, for example, at store separation from a cavity or at slender body motion in the wake of aircraft.

2. The boundary conditions on the parent-body surface affect on the store motion. This effect was analyzed in our previous studies for store separations from a flat wall or slip surface to subsonic and transonic free streams.

3. Inhomogeneous pressure distribution in the external flow leads to additional drag force, lift force and pitch moment. This effect can be dominant if the external flow perturbations are larger than the store induced perturbations.

In supersonic flow, the store diffraction of weak shock waves induced by another body leads to new effects. At the initial stage of separation, a system of reflected shocks may generate rather complicated flow structure that is challenging problem even for up-to-date CFD methods.

Scattering of a weak shock by a slender body is a key unit problem for analysis of 3-D flow. This problem was treated using asymptotic methods. In the first order approximation, the perturbation potential in the scattering region is governed by the linear three-dimensional acoustic equation.

To simplify modeling of shock-body interaction and understand basic features of the scattering region, the solution of governing equation is obtained using the geometric acoustics approximation. A simple formula for the pressure rise across incident and

reflected shocks is derived. This result is useful for quick first-cut estimates of the shock-body interaction effect on the body aerodynamics and trajectory.

Parametric studies of the parent body effect on store trajectories are performed for supersonic free stream with emphasis to the store-shock interaction. These calculations lead to the conclusions:

1. The interaction of the body with shocks plays a dominant role in store separation to supersonic free stream. The obtained results show that this effect leads to crucial changes of the trajectory parameters, especially, the angle of attack.

2. The initial vertical speed strongly affects on the body trajectory. At sufficiently large initial vertical speeds the body crosses the leading-edge shock that leads to sharp changes of the angle of attack and trajectory.

3. The CG trajectory becomes more slanting with the body mass decreasing. The angle-of-attack oscillation period is inversely proportional to the body mass that is consistent with our theoretical analysis.

4. The body trajectories linearly depend on the initial vertical CG coordinate in the case of small vertical velocities. It is not essential at relatively large initial vertical speeds.

5. By variation of the streamwise CG locus it is feasible to keep the separated body in between the leading-edge and trailing-edge shocks for a long time period. The body drops between the shocks with small oscillations of trajectory parameters.

6. At small vertical speeds the main effect is related to the body interaction with the trailing-edge shock.

References

[1]Wood, M.E., "Application of Experimental Techniques to Store Release Problems," Proceedings of NEAR Conference on Missile Aerodynamics, Monterey, California, 1988.

[2]Schindel , L.H., "Store separation," AGARD-AG-202, June 1975.

[3]Jordan, J.K., "Computational Investigation of Predicted Store Loads in Mutual Interference Flow Fields," AIAA Paper 92-4570, Aug. 1992.

[4]Malmuth, N. D., Hites, M., Williams, D., "Experimental Investigations of an Ogive-Cylinder Model Transversing a

2:1 Cavity," Illinois Institute of Technology, Rockwell Science Center, Final Report, September 1999.

[5]Shalaev, V.I, Fedorov, A.V., and Malmuth, N.D. "Dynamics of Slender Bodies Separating from Rectangular Cavities," *AIAA J.*, v. 40, No. 3, 2002.

[6]Belk, D. M., Janus, J. M., and Whitfield, D. L., "Three-Dimensional Unsteady Euler Equations Solution on Dynamic Grids," *AIAA Journal*, **25**, No. 9, pp. 1160-1161, 1987.

[7]Lijewski, L. E., and Suhs, N., "Time-Accurate Computational Fluid Dynamics Approach to Transonic Store Separation Trajectory Prediction," *Journal of Aircraft*, **31**, No. 4, pp. 886-891, 1994.

[8]Thoms, R. D., and Jordan, J.K., "Investigation of Multiple Body Trajectory Prediction Using Time Accurate Computational Fluid Dynamics," AIAA Paper, 95-870, June, 1995.

[9]Prewitt, N. C., Belk, D. M., and Maple, R. C. "Multiple-Body Trajectory Calculations Using the Beggar Code," *J. Aircraft*, **36**, No. 5, pp. 802-808, 1999.

[10]Goodwin, F.K., Dillenius, M.F.E., Nielsen, J.N., "Prediction of Six-Degree-of-Freedom Store Separation Trajectories at Speeds up to the Critical Speed. V.1. Theoretical Methods and Comparison with Experiment," AFFDL-TR-72-83, 1972.

[11]Fernandes, F. D., "Theoretical Prediction of Interference Loading on Aircraft Stores: Part I – Subsonic Speeds," NASA Report CR 112065-1, June 1972.

[12]Fernandes, F. D., "Theoretical Prediction of Interference Loading on Aircraft Stores: Part II – Supersonic Speeds," NASA Report CR 112065-2, June 1972.

[13]Malmuth, N.D., Fedorov, A.V., Shalaev, V., Cole, J., Khokhlov, A., Hites, M., and Williams, D., "Problems in High Speed Flow Prediction Relevant to Control," AIAA Paper No. 98-2695, 1998, also unpublished notes and memoranda 1999-2001.

[14]Malmuth, N.D., Shalaev, V.I., Fedorov, A.V. "Combined Asymptotics and Numerical Methods for Store Interactions," Rockwell Science Center, Technical Report of Contract F49620-96-C-0004, AFOSR/NM, October 1998 (available in Defense Technical Information Center, stient.dtic.mil).

[15]Malmuth, N.D., Shalaev, V.I., Fedorov, A.V. "Combined Asymptotics and Numerical Methods for Store Interactions," Rockwell Scientific, Technical Report of Contract F49620-99-0005, AFOSR/NM, February 2002 (available in Defense Technical Information Center, stient.dtic.mil).

[16]Shalaev, V., Malmuth, N., and Fedorov A., "Analytical Modeling of Transonic Store Separation from a Cavity," 41th AIAA Aerospace Science Meeting and Exhibit, January 6-9, 2003, Reno, Nevada, AIAA Paper No. 0004, 2003.

[17]Morse, Ph. M., Feshbach, H. *Methods of Theoretical Physics.* New York – Toronto – London, McGraw-Hill Book Company, Inc. !953.

[18]Sauer, R. *Écoulements des Fluides Compressibles*, Paris et Liege, 1951.

[19]Whitham, G.B. *Linear and Nonlinear Waves.* John Willey & Sons, New York-London-Sydney-Toronto, 1974.
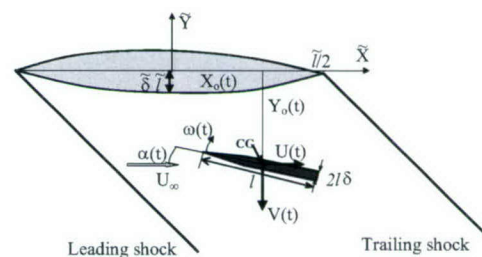
Fig. 1 Flow scheme and coordinate systems.
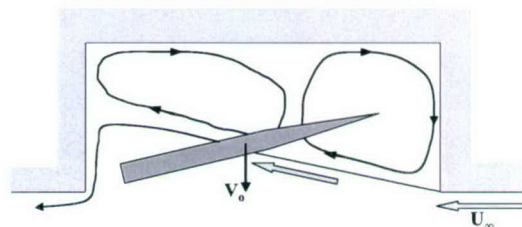
Fig. 2 Flow scheme for the store dropping inside a shallow cavity.
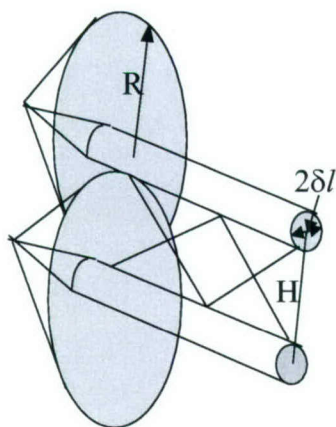
Fig. 3 Wave train between two slender bodies.

Fig. 6 Effect of the initial vertical speed on the CG trajectory. $X_0 = -20D$, $Y_0 = -2.5D$

Fig. 4 Scattering region for a weak shock interacting with a cylinder; side view.
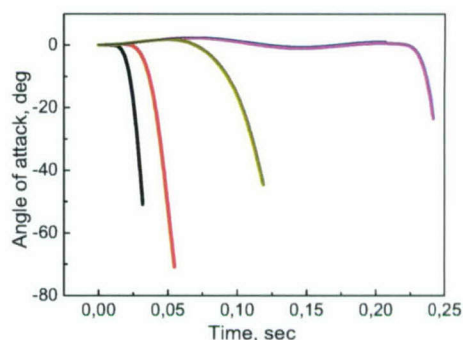
Fig. 7 Effect of initial vertical speed on the angle of attack history; for caption see Fig. 5, $X_0 = -20D$, $Y_0 = -2.5D$.


Fig. 5 Scheme of a weak shock scattering by a slender body.
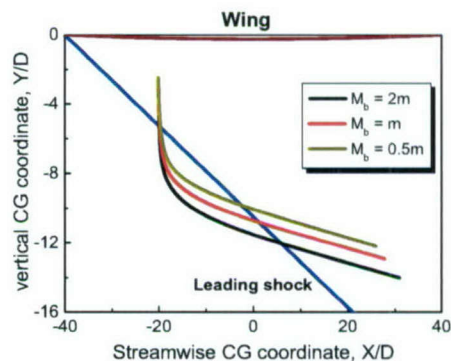
Fig 8 Effect of the body mass on the CG trajectory at the interaction with the leading shock.. $X_0 = -20D$, $Y_0 = -2.5D$, $V_0 = -5$ m/s.
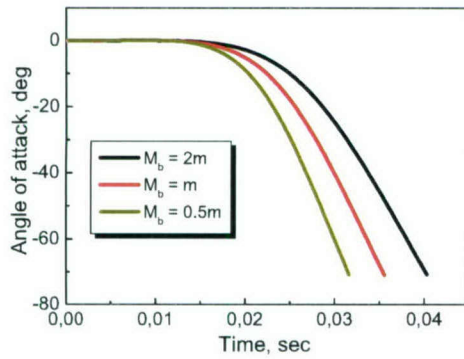
Fig. 9 Effect of the body mass on the angle of attack history at interaction with the leading shock. $X_0 = -20D$, $Y_0 = -2.5D$, $V_0 = -5$ m/s.

Fig. 10 Effect of the body mass on body at interaction with the trailing shock. $X_0 = -20D$, $Y_0 = -2.5D$, $V_0 = 0$ m/s.

Fig. 11 Effect of the body mass on the angle of attack history at interaction with the trailing shock. $X_0 = -20D$, $Y_0 = -2.5D$, $V_0 = 0$ m/s.
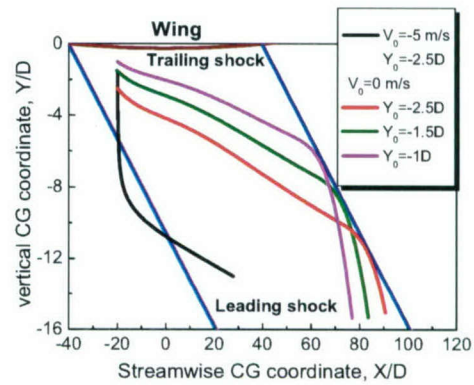
Fig. 12 Effect of the initial CG vertical location on CG trajectory. $X_0 = -20D$.
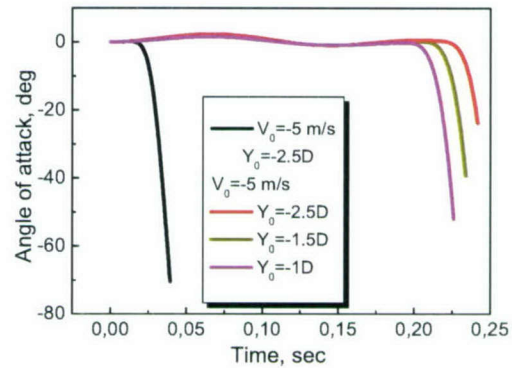
Fig. 13 Effect of the initial CG vertical location on the angle of attack history. $X_0 = -20D$.
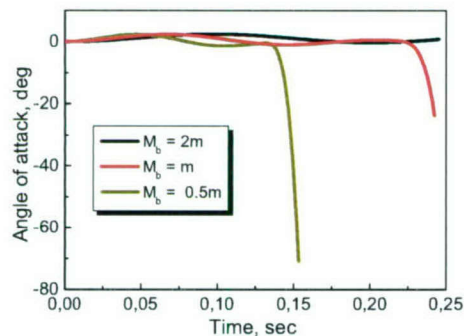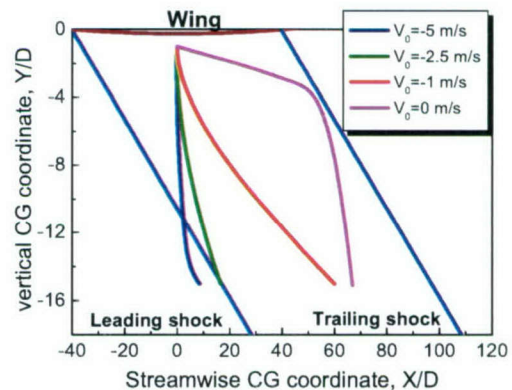
Fig. 14 CG trajectories at $X_0 = 0$ and different initial vertical velocities. $Y_0 = D$.
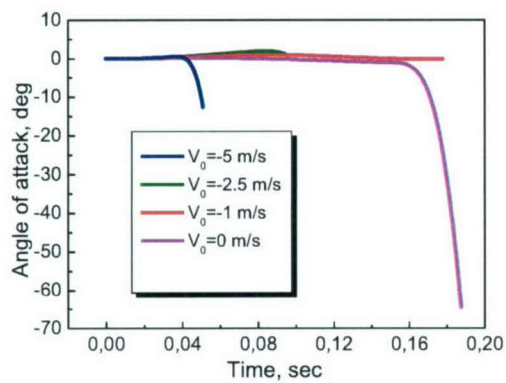
Fig. 15 Angle-of-attack histories at $X_0 = 0$ and different initial vertical velocities. $Y_0 = D$.
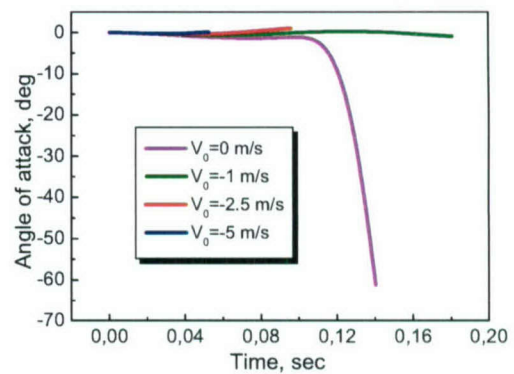
Fig. 17 Angle-of-attack histories at $X_0 = 20D$ and different initial vertical velocities. $Y_0 = D$.
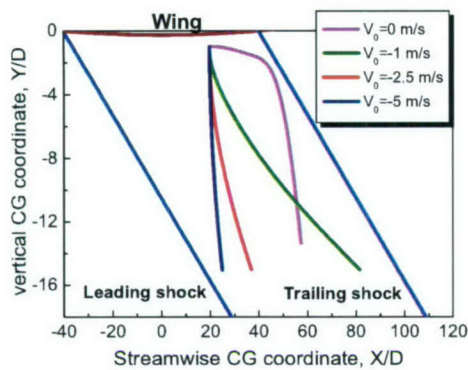
Fig. 16 CG trajectories at $X_0 = 20D$ and different initial vertical velocities. $Y_0 = D$.

Wave drag due to lift for transonic airplanes

By Julian D. Cole[1]† and Norman D. Malmuth[2,3]

[1] *Rensselaer Polytechnic Institute, 110 8th Street, Troy, NY 12180, USA*
[2] *Rockwell Scientific Company, 1049 Camino Dos Rios,*
Thousand Oaks, CA 91360, USA (nmalmuth@rwsc.com)
[3] *Departments of Aeronautics and Engineering and Applied Sciences,*
California Institute of Technology, 1200 East California Boulevard,
Pasadena, CA 91125, USA

Lift-dominated pointed aircraft configurations are considered in the transonic range. To make the approximations more transparent, two-dimensionally cambered untwisted lifting wings of zero thickness with aspect ratio of order one are treated. An inner expansion, which starts as Jones's theory, is matched to a nonlinear outer transonic theory as in Cheng and Barnwell's earlier work. To clarify issues, minimize ad hoc assumptions existing in earlier studies, as well as provide a systematic expansion scheme, a deductive rather than inductive approach is used with the aid of intermediate limits and matching not documented for this problem in previous literature. High-order intermediate-limit overlap-domain representations of inner and outer expansions are derived and used to determine unknown gauge functions, coordinate scaling and other elements of the expansions. The special role of switchback terms is also described. Non-uniformities of the inner approximation associated with leading-edge singularities similar to that in incompressible thin airfoil theory are qualitatively discussed in connection with separation bubbles in a full Navier–Stokes context and interaction of boundary-layer separation and transition. Non-uniformities at the trailing edge are also discussed as well as the important role of the Kutta condition. A new expression for the dominant approximation of the wave drag due to lift is derived. The main result is that although wave drag due to lift integral has the same form as that due to thickness, the source strength of the equivalent body depends on streamwise derivatives of the lift up to a streamwise station rather than the streamwise derivative of cross-sectional area. Some examples of numerical calculations and optimization studies for different configurations are given that provide new insight on how to carry the lift with planform shaping (as one option), so that wave drag can be minimized.

Keywords: asymptotic expansions; transonic flow; slender body theory; mixed type

1. Introduction

Performance of high-speed airplanes and missiles is closely related to our ability to accurately predict and reduce drag. The transonic regime is quite challenging because

† Deceased 17 April 1999.

of the strong nonlinearities in the flow and the occurrence of shock waves. Many commercial aircraft, as well as high-speed fighters, operate in this Mach number range. Other flight vehicles such as hypersonic aircraft and spacecraft accelerate through the same regime. However short the duration of exposure, the drag encountered during transonic flight is critical to overall mission performance, fuel expended and cost.

In the 1970s, a revolution occurred in computing nonlinear transonic and other high-speed flows with computational algorithms and computers. From this pioneering effort, computational fluid mechanics (CFD) has been an asset and workhorse for the aerospace engineer and designer in obtaining transonic flow patterns around realistic shapes. In spite of CFD's power, challenges still exist to predict drag and other quantities, such as pitching and hinge moments, rapidly enough for the phase of aircraft development known as conceptual design. Typical CFD calculations require significant amounts of pre-processing, a large portion of which involves grid generation. Conceptual design optimization also requires the study of hundreds to thousands of airplane geometry and related parametric variations as well as the interplay of physical intuition and compromises based on aerodynamic reasoning and systems impacts. Conflicting demands exist between quick response and pre-processing. Because the latter cannot yet be adapted to quickly restructure the grid for rapidly changing parameter sets, CFD's role is emphasized in later phases of preliminary and advanced design than the conceptual one. Alternatively, it is used to anchor a selected small subset of the conceptional (basepoint) design aerodynamic predictions using other methods.

Recent reviews, assessments and surveys of CFD approaches currently used in industry to estimate drag as well as other forces and moments are typified by Cosner (2000) and Lee-Rausch et al. (2003). As an alternate to CFD, empirical methods have been employed in conceptual design. One such application is the use of algebraic fairings to estimate zero-lift transonic drag rise, a salient performance obstacle. Such fairings of are of limited value because their validity is restricted to their supporting datasets and they do not apply physical ideas in a self-consistent way based on first principles. At the other extreme, large-scale CFD, with careful application and study, is capable of providing excellent, high-accuracy results for a family of shapes for which there are wind-tunnel and flight tests to benchmark and, even in some cases, calibrate them. However, it provides limited design direction based on gasdynamic ideas for rapid-response, optimal aerodynamic shaping. Mathematical shaping guidance is possible from modern optimization techniques such as adjoint methods, stimulated annealing and control theory, but is implicitly restricted to small perturbations around an initial iterate. Such methods currently require high-end workstations, which, with the exception of computer-aided design platforms, is atypical in today's conceptual design environment, but perhaps not in the future. Accordingly, the question of global optimality is a challenge in such techniques. New approaches such as continuation may be a possibility in this connection.

To provide an important complement to the aforementioned existing conceptual aerodynamic design 'toolbox', traditional asymptotic methods in a modern computational setting are attractive. Transonic application of combined asymptotics and numerics that stem from this idea is based on concepts that derive from the early work of Jones (1946), who published a paper giving a formula for the lift and induced drag of 'low aspect ratio pointed wings below and above the speed of sound'. Related work on the equivalence and area rule appear in Oswatitisch & Keune (1955) and
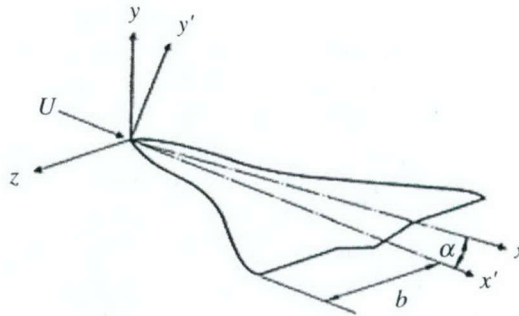
Figure 1. Pointed transonic wing.

Whitcomb (1956), which correlate the aerodynamic characteristics of a full aircraft configuration to that of a body of revolution having the same cross-sectional area distribution along its length as the full airplane's. In Malmuth (1993), the area rule and equivalence rule have been systemized into a combined asymptotic and numerical method that can be used as a conceptual design tool. This approach reduces the three-dimensional drag shaping optimization problem to one in one less space dimension and is capable (in principle) of systematic refinement. It is an example of how intuitive concepts based on systematic asymptotic approximation procedures combined with modern computational methods can be used to provide a rapid-response complement to the previously mentioned tools in a preliminary configuration environment. In addition, the shaping concepts are intuitive, being based on shape smoothing to remove shocks of an 'equivalent' body of revolution as contrasted to that of the complete airplane.

The work presented here, and earlier in the references cited below, represents an extension of Jones's ideas to the transonic range with emphasis on a special concept, *wave drag due to lift*. In this connection, it is reassuring that, under suitable circumstances, Jones's formula for the lift and induced drag not only continues to hold, but is even valid for wings whose aspect ratio is order one. Under these circumstances, shock waves and associated wave drag generally appear.

The basic ideas of how this type of flow behaves are set out in the papers by Cheng & Hafez (1973*a,b*) and the report of Barnwell (1975). The principal result is that the lift produces a flow that looks, in the outer region, like the flow past an equivalent axisymmetric body. This physical effect shows up in the inner and outer expansions used by Barnwell. Cheng & Hafez used similar ideas to define the apparent body and general equivalence rule in a series of papers. Cramer (1979) also studied the problem (with zero thickness as is done here). He discusses thickness effects and essentially verified the results of Cheng & Hafez.

In this paper and Malmuth *et al.* (1987), we have also considered wing-like configurations with zero thickness and aspect ratio $O(1)$ as in figure 1. Thickness effects can be incorporated relatively easily (see Cole & Cook 1988), where the angle of attack α is $O(\delta)$, where δ is the wing-thickness ratio.† This analysis is an approximation of the case $\alpha \gg \delta$. Inner and outer expansions are defined in essentially the same manner

---

† The thickness theory applied in Malmuth *et al.* (1987) is applicable away from the nose. Studies of local corrections and uniformly valid approximations valid for two-dimensional airfoils as contrasted to the three-dimensional wings considered here are given in Rusak (1993, 1994).

as Barnwell, although the asymptotic matching is carried out in a different way using intermediate limit process expansions which, in our opinion, provides greater clarity. A special new result of the paper is the formula for transonic wave drag due to the lift associated with the outer expansion.

To show the implications of this work and in contrast with previous strictly analytical effort, this paper will describe the modern computational implementation of this concept to provide a tool for rapid conceptual design with particular emphasis on planform shaping to avoid wave drag due to lift. Several computations and an optimization are carried out to show the effect of planform and longitudinal distribution of lift on the transonic wave drag and give hints on how effective planform design can reduce it in the reduced-dimension equivalent body of revolution analogue. Of other significant importance is the fact that the combined asymptotic method provides a method of segregating out wave drag due to lift as contrasted to induced drag. This can provide a framework to deal with trade-offs between the two sources of drag.

2. Basic equations and boundary conditions

The problem is studied in the framework of inviscid aerodynamics. Since entropy increases across the shock waves are of third order in the flow perturbation, the full potential equation can be used as a starting point. The flow is thus, to this approximation, isentropic, i.e.

$$\frac{p}{p_\infty} = \left(\frac{\rho}{\rho_\infty}\right)^\gamma, \tag{2.1}$$

where p is the static pressure, ρ is the density, γ is the specific heat ratio and '∞' subscripts signify free-stream values.

The potential equation is an expression of the continuity equation

$$\nabla \cdot \rho \boldsymbol{q} = 0, \tag{2.2}$$

where $\boldsymbol{q}$ is the velocity. Φ is the velocity potential such that $\boldsymbol{q} = \nabla\Phi$. Equations (2.2) and (2.1) imply that

$$(a^2 - \Phi_x^2)\Phi_{xx} + a^2(\Phi_{yy} + \Phi_{zz}) = 2\Phi_x(\Phi_y\Phi_{xy} + \Phi_z\Phi_{xz}) + 2\Phi_y\Phi_z\Phi_{yz} + \Phi_y^2\Phi_{yy} + \Phi_z^2\Phi_{zz} \tag{2.3}$$

and a is the local speed of sound $\sqrt{\gamma p/\rho}$. The total enthalpy integral can be written as

$$\frac{a^2}{U^2} = \frac{1}{M_\infty^2} + \tfrac{1}{2}(\gamma - 1)\left(1 - \frac{q^2}{U^2}\right), \tag{2.4}$$

where U is the free-stream speed, M_∞ is the Mach number at infinity and $M = U/a$ is the local Mach number.

The boundary condition of flow tangency to the surface can be written as

$$\nabla\Phi \cdot \nabla B = 0 \tag{2.5}$$

on $B(x, y, z) = 0$, which defines the surface.

We consider here an untwisted wing of zero thickness specified by an angle of attack α and a camber function $m(x)$. The chord of the wing $c = 1$ and the span $2b$ is $O(1)$. Thus

$$B(x, y, z) = 0 = y - \alpha f(x) + O(\alpha^3), \quad 0 < x < 1, \quad -z_{\mathrm{LE}} < z < z_{\mathrm{LE}}, \tag{2.6}$$

where $f(x) = m(x) - x$ and $m(1) = 1$. For a straight trailing edge at $y = 0$, the trailing vortex sheet lies in the plane $y = 0$, $x > 1$. The planform is specified by $(\pm z_{\mathrm{LE}}(x), z_{\mathrm{LE}}(1)) = b$.

Cheng & Hafez (1973a) considers the breakdown of the expansions associated with separation at the leading edges. Rigorous consideration of this effect is beyond the scope of this analysis since this flow is actually one involving the interaction of *viscous* boundary-layer separation and *non-parallel flow* transition in a reattaching separation bubble. Even an inviscid flow model in which a single rectilinear vortex is introduced into the flow by *inductive* ad hoc procedures needs to be checked against *deductive* solutions of the full unsteady Navier–Stokes equations derived from first principles.[†] The solution of the unit problem presented here should therefore be regarded as one significant component of a more general problem that accounts for this local breakdown region. Another viewpoint is that it is for the case when $\delta = o(\alpha)$ as $\alpha \to 0$, in which the thickness at the leading edge is not zero. For $\delta = 0$, this component represents an outer expansion that should be matched with the local leading-edge flow. The matching might involve intermediate expansions. Inviscidly, this leading-edge neighbourhood acts like the local leading-edge singularities of thin-airfoil and slender-wing theory to dominant order. Possible non-uniformities occur in the higher approximations. In both these examples, the solution ignoring this non-uniformity gives reasonably accurate approximations since the square-root singularity in many cases is weak in an appropriate parameter space. In other cases, such as blunt leading edges, this approximation is not so elastic and the local breakdown regions are more important.

Another boundary condition that must be satisfied is the 'Kutta condition' at a trailing edge where the flow is locally subsonic. This condition implies that the pressure loading at a trailing edge is zero. In approximations such as the inner expansion, which follows, each term satisfies this condition. Another interpretation of this condition is that unphysical pressure jumps are not allowed in the inner solutions.

3. Inner expansion and far field ($r^* \to \infty$)

The approximation in general is based on $\alpha \to 0$, $M_\infty \to 1$ and in the usual transonic way ($K = (1 - M_\infty^2)/\varepsilon_1(\alpha)$ is the transonic similarity parameter, fixed, where $\varepsilon_1(\alpha)$ is the parameter of outer expansion, defined later). In the inner expansion, the observer remains a fixed distance $O(1)$ from the wing, and distances are measured from the wing surface.

The inner limit process thus has

$$\alpha \to 0 \quad (x, y^*, z; K \text{ fixed}),$$

where

$$y^* = \begin{cases} y - \alpha f(x), & 0 < x < 1, \\ y, & x > 1. \end{cases} \tag{3.1}$$

The form of the inner expansion for the potential is thus

$$\Phi(x, y, z; \alpha; M_\infty) = U\{x + \alpha \varphi_1(x, y^*, z) + \alpha^2 \bar{\varphi}_2(x, y^*, z) + \bar{O}(\alpha^3)\}. \tag{3.2}$$

[†] Actually, an infinite cascade of eddies may occur in such a leading-edge bubble as contrasted to a single vortex.

The presence of the overbar denotes the possibility of logarithmic switchback terms introduced into the inner expansion for purposes of matching with the outer expansion. Anticipating the result, we note here that

$$\bar{\varphi}_2(x, y^*, z) = \log^2 \frac{1}{\sqrt{\varepsilon_1}} \varphi_{22}(x) + \log \frac{1}{\sqrt{\varepsilon_1}} \varphi_{21}(x) + \varphi_2(x, y^*, z). \qquad (3.3)$$

Note also that the velocity components of the inner expansion are

$$\frac{q_x}{U} = 1 + \alpha\varphi_{1_x} + \alpha^2(\bar{\varphi}_{2_x} - f'\varphi_{1_{y^*}}) + \bar{O}(\alpha^3),$$

$$\frac{q_y}{U} = \alpha\varphi_{1_{y^*}} + \alpha^2\varphi_{2_{y^*}} + \bar{O}(\alpha^3), \quad \text{etc.}$$

Substituting the assumed expansion into the full potential equation, we obtain the equations for the first two approximations (in divergence forms, as follows from (2.2)) and the corresponding conditions of tangent flow to the wing surface

$$O(\alpha): \quad \nabla^{*2}\varphi_1 = 0, \quad \varphi_{1_{y^*}}(x, 0, z) = f'(x), \quad x_{LE} < x < 1, \quad -z_{LE} < z < z_{LE},$$
$$(3.4)$$

$$O(\alpha^2): \quad \nabla^{*2}\varphi_2 = \frac{\partial}{\partial x}\{\tfrac{1}{2}(\gamma+1)\varphi_{1_x}^2 + |\nabla^*\varphi_1|^2\},$$

$$\varphi_{2_{y^*}}(x, 0\pm, z) = f'(x)\varphi_{1_x}(x, 0\pm, z), \qquad (3.5)$$

where

$$\nabla^* = \left(\frac{\partial}{\partial y^*}, \frac{\partial}{\partial z}\right) \text{ is the inner transverse gradient,}$$

$$\nabla^*\varphi_1 \text{ is the inner transverse velocity perturbation,}$$

$$\nabla^{*2} = \left(\frac{\partial^2}{\partial y^{*2}} + \frac{\partial^2}{\partial z^2}\right) \text{ is the inner transverse Laplacian}$$

and, heuristically†,

$$\varepsilon_1 = o(\alpha), \qquad (3.6)$$

so that the term involving K does not appear in the inner equations to this order, since these terms are to dominant order $O(\alpha\varepsilon_1) = o(\alpha^2)$.

The first equation (3.4) can be thought of as the Prandtl–Glauert equation of linearized theory, but with M_∞ close to unity. The second equation (3.5) shows how, in the inner representation, either compression $\varphi_{1_x} < 0$ or expansion $\varphi_{1_x} > 0$ provides an effective volume source and can cause stream tube divergence. We note the expression for the x component of the mass flux vector,

$$\frac{\rho q_x}{\rho_\infty U} = 1 - \alpha^2(\tfrac{1}{2}(\gamma+1)\varphi_{1_x}^2 + \tfrac{1}{2}(\nabla^*\varphi_1)^2) + \bar{O}(\alpha^3). \qquad (3.7)$$

The x derivative of the quadratic form in (3.7) is almost the right-hand side of (3.5); the additional term $\tfrac{1}{2}|\nabla\varphi_1|^2$ in (3.5) comes from $\nabla^* \cdot (\varphi_{1_x}\nabla^*\varphi_1)$, which is related to

† In this connection, From (5.5) ff., $\varepsilon_1 = \alpha^2 \log(1/\sqrt{\varepsilon_1})$, equation (3.6) follows from a study of inequalities and can also be verified by solution of this identity by rapidly converging Picard iterations.

the dominant approximation of the left side of the continuity equation $\nabla^* \cdot (\rho \boldsymbol{q}) = 0$ in the inner approximation.

The inner expansion is the driver of the entire procedure. But, as is now shown, it is not valid as $r^* = \sqrt{y^{*2} + z^2}$ tends to infinity. On physical grounds, we would expect the transonic flow far away, which, in general, contains shock waves, to be described by an equation of mixed elliptic–hyperbolic type. The Laplace equation (3.4) is, of course, always elliptic.

Furthermore, we show that the second term $\alpha^2 \varphi_2$ becomes much greater than the first, $\alpha \varphi_1$, as $r^* \to \infty$. The general symmetry of the solution φ_1, φ_2 is

$$\varphi_1(x; y^*, z) = -\varphi_1(x; -y^*, z) \quad \text{odd, lifting, vortex sheet,}$$
$$\varphi_2(x; y^*, z) = \varphi_2(x; -y^*, z) \quad \text{even, non-lifting, source.}$$

We now study the behaviour of these solutions near infinity in r^*. The solution for φ_1 can be represented by a dipole sheet (or vortices) or, most directly, by the use of the complex variable

$$\xi = z + iy^* = r^* e^{i(\pi/2 - \theta^*)}. \tag{3.8}$$

The complex potential for the wing, which is flat in a cross-plane $x = \text{const.}$, and for the trailing vortex sheet is

$$\varphi_1 + i\psi_1 = \begin{cases} if'(x)\{\xi - \sqrt{\xi^2 - z_{\text{LE}}^2(x)}\}, & 0 < x < 1, \\ -if'(1)\{\xi - \sqrt{\xi^2 - b^2}\}, & x > 1. \end{cases} \tag{3.9}$$

The transverse components of velocity perturbation $\nabla^* \varphi_1 = (v_1, w_1)$ are found from

$$w_1 - iv_1 = \begin{cases} if'(1)\left\{1 - \dfrac{\xi}{\sqrt{\xi^2 - z_{\text{LE}}^2(x)}}\right\}, & 0 < x < 1, \\ -if'(1)\left\{1 - \dfrac{\xi}{\sqrt{\xi^2 - b^2}}\right\}, & x > 1. \end{cases} \tag{3.10}$$

The first approximation to the pressure distribution and the lift can be found from

$$\left. \begin{aligned} \frac{p}{p_\infty} &= \left(\frac{a^2}{a_\infty^2}\right)^{\gamma/(\gamma-1)}, \\ \frac{a^2}{a_\infty^2} &= 1 + \tfrac{1}{2}(\gamma - 1)M_\infty^2\left(1 - \frac{q^2}{U^2}\right) = 1 - \alpha(\gamma - 1)\varphi_{1_x} + \cdots, \\ \frac{p}{p_\infty} &= 1 - \alpha\gamma\varphi_{1_x} + \cdots. \end{aligned} \right\} \tag{3.11}$$

Equation (3.10) shows the leading-edge singularity at $\xi = z_{\text{LE}}$, whose ramifications were discussed after (2.6). In accord with the remarks in § 1, resolution of this non-uniformity is a subject for future investigation. However, as in thin-airfoil theory, this effect will be localized in the dominant approximation but may have other consequences in the higher orders.

Thus the lift up to a station x is given by

$$L_1(x) = \gamma p_\infty \alpha c^2 \int_{-z_{\text{LE}}(x)}^{z_{\text{LE}}(x)} \mathrm{d}z' \int_{x_{\text{LE}}(x)}^{x} [\varphi_{1_x}(x', 0, z')]_w \, \mathrm{d}x', \tag{3.12}$$

where $[\varphi_{1_x}]_w = \varphi_{1_x}(x, 0+, z) - \varphi_{1_x}(x, 0-, z)$.

Also,

$$l_1(x) = \frac{L_1(x)}{\rho_\infty U^2 \alpha c^2}$$

$$= \int_{-z_{\mathrm{LE}}(x)}^{z_{\mathrm{LE}}(x)} [\varphi_1]_w \, \mathrm{d}z$$

$$= \text{dimensionless (lift}/\alpha) \text{ up to station } x; \ (l_1,(0) = 0). \tag{3.13}$$

From (3.9),

$$\varphi_1(x; 0\pm, z) = \mp f'(x)\sqrt{z_{\mathrm{LE}}^2 - z^2}, \tag{3.14}$$

$$[\varphi_1]_w = -2f'(x)\sqrt{z_{\mathrm{LE}}^2 - z^2}, \tag{3.15}$$

so that

$$l_1(x) - \pi f'(x) z_{\mathrm{LE}}^2(x). \tag{3.16}$$

Thus the total lift is

$$l_1(1) = -\pi f'(1) b^2. \tag{3.17}$$

These results are, of course, the same as those of Jones's theory. The pressure loading depends on (cf. (3.15))

$$[\varphi_{1_x}]_w = -2\left\{ f''(x)\sqrt{z_{\mathrm{LE}}^2 - z^2} + f'(x)\frac{z_{\mathrm{LE}}(x) z_{\mathrm{LE}}'(x)}{\sqrt{z_{\mathrm{LE}}^2(x) - z^2}} \right\}. \tag{3.18}$$

The Kutta condition $[\varphi_{1_x}]_w = 0$ at the straight trailing edge $x = 1$, $z_{\mathrm{LE}} = b$ can be satisfied by controlling the planform and camber so that $z_{\mathrm{LE}}'(1) = 0$, $f''(1) = 0$. Otherwise, the theory has a local non-uniformity at the trailing edge, which has to be accounted for by a local asymptotic expansion.

The far-field behaviour of φ_1 follows from (3.9) as $\xi \to \infty$,

$$\varphi_1 + \mathrm{i}\psi_1 = \mathrm{i}f'(x)\frac{z_{\mathrm{LE}}^2(x)}{2\xi} + O\left(\frac{1}{\xi^3}\right), \quad 0 < x < 1, \tag{3.19}$$

so that

$$\varphi_1(r^*, \theta^*; x) = \tfrac{1}{2} f'(x) z_{\mathrm{LE}}^2(x) \frac{\cos\theta^*}{r^*} + O\left(\frac{1}{r^{*3}}\right). \tag{3.20}$$

The dominant term is a dipole potential where the dipole strength $D_1(x)$ is equal to the lift $l_1(x)$ up to the station x (cf (3.16)),

$$\varphi_1(r^*, \theta^*, x) = -\frac{l_1(x)}{2\pi}\frac{\cos\theta^*}{r^*} + O\left(\frac{1}{r^3}\right). \tag{3.21}$$

An unyawed symmetric planform has been assumed. For more general planforms, we can use

$$D_1(x) = \int_{-z_{\mathrm{LE}}}^{z_{\mathrm{LE}}} [\varphi_1]_{y=0} \, \mathrm{d}z.$$

The potential problem for φ_2 can be thought of as describing the flow past a thin wing with thickness and a volume distribution of sources. Thus the far-field contains

a source term like $\log r^*$ and a particular solution due to the right-hand side of (3.5). From (3.21), the right-hand side has a term

$$\tfrac{1}{2}(\gamma+1)\varphi_{1_x}^2 + \varphi_{1_{r^*}}^2 + \frac{1}{r^{*2}}\varphi_{1_{\theta^*}}^2 = \tfrac{1}{2}(\gamma+1)\left(\frac{l_1'}{2\pi}\right)^2 \frac{\cos^2\theta^*}{r^{*2}} + O\left(\frac{1}{r^{*4}}\right).$$

Thus

$$\frac{\partial^2\varphi_2}{\partial r^{*2}} + \frac{1}{r^*}\frac{\partial\varphi_2}{\partial r^*} + \frac{1}{r^{*2}}\frac{\partial^2\varphi_2}{\partial r^{*2}} = \tfrac{1}{4}(\gamma+1)\frac{\partial}{\partial x}\left\{\left(\frac{l_1'}{2\pi}\right)^2\right\}\frac{1+\cos 2\theta^*}{r^{*2}} + O\left(\frac{1}{r^{*4}}\right). \quad (3.22)$$

Taking account of the particular solution, the far-field of φ_2 is

$$\varphi_2(r^*,\theta^*;x) = \tfrac{1}{4}(\gamma+1)\frac{l_1'l_1''}{(2\pi)^2}\log^2 r^* + S_2(x)\log r^* + g_2(x)$$

$$- \tfrac{1}{8}(\gamma+1)\frac{l_1'l_1''}{(2\pi)^2}\cos 2\theta + \bar{O}\left(\frac{1}{r^{*2}}\right). \quad (3.23)$$

Thus there is a non-uniformity as $r^* \to \infty$ (since $\alpha\varphi_1 \sim \alpha/r^*$, $\alpha^2\varphi_2 \sim \alpha^2\log^2 r^*$), roughly when $r^*\log^2 r^* \sim 1/\alpha$. This shows the need for an outer expansion. An expression for the source strength $S_2(x)$ can be found from the boundary-value problem for φ_2, but $g_2(x)$ is undetermined from an inner problem. $g_2(x)$ must be found by matching with the outer nonlinear boundary-value problem. The presence of shock waves in the outer flow is reflected in g_2.

4. Outer expansion and near field ($\tilde{r} \to 0$)

The first few terms of the outer expansion necessary to match with φ_1, φ_2 are considered in what follows. The limit process associated with this expansion is the typical transonic expansion necessary to give the small disturbance equation (Cole & Cook 1986). The representative point runs to infinity as $\alpha \to 0$, $M_\infty \to 1$. More precisely, if $\mu = \sin^{-1}(1/M_\infty)$ is the Mach angle of the Mach waves, then the vertical and lateral scales y, z are such that

$$y, z = O(\tan\mu) = O\left(\frac{1}{\sqrt{M_\infty^2 - 1}}\right) = O\left(\sqrt{\frac{\varepsilon_1}{K}}\right) = O(\sqrt{\varepsilon_1}),$$

since $K = O(1)$ is fixed in the transonic limit considered here. We consider an outer limit in which the flow pattern is invariant by rescaling all the lengths to the expanding vertical and lateral length-scales. From the just-mentioned orders of magnitude, this invariant picture is achieved in an outer limit in which the strained coordinates $\sqrt{\varepsilon_1}(y,z) \equiv \tilde{y}, \tilde{z}$ are held fixed to keep the flow field in view to the observer in the rescaled frame as $\alpha \to 0$, in accord with the aforementioned Mach wave scaling. The flow variables are functions of the scaled independent variables $(x, \tilde{y}, \tilde{z}, K)$ in this limit.

Accordingly, the general form of the expansion for the potential is

$$\Phi(x, y, z; M_\infty, \alpha)$$
$$= U\{x + \varepsilon_1(\alpha)\phi_1(x,\tilde{y},\tilde{z};K) + \varepsilon_2(\alpha)\phi_2(x,\tilde{y},\tilde{z};K) + \varepsilon_3(\alpha)\phi_3(x,\tilde{y},\tilde{z};K)\cdots\},$$
$$(4.1)$$

where ε_1, ε_2, ε_3 are found from matching and $\varepsilon_3 \ll \varepsilon_2 \ll \varepsilon_1$, where $\tau_1 \ll \tau_2$ signifies $\tau_1 = o(\tau_2)$ hereinafter. In order to match, it is necessary to obtain a right-hand side term similar to that in (3.5), $\frac{1}{2}(\gamma + 1)(\varphi_x^2)_x$. ϕ_2 can be made to match with the dominant dipole of inner φ_1, and this forcing term then appears in the right-hand side of the equation for ϕ_3. ϕ_1 is termed a 'switchback' type of function (that needs to be inserted for matching), and turns out to be the axisymmetric flow produced by an equivalent body of revolution. This forcing term can be made to appear in this way by adjusting the relative orders of magnitude of the gauge functions ε_1, ε_2, ε_3.

Some details are now shown.

$$\frac{q_x}{U} = \frac{1}{U}\frac{\partial \Phi}{\partial x} = 1 + \varepsilon_1 \phi_{1_x} + \varepsilon_2 \phi_{2_x} + \varepsilon_3 \phi_{3_x} + \cdots ,$$

$$\frac{q_y}{U} = \frac{1}{U}\frac{\partial \Phi}{\partial y} = \varepsilon_1^{3/2} \phi_{1_{\tilde{y}}} + \varepsilon_2 \varepsilon_1^{1/2} \phi_{2_{\tilde{y}}} + \varepsilon_3 \varepsilon_1^{1/2} \phi_{3_{\tilde{y}}} + \cdots , \quad \text{etc.,}$$

$$\frac{a^2}{U^2} = 1 + \varepsilon_1(K - (\gamma - 1)\phi_{1_x}) - \varepsilon_2(\gamma - 1)\phi_{2_x} - \varepsilon_3(\gamma - 1)\phi_{3_x} + O(\varepsilon_1^2).$$

The full potential equation (2.3) takes the form

$$\{1 + \varepsilon_1(K - (\gamma - 1)\phi_{1_x}) - \varepsilon_2(\gamma - 1)\phi_{2_x} - \varepsilon_3(\gamma - 1)\phi_{3_x}$$
$$- \cdots - 1 - 2\varepsilon_1 \phi_{1_x} - 2\varepsilon_2 \phi_{2_x} - 2\varepsilon_3 \phi_{3_x} - \cdots \}$$
$$\times \{\varepsilon_1 \phi_{1_{xx}} + \varepsilon_2 \phi_{2_{xx}} + \varepsilon_3 \phi_{3_{xx}} + \cdots \}$$
$$+ \{1 + O(\varepsilon_1)\}\{\varepsilon_1^2 \tilde{\nabla}^2 \phi_1 + \varepsilon_1 \varepsilon_2 \tilde{\nabla}^2 \phi_2 + \varepsilon_1 \varepsilon_3 \tilde{\nabla}^2 \phi_3\}$$
$$= 2\{1 + \cdots \}\varepsilon_1^3(\phi_{1_{\tilde{y}}}\phi_{1_{x\tilde{y}}} + \phi_{1_{\tilde{z}}}\phi_{1_{x\tilde{z}}}) + \cdots ,$$

$$\tilde{\nabla}^2 = \frac{\partial^2}{\partial \tilde{y}^2} + \frac{\partial^2}{\partial \tilde{z}^2}. \tag{4.2}$$

Thus, choosing $\varepsilon_1 \varepsilon_3 = \varepsilon_2^2$, we have

$$O(\varepsilon_1^2): \qquad\qquad (K - (\gamma + 1)\phi_{1_x})\phi_{1_{xx}} + \tilde{\nabla}^2 \phi_1 = 0, \tag{4.3}$$

$$O(\varepsilon_1 \varepsilon_2): \quad (K - (\gamma + 1)\phi_{1_x})\phi_{2_{xx}} - (\gamma + 1)\phi_{2_x}\phi_{1_{xx}} + \tilde{\nabla}^2 \phi_2 = 0, \tag{4.4}$$

$$O(\varepsilon_1 \varepsilon_3): \quad (K - (\gamma + 1)\phi_{1_x})\phi_{3_{xx}} - (\gamma + 1)\phi_{3_x}\phi_{1_{xx}} + \tilde{\nabla}^2 \phi_3 = (\gamma + 1)\phi_{2_x}\phi_{2_{xx}}. \tag{4.5}$$

Here, ϕ_1 satisfies the usual nonlinear transonic small-disturbance Karman–Guderley (K–G) equation, ϕ_2 satisfies a linear variational equation and ϕ_3 a forced variational equation. All the equations are of conservation type and can be written as

$$(K\phi_{1_x} - \frac{1}{2}(\gamma + 1)\phi_{1_x}^2)_x + \tilde{\nabla} \cdot (\tilde{\nabla}\phi_1) = 0, \tag{4.6}$$

$$(K\phi_{2_x} - (\gamma + 1)\phi_{1_x}^2 \phi_{2_x})_x + \tilde{\nabla} \cdot (\tilde{\nabla}\phi_2) = 0, \tag{4.7}$$

$$(K\phi_{3_x} - (\gamma + 1)\phi_{1_x}^2 \phi_{3_x})_x + \tilde{\nabla} \cdot (\tilde{\nabla}\phi_3) = \frac{1}{2}(\gamma + 1)(\phi_{2_x}^2)_x. \tag{4.8}$$

Heuristically anticipating matching, we anticipate that the near-field behaviour $\tilde{r} \to 0$ of these solutions, obtained from $\tilde{\nabla}^2 \phi_1 = RHS$, where $i = 1, 2, 3$, is given

by

$$\phi_1(x_1\tilde{r}) = S_1(x)\log\tilde{r} + G_1(x) + O(\tilde{r}^2\log^2\tilde{r}), \tag{4.9}$$

$$\phi_2(x_1\tilde{r},\theta) = \frac{D_2(x)}{2\pi}\frac{\cos\theta}{\tilde{r}} + (\gamma+1)\frac{S_1'D_2'}{2\pi}\cos\theta\{\tfrac{1}{4}\tilde{r}\log^2\tilde{r} - \tfrac{1}{4}\tilde{r}\log\tilde{r} + \tfrac{1}{4}\tilde{r}\}$$
$$+ \left((\gamma+1)\frac{(G_1'D_2')'}{2\pi} - K\frac{D_2''}{2\pi}\right)\cos\theta\{(\tfrac{1}{2}\tilde{r}\log\tilde{r} - \tfrac{1}{4}\tilde{r}) + O(\tilde{r}^3)\}, \tag{4.10}$$

$$\phi_3(x_1\tilde{r},\theta) = \tfrac{1}{4}(\gamma+1)\frac{D_2'D_2''}{(2\pi)^2}\log^2\tilde{r} + S_3(x)\log\tilde{r} + G_3(x) - \tfrac{1}{8}(\gamma+1)\frac{D_2'D_2''}{(2\pi)^2}\cos2\theta$$
$$+ \tfrac{1}{16}(\gamma+1)^2\frac{(S_1'D_2'D_2'')'}{(2\pi)^2}\tilde{r}^2\log^3\tilde{r} + O(\tilde{r}^2\log^2\tilde{r}), \tag{4.11}$$

where

$$\tilde{r} = \sqrt{\tilde{y}^2 + \tilde{z}^2}, \qquad \theta = \tan^{-1}\frac{\tilde{z}}{\tilde{y}} = \tan^{-1}\frac{z}{y}.$$

The foregoing structure is obtained from anticipated matching with the source and dipole representing homogeneous solutions of the first- and second-order problems and correction particular solutions from the forcing terms in the dominant part of the recursive procedure based on the right-hand-side structure previously outlined. The source strength S_3 and doublet strength D_2 are found by matching with the inner solution. The source strength S_1 is found in a special way in the matching. The functions $G_1(x)$, $G_3(x)$ are found when the boundary-value problems defined by the singular behaviour as $\tilde{r} \to 0$ in (4.9)–(4.11) are solved (numerically).

5. Asymptotic matching

A matching limit, intermediate to the inner and outer limits, is defined by a class of functions $\eta(\alpha)$ such that $\sqrt{\varepsilon_1} \ll \eta(\alpha) \ll 1$. A coordinate

$$r_\eta = \eta(\alpha)r \tag{5.1}$$

is held fixed in this limit. Thus

$$r = \frac{r_\eta}{\eta} \to \infty, \qquad \tilde{r} = \frac{\sqrt{\varepsilon_1}}{\eta}r_\eta \to 0.$$

In the intermediate limit, the representative physical radius again runs to infinity as $\alpha \to 0$, $M_\infty \to 1$, but not as fast as in the outer limit. For matching, the inner- and outer-limit expansions must read the same in the intermediate coordinate. Thus

$$\alpha\varphi_1 + \alpha^2\varphi_2 + \cdots \leftrightarrow \varepsilon_1\phi_1 + \varepsilon_2\phi_2 + \varepsilon_3\phi_3 + \cdots,$$

where $\leftrightarrow$ denotes 'matches to'.

Note that, in the matching,

$$\log\tilde{r} = \log\frac{\sqrt{\varepsilon_1}r_\eta}{\eta} = \log\frac{r_\eta}{\eta} - \log\frac{1}{\sqrt{\varepsilon_1}} \tag{5.2a}$$

and

$$\log^2 \tilde{r} = \log^2 \frac{r_\eta}{\eta} - 2\log \frac{r_\eta}{\eta} \log \frac{1}{\sqrt{\varepsilon_1}} + \log^2 \frac{1}{\sqrt{\varepsilon_1}}. \tag{5.2 b}$$

Note also that

$$\frac{\cos \theta^*}{r^*} = \frac{y - \alpha f(x)}{y^2 + z^2 - 2\alpha y f(x)} = \frac{\cos \theta}{r} + \alpha f(x)\frac{\cos 2\theta}{r^2} + \cdots. \tag{5.3}$$

Writing these out using the near-field expansions of this section and the far-field expansion of the previous section, we have

$$\alpha\left(\frac{l_1 \cos \theta}{r_\eta/\eta} + \cdots\right) + \alpha^2 \log^2 \frac{1}{\sqrt{\varepsilon_1}}\varphi_{22}(x) + \alpha^2 \log \frac{1}{\sqrt{\varepsilon_1}}\varphi_{21}(x)$$

$$+ \alpha^2\left\{\tfrac{1}{4}(\gamma+1)\frac{l_1' l_1''}{(2\pi)^2}\log^2 \frac{r_\eta}{\eta} + S_2(x)\log \frac{r_\eta}{\eta} + g_2(x)\right.$$

$$\left. - \tfrac{1}{8}(\gamma+1)\frac{l_1' l_1''}{(2\pi)^2}\cos 2\theta + \bar{O}(\eta^2)\right\} + \cdots$$

$$\leftrightarrow \varepsilon_1\left\{S_1(x)\left(\log \frac{r_\eta}{\eta} - \log \frac{1}{\sqrt{\varepsilon_1}}\right) + G_1(x) + \cdots\right\} + \varepsilon_2\left\{\frac{D_2(x)\cos \theta}{2\pi\sqrt{\varepsilon_1}r_\eta/\eta} + \cdots\right\}$$

$$+ \varepsilon_3\left\{\tfrac{1}{4}(\gamma+1)\frac{D_2' D_2''}{(2\pi)^2}\left(\log^2 \frac{r_\eta}{\eta} - 2\log \frac{r_\eta}{\eta}\log \frac{1}{\sqrt{\varepsilon_1}} + \log^2 \frac{1}{\sqrt{\varepsilon_1}}\right)\right.$$

$$+ S_3(x)\left(\log \frac{r_\eta}{\eta} - \log \frac{1}{\sqrt{\varepsilon_1}}\right) + G_3(x)$$

$$\left. - \tfrac{1}{8}(\gamma+1)\frac{D_2' D_2''}{(2\pi)^2}\cos 2\theta + \cdots\right\}. \tag{5.4}$$

Comparison of these two expansions shows that they match in an intermediate region with the choices

$$\left.\begin{aligned}
\frac{\varepsilon_2}{\sqrt{\varepsilon_1}} &= \alpha, & D_2(x) &= l_1(x), \\
\varepsilon_3 &= \alpha^2, & S_1(x) &= \tfrac{1}{2}(\gamma+1)\frac{D_2' D_2''}{(2\pi)^2} = \tfrac{1}{2}(\gamma+1)\frac{l_1' l_1''}{(2\pi)^2}, \\
\varepsilon_3 \log \frac{1}{\sqrt{\varepsilon_1}} &= \varepsilon_1, & S_3(x) &= S_2(x), \quad G_3(x) = g_2(x).
\end{aligned}\right\} \tag{5.5}$$

In summary,

$$\varepsilon_1 = \alpha^2 \log \frac{1}{\sqrt{\varepsilon_1}}, \qquad \varepsilon_2 = \alpha^2 \log^{1/2}\frac{1}{\sqrt{\varepsilon_1}}, \qquad \varepsilon_3 = \alpha^2,$$

where $\varepsilon_1(\alpha)$ is defined implicitly by the relationship above and $S_1(x)$ is chosen by an internal switchback in the outer expansion. Note that the first member of the above equation giving $\varepsilon_1(\alpha)$ agrees with that anticipated by Cramer (1979). The

switchback functions in the inner expansion are

$$\varphi_{22}(x) = -\tfrac{1}{2}S_1(x) = -\tfrac{1}{4}(\gamma+1)\frac{l_1'l_1''}{(2\pi)^2}, \tag{5.6}$$

$$\varphi_{21}(x) = G_1(x) - S_3(x) = G_1(x) - S_2(x). \tag{5.7}$$

The principal physical result of the matching is the source distribution for the apparent body that generates the first axisymmetric outer potential $\phi_1(x, \tilde{r})$,

$$S_1(x) = \tfrac{1}{2}(\gamma+1)\frac{l_1'l_1''}{(2\pi)^2}. \tag{5.8}$$

This body depends only on the longitudinal distribution of lift $l_1(x)$. A correction axisymmetric flow is provided by the source S_3,

$$S_3(x) = S_2(x), \tag{5.9}$$

which generates the axisymmetric part of $\phi_3(x, \tilde{r}, \theta)$. $\phi_3(x, \tilde{r}, \theta)$ can be decomposed into

$$\varphi_3(x, \tilde{r}, \theta) = \Omega_3(x, \tilde{r}) + \Psi_3(x, \tilde{r})\cos 2\theta \tag{5.10}$$

using the form of ϕ_2,

$$\varphi_2(x, \tilde{r}, \theta) = \psi_2(x, \tilde{r})\cos\theta. \tag{5.11}$$

Then, for $\Omega_3(x, \tilde{r})$,

$$(K - (\gamma+1)\phi_{1_x})\Omega_{3_{xx}} - (\gamma+1)\Omega_{3_x}\phi_{1_{xx}} + \tilde{\nabla}\Omega_3 = \tfrac{1}{4}(\gamma+1)(\Psi_{2_x}^2)_x. \tag{5.12}$$

By considering the omitted terms, an overlap domain can be shown to exist for matching to this order. Also, consideration of higher-order terms in both expansions shows that the matching can be continued. Thus the outer expansion reads

$$\Phi = U\left\{ x + \alpha^2 \log\frac{1}{\sqrt{\varepsilon_1}}\bar{\phi}(x, \tilde{r}, \theta) + \bar{O}(\alpha^4) \right\}, \tag{5.13}$$

where

$$\bar{\phi} = \phi_1(x, \tilde{r}) + \frac{1}{\log^{1/2}(1/\sqrt{\varepsilon_1})}\phi_2(x, \tilde{r}, \theta) + \frac{1}{\log(1/\sqrt{\varepsilon_1})}\phi_3(x, \tilde{r}, \theta).$$

It can thus be noted that the collection of terms ϕ_1, ϕ_2, ϕ_3 that can be computed individually satisfy together the small disturbance (K–G) equation

$$(K - (\gamma+1)\bar{\phi}_x)\bar{\phi}_{xx} + \tilde{\nabla}^2\bar{\phi} = O\left(\frac{1}{\log^{3/2}(1/\sqrt{\varepsilon_1})}\right). \tag{5.14}$$

We remark that, as in the discussions by Cheng & Hafez, the gauge function *analytical* orders are close to each other. Further analysis is required to assess their importance with respect to wave drag due to lift. These studies should examine the question of the *numerical* order of magnitude of the coefficients of these gauge functions. In many engineering applications, the magnitude of these coefficients can be small enough to offset the closeness of the gauge functions, allowing an accurate estimation from the dominant orders.

J. D. Cole and N. D. Malmuth

6. Wave drag

There is, of course, induced drag associated with the trailing vortex system; the drag in dominant order, associated with φ_1, is just that of Jones's theory. From the point of view of induced drag, the wing considered here, which is flat spanwise, is an optimum. The spanwise circulation distribution (cf. (3.15)) is elliptical. The wave drag is connected to the shock-wave system in the outer flow field. It could be calculated from the entropy increase in the wave system.

For small disturbances to a free-stream, we have the result for the wave drag D_{w},

$$D_{\mathrm{w}} = \rho_\infty T_\infty c^2 \int \int_{-\infty}^{\infty} [S]_{\mathrm{s}} \, \mathrm{d}y \, \mathrm{d}z + \cdots, \tag{6.1}$$

where $[S]_{\mathrm{s}}$ is the jump in specific entropy across a shock. The integral is taken over all the shocks in the system. Using the expression for the entropy jump in transonic small disturbance theory (cf. Cole & Cook (1986, p. 165 ff.) for a discussion of wave drag), we have

$$D_{\mathrm{w}} = -\tfrac{1}{12}\rho_\infty U^2 (\gamma+1)\alpha^4 \log^2 \frac{1}{\sqrt{\varepsilon_1}} c^2 \int_0^{\infty} \tilde{r}\,\mathrm{d}\tilde{r} \int_0^{2\pi} [\bar{\phi}_x]_{\mathrm{s}}^3 \, \mathrm{d}\theta + \cdots. \tag{6.2}$$

Consider the differential conservation form associated with (5.14),

$$\tilde{r}(\tfrac{1}{2}K\bar{\phi}_x^2 - \tfrac{1}{3}(\gamma+1)\bar{\phi}_x^3 - \tfrac{1}{2}(\tilde{\nabla}\phi)^2)_x + (\tilde{r}\bar{\phi}_{\tilde{r}}\bar{\phi}_x)_{\tilde{r}} + \frac{1}{\tilde{r}}(\bar{\phi}_x\bar{\phi}_\theta)_\theta = 0. \tag{6.3}$$

Integrating this divergence form over all space outside a small cylinder,

$$(-\infty < x < \infty) \quad \tilde{r}_{\mathrm{c}} \to 0,$$

around the x-axis enables the entropy jump of (6.2) to be related to radial momentum flow. Equation (6.3) is not conserved across shocks, so that shock jumps appear such as

$$[\tfrac{1}{2}K\bar{\phi}_x^2 - \tfrac{1}{3}(\gamma+1)\bar{\phi}_x^3 - \tfrac{1}{2}(\tilde{\nabla}\phi)^2]_{\mathrm{s}},$$

where the square brackets signify jumps.

Let

$$\tilde{D}_{\mathrm{w}} = \frac{D_{\mathrm{w}}}{\rho_\infty U^2 c^2 \varepsilon_1^2}.$$

Then

$$\tilde{D}_{\mathrm{w}} = -\lim_{\tilde{r}_{\mathrm{c}}\to 0} \tilde{r}_{\mathrm{c}} \int_{-\infty}^{\infty} \mathrm{d}x \int_0^{2\pi} \mathrm{d}\theta \, \bar{\phi}_x\bar{\phi}_{\tilde{r}}|_{\tilde{r}_{\mathrm{c}}} - \lim_{\substack{\tilde{r}_{\mathrm{c}}\to 0 \\ x_2\to\infty}} \int_{\tilde{r}_{\mathrm{c}}}^{\infty} r\,\mathrm{d}r \int_0^{2\pi} \mathrm{d}\theta \, \tfrac{1}{2}(\tilde{\nabla}\bar{\phi})^2|_{x_2}. \tag{6.4}$$

If we consider the dominant term in (6.4), then

$$\tilde{D}_{\mathrm{w}1} = \int_0^1 \mathrm{d}x \int_0^{2\pi} \mathrm{d}\tilde{\theta} \lim_{\tilde{r}_{\mathrm{c}}\to 0} (\tilde{r}_{\mathrm{c}}\phi_1\phi_{1_x}\phi_{1_{\tilde{r}}}). \tag{6.5}$$

From (4.9),

$$\phi_{1_x} = S_1'(x)\log\tilde{r} + G_1'(x), \qquad \phi_{1_{\tilde{r}}} = \frac{S_1(x)}{\tilde{r}}.$$
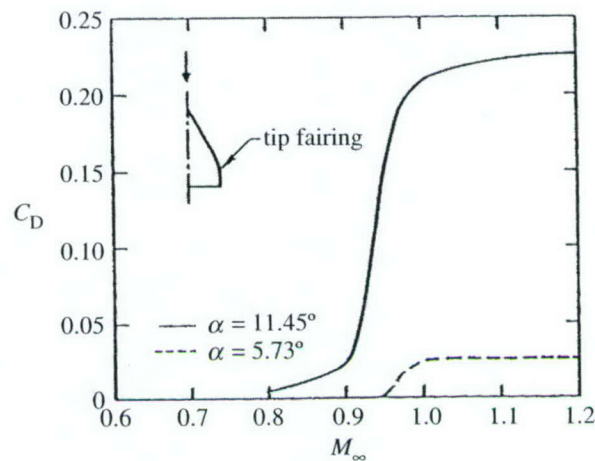
Figure 2. Drag rise due to lift characteristics of model fighter planform.
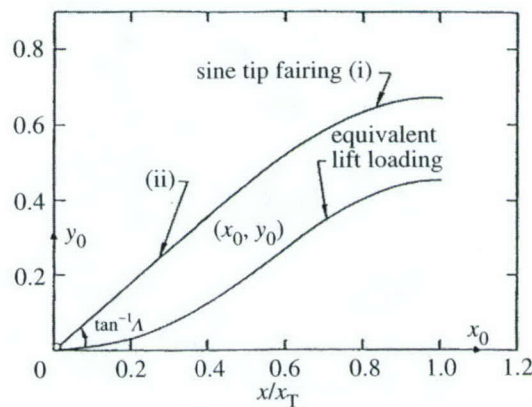
Figure 3. Lift loading of model wing with sine tip fairing.
(i) $y - y_0 = (2\Lambda(x_T - x_0)/\pi)\sin(\pi(x - x_0)/2(x_T - x_0))$; (ii) $y_0/x_0 = \Lambda$.

and using

$$\int_0^1 S_1(x)S_1'(x)\,\mathrm{d}x = \tfrac{1}{2}S_1^2(1) - \tfrac{1}{2}S_1^2(0) = 0,$$

in which $S_1(1) = S_1(0) = 0$, we have

$$\tilde{D}_{w1} = -2\pi \int_0^1 S_1(x)G_1'(x)\,\mathrm{d}x = 2\pi \int_0^1 S_1'(x)G_1(x)\,\mathrm{d}x. \qquad (6.6)$$

This wave drag due to lift 'area rule' formula is exactly that of a slender body in transonic flow (cf. Cole & Cook 1986, p. 161), *except with the new interpretation of $S_1(x)$ given by* (5.5). Higher-order terms in the drag formula can be found.

7. Applications and remarks

Several applications have been made of the theory in its present form. For flat wings, $f'(x) = -1$ and $l_1(x)$ is given by (3.16) to get $\pi z_{\mathrm{LE}}^2(x)$. The effective source strength
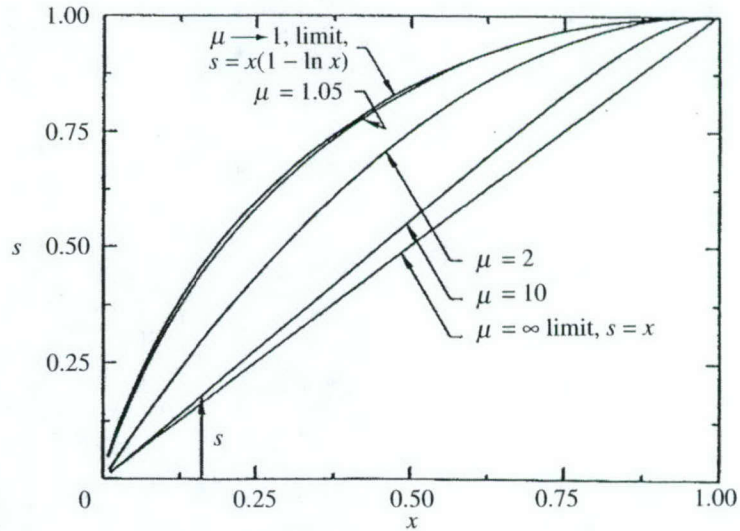
Figure 4. μ family of wing bodies in which semi-span equals $x(\mu - x^{\mu-1})/(\mu - 1)$.

for the equivalent body is

$$S_1(x) = \tfrac{1}{2}(\gamma + 1)\frac{l_1' l_1''}{(2\pi)^2} = \tfrac{1}{8}(\gamma + 1)(z_{LE}^2(x))'(z_{LE}^2(x))''$$

(cf. (5.5)).

Equation (4.3), which, for axisymmetric flow, reads

$$(K - (\gamma + 1)\bar{\phi}_{1_x})\bar{\phi}_{1_{xx}} + \bar{\phi}_{1_{\bar{r}\bar{r}}} + \frac{1}{\bar{r}}\bar{\phi}_{1_{\bar{r}}} = 0, \tag{7.1}$$

is solved numerically with a small disturbance code NLWAVE for various K using (4.9) as the boundary condition. It is similar to that given in Krupp & Murman (1972), except that the source strength is given by (5.5) and (3.16) instead of that related to streamwise derivatives of the cross-sectional area for axisymmetric bodies at zero angle of attack treated in Krupp & Murman (1972). NLWAVE uses the successive line over-relaxation scheme (SLOR) with global iterative streamwise sweeps and their type-dependent switch for elliptic (subsonic), hyperbolic (supersonic), parabolic (sonic) and shock points developed by Murman and the first author. Jameson operators are also used to weight current and previous time iterations for nonlinear source terms in the finite-difference discretization of (7.1). A new version of the usual SLOR scheme is included in NLWAVE. Therein, the Neumann boundary condition associated with (4.9),

$$\lim_{\bar{r} \to 0} \bar{r}\phi_{\bar{r}} = S_1'(x)$$

is treated by using the local inner expansion corresponding to (4.9) for the boundary points $\bar{r} = \sigma$, where σ is a small constant. During the iterative scheme, the second term in the inner expansion is obtained from (4.9) written in the form at $\bar{r} = \sigma$,

$$G_1^{i+1}(x) = \phi_1^i(x) - S_1(x)\log\tilde{r},$$

where i indicates the previous SLOR iterate and $i + 1$ the current one. This value of $G_1(x)$ is used to compute the dominant term of the wave-drag coefficient. Although
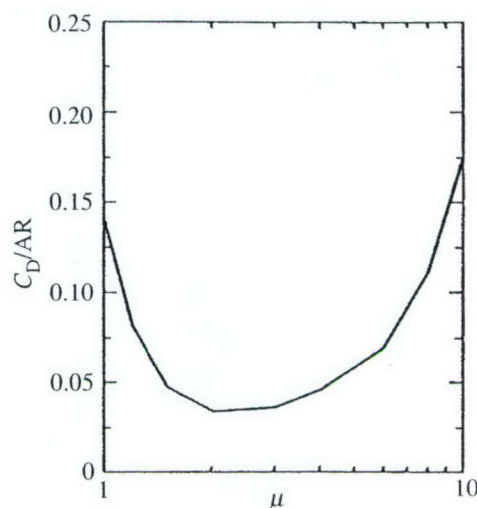
Figure 5. Wave drag/aspect ratio, L/D figure of merit for
μ wing–body family, $M_\infty = 0.9951$, $\alpha = 0.2$ rad.

the far-field boundary conditions at the outer edges of the computational domain could have used the doublet ideas in Krupp & Murman (1972), the extent of these boundaries justified a simpler approach involving homogenous Neumann data. On a modern PC, the SLOR iterations converge rapidly for non-pathological or 'bumpy' lift distributions $l_1(x)$. Pathologies and non-uniformities of the theory can occur for special classes of pointed wing tips and reentrant corners (largely of academic interest) where the theory herein could be improved with local solutions. Typical cases involving of the order of 1000 SLOR iterations require less than 1 min on an AMD Athlon, 524 MB RAM, 1.1 GHz Processor, Windows 2000 operating system. More iterations are required for near-sonic and thicker equivalent lift bodies in which the shock patterns become complex and take longer to converge as well as resolve.

Once adequate convergence is obtained, C_{D_w} is calculated from (6.6).

NLWAVE results are plotted as C_{D_w} versus M_∞ for two different angles of attack in figure 2. Substantial drag due to lift is evident. The planform shape and the distribution of $l_1(x)$ which is typical appears in figure 3.

Another set of calculations incorporates a parabolic body of revolution (thickness ratio 0.057) and adds the source strength of this body to $S_1(x)$. A series of planforms with semi-span $z_{LE}(x)$ given by

$$z_{LE}(x) = \frac{x(\mu - x^{\mu-1})}{\mu - 1} \tag{7.2}$$

and shown in figure 4 was considered for various μ, $M_\infty = 0.995$, $\alpha = 0.2$ rad. The idea is to optimize the L/D figure of merit C_{D_w}/AR (where AR denotes aspect ratio) by a choice of planform. Here,

$$C_{D_w} = \frac{D_w}{\frac{1}{2}\rho_\infty U^2 S}, \qquad \text{AR} = \frac{b^2}{S},$$

where S is the planform area and b is the wing span.
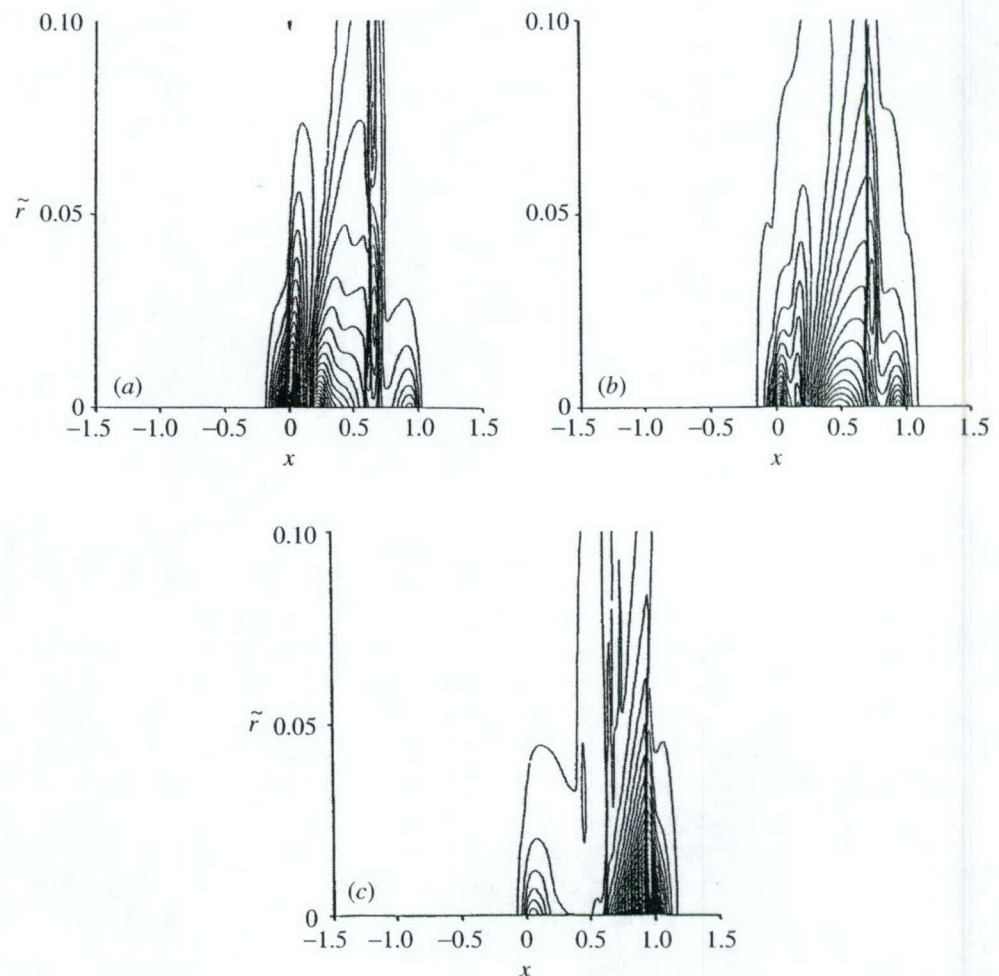
Figure 6. Isomachs of (a) $\mu = 1.2$, (b) $\mu = 2.0$ and (c) $\mu = 10.0$ wing–body; $M_\infty = 0.995$, $\alpha = 0.2$ rad, $\Delta M = 0.1$.

A minimum drag occurs for $\mu = 2.5$. The planform shape and curve of C_{D_w} versus μ appears in figure 5. Also shown in figure 6 for $\mu = 1.2, 2, 10$ are isobars which make evident the shock wave that occurs. The wave drag for small μ is large because of the small sweep and for large μ because of rapid changes of l_1 near the wing tip. These preliminary studies are meant to show the relative effectiveness of various planforms and the utility of the theory in this article to select them.

It would be very useful to extend this work to give efficient ways of calculating the higher-order terms in the wave drag. It is also possible to incorporate the effects of wing thickness $\delta \sim (\alpha^2 \log(1/\sqrt{\varepsilon_1}))$ into the formulation in a more systematic way. First steps in this direction are given in Malmuth *et al.* (1987) and Cole & Cook (1988).

In summary, the analysis given herein provides a new result for the transonic drag due to lift of zero-thickness untwisted two-dimensionally cambered wings. Intermediate limits and matching provides an effective tool to determine the unknown scales and switchback terms to uniquely and deductively determine inner and outer rep-

resentations. The formula for the wave drag is identical to that due to thickness except for a new interpretation of the equivalent body or source distribution factor $S_1(x)$ in (6.6). This changes the boundary conditions for the Karman–Guderley solution that determines the inner behaviour given by the function $G_1(x)$ in (6.6). Dramatic influence of the planform shape on shock drag has been demonstrated by the numerical studies shown here. Optimum planforms can be determined by the methods illustrated. In addition, our analysis can be extended to more arbitrary shapes including twist and thickness. Interesting optima are possible with these generalizations and should be studied in the future.

References

Barnwell, R. W. 1975 Analysis of transonic flow about lifting wing–body configurations. NASA TR R-440.

Cheng, H. K. & Hafez, M. M. 1973a Equivalence rule and transonic flow theory involving lift. *AIAA J.* **11**, 1210–1212.

Cheng, H. K. & Hafez, M. M. 1973b Equivalence rule and transonic flows involving lift. USCAE Report 124. Los Angeles, CA: University of Southern California.

Cole, J. D. & Cook, L. P. 1986 *Transonic aerodynamics*. Amsterdam: North-Holland.

Cole, J. D. & Cook, L. P. 1988 Some asymptotic problems of transonic flow theory. In *Symp. Transsonicum III, IUTAM Symp., Gottingen, Germany, 24–27 May 1988*, pp. 158–170.

Cosner, R. R. 2000 Assessment of vehicle performance predictions using CFD. AIAA Paper 2000-0384.

Cramer, M. S. 1979 Lifting three-dimensional wings in transonic flow. *J. Fluid Mech.* **95**, 223–240.

Jones, R. T. 1946 Properties of low-aspect-ratio pointed wings at speeds below and above the speed of sound. NACA Report 835.

Krupp, J. A. & Murman, E. M. 1972 Computation of transonic flows past lifting airfoils and slender bodies. *AIAA J.* **10**, 880–886.

Lee-Rausch, E. M., Buning, P. G., Mavriplis, D., Morrison, J. H., Park, M. A., Rivers, S. M. & Rumsey, C. L. 2003 CFD sensitivity analysis of a drag prediction workshop wing/body transport configuration. AIAA Paper 2003-3400.

Malmuth, N. D. 1993 Some applications of combined asymptotics and numerics in fluid mechanics and aerodynamics in transonic aerodynamics. In *Problems in asymptotic theory* (ed. P. Cook), Frontiers in Applied Mathematics, vol. 12, pp. 65–88. Philadelphia, PA: SIAM.

Malmuth, N., Wu, C. C. & Cole, J. D. 1987 Transonic wave drag-estimation and optimization using the nonlinear area rule. *J. Aircraft* **24**, 203–210.

Oswatitisch, K. & Keune, F. 1955 Ein Äquivalenzsatz für Nichtangestellet Flügel Kleiner Spannweite in Schallnaher Strömung. *S. Flugwiss.* **3**, 29–46.

Rusak, Z. 1993 Transonic flow around the leading edge of a thin airfoil with a parabolic nose. *J. Fluid Mech.* **248**, 1–26.

Rusak, Z. 1994 Subsonic flow around the leading edge of a thin airfoil with a parabolic nose. *Eur. J. Appl. Math.* **5**, 283–311.

Whitcomb, R. T. 1956 A study of zero-lift drag-rise characteristics of wing–body combinations near the speed of sound. NASA Report 1273.

Thin Shock Layer Theory Model for a Jet in a Hypersonic Cross Flow

Norman Malmuth[*]
Rockwell Scientific, Thousand Oaks, California 91360
California Institute of Technology, Pasadena, California 91125

and

Alexander Fedorov [†]
Department of Aeromechanics and Flight Engineering, Moscow Institute of
Physics and Technology, Zhukovski 140180, Russia

Transverse fuel injection into a supersonic cross-flow is analyzed using approximations resembling thin shock-layer theory in the Newtonian limit. The theoretical model is based on the balance of pressures with centrifugal force inside the jet-shock filament formed between the jet-induced bow shock and the jet outer edge. A solution describing the jet-shock filament shape is obtained in a compact analytical form convenient for quick estimates of the jet penetration depth and total pressure losses. Near-field asymptotic behavior of this solution reveals a square-root singularity, which agrees with empirical fits of experimental data. The theoretical model is verified by comparisons with experiments on combustion and mixing of a transverse hydrogen jet injected into a supersonic cross flow. In the near-field region, the analytical solution agrees well with the average position of the jet plume outer edge and the OH fluorescence filament indicating combustion regions.

Nomenclature

C_P	=	pressure coefficient
d^*	=	jet exit width
$f(x)$	=	shape of shock-jet filament
$F = f/\alpha$	=	normalized shape of shock-jet filament
h	=	jet penetration depth
M	=	freestream Mach number
p	=	pressure
q	=	dynamic pressure
T	=	temperature
U	=	longitudinal velocity
x, y	=	Cartesian coordinates
$X = x/\alpha$	=	normalized streamwise coordinate
α	=	jet-to-freestream momentum flux ratio
δ	=	characteristic flow deflection slope
γ	=	specific heat ratio
ρ	=	density
θ	=	jet injection angle

Superscripts
*	=	dimensional

Subscripts
j	=	jet
S	=	shock-jet filament

[*] Senior Scientist, Program Manager, Fluid Mechanics, Fellow AIAA, APS
[†] Associate Professor, Dept. of Aeromechanics and Flight Engineering, Member AIAA

∞ = freestream

I.   Introduction

PERFORMANCE of hypersonic air breathing propulsion systems strongly depends on efficiencies of fuel injection and mixing in the supersonic combustion chamber. Mixing and flame stabilization may be achieved in recirculation regions and coherent structures containing unmixed fuel and air. Transverse injection, which is commonly used in the design of supersonic combustors, involves these mechanisms.

As shown in Fig. 1, the flow pattern induced by under-expanded transverse injection is rather complicated.[1-3] The fuel jet displaces the supersonic crossflow as if a bluff body was inserted into the flow. A bow shock (3) upstream of the injector exit is formed causing the upstream boundary layer to separate at the point S. In the separation region (1), the boundary layer and jet mix subsonically. The jet turns to the freestream direction and reattaches to the wall at the point R forming another recirculation region (6) downstream from the jet exit. This process is accompanied by formation of shocks (2, 8) and expansion waves (7). Nevertheless, in the near-field region, the time-averaged jet-penetration profile mimics the bow shock shape and looks smooth. In the far-field region (downstream from the point A), the jet thickness continues to grow. However, this growth, which is due to the turbulent mixing rather than the pressure gradient, is much slower than that in the near-field region.

The near-field mixing is driven by large-scale jet-shear layer vortices generated by the jet-freestream interaction.[2-3] These vortices are formed along the jet-freestream interface starting near the injector exit. They periodically grab large quantities of free-stream air and draw them into the jet shear layer. In the far field, the eddies travel with velocities close to the freestream velocity. These coherent structures, where the fuel and air are mixed by slow molecular diffusion, also travel at high speeds. Consequently the combustion process is mixing (vorticity diffusion) controlled.

Experiments[2-3,8] show that ignition is likely to occur in the recirculation region ahead of the jet exit. The flame is convected downstream along with the large eddies and observed near the outer edge of the jet plume. To estimate flame-holding capability of the transverse injection and stagnation pressure losses due to the jet-induced shock, it is necessary to predict the bow-shock shape and the average penetration profile of the jet plume. This could be done empirically using correlations of experimental data.[1] The average penetration profile is commonly approximated by a power law fit, [1,4-6] that couples the jet outer edge with the downstream distance from the jet exit. However, this correlation varies widely between experimental studies. Although CFD approaches such as RANS and DES are nominally capable of handling jets in a cross-flow, depending on turbulence modeling and use of implicit algorithms, they are time-consuming in engineering practice. Quicker response, analytical models are required to shed light on the physics of jet penetration and interpolate between large-scale CFD solutions. These are also useful for conceptual and preliminary design phases associated with turn-around parametric studies. This motivated us to analyze the transverse injection into supersonic cross flow using asymptotic-related methods. We believe that such a model can shed light on previous experiments and recent large simulations. An excellent example of the latter is Ref. 9.

In Section II, the cross-flow jet problem is formulated for a hypersonic freestream in the Newtonian limit[10] of the Euler equations. Although, some sort of blast wave theory[11-15] seems appropriate associated with hypersonic blunt bodies, basic ideas of the thin layer Newtonian theory are also appropriate. It is shown that a shape of the thin shock-jet filament is governed by an ordinary differential equation, which is solved analytically in Section III. In Section IV, the analytical solution is compared with the experiments[2,3-8] on combustion and mixing of the transverse hydrogen jet injected into supersonic cross flows. Results of the analysis are summarized in Section V.

II.   Basic Formulation

Consider normal injection of a fuel jet into a supersonic cross-flow shown in Fig. 1. The jet displaces the supersonic flow, qualitatively as if a blunt body was inserted into the flow. In this situation, the characteristic flow deflection slope is $\delta \equiv U_j^* / U_\infty^* = O(1)$, where U_j^* is speed at the jet exit, U_∞^* is the freestream speed, and asterisks denote dimensional quantities. Assuming that the freestream Mach number $M \to \infty$ and the specific heat ratio $\gamma \to 1$, consider the Newtonian limit[10] of the Euler equations: $H \equiv (M\delta)^{-2} \to 0$ and $\lambda \equiv (\gamma - 1)/(\gamma + 1) \to 0$ so that $N = H / \lambda$ is fixed. Neglecting viscous shear-layer processes, we assume that U_j is constant along the jet, and the jet thickness approximately equals to the jet exit width d^*. With these assumptions, the flow pattern is

schematically shown in Fig. 2. The bow shock and the outer edge of the fuel jet form a thin shock-jet filament, which is approximated by a single line $y = f(x)$ with $x = x^*/d^*$ and $y = y^*/d^*$.

Following results of the Newtonian theory[10, 11, 14], an approximate model is based on the balance of pressure with centrifugal force inside the jet-shock filament. It is assumed that the pressure p_C^* behind the downstream boundary of the jet is of the order of the pressure in the downstream recirculation region (see the dead-water cavity eddy (6) in Fig. 1). This pressure is small compared to the static pressure p_S^* inside of the shock-jet filament shown in Fig. 2. The latter approximately equals the pressure directly behind the shock, which is determined by the 2-D shock relations for a blunt body Newtonian limit. The pressure coefficient $C_{P_S} \equiv (p_S^* - p_\infty^*)/q_\infty^*$ is estimated as,

$$C_{P_S} \cong 2\sin^2\theta_S = 2\frac{f'^2}{1+f'^2},$$

where $\tan\theta_S = f'$ specifies the local slope of the shock-jet filament (Fig. 2). This equation leads to the relation

$$p_S^* \cong 2q_\infty^* \frac{f'^2}{1+f'^2}. \tag{1}$$

Along the jet-shock filament, the centrifugal force is balanced by the pressure gradient across the filament that gives[7]

$$\frac{\partial p^*}{\partial n^*} \cong \frac{\Delta p^*}{d^*} = \frac{p_S^* - p_C^*}{d^*} \cong \frac{\rho_j^* U_j^{*2}}{R^*(x)}, \tag{2}$$

where n signifies the direction normal to the jet-shock filament; ρ_j is jet density, which is approximately constant along the jet length; $d^*/R^*(x) = |f''(1+f'^2)^{-3/2}|$ is the normalized curvature of the shock-jet filament. The absolute value sign is important since for the normal injection $f'' < 0$, and imaginary limiting solutions for small x can arise if this is not taken into account.

Using the approximation $\Delta p^* \cong p_S^*$ and (1) we obtain the nonlinear ordinary differential equation

$$f'^2 = \alpha |f''(1+f'^2)^{-1/2}|, \tag{3}$$

where $\alpha \equiv q_j^*/q_\infty^*$ is the jet-to-freestream momentum flux ratio, $q_j^* = \rho_j^* U_j^{*2}/2$. The appropriate initial conditions for (3) are

$$f(0) = 0, \ f'(0) \to \infty. \tag{4}$$

III. Solution

The problem (3)-(4) gives a one-parameter family of solutions with α as the parameter. This parameter may be scaled out of Eq. (3) by the transformations

$$F(X) = f(x)/\alpha, \ X = x/\alpha. \tag{5}$$

Substitution of (5) into (3) and (4) gives the initial-value problem

$$\begin{aligned} F'' &= -F'^2\sqrt{1+F'^2} \\ F(0) &= 0, \ F'(0) = \infty \end{aligned} \tag{6}$$

where the primes signify differentiation with respect to X. An exact solution of (6) is expressed in the analytical form

$$F(X) = \log\left|(1+X) + \sqrt{(1+X)^2 - 1}\right| = \cosh^{-1}\left|(1+X)\right|.$$

(7)

For small X relevant to the near field, the solution (7) is approximated as

$$F(X) = \log\left|1 + \sqrt{2X} + X + ...\right| \cong \sqrt{2X}\ ,\ X \to 0.$$

(8)

Note in contrast to the blast wave theory, (see for example Ref. 11), the exponent in (8) should be 2/3 rather than 1/2 for this 2-D flow. This appears appropriate since the equations are not embedded in the blast wave similitude. Note that the 1/2 exponent applies for an axisymmetric body in the blast wave theory.

For large X, we obtain

$$F(X) \cong \log X\ ,\ X \to \infty.$$

(9)

Equation (9) shows that the shock does not become asymptotic to a Mach line, as it should. This is associated with a breakdown of thin shock layer approximations in the far-field region, where the strong shock and hypersonic approximations are inappropriate and some form of the Prandtl-Glauert linearized theory approximations is more valid. In some form of an outer limit and asymptotic matching that has yet to be discovered, (although unified supersonic-hypersonic similarity has been proposed), the body appears as a supersonic source generating a Mach wave in the far field. The yet-to-be-determined unified theory would systematically match thin shock layer, blast wave and linearized regions as well as provide a uniformly valid description of the flow. Nevertheless, the physics-based "engineering" approximation used here provides a useful estimate for the jet penetration as will be shown in the next section. .

IV.   Comparison with experiment

In the engineering model,[1] the jet penetration depth h^* is defined as a distance from the point A to the wall (see Fig. 1). The experimental data discussed in Ref. 1 are correlated as

$$h \equiv \frac{h^*}{d^*} = \frac{1.51}{(1 + \cos\theta_j)}\sqrt{\alpha}\ ,$$

(10)

where θ_j is the jet injection angle. For the normal injection, $\theta_j = 90°$, the relation (10) gives $h = 1.51\sqrt{\alpha}$. Using the near-field asymptotic form (8) and assuming that the point A corresponds to $x \approx 1$, we obtain $h = \sqrt{2\alpha} \approx 1.41\sqrt{\alpha}$, which is close to the correlation (10). More importantly, the square-root singularity near the jet origin $x = 0$ predicted by the theory agrees with the empirical fit. This indicates that the analytical solution (7) resulting from the inviscid approximate thin shock layer model captures basic features of the near-field flow. As previously mentioned, the approximation is not strictly embedded in blast wave similitude and therefore gives a different singular behavior near the origin than that from the blast wave theory.

Ben-Yakar and Hanson[2, 3,8] performed experimental studies of combustion and mixing in high total enthalpy supersonic flows. The experiments, conducted in an expansion tube facility of Stanford University, were designed to investigate the near-field mixing and auto ignition of a three-dimensional under-expanded transverse hydrogen jet injected through a cylindrical hole. Simultaneous OH-PLIF and schlieren imaging were performed at the jet centerline to obtain information on the location of shock waves, the jet penetration, and the region of combustion. These data are used hereinafter for testing the theoretical model discussed in Sections II and III.

Figures 3a, 4a,b and 5 compare the theoretical solution (7) with the instantaneous schlieren images[2,8] of hydrogen injection into the cross flow at $M \approx 3.5$, static temperature $T^* = 1300\ \text{K}$, static pressure $p^* = 0.32\ \text{psi}$ and

freestream velocity $U_\infty^* = 2420$ m/s. The jet-to-freestream momentum flux ratios are $\alpha = 1.4$ (Fig. 3) and $\alpha = 2$ (Fig. 4). Large-scale coherent vortical structures generated by the jet-stream interaction are clearly observed along the jet-freestream interface (Fig. 5). These structures cause local fluctuations of the bow shock (Fig. 4b). Nevertheless, the time-averaged shock position is smooth rather than a bumpy instantaneous shape. In the near-field region $x < 3$, the jet outer edge is located close to the bow shock forming a thin shock-jet filament that confirms our theoretical concept. In this region, the solution (7) agrees well with the average position of the jet outer edge as shown in Fig. 6. Some of this agreement needs to be explained in view of the two-dimensional nature of the model, which is applicable to slot injection and the three-dimensional nature of the flow out of a round hole in the experiments. As shown in Refs. 16 and 17, round jets in cross flows flatten out due to vortical kinematics as soon as one jet exit diameter along their length. The flattening process can legitimize the approximation that the curvature of the jet axis is more important than the circumferential one in determining the pressure jump across the jet.

In Figures 3b and 7, the theoretical prediction is compared with instantaneous OH-PLIF images, which indicate the presence of the OH radicals formed by the auto ignition of jet hydrogen. The OH radicals are primarily produced in the hot separation region upstream of the jet exit (see region (1) in Fig. 1) and directly behind the bow shock and convected downstream with the shear-layer vortices. The OH-mole fraction decreases as the gases expand around the jet and the local mixture temperature falls.[2] In the near-field region, the solution (7) mimics the shape of a thin filament along the outer edge of the plume.

Figure 8 shows similar comparisons with simultaneous OH-PLIF and schlieren visualizations overlaid in a single image. The experimental data correspond to hydrogen injection into the cross-flow at $M = 4.7$, $T^* = 1300$ K, $p^* = 0.75$ psi and $U_\infty^* = 3300$ m/s.[8] The jet-to-freestream momentum flux ratios are $\alpha = 2, 3, 5$. Again, in the near-field region $x < 3$, the solution (7) agrees well with the OH fluorescence filaments, which are mainly observed along the outer edge of the jet plume.

V.   Summary

Transverse fuel injection into a supersonic cross-flow was analyzed using a thin shock-layer model relevant to the Newtonian limit of inviscid gasdynamics. The theoretical model is based on the balance of pressures with centrifugal forces inside the jet-shock filament formed between the jet-induced bow shock and the jet outer edge. A solution describing the jet-shock filament shape was obtained in a compact analytical form convenient for quick estimates of the jet penetration depth and total pressure losses. The near-field asymptotic behavior of this solution gives square-root similarity, e.g., $\sim x^{1/2}$ as $x \to 0$, where x is the streamwise coordinate from the jet exit. This behavior agrees with the empirical fit of Ref. 1. Since the present model does not use blast wave theory, the shock fuel interface is not $\sim x^{2/3}$ as $x \to 0$ as for blast wave over a cylindrically blunted slab (2-D case). Coincidentally, the blast wave theory for a hemispherically blunted cylinder (axisymmetric case), rather than the 2-D one assumed here gives the square root behavior at the origin $x \to 0$. The theoretical model was verified by comparisons with the experiments[2,3-8] on combustion and mixing of the transverse hydrogen jet injected into supersonic cross flows. In the near-field region $x^* / d^* < 3$, the analytical solution agrees well with the average position of the jet plume outer edge and the OH fluorescence filaments indicating combustion regions.

The theory breaks down and does not give the jet shock as a Mach line in the far-field region. This is because the jet interface is no longer close to the shock. In addition, the shock is attenuated and becomes weak. Accordingly, the thin-layer Newtonian assumptions are no longer applicable and a linearized model involving the jet flow appearing as a Prandtl-Glauert supersonic source-like singularity in the far field may be applicable. Asymptotic modeling of this region and its matching with the near-field solution needs attention. Although the present model is not a formal asymptotic solution, it is a good starting point for such a systematic approximation scheme, using the Newtonian distinguished limit. In spite of the aforementioned limitations, comparison of the theory in this paper and experiment reveals that it gives a good account of the physics important for fuel penetration estimation. The scaling arising in terms of the jet to freestream momentum ratio parameter α (sometimes denoted as J in the literature) a means of collapsing normalized penetration data in units of jet exit width on to a universal curve shown by Bowersox and others arises naturally in our analysis. Indications are that the ideas of the present model with some modification apply to oblique injection. An important aspect of this work is that it can be used for a good first quantitative, non-

empirical estimate of penetration of fuel into a hypersonic stream. The associated time and distance scales may be decisive in determining the fraction of fuel burned and other scramjet combustion metrics.

Acknowledgments

References

[1]Krasnov, N.F., Koshevoy, V.N., and Kalugin, V.T., *Aerodynamics of Separated Flows*, Moscow, Vysshaya Shkola, 1988 (in Russian).

[2]Ben-Yakura, A., and Hanson, R.K., "Supersonic Combustion of Cross-Flow Jets and the Influence of Cavity Flame-Holders," AIAA Paper No. 99-0484, 1999.

[3]Ben-Yakura, A., and Hanson, R.K., "Experimental Investigation of Flame-Holding Capability of Hydrogen Transverse Jet in Supersonic Cross-Flow," 27th Symposium on Combustion, The Combustion Institute, 1998, pp. 2173-2180.

[4]McDaniel, J.C., and Graves, J., "Laser Induced Fluorescence Visualization of Transverse Gaseous Injection in a Nonreacting Supersonic Combustor," *Journal of Propulsion and Power*, Vol. 4, No. 6, 1988, pp. 591-597.

[5]Gruber, M.R., Nejad, A.S., Chen, T.H., and Dutton, J.C., "Mixing and Penetration Studies of Sonic Jets in a Mach 2 Freestream," *Journal of Propulsion and Power*, Vol. 11, No. 2, 1995, pp. 315-323.

[6]Rothstein, A.D., and Wantuck, P.J., "A Study of the Normal Injection of Hydrogen into a Heated Supersonic Flow Using Planar Laser-Induced Fluorescence," AIAA Paper No. 92-3423, 1992.

[7]Liepmann, H. and Roshko, A. *Gasydnamics*, 1957.

[8]Ben-Yakura, A., Kamel, M.R., Morris, C.I., and Hanson, R.K., "Experimental Investigation of H_2 Transverse Jet Combustion in Hypervelocity Flows," AIAA Paper No. 97-3019, 1997.

[9]Srnivesan, R. and Bowersox, R., "Detached Eddy Simulation of Gaseous into a Mach 5.0 Freestream," AIAA 2005-0893, 43rd AIAA Aerospace Sciences Meeting, Reno, Nevada, 10-13 January 2005.

[10]Cole, J.D., "Newtonian Flow Theory for Slender Bodies," *J. Aero, Sci*, Vol. 24, pp. 448-455, 1957

[11]Chernyi, G. G, *Introduction Hypersonic Flow*, translated by Ronald F. Probstein, Academic Press, New York and London, 1961, pp. 209, 215.

[12]Sedov, L.I., *Similarity and Dimensional Methods in Mechanics*, English translation, (M. Holt ed.) Academic Press, New York and London, 1959.

[13]Taylor, G.I., "The Formation of Blast Wave by a Very Intense Explosion," *Proc. Roy. Soc., London, Ser. A*. Vol. 201, 159 – 186, 1950.

[14]Hayes, W, and Probstein, R., *Hypersonic Flow Theory*, Academic Press, New York, 1959.

[15]Cheng, H.K., "Inviscid Leading Edge Effect in Hypersonic Flow," *J. Aero. Sci.*, Vol. 23, pp. 898-900, 1956.

[16]Abramovich, G., *The Theory of Turbulent Jets*, English Translation by Scripta Technica, MIT Press, 1963, pp. 541-556.

[17]Shandorov, G., "Flow from a Channel into Stationary and Moving Media," *Zh. Tekn. Fiz*, Vol. 37, 1, 1957.
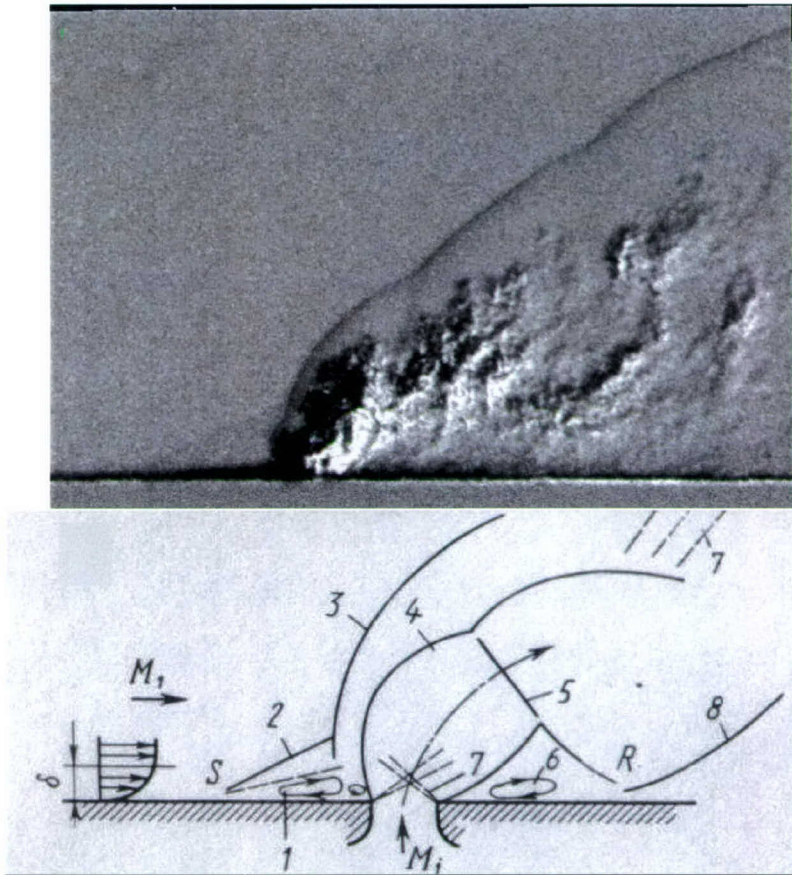
Figure 1. Schlieren image of the normal under-expanded hydrogen injection into supersonic cross-flow[2], and schematics of the flow pattern (from Ref. 1): 1 – separation bubble upstream the jet exit; 2 – shock due to upstream separation at the point S; 3 – bow shock induced by the jet; 5 – Mach discus; 6 – separation bubble downstream from the slot; 7 – expansion waves; 8 – shock induced by the jet reattachment R; M_1 - freestream Mach number; M_j - Mach number of the out-coming jet.
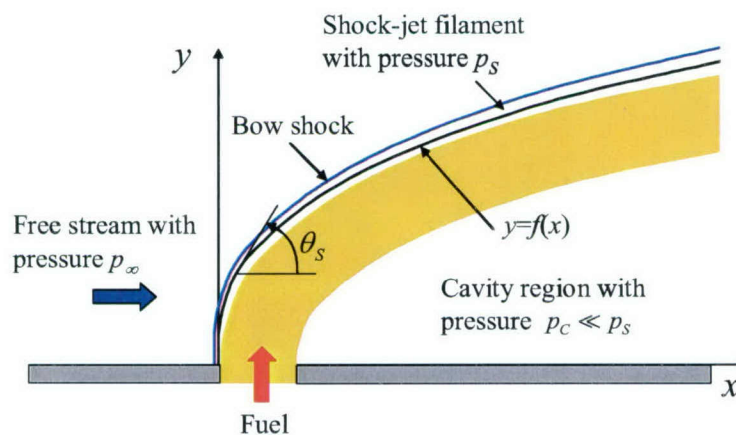
Figure 2. Approximate flow pattern in the inviscid Newtonian limit.
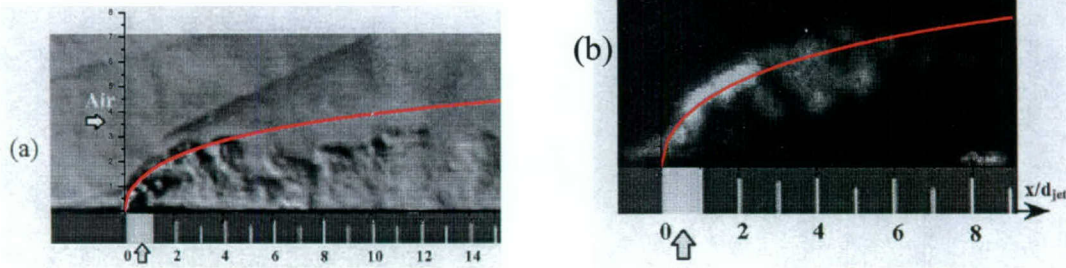
Figure 3. Comparison of the theoretical solution (7) (red line) with simultaneous schlieren (a) and OH-PLIF (b) images of hydrogen injection into supersonic cross-flow;[8] $M = 3.46$, $T^* = 1300$ K, $p^* = 0.32$ psi, $U_\infty^* = 2420$ m/s; the jet-to-freestream momentum flux ratio $\alpha = 1.4$.
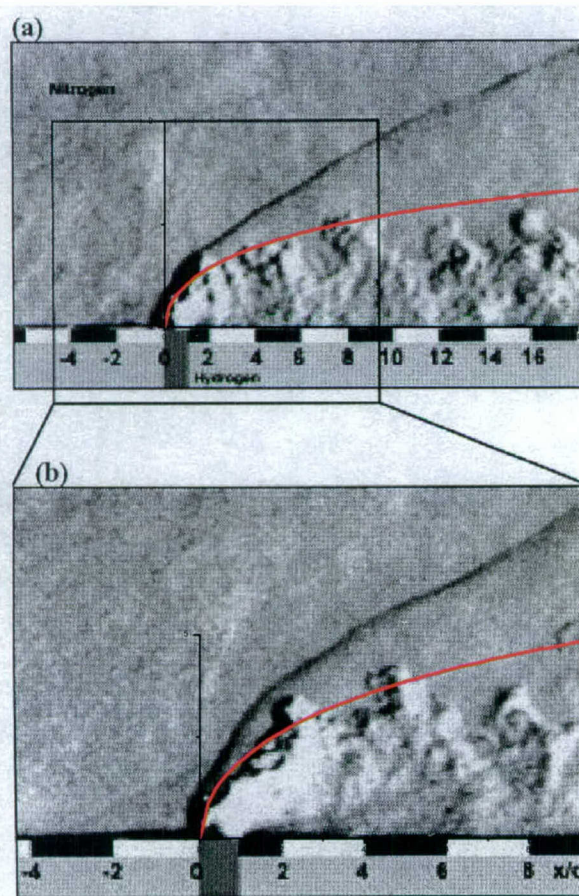
Figure 4. Comparison of the theoretical solution (7) (red line) with simultaneous schlieren image of hydrogen injection into supersonic cross-flow;[2] $M = 3.5$, $T^* = 1300$ K, $p^* = 0.32$ psi, $U_\infty^* = 2420$ m/s; the jet-to-freestream momentum flux ratio $\alpha = 2$.
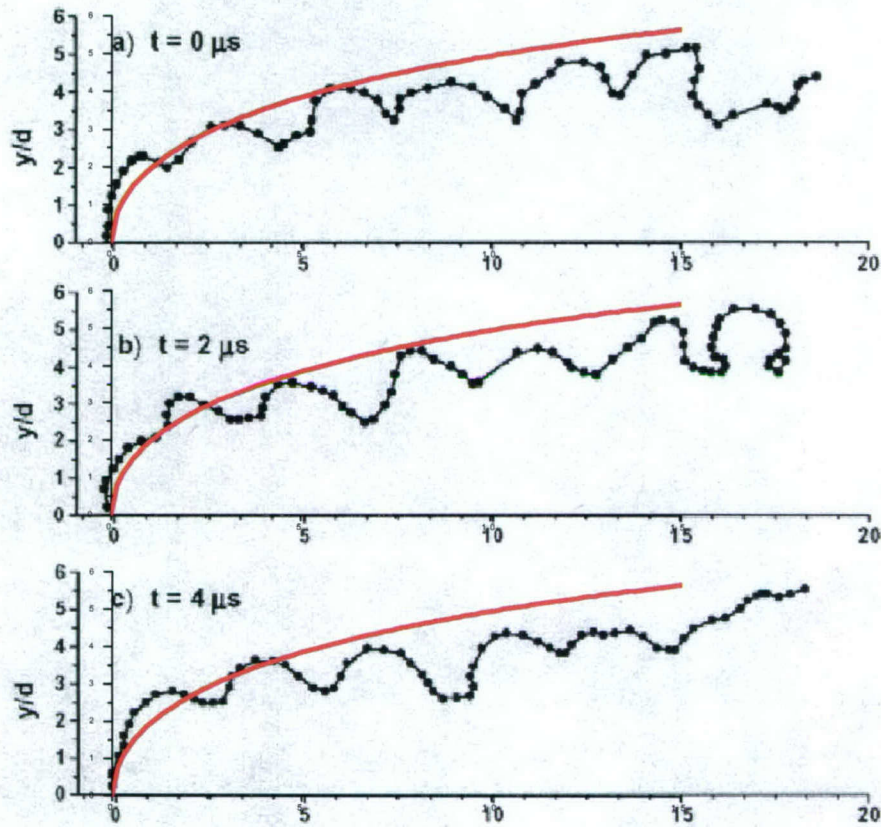
Figure 5. Comparison of the theoretical solution (7) (red lines) with the jet penetration measured from schlieren images of hydrogen injection into supersonic cross-flow;[2] $M = 3.5$, $T^* = 1300$ K, $p^* = 0.32$ psi, $U_\infty^* = 2420$ m/s; the jet-to-freestream momentum flux ratio $\alpha = 2$.
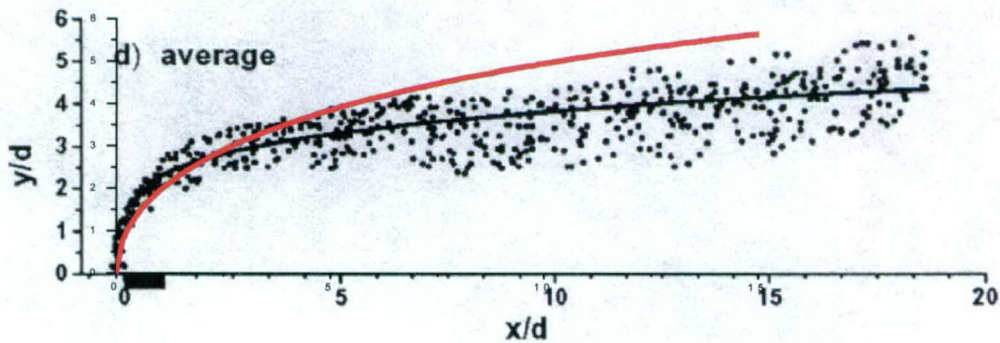
Figure 6. Comparison of the theoretical solution (7) (red lines) with the jet penetration measured from 8 consecutive schlieren images of hydrogen injection into supersonic cross-flow;[2] $M = 3.5$, $T^* = 1300$ K, $p^* = 0.32$ psi, $U_\infty^* = 2420$ m/s; the jet-to-freestream momentum flux ratio $\alpha = 2$.
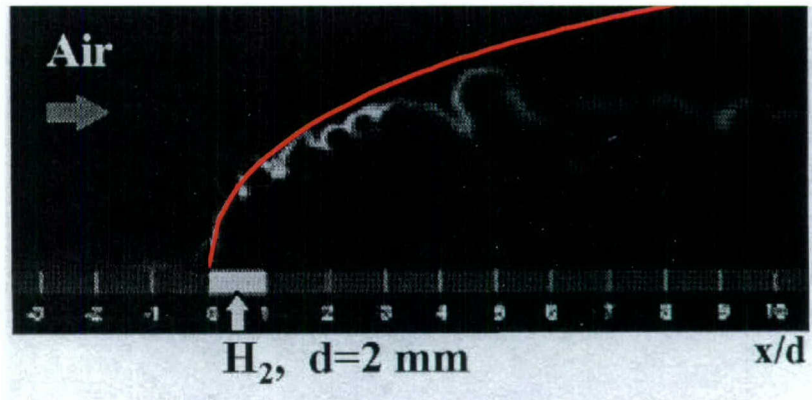
Figure 7. Comparison of the theoretical solution (7) (red line) with simultaneous OH-PLIF image of hydrogen injection into supersonic cross-flow;[2] $M = 3.5$, $T^* = 1300$ K, $p^* = 0.32$ psi, $U_\infty^* = 2420$ m/s; the jet-to-freestream momentum flux ratio $\alpha = 2$.

$\alpha = 2$ $\alpha = 3$

$\alpha = 5$
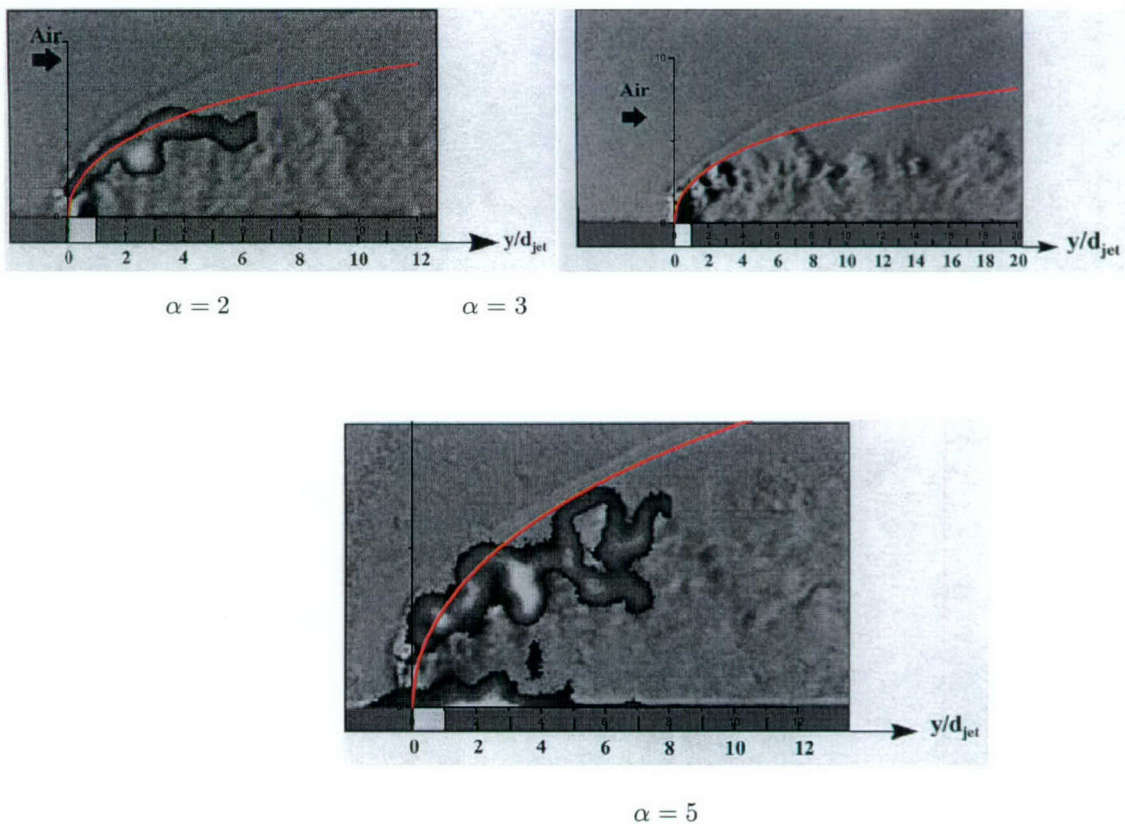
Figure 8. Comparison of the theoretical solution (7) (red line) with simultaneous combined OH-PLIF and schlieren images of hydrogen injection into supersonic cross-flow;[8] $M = 4.7$, M=4.7, $T^* = 1300$ K, $p^* = 0.75$ psi, $U_\infty^* = 3300$ m/s.

Stabilization of Hypersonic Boundary Layers by Porous Coatings

Alexander V. Fedorov*
Moscow Institute of Physics and Technology, Zhukovski 140160, Russia
Norman D. Malmuth[†]
Rockwell Science Center, Thousand Oaks, California 91630
and
Adam Rasheed[‡] and Hans G. Hornung[§]
California Institute of Technology, Pasadena, California 91125

A second-mode stability analysis has been performed for a hypersonic boundary layer on a wall covered by a porous coating with equally spaced cylindrical blind microholes. Massive reduction of the second mode amplification is found to be due to the disturbance energy absorption by the porous layer. This stabilization effect was demonstrated by experiments recently conducted on a sharp cone in the T-5 high-enthalpy wind tunnel of the Graduate Aeronautical Laboratories of the California Institute of Technology. Their experimental confirmation of the theoretical predictions underscores the possibility that ultrasonically absorptive porous coatings may be exploited for passive laminar flow control on hypersonic vehicle surfaces.

Nomenclature

A	=	admittance
B	=	thermal admittance
F	=	frequency parameter
h	=	porous layer thickness
n	=	porosity
p	=	pressure perturbation
Pr	=	Prandtl number
Re	=	displacement thickness Reynolds number
Re_{tr}	=	transition Reynolds number
r	=	pore radius
s	=	pore spacing
T	=	mean flow temperature
t	=	time
U	=	mean flow velocity
u, v, w	=	perturbation velocity components
x, y, z	=	Cartesian coordinates
α, β	=	wavenumber components
γ	=	specific heat ratio
δ^*	=	displacement thickness
θ	=	temperature perturbation
κ	=	thermal conductivity
μ	=	viscosity
ρ	=	mean flow density
σ	=	spatial growth rate
φ	=	wave front angle
ω	=	angular frequency

Subscripts

ad	=	adiabatic
e	=	upper boundary-layer edge
m	=	maximum value
w	=	wall surface

Superscript

*	=	dimensional

Introduction

THE ability to stabilize a hypersonic boundary layer and increase its laminar run is of critical importance in the hypersonic vehicle design.[1] Early transition causes significant increases in heat transfer and skin friction. Higher heating requires an increased performance thermal protection system (TPS), active cooling, or trajectory modification. This translates to higher cost and weight of hypersonic vehicles due to increased TPS weight. Moreover, with the low payload mass fraction, even small savings in TPS weight can provide a significant payload increase. Vehicle maintainability and operability are also affected by transition. Robust metallic TPS have temperature limits lower than ceramic TPS. Laminar flow control (LFC) can help meet these more severe constraints. For a streamlined vehicle with large wetted area, viscous drag becomes important. It can be from 10% (fully laminar) to 30% (fully turbulent) of the overall drag.[2] For optimized hypersonic wave/riders, viscous drag may represent up to 50% of the total drag.[3] Vehicle aerodynamics is another area impacted by laminar–turbulent transition. Asymmetry of the transition locus can produce significant yawing moments. Aerodynamic control surfaces and reaction control systems are also affected due to sensitivity of boundary-layer separation to the flow state (laminar or turbulent).

If freestream disturbances and TPS-induced perturbations are small, transition to turbulence is due to amplification of unstable boundary-layer modes.[1,4] In this case, LFC methods and transition prediction tools are predominantly based on stability theory and experiment.[5-8] LFC systems are aimed at slowing down or eliminating amplification of unstable disturbances using passive and/or active control techniques. A third form of flow control is known as reactive control, in which boundary-layer disturbances are canceled by artificially introducing out-of-phase disturbances. Typical passive LFC techniques are pressure gradient and shaping. Active techniques include wall suction and heat transfer. In reactive control methods, periodic suction/blowing, heating/cooling or wall vibrations are used for artificial excitation of counter-phase disturbances.

In hypersonic boundary layers, amplification of the following instability mechanisms may drive the transition process:

1) The first instability mechanism is the first mode associated with Tollmien–Schlichting waves. This instability may be dominant at relatively small local Mach numbers (normally less than 5). This mode is strongly stabilized on cool surfaces. At low wall-temperature ratios, the stabilization effect may be so strong that the first-mode mechanism becomes unimportant.

2) The second mode associated with an inviscid instability present due to a region of supersonic mean flow relative to the disturbance phase velocity[5] belongs to the family of trapped acoustic modes and becomes the dominant instability in two-dimensional and
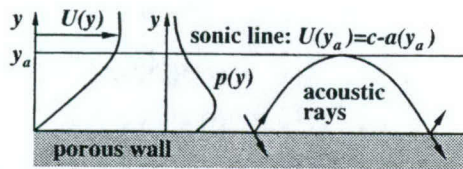
Fig. 1 Acoustic mode in a supersonic boundary layer on semitransparent wall.

quasi-two-dimensional boundary layers at Mach numbers $M > 4$. The existence of the second mode was established by the experiments of Kendall,[9] Demetriades,[10] Stetson et al.,[11] Stetson and Kimmel,[12] and Kimmel et al.[13] The most amplified second-mode wavelength is approximately twice the boundary-layer thickness, and its phase velocity tends to the boundary-layer edge velocity of mean flow. As a result, the second-mode disturbances are in the ultrasonic frequency band. For example, the most amplified waves observed in the experiment of Stetson et al.[11] at Mach 8 correspond to a frequency about 100 kHz. In contrast to the first mode, the second mode is destabilized by cooling.

3) Crossflow vortices are observed in three-dimensional boundary layers on the leading edge of a swept wing, axisymmetric bodies at high angles of attack, etc. This instability is weakly sensitive to wall cooling. It can be effectively stabilized by shaping. For example, two-dimensional shaping of air breathers helps to avoid crossflow instabilities on large acreage regions of the vehicle surface.

4) Görtler vortices play a major role in transition on concave surfaces. Similar to the crossflow instability, their growth rate can be reduced by shaping.

Because severe environmental conditions make it difficult to use active and reactive LFC concepts for hypersonic vehicles, passive LFC techniques are of great interest. Thus, Malmuth et al.[14] proposed a new passive method of second- and higher-mode stabilization. They exploited the hypersonic boundary layer's behavior as an acoustic waveguide, schematically shown in Fig. 1. Therein, acoustic rays are reflected by the wall and turn around near the sonic line: $y = y_a$, $U(y_a) = Re(c) - a(y_a)$, where c is the disturbance phase speed and a is local sound speed. The second, third, and higher boundary-layer modes correspond to the waveguide normal modes. Malmuth et al.[14] assumed that the absorption of acoustic energy by an ultrasonically absorptive coating can stabilize these disturbances. This assumption was examined using stability theory for inviscid disturbances. It was found that an ultrasonically semitransparent wall provides substantial reduction of the second-mode growth rate.

In this paper, we study this stabilization mechanism, including viscous effects and an absorptive skin microstructure. We formulate the eigenvalue problem for viscous disturbances in a hypersonic boundary layer on a wall covered by an ultrasonically absorptive coating of special type, namely, a porous layer with equally spaced cylindrical blind microholes. We obtain the analytical form of boundary conditions on the porous surface and solve the viscous eigenvalue problem numerically. We discuss results of calculations showing the second-mode stabilization on porous surfaces of various pore radii, spacing, and thickness. Then we briefly describe the experimental data of Rasheed et al.[15] that confirm the theoretically based hypersonic boundary-layer stabilization by porous coatings given in this paper. These results were obtained in the T-5 Graduate Aeronautical Laboratories of the California Institute of Technology high-enthalpy wind tunnel on a sharp cone that they detail in Ref. 15. Finally, we conclude the paper with a summary discussion and indicate possible future directions.

Eigenvalue Problem

We consider supersonic boundary-layer flow over a flat plate or sharp cone as schematically shown in Fig. 2. The fluid is a perfect gas with Prandtl number Pr, specific heat ratio γ, and viscosity μ. The coordinates x, y, and z are made nondimensionless using the boundary-layer displacement thickness δ^*. In the locally parallel approximation, the mean flow is characterized by the profiles of x-component velocity $U(y)$ and temperature $T(y)$, referenced to the quantities U_e^* and T_e^* at the upper boundary-layer edge. Three-
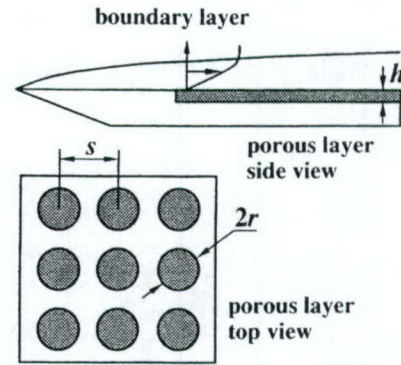

Fig. 2 Schematic of a wall covered by porous layer.

dimensional disturbances are represented in the traveling wave form

$$\tilde{q} = \text{Re}\{q(y)\exp[i(\alpha x + \beta z - \omega t)]\}, \qquad \tilde{q} = [\tilde{u}, \tilde{v}, \tilde{w}, \tilde{p}, \tilde{\theta}] \quad (1)$$

where $\tilde{u}$, $\tilde{v}$, and $\tilde{w}$ are velocity components; $\tilde{p}$ is the pressure referenced to the double dynamic pressure $\rho_e^* U_e^{*2}$; $\tilde{\theta}$ is the temperature; $\alpha = \alpha^* \delta^*$ and $\beta = \beta^* \delta^*$ are wave number components; and $\omega = \omega^* \delta^*/U_e^*$ is the angular frequency. The system of stability equations that is derived from the full Navier–Stokes equations for a locally parallel compressible boundary layer can be represented in the form[16]

$$\frac{dz}{dy} = S \cdot z, \qquad z = \left(u, \frac{du}{dy}, v, p, \theta, \frac{d\theta}{dy}, w, \frac{dw}{dy}\right)^T \quad (2)$$

where S is an 8×8 matrix. Its elements are functions of the mean flow profiles, the displacement thickness Reynolds number $Re = \delta^* U_e^* \rho_e^*/\mu_e^*$, and disturbance characteristics ω, α, and β.

We consider a wall covered by a porous layer of the thickness h^*. The pores are equally spaced cylindrical blind holes of radius r^* perpendicular to the wall surface, as schematically shown in Fig. 2. The hole spacing s^* and diameter are assumed to be much less than the boundary-layer displacement thickness δ^*. Because the pore radius is small and interactions between neighboring pores are weak, perturbations of longitudinal and transverse velocity produced by the porous layer are neglected. However, the porous structure is semitransparent relative to the vertical velocity and temperature perturbations. In this case, the wall boundary conditions can be expressed as

$$u(0) = 0, \qquad w(0) = 0, \qquad v(0) = Ap(0), \qquad \theta(0) = Bp(0) \quad (3)$$

where the admittance A and thermal admittance B are complex quantities that depend on properties of the wall material, porosity parameters, mean flow characteristics on the wall surface, and flow perturbation parameters such as a wave frequency and wavelength. These dependencies are derived in the next section. Because boundary-layer modes decay outside the boundary layer, we have

$$u(\infty) = v(\infty) = w(\infty) = \theta(\infty) = 0 \quad (4)$$

The eigenvalue problem (2–4) provides the dispersion relation $F(\alpha, \beta, \omega) = 0$. For temporal stability, the wave number components α and β are real quantities, and ω is a complex eigenvalue. If $\text{Im}(\omega) > 0$, then the disturbance is unstable. For spatial instability in two-dimensional boundary layers, the frequency ω and transverse wave number component β are real, whereas α is a complex eigenvalue. If $\text{Im}(\alpha) < 0$, then the disturbance amplifies downstream with the spatial growth rate $\sigma = -\text{Im}(\alpha)$.

Admittance of Porous Layer

The porous layer is characterized by the porosity n, which is the fraction of the overall volume taken up by the pores. For the pore spacing shown in Fig. 2, the porosity, $n = \pi(r^*/s^*)^2$, can be varied in the range $0 < r^*/s^* < \pi/4$, where the upper limit corresponds to $s^* = 2r^*$. The pore radius and spacing are considered to be much less than the disturbance wavelength, which is of the order of the

boundary-layer displacement thickness. In this case, the porosity is fine enough to avoid disturbing the laminar boundary layer by other mechanisms associated with effective surface roughness. The porous layer thickness h^* is assumed to be much larger than the pore radius r^*, that is, each pore is treated as a long tube.

To obtain the relationship between the admittance A and porous layer parameters, we use the theoretical model developed by Gaponov for subsonic[17,18] and moderate supersonic speeds.[19] These studies addressed the porosity effect on Tollmien–Schlichting (TS) waves. As contrasted to second-mode waves of acoustic type discussed in this paper, the TS waves over porous walls analyzed by Gaponov are vortical disturbances that become unstable due to viscous mechanisms. For this reason, the second-mode interaction with a porous surface is fundamentally different from that of TS waves. Yet, the results[18] for the disturbance propagation within a porous wall are independent of the nature of the boundary-layer disturbances, for example, second-mode acoustic or TS waves. In particular, they can be used in formulating the porous wall boundary conditions for the vertical velocity of second-mode disturbances considered herein. The thermal admittance B is derived using an explicit coupling between the pressure, temperature, and velocity perturbations within a uniform pore.[20]

Following the analysis,[18] we apply the theory of sound wave propagation in thin and long tubes (see, for example, Ref. 21). Because $h^* \gg r^*$, the pressure is approximately constant across the pore. In this case, the acoustic field within each pore is characterized by the propagation constant Λ and the characteristic impedance Z_0. These parameters can be expressed as a function of the series impedance Z and the shunt admittance Y for the tube element of unit length using the transmission line formalism.[22,23] The series impedance properties of the tube element are associated with the storage of kinetic energy and its dissipation due to viscous losses at the tube wall. The shunt admittance is associated with the potential energy of compression and the thermal energy losses due to the wall heat conductivity. We assume that the mean gas temperature along the tube is constant and equal to the wall surface temperature T_w. Daniels[22] and Benade[23] showed that the dimensional series impedance Z^* and shunt admittance Y^* per unit length of a tube with radius r^* are expressed as

$$Z^* = -\frac{i\omega^* \rho_w^*}{\pi r^{*2}} \left[1 - \frac{2}{k_v} \cdot \frac{J_1(k_v)}{J_0(k_v)} \right]^{-1} \tag{5}$$

$$Y^* = -\frac{i\omega^* \pi r^{*2}}{\rho_w^* a_w^{*2}} \left[1 + (\gamma - 1)\frac{2}{k_t} \cdot \frac{J_1(k_t)}{J_0(k_t)} \right] \tag{6}$$

where, ρ_w^* and a_w^* are mean density and sound speed in a tube. J_0 and J_1 are Bessel functions of the arguments $k_v = r^* \sqrt{(i\omega^* \rho_w^*/\mu_w^*)}$ and $k_t = k_v \sqrt{(Pr)}$, which measure the ratio of the tube radius to the viscous boundary-layer thickness and to the thermal boundary-layer thickness on the tube surface, respectively. Using the relation

$$J_0(x) + J_2(x) = 2J_1(x)/x \tag{7}$$

we express Z^* and Y^* in the form

$$Z^* = \frac{i\omega^* \rho_w^*}{\pi r^{*2}} \cdot \frac{J_0(k_v)}{J_2(k_v)} \tag{8}$$

$$Y^* = -\frac{i\omega^* \pi r^{*2}}{\rho_w^* a_w^{*2}} \left[\gamma + (\gamma - 1)\frac{J_2(k_t)}{J_0(k_t)} \right] \tag{9}$$

For the average velocity through the pore, the transmission line is characterized by the impedance $Z_1^* = S^* Z^*$ and shunt admittance $Y_1^* = Y^*/S^*$, where $S^* = \pi r^{*2}$ is pore cross-sectional area. Choosing the boundary-layer displacement thickness and mean flow parameters at the upper boundary-layer edge as reference scales, we have

$$Z_1 \equiv \frac{\pi r^{*2} \delta^*}{\rho_e^* U_e^*} Z^* = \frac{i\omega}{T_w}\frac{J_0(k_v)}{J_2(k_v)}, \qquad k_v = r\sqrt{\frac{i\omega \rho_w}{\mu_w}} R \tag{10}$$

$$Y_1 \equiv \frac{\rho_e^* U_e^* \delta^*}{\pi r^{*2}} Y^* = -i\omega M^2 \left[\gamma + (\gamma - 1)\frac{J_2(k_t)}{J_0(k_t)} \right] \tag{11}$$

where $r = r^*/\delta^*$ is nondimensional pore radius. The characteristic impedance Z_0 and the propagation constant Λ are expressed in the form

$$Z_0 = \sqrt{Z_1/Y_1}, \qquad \Lambda = \sqrt{Z_1 Y_1}, \qquad \mathrm{Re}(\Lambda) < 0 \tag{12}$$

The coupling between the pressure amplitude p and the average velocity disturbance amplitude $\bar{v}$ at the pore end, $y = -h$, can be expressed as $p(-h) = X \cdot \bar{v}(-h)$, where the impedance X depends on characteristics of the backup structure. If the lower pore end is closed by a solid wall (blind pores), then $\bar{v}(-h) = 0$. In this case, the impedance is $X = \infty$, and the velocity–pressure ratio at the upper end of the pore is

$$[\bar{v}(0)/p(0)] = (1/Z_0)\tanh(\Lambda h) \tag{13}$$

Averaging the vertical velocity amplitude at the wall over the surface area, we have $v(0) = n \cdot \bar{v}(0)$. Then the admittance in the boundary conditions (3) is expressed as

$$A = (n/Z_0)\tanh(\Lambda h) \tag{14}$$

If the porous layer is relatively thick ($\Lambda h \to \infty$), then Eq. (14) is reduced to the form

$$A = -(n/Z_0) \tag{15}$$

Note that the limit $\Lambda h \to \infty$ leads to Eq. (15) at any finite value of X (i.e., the disturbance at the upper end of each hole does not feel the lower end due to the decay of sound propagating along a tube).

According to the analysis of Stinson and Champoux,[20] the pressure disturbance, average temperature disturbance, and average velocity disturbance within a cylindrical pore are coupled as

$$\bar{v}^*(\omega^*) = \frac{1}{i\omega^* \rho_w^*}\frac{dp^*}{dy^*}(\omega^*)\left[1 - \frac{2}{k_v}\frac{J_1(k_v)}{J_0(k_v)} \right] \tag{16}$$

$$\bar{\theta}^*(\omega^*) = \frac{i\omega^* \mu^*}{\kappa_w^*}\left[p^*(\omega^*) \middle/ \frac{dp^*}{dy^*}(Pr\omega^*) \right]\bar{v}^*(Pr\omega^*) \tag{17}$$

Substituting Eq. (16) into Eq. (17), accounting for Eq. (7), and nondimensionalizng the result, we obtain

$$\bar{\theta} = -(\gamma - 1)M^2 T_w p J_2(k_t)\middle/ J_0(k_t) \tag{18}$$

Thus, the thermal admittance in the boundary condition (3) for the temperature disturbance is expressed as

$$B = -n(\gamma - 1)M^2 T_w J_2(k_t)\middle/ J_0(k_t) \tag{19}$$

Computational and Parametric Studies

To evaluate the porous layer effect on the second-mode stability, we solve the eigenvalue problem (2–4) numerically using the admittance (14) or its limiting form (15) and the thermal admittance (19). We consider the boundary layer of a perfect gas with Prandtl number $Pr = 0.71$ and specific heat ratio $\gamma = 1.4$. The temperature–viscosity law is specified as $\mu = \mu_0(T/T_0)^m$ with the exponent $m = 0.75$; the second viscosity is zero. Figure 3 shows the spatial growth rate σ as a function of the Reynolds number Re for two-dimensional unstable waves ($\beta = 0$) of nondimensional frequency $F \equiv \omega^* v_e^*/U_e^{*2} = 2.8 \times 10^{-4}$ in the boundary layer at the Mach number $M = 6$. The wall temperature $T_w = 1.4$ approximately corresponds to the wall temperature ratio $T_w/T_{ad} = 0.2$. Calculations were conducted for a thick porous layer ($\Lambda h \to \infty$) with the porosity $n = 0.5$ at various values of the nondimensional pore radius $r = r^*/\delta^*$. Note that the porous layer causes massive reduction of the second-mode growth rate. In Figs. 3–6, symbols correspond to the case of zero thermal admittance, $B = 0$. For all cases considered, temperature perturbations on the porous surface weakly affect the disturbance growth rate and can be neglected.

Figure 4 shows that deep pores of fixed radius ($r = 0.03$ at $Re = 2 \times 10^3$) and spacing (porosity $n = 0.5$) strongly stabilize the second-mode waves in a wide frequency band at various Reynolds numbers Re (dashed lines). This example illustrates that it is possible to cause significant reduction of the disturbance growth rate on large surface areas without fine tuning the pore size. As contrasted to
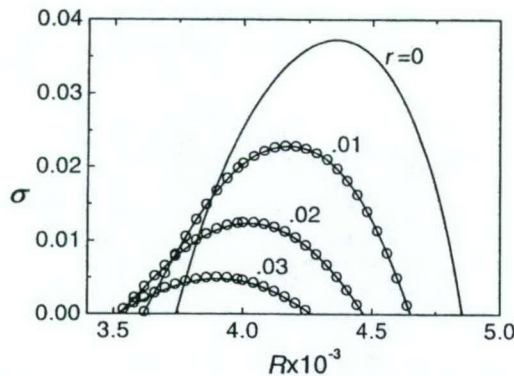
Fig. 3 Growth rate σ as a function of Reynolds number Re at various pore radii r: $M = 6$, $T_w = 1.4$, $F = 2.8 \times 10^{-4}$, $n = 0.5$, and $\Lambda h \to \infty$ (solid lines); symbols indicate zero thermal admittance. (R = Reynolds number in figure.)
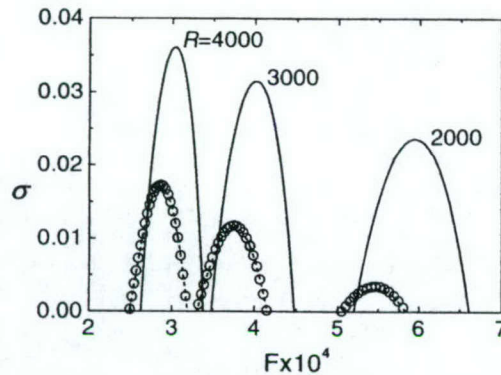

Fig. 4 Growth rate σ as a function of disturbance frequency F at various Reynolds numbers Re: $M = 6$, $T_w = 1.4$, $n = 0.5$, and $\Lambda h \to \infty$; solid lines $r = 0$, dashed lines $r = 0.03$ at $Re = 2.0 \times 10^3$, symbols indicate zero thermal admittance. (R = Reynolds number in figure.)

reactive flow control techniques, a porous coating provides passive stabilization of the boundary-layer flow regardless the disturbance phase and amplitude distributions in space and time and with no external energy input. Note that the waveguide behavior described earlier in this paper in connection with the instability of the acoustic second mode that is quenched by the ultrasonic absorbing wall concept described herein resembles amplification processes studied by the second author in connection with the stability of hypersonic strong interaction flows.[24]

Figure 5 shows distributions of the maximum growth rate, $\sigma_m(Re) = \max_\omega[\sigma(\omega, Re)]$, at the wall temperatures $T_w = 1.4$, 3.5, and 7.0, that approximately corresponds to the wall temperature ratio $T_w/T_{ad} = 0.2, 0.5$, and 1. The stabilization effect decreases as the wall temperature increases. A strong reduction of the growth rate is observed in the boundary layer on a cool wall (see Fig. 5), a more practical case for hypersonic applications. This trend is consistent with the admittance asymptotic behavior associated with Eqs. (10–12) and (15). For deep pores ($\Lambda h \gg 1$) of relatively small radius ($|k_v| \ll 1$), the admittance A is proportional to $k_v M \sqrt{(T_w)}$ and decreases with the wall temperature as $T_w^{-m/2}$.

Figure 6 shows the maximum growth rate σ_m as a function of the porosity n for $Re = 4 \times 10^3$ and $r = 0.03$ for the boundary layer at $M = 6$ and $T_w = 1.4$. The porous layer of spacing $s = 4r$ ($n \approx 0.2$) reduces the growth rate by a factor of 2 compared to the solid wall case $n = 0$. Our calculations using the e^N method indicates that this stabilization translates to extending the transition onset point more than three times its value without porosity. In Fig. 7, the second-mode growth rate is shown as a function of the nondimensional porous layer thickness $h = h^*/\delta^*$ at $n = 0.4$, $r = 0.03$, $Re = 4 \times 10^3$, and $F = 3 \times 10^{-4}$. The limit $\Lambda h \to \infty$ is achieved at a relatively small value of $h \approx 0.3$ (pore depth is about five diameters) that is due to strong damping of sound waves in thin pores. There is an optimal thickness, $h \approx 0.12$, at which the porous
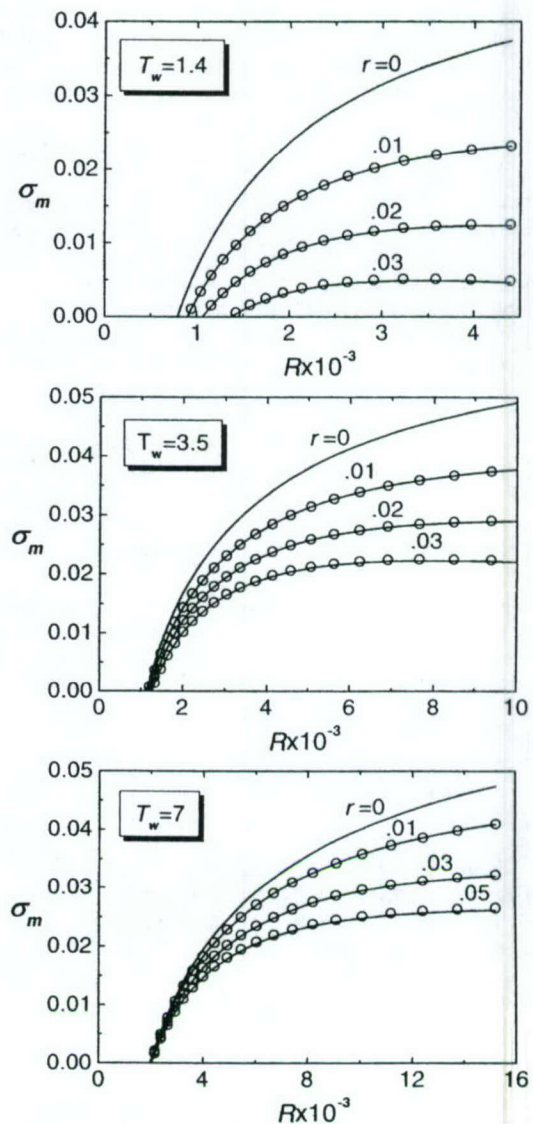

Fig. 5 Distributions of maximum growth rate $\sigma_m(Re)$ at various pore radii r: $M = 6$, $n = 0.5$, and $\Lambda h \to \infty$ (———); symbols indicate zero thermal admittance. (R = Reynolds number in figure.)
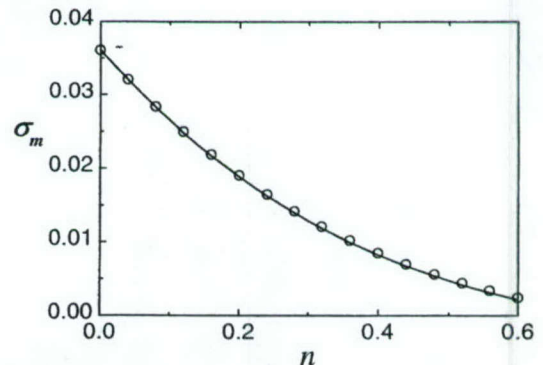

Fig. 6 Maximum growth rate σ_m as a function of porosity n at $Re = 4 \times 10^3$: $M = 6$, $T_w = 1.4$, $r = 0.03$, and $\Lambda h \to \infty$ (———); symbols indicate zero thermal admittance.

wall effect is able to stabilize the disturbance completely. In this case, the disturbance reflected from the pore bottom is in counter phase with the boundary-layer disturbance. However, the optimal thickness strongly depends on the disturbance frequency and the thick porous layer is more robust. Figure 8 illustrates the stabilization effect for three-dimensional waves of the second-mode family. The growth rate is shown as a function of the wave front angle $\varphi = \arctan(\beta_r/\alpha_r)$ at various pore radii. The porous coating causes massive reduction of the disturbance growth rate and substantially
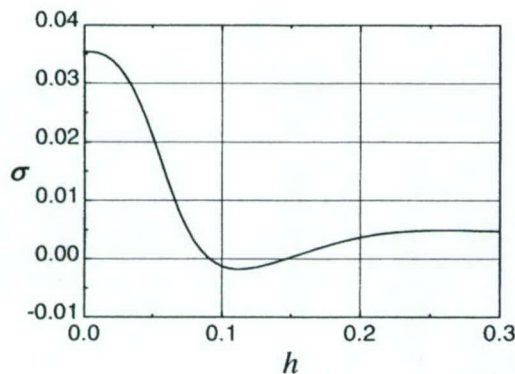
Fig. 7 Growth rate σ as a function of porous layer thickness h at $n = 0.4, r = 0.03, Re = 4 \times 10^3, F = 3 \times 10^{-4}$, $M = 6$, and $T_w = 1.4$ for zero thermal admittance.
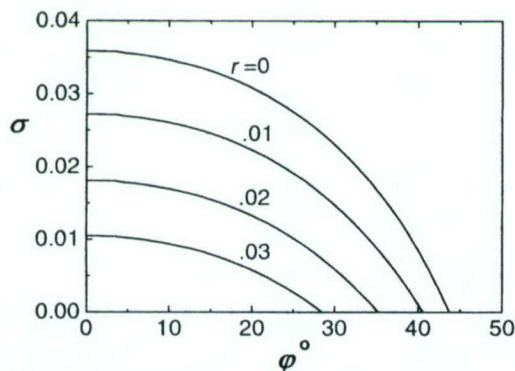

Fig. 9 Microphotograph of porous surface.

Fig. 8 Growth rate σ as a function of wave front angle φ at various pore radii r: $M = 6$, $T_w = 1.4$, $Re = 4287$, $F = 3 \times 10^{-4}$, $n = 0.3$, and $\Lambda h \rightarrow \infty$.

Fig. 10 Transition onset Reynolds number Re_{tr} vs total enthalpy H_0: ■, solid wall; ○, porous wall; and ⊙, boundary layer on porous wall is laminar up to the model base.

decreases the unstable range of wave front angles. These examples show that a relatively thin porous coating can dramatically reduce the second-mode amplification and increase the laminar run if transition is driven by second-mode disturbances.

Experimental Validation of Theory

Rasheed et al.[15] have recently verified the theoretical concept by testing a 5-deg half-angle sharp cone with an ultrasonically absorptive coating in the California Institute of Technology T5 high-enthalpy shock tunnel. The cone was 1 m in length, with half of its surface solid and the other a porous sheet perforated with equally spaced blind cylindrical holes. Porosity parameters were chosen from the preliminary theoretical analysis of Fedorov and Malmuth as well as manufacturing constraints. The average pore radius r^* was 30 μm, the depth h^* was 500 μm, and the average spacing s^* was 100 μm. Figure 9 shows a microphotograph of a portion of the porous surface. For typical runs, the boundary-layer thickness was about 1 mm, and the estimated number of holes per boundary-layer disturbance wavelength was about 20. Static measurements of ultrasound reflectivity of perforated sheet coupons (without flow) showed that the porous coating attenuated the incident ultrasonic signal of 400-kHz frequency by 3.0 dB relative to a solid wall.

The model was instrumented by thermocouples, and the transition onset point was determined from the Stanton number distributions $St(x)$ measured simultaneously on both sides of the model for each run. Nitrogen was selected as the test gas to minimize the chemistry effects, which were not included in the theoretical analysis. Runs were performed for the ranges of the freestream total enthalpy $4.18 \leq H_0 \leq 13.34$ MJ/kg and Mach number $4.59 \leq M_\infty \leq 6.4$. Figure 10 shows a summary plot of the transition onset Reynolds number $Re_{tr} = x_{tr}^* U_e^* \rho_e^* / \mu_e^*$ vs H_0. The solid squares correspond to transition on the solid wall, and the open circles correspond to transition on the porous surface. The circles with arrows indicate that the boundary layer on the porous surface was
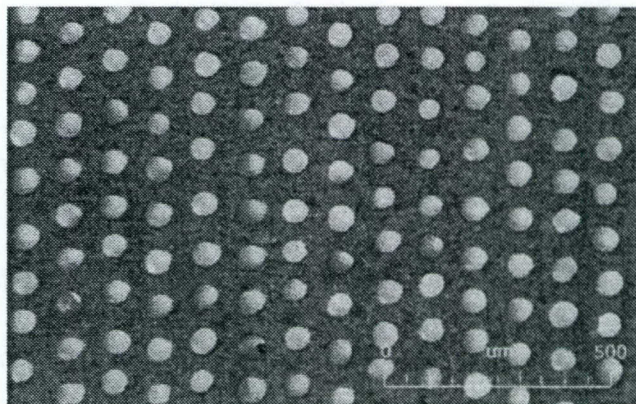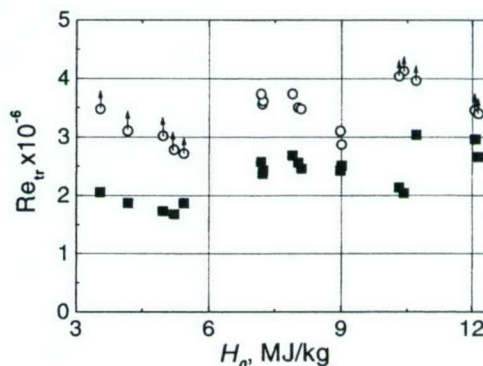
laminar up to the model base, that is, the value plotted is not a real data point because the cone was not long enough to measure the transition locus. In all cases, the circles are well above the squares. This indicates that the porous coating always delays transition by a significant amount.

Summary

A second-mode stability analysis has been performed for hypersonic boundary layers over walls covered by porous coatings with equally spaced blind microholes. Absorption of the disturbance energy by porous layers was modeled using the theory of disturbance wave propagation in thin and long tubes. The admittance and thermal admittance coupling the pressure disturbance with the vertical velocity and temperature disturbances on the porous surface are expressed as explicit functions of porosity characteristics. Stability calculations showed that the absorption of disturbance energy by the porous coating provides massive reduction of the second-mode growth rate in a wide range of disturbance frequencies and Reynolds numbers. The flow stabilization is due to vertical velocity perturbations on the porous surface associated with nonzero admittance of porous medium. Temperature perturbations weakly affect the boundary-layer disturbance and can be neglected. This indicates that temperature disturbances play a passive role in the second-mode instability mechanism.

Our conclusions are consistent with the results of Malmuth et al.,[14] obtained from their inviscid stability analysis. The most profound effect is observed on a cool wall that is typical for hypersonic vehicle TPS surfaces. A relatively thin porous coating (of thickness about 30% of the laminar boundary-layer displacement thickness) provides a strong stabilization effect. Such porous coatings can be designed for passive LFC in hypersonic vehicle surfaces. Note that the disturbance absorption should be introduced at the initial phase of transition process, where the unstable disturbance amplitude is about 0.01–0.1% of its level in transitional and turbulent boundary layers. In this phase, additional heating of the porous coating

associated with partial absorption of the disturbance energy is negligibly small compared to the turbulent heating.

The first series of experiments conducted by Rasheed et al.[15] on a sharp cone in the T5 shock tunnel at the Graduate Aeronautical Laboratories at the California Institute of Technology qualitatively confirms the theoretical prediction. Quantitative comparison of the theory with these data is planned for the future. Because the boundary-layer stabilization is due to the disturbance energy extraction mechanism, we believe that similar effects may occur for other types of high-frequency instabilities. Absorptive coatings may also affect the bypass mechanism, which is responsible for transition past TPS roughness elements. These assumptions could be examined by further theoretical modeling and verified by experiments.

Many TPS materials, which can provide efficient absorption of acoustic disturbances, have a random porosity. The interaction of the boundary layer and unstable disturbances with a random porous coating may be different from the case of the regular pore structure discussed earlier. Because of communication between randomly distributed pores, a mean flow may occur inside the coating that leads to a slip effect on the coating surface. Boundary conditions for unstable disturbances may be also affected. These effects will also be addressed in our future studies.

Acknowledgments

References

[1]Malik, M. R., Zang, T. A., and Bushnell, D. M., "Boundary-Layer Transition in Hypersonic Flows," AIAA Paper 90-5232, 1990.

[2]Reed, H. L., Kimmel, R., Schneider, S., and Arnal, D., "Drag Prediction and Transition in Hypersonic Flow," AIAA Paper 97-1818, June 1997.

[3]Bowcutt, K. G., Anderson, J. D., and Capriotti, D., "Viscous Optimized Hypersonic Waveriders," AIAA Paper 87-0272, 1987.

[4]Reshotko, E., "Boundary-Layer Instability, Transition, and Control," AIAA Paper 94-0001, Jan. 1994.

[5]Mack, L. M., "Boundary-Layer Stability Theory," Special Course on Stability and Transition of Laminar Flow, edited by R. Michel, Rept. 709, AGARD, 1984, pp. 3-1–3-81.

[6]Reshotko, E., "Stability Theory as a Guide to the Evaluation of Transition Data," AIAA Journal, Vol. 7, No. 6, 1969, pp. 1086–1091.

[7]Malik, M. R., "Prediction and Control of Transition in Supersonic and Hypersonic Boundary Layers," AIAA Journal, Vol. 27, No. 11, 1989, pp. 1487–1493.

[8]Malik, M. R., "Stability Theory for Laminar Flow Control Design," Viscous Drag Reduction in Boundary Layers, edited by D. M. Bushnell and J. N. Hefner, Vol. 123, Progress in Astronautics and Aeronautics, AIAA, Washington, DC, 1990, pp. 3–46.

[9]Kendall, J. M., "Wind-Tunnel Experiments Relating to Supersonic and Hypersonic Boundary-Layer Transition," AIAA Journal, Vol. 13, No. 3, 1975, pp. 290–299.

[10]Demetriades, A., "Hypersonic Viscous Flow over a Slender Cone, Part III: Laminar Instability and Transition," AIAA Paper 74-535, 1974.

[11]Stetson, K. F., Thompson, E. R., Donaldson, J. C., and Siler, L. G., "Laminar Boundary-Layer Stability Experiments on a Cone at Mach 8, Part 1: Sharp Cone," AIAA Paper 83-1761, 1983.

[12]Stetson, K. F., and Kimmel, R. G., "On the Breakdown of a Hypersonic Laminar Boundary Layer," AIAA Paper 93-0896, 1993.

[13]Kimmel, R., Demetriades, A., and Donaldson, J., "Space–Time Correlation Measurements in a Hypersonic Transitional Boundary Layer," AIAA Paper 95-2292, 1995.

[14]Malmuth, N. D., Fedorov, A. V., Shalaev, V., Cole, J., and Khokhlov, A., "Problems in High-Speed Flow Prediction Relevant to Control," AIAA Paper 98-2995, June 1998.

[15]Rasheed, A., Hornung, H. G., Fedorov, A. V., and Malmuth, N. D., "Experiments on Passive Hypervelocity Boundary-Layer Control Using a Porous Surface," AIAA Paper 2001-0274, Jan. 2001.

[16]Mack, L. M., "Boundary-Layer Stability Theory," Jet Propulsion Lab., Rept. 900-277, rev. B, California Inst. of Technology, Pasadena, CA, 1969.

[17]Gaponov, S. A., "Influence of Porous Layer on Boundary-Layer Stability," Izevestia SO AN SSSR, Seria Technicheskich Nauk, Vyp. 1, No. 3, 1971, pp. 21–23 (in Russian).

[18]Gaponov, S. A., "Influence of Gas Compressibility on Stability of Boundary Layer on Porous Surface at Subsonic Speeds," Zhurnal Prikladnoi Mechaniki i Technicheskoi Fiziki, No. 1, 1975, pp. 121–125 (in Russian).

[19]Gaponov, S. A., "Stability of Supersonic Boundary Layer on Porous Wall with Heat Conductivity," Izvestia AN SSSR, Mechanika Zhidkosti i Gaza, No. 1, 1977, pp. 41–46 (in Russian).

[20]Stinson, M. R., and Champoux, Y., "Propagation of Sound and the Assignment of Shape Factors in Model Porous Materials Having Simple Pore Geometries," Journal of the Acoustical Society of America, Vol. 91, No. 2, 1992, pp. 685–695.

[21]Rzhevkin, S. N., Lectures on Theory of Sound, Moscow State Univ., Moscow, 1960 (in Russian).

[22]Daniels, F. B., "On the Propagation of Sound Waves in a Cylindrical Conduit," Journal of the Acoustical Society of America, Vol. 22, No. 2, 1950, pp. 563–564.

[23]Benade, A. H., "On the Propagation of Sound Waves in a Cylindrical Conduit," Journal of the Acoustical Society of America, Vol. 44, No. 2, 1968, pp. 616–623.

[24]Malmuth, N., "Stability of the Inviscid Shock Layer in Strong Interaction Flow over a Hypersonic Flat Plate," Fluid Mechanics and Its Applications, edited by D. E. Ashpis, T. B. Gatski, and R. Hirsch, Kluwer Academic, Boston, 1993, pp. 189–223.

M. Sichel
Associate Editor

Experiments on Passive Hypervelocity Boundary-Layer Control Using an Ultrasonically Absorptive Surface

A. Rasheed* and H. G. Hornung†
California Institute of Technology, Pasadena, California 91125
A. V. Fedorov‡
Moscow Institute of Physics and Technology, Zhukovski, 140160, Russia
and
N. D. Malmuth§
Rockwell Science Center, Thousand Oaks, California 91630

Recently performed linear stability analyses suggested that transition could be delayed in hypersonic boundary layers by using an ultrasonically absorptive surface to damp the second mode (Mack mode). Boundary-layer transition experiments were performed on a sharp 5.06-deg half-angle round cone at zero angle of attack in the T5 Hypervelocity Shock Tunnel to test this concept. The cone was constructed with a smooth surface around half the cone circumference (to serve as a control) and an acoustically absorptive porous surface on the other half. Test gases investigated included nitrogen and carbon dioxide at $M_\infty \simeq 5$ with specific reservoir enthalpy ranging from 1.3 to 13.0 MJ/kg and reservoir pressure ranging from 9.0 to 50.0 MPa. Comparisons were performed to ensure that previous results obtained in similar experiments (on a regular smooth surface) were reproduced, and the results were extended to examine the effects of the porous surface. These experiments indicated that the porous surface was highly effective in delaying transition provided that the pore size was significantly smaller than the viscous length scale.

Nomenclature

h	=	enthalpy, MJ/kg
M	=	Mach number
P	=	pressure, MPa
$\dot{q}$	=	heat flux, MW/m^2
Re	=	Reynolds number
St	=	Stanton number
ρ	=	density, kg/m^3
μ	=	viscosity, N · s/m^2

Subscripts

aw	=	adiabatic wall
D	=	hole diameter
e	=	edge condition
k	=	roughness height
s	=	slot width
tr	=	transition
x	=	location on cone measured along surface, mm
0	=	stagnation condition
∞	=	freestream

Superscript

*	=	reference condition

*Graduate Research Assistant, Graduate Aeronautical Laboratories. Student Member AIAA.

†Clarence L. Johnson Professor of Aeronautics, Director of Graduate Aeronautical Laboratories. Member AIAA.

‡Associate Professor, Department of Aeromechanics and Flight Engineering. Member AIAA.

§Senior Scientist, Fluid Dynamics. Fellow AIAA.

Introduction

HEAT loads and forces on hypervelocity vehicles depend critically on the location of transition from laminar to turbulent flow. Although significant progress has been and is being made in the theoretical understanding of transition, it is still one of the most severe uncertainties in the aerodynamic design of such vehicles.

An extensive series of experiments studying boundary-layer transition over a 5-deg smooth surfaced cone has previously been performed in the T5 Hypervelocity Shock Tunnel by Germain and Hornung[1] and Adam and Hornung.[2] In addition to capturing a flow visualization (shadowgraph) image of the boundary-layer transition process, these experiments determined the dependence of transition Reynolds number on specific stagnation enthalpy. One of the main results obtained by Germain and Hornung[1] was that the transition Reynolds number correlated with specific stagnation enthalpy provided that the Reynolds number was calculated at a reference temperature[3] rather than the boundary-layer edge conditions. As shown by Adam and Hornung,[2] the reference condition characterizes the conditions in the boundary layer better than the edge conditions, especially when comparisons are made between flows at different Mach numbers. These experiments also observed a trend of delayed transition as enthalpy increased. It is known that acoustic waves are absorbed by chemical activity, and the delayed transition was attributed to the increased chemical activity acting as a damping mechanism on the growth rate of the second mode acoustic instability waves.

In the absence of large freestream disturbances or surface perturbations, transition is caused by the amplification of unstable boundary-layer modes.[4] At hypersonic conditions ($M \gtrsim 4$), the dominant instability mode in two-dimensional or quasi-two-dimensional boundary layers is the so-called second mode or Mack mode.[5] In this mode, freestream acoustic perturbations become trapped in the boundary layer, grow in amplitude, and eventually cause the boundary layer to become turbulent. The most strongly amplified wavelength of these acoustic perturbations is approximately twice the boundary-layer thickness and propagates with a phase velocity approximately equal to the boundary-layer edge velocity.[6] This is entirely different from lower speed flows, where transition is dominated by the Tollmien–Schlichting mode. Linear stability computations by Johnson et al.[7] indicated that, at T5 tunnel experimental

conditions, the most unstable mode had frequencies of the order of 1–3 MHz. Such high frequencies are highly indicative of the second mode and confirmed that the Mack mode was indeed the most strongly amplified mode. These computations also confirmed the experimental observation that increased chemical activity at higher enthalpies damped the second mode growth rates and delayed transition at the T5 tunnel conditions.

Even more desirable than being able to predict the transition location would be to control it, specifically to move it downstream. Inviscid and viscous second mode stability analyses recently performed by Fedorov and Malmuth[8] and Fedorov et al.[9,10] suggested that transition could be delayed in hypersonic flow by using a suitably porous surface that would absorb and dissipate the most unstable second mode acoustic waves. The porous surface considered in the analysis was a surface pitted by equally spaced cylindrical blind microholes, that is, holes with closed bottoms, whose size and spacing were determined by the frequencies (or rather, the wavelengths) of the most unstable mode. The scale of the required porosity at the high frequencies of the second mode is extremely fine and would not prematurely trip the boundary layer by other mechanisms. Note that the proposed control mechanism is purely passive and that there is no net flow (suction or blowing) through the holes. This paper will discuss the details of the experiments performed in the T5 Hypervelocity Shock Tunnel to test the computational prediction by Fedorov et al.[10] that suitable wall porosity delays transition in hypersonic boundary layers.

Experimental Objective

The main objective was to test the boundary-layer control scheme by testing a nominal 5-deg half-angle cone with a smooth surface on one side and the ultrasonically absorbing porous surface on the other side. In this manner, each experiment was self-contained in that the smooth surface transition Reynolds number provided a direct baseline for the porous surface results. In addition, these experiments were used to verify agreement with previous data obtained by Germain and Hornung[1] and Adam and Hornung,[2] to test repeatability and to confirm that nonaxisymmetry or angle-of-attack issues were not affecting the results.

The previous set of experiments and linear stability analyses provided the basis for the current experimental study. In particular, the Mack mode was identified as being dominant at T5 tunnel conditions, and the proposed control scheme addresses this mode. Furthermore, the transition data from previous experiments provided important comparison data and served as a checkpoint for the new results. Finally, Adam and Hornung's comparison[2] with flight data ensured that the experimental results obtained were relevant to actual future flight vehicles.

Experimental Setup

T5 Hypervelocity Shock Tunnel

This series of experiments was performed in the Graduate Aeronautical Laboratories, California Institute of Technology, T5 Hypervelocity Free-Piston Shock Tunnel. In this reflected shock tunnel facility, a piston is initially launched by high-pressure air. The resulting adiabatic compression of a helium–argon mixture bursts a diaphragm ($P_{burst} \simeq 90$ MPa) causing a shock wave to travel into a shock tube, whose end wall is closed except for the small throat of the nozzle. The reflected shock from the end wall creates a quasi-constant pressure reservoir for the subsequent steady expansion

through the nozzle. Shock speeds of up to 5 km/s can be obtained to produce nominal Mach 5 flows with a specific reservoir enthalpy of up to 25 MJ/kg, reservoir pressure of 60 MPa, and reservoir temperature of 8000 K. Typical flow velocities for the present experiments were of the order of 3–4 km/s with typical useful test times ranging from 1 to 2 ms. Existing shock tunnel diagnostic instrumentation provided the shock speed and reservoir pressure from which the freestream conditions were calculated. The stagnation enthalpy was calculated by solving the one-dimensional equilibrium gasdynamics reflected shock problem using the measured shock speed, the measured initial shock tube pressure, and room temperature as inputs. The freestream conditions were calculated using a one-dimensional, inviscid, vibrational equilibrium, chemical nonequilibrium nozzle code, which used the computed stagnation temperature and measured stagnation pressure as inputs. Detailed descriptions regarding T5 operations and performance may be found in Hornung.[11]

Model and Instrumentation

Model Configuration

The model used for these experiments was a heavily modified version of the same model used by Germain and Hornung[1] and Adam and Hornung.[2] The final configuration was a sharp 5.06-deg half-angle round cone consisting of five pieces with an overall length of 999 mm. It had a smooth surface over half the cone and the absorptive porous surface over the other half beginning at 148 mm from the cone tip (Fig. 1). The aluminum base cone used by Germain and Hornung[1] and Adam and Hornung[2] was lengthened by the cone insert for the purposes of this project. The base cone was already hollow to allow room for instrumentation, and this aspect was preserved. An intermediate piece made of stainless steel 304 referred to as the cone tip holder was screwed into this assembly. The molybdenum cone tip was then screwed into this intermediate piece and was easily replaceable in the event of excessive blunting or other damage. Extreme care was taken during the manufacturing process to minimize the steps at these junctions.

The cone sheet was manufactured by rolling two initially flat sheets of metal (one perforated, one smooth) to form two longitudinal halves of a cone and then laser fusion welding them along the seams. Refer to Fig. 2a for a micrograph of the final weld. The resulting stainless steel cone sheet was fitted over the aluminum base cone using a thermal interference fit that took advantage of the mismatch in thermal coefficients of expansion of the two materials. This was accomplished by cooling both parts down to 190 K in special freezers used to store biological cell samples. This assembly technique resulted in the cone sheet being stretched tightly over the base cone providing the blind microholes for the porous surface and eliminating any surface imperfections. In addition, it eliminated the need for any mechanical fasteners that would disturb the boundary layer. Finally, this attachment method allowed the cone sheet to be nondestructively removable (and thus reusable) by simply reversing the thermal interference fit process. Note that all surfaces that were exposed to the flow were made of stainless steel 304, with the exception of the removable tip, which was made of molybdenum.

The final fully assembled model was placed in a lathe, and indicators were used to verify the geometry of the cone. In particular, the half-angle of the cone was verified to be 5.06 deg, and the steps the two junctions (cone tip/cone tip holder and cone tip holder/con sheet junctions) were measured to be less than 0.038 ± 0.006 mr Table 1 summarizes the angular distribution of the measured ste
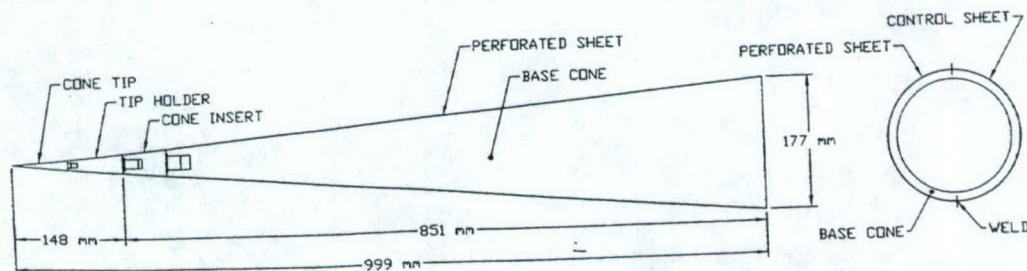

Fig. 1   Schematic diagram of the assembled test model from the profile and rear view.

heights. This was acceptable because previous experiments by Germain and Hornung[1] at similar run conditions indicated that roughness elements, and steps as large as 0.1 mm placed at the $x = 76$ and 203 mm locations had no measurable effect on the transition location.

As expected, there were highly localized imperfections along the welded seams of the cone sheet, even after the thermal interference fit assembly process. The size of the bumps was approximately constant along the length of the cone such that the local increase in diameter was about 0.3 mm. Note that this effect was very small. The cross-sectional diameter at the front edge of the cone sheet (where the effect was most pronounced) was 26.1 mm, resulting in the bump height being less than 1% of the local diameter. The cone tip was sharp with a measured radius of 0.076 ± 0.005 mm. A limited amount of blunting of the tip occurred over the course of these experiments (blunted radius of 0.130 ± 0.005 mm) due to the high heat loads at the stagnation point. Studies by Germain and Hornung[1] (and confirmed in the present work) indicated that the effect of this minimal blunting on transition Reynolds number fell well within the overall error tolerance and, therefore, was not relevant for this series of experiments. New and blunted nose tips were examined under a microscope and were observed to be perfectly straight. The most significant imperfection was a small gap that existed between the cone sheet and the base cone. This gap was localized near the beginning edge of the cone sheet and was the result of imperfect rolling/welding of the cone sheet halves. This was of concern because the gap causes suction through the perforated sheet during the time it takes the test gas to fill the cavity between the cone sheet and the base cone. This would, of course, have a strong stabilizing effect on the boundary layer. After the pressure equalizes, however, the suction effect would no longer occur. The maximum gap height was measured to be less than 0.05 mm and extended no more than 50 mm downstream on the porous side of the cone only, that is, the affected area extended from approximately 150 to 200 mm as measured from the cone tip along the surface. The quoted numbers are considered to be conservative estimates and result in a maximum cavity volume of 0.3 cm³. The affected

surface area was about 48 cm² resulting in approximately 480,000 holes connecting the gap to the freestream. Conservative estimates with an assumed cavity volume of 1 cm³ indicated that it would take approximately 25 μs to fill the gap. This is well within the 0.5 ms required for the nozzle to start and for steady flow to be established. Furthermore, data were never taken earlier than 1.0 ms after the start of the experiment, which allowed more than sufficient time for the gap to be filled and the pressure to be equalized. Note that no flow could enter this gap in the streamwise direction because the front edge of the cone sheet at the gap location butted solidly against the back of the cone tip holder. For these reasons, it is felt that the small gap had no appreciable effect on the results.

Porous Sheet

As indicated earlier, the very high frequencies, that is, small wavelengths, of interest necessitated extremely fine porosity. The desired parameters for the porous surface were determined based on the estimated wavelength of the most unstable mode. Numerical simulations by Adam[12] indicated that the boundary-layer thickness was approximately 0.5–1 mm (computed at the $x = 305$ and 914 mm locations); therefore, the most unstable mode had a wavelength of approximately 1–2 mm. The final porous sheet had 60 ± 4 μm diameter holes spaced 100 ± 7 μm apart in a rectangular grid arrangement. This resulted in approximately 10–20 holes per disturbance wavelength and an open area (or porosity) of 28%. Because of the nature of the laser drilling process, the holes were slightly conical (taper angle of about 0.5-deg) with the small diameter exposed to the flow. The thickness of the sheet (thus, the depth of the holes) was 450 μm (26 gauge sheet) and followed the Fedorov et al.[10] analysis that the depth of the holes be approximately 30% of the boundary-layer displacement thickness. The porous surface began at approximately 148 mm from the tip of the cone as per the Fedorov et al. analysis[10] using the lower branch of the neutral stability curve for the Mack mode at a frequency of 1 MHz. Refer to Fig. 2b for a micrograph of the porous surface.

Instrumentation

The model was instrumented with 56 Type E flush-mounted coaxial thermocouples of which 52 (26 per side) were actually used to collect data because this was the maximum number of channels available on the data acquisition system. The thermocouples were arranged in a staggered pattern 24.5 mm apart with the first one located at 255 mm and the last one located at 814 mm from the tip. Figure 3 is a schematic diagram showing the location of the thermocouples on a developed view of half the cone, that is, the smooth surface side. The azimuthal lines are drawn at 12.7-mm (0.5-in.) intervals with the third line located at 165 mm (6.5 in.). The second line shows the location of the cone tip holder/cone sheet interface at 148 mm (5.8 in.). The porous surface side had the mirror image of the same layout. Note that the thermocouples were deliberately placed as far from the weld as possible, with the closest one being

Table 1 Measured step heights[a] at cone tip/cone tip holder[b] and cone tip holder/cone sheet[c] interfaces

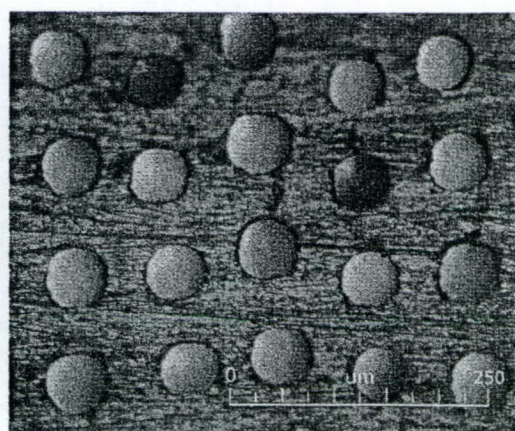| Angle, deg	Junction A, mm	Junction B, mm
0 (weld)	0.000	0.025
90 (smooth surface)	0.013	−0.013
180 (weld)	0.013	0.025
270 (porous surface)	0.013	0.038

[a] All step height measurements are ± 0.006 mm. Positive quantities indicate forward facing steps; negative quantities indicate backward facing steps; angular locations are further defined in Fig. 3.
[b] Junction A, $x = 75$ mm.
[c] Junction B, $x = 148$ mm.
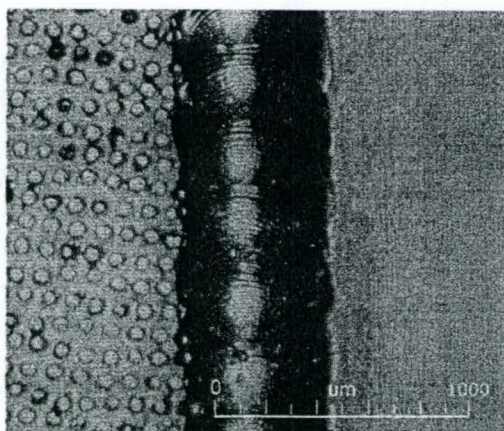
a)   b)

Fig. 2 Magnified image of a) weld joining the porous and solid sheets and b) stainless-steel perforated sheet.
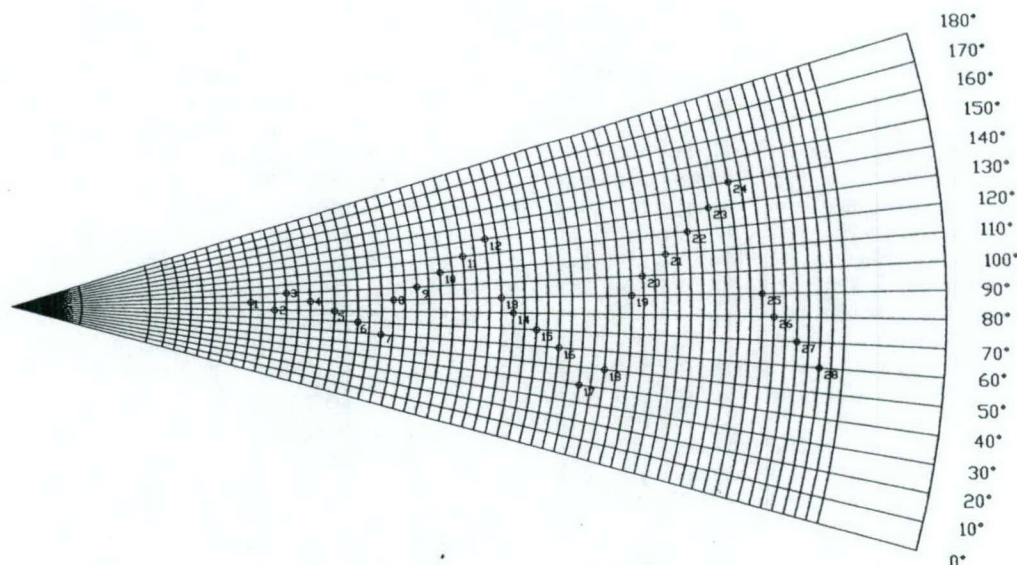
Fig. 3   Schematic diagram showing the locations of the thermocouples on a developed view of half the cone.

placed along the 40-deg ray. This is deemed more than adequate because shock tunnel experiments by Mee[13] in Mach 5 hypervelocity flow over a flat plate indicated that the spreading half-angle of turbulent bursts is approximately 3–4 deg.

The small (0.8-mm-diam) and fast-response (1-μs) thermocouples were manufactured in-house based on a modified design originally developed by Sanderson[14] and whose performance was tested in detail by Davis.[15] During the shot, the thermocouple signal was amplified by a factor of 500 and then sampled at 200 kHz. The sampled voltage levels were converted to temperature using correlations for Type E thermocouples. The heat flux for each thermocouple was subsequently computed using a spectral deconvolution technique[14–16] based on the heat equation for one-dimensional unsteady heat transfer in a semi-infinite solid.

Results

A total of 29 shots were carried out in nitrogen, and 19 shots were performed in carbon dioxide. The nitrogen shots were performed with reservoir pressures ranging from 11 to 50 MPa and specific reservoir enthalpies ranging from 3.0 to 13 MJ/kg. Above 13 MJ/kg, the Reynolds numbers achieved in T5 were too low to observe transition on the cone. The carbon dioxide shots were performed with reservoir pressures ranging from 9.0 to 40 MPa with specific reservoir enthalpies ranging from 1.3 to 9.0 MJ/kg. The complete set of data and results is available.[16]

Transition Reynolds Number

The transition Reynolds number was determined by examining the heat transfer traces measured at each thermocouple station. For each shot, a heat flux level for each thermocouple was obtained by averaging over a short time period after the nozzle starting process but before the onset of driver gas contamination and always within the constant reservoir pressure window.

The heat flux levels were used to produce nondimensional plots of Stanton number vs Reynolds number (evaluated at edge conditions) such as in Fig. 4. The Stanton number was computed as

$$St = \frac{\dot{q}(x)}{\rho_e U_e h_{aw}} \qquad (1)$$

where $\dot{q}$ is the heat transfer rate, ρ_e is the edge density, U_e is the edge velocity, and h_{aw} is the enthalpy assuming an adiabatic wall. The Reynolds number was computed as

$$Re_x = \rho_e U_e x / \mu_e \qquad (2)$$

where ρ_e and U_e are as before, x is the distance along the surface of the cone, and μ_e is the viscosity evaluated at the edge conditions. The viscosity was calculated using a simple code based on

a viscosity model for reacting gases developed by Blottner et al.[17] to determine the viscosity of each species in the gas mixture at the edge temperature. Coefficients for the model for the different gases were obtained from Olynick et al.[18] When the computed gas composition at the edge condition was used, the code then used Wilke's[19] semi-empirical mixing rule to calculate the overall viscosity of the gas mixture.

In Figs. 4a–4f, each point represents a heat flux value (or Stanton number St) for the thermocouple at that particular location (or Reynolds number Re_x). The dark black data points correspond to the data collected in the current series of experiments, whereas the gray data points correspond to previous results. The state of the boundary layer was determined by comparing the experimental results with theoretical models assuming frozen chemistry. The solid line that essentially runs through the data points represents the theoretical value for a frozen, noncatalytic surface laminar boundary layer. The dashed–dotted and dotted lines represent the expected values for turbulent boundary layer as computed using semi-empirical models developed by Van Driest and White/Christoph, respectively. These models are described in detail by White,[20] Adam,[12] and Rasheed.[16] Although error bars are not shown in Figs. 4a–4f for clarity, the uncertainty in the Stanton number was computed based on the uncertainty in the dimensional heat flux (from ±13 to ±18%), the stagnation enthalpy (±8%), the edge velocity (±4%), and the edge density (±8%). The details of the estimation of these uncertainties are presented by Rasheed.[16] The final uncertainty in the Stanton number for each thermocouple ranged from about ±18 to ±22%.

The transition location was determined by first fitting a line through the data points in the laminar region (the dashed–triple dotted line near the solid line) while enforcing the Reynolds number $Re^{-0.5}$ law expected for a zero pressure gradient laminar boundary-layer. Another line was then fitted through the data points in the transition region (the other dashed–triple dotted line). The intersection of these two lines was determined to be the transition Reynolds number, that is, the onset of transition. Note that, although including fewer or more data points in the curve fit for the transition region changes the slope of the dashed–triple dotted line, it does not significantly change the intersection with the laminar line. The uncertainty in the transition Reynolds number was computed by first determining upper and lower uncertainty bounds for the laminar experimental data fit from the linear regression assuming the 95% confidence level using the small sample T distribution. Although not shown in Figs. 4a–4f for clarity, these upper and lower uncertainty bounds would be represented as parallel lines above and below the laminar experimental fit. Similarly, another pair of lines was drawn above and below the transitional experimental fit. The intersections of these two sets of upper and lower bounds formed an error rhombus around the transition location. The minimum and
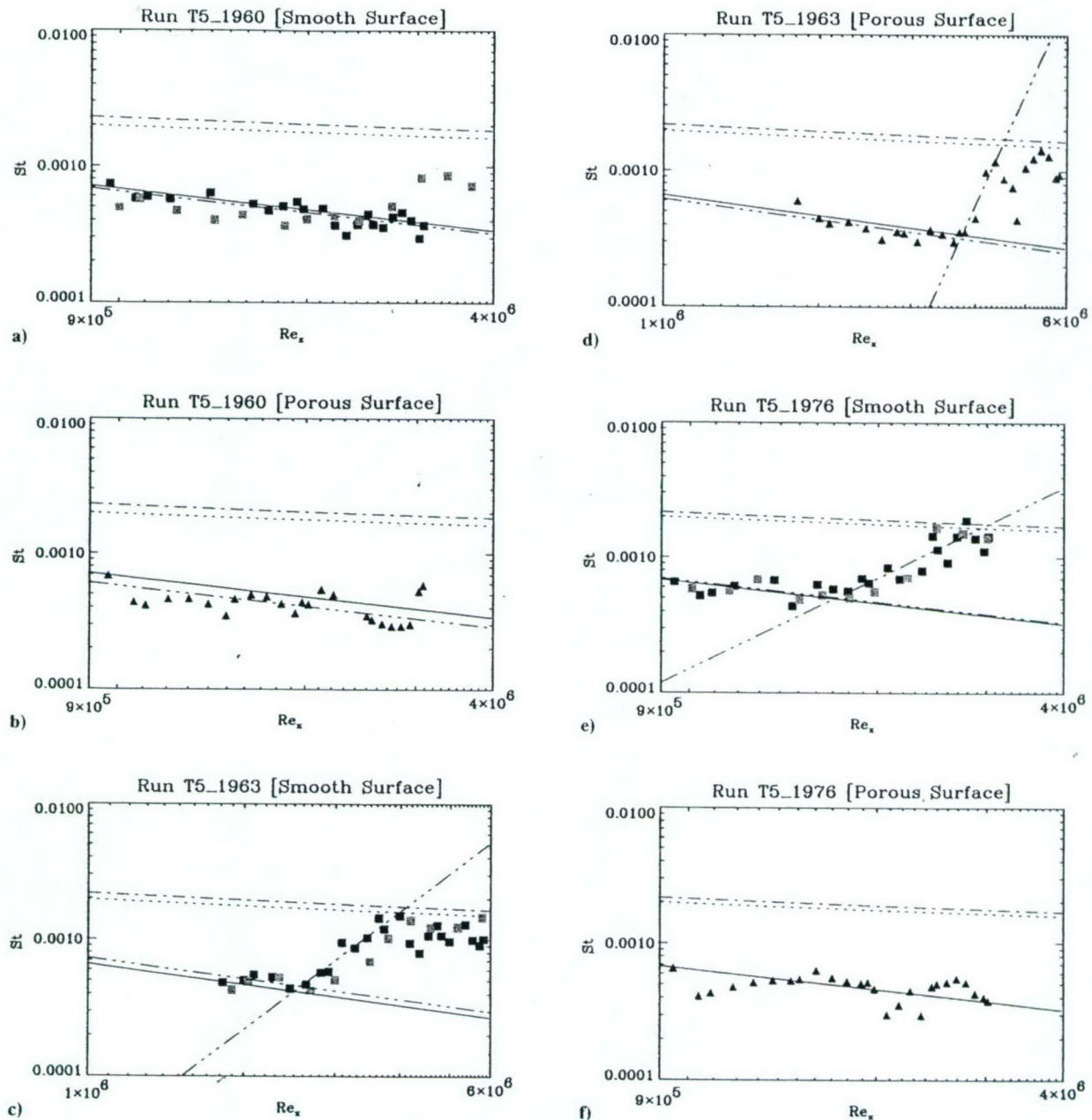
Fig. 4   Stanton number St vs Reynolds number Re_x.

maximum vertices (in terms of absissca coordinates) of the error rhombus were used as the upper and lower uncertainty bounds, and the average percent error of these two values was used as the estimate for the uncertainty in the transition location. This uncertainty varied from shot to shot, but it ranged from ±3 to ±15%, depending on the slope of the transitional fit. When the additional uncertainty due to density (±8%), velocity (±4%) and viscosity (±5%) were factored in, the overall uncertainty in transition Reynolds number ranged from ±11 to ±19%, with a median of ±13%.

Case 1: Both Sides Laminar

Figures 4a and 4b show plots of Stanton number St vs Reynolds number Re_x obtained from shot 1960, a high-enthalpy shot ($p_0 = 51.5$ MPa, $h_0 = 12.8$ MJ/kg) in nitrogen. Figures 4a and 4b show that the boundary layer was laminar over the entire length of the cone for both the smooth and porous surfaces. Furthermore, the results obtained on the smooth surface are shown to be in excellent agreement with previous results obtained by Germain and Hornung[1] for essentially the same run condition. Note that the Ref. 1 data indicate that the boundary layer is just beginning to transition toward the back of the model, whereas this effect is not evident in the present

experiment. This is attributed to the slightly higher unit Reynolds number obtained in Germain and Hornung's experiments.

Case 2: Both Sides Transitional

Figures 4c and 4d show plots of Stanton number St vs Reynolds number Re_x for shot 1963, which was a midenthalpy shot ($p_0 = 45.6$ MPa, $h_0 = 7.2$ MJ/kg) in nitrogen. Figures 4c and 4d show typical transition behavior with the data following the theoretical laminar curve at low Reynolds number and moving to the expected turbulent curve farther downstream. Figures 4c and 4d show that the boundary layer on the smooth surface transitions well upstream as compared to the porous surface and appears to validate the prediction by Fedorov et al.[10] Once again, the Germain and Hornung[1] data for a similar run condition is shown for comparison with excellent agreement as to the transition location.

Case 3: Porous Side Laminar, Smooth Side Transitional

Figures 4e and 4f show plots of Stanton number St vs Reynolds number Re_x obtained from shot 1976, a low-enthalpy shot ($p_0 = 14.5$ MPa, $h_0 = 5.0$ MJ/kg) in nitrogen. In this particular case, the smooth surface boundary layer transitions roughly at the halfway

point on the cone whereas the porous sheet boundary layer is laminar all of the way to the end of the cone. This shot clearly demonstrates the dramatic effect of the porous surface in delaying boundary-layer transition. Once again, notice the good agreement with the previous experiment performed by Germain and Hornung.[1]

Summary Data

The summary data are presented in the form of plots of Reynolds number Re_{tr}^* vs stagnation enthalpy h_0 (Figs. 5 and 6). The data are presented in this manner because both Germain and Hornung[1] and Adam and Hornung[2] found a correlation of Reynolds number Re_{tr}^* with stagnation enthalpy h_0, where the transition Reynolds number (evaluated at reference conditions) is calculated as

$$Re_{tr}^* = \rho^* U_e x_{tr} / \mu^* \qquad (3)$$

where ρ^* is the density evaluated at the reference condition, U_e is the edge velocity, x_{tr} is the transition location (as defined earlier) measured along the surface of the cone, and μ^* is the viscosity evaluated at the reference condition. In addition, there was reason to believe that the effectiveness of the porous surface would depend on h_0 because calculations by Johnson et al.[7] in air indicated that the most unstable mode frequencies varied with h_0.

Nitrogen Shots

Figure 5 gives a summary of the data for the nitrogen shots. The first observation is that the present experimental results (dark data points) agree fairly well with the previous results obtained by Germain and Hornung[1] (gray data points). The diamonds represent the Re_{tr}^* on the porous surface, whereas the squares represent the Re_{tr}^* on the smooth surface for the same shot. The second observation is that, in all cases, the porous surface delayed transition by a significant amount. The open diamonds with an upward-facing arrow ↑ indicate that the porous surface boundary layer was laminar to the very end of the cone. The value plotted assumes that transition occurred at the last thermocouple, that is, unit Reynolds number
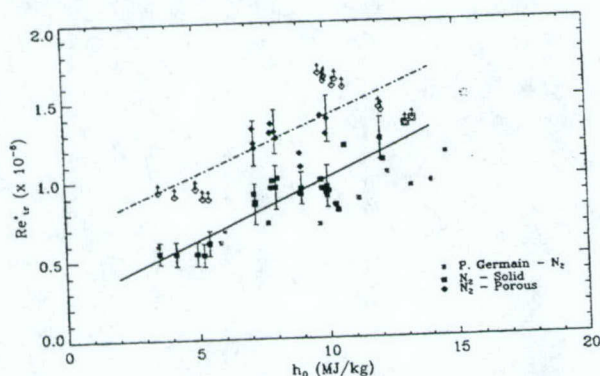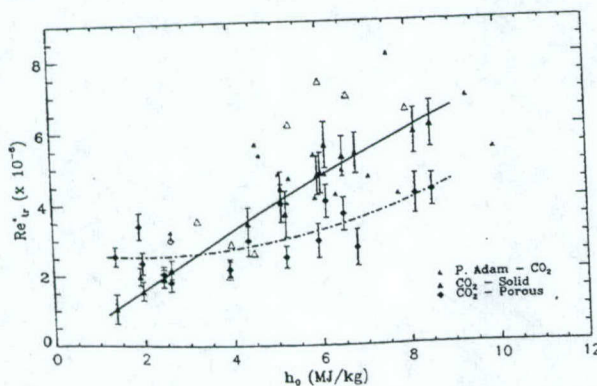
multiplied by the last thermocouple location. This is not a valid data point but rather a manner in which to show that the boundary layer was entirely laminar. The same discussion applies for the open square symbols with an ↑ for the smooth surface side. The two data points at 13 MJ/kg are actually open diamonds superimposed on open squares, with an ↑, indicating that both the smooth and porous surface boundary layers were entirely laminar. The lines are linear curve fits to help guide the eye (dashed–dotted for porous and solid for smooth). Note that the porous sheet appears to be less effective at midenthalpies as compared to low and high enthalpies.

Carbon Dioxide Shots

An analysis similar to that performed for the nitrogen shots was also performed for each carbon dioxide shot. The resulting summary plot of Reynolds number Re_{tr}^* vs h_0 is shown in Fig. 6. Once again there is fairly good agreement between the present smooth surface results (dark data points) and those obtained in previous experiments by Adam and Hornung[2] (gray data points), although there is much more scatter. Figure 6 shows that the porous sheet (diamonds) was, in fact, detrimental at higher enthalpies, but was effective at lower enthalpies with a crossover point at roughly 3.0 MJ/kg. The diamonds represent the Re_{tr}^* on the porous surface, whereas the triangles represent Reynolds number Re_{tr}^* on the smooth surface for the same shot. The lines are second-order curve fits to help guide the eye (dash–dotted for porous and solid for smooth).

Resonantly Enhanced Shadowgraph

Further evidence of the effectiveness of the porous sheet is seen in Fig. 7, which is a resonantly enhanced shadowgraph showing the boundary-layer transitioning on the smooth surface (top) while remaining perfectly laminar on the porous surface (bottom). Flow is left to right and the schematic at the top right indicates the window position relative to the model. The rectangular boxes in the main image indicate the location of the magnified images whose left and right edges are 495 and 615 mm from the cone tip, respectively (as measured along the surface of the cone). The white line on the magnified image of the smooth surface was digitally added to indicate the approximate surface of the model. This shadowgraph corresponds to shot 2008 ($P_0 = 48.2$ MPa, $h_0 = 9.8$ MJ/kg) and was obtained by seeding the flow with sodium and tuning the frequency of the dye laser light source to one of the sodium D lines. The transition location on the smooth surface identified by the analysis of the heat transfer data is approximately at the left edge of the magnified image of the smooth surface. The magnified images were also used to measure the boundary-layer thickness, and this value was found to be approximately 1 mm, which is in agreement with Adam's computations.[12]

Discussion

As already indicated, to validate the effectiveness of the porous surface, it was necessary to ensure that angle-of-attack or nonaxisymmetry issues were not affecting the results and that the results were repeatable. Angle of attack was eliminated as a cause for the delayed transition by carefully aligning the model to within ±0.05 deg of the tunnel axis. Furthermore, it was noted that the observed effect was to delay transition as much as 100% (or more because the cone was not long enough). This is significantly larger than the 5% variation in Reynolds number Re_{tr} that could be attributed to an angle of attack of 0.1 deg as observed by Krogmann (and reported by Stetson[21]) in his study of the effects of angle of attack on Reynolds number Re_{tr} in hypersonic flow ($M_\infty \simeq 5$) over a 5-deg half-angle cone.

Flow asymmetry issues were addressed by rotating the model to the 0-, 90-, and 180-deg orientations and repeating the experiments. In particular, two run conditions were repeated and can be seen in Fig. 5 as the data points clustered at 5 and 8 MJ/kg, respectively. Clearly, there is excellent agreement, and there appears to be no effects from rotating the model. The model asymmetries due to imperfections were discussed earlier and were determined to be irrelevant in the context of the present results.

Repeatability was tested by repeating selected experimental run conditions at various stages in the test program and noting that there

Fig. 5 Reynolds number Re_{tr}^* vs h_0 summary of nitrogen data.

Fig. 6 Reynolds number Re_{tr}^* vs h_0 summary of the carbon dioxide data.

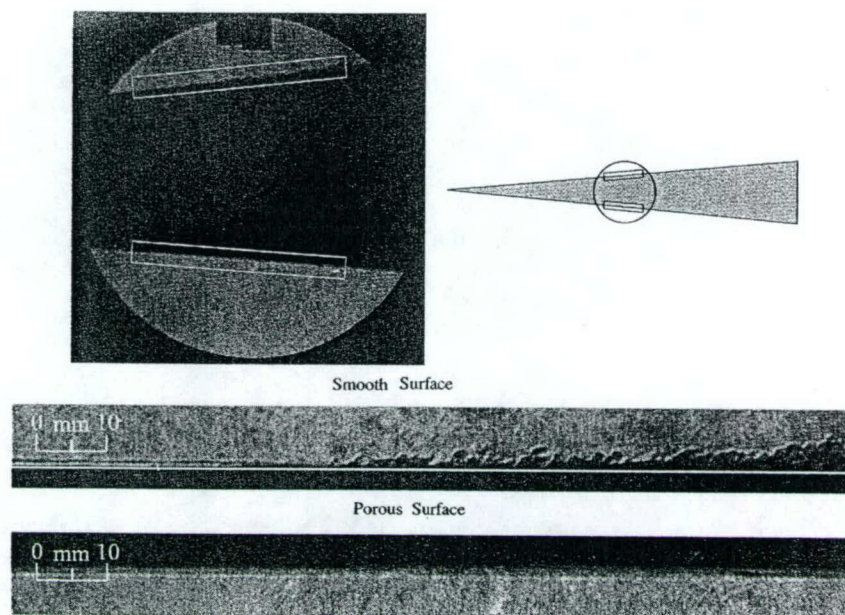Smooth Surface

Porous Surface

Fig. 7 Resonantly enhanced shadowgraph.

was no observable effect on transition location. This was of particular importance because it confirmed that the slight accumulation of soot on the surface of the model over the course of the experiments had no effect on the results. The soot was generated by the pyrolization of the polyurethane buffers used to stop the piston in this facility and was carried by the driver gas at the end of each shot, that is, the soot arrived at the model after the useful test time. Extensive testing performed on two sample test pieces of the porous surface mounted on Plexiglas® backings (flat plate normal to the flow and cylinder inclined at 5 deg to the flow) before testing the actual cone model had previously suggested that the soot would not be a problem. The Plexiglas mountings allowed the samples to be backlit so that it was possible to determine whether the holes were clogged (no light passing through). Based on these tests it was decided to allow the soot to accumulate over the course of the series of experiments. The repeatability tests confirmed that the soot had no effect on the results and also provided an indication of the robustness of this boundary-layer control scheme to small amounts of contamination.

As already mentioned, for the nitrogen experiments, the porous surface was effective over the whole enthalpy range tested, although it was more effective at low- and high-enthalpy conditions than at midenthalpy conditions. For the carbon dioxide shots, however, the porous surface was only effective at very low-enthalpy conditions and was counterproductive at mid- to high enthalpies. This behavior suggested that another parameter was important in the carbon dioxide flows.

A possible explanation for the observed behavior lies in the expectation that the porous surface must be hydraulically smooth, that is, pore size must be sufficiently small in relation to the viscous length scale, for the proposed mechanism to effectively delay transition. If this were not the case, then the holes would act as distributed surface roughness and prematurely trip the boundary layer. A plot of $Re^*_{tr,porous} - Re^*_{tr,smooth}$ vs Reynolds number based on pore diameter Re^*_D clearly shows that the delay in transition becomes much smaller as Reynolds number Re^*_D increases (Fig. 8). Note that no such trend was observed when the results were plotted using the Reynolds number evaluated at the edge conditions (Re_D), and it is, therefore, concluded that the reference Reynolds number is the proper Reynolds number to use in this analysis for these flows. The grayscale indicates the qualitative effectiveness of the porous surface. Black indicates laminar over the entire length of the cone on the porous side, medium gray indicates delayed transition was observed on the cone, and light gray indicates premature transition. Squares and triangles correspond to N_2 and CO_2, respectively. Figure 8 shows that the mechanism becomes qualitatively less effective at an Reynolds number Re^*_D of about 130 and actually prematurely trips the boundary layer at an Reynolds number
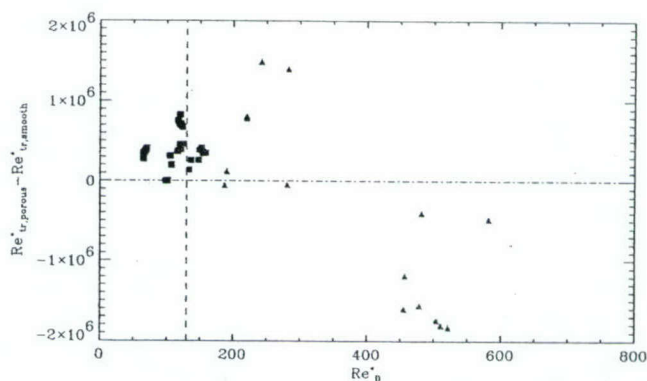
Fig. 8 Decreased effectiveness as Reynolds number Re^*_D increases beyond 130 (vertical line).

Re^*_D greater than 300. The most relevant experiment (to the present case) regarding distributed surface roughness effects was performed by Germain and Hornung,[1] who found that 0.1-mm salt crystals ($Re^*_k = 220$, based on salt crystal height) randomly distributed over the first 206 mm of the model tripped the boundary layer. No attempt was made to identify the critical roughness Reynolds number below which the surface roughness had no effect on transition. For such a comparison, it is useful to recognize that the present results correspond reasonably well with experiments in incompressible flow by Feindt (as reported by Schlichting[22]), who examined the effect of distributed surface roughness (in the form of sand grains) on transition Reynolds number. Although the type of roughness differed from the present experiments (sand grains vs porous surface), Feindt also found that the surface roughness became important when Reynolds number Re_k (based on the sand grain height) was greater than 120. Similarly, Pfenninger[23] reported that surface roughness issues were important in laminar flow control experiments (suction through slots) when Reynolds number Re_s (based on slot width) was approximately greater than 100.

More recently, Reda[24] reviewed the effects of distributed surface roughness in hypervelocity flows on nose tips, attachment lines, and lifting entry vehicles. Reda concluded that there exists no universal value for critical Reynolds number Re_k (based on roughness height) for transition to turbulence and that this critical roughness Reynolds number was highly dependent on the particular flowfield and roughness characteristics. Despite this observation, Reda indicated that a number of different experiments suggested that the critical roughness Reynolds number ranges between 100 and 200. Reda's earlier experiments on nose tip transition in a ballistic range yielded values
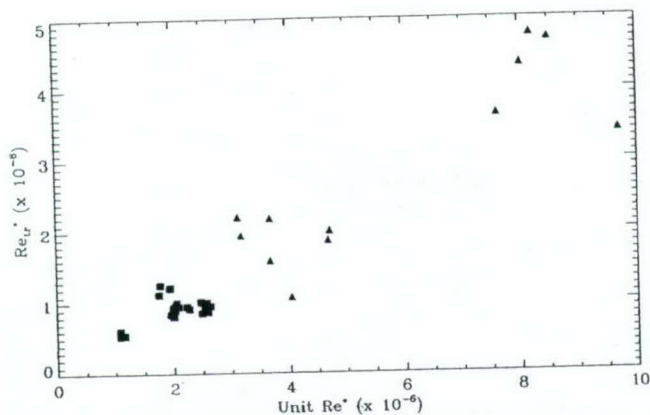
Fig. 9 Reynolds number Re_{tr}^* vs Unit Re^* showing unit Reynolds number effect observed in the transition data on the smooth surface.

Fig. 10 Reynolds number Re_{tr}^* vs Unit Re^* showing that unit Reynolds number effect was not observed in the transition data on the porous surface.

for the critical Reynolds number Re_k of 192. Bertin et al. (as reported by Reda[24]) found $Re_k = 110$ to be the critical value at which roughness effects began to dominate in wind-tunnel tests of a 0.0175 scale model of the Space Shuttle Orbiter at Mach 8–12. Finally, Goodrich et al. (as reported by Reda[24]) found that the transition data on the windward centerline of the Space Shuttle Orbiter during reentry for missions STS-1 to STS-5 suggested a critical Reynolds number Re_k of 120. Note that in these cases, the Reynolds number Re_k value was for surface bumps (as opposed to holes in the present work) and were calculated using the conditions in the boundary layer at the roughness height. This may or may not allow direct comparison with the Reynolds number Re_D^* used to analyze the present results, but it is clear that the critical Reynolds number Re_D^* is in the same range as previous experiments.

Note, however, that closer examination of Fig. 8 also indicates that some parameter is still not fully accounted for because the effectiveness of the porous sheet does not decrease monotonically with increasing Reynolds number Re_D^*. Specifically, the porous sheet appeared to be more effective in the carbon dioxide shots at $Re_D^* \simeq 200$ than the nitrogen shots at $Re_D^* \simeq 130$. Although unexpected, it is not entirely surprising that nitrogen and carbon dioxide behave slightly differently because the different chemistry involved could affect the second mode amplification.

A final interesting observation is noted if one examines the so-called unit Reynolds number effect. Figure 9 is a plot of Reynolds number Re_{tr}^* vs Unit Re^* for the smooth surface (squares and triangles correspond to N_2 and CO_2, respectively). As expected, it shows the typically strong dependence of transition Reynolds number on unit Reynolds number. Of course, the dependence of a nondimensional quantity on a dimensional quantity simply means that there is another factor that has not been taken into account. In the case of transition data, this other factor is typically associated with the acoustic noise generated by the nozzle wall boundary layer, as was shown by Pate and Schueler.[25] Note that, as before, this trend is not observed in the present data if one plots the Reynolds number based on edge conditions (as opposed to the reference conditions). This seems to further support the conclusion by Germain and Hornung[1] and Adam and Hornung[2] that the reference conditions are the appropriate conditions to use when evaluating these flows. An even more interesting observation is noted if one examines a similar plot for the porous surface as shown in Fig. 10, where squares and triangles correspond to N_2 and CO_2, respectively. In this case, there is no observed unit Reynolds number effect (when plotted using either edge conditions or reference conditions). At this time, it is unclear why this would be the case. A very reasonable explanation, however, is that the effect of the porous surface is to damp out the second mode acoustic perturbations. As such, it definitely also attenuates the acoustic noise from the nozzle wall boundary layer, and it is entirely possible that the porous surface is so effective that it completely removes the unit Reynolds number effect. Such a conclusion would have very far-reaching implications and would need to be considered very carefully in much more detail in the future.
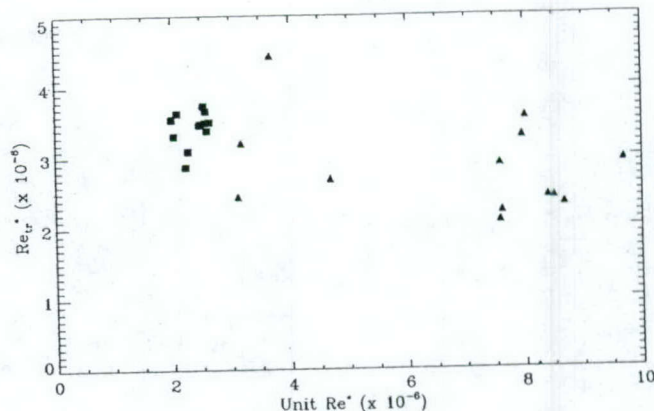
Conclusions

Extensive experiments on hypervelocity boundary-layer transition control have been carried out in the T5 on a 5.06-deg half-angle sharp cone with a smooth surface over half the cone and an ultrasonically absorptive porous surface over the other half. These experiments, performed in nitrogen and carbon dioxide, used heat transfer measurements to determine simultaneously the transition location on the smooth and porous surfaces for each shot. These new measurements for the smooth surface transition location compared very well with experimental results obtained by previous researchers in the same facility. The theoretical result that transition may be delayed by suitable wall porosity has been confirmed convincingly in nitrogen flows, and the reversal of the phenomenon in carbon dioxide flows appears to be due to the chosen wall porosity scale being too coarse in carbon dioxide. These results were tested for repeatability and were checked to ensure that they were not induced by angle-of-attack or other effects. The effectiveness of the porous sheet was further evidenced by a resonantly enhanced shadowgraph that clearly showed transition occurring over the smooth surface but not the porous surface.

References

[1]Germain, P., and Hornung, H. G., "Transition on a Slender Cone in Hypervelocity Flow," *Experiments in Fluids*, Vol. 22, No. 3, 1997, pp. 183–190.

[2]Adam, P., and Hornung, H. G., "Enthalpy Effects on Hypervelocity Boundary Layer Transition: Ground Test and Flight Data," *Journal of Spacecraft and Rockets*, Vol. 34, No. 5, 1997, pp. 614–619.

[3]Eckert, E. R. G., "Engineering Relations for Friction and Heat Transfer to Surfaces in High Velocity Flow," *Journal of the Aeronautical Sciences*, Vol. 22, Aug. 1955, pp. 585–587.

[4]Stetson, K. F., "Hypersonic Boundary-Layer Transition," *Advances in Hypersonics: Volume I, Defining the Environment*, edited by J. J. Bertin, J. Periaux, and J. Ballmann, Birkhäuser, Boston, 1992, pp. 324–417.

[5]Mack, L. M., "Boundary-Layer Stability Theory," *Special Course on Stability and Transition of Laminar Flow*, Rept. 709, AGARD, 1984.

[6]Stetson, K. F., Thompson, E. R., Donaldson, J. C., and Siler, L. G., "Laminar Boundary Layer Stability Experiments on a Cone at Mach 8, Part 1: Sharp Cone," AIAA Paper 83-1761, July 1983.

[7]Johnson, H. B., Seipp, T., and Candler, G. V., "Numerical Study of Hypersonic Reacting Boundary Layer Transition on Cones," *Physics of Fluids*, Vol. 10, No. 10, 1998, pp. 2676–2685.

[8]Fedorov, A. V., and Malmuth, N. D., "Hypersonic Flow Stabilization by Ultrasonically Transparent Wall," Rockwell Science Center, TR SCNM96-1, Thousand Oaks, CA, 1996.

[9]Fedorov, A. V., Malmuth, N. D., Shalaev, V., Cole, J., and Khokhlov, A., "Problems in High Speed Flow Prediction Relevant to Control," AIAA Paper 98-2995, June 1998.

[10]Fedorov, A. V., Malmuth, N. D., Rasheed, A., and Hornung, H. G., "Stabilization of Hypersonic Boundary Layers by Porous Coatings," *AIAA Journal*, Vol. 39, No. 4, 2001, pp. 605–610.

[11] Hornung, H. G., "Performance Data of the New Free-Piston Shock Tunnel T5 at GALCIT," AIAA Paper 92-3943, July 1992.

[12] Adam, P., "Enthalpy Effects on Hypervelocity Boundary Layers," Ph.D. Dissertation, California Inst. of Technology, Pasadena, CA, 1997.

[13] Mee, D. J., "Boundary Layer Transition Measurements in Hypervelocity Flows in a Shock Tunnel," AIAA Paper 2001-0208, Jan. 2001.

[14] Sanderson, S. R., "Shock Wave Interaction in Hypervelocity Flow," Ph.D. Dissertation, California Inst. of Technology, Pasadena, CA, 1995.

[15] Davis, J. P., "High-Enthalpy Shock/Boundary-Layer Interaction on a Double Wedge," Ph.D. Dissertation, California Inst. of Technology, Pasadena, CA, 1999.

[16] Rasheed, A., "Passive Hypervelocity Boundary Layer Control Using an Ultrasonically Absorptive Surface," Ph.D. Dissertation, California Inst. of Technology, Pasadena, CA, 2001.

[17] Blottner, F. G., Johnson, M., and Ellis, M. G., "Chemically Reacting Viscous Flow Program for Multi-Component Gas Mixtures," Sandia Lab., TR SC-RR-70-754, Albuquerque, NM, Dec. 1971.

[18] Olynick, D., Chen, Y.-K., and Tauber, M., "Aerothermodynamics of the Stardust Sample Return Capsule," Journal of Spacecraft and Rockets, Vol. 36, No. 3, 1999, pp. 442–462.

[19] Wilke, C. R., "A Viscosity Equation for Gas Mixtures," Journal of Chemical Physics, Vol. 18, No. 4, 1950, pp. 517–519.

[20] White, F. M., Viscous Fluid Flow, 2nd ed., McGraw-Hill, New York, 1991, pp. 549–554.

[21] Stetson, K. F., "Mach 6 Experiments of Transition on a Cone at Angle of Attack," Journal of Spacecraft and Rockets, Vol. 19, No. 5, 1982, pp. 397–403.

[22] Schlichting, H., Boundary Layer Theory, McGraw–Hill, New York, 1987, Chap. 17, Sec. g, p. 542.

[23] Pfenninger, W., "Laminar Flow Control," Special Course on Concepts for Drag Reduction, Rept. 654, AGARD, 1977.

[24] Reda, D. C., "Roughness-Dominated Transition on Nosetips, Attachment Lines and Lifting-Entry Vehicles," AIAA Paper 2001-0205, Jan. 2001.

[25] Pate, S. R., and Schueler, C. J., "Radiated Aerodynamic Noise Effects on Boundary-Layer Transition in Supersonic and Hypersonic Wind Tunnels," AIAA Journal, Vol. 7, No. 2, 1969, pp. 450–457.

W. J. Devenport
Associate Editor

Stabilization of a hypersonic boundary layer using an ultrasonically absorptive coating

By A. FEDOROV[1], A. SHIPLYUK[2], A. MASLOV[2],
E. BUROV[2] AND N. MALMUTH[3]

[1]Department of Aeromechanics and Flight Engineering, Moscow Institute of Physics and Technology,
Zhukovski, 140180, Russia
[2]Institute of Theoretical and Applied Mechanics, Novosibirsk, 630090, Russia
[3]Rockwell Scientific Company, Thousand Oaks, CA 91360, USA

Experimental and theoretical studies of the effect of an ultrasonically absorptive coating (UAC) on hypersonic boundary-layer stability are described. A thin coating of fibrous absorbent material (felt metal) was selected as a prototype of a practical UAC. Experiments were performed in the Mach 6 wind tunnel on a 7° half-angle sharp cone whose longitudinal half-surface was solid and other half-surface was covered by a porous coating. Hot-wire measurements of 'natural' disturbances and artificially excited wave packets were conducted on both solid and porous surfaces. Stability analysis of the UAC effect on two- and three-dimensional disturbances showed that the porous coating strongly stabilizes the second mode and marginally destabilizes the first mode. These results are in qualitative agreement with the experimental data for natural disturbances. The theoretical predictions are in good quantitative agreement with the stability measurements for artificially excited wave packets associated with the second mode. Stability calculations for the cooled wall case showed the feasibility of achieving a dramatic increase of the laminar run using a thin porous coating of random microstructure.

1. Introduction

For small free-stream disturbances and negligible surface roughness, laminar–turbulent transition is due to amplification of unstable modes in the boundary layer (Malik, Zang & Bushnell 1990; Reshotko 1994). In this case, stability theory and experiment are basic tools for predicting transition loci and developing laminar flow control methods (Mack 1984; Reshotko 1969; Malik 1989). For essentially two-dimensional supersonic and hypersonic flows, the initial phase of transition is associated with excitation and amplification of the first and/or second modes.

The first mode is an extension to high speeds of the Tollmien–Schlichting (TS) waves, which represent viscous instability at low Mach numbers. The inviscid nature of the first mode begins to dominate when the Mach number increases, since compressible boundary-layer profiles contain a generalized inflection point (Mack 1984). This mode may be stabilized by wall cooling, suction and favourable pressure gradient. Another way to damp the first mode is by a very thin perforated sheet stretched over a plenum chamber (Carpenter & Porter 2001). When the TS waves propagate along the boundary layer, the fluctuating pressure forces air in and out of the plenum chamber that modifies the wall boundary conditions for

the disturbances. Carpenter & Porter (2001) conducted a stability analysis for the incompressible boundary layer on a flat plate and showed that the TS waves are stabilized when the wall admittance phase is close to $\frac{1}{2}\pi$. Their analysis is based on linear stability theory for the boundary layer with modified boundary conditions on the perforated wall. Certain aspects of this theoretical modelling are similar to the approach developed by Gaponov (1971, 1975) and Lecoudis (1978) for subsonic boundary layers and by Gaponov (1977) for moderate supersonic flows. Whether the experiments will confirm the theoretical predictions remains to be seen. Carpenter & Porter (2001) indicated several factors that could lead to problems in practice. The theory requires the admittance phase to be very close to $\frac{1}{2}\pi$. This can be achieved only by minimizing the losses through the pores, which leads to severe constraints on the perforated sheet thickness. Another difficulty is associated with pressure variations along the perforated panel. This may lead to areas of quasi-steady inflow and outflow, thereby modifying the mean flow and its stability characteristics.

The second mode results from an inviscid instability driven by a region of supersonic mean flow relative to the disturbance phase velocity. This instability belongs to the family of trapped acoustic modes propagating in a waveguide between the wall and the sonic line (Mack 1984; Guschin & Fedorov 1989). The existence of the second mode was established by the experiments of Kendall (1975), Demetriades (1974), Stetson *et al.* (1983) Stetson & Kimmel (1992*a*, *b*) and Kimmel, Demetriades & Donaldson (1995). Once the second mode sets in, it becomes the dominant instability since its growth rate tends to exceed that of the first mode. For insulated surfaces, this occurs for Mach numbers larger than 4. For cooled surfaces, the second mode can dominate at even lower Mach numbers (Lysenko & Maslov 1984). In contrast to the TS instability, wall cooling destabilizes the second mode. This effect can be important in the transition of hypersonic flows. Since the temperature of a hypersonic vehicle surface is relatively small (less than 0.2 of the adiabatic wall temperature), the TS instability is eliminated by natural cooling, whereas the second mode remains unstable and may trigger early transition. Increasing the laminar run requires the second-mode instability to be diminished.

In high-speed flows, the second mode is associated with disturbances of relatively high frequency corresponding to the ultrasonic band. Malmuth *et al.* (1998) assumed that a passive ultrasonically absorptive coating (UAC) of fine porosity may suppress these fluctuations and, at the same time, may not trip the boundary layer owing to roughness effects, i.e. the passive UAC may stabilize the second and higher modes by a disturbance energy extraction mechanism. This hypothesis was examined by an inviscid linear stability analysis. Using the WKB method, Malmuth *et al.* (1998) formulated the boundary condition on an ultrasonically absorptive wall for the second and higher modes, and showed that the absorption does cause a strong stabilization of the second mode. Later, Fedorov & Malmuth (2001) analysed the absorption effect at finite Reynolds numbers using viscous stability theory and found that viscosity weakly affects the stabilization mechanism. They also considered an ultrasonically absorptive surface of a particular type, namely, a wall covered by a porous coating with cylindrical blind micro-holes, and showed that a relatively thin coating (of thickness ~ 0.1 of the boundary-layer displacement thickness) can dramatically reduce the second-mode growth rate. In contrast to the TS waves (Carpenter & Porter 2001), the second mode is effectively suppressed without a plenum chamber underneath the porous sheet. This significantly simplifies practical application.

These theoretical findings lead to the expectation that a passive porous coating may be exploited for hypersonic laminar flow control. The concept was verified in the

California Institute of Technology GALCIT T-5 shock tunnel (Rasheed *et al.* 2002) by testing a 5° half-angle sharp cone. The cone in these tests had one half of its surface solid and the other a porous sheet that was perforated with equally spaced blind cylindrical holes. The average hole diameter and depth were respectively 60 μm and 500 μm. Average spacing between the holes was 100 μm. The model was instrumented by thermocouples, and the transition onset point was determined from the Stanton number distributions measured simultaneously on both sides of the model for each run. The experiments were performed for the ranges of the free-stream total enthalpy $4.18 \leqslant H_0 \leqslant 13.34 \, \mathrm{MJ \, kg^{-1}}$ and the free-stream Mach number $4.59 \leqslant M_\infty \leqslant 6.4$. This study revealed that the porous coating delays transition by a significant amount. For the majority of runs, the boundary layer on the porous surface was laminar up to the model base, whereas transition on the untreated solid surface was observed halfway along the cone. These experiments qualitatively confirmed the theoretical prediction of Fedorov & Malmuth (2001). However, quantitative comparison was not feasible because the cone was not long enough to measure the transition locus on the porous surface. Since the boundary-layer disturbances were not measured, these experiments did not give direct evidence of the second mode instability, and its effect on the transition process was not clear.

A regular microstructure UAC is one possible good starting point for validation of the hypersonic laminar flow control concept. However, most porous materials, which provide efficient absorption of acoustic disturbances, have a random porosity. A practical UAC should be symbiotic with thermal protection systems (TPS) of actual hypersonic vehicles. Since the majority of TPS materials have random microstructures, a randomly porous coating is of most interest for applications. This motivated the theoretical and experimental studies of a randomly porous UAC to be discussed herein. The investigation is focused on direct measurements of the boundary-layer disturbances and verification of the stability theory predictions.

2. Experimental apparatus

2.1. *Wind tunnel*

The experiments were conducted in the T-326 hypersonic blow-down wind tunnel with open-jet test section (Grigoriev *et al.* 1972) at the Institute of Theoretical and Applied Mechanics (ITAM) of the Siberian Branch of Russian Academy of Sciences in Novosibirsk. The diameter of the axisymmetric contoured nozzle of this facility is 200 mm. Run-time can be as long as 30 min, subject to a Mach number flow-field non-uniformity of 0.7% in the flow core at a freestream Mach number $M_\infty \approx 6$. The test core diameter is approximately 180 mm. Typical of conventional hypersonic wind tunnels, the noise level is about 1%. During the experiment, pressure, P_0, and temperature, T_0, in the settling chamber are kept constant, with accuracies of 0.06% and 0.25%, respectively.

2.2. *UAC parameters*

Characteristics of a porous coating must meet certain requirements to suppress the boundary-layer instability effectively. For the wind tunnel tests, the boundary-layer thickness on a 7° half-angle cone is approximately 1 mm (see §4.1 and figure 8). According to the experimental observations of Kendall (1975), Demetriades (1974), Stetson *et al.* (1983), Stetson & Kimmell (1992*a*, *b*) and Kimmel *et al.* (1995), the second-mode wavelength is approximately twice the boundary-layer thickness, i.e. it is ~ 2 mm in the case considered. The characteristic size of the porous coating should
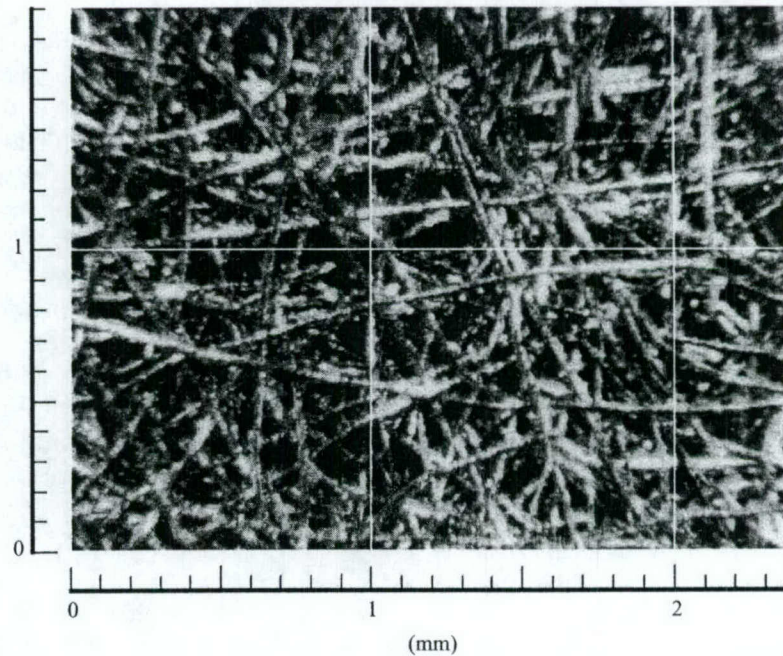
FIGURE 1. Magnified sixty-fold image of the upper surface of the felt-metal coating; $1 \times 1 \, \text{mm}^2$ grid.

be much smaller than the disturbance wavelength to avoid resonant interactions with the porous-layer microstructure and minimize roughness effects. On the other hand, the pore size should be large enough to diminish the rarefied gas effect and provide intensive absorption of the boundary-layer disturbances in the frequency band 200–400 kHz associated with the second mode. Compromising these constraints we chose the felt-metal coating, which is composed of stainless steel fibres of diameter $d = 30 \, \mu\text{m}$. To provide integrity of the coating, the fibres were hard sintered randomly on a solid stainless steel sheet of thickness 0.245 mm. Then, they were rolled to a porosity of 75%. The porous layer has a thickness of 0.75 mm resulting in a total thickness of the felt metal sheet of 1 ± 0.1 mm. Magnified images of the porous surface (one of them is shown in figure 1) reveal that the average pore size is $\approx 100 \, \mu\text{m}$. This results in 20 pores per boundary-layer disturbance wavelength.

2.3. *Model*

The model was a 7° half-angle sharp cone of 500 mm length (see figure 2) consisting of three parts: (i) a sharp cone 65 mm in length and 0.1 mm nose radius; (ii) a middle part 65 mm in length containing an electric glow discharge perturber; and (iii) a base portion 370 mm in length. Half of the base part is covered by a felt-metal sheet as shown in figure 2. Roughness of the solid surface is 0.6 μm. The model is equipped with a three-dimensional perturber providing a high-frequency glow discharge in a small chamber. Artificial disturbances generated by the perturber are introduced into the boundary layer through an orifice of 0.4 mm diameter located at a distance of 69 mm from the model nose. The perturber construction is similar to that used for excitation of artificial wave packets in supersonic boundary layers (Kosinov, Maslov & Shevelkov 1990). Maslov *et al.* (2001) have successfully applied this technique to hypersonic flows.
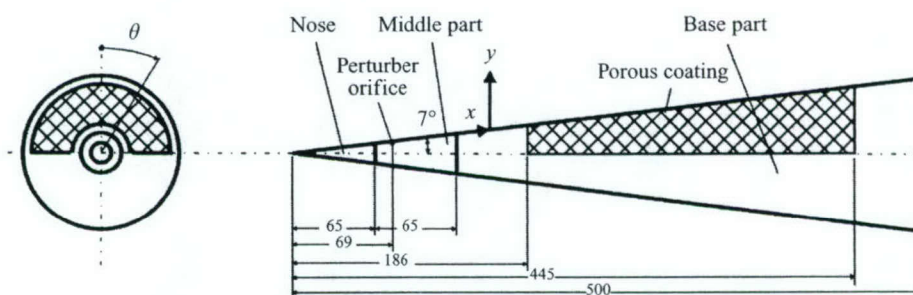
FIGURE 2. Schematics of the model; dimensions are in mm.

A major challenge in the construction of the model was attachment of the felt-metal sheet to the basic cone. After bending, the porous layer expanded, leading to its thickening by approximately 20%. This complicated the determination of the undercut of the basic cone to allow flash attachment of the felt-metal sheet. To minimize mismatch between the porous and solid surfaces, the felt-metal sheet was attached to the base cone and then ground until the surface irregularity was reduced to 0.05 mm.

Another difficulty was detachment of the felt-metal filaments because of sheet stretching. Examination of the porous surface under a microscope showed that some of the detached filaments protrude from the surface approximately 3–4 mm. These filaments (about 1500–2000) were manually trimmed off.

The model was installed at zero angle of attack. The estimated misalignment between the cone axis and the free-stream direction was less than 0.05°. This allows three-dimensional distortions of the mean flow to be neglected.

2.4. *The measuring system*

To determine the free-stream parameters, IPD-89008 pressure gauges and k-type thermocouples measured pressures and temperatures in the settling chamber and provided accuracies of 0.15% and 0.1%, respectively. The free-stream Mach number was determined using Pitot measurements.

Two traverse gears were used in the experiment. A three-component traverse system provided X, Y, Z displacements of the hot-wire probe to an accuracy of 0.01 mm. A special unit was used to roll the whole cone around its X-axis and measure transverse distributions of wave packets. The roll angle, Θ, was controlled within an accuracy 0.1°.

The high-frequency glow discharge system consisted of clock and high-voltage generators. The clock generator signal was used to trigger the high-voltage generator and synchronize hot-wire measurements with the high-voltage generator initiation. The high-voltage generator produced voltage pulses up to 2000 V, of 1 μs duration and pulse frequency up to 400 kHz. During the run, the glow discharge was controlled visually through optical windows and a mirror in the test section.

A constant-current hot-wire anemometer, custom built at ITAM, was used to measure mass flow fluctuations. The hot-wire probes were made of tungsten wire of 5 μm diameter and 1 mm length which was welded to pointed stings. The overheat ratio was 0.5 and the frequency response of the hot-wire anemometer was 500 kHz. The constant and alternating components of the hot-wire signal were measured by a 12-bit analogue-digital converter with a sampling frequency of 5 MHz. At each measurement station, 98 time-series of 4096 samples were acquired. An analogue

Surface	P_0 (MPa)	T_0 (K)	M_∞	M_e	$Re_{1\infty}$ (m^{-1})	Re_{1e} (m^{-1})	T_w/T_0	f (kHz)
Solid	1.0 ± 0.002	395 ± 3	5.92	5.3	11.8×10^6	15.4×10^6	0.79–0.83	280
Porous	1.0 ± 0.002	391 ± 1	5.92	5.3	12.0×10^6	15.6×10^6	0.81–0.84	280

TABLE 1. Basic parameters.

signal of the main generator initiating glow discharge was used to trigger ADC. Details of the processing techniques have been discussed by Maslov *et al.* (2001).

2.5. *Processing of the disturbance characteristics*

To obtain the amplitude, A, and phase, Φ, of artificially excited disturbances, the discrete Fourier transform is used

$$A(X, Y, \Theta) \exp(i\Phi(X, Y, \Theta)) = \frac{2}{N} \sum_{j=1}^{N} \rho U_n(X, Y, \Theta, t_j) \exp(-2i\pi f t_j),$$

where N is the sample count in the time-series, f is the disturbance frequency, and $\rho U_n(X, Y, \Theta, t_j)$ is the time-series of mass flow pulsations. The artificial wave packet is represented as a decomposition of elementary waves. For this purpose the transverse wave spectra are calculated as

$$SA(x, \beta) \exp(iSF(x, \beta)) = \int_{-\Theta_0}^{\Theta_0} A(x, \Theta) \exp(i\Phi(x, \Theta)) \exp(-i\beta\Theta) d\Theta,$$

where SA and SF are the amplitude and phase spectra with respect to the transverse wave number β.

3. Measurement results

Basic experimental parameters are given in table 1, where Re_1 is the unit Reynolds number, T_w is the wall temperature, f is the frequency of artificial disturbances, and the subscript e denotes quantities at the upper boundary-layer edge. Hypersonic viscous–inviscid interaction is neglected, since the interaction parameter $\chi = M_e^3/\sqrt{Re_X}$ (Hayes & Probstein 1959) is less than 0.1 for the region $X > 94$ mm, where all measurements are conducted.

Figures 3(*a*) and 3(*b*) show the mean flow velocity U/U_e and the r.m.s. mass flow pulsations versus the vertical coordinate, Y, normalized with respect to the boundary-layer thickness δ ($U(\delta) = 0.99U_e$). Symbols correspond to the hot-wire measurements on the (i) porous and (ii) solid surfaces at $X = 224.9$ mm; the solid line (iii) in figure 3(*a*) shows the self-similar solution of the laminar boundary-layer equations discussed in § 4.1. The good agreement between the theoretical and experimental mean flow profiles indicates that the boundary layers on both surfaces are laminar. Similar results were obtained at the cross-sections where hot-wire measurements were made. Note that the disturbance profiles for both surfaces have maxima located at $Y/\delta = 0.8$ (see figure 3*b*).

Mass flow disturbance spectra were measured at the normal coordinate Y corresponding to the disturbance maxima. Hot-wire measurements were conducted at the equally spaced X-stations given in table 2. The first station S1 was chosen near the leading edge of the porous surface ($X = 185$ mm). Disturbance spectra are
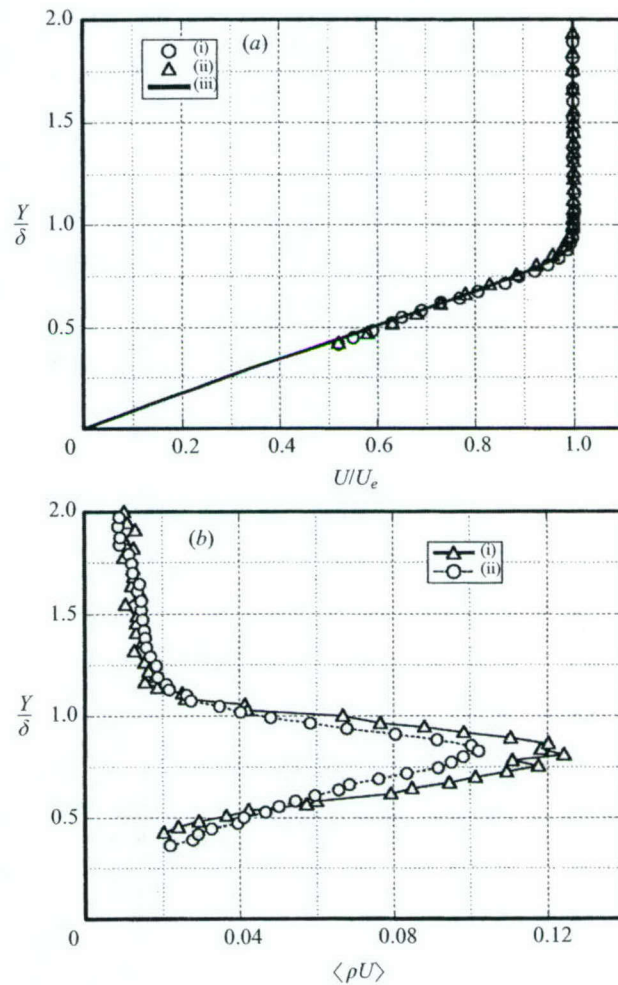
FIGURE 3. Comparison profiles of (*a*) mean velocity and (*b*) r.m.s. mass-flow pulsations for (i) porous and (ii) solid surfaces; (iii) self-similar profile.

Surface	S1	S2	S3	S4	S5
Solid	192.8	217.8	242.9	268.0	293.0
Porous	189.1	214.2	239.2	264.3	289.4

TABLE 2. Locations of the measurement stations (*X* mm).

shown in figures 4(*a*) and 4(*b*) for the solid and porous surfaces, respectively. At the upstream station S1, the spectra are similar on both surfaces. Downstream from S1, the spectrum evolutions are quite different. On the solid surface the disturbance spectra look very similar to those measured by Stetson & Kimmel (1992*b*) on a sharp cone at $M_\infty = 8$; they correspond to the second mode instability. At the upstream station S1, the second mode is observed at the frequency $f \approx 340$ kHz. Downstream from S1, its amplitude quickly increases, whereas its central frequency decreases to 275 kHz at the last station S5. On the porous surface, the low-frequency disturbances
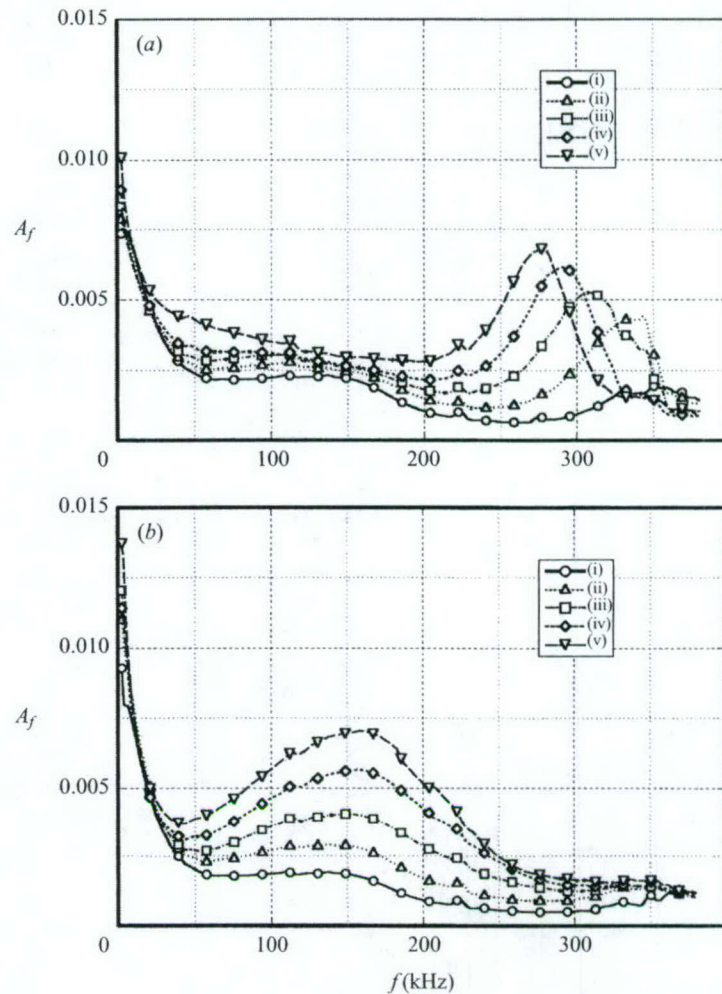
FIGURE 4. Disturbance spectra for (*a*) solid and (*b*) porous surfaces; curves (i)–(v) correspond to stations S1–S5 of table 2.

associated with the first mode are destabilized in the frequency band 100–200 kHz. At the upstream station S1, a small increase of the disturbance spectrum is noticeable near the frequency 350 kHz that may be relevant to the second mode. However, there is no evidence of the second mode at stations S2–S5. These data demonstrate that the porous coating strongly stabilizes the second mode and destabilizes the first mode under natural flow conditions.

To investigate the second-mode stabilization effect a series of experiments was conducted with artificially excited wave packets. The artificial disturbances were generated at a frequency of 280 kHz, which corresponds to the maximum of the second-mode amplitude observed on the solid surface at station S5 for natural disturbances (see the spectrum (v) in figure 4*a*). At first, the artifical wave packet was measured on the solid surface. Then, the middle part with the perturber was rolled 180°, and experiments were carried out on the porous surface. This approach allows for excitation of the wave packets with almost identical initial amplitudes on both surfaces. The disturbance characteristics were measured at the same stations as for natural disturbances (see table 2).
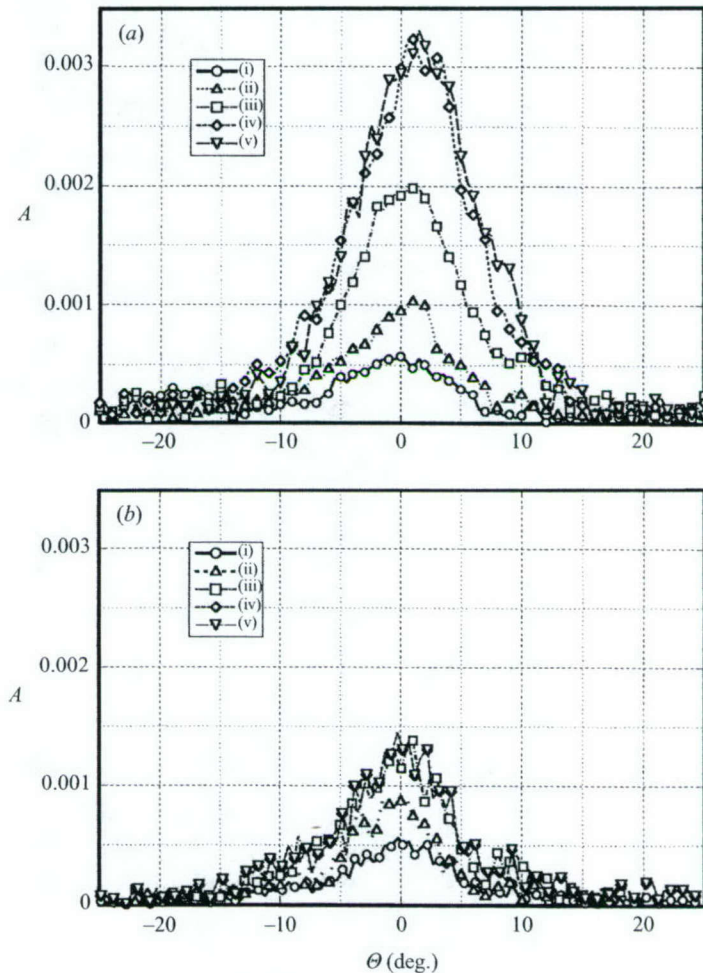
FIGURE 5. Transverse distributions of amplitude of artificial wave packet for (*a*) solid and (*b*) porous surfaces; curves (i)–(v) correspond to stations S1–S5 of table 2.

The disturbance phase measured at the wave packet centre is a linear function of X in the range $X = 240$–300 mm. For the solid and porous surfaces, the phase velocities are equal to $(0.896 \pm 0.03)U_e$, which is consistent with the value $0.916U_e$ calculated for the second mode using the theoretical model of §4.

Transverse distributions of the wave packet amplitude are shown in figures 5(*a*) and 5(*b*) for the solid and porous surfaces, respectively. These distributions have a single peak in the middle of the wave packet (at $\Theta \approx 0$) for all X-stations. The porous coating reduces the disturbance amplitude more than twice. The transverse wave spectra (the β-spectra resulting from the Fourier transform of the transverse distributions) are shown in figures 6(*a*) and 6(*b*). These spectra have a single peak at $\beta = 0$ for all X-stations, i.e. two-dimensional waves are dominant. This is typical for the second mode. On the porous surface, the maximum amplitude is essentially smaller than on the solid surface, clearly demonstrating boundary-layer stabilization.

Longitudinal distributions of the mass flow disturbance amplitude SA_0 at $\beta = 0$ are shown in figure 7 for the solid (i) and porous (ii) surfaces. The amplitudes of natural disturbances with a frequency $f = 280$ kHz are also shown for comparison. They were normalized to match the distributions at the initial X-station. On the solid surface,
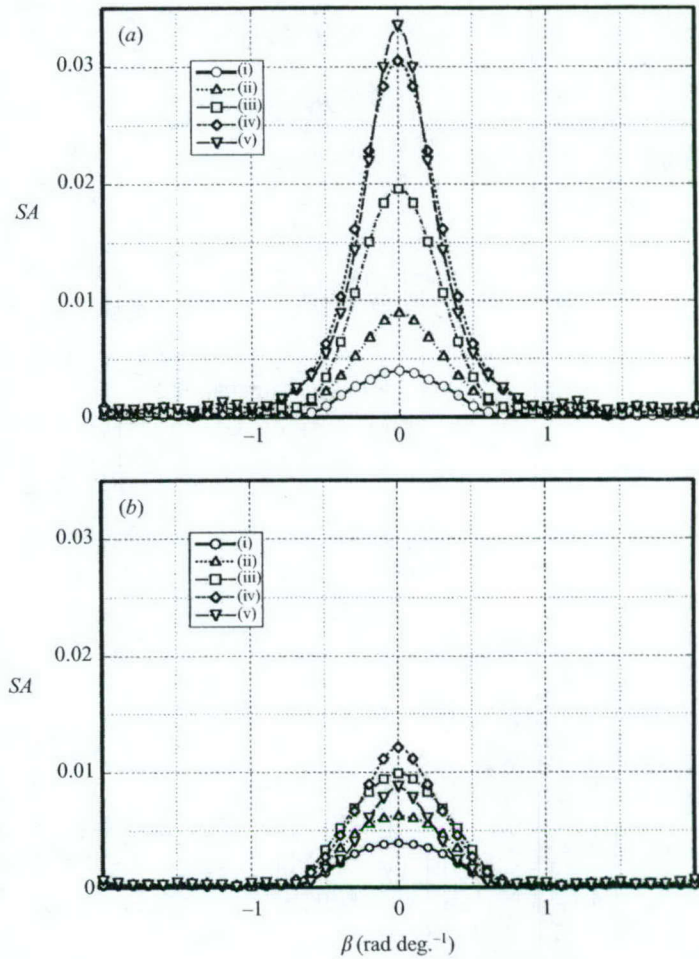
FIGURE 6. β-spectra for (*a*) solid and (*b*) porous surfaces; curves (i)–(v) correspond to stations S1–S5 of table 2.
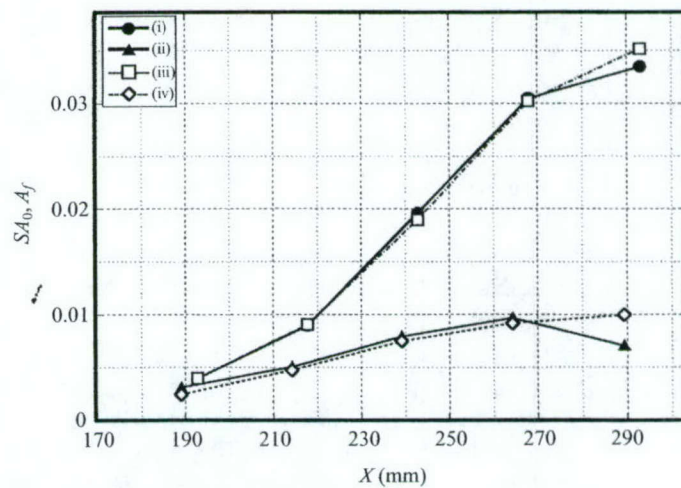

FIGURE 7. Longitudinal distribution of mass flux pulsations amplitude for solid ((i) artificial and (iii) natural disturbances) and porous ((ii) artificial and (iv) natural disturbances) surfaces.

the disturbance amplitude exponentially grows up to $X = 243$ mm. Downstream of this location, the amplification rate decreases. On the porous surface, the amplitude increases approximately twice as slowly as on the solid surface. Moreover, disturbance decay begins downstream of the station $X = 264$ mm. The amplitude distributions of artificial and natural disturbances are very close to each other. This indicates that two-dimensional waves are dominant in the natural disturbance field in the same manner as for artificial wave packets.

4. Stability analysis

4.1. Mean flow

For the laminar boundary layer on a flat plate or a sharp cone at zero angle of attack, the boundary-layer equations are written in the self-similar form (Hayes & Probstein 1959)

$$(Cf'')' + ff'' = 0, \tag{4.1}$$

$$\left(\frac{C}{Pr}g'\right)' + fg' + \frac{U_e^{*2}}{H_e^*}\left[C\left(1 - \frac{1}{Pr}\right)f'f''\right]' = 0, \tag{4.2}$$

$$C = \frac{\rho^*\mu^*}{\rho_e^*\mu_e^*}, \quad \frac{U_e^{*2}}{H_e^*} = \frac{(\gamma-1)M_e^2}{1 + \frac{1}{2}(\gamma-1)M_e^2}, \quad \frac{\rho_e^*}{\rho^*} = \left(1 + \frac{1}{2}(\gamma-1)M_e^2\right)g - \frac{1}{2}(\gamma-1)M_e^2 f'^2. \tag{4.3}$$

Hereinafter, $f'(\eta) = U^*/U_e^*, g(\eta) = H^*/H_e^*, \rho, \mu, Pr$ and γ denote the streamwise velocity, total enthalpy, density, viscosity, Prandtl number and specific heat ratio, respectively; primes denote differentiation with respect to η, and asterisks denote dimensional quantities. The independent variables are given by the Howarth–Dorodnitsyn transformations and Mangler transformation by the coordinates

$$\xi = \int_0^{x^*} \rho_e^*\mu_e^*U_e^*r_w^{*2j}\, dx^*, \quad \eta = \frac{U_e^*r_w^{*j}}{\sqrt{2\xi}}\int_0^{y^*}\rho^*\, dy^*, \tag{4.4}$$

where x is along an external streamline, y is normal to the body surface, r_w is the distance from the symmetry axis to the wall surface; $j = 0$ for two-dimensional flow and $j = 1$ for axisymmetric flow. The porous coating is assumed to affect the mean flow only weakly. Accordingly, the conventional no-slip boundary conditions are imposed on the wall surface

$$\eta = 0: \quad f = f' = 0, \quad g = g_w \quad (\text{or } g' = 0 \text{ for adiabatic wall}), \tag{4.5}$$

$$\eta \to \infty: \quad f' = 1, \quad g = 1. \tag{4.6}$$

In all calculations discussed hereinafter, the fluid is a perfect gas of $\gamma = 1.4$ and $Pr = 0.708$. The viscosity temperature dependency is approximated by Sutherland's law

$$\mu(T) = \frac{(1+S)}{(T+S)}T^{3/2}, \tag{4.7}$$

where $S = 110/T_e^*, \mu = \mu^*/\mu_e^*$ and $T = T^*/T_e^*$ are non-dimensional viscosity and temperature. The mean-flow parameters correspond to the experimental conditions discussed in §3: $M_e = 5.3; T_e^* = 59.3$ K; the local unit Reynolds number $Re_{1e} = U_e^*/v_e^* = 15.5 \times 10^6$ m^{-1}; the wall temperature, $T_w^* = 5.5 T_e^*$, is close to the adiabatic wall temperature.
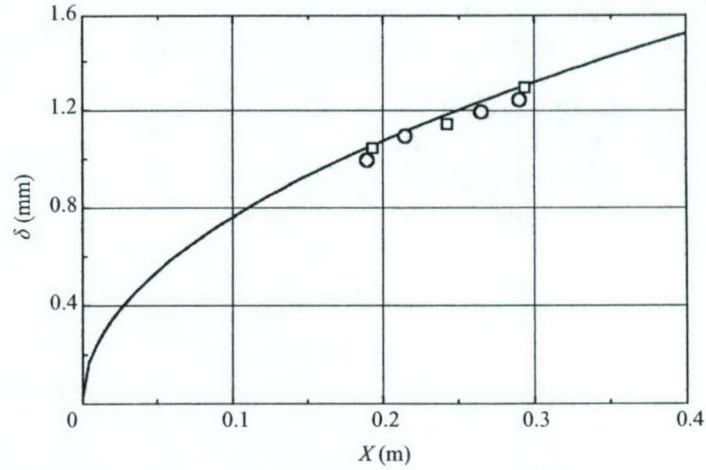
FIGURE 8. Boundary-layer thickness at $Re_1 = 15.5 \times 10^6 \, \text{m}^{-1}$, $M_e = 5.3$, $T_e = 59.3 \, \text{K}$, and the wall temperature $T_w = 5.5 \, T_e$. —, theory; ○, experiment, porous surface; □, experiment, solid surface.

Figure 8 shows that the theoretical boundary-layer thickness δ correlates well with the experimental data for the solid and porous surfaces of the cone. Since wall temperature, $T_w^* \approx 326 \, \text{K}$, is close to room temperature, thermal deformations of the porous coating during the wind-tunnel run are neglected.

4.2. *Linear stability problem*

The stability analysis herein includes the non-parallel effect associated with downstream growth of the boundary-layer thickness. Cone surface curvature and conical divergence of streamlines are neglected in this model. It is based on the method developed by Gaster (1974) for incompressible boundary layers and extended by Padhye & Nayfeh (1979) to compressible flows. This method (with insignificant variations) has been used to investigate the non-parallel effect on stability of supersonic boundary layers (Gaponov 1980; El-Hady 1980; Tumin & Fedorov 1982). Its extension to the case of multiple modes was discussed in Zhigulev & Tumin (1982) and Fedorov & Khokhlov (2002).

Following Fedorov & Khokhlov (2002), we outline the non-parallel stability analysis for a monochromatic wave. The coordinates (x, y, z) are made non-dimensional using the boundary-layer scale $l^* = \sqrt{v_e^* L^* / U_e^*}$, where the distance L^* from the leading edge is assumed to be much larger than l^*, and the ratio $\varepsilon = l^*/L^*$ is treated as a small parameter. Time t and pressure P are referenced to l^*/U_e^* and $\rho_e^* U_e^{*2}$, respectively; other flow characteristics are non-dimensionized by normalizing them to upper boundary-layer edge quantities. Introducing the slow variable, $x_1 = x^*/L^* = \varepsilon x$, we specify the mean-flow velocity components (U, V) and temperature T as

$$U = U(x_1, y), \quad V = \varepsilon V_0(x_1, y), \quad T = T(x_1, y). \tag{4.8}$$

A monochromatic disturbance is represented by the vector function

$$\mathbf{Z} = \left(u, \frac{\partial u}{\partial y}, v, p, \theta, \frac{\partial \theta}{\partial y}, w, \frac{\partial w}{\partial y} \right)^T,$$

$$\mathbf{Z}(x, y, z, t) = \mathbf{F}(x, y) \exp(i \beta z - i \omega t), \tag{4.9}$$

where u, v, w, p and θ are velocity components, pressure and temperature; $\beta = \beta^* l^*$ and $\omega = \omega^* l^* / U_e^*$. The amplitude vector-function $F(x, y)$ satisfies a system of partial differential equations that result from a Fourier transform of the linearized Navier–Stokes equations with respect to time and the z-coordinate. These equations with the boundary conditions can be written in the matrix-operator form

$$\mathbf{H}(y, \partial_y, x_1, \varepsilon \partial_{x_1}, \omega, \beta)\mathbf{F} = 0. \tag{4.10}$$

$$y = 0: \quad F_1 = A_x F_4, \quad F_3 = A_y F_4, \quad F_5 = A_\theta F_4, \quad F_7 = A_z F_4, \tag{4.11}$$

$$y \to \infty: \quad F_1, F_3, F_5, F_7 \to 0. \tag{4.12}$$

Here admittances A_x, A_y, A_z and thermal admittance A_θ are complex quantities, which couple velocity and temperature disturbances with the pressure perturbations on the porous surface. They depend on properties of the porous material, mean flow characteristics on the wall surface, and disturbance frequency. These dependencies will be specified in §4.3. For the solid wall $A_x = A_y = A_z = A_\theta = 0$, which corresponds to no-slip conditions and zero temperature perturbation on a surface of high thermal conductivity.

We consider a partial solution of the problem (4.10)–(4.12), which is a discrete mode of the complex eigenvalue $\alpha(x_1, \beta, \omega)$. The amplitude vector-function is expressed as

$$\mathbf{F} = (\mathbf{F}_0 + \varepsilon \mathbf{F}_1 + \ldots) \exp(\mathrm{i}\varepsilon^{-1} S), \quad S = \int \alpha(x_1) \mathrm{d}x_1 \tag{4.13}$$

Substituting (4.13) into (4.10)–(4.12) and grouping terms of the same order of magnitude with respect to ε we obtain a sequence of problems for $\mathbf{F}_j(x_1, y), j = 0, 1, \ldots$. In the zeroth-order approximation, the eigenvalue problem for a locally parallel mean flow is written as

$$\left(\frac{\partial}{\partial y} - \mathbf{H}_0\right) \mathbf{F}_0 = 0, \tag{4.14}$$

$$y = 0: \quad F_{01} = A_x F_{04}, \quad F_{03} = A_y F_{04}, \quad F_{05} = A_\theta F_{04}, \quad F_{07} = A_z F_{04}, \tag{4.15}$$

$$y \to \infty: \quad F_{01}, F_{03}, F_{05}, F_{07} \to 0. \tag{4.16}$$

Here, the matrix $\mathbf{H}_0$ has dimension 8×8; its non-zero elements are given in the Appendix. Solution of the problem (4.14)–(4.16) is expressed as

$$\mathbf{F}_0 = c(x_1)\boldsymbol{\zeta}(x_1, y, \alpha), \tag{4.17}$$

where $\boldsymbol{\zeta}$ is the eigenvector normalized by a certain condition, such as the pressure disturbance amplitude on the wall surface is $\zeta_4(x_1, 0, \alpha) = 1$. For spatial instability of two-dimensional boundary layers, the frequency ω and the transverse wavenumber component β are real, whereas α is a complex eigenvalue. If $\mathrm{Im}\,\alpha < 0$, then the disturbance amplifies downstream with the spatial growth rate $\sigma_\alpha = -\mathrm{Im}\,\alpha$. The amplitude coefficient $c(x_1)$ is determined from the first-order approximation, which leads to the inhomogeneous problem

$$\left(\frac{\partial}{\partial y} - \mathbf{H}_0\right) \mathbf{F}_1 = -\mathrm{i}\frac{\partial \mathbf{H}_0}{\partial \alpha}\frac{\partial \mathbf{F}_0}{\partial x_1} + \mathbf{H}_1 \mathbf{F}_0, \tag{4.18}$$

$$y = 0: \quad F_{01} = A_x F_{04}, \quad F_{03} = A_y F_{04}, \quad F_{05} = A_\theta F_{04}, \quad F_{07} = A_z F_{04}, \tag{4.19}$$

$$y \to \infty: \quad F_{01}, F_{03}, F_{05}, F_{07} \to 0. \tag{4.20}$$

The right-hand side of (4.18) is associated with the non-parallel effect; the vector $\mathbf{G} = \mathbf{H}_1 \mathbf{F}_0$ is given in the Appendix. The problem (4.18)–(4.20) has a non-trivial

solution if its right-hand side is orthogonal to the eigenvector $\xi(x_1, y, \alpha)$ of the adjoint problem

$$\left(\frac{\partial}{\partial y} + \boldsymbol{H}_0^T\right) \bar{\boldsymbol{\xi}} = 0, \tag{4.21}$$

$$y = 0: \quad \bar{\xi}_2 = \bar{\xi}_6 = \bar{\xi}_8 = 0, \quad \bar{\xi}_4 + A_x\bar{\xi}_1 + A_y\bar{\xi}_3 + A_\theta\bar{\xi}_5 + A_z\bar{\xi}_7 = 0, \tag{4.22}$$

$$y \to \infty: \quad \bar{\xi}_2, \bar{\xi}_4, \bar{\xi}_6, \bar{\xi}_8 \to 0, \tag{4.23}$$

where the upper bar denotes a complex conjugate value. The orthogonality condition leads to the ordinary differential equation for the amplitude function $c(x_1)$

$$\left\langle \boldsymbol{\xi}, \frac{\partial \boldsymbol{H}_0}{\partial \alpha}\boldsymbol{\zeta} \right\rangle \frac{\mathrm{d}c}{\mathrm{d}x_1} = \left[-\left\langle \boldsymbol{\xi}, \frac{\partial \boldsymbol{H}_0}{\partial \alpha}\frac{\partial \boldsymbol{\zeta}}{\partial x_1} \right\rangle - \mathrm{i}\langle \boldsymbol{\xi}, \boldsymbol{H}_1\boldsymbol{\zeta} \rangle \right] c, \tag{4.24}$$

where the scalar product is defined as

$$\langle \boldsymbol{f}, \boldsymbol{g} \rangle = \int_0^\infty \sum_{j=1}^8 \bar{f}_j g_j \mathrm{d}y. \tag{4.25}$$

Substituting the solution of (4.24) into (4.17) and (4.13), we express the amplitude vector in the form

$$\boldsymbol{F} = [c_0\boldsymbol{\zeta}(x_1, y) + O(\varepsilon)]\exp\left(\mathrm{i}\varepsilon^{-1}\int [\alpha(x_1) + \varepsilon W(x_1) + O(\varepsilon^2)]\mathrm{d}x_1\right), \tag{4.26}$$

$$W(x_1) = \frac{\mathrm{i}\left\langle \boldsymbol{\xi}, \frac{\partial \boldsymbol{H}_0}{\partial \alpha}\frac{\partial \boldsymbol{\zeta}}{\partial x_1} \right\rangle - \langle \boldsymbol{\xi}, \boldsymbol{H}_1\boldsymbol{\zeta} \rangle}{\left\langle \boldsymbol{\xi}, \frac{\partial \boldsymbol{H}_0}{\partial \alpha}\boldsymbol{\zeta} \right\rangle}, \tag{4.27}$$

where c_0 is constant. The amplification rate of any physical quantity can be calculated using (4.26) and (4.27). For example, the x-component of mass flow disturbance is

$$Q(x_1, y) = [c_0 q(x_1, y) + O(\varepsilon)]\exp\left(\mathrm{i}\varepsilon^{-1}\int [\alpha(x_1) + \varepsilon W(x_1) + O(\varepsilon^2)]\mathrm{d}x_1\right), \tag{4.28}$$

$$q = [\zeta_1 + (\gamma M_e^2\zeta_4 - \zeta_5/T)U]/T. \tag{4.29}$$

The disturbance growth rate is a logarithmic derivative of (4.28), which is expressed in the form

$$\sigma_\alpha(x_1, y) = -\mathrm{Im}\,\alpha + \varepsilon\left(\frac{\partial \ln|q(x_1, y)|}{\partial x_1} - \mathrm{Im}\,W\right) + O(\varepsilon^2). \tag{4.30}$$

Because of the non-parallel effect, the growth rate depends on the vertical coordinate y. According to the experimental measurements, $\sigma_\alpha(x_1, y)$ is calculated at $y = y_m$ relevant to the maximum of mass-flow disturbance in the boundary layer. This maximum lies in the critical layer, where the mean-flow velocity is close to the phase velocity, $U(y) = c$.

The zeroth-order and first-order approximations of σ_α were validated by comparison with the experimental data of Kendall (1967) and the calculations of Chang et al. (1991) performed in the framework of linear parabolized stability equations (PSE). Figure 9 shows the first-mode growth rate as a function of the non-dimensional frequency, $F = \omega^* v_e^*/U_e^{*2}$, for the boundary layer on a flat plate at the Mach number $M_e = 2.2$ and the Reynolds number $R = \sqrt{U_e^* L^*/v_e^*} = 1000$. The wave angle is $\psi = \arctan(\beta/\alpha_r) = 60°$. This approximately corresponds to the most unstable waves.
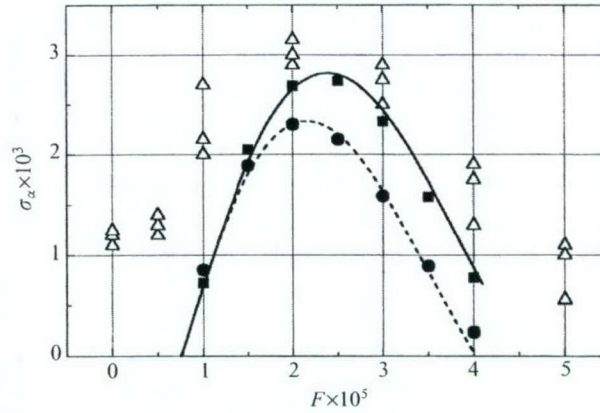
FIGURE 9. The first-mode growth rate as a function of frequency; boundary layer on a flat plate at $M_e = 2.2$, $R = 1000$, the wave angle $\psi = \arctan(\beta/\alpha_r) = 60°$: △, experiment of Kendall (1967); ---, parallel theory (present); ●, parallel theory, Chang *et al.* (1991); —, non-parallel theory (present); ■, non-parallel PSE, Chang *et al.* (1991).
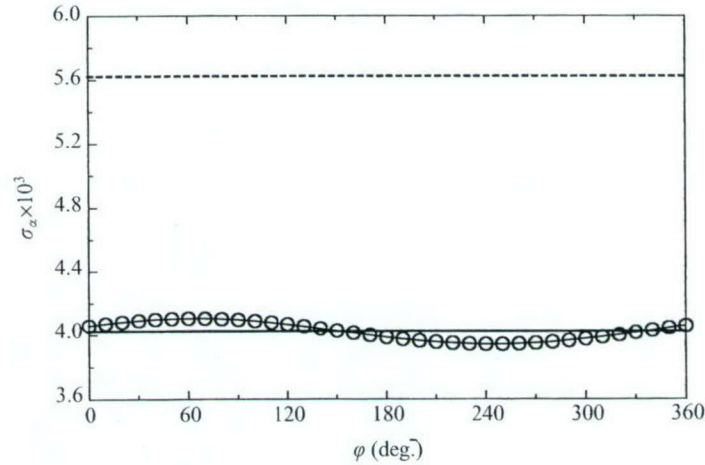

FIGURE 10. Effect of longitudinal admittance on the second-mode stability: $F = 1.2385 \times 10^{-4}$, $R = 2095$; ---, solid wall; —, $A_y = -1$, $A_x = 0$; ○, $A_y = -1$, $A_x = \exp(i\varphi \pi/180)$.

The results are in good agreement with the linear PSE calculations, thereby confirming the aforementioned model.

4.3. *Admittance of porous layer and boundary conditions*

Fedorov & Malmuth (2001) showed that thermal admittance produces a negligible effect on boundary-layer stability. This finding allows us to use the boundary condition $\theta = 0$ at $y = 0$. To estimate effects of the admittance components A_x and A_z, associated with non-zero perturbations of the velocity components u, w on the porous surface, we conducted stability calculations in a wide range of A_x and A_z. This parametric study indicates that the second-mode growth rate weakly depends on A_x and A_z. As an example, figure 10 shows the growth-rate distribution $\sigma_\alpha(\varphi)$ for a two-dimensional disturbance of non-dimensional frequency $F \equiv \omega^* l^* / U_e^* = 1.2385 \times 10^{-4}$ for a Reynolds number $R \equiv U_e^* l^* / \nu_e^* = 2.095 \times 10^3$. This case corresponds to the

114   A. Fedorov, A. Shiplyuk, A. Maslov, E. Burov and N. Malmuth

disturbance of the frequency $f = 250\,\text{kHz}$ at $x^* = 283.2\,\text{mm}$. The calculations were conducted at normal admittance $A_y = -1.0$, transverse admittance $A_z = 0$ and longitudinal admittance $A_x = \exp(i\varphi\pi/180)$ with φ being measured in degrees. The longitudinal admittance effect is small compared to the normal admittance effect. This feature is due to instability of the hypersonic boundary layer being predominantly governed by an inviscid process. For the limit $R \to \infty$, the system of stability equations is reduced to the two equations coupling the vertical velocity disturbance v and the pressure disturbance p (Mack 1984). Since the other components u, w and θ are passive, their interference with the porous layer weakly affects the disturbance growth rate. Moreover, the felt-metal fibres lie predominantly in the planes, which are orthogonal to the y-axis (see figure 1). Because of this anisotropy, disturbances weakly penetrate in the x- and z-directions compared with the y-direction, i.e. $|A_x| \sim |A_z| \ll |A_y|$. Summarizing, we approximate the boundary conditions on the felt-metal coating as

$$y = 0: \quad u = w = \theta = 0, \quad v = A_y p, \tag{4.31}$$

that is equivalent to the assumption that $A_x = A_z = A_\theta = 0$.

Fedorov & Malmuth (2001) showed that the porous-layer admittance A_y is expressed in the form

$$A_y = \frac{\phi}{Z_0} \tanh(\Lambda h), \tag{4.32}$$

where ϕ is porosity, $h = h^*/l^*$ is the porous-layer thickness, Z_0 and Λ are the characteristic impedance and propagation constant of a porous media, respectively. In the case of cylindrical holes perpendicular to the surface, the characteristic impedance and propagation constant are expressed as a function of the series impedance and the shunt admittance for the tube element of unit length using the transmission line formalism (Daniels 1950; Benade 1968). The same analytical solution can be obtained in terms of the complex dynamic density $\tilde{\rho}$ and the complex dynamic compressibility $\tilde{C}$ (see, for example, Johnson, Koplik & Dashen 1987). Hereafter, we use the latter approach, which is more convenient for analysis of acoustic disturbances in randomly porous media. Accordingly, the characteristic impedance and the propagation constants are expressed as

$$Z_0 = -\frac{\sqrt{\tilde{\rho}/\tilde{C}}}{M_e\sqrt{T_w}}, \quad \Lambda = \frac{i\omega M_e}{\sqrt{T_w}}\sqrt{\tilde{\rho}/\tilde{C}}, \tag{4.33}$$

where $\tilde{\rho} = \rho^*(\omega)/\rho_w^*$ and $\tilde{C} = \gamma P_w^*/K^*(\omega)$; $K^*(\omega)$ is the dynamic bulk modulus; ρ_w^* and P_w^* are mean density and static pressure in the porous layer, respectively.

The problem of disturbance propagation within the porous layer is decoupled from the boundary-layer stability problem. The former can be treated as a problem of acoustic wave propagation in a porous media, which is characterized by the quantities $\tilde{\rho}$ and $\tilde{C}$. Unfortunately, there is no rigorous theory to predict these characteristics for porous materials of random microstructure. Delany & Bazley (1970) gave empirical relations for $\tilde{\rho}$ and $\tilde{C}$ for fibrous absorbent materials. These relations are widely used in various applications such as sound attenuation in ducts, room acoustics and the transmission loss through walls. Allard & Champoux (1992) modified the correlation of Delany & Bazley (1970) using the theoretical results of Johnson et al. (1987). They
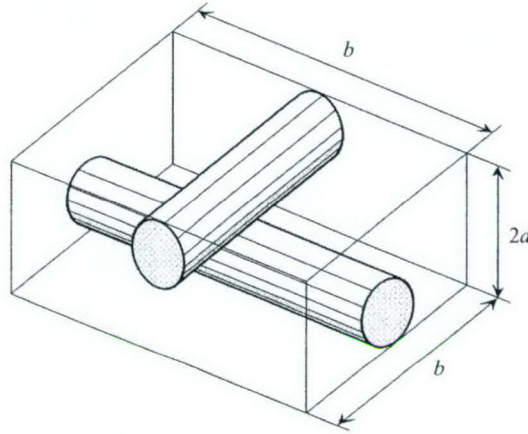
FIGURE 11. An elementary cell of the felt-metal microstructure; $b \times b \times 2d$ parallelepiped including two adjoining sections of fibres with diameter d and mutually orthogonal axes.

derived the semi-empirical relations

$$\tilde{\rho} = a_\infty \left[1 + \frac{g(\lambda_1)}{\lambda_1} \right], \quad \tilde{C} = \gamma - \frac{\gamma - 1}{1 + g(\lambda_2)/\lambda_2}, \tag{4.34}$$

$$g(\lambda) = \sqrt{1 + \frac{4a_\infty \mu^* \lambda}{\sigma^* \phi r_p^{*2}}}, \tag{4.35}$$

$$\lambda_1 = \mathrm{i} a_\infty \rho_w^* \omega^* / (\phi \sigma^*), \quad \lambda_2 = 4 \mathrm{Pr} \lambda_1. \tag{4.36}$$

Here, σ^* is the flow resistivity determined from the equation

$$\Delta P^* = -\sigma^* \Delta Z^* \bar{W}^*, \tag{4.37}$$

which couples the steady pressure drop ΔP^* of viscous flow with the mean flow velocity $\bar{W}^*$ through the porous layer of thickness ΔZ^*. The parameter a_∞ is the tortuosity, which is equivalent to the structure form factor k_s of Zwikker & Kosten (1949) or to the parameter q^2 of Attenborough (1987). It is coupled with the dynamic density $\tilde{\rho}(\omega)$ as $a_\infty = \lim_{\omega \to 0} \tilde{\rho}(\omega)$. The characteristic pore size is defined as

$$r_p^* = \frac{2 \int_V |W^*(r^*)|^2 \, \mathrm{d}V^*}{\int_S |W^*(r_S^*)|^2 \, \mathrm{d}S}. \tag{4.38}$$

The integral in the numerator is evaluated over the pore volume, and $W^*(r^*)$ is the velocity vector of inviscid fluid within the pore; r^* is the radius vector of the point inside the pore volume for which the fluid-velocity vector is defined. The integral in the denominator is taken over the pore surface, and $W^*(r_s^*)$ is the fluid velocity vector on the pore surface. For isotropic porous materials, Allard & Champoux (1992) showed that $r_p^* = s_h \sqrt{8 \mu^* a_\infty / \sigma^* \phi}$, where s_h is the dimensionless shape factor. However, this relation seems not to be valid for the felt-metal, which is highly anisotropic. To resolve this difficulty, we note that the shape factor is $s_h \approx 1$ in the case of cylindrical pores (not necessarily circular), if the fluid velocity is constant. Accordingly, the characteristic pore size r_p^* can be treated as a hydraulic radius, i.e. it is a ratio of the doubled cross-sectional area to the cross-sectional perimeter. To
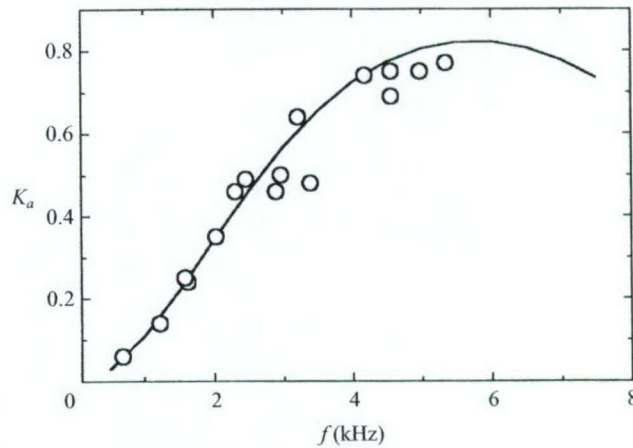
FIGURE 12. The absorption coefficient K_a versus the sound frequency f at the ambient pressure; —, correlation (4.34)–(4.36); ○, laboratory measurements.

estimate r_p^*, we consider an elementary cell (see figure 11) simulating topology of the felt-metal microstructure. The cell is assumed to have the same average statistical properties as the actual porous layer. Accordingly, the characteristic pore size r_p^* and the porosity ϕ are expressed in terms of the fibre diameter d^* and the cell size b^* as

$$r_p^* = 4b^*/(1 + \pi d^*/4b^*), \quad \phi = 1 - \pi d^*/4b^*. \tag{4.39}$$

Using (4.39), we represent r_p^* as a function of the quantities ϕ and d^*, which can be measured experimentally,

$$r_p^* = \frac{\pi d^*}{2(1 - \phi)(2 - \phi)}. \tag{4.40}$$

Using the method of acoustic standing waves S. Mironov (ITAM) performed laboratory measurements of the felt-metal energy absorption coefficient $K_a = 1 - |R_{ref}|^2$ (where R_{ref} is the reflection coefficient for plane acoustic waves of normal incidence) and coordinates of nodes for standing waves in the resonance tube. The measurements were conducted in the frequency band 1–6 kHz, for which the non-dimensional arguments $\lambda_{1,2}$ of the correlation (4.34)–(4.36) correspond to the wind-tunnel conditions. The best fit of the experimental data gives the felt-metal flow resistivity $\sigma^* = (1.66 \pm 0.21) \times 10^5 \, \mathrm{kg \, (m^3 \, s^{-1})}$ assuming that the tortuosity $a_\infty = 1$ and the porosity $\phi = 0.75$. With these parameters the relations (4.34)–(4.36) have been used for stability calculations discussed in §5. Note that 12.6% uncertainty of σ^* is due to a relatively large scatter of the absorption coefficient measurements shown in figure 12 along with the prediction based on (4.34)–(4.36). However, stability calculations of §5 show that this uncertainty weakly affects the second mode amplification (see figure 16).

Under wind-tunnel conditions, the flow density is relatively small ($\sim 1\%$ of the normal density). Because the characteristic pore diameter is also small, rarefied gas effects need to be evaluated. Our estimates show that the mean free path in the porous layer is $\lambda_{mfp}^* \sim 10 \, \mu m$. Using the pore diameter $2r_p^*$ as a characteristic length scale we obtain the Knudsen number $Kn = \lambda_{mfp}^*/2r_p^* \sim 3 \times 10^{-2}$, i.e. the Knudsen-layer thickness is only a few per cent of the pore diameter, and rarefaction effects can be neglected.
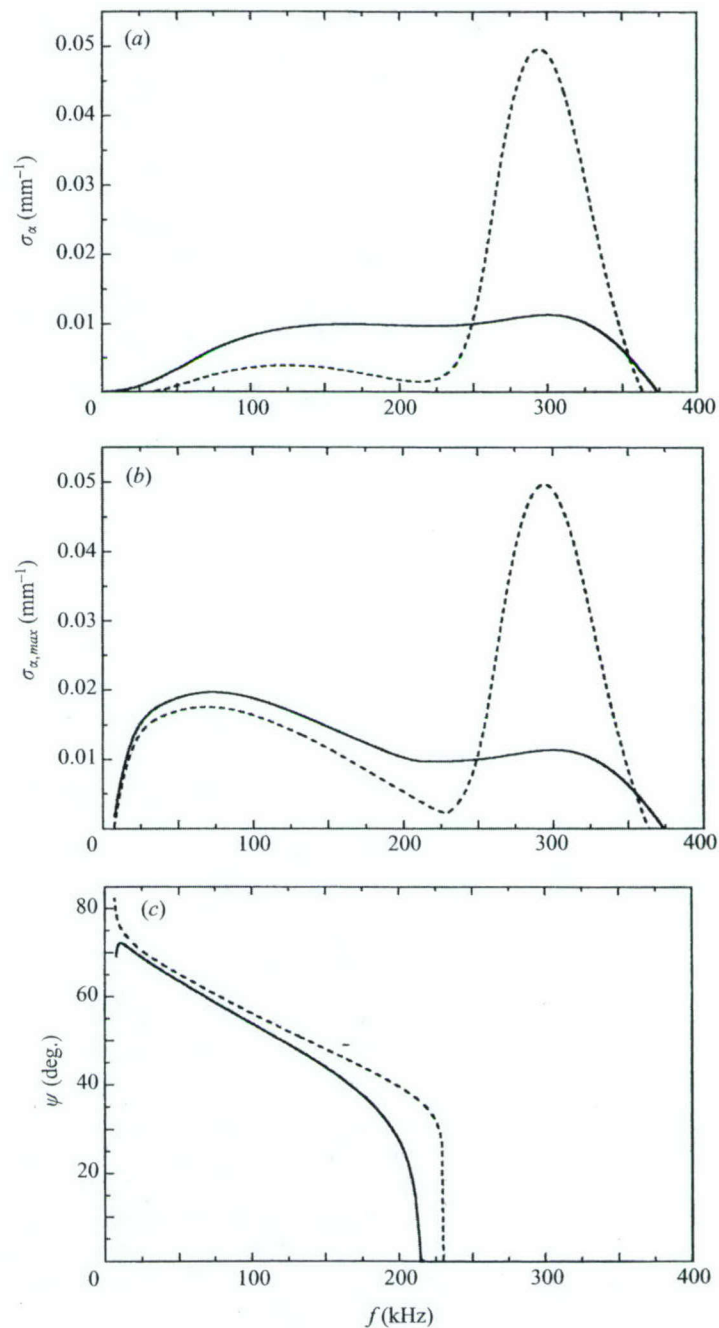
FIGURE 13. (a) Growth rate of two-dimensional disturbances *vs.* frequency at $x = 200.1\,\text{mm}$ ($R = 1761.2$); locally parallel approximation. (b) Maximum growth rate of three-dimensional disturbances *vs.* frequency at $x = 200.1\,\text{mm}$ ($R = 1761.2$); locally parallel approximation. (c) The wave angle $\psi = \arctan(\beta/\alpha_r)$ of the most unstable three-dimensional waves *vs.* frequency at $x = 200.1\,\text{mm}$ ($R = 1761.2$); locally parallel approximation. —, porous wall; ---, solid wall.

5. Stability calculations and comparison with experiment

The first series of stability calculations has been conducted in the local parallel approximation using the system of equations (4.14)–(4.16). Figure 13(a) shows the
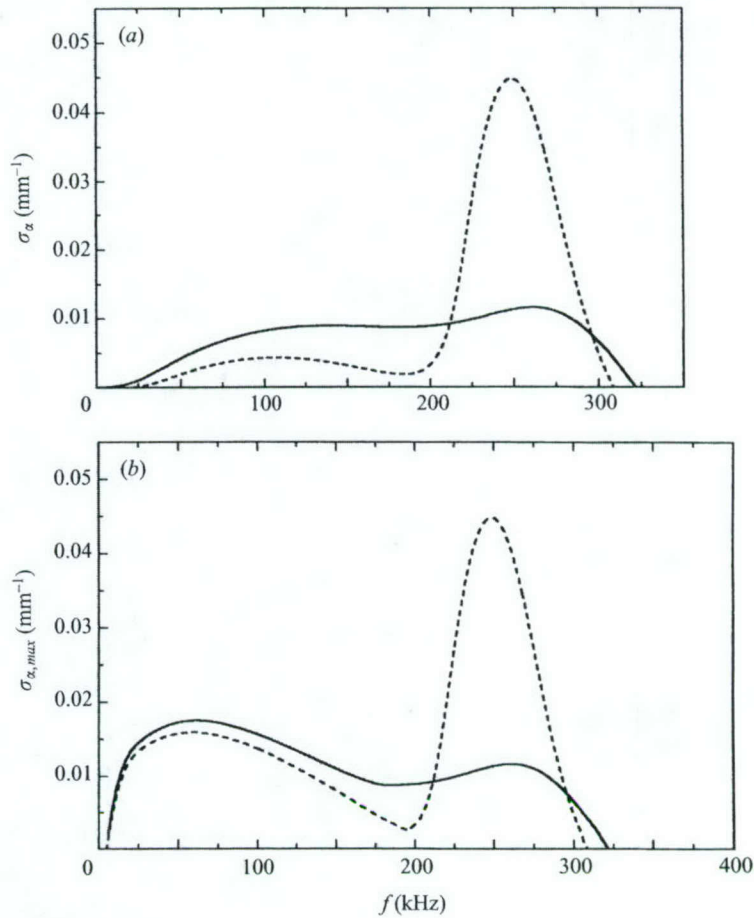
FIGURE 14. Growth rate of two-dimensional disturbances *vs.* frequency at $x = 283.2$ mm ($R = 2095$); locally parallel approximation. Maximum growth rate of three-dimensional disturbances *vs.* frequency at $x = 283.2$ mm ($R = 2095$); locally parallel approximation. ---, solid wall; —, porous wall.

growth rate, $\sigma_\alpha^* = -\mathrm{Im}\,\alpha^*$, of two-dimensional disturbances ($\beta = 0$) as a function of the disturbance frequency f at the streamwise coordinate $x^* = 200.1$ mm. The porous coating strongly stabilizes the second mode relevant to the high-frequency band, $225 < f < 375$ kHz; whereas the first mode associated with low frequencies, $f < 225$ kHz, is marginally destabilized. Figure 13(b) shows similar trends for the maximum growth rate, $\sigma_{\alpha,max}^* = \max[\sigma_\alpha^*(\beta)]$, of three-dimensional disturbances. Figure 13(c) shows the wave angle, $\psi = \arctan(\beta/\alpha_r)$, of the most unstable waves. The low-frequency disturbances of maximum amplification are oblique waves relevant to the first mode. In the high-frequency band, the most unstable disturbances are two-dimensional waves (with $\psi = 0$) of the second mode. Similar trends are observed in the case of $x^* = 283.2$ mm shown in figure 14. These results are in qualitative agreement with the experimental data for 'natural' disturbances discussed in § 3.

   Figure 15 compares theoretical amplification curves with experimental data for the two-dimensional component of an artificially excited wave packet of frequency $f = 280$ kHz. (See curves (i) and (ii) in figure 7.) In these calculations, the initial amplitudes are adjusted to experimental data at the first data point. For the solid-wall case, the theoretical growth rate is essentially larger than the experimental one,
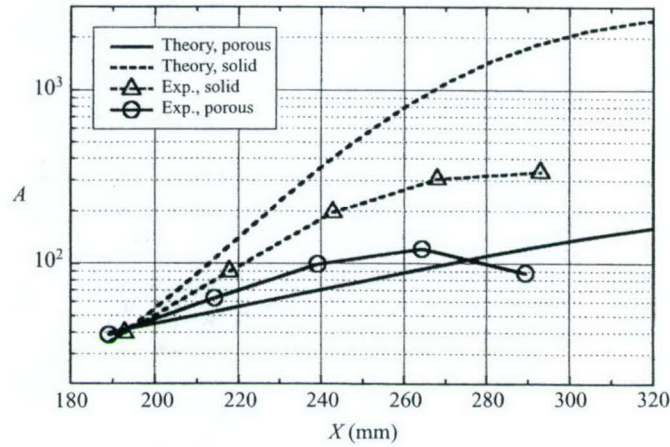
FIGURE 15. Amplification of the two-dimensional component for the artificially excited wave packet of frequency $f = 280\,\text{kHz}$; locally parallel theory versus experiment.
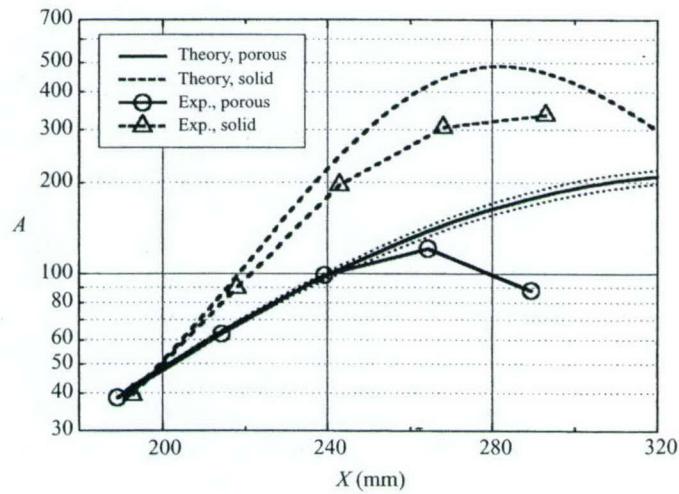

FIGURE 16. Amplification of the two-dimensional component for the artificially excited wave packet of frequency $f = 280\,\text{kHz}$; non-parallel theory versus experiment; —, the felt-metal flow resistivity $\sigma^* = 1.66 \times 10^5\,\text{kg}\,\text{m}^{-3}\,\text{s}^{-1}, \cdots, \sigma^* = (1.66 \pm 0.21) \times 10^5\,\text{kg}\,\text{m}^{-3}\,\text{s}^{-1}$.

i.e. the locally parallel approximation gives only qualitative agreement with stability measurements.

To perform a more accurate comparison, we accounted for the non-parallel effect using the first-order approximation, (4.30). According to experimental measurements, the disturbance growth rate $\sigma_\alpha^*(x_1, y)$ was calculated at the vertical coordinate, $y = y_m$, relevant to the maximum of mass-flow pulsations. Figure 16 shows that with this correction, theoretical growth rates (slopes of the amplification curves) are remarkably close to experimental data in the region $190 < x < 260\,\text{mm}$, especially for the porous surface. The dotted lines indicate that an approximately 12% uncertainty in the laboratory measurements of the felt-metal resistivity σ^* leads to much smaller changes of the amplification curve.
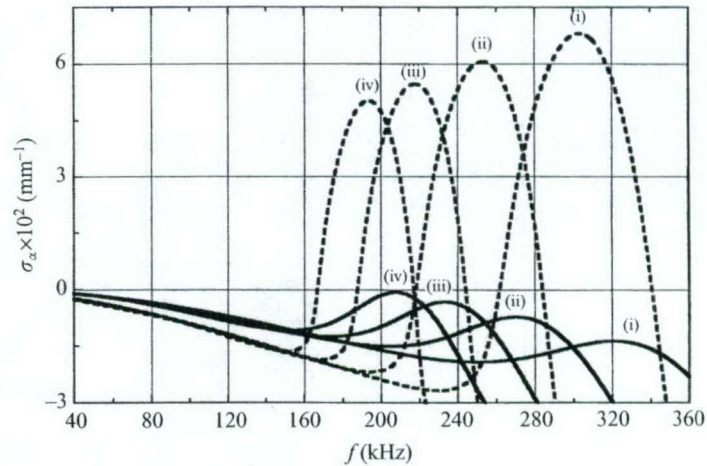
120   *A. Fedorov, A. Shiplyuk, A. Maslov, E. Burov and N. Malmuth*

FIGURE 17. Growth rate of two-dimensional disturbances as a function of frequency f at various x, $T_w = 2T_e$, $Re_1 = 10^7\,\mathrm{m}^{-1}$; locally parallel approximation; (i) $x^* = 206.35\,\mathrm{mm}$, (ii) $x^* = 298.72\,\mathrm{mm}$, (iii) $x^* = 406.05\,\mathrm{mm}$, (iv) $x^* = 515.79\,\mathrm{mm}$. ---, solid wall; —, porous wall.

Finally, we discuss a combination of the UAC and wall cooling effects on the boundary-layer disturbances. We consider the boundary layer at local Mach number $M_e = 5.3$, wall temperature $T_w^* = 2T_e^*$ ($T_w/T_{ad} \approx 0.35$) and the local unit Reynolds number $Re_{1e} = 10^7\,\mathrm{m}^{-1}$. Stability calculations for various β show that, in contrast to the adiabatic wall case, the most unstable waves are two-dimensional for both low and high frequencies. Seemingly, wall cooling leads to a stronger stabilization of the first-mode oblique waves than the two-dimensional waves. Figure 17 shows the growth rates of two-dimensional disturbances as functions of the frequency f at various x^* stations. The porous coating leads to a dramatic reduction of σ_α for high frequencies associated with the second mode instability. In the low-frequency band of the first mode, the coating causes a marginal increase of σ_α. However, the wall cooling leads to such a strong stabilization of the first mode that the low-frequency waves are stable everywhere. This example demonstrates that the porous coating on a cold wall causes a massive damping of unstable disturbances. Note that for actual hypersonic vehicles, the wall temperature ratio is small (less than 0.2) enough to eliminate the first-mode instability. With the help of a passive porous coating, it is feasible to diminish the second-mode instability and significantly increase the laminar run on hypersonic vehicle surfaces.

6. Conclusions

Experimental and theoretical studies of hypersonic boundary-layer stability were performed for ultrasonically absorptive coatings (UAC) of random microstructure. Such structures typify practical TPS materials. Stability of natural disturbances and artificially excited wave packets in the boundary layer on solid and porous surfaces of a sharp cone were measured in the ITAM Mach 6 wind tunnel. These results were compared with stability analyses that included theoretical simulations of the UAC characteristics.

The experiments were conducted on a 7° half-angle sharp cone, one half of which is solid and the other covered by a thin porous coating of random microstructure. Hot-wire measurements showed that boundary layers on solid and porous surfaces

are laminar. The mean flow profiles are similar in both cases and agree with the self-similar solution of the boundary-layer equations. The hot-wire measurements of 'natural' disturbances showed that the disturbance spectra on the solid surface are typical for hypersonic boundary layers, with the second mode being dominant. On the porous surface, the second mode is so strongly suppressed that it is not observable in the measurement region, while the first mode becomes unstable. To investigate the second mode stabilization effect, artificial wave packets were generated in the boundary layer at a frequency relevant to the second mode instability. Two-dimensional waves of the wave packets were dominant and unstable on the solid surface. Additionally, the porous coating reduced the second-mode growth rate.

A linear stability problem was formulated for the boundary layer on a sharp cone with and without a porous coating. A major effect of the coating is associated with porous-layer admittance to vertical velocity disturbances. Non-zero perturbations of the longitudinal and transverse velocity components on the porous surface weakly affect the second-mode instability and can be neglected. With this approximation, the porous coating admittance was determined using the semi-empirical relations of Allard & Champoux (1992) and laboratory measurements of the felt-metal characteristics.

Stability calculations for two- and three-dimensional disturbances showed that the felt-metal coating strongly stabilizes the second mode relevant to the high-frequency band and marginally destabilizes the first mode of relatively low frequencies. These results are in qualitative agreement with experimental data for natural disturbances.

Comparison of the theoretical amplification curves with the experimental data for a two-dimensional component of an artificially excited wave packet showed that the theoretical growth rate is larger than the experimental one. The locally parallel approximation of the stability problem gives only qualitative agreement with the stability measurements. The mean-flow non-parallel effect, associated with the downstream growth of the boundary layer, was incorporated into the stability analysis. With this correction, theoretical growth rates are remarkably close to experimental data (especially for the porous wall case), which confirms the theoretical model.

Stability calculations for the cooled-wall case indicated that wall cooling leads to a strong stabilization of the first mode, while the second mode is effectively suppressed by the porous coating. For actual hypersonic vehicles, the wall temperature ratio is small (less than 0.2), which eliminates the first-mode instability. Using a passive porous coating, it is feasible to diminish the second-mode instability and significantly increase the laminar run on actual hypersonic vehicle surfaces with predominantly two-dimensional boundary layers.

Appendix

$D = d/dy$, $\mu' = d\mu/dT$, $m = \frac{2}{3}(e - 1)$, $r = (e + 2)$, where $e = 1.2$ corresponds to the ratio of the second viscosity to the first viscosity $\mu_2/\mu = \frac{2}{3}e = 0.8$; $\chi = [(R/\mu) + ir\gamma M_e^2(\alpha U - \omega)]^{-1}$. Non-zero elements of the matrix $\boldsymbol{H}_0$ in (4.14) are

$$H_{12} = H_{56} = H_{78} = 1;$$

$$H_{21} = \alpha^2 + \beta^2 + i(\alpha U - \omega)\frac{R}{\mu T}, \quad H_{22} = -\frac{D\mu}{\mu},$$

$$H_{23} = -i\alpha\left[(m+1)\frac{DT}{T} + \frac{D\mu}{\mu}\right] + \frac{RDU}{\mu T},$$

$$H_{24} = i\frac{\alpha R}{\mu} - (m+1)\gamma M_e^2\alpha(\alpha U - \omega), \quad H_{25} = (m+1)\frac{\alpha}{T}(\alpha U - \omega) - \frac{D(\mu'DU)}{\mu},$$

$$H_{26} = -\frac{\mu'DU}{\mu};$$

$$H_{31} = -i\alpha, \quad H_{33} = \frac{DT}{T}, \quad H_{34} = -i\gamma M_e^2(\alpha U - \omega), \quad H_{35} = \frac{i}{T}(\alpha U - \omega), \quad H_{37} = -i\beta;$$

$$H_{41} = -i\alpha\chi\left(r\frac{DT}{T} + 2\frac{D\mu}{\mu}\right), \quad H_{42} = -i\alpha\chi,$$

$$H_{43} = \chi\left[-\alpha^2 - \beta^2 + r\frac{D\mu DT}{\mu T} + r\frac{D^2 T}{T} - i\frac{R}{\mu T}(\alpha U - \omega)\right],$$

$$H_{44} = -i\chi r\gamma M_e^2\left[\alpha DU + \left(\frac{DT}{T} + \frac{D\mu}{\mu}\right)(\alpha U - \omega)\right],$$

$$H_{45} = i\chi\left[r\alpha\frac{DU}{T} + \alpha\frac{\mu'DU}{\mu} + r\frac{D\mu}{\mu T}(\alpha U - \omega)\right],$$

$$H_{46} = i\chi\frac{r}{T}(\alpha U - \omega), \quad H_{47} = -i\beta\chi\left(r\frac{DT}{T} + 2\frac{D\mu}{\mu}\right), \quad H_{48} = -i\beta\chi;$$

$$H_{62} = -2\Pr(\gamma - 1)M_e^2 DU, \quad H_{63} = R\Pr\frac{DT}{\mu T} - 2i\alpha(\gamma - 1)M_e^2\Pr DU,$$

$$H_{64} = -iR\Pr\frac{(\gamma - 1)M_e^2}{\mu}(\alpha U - \omega),$$

$$H_{65} = \alpha^2 + \beta^2 + iR\Pr\frac{(\alpha U - \omega)}{\mu T} - (\gamma - 1)M_e^2\Pr\frac{\mu'(DU)^2}{\mu} - \frac{D^2\mu}{\mu}, \quad H_{66} = -2\frac{D\mu}{\mu};$$

$$H_{83} = -i\beta\left[(m+1)\frac{DT}{T} + \frac{D\mu}{\mu}\right], \quad H_{84} = i\frac{\beta R}{\mu} - (m+1)\gamma M_e^2\beta(\alpha U - \omega),$$

$$H_{85} = (m+1)\frac{\beta}{T}(\alpha U - \omega), \quad H_{87} = \alpha^2 + \beta^2 + i(\alpha U - \omega)\frac{R}{\mu T}, \quad H_{88} = -\frac{D\mu}{\mu}.$$

The vector $\boldsymbol{G} = \boldsymbol{H}_1\boldsymbol{F}_0$ in (4.18) is expressed as

$$\boldsymbol{F}_0 \equiv (f_1, f_2, \ldots, f_8)^T,$$
$$G_1 = G_5 = G_7 = 0,$$
$$G_2 = \frac{R}{\mu}\left[\frac{f_1}{T}\frac{\partial U}{\partial x_1} + \frac{V_0}{T}\frac{\partial f_1}{\partial y} + \left(\frac{\gamma M_e^2 f_4}{T} - \frac{f_5}{T^2}\right)\left(U\frac{\partial U}{\partial x_1} + V_0\frac{\partial U}{\partial y}\right)\right],$$

$$G_3 = \frac{f_1}{T}\frac{\partial T}{\partial x_1} + \gamma M_e^2 f_4 \frac{U}{T}\frac{\partial T}{\partial x_1} - f_5 \frac{2U}{T^2}\frac{\partial T}{\partial x_1} - \left(\gamma M_e^2 f_4 - \frac{f_5}{T}\right)\left(\frac{\partial U}{\partial x_1} + \frac{\partial V_0}{\partial y}\right)$$
$$- \gamma M_e^2 V_0 \left[\left(\frac{\partial f_4}{\partial y} - \frac{f_4}{T}\frac{\partial T}{\partial y}\right) - \frac{1}{T}\frac{\partial f_5}{\partial y} + \frac{2f_5}{T^2}\frac{\partial T}{\partial y}\right],$$

$$G_4 = -\frac{1}{T}\left(V_0 \frac{\partial f_3}{\partial y} + f_3 \frac{\partial V_0}{\partial y}\right),$$

$$G_6 = -\frac{RPr}{\mu}\left[-\frac{V_0}{T}\frac{\partial f_5}{\partial y} - \left(\frac{\gamma M_e^2 f_4}{T} - \frac{f_5}{T^2}\right)\left(U\frac{\partial T}{\partial x_1} + V_0 \frac{\partial T}{\partial y}\right)\right.$$
$$\left. + (\gamma - 1)M_e^2 \left(V_0 \frac{\partial f_4}{\partial y} - \frac{f_1}{T}\frac{\partial T}{\partial x_1}\right)\right],$$

$$G_8 = \frac{R}{\mu}\frac{V_0}{T}\frac{\partial f_7}{\partial y}.$$

REFERENCES

ALLARD, J.-F. & CHAMPOUX, Y. 1992 Empirical equations for sound propagation in rigid frame porous materials. *J. Acoust. Soc. Am.* **91**, 3346–3353.

ATTENBOROUGH, K. 1987 On the acoustic slow wave in air-filled granular media. *J. Acoust. Soc. Am.* **81**, 93–102.

BENADE, A. H. 1968 On the propagation of sound waves in a cylindrical conduit. *J. Acoust. Soc. Am.* **44**, 616–623.

CARPENTER, P. W. & PORTER, L. J. 2001 Effects of passive porous walls on boundary-layer stability. *AIAA J.* **39**, 597–604.

CHANG, C.-L., MALIK, M. R., ERLEBACHER, G. & HUSSAINI, M. Y. 1991 Compressible stability of growing boundary layers using parabolized stability equations. *AIAA Paper* 91-1636.

DANIELS, F. B. 1950 On the propagation of sound waves in a cylindrical conduit. *J. Acoust. Soc. Am.* **22**, 563–564.

DELANY, M. A. & BAZLEY, E. N. 1970 Acoustic properties of fibrous absorbent materials. *Appl. Acoust.* **3**, 105–116.

DEMETRIADES, A. 1974 Hypersonic viscous flow over a slender cone. Part III: Laminar instability and transition. *AIAA Paper* 74-535.

EL-HADY, N. M. 1980 On the stability of three-dimensional compressible nonparallel boundary layers. *AIAA Paper* 80-1374.

FEDOROV, A. V. & KHOKHLOV, A. P. 2002 Receptivity of hypersonic boundary layer to wall disturbances. *Theor. Comput. Fluid Dyn.* **15**, 231–254.

FEDOROV, A. V. & MALMUTH, N. D. 2001 Stabilization of hypersonic boundary layers by porous coatings. *AIAA J.* **39**, 605–610.

GAPONOV, S. A. 1971 Influence of porous layer on boundary layer stability. *Izv. SO AN SSSR Ser. Tekh. Nauk* **1**, 21–23 (in Russian).

GAPONOV, S. A. 1975 Influence of gas compressibility on stability of boundary layer on porous surface at subsonic speeds. *Zh. Prikl. Mekh. i Tekh. Fiz.* **1**, 121–125 (in Russian).

GAPONOV, S. A. 1977 Stability of supersonic boundary layer on porous wall with heat conductivity. *Izv. AN SSSR Mekh. Zhid. i Gaza* **1** (in Russian).

GAPONOV, S. A. 1980 Effect of nonparallel flow on propagation of disturbances in a supersonic boundary layer. *Izv. AN SSSR Mekh. Zhid. i Gaza* **2**, pp. 26–31 (in Russian).

GASTER, M. 1974 On the effects of boundary-layer growth on the flow stability. *J. Fluid Mech.* **66**, 465–480.

GRIGORIEV, V. D., KLEMENKOV, G. P., OMELAEV, A. I. & KHARITONOV, A. M. 1972 Hypersonic wind tunnel T-326. In *Aerofizicheskie Issledovania* (ed. A. M. Kharitonov), pp. 16–18. Novosibirsk (in Russian).

GUSHCHIN, V. R. & FEDOROV, A. V. 1989 Asymptotic analysis of inviscid perturbations in a supersonic boundary layer. *Zh. Prikl. Mekh. i Tekh. Fiz.* **1**, 69–75 (in Russian).

HAYES, W. D. & PROBSTEIN, R. F. 1959 *Hypersonic Flow Theory*. Academic.

JOHNSON, D. L., KOPLIK, J. & DASHEN, R. 1987 Theory of dynamic permeability and tortuosity in fluid saturated porous media. *J. Fluid Mech.* **176**, 379–402.

KENDALL, J. M. 1967 Supersonic boundary layer stability experiments. *Proc. of Transition Study Group Meeting*, vol. 2 (ed. W. D. McCauley). Aerospace Corp., San Bernardino, CA.

KENDALL, J. M. 1975 Wind tunnel experiments relating to supersonic and hypersonic boundary-layer transition. *AIAA J.* **13**, 290–299.

KIMMEL, R., DEMETRIADES, A. & DONALDSON, J. 1995 Space–time correlation measurements in a hypersonic transitional boundary layer. *AIAA paper* 95-2292.

KOSINOV, A. D., MASLOV, A. A. & SHEVELKOV, S. G. 1990 Experiments on the stability of supersonic laminar boundary layers. *J. Fluid Mech.* **219**, 621–633.

LECOUDIS, S. G. 1978 Stability of boundary layers over permeable surfaces. *AIAA Paper* 78-203.

LYSENKO, V. I. & MASLOV, A. A. 1984 The effect of cooling on supersonic boundary-layer stability. *J. Fluid Mech.* **147**, 38–52.

MACK, L. M. 1984 Boundary-layer stability theory. Special course on stability and transition of laminar flow (ed. R. Michel), *AGARD Rep.* **709**, pp. 3-1–3-81.

MALIK, M. R. 1989 Prediction and control of transition in supersonic and hypersonic boundary layers. *AIAA J.* **27**, 1487–1493.

MALIK, M. R., ZANG, T. A. & BUSHNELL, D. M. 1990 Boundary layer transition in hypersonic flows. *AIAA Paper* 90-5232.

MALMUTH, N. D., FEDOROV, A. V., SHALAEV, V., COLE, J. & KHOKHLOV, A. 1998 Problems in high speed flow prediction relevant to control. *AIAA Paper* 98-2695.

MASLOV, A. A., SHIPLYUK, A. N., SIDORENKO, A. A. & ARNAL, D. 2001 Leading-edge receptivity of a hypersonic boundary layer on a flat plate. *J. Fluid Mech.* **426**, 73–94.

PADHYE, A. R. & NAYFEH, A. H. 1979 Nonparallel stability of three-dimensional flows. *AIAA Paper* 79-1278.

RASHEED, A., HORNUNG, H. G., FEDOROV, A. V. & MALMUTH, N. D. 2002 Experiments on passive hypervelocity boundary layer control using an ultrasonically absorptive surface. *AIAA J.* **40**, 481–489.

RESHOTKO, E. 1969 Stability theory as a guide to the evaluation of transition data. *AIAA J.* **7**, 1086–1091.

RESHOTKO, E. 1994 Boundary layer instability, transition and control. *AIAA Paper* 94-0001.

STETSON, K. F. & KIMMEL, R. G. 1992a On hypersonic boundary-layer stability. *AIAA Paper* 92-0737.

STETSON, K. F. & KIMMEL, R. G. 1992b Example of second-mode instability dominance at a Mach number of 5.2. *AIAA J.* **30**, 2974–2976.

STETSON, K. F., THOMPSON, E. R., DONALDSON, J. C. & SILER, L. G. 1983 Laminar boundary layer stability experiments on a cone at Mach 8. Part 1: Sharp cone. *AIAA Paper* 83-1761.

TUMIN, A. M. & FEDOROV, A. V. 1982 On the weakly nonparallel effect on characteristics of flow stability. *Uchenye Zapiski TsAGI* **13**(6), 91–96 (in Russian).

ZHIGULEV, V. N. & TUMIN, A. M. 1987 *Onset of Turbulence*. Nauka, Novosibirsk (in Russian).

ZWIKKER, C. & KOSTEN, C. W. 1949 *Sound Absorbing Materials*. Elsevier.

Stability of Hypersonic Boundary Layer on Porous Wall with Regular Microstructure[‡]

A. Fedorov[*] and V. Kozlov[†]

Department of Aeromechanics and Flight Engineering, Moscow Institute of Physics and Technology, Zhukovski, 140180, Russia

A. Shiplyuk[‡], A. Maslov[§]

Institute of Theoretical and Applied Mechanics, Novosibirsk, 630090, Russia

and

N. Malmuth[**]

Rockwell Scientific Company, Thousand Oaks, California 91360, USA

Theoretical and experimental studies of hypersonic boundary layer stabilization using a passive porous coating of regular microstructure are discussed. Propagation of disturbances inside pores is simulated with linear acoustic theory including the gas rarefaction effect, which is associated with Knudsen layer on the pore wall. This model provides boundary conditions for stability analysis of boundary-layer disturbances on the porous wall. Experiments are conducted in the Mach 6 wind tunnel on a 7° half-angle sharp cone whose longitudinal half surface is solid and whose other half surface is covered by a perforated sheet comprising equally spaced cylindrical blind micro-holes. Hot-wire measurements of "natural" disturbances and artificially excited wave packets are conducted on both solid and porous surfaces. Natural disturbance spectra indicate that the second mode is a dominant instability. The porous coating stabilizes the second mode and weakly affects the first mode. Measurements of artificially excited wave packets show that the porous coating leads to substantial decreasing of the wave-packet growth. The experimental data on phase speeds and amplitudes of the second-mode disturbances are compared with theoretical predictions. Satisfactory agreement is obtained for both solid and porous surfaces. This study confirms the concept of hypersonic boundary-layer stabilization by passive porous coatings, which can be used for laminar flow control.

Nomenclature

A	=	disturbance amplitude
A_x, A_y, A_z	=	admittance components
A_n	=	thermal admittance
$\tilde{C}$	=	dynamic compressibility
f	=	frequency
F	=	$\omega^* \nu_e^* / U_e^{*2}$
h	=	porous layer thickness
l^*	=	$\sqrt{\nu_e^* L^* / U_e^*}$
Kn	=	Knudsen number

1

M	=	Mach number
p	=	pressure disturbance
P	=	mean pressure
Pr	=	Prandtl number
r_0	=	pore radius
Re_X	=	$U_e^* X / \nu_e^*$ local Reynolds number
Q	=	mass flux disturbance
T	=	temperature
u, v, w	=	velocity disturbance
U, V	=	mean-flow velocity components
x, y, z	=	Cartesian coordinates
X, Y, Z	=	hot wire coordinates
Z_0	=	characteristic impedance
α, β	=	wavenumber components
γ	=	specific heat ratio
ρ	=	density
$\tilde{\rho}$	=	dynamic density
Λ	=	propagation constant
μ	=	viscosity
ν	=	kinematic viscosity
σ	=	spatial growth rate
θ	=	temperature disturbance
ϕ	=	porosity
ω	=	angular frequency

Subscripts

e	=	upper boundary-layer edge
w	=	wall
∞	=	free stream
0	=	initial
LST	=	linear stability theory

I. Introduction

LAMINAR turbulent transition leads to substantial increase of the aerodynamic drag and surface heating of hypersonic vehicles.[1,2] The ability to increase the laminar run is of critical importance in design and optimization of aerospace planes. Aspects of hypersonic boundary-layer transition control are discussed in Ref. 3. Smoothing and shaping of the vehicle surface help to avoid early transition due to roughness, leading-edge contamination as well as cross-flow and Görtler instabilities. However, with these measures the laminar run may be still short because of the first and/or second mode instability.[4,5] The wall cooling, which naturally occurs on hypersonic vehicle surfaces, strongly stabilizes the first mode[6] while destabilizes the second mode.[7] This indicates that hypersonic laminar flow control concepts should address the second-mode instability.

The second mode is associated with instability of trapped acoustic waves of relatively high frequency.[4] Malmuth et al.[8] assumed that a passive ultrasonically absorptive porous coating (UAC) may stabilize the second mode and, at the same time, may be aerodynamically smooth. This hypothesis was confirmed by the linear stability analyses,[8,9] which showed that the porous coating causes a massive reduction of the second-mode growth rate. The theoretical predictions were qualitatively confirmed by the experiments[10,11] conducted in the high-enthalpy GALCIT T-5 shock tunnel of California Institute of Technology on a sharp cone at the freestream Mach number $4.59 \leq M_\infty \leq 6.4$.

However, quantitative comparison was not feasible because stability characteristics of the boundary-layer disturbances were not measured. This motivated us to perform a series of stability experiments on cones covered by porous coatings of various microstructures. Further theoretical research was also needed to address randomly porous coatings as well as to account for rarefied gas effects occurring in pores of small size.

The first series of stability experiments was conducted in the T-326 Mach 6 wind tunnel of the Institute Theoretical of Applied Mechanics (ITAM, Novosibirsk, Russia) on a $7°$ half-angle sharp cone whose longitudinal half surface was solid and other half surface was covered by a thin porous coating of random structure, namely, a fibrous absorbent material (felt metal).[12,13] Hot-wire measurements of "natural" disturbances and artificially excited

wave packets were performed on both solid and porous surfaces. Stability analyses for two- and three-dimensional disturbances showed that the porous coating stabilizes the second mode and marginally destabilizes the first mode. These results are in qualitative agreement with the experimental data for natural disturbances. The theoretical predictions are in good quantitative agreement with stability measurements for artificially excited wave packets associated with the second mode. [12,13]

In this paper, we discuss the second series of stability experiments and calculations, which has been performed for the UAC of regular microstructure similar to that tested in the GALCIT T-5 shock tunnel.[10,11]

II. Theoretical Modeling

In this section, we formulate the linear stability problem on a porous wall and discuss the disturbance dynamics inside micropores with emphasis on rarefied gas effects associated with Knudsen layer on the pore wall.

A. Linear Stability Problem

Consider a supersonic laminar boundary layer on a sharp cone at zero angle of attack. The fluid is a perfect gas with constant Prandtl number Pr and specific heat ratio γ. Viscosity μ is a function of temperature given by Sutherland's formula. The Cartesian coordinates (x, y, z) are made nondimensional using the boundary-layer scale $l^* = \sqrt{\nu_e^* L^* / U_e^*}$, where the distance L^* from the leading edge is assumed to be much larger than l^*; i.e., the ratio $\varepsilon = l^* / L^*$ is treated as a small parameter. Time t and pressure P are referenced to l^* / U_e^* and $\rho_e^* U_e^{*2}$ respectively; other flow characteristics are made nondimensional using their quantities at the upper boundary-layer edge. Introducing the slow variable, $x_1 = x^* / L^* = \varepsilon x$, we specify the mean-flow velocity components (U, V) and temperature T as

$$(U, V) = (U(x_1, y), \varepsilon V_0(x_1, y)), T = T(x_1, y).$$ (1)

A three-dimensional monochromatic disturbance is represented by the vector function

$$\mathbf{Z} = (u, \frac{\partial u}{\partial y}, v, p, \theta, \frac{\partial \theta}{\partial y}, w, \frac{\partial w}{\partial y})^T,$$ (2)

$$\mathbf{Z}(x, y, z, t) = \mathbf{F}(x, y) \exp(i\beta z - i\omega t),$$

where u, v, w, p and θ are velocity components, pressure and temperature; $\beta = \beta^* l^*$ and $\omega = \omega^* l^* / U_e^*$. The amplitude vector-function $\mathbf{F}(x, y)$ satisfies a system of partial differential equations that resulted from Fourier transform of the linearized Navier-Stokes equations with respect to time and z-coordinate. These equations with the boundary conditions are written in the matrix-operator form[12,13]

$$\mathbf{H}(y, \partial_y; x_1, \varepsilon\partial_{x_1}, \omega, \beta)\mathbf{F} = 0,$$ (3)

$$y = 0: F_1 = A_x F_4, F_3 = A_y F_4, F_5 = A_\theta F_4, F_7 = A_z F_4,$$

$$y \to \infty: F_1, F_3, F_5, F_7 \to 0.$$

Here the admittance components A_x, A_y, A_z and the thermal admittance A_θ are complex quantities, which couple velocity and temperature disturbances with the pressure disturbance on the porous surface. The admittances depend on properties of the porous material, mean flow characteristics on the wall surface, and disturbance frequency. These dependencies are specified in Section B. For the solid wall $A_x = A_y = A_z = A_\theta = 0$, which corresponds to no-slip conditions and zero temperature perturbation on the surface of high thermal conductivity.

We consider a partial solution of Eq. (3), which is a discrete mode of the complex eigenvalue $\alpha(x_1, \beta, \omega)$; this may be the first or second mode. The amplitude vector-function is expressed as

$$\mathbf{F} = (\mathbf{F}_0 + \varepsilon\mathbf{F}_1 + ...) \exp(S),$$ (4)

$$S = i\varepsilon^{-1} \int \alpha(x_1) dx_1.$$

According to the analysis of Refs. 12,13 the amplitude vector-function is

$$\mathbf{F}_0 = c(x_1)\zeta(x_1, y, \alpha),$$ (5)

3

where ζ is eigenfunction of the local-parallel stability problem

$$\left(\frac{\partial}{\partial y} - \mathbf{H}_0\right)\zeta = 0,\tag{6}$$

$$y = 0: \ \zeta_1 = A_x\zeta_4, \ \zeta_3 = A_y\zeta_4, \ \zeta_5 = A_\theta\zeta_4, \ \zeta_7 = A_z\zeta_4,$$

$$y \to \infty: \ \zeta_1, \zeta_3, \zeta_5, \zeta_7 \to 0.$$

The 8×8 matrix $\mathbf{H}_0$ is given in Appendix of Refs. 12,13. The amplitude coefficient $c(x_1)$ is resulted from analysis of the next-order problem for $\mathbf{F}_1$. The mass-flow disturbance Q, which is measured in experiments, is calculated as [12,13]

$$Q(x_1, y) = c_0 q(x_1, y)\exp[S(x_1)],\tag{7}$$

$$S(x_1) = i\varepsilon^{-1}\int[\alpha(x_1) + \varepsilon W(x_1) + O(\varepsilon^2)]dx_1,$$

$$q = [\zeta_1 + (\gamma M_e^2\zeta_4 - \zeta_5/T)U]/T,$$

where c_0 is constant; $W(x_1)$ is relevant to the nonparallel effect. The spatial growth rate σ is the logarithmic derivative of Eq. (7) with respect to x

$$\sigma \equiv \frac{1}{|Q|}\frac{\partial|Q|}{\partial x} = -\operatorname{Im}\alpha + \varepsilon\left(\frac{\partial\ln|q|}{\partial x_1} - \operatorname{Im}W\right) + O(\varepsilon^2).\tag{8}$$

Due to the nonparallel effect the growth rate depends on the vertical coordinate y. In accordance with experimental measurements, $\sigma(x_1, y)$ is calculated at $y = y_m$ relevant to the maximum of mass-flow disturbance in the boundary layer.

B. Admittance of Porous Layer

Consider a porous layer of thickness h^* with equally spaced cylindrical blind holes of the radius r_0^*, as schematically shown in Fig. 1. The spacing s^* between holes is assumed to be much smaller than the boundary-layer displacement thickness. Mean perturbations of longitudinal and transverse velocities induced by the pores are neglected. As shown in Refs. 9,12,13, the admittances A_x, A_z and A_θ produce small effects on the boundary-layer instability, compared to the effect of A_y. This allows us to approximate the wall boundary conditions as

$$\zeta_1(0) = \zeta_5(0) = \zeta_7(0) = 0, \ \zeta_3(0) = A_y\zeta_4(0).\tag{9}$$

The admittance component A_y is expressed in the form [9]

$$A_y = -\frac{\phi}{Z_0}\tanh(\Lambda h),\tag{10}$$

where ϕ is porosity, $h = h^*/l^*$ is the porous-layer thickness, Z_0 and Λ are the characteristic impedance and propagation constant of a porous medium, respectively. The two latter are functions of the complex dynamic density $\tilde{\rho}$ and the complex dynamic compressibility $\tilde{C}$

$$Z_0 = \frac{\sqrt{\tilde{\rho}/\tilde{C}}}{M_e\sqrt{T_w}}, \ \Lambda = \frac{i\omega M_e}{\sqrt{T_w}}\sqrt{\tilde{\rho}\tilde{C}}.\tag{11}$$

The porous-media characteristics $\tilde{\rho}$ and $\tilde{C}$ are solutions of the problem related to propagation of disturbances within an isolated cylindrical pore. This problem was solved in Refs. 14,15. Its solutions are widely used for analyses of acoustic disturbances in wave-guides and perforated panels. They serve as a basis for the semi-empirical models[16-22] predicting absorption of sound in porous media of random microstructures. However, these solutions cannot be directly applied to low ambient pressures at which the gas rarefaction is essential.

4

Hereafter we consider the case when the most part of the pore interior may be treated as a continuum medium. The rarefaction effects are appreciable near the pore wall in Knudsen layer of thickness ~ the molecular mean free path λ^*. They revile themselves as slip and temperature jump on the pore surface. Detailed reviews of this phenomenon and its modeling for stationary flows are presented in Refs. 23-25.

Disturbances of velocity v^* and temperature θ^* within an infinitely long circular tube, which typifies an isolated cylindrical pore, are governed by the linearized Navier-Stokes equations. A fundamental solution of these equations is expressed in terms of the Bessel function of first kind

$$v^* = \frac{1}{i\omega^* \rho_w^*} \frac{d\hat{p}^*}{dy^*} \left[1 - D_1 J_0(\varsigma r) \right] \exp(-i\omega^* t^*), \tag{12}$$

$$\theta^* = \frac{\hat{p}^*}{\rho_w^* C_p^*} \left[1 - D_2 J_0(\varsigma r \sqrt{\mathrm{Pr}}) \right] \exp(-i\omega^* t^*), \tag{13}$$

where D_1 and D_2 are constants; the y-axis is directed along the pore axis; r is radius referenced to r_0^*; C_p^* is specific heat capacity under constant pressure; $\hat{p}^*$ is amplitude of pressure disturbance; $\varsigma = \sqrt{i\omega^* \rho_w^* r_0^{*2} / \mu_w^*}$ is the complex ratio of the pore radius to the viscous-layer thickness $\delta_{vis}^* = \sqrt{\mu_w^* / \omega^* \rho_w^*}$; ρ_w^* is gas density; subscript "w" denotes gas characteristics within the pore.

The boundary conditions on the pore wall are approximated as[23]

$$v_g^* = -B_v \left(\frac{\partial v^*}{\partial r} \right)_w, \quad \theta_g^* = -B_E \left(\frac{\partial \theta^*}{\partial r} \right)_w, \tag{14}$$

where v_g^* and θ_g^* are disturbances of velocity and temperature on the solid surface; the dimensionless factors $B_v = (\alpha_v^{-1} - 0.5)\mathrm{Kn}$ and $B_E = \left[2\gamma \left(\alpha_E^{-1} - 0.5 \right) / (\gamma + 1)\mathrm{Pr} \right]\mathrm{Kn}$ depend on the molecular tangential impulse, α_v, and energy, α_E, accommodation coefficients as well as the Knudsen number $\mathrm{Kn} = \lambda^* / r_0^*$. In turn, α_v and α_E depend on interaction of gas molecules with the solid surface. Usually, they are determined experimentally. In the framework of elementary kinetic theory (see, for example, Ref. 23), the Knudsen number is expressed as $\mathrm{Kn} = 4\mu_w^* / (\rho_w^* \bar{c}^* r_0^*)$, where $\bar{c}^* = \sqrt{8R_g T_w^* / \pi}$ is the mean module of molecular velocity vector, R_g is gas constant per unit mass. The pore surface temperature T_w^* is assumed to be constant. With the boundary conditions (14) the constants of integration in Eqs. (12), (13) are

$$D_1 = \frac{1}{J_0(\varsigma)\left[1 - 0.5B_v \varsigma^2 Q(\varsigma) \right]}, \tag{15}$$

$$D_2 = \frac{1}{J_0(\varsigma \sqrt{\mathrm{Pr}})\left[1 - 0.5B_E (\varsigma \sqrt{\mathrm{Pr}})^2 Q(\varsigma \sqrt{\mathrm{Pr}}) \right]},$$

where $Q(\xi) = 2J_1(\xi) / [\xi J_0(\xi)]$. The relations (15) differ from the case of continuum media due to the presence of the factors $\left[1 - 0.5B_E (\varsigma \sqrt{\mathrm{Pr}})^2 Q(\varsigma \sqrt{\mathrm{Pr}}) \right]^{-1}$ and $\left[1 - 0.5B_v \varsigma^2 Q(\varsigma) \right]^{-1}$, which depend on the ratio $\lambda^* / \delta_{vis}^*$. They are valid for $\mathrm{Kn}|\varsigma| \ll 1$ if $|\varsigma| \sim 1$, and for $\mathrm{Kn} \ll 1$ if $|\varsigma| < 1$. The latter case corresponds to disturbances of relatively low frequency, when the viscous-layer thickness is $\delta_{vis}^* > r_0^*$.

Substituting Eq. (15) into Eqs. (12), (13) we average v^* and θ^* over the pore cross-section as $\langle f \rangle = 2 \int_0^1 f(r) r \, dr$. Using the general relations for the average characteristics (see, for example, Ref. 16)

$$i\omega^* \hat{\rho}^*(\omega^*) \langle \hat{v}(y^*) \rangle = \frac{d\hat{p}^*}{dy^*}, \tag{16}$$

$$\hat{C}^*(\omega^*) \equiv \frac{\langle \hat{\rho}^* \rangle}{\rho_w^* \hat{p}^*} = \frac{1}{P_w^*} - \frac{\langle \hat{\theta}^* \rangle}{T_w^* \hat{p}^*}, \tag{17}$$

we express the dimensionless dynamic density $\tilde{\rho}$ and the dynamic compressibility $\tilde{C}$ of Eq. (11) in the form

5

$$\tilde{\rho} \equiv \frac{\tilde{\rho}^*}{\rho_w^*} = \frac{1}{1 - F(B_v, \varsigma)}, \tag{18}$$

$$\tilde{C} \equiv \gamma P_w^* \hat{C}^* = 1 + (\gamma - 1)F\left(B_E, \varsigma\sqrt{\mathrm{Pr}}\right), \tag{19}$$

where

$$F(B_v, \varsigma) = \frac{Q(\varsigma)}{1 - 0.5 B_v \varsigma^2 Q(\varsigma)}, \tag{20}$$

$$F\left(B_E, \varsigma\sqrt{\mathrm{Pr}}\right) = \frac{Q(\varsigma\sqrt{\mathrm{Pr}})}{1 - 0.5 B_E (\varsigma\sqrt{\mathrm{Pr}})^2 Q(\varsigma\sqrt{\mathrm{Pr}})}. \tag{21}$$

The relations (18)-(21) coincide with the known relations for $\mathrm{Kn} = 0$ (see, for example, Ref. 16). The latter were used for modeling of the UAC admittance A_y in Ref. 9.

Parametric calculations show that the rarefaction effect leads to increasing of the pore admittance that, in turn, enhances the UAC performance. As an example, Figure 2 shows the second-mode maximum growth rate, $\sigma_{max} = \max \sigma(\omega)$, as a function of the longitudinal coordinate for the boundary layer at $M_e = 5.3$, $T_e = 56.4$ K, the local unit Reynolds number $\mathrm{Re}_{e1} \equiv U_e^* / \nu_e^* = 2 \times 10^7$ m^{-1} and the wall temperature $T_w = T_{ad}$. Stability calculations are conducted using the locally parallel theory; i.e., the second term in Eq. (8) is neglected. The UAC characteristics are: $r_0^* = 25$ μm, $s^* = 100$ μm, the porous-layer thickness $h^* \gg r_0^*$, the accommodation coefficients $\alpha_v = \alpha_E = 1$. At these parameters, which are typical for the wind-tunnel experiment discussed in Section III, the Knudsen number is $\mathrm{Kn} \approx 0.4$. The second-mode stabilization, predicted at this Knudsen number (dotted line), is essentially stronger than in the case of $\mathrm{Kn} = 0$ (dashed line).

III.   Experimental Setup and Instrumentation

Experiments are conducted in the hypersonic blow-down wind tunnel T-326 with open-jet test section at ITAM.[26] The diameter of the axisymmetric contoured nozzle is 200 mm. The Mach number in the flow core is M_x=5.95. The noise level is $\approx 1\%$, which is typical for conventional hypersonic wind tunnels. During the experiments, the total pressure, $P_0 = 10^3$ kPa, and the stagnation temperature, $T_0 = 385 - 400$ K, in the settling chamber are kept constant with accuracy 0.06% and 0.25%, respectively. The freestream unit Reynolds number is $\mathrm{Re}_{1\infty} = (11.5 - 12.3) \times 10^6$ m^{-1}; the wall-temperature ratio, $T_w / T_0 = 0.80 - 0.84$, approximately corresponds to the adiabatic wall.

The model is a $7°$ half-angle sharp cone of 500 mm length (see Fig. 3) consisting four parts: the sharp nose of 65 mm length and 0.1 mm tip radius; the middle part of 65 mm length with an electric glow-discharge actuator; the base part of 370 mm length; a unit providing turning of the cone around its axis. The solid surface roughness is approximately 0.5 μm. The cone is installed at zero angle of attack with accuracy 0.05°.

A longitudinal half of the base part is covered by the stainless steel perforated sheet, which has equally spaced cylindrical holes of depth $h^* = 450$ μm and the average spacing $s^* = 100 \pm 4$ μm. The average hole diameter is $d^* = 50 \pm 6$ μm on the face side and $d^* = 64 \pm 6$ μm on the back side (see Figs. 4a,b); i.e., holes are slightly conical with taper angle $\approx 0.9°$. The perforated sheet is flash mounted on the cone surface. With the help of a custom-built tension mechanism the sheet is tightly tensed onto the model to avoid cavities underneath the porous coating. The UAC leading edge is located at the distance $X = 182$ mm from the cone tip.

The model is equipped with a three-dimensional actuator providing a high-frequency glow discharge in a small chamber. Artificial disturbances generated by the actuator are introduced into the boundary layer through an orifice of 0.4 mm diameter located at the distance of 69 mm from the cone tip.

The actuator, instrumentation and measuring system are the same as in the experiment with the porous coating of random microstructure.[12,13] A constant-current hot-wire anemometer is used to measure mass-flow fluctuations. Details of hot-wire probes and processing techniques are given in Refs. 12,13,27.

The amplitude A and phase Φ of disturbances are obtained using the discrete Fourier transformation

$$A(X, Y, \Theta)e^{i\Phi(X, Y, \Theta)} = \frac{2}{N} \sum_{j=1}^{N} \rho U_n(X, Y, \Theta, t_j)e^{-i\omega t_j}, \tag{22}$$

where N is the samples count in the time-series, $\rho U_n(X,Y,\Theta,t_j)$ is the time-series of mass-flow pulsations; Θ is circumferential angle in the cone cross section.

To compare the experimental and theoretical data, the artificially excited wave packet is decomposed to waves. The transversal wave spectra are calculated as

$$SA(x,\beta)e^{iSF(x,\beta)} = \int_{-\theta_0}^{\theta_0} A(x,\Theta)e^{i\Phi(x,\Theta)}e^{-i\beta\Theta}d\Theta , \qquad (23)$$

where SA, SF – are the amplitude and phase spectra with respect to the transversal wave number β measured in rad/deg.

IV.   Experimental Results

Hot-wire measurements of mean profiles and root-mean-square pulsations of $\rho^*U^* / \rho_e^*U_e^*$ at the stations X=138-287 mm show that the boundary layer is laminar on the solid and porous sides; i.e., roughness of the porous coating does not cause premature tripping of the boundary-layer flow.

A. Natural Disturbances

Spectra of maximum (versus the vertical coordinate Y) mass-flow disturbances are measured at equally spaced X-stations. The first three stations are located upstream from the UAC leading edge. The disturbance spectra $A(f)$ are shown in Figs. 5a,b. for the solid and porous sides, respectively. At the first three stations, the spectra practically coincide on both sides. Downstream from the UAC leading edge, spectrum behaviors are quite different:

On the solid side, spectra look very similar to those reported in Ref. 28 for a sharp cone at $M_\infty = 8$; they indicate that the second-mode instability is dominant. At the first upstream station, the second mode is observed at frequencies $\approx$ 430-450 kHz. Its amplitude quickly increases downstream, whereas its central frequency decreases to 270 kHz at the last station. In the middle of the measurement region ($\mathrm{Re}_{eX} \approx 3.42 \times 10^6$), the second mode becomes lager than the first mode associated with the frequency band 50-200 kHz; *i.e.*, the first mode grows slower than the second mode. Measurements at the last downstream station (on both solid and porous sides) indicate the beginning of boundary-layer turbulization.

On the porous side, the second mode grows quickly in the first three stations located upstream from UAC. Further downstream this growth is slowed down due to the presence of the porous coating. Over the entire measurement region, the second-mode amplitudes are smaller than the first-mode ones.

To evaluate the downstream growth of boundary-layer disturbances, the spectra $A(f)$ are referenced to the initial spectrum $A_0(f)$ measured at the first X-station. These normalized spectra A / A_0 are shown in Figs. 6a,b for the solid and porous sides respectively. The first-mode disturbances have nearly equal growth on the both sides; *i.e.*, the porous coating weakly affects the first-mode instability. Maximum amplifications are observed in the range 100–130 kHz; they are 3.3 and 3.6 for solid and porous sides, respectively. The second-mode disturbances grow faster than the first-mode disturbances. Their maximum amplifications are 6.9 and 20.4 on the porous and solid sides, respectively; *i.e.*, the UAC effectively stabilizes the second mode.

B. Artificial Wave Packets

Artificial disturbances are generated in the boundary layer at frequency 275 kHz, which is relevant to the maximum amplitude of the second mode, measured on the solid side under natural conditions (see Fig. 5a) Figure 7 shows transversal distributions of the amplitude at various Re_{eX}. They are nearly symmetric and similar to each other in all cross sections. The amplitudes are maximal at the wave-packet center indicating that the two-dimensional wave component is dominant. The phase distributions are very flat and give nearly constant phase speeds $C_X \equiv C_X^* / U_e^*$ shown in Fig. 8.

Figure 9 shows the amplitude wave spectra with respect to the transversal wave number β. The wave packets lie within the range $\beta = \pm 0.5$ rad/deg corresponding to the range of the wave-vector inclination $\pm 20°$. The amplitude maximums are observed at β=0. These features indicate that the dominant component of the artificially excited wave packets is two-dimensional.

Amplitudes of natural and artificial disturbances of 275 kHz are shown by symbols in Fig. 10. On the porous side, these amplitudes practically coincide (compare circles and squares); *i.e.*, natural disturbances of this frequency are predominantly two-dimensional waves of the second mode. It is clearly seen that the UAC leads to substantial

decreasing of the amplitude growth: the maximum amplitude on the porous side (circles and squares) is approximately 3 times smaller than that on the solid side (triangles).

V.   Comparison with Linear Stability Theory

Stability calculations are conducted for two-dimensional disturbances ($\beta = 0$) of the second mode at flow parameters relevant to the experiment. Namely: the local Mach number $M_e = 5.325$; the wall temperature $T_w^* = 320$ K corresponds to the wall temperature ratio $T_w^* / T_e^* = 5.471$; $\gamma = 1.4$ and $\mathrm{Pr} = 0.708$. The local unit Reynolds number is $\mathrm{Re}_{1e} = 15.2 \times 10^6$ m^{-1}; the disturbance frequency $f = 275$ kHz corresponds to the frequency parameter $F = 1.393 \times 10^{-4}$.

The spatial growth rate is calculated with the relation (8) including the nonparallel effect. For the porous wall, stability calculations are conducted using the boundary conditions (9), in which the admittance is given by Eqs. (10), (11) with the dynamic density (18) and compressibility (19). The UAC parameters are specified as: $r_0^* = 25$ μm, $s^* = 100$ μm, the porosity $\phi = 0.2$, the porous-layer thickness $h^* = 450$ μm.

Figure 102 compares theoretical amplification curves (solid lines) with the experimental data (symbols). In these calculations, the amplitudes are adjusted to the experimental values at the initial X-station. The theory agrees well with the experiment on the solid side (compare the solid line with triangles). The amplification curve calculated for the porous surface (dashed line) lies above the experimental points (red triangles and blue squares); $i.e.$, the theory underestimates the UAC stabilization effect. Assuming that this discrepancy is due to the conical shape of actual pores, we calculated the amplification curve for the pore radius averaged over the pore length ($r_0^* = 28.5$ μm). With this correction the agreement of theory (dashed-dotted line in Fig. 10) with the experiment is satisfactory.

Another reason of discrepancy between theory and experiment may be due to nonlinear effects, which decrease the second-mode amplification. As mentioned in Section A, the nonlinear breakdown of natural disturbances is observed at the last X-station. Since amplitudes of artificially excited wave packets are significantly larger than those of natural disturbances, the nonlinear effect may be exposed earlier. This assumption is consistent with decreasing of the disturbance amplitude at the last station (see the right square in Fig. 10).

As shown in Figure 8, the theoretical phase speeds agree well with the experimental data for artificially excited wave packets on both solid and porous sides of the cone.

VI.   Summary

Experimental and theoretical studies of hypersonic boundary-layer stabilization using a passive porous coating of regular microstructure were conducted in order to evaluate the UAC performance for further applications to hypersonic laminar-flow control.

Linear stability problem for disturbances in the boundary layer on a porous wall was formulated using the asymptotic method of multiple scales. This problem differs from the typical stability problem because of new boundary conditions associated with absorption of disturbance energy by the porous coating. The boundary conditions are formulated in terms of the porous-layer acoustic admittances, which depend on the UAC microstructure. Acoustic properties of cylindrical pores were analyzed in the framework of linear acoustic theory including gas rarefaction effects. This analysis is focused on the most practical case when the molecular mean free path is smaller (or much smaller) than the pore radius.

Stability experiments were carried out on a 7° half-angle sharp cone with a longitudinal half of its surface solid and the other a porous sheet perforated with equally spaced cylindrical blind microholes. The cone was tested at zero angle of attack in hypersonic free stream of Mach number 5.95. Hot-wire measurements were conducted in the boundary layer on the porous and solid sides of the cone. Spectra of natural and artificially excited wave packets were obtained at various cross sections of the cone.

Measurements of mean profiles and root-mean-square pulsations of the mass flow showed that the boundary layer was laminar on the solid and porous sides; $i.e.$, the coating roughness did not cause premature transition.

Under natural conditions, the first (low frequency) and second (high frequency) modes were observed in the boundary layer. Analysis of natural-disturbance spectra showed that the second mode was dominant on the solid side. The porous coating stabilizes the second mode and weakly affects the first mode that is consistent with the theoretical predictions.[12,13]

To evaluate the UAC stabilization effect, the wave packets were artificially exited at the frequency relevant to the second-mode instability. It was found that the two-dimensional wave is a dominant component of the wave packets. The amplification of this component practically coincides with the amplification of natural disturbance of the same frequency. This indicates that natural disturbances of high-frequency band are predominantly two-dimensional waves of the second mode. It was shown that the UAC leads to substantial decreasing of the wave-

packet growth: the maximum amplitude on the porous side is approximately 3 times lower than that on the solid side.

Stability calculations were conducted for the second mode and compared with the experimental data. The theoretical amplification curve agrees well with the experiment on the solid side. In the case of the porous wall, the theory underestimates the UAC stabilization effect. With the correction accounting for conical shape of actual pores, the agreement is satisfactory.

In summary, the present theoretical and experimental results confirm the concept of hypersonic boundary-layer stabilization by passive porous coatings. The following issues remain to be addressed in future:

1) The wall temperatures of actual hypersonic vehicles are substantially lower than the adiabatic wall temperature. Stability calculations[9,12,13] showed that the UAC performance dramatically increases as the wall temperature ratio decreases. These theoretical predictions need to be verified by stability experiments on the model with cooled wall.

2) Roughness of the porous coating may lead to premature tripping of the boundary layer. Detailed studies of this detrimental effect will help to formulate criteria for the pore size and spacing.

3) It needs to be shown that the second-mode stabilization leads to the increase of laminar run. At present, we have only indirect experimental evidence in favor of this connection. Namely, the experiments[10,11] in the GALCIT T-5 shock tunnel showed significant increase of the transition Reynolds number on the porous surface. Further experimental studies are needed to clarify this issue.

4) Refinements of the theoretical model are also needed to address the pore end effects and treat disturbance absorption by coatings of complex microstructures.

Acknowledgments

References

[1]Lin, T.C., Grabowsky, W.R., and Yelmgren, K.E., "The Search for Optimum Configurations for Re-Entry Vehicles," *J. Spacecraft and Rockets*, Vol. 21, No. 2, 1984, pp. 142-149.

[2]Tartabini, P.V., Lepsch, R.A., Korte, J.J., and Wurster, K.E., "A Multidisciplinary Performance Analysis of a Lifting-Body Single-Stage-to-Orbit Vehicle," AIAA Paper No. 2000-1045, Jan. 10-13, 2000.

[3]Kimmel, R., "Aspects of Hypersonic Boundary Layer Transition Control," AIAA Paper No. 2003-0772, Reno NV, Jan. 6-9, 2003.

[4]Mack, L.M., "Boundary-Layer Stability Theory," *Special Course on Stability and Transition of Laminar Flow*, edited by R. Michel, AGARD Rep. No. 709, 1984, pp. 3-1 to 3-81.

[5]Malik, M.R., Zang, T.A., and Bushnell, D.M., "Boundary Layer Transition in Hypersonic Flows," AIAA Paper No. 90-5232, 1990.

[6]Lysenko, V.I., and Maslov, A.A., "The Effect of Cooling on Supersonic Boundary-Layer Stability," *J. Fluid Mech.*, Vol. 147, 1984, pp. 38-52.

[7]Malik, M.R., "Prediction and Control of Transition in Supersonic and Hypersonic Boundary layers," *AIAA Journal*, Vol. 27, No. 11, 1989.

[8]Malmuth, N.D., Fedorov, A.V., Shalaev, V., Cole, J., and Khokhlov, A., "Problems in High Speed Flow Prediction Relevant to Control," AIAA Paper No. 98-2695, 1998.

[9]Fedorov, A. V., Malmuth, N. D., Rasheed, A., Hornung, H.G., "Stabilization of Hypersonic Boundary Layers by Porous Coatings," *AIAA Journal*, Vol. 39, No. 4, 2001, pp. 605-610.

[10]Rasheed, A., Hornung, H.G., Fedorov, A.V., and Malmuth, N.D., "Experiments on Passive Hypervelocity Boundary Layer Control Using a Porous Surface," AIAA Paper No. 2001-0274, 2001.

[11]Rasheed, A., Hornung, H.G., Fedorov, A.V., and Malmuth, N.D., "Experiments on Passive Hypervelocity Boundary Layer Control Using a Ultrasonically Absorptive Surface," *AIAA Journal*, Vol. 40, No. 3, 2002, pp. 481-489.

[12]Fedorov A., Shiplyuk, A., Maslov, A., Burov, E., and Malmuth, N., "Stabilization of High Speed Boundary Layer Using a Porous Coating," AIAA Paper No. 2003-1270, Reno NV, Jan. 6-9, 2003.

[13]Fedorov, A., Shiplyuk, A., Maslov, A., Burov, E., and Malmuth, N., "Stabilization of a Hypersonic Boundary Layer Using an Ultrasonically Absorptive Coating," *Journal of Fluid Mechanics*, Vol. 479, 2003, pp. 99-124.

[14]Kirchoff, G., "Über den Einfluss der Wärmeleitung in einem Gase auf die Schallbewegung," *Poggendorfer Annalen*, Vol. 134, 1868, pp. 177-193.

[15]Strutt, J. (Lord Rayleigh), *Theory of Sound*, Vol. 2, Dover, 1894.

[16]Zwikker, C., and Kosten, C. W., *Sound Absorbing Materials*. Elsevier, New York, 1949.

[17]Biot, M.A., "Theory of Propagation of Elastic Waves in a Fluid-Saturated Porous Solid. Part I. Low-Frequency Range," *J. Acoust. Soc. Am.*, Vol. 28, No. 1, 1956, pp. 168-178.

[18]Biot, M.A., "Theory of Propagation of Elastic Waves in a Fluid-Saturated Porous Solid. Part 2. High-Frequency Range," Vol. 28, No. 2, 1956, pp. 179-191.

[19]Delany, M.A., and Bazley, E.N., "Acoustic Properties of Fibrous Absorbent Materials," *Appl. Acoust.*, Vol. 3, pp. 105-116, 1970.

[20]Attenborough, K., "On the acoustic slow wave in air-filled granular media," *J. Acoust. Soc. Am.*, Vol. 81, No. 1, 1987, pp. 93-102.

[21]Johnson, D.L., Koplik, J., Dashen, R., "Theory of Dynamic Permeability and Tortuosity in Fluid Saturated Porous Media," *J. Fluid Mech.*, Vol. 176, pp. 379-402, 1987.

[22]Allard, J.-F., and Champoux, Y., "Empirical Equations for Sound Propagation in Rigid Frame Porous Materials," *J. Acoust. Soc. Am.*, Vol. 91, No. 6, 1992, pp. 3346-3353.

[23]Goodman, F. O., and Wachman, H. Y., *Dynamic of Gas-Surface Scattering*, Academic Press, N.-Y., 1976.

[24]Patterson, G. N., *Molecular Flow of Gases*, John Wiley & Sons. Inc., New York, Chapmen & Hall, Lmtd, London, 1956.

[25]Shidlovsky V. P., *The Introduction into Rarefied Gas Dynamics*. Nauka, Moscow, 1965 (in Russian).

[26]Grigoriev, V.D., Klemenkov, G.P., Omelaev, A.I., and Kharitonov, A.M., "Hypersonic Wind Tunnel T-326," In: *Aerofizicheskie Issledovania*, ed. A.M. Kharitonov, Novosibirsk, 1972, pp. 16–18. (in Russian).

[27]Maslov, A.A., Shiplyuk, A.N., Sidorenko, A.A., and Arnal, D., "Leading-Edge Receptivity of a Hypersonic Boundary Layer on a Flat Plate," *J. Fluid Mech.*, Vol. 426, 2001, pp. 73-94.

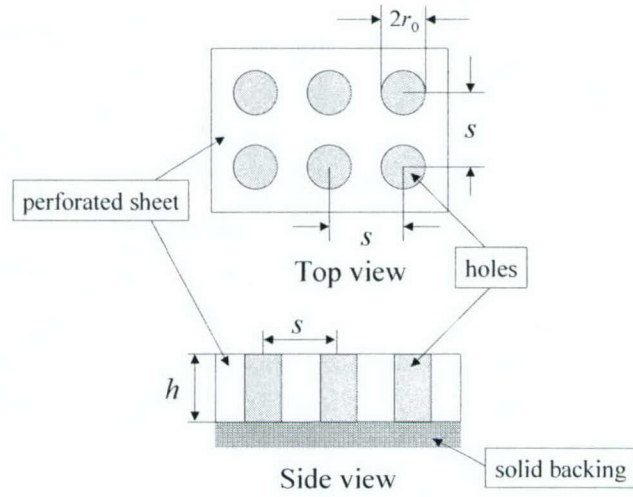[28]Stetson, K.F., and Kimmel, R.G., "On Hypersonic Boundary-Layer Stability," *AIAA Paper* No. 92-0737, 1992.

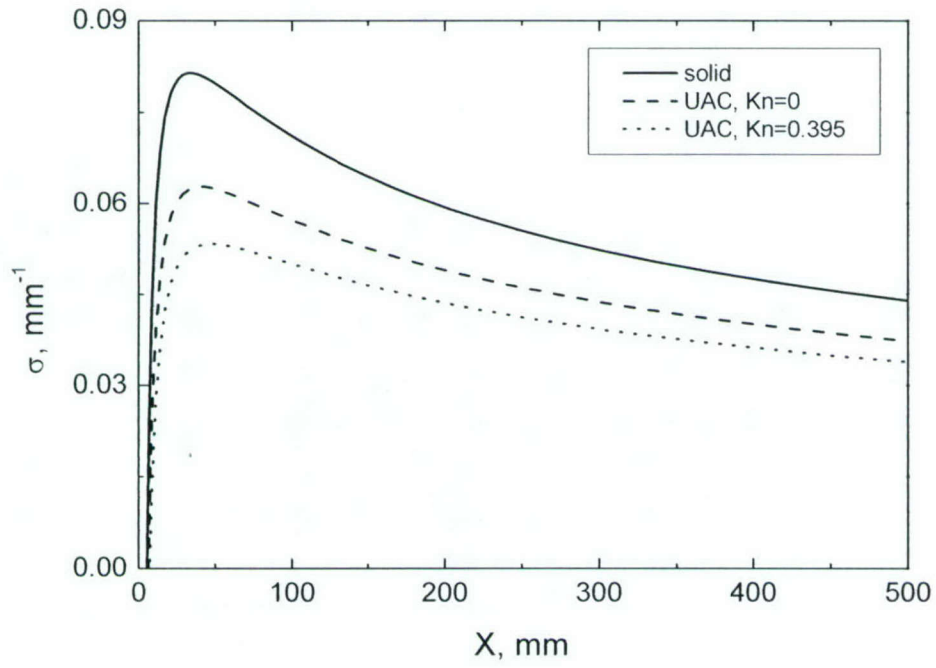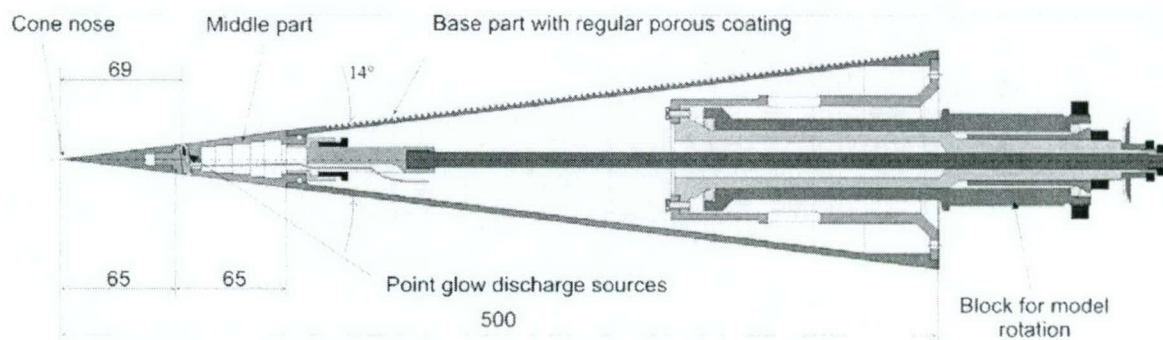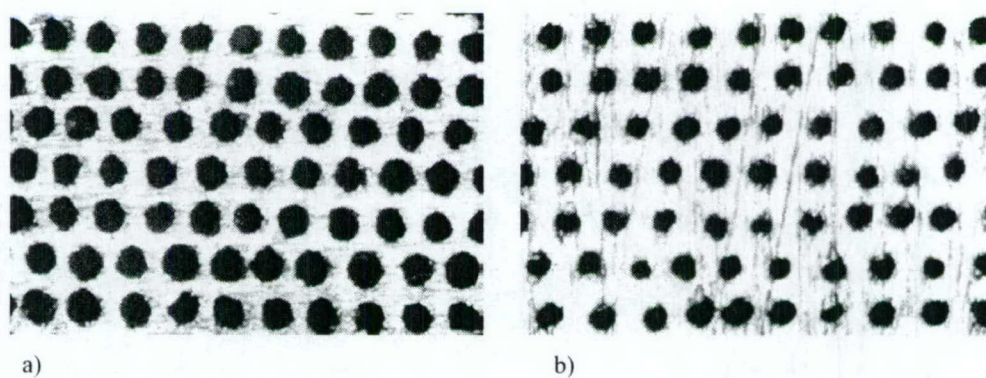**Fig. 1 Sketch of the wall covered by the perforated sheet.**

Fig. 2 Rarefaction effect on the UAC performance; $T_w = T_{ad}$, $\mathrm{Re}_1 = 2 \times 10^7$ $\mathbf{m^{-1}}$, $M_e = 5.3$, $T_e = 56.4$ **K.**

Cone nose   Middle part   Base part with regular porous coating

69

14°

65   65   Point glow discharge sources

500

Block for model rotation

Fig. 3 General view of the sharp cone model.

a)   b)

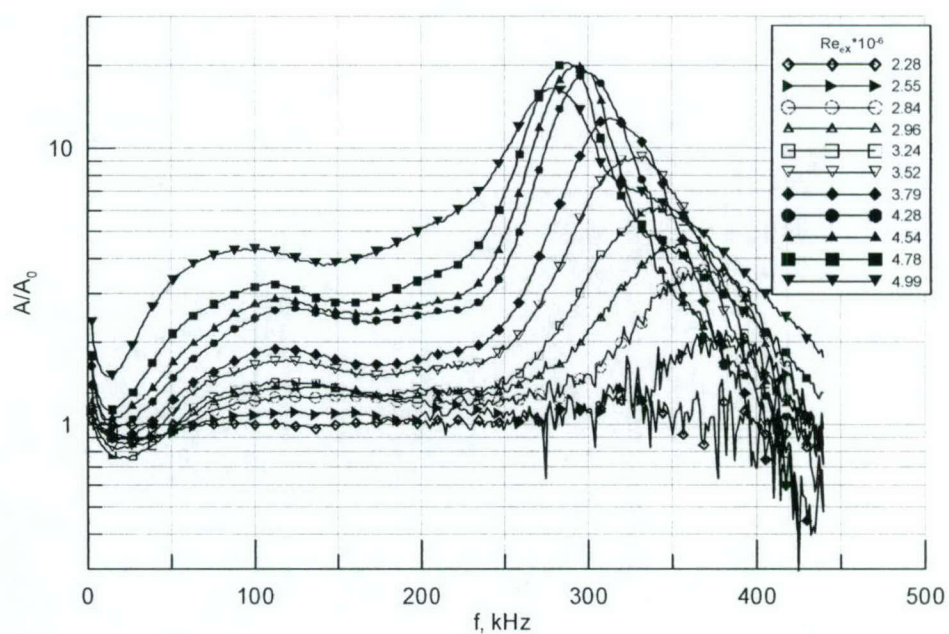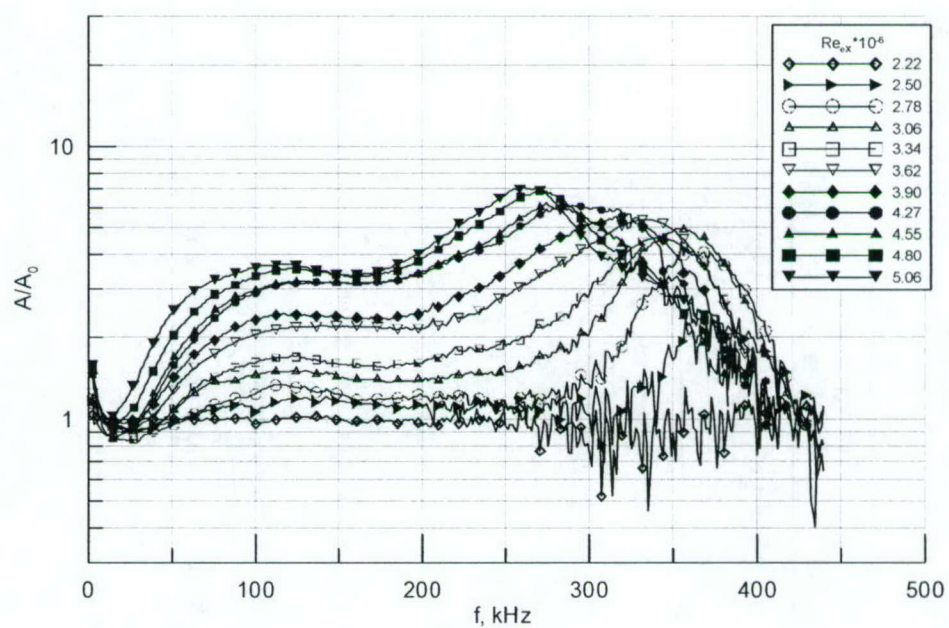**Fig. 4 Micrographs of back (a) and face (b) sides of the perforated sheet.**
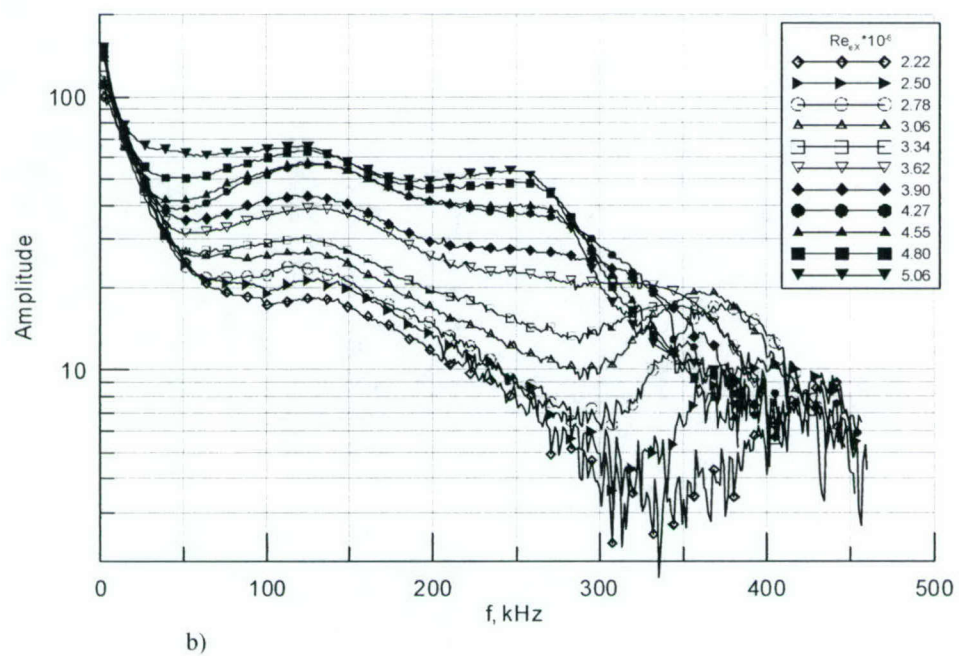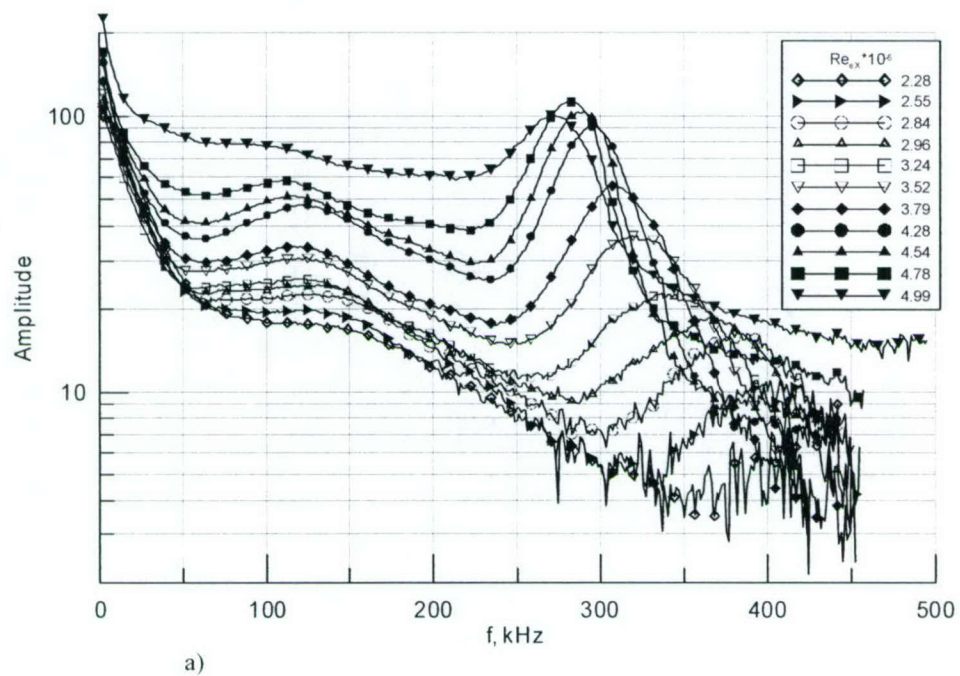
Fig. 5 Natural disturbances spectra in the boundary layer on the solid (a) and porous (b) sides at various Re_{eX}.

13

Fig. 6 Normalized natural-disturbance spectra on the solid (a) and porous (b) sides at various Re_{eX}.
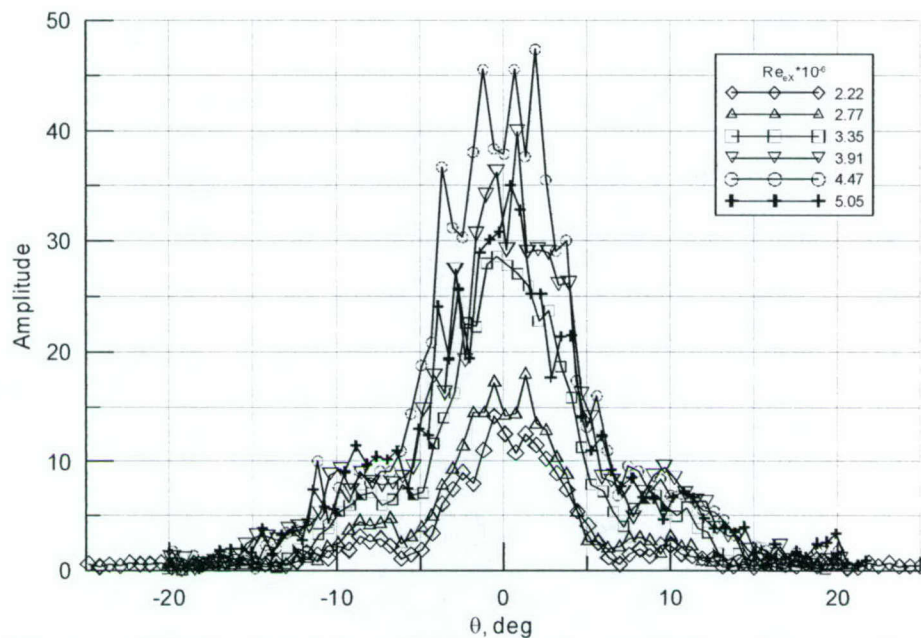
Fig. 7 Transversal distributions of the artificial wave-packet amplitude on the porous side; $\theta \equiv \Theta$.
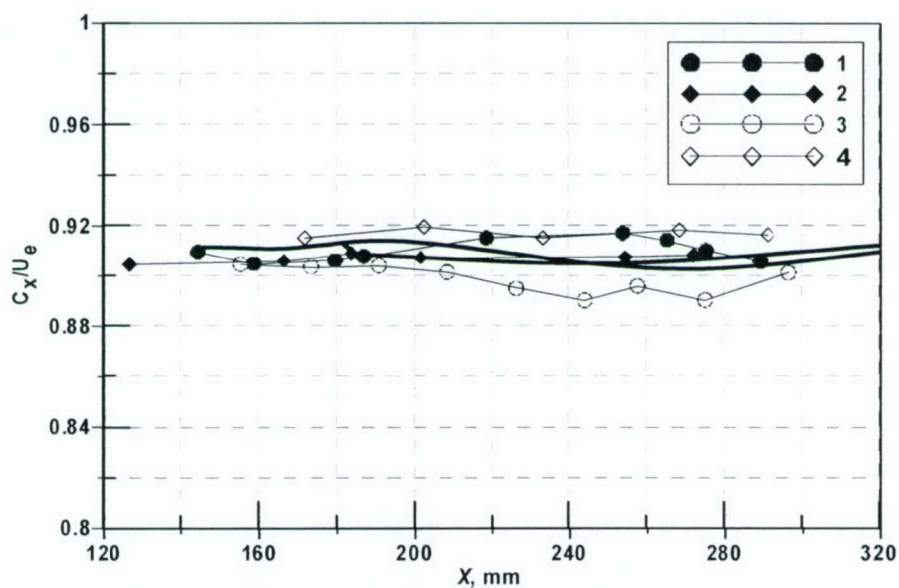

Fig. 8 Phase speeds for artificial disturbances on the porous and solid sides; $f = 275$ kHz. 1, 2 – solid side; 3, 4 – porous side; black lines – theory.
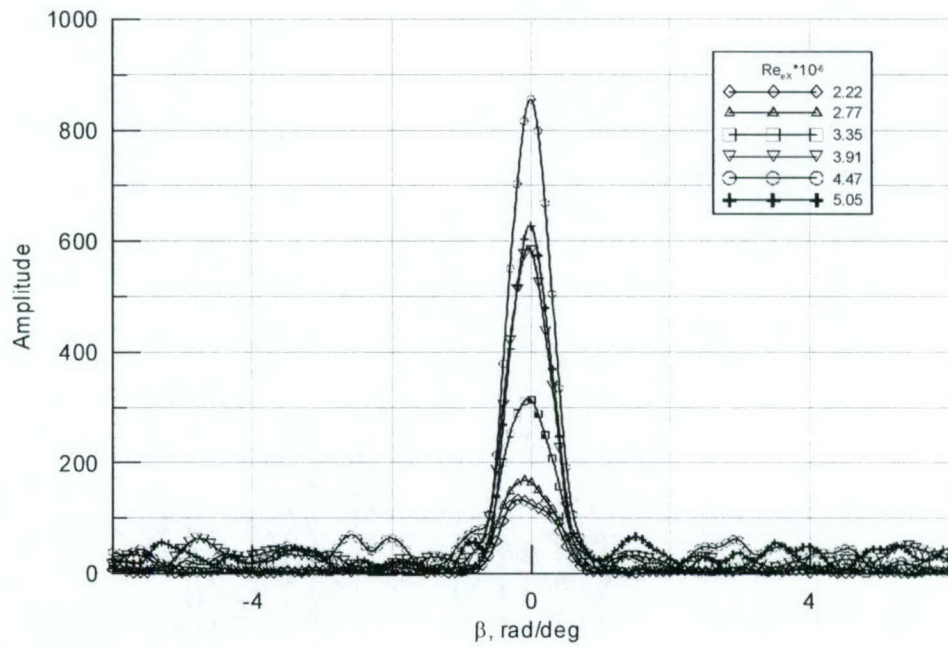
Fig. 9 Amplitude wave spectra with respect to the transversal wavenumber β on the porous side at various Re_{ex}.
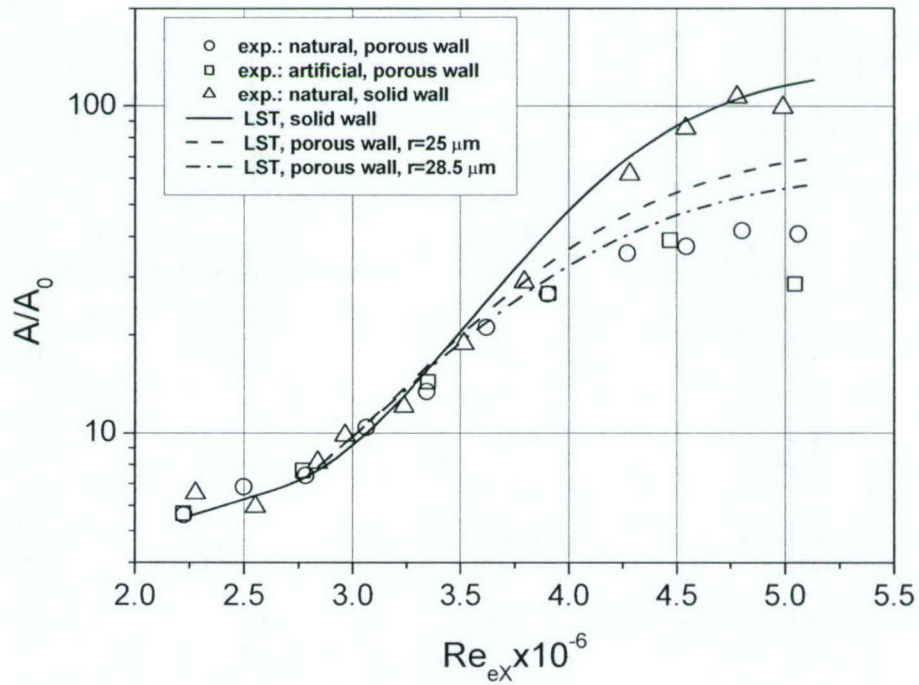

Fig. 10 Downstream development of the second-mode disturbances of frequency 275 kHz.

16

Acoustic properties of rarefied gases inside pores of simple geometries

Vitaly F. Kozlov[a)] and Alexander V. Fedorov
Department of Aeromechanics and Flight Engineering, Moscow Institute of Physics and Technology, Gagarin Str., 16, Zhukovsky, Moscow Reg., Russia, 140187

Norman D. Malmuth
Rockwell Scientific Company, Thousand Oaks, California 91360

Analytical solutions describing propagation of monochromatic acoustic waves inside long pores of simple geometries and narrow flat slits are obtained with accounting for gas rarefaction effects. It is assumed that molecular nature of gas is important in Knudsen layers near solid boundaries. Outside the Knudsen layers, the continuum approach is used. This model allows for extension of acoustic analysis to regions of low pressures and microscopic cross-sectional sizes of channels. The problem is solved using linearized Navier-Stokes equations with the boundary conditions that resulted from the first-order approximation with respect to small Knudsen number Kn. For slits and pores of circular and square cross sections, the theoretical dependencies of the dynamic density in the low-frequency range are compared with those that resulted from known experimental data on steady-state flows of rarefied gases in uniform channels. Despite the formal restriction Kn≪1 of asymptotic analysis, the theoretical model agrees well with experiments up to Kn~5. It is shown that the molecular phenomena affect acoustic characteristics of micro-channels and pores starting from relatively small Knudsen numbers Kn>0.01, especially at low frequencies. The obtained results may be used for analyses of acoustic properties of waveguides, perforated panels, micro-channels and pores in wide range of gas pressures as well as for stationary flows of rarefied gases through long uniform pipes etc. © 2005 Acoustical Society of America.
[DOI: 10.1121/1.1893428]

I. INTRODUCTION

The classic solutions[1,2] of Navier-Stokes equations, which describe acoustic waves traveling inside a long circular tube, are widely used for analyses of acoustic properties of waveguides and perforated panels. They also form a foundation for the semi-empirical models[3–9] predicting the absorption of sound by rigid frame porous media of complex structures. The exact solutions describing acoustic waves inside pores of rectangular and triangular cross-sectional shapes were presented in Refs. 10–13. These results have been obtained with the assumption that gas inside pores is a continuum.

However, there are practical cases in which the continuum assumption is not valid. In particular, rarefaction effects become important in flows within porous materials, which have ultra-fine structure and/or are exploited at so low ambient pressures that the molecular mean free path λ is comparable to a characteristic length scale. For example, in the ultrasonically absorptive coating[14,15] designed for the laminar flow control at hypersonic speeds, the mean free path was approximately 40% of the pore radius r_p $=25\ \mu$m. This leads to 20% increase of the boundary-layer stabilization effect produced by the coating.[15] Similar situations occur in microfluids[16] dealing with gas flows in capillaries and ducts of ~1-μm diameter. Many of these cases

may be modeled using the concept of slip flows, in which the gas is treated as a continuum except thin Knudsen layers on solid walls. Within the Knudsen layer of thickness ~λ, the thermodynamic equilibrium is violated. As shown in the kinetic theory of rarefied gases, slip flows are governed by the Navier-Stokes equations with the boundary conditions that resulted from the first-order (instead of zeroth-order) approximation with respect to the small Knudsen number Kn $=\lambda/L_p$, where L_p is a macroscopic length scale.

Kundt and Warburg[17] were the first who revealed experimentally the slip effects in the gas outflow from a circular tube. They showed that the volume rate of laminar low-density flow inside a circular tube exceeded that predicted by the Poiseuille law. Maxwell[18] gave a qualitative explanation of this phenomenon by means of molecular-kinetic consideration. Smoluchowski[19] discovered physical reasons causing the temperature discontinuity on the solid wall submerged into nonuniformly heated gas of low density. These effects were thoroughly studied both experimentally and theoretically. Detailed reviews of the main results are given in Refs. 20–22 and many other monographs dealing with the interaction of molecular gas with solid surfaces.

Similar to the case of stationary flows through pipes, the gas rarefaction may affect acoustic disturbances propagating in pores. To our knowledge, this problem has not yet been studied. This motivated us to analyze propagation of sound in isolated long pores of various cross-sectional shapes and determine their acoustic characteristics accounting for the
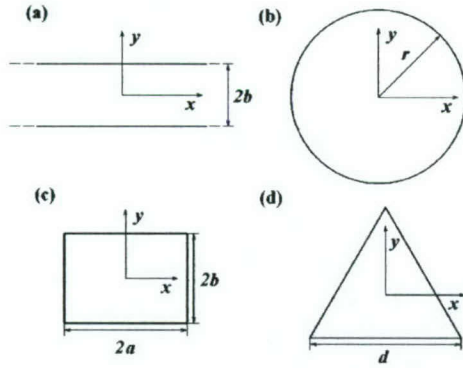
[a)]Electronic mail: afedorov@pt.comcor.ru

FIG. 1. The pore cross-sectional shapes. They are (a) slit of half-height b, (b) circle of radius r_0, (c) rectangle of half-width a and half-height b, and (d) equilateral triangle with sides d.

rarefaction effects. The acoustic problem for straight, uniform, and infinitely long pores is formulated in Sec. II. Its analytical solutions for flat slits and pores of circular, rectangular, and triangular cross-sections are obtained in Section III. The theoretical results are compared with available experimental data in Sec. IV and summarized in Sec. V.

II. FORMULATION OF THE PROBLEM

Consider a pulsating flow of rarefied gas inside flat slits and straight uniform pores. It is assumed that the rarefaction effects are appreciable in thin layers (Knudsen layers) forming on the solid boundaries. Outside the Knudsen layers, the fluid is treated as a continuum medium. The corpuscular effects are taken into account via boundary conditions. In the kinetic theory (see, for example, Refs. 21 and 22) this model corresponds to the first-order asymptotic approximation with respect to small Knudsen number Kn. As usual for asymptotic models, the range of Knudsen numbers in which the first-order approximation is robust can be estimated by comparison with experimental data.

The Cartesian coordinate system (x,y,z) is used for pores of arbitrary cross-sectional shape, and the cylindrical system (r,φ,z) is used for circular pores, where z is measured along the longitudinal axis of the pore. The origin of each coordinate system is located at the cross-sectional center of the pore as sketched in Fig. 1. With the assumption that the longitudinal pore length is much larger than its cross-sectional size L_p, the end effects are neglected. Gas motions inside the pore are caused by an infinitesimal periodic pressure gradient $\mathrm{Re}\{(d\tilde{p}/dz)\exp(i\omega t)\}$, where $i=\sqrt{-1}$, $\omega=2\pi f$ is angular frequency, t is time, and $d\tilde{p}/dz$ is complex amplitude. Solutions of the linearized Navier-Stokes equations for the particle velocity u and temperature disturbances T' are expressed in the form $u=\tilde{u}\exp(i\omega t)$ and $T'=\tilde{T}\exp(i\omega t)$. The momentum and energy equations lead to the equations for complex amplitudes $\tilde{u}$ and $\tilde{T}$:

$$\Delta\tilde{u}+\Lambda^2\tilde{u}=-\frac{\Lambda^2}{i\omega\rho_0}\frac{d\tilde{p}}{dz}, \tag{1a}$$

$$\Delta\tilde{T}+\mathrm{Pr}\Lambda^2\tilde{T}=\frac{\mathrm{Pr}\Lambda^2}{\rho_0 C_\mathrm{p}}\tilde{p}, \tag{1b}$$

where Pr is Prandtl number ($\mathrm{Pr}=\eta C_\mathrm{p}/\kappa$), C_p is the specific heat capacity under constant pressure, η and κ are the dynamic viscosity and heat conductivity of gas, respectively; $\Lambda=\sqrt{-i\omega\rho_0 L_p^2/\eta}$ is the dimensionless parameter, the modulus of which is the ratio of the characteristic length L_p to the viscous skin depth $\delta_\mathrm{visc}=\sqrt{\eta/\omega\rho_0}$, and ρ_0 is gas density in equilibrium; the Laplacian $\Delta=\partial^2/\partial y^2$ for slits, $\Delta=(1/r)(\partial/\partial r)(r\partial/\partial r)$ for the pore of circular cross section, and $\Delta=\partial^2/\partial x^2+\partial^2/\partial y^2$ for pores of rectangular and triangular cross-sections. The coordinates x, y, r are dimensionalized using L_p. The cross-sectional length scale L_p is specified as $L_p=b$ is the half-height of the slit; $L_p=r_0$ is the radius of the cylindrical pore; $L_p=\sqrt{3}d/4$ is the half-height of the equilateral triangle. For the rectangular pore, the characteristic size, L_C, may be determined as the pore half-width a or half-height b, the diagonal $2\sqrt{a^2+b^2}$, the hydraulic radius $2ab/(a+b)$ depending on applications. Thus, the key macroscopic parameter Λ is specified as

$$\Lambda=\begin{cases} \sqrt{-i\omega\rho_0 b^2/\eta}, & \text{slit;} \\ \sqrt{-i\omega\rho_0 r_0^2/\eta}, & \text{circle;} \\ \sqrt{-i\omega\rho_0 L_C^2/\eta}, & \text{rectangle;} \\ \sqrt{-3i\omega\rho_0 d^2/16\eta}, & \text{triangle.} \end{cases} \tag{2}$$

In accordance with the concept of slip flow, the boundary conditions on the solid surfaces are written as[23] (in our notations)

$$u_g=B_u\left(\frac{\partial u}{\partial N}\right)_w, \tag{3a}$$

$$T_g=B_E\left(\frac{\partial T}{\partial N}\right)_w, \tag{3b}$$

where $\partial/\partial N$ is the directional derivative calculated along the unit normal drawn into the pore, the subscript "w" denotes quantities on the pore wall, and u_g and T_g are perturbations of gas velocity and temperature on the wall surface. The factors B_u and B_E are introduced for brevity. They are expressed in terms of the molecular tangential impulse α_u and energy α_E accommodation coefficients, the specific heat ratio γ, Prandtl number Pr and Knudsen number Kn, as

$$B_u=(2\alpha_u^{-1}-1)\mathrm{Kn}, \quad B_E=(2\gamma/\mathrm{Pr}(\gamma+1))(2\alpha_E^{-1}-1)\mathrm{Kn}.$$

The accommodation coefficients α_u and α_E depend, mainly, on collision interaction laws between gas molecules and the solid wall, and on gas temperature, and depend almost not at all on pressure (see, for example, Ref. 20). In practice, an approximation $\alpha_u\approx\alpha_E$ is often used.

Hereafter, we use the well-known theoretical expression for the dynamic viscosity of monatomic gas modeled by hard spheres[23] $\eta\approx0.5\rho_0\bar{c}\lambda$ to express the molecular mean free path λ through experimentally determined parameters ρ_0, T_0, and η. Accordingly, the Knudsen number is specified as $\mathrm{Kn}\approx2\eta/(\rho_0\bar{c}L_p)$, where $\bar{c}=\sqrt{8R_gT_0/\pi}$ is the mean molecular speed, R_g is gas constant per unit mass, and T_0 is gas temperature in equilibrium. In addition, the unperturbed solid surface temperature T_w in (3b) is assumed to be constant.
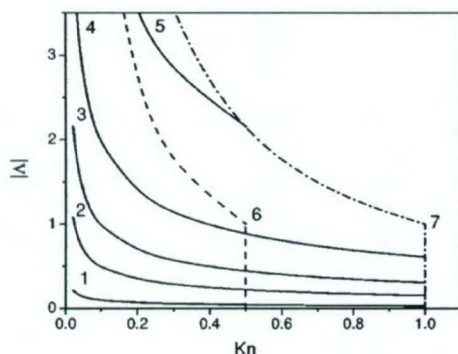
Kozlov et al.: Acoustic properties of rarefied gases

FIG. 2. The $|\Lambda|$-Kn diagram of the regimes of validity of the asymptotic theory. Isolines 1–5 correspond to constant ratios $L_p/\lambda: 1 - L_p/\lambda = 10^{-4}$, $2 - L_p/\lambda = 2.5 \cdot 10^{-3}$, $3 - L_p/\lambda = 10^{-2}$, $4 - L_p/\lambda = 0.04$, and $5 - L_p/\lambda = 0.25$. The dashed curve 6 restricts the parameter plane by Kn<0.5 in the low-frequency range and by Kn$|\Lambda|<0.5$ in the high-frequency range, respectively. The dash-and-dot line 7 does the same for the corresponding restrictions Kn<1 and Kn$|\Lambda|<1$.

The boundary conditions (3a) and (3b), which are obtained in the first-order approximation with respect to the small ratio of molecular mean free path λ to a macroscopic length scale, give a nonzero relative macroscopic gas velocity and temperature jump on the solid wall. More general forms of these conditions, in particular, for varying wall temperature T_w, are discussed, for example, in Refs. 21 and 22.

In the problem considered herein, there are two important macroscopic length scales: the cross-sectional pore size L_p and the viscous skin depth δ_{visc}. The asymptotic analysis should be conducted using a small parameter to be determined as the largest of ratios λ/L_p and $\lambda/\delta_{\text{visc}}$. In the low-frequency range ($|\Lambda|<1$) the viscous skin depth δ_{visc} exceeds the cross-sectional size L_p, and the small parameter is the Knudsen number Kn$=\lambda/L_p$. In the high-frequency range ($|\Lambda|>1$) the characteristic cross-sectional size L_p is larger than δ_{visc}, and the proper small parameter is Kn$|\Lambda|$ (assuming that Pr$\sim$1). Figure 2 illustrates these two cases for air ($\gamma=1.4$) in the parameter space Kn$-|\Lambda|$. Using definition of Kn and (2) we obtain the relation $|\Lambda| = (\pi\gamma/2)^{1/4}\sqrt{kL_p/\text{Kn}}$, where $k = 2\pi/\lambda$ is the wave number and $\lambda = f^{-1}\sqrt{\gamma R_g T_0}$ is the wavelength of a monochromatic acoustic wave propagating in unbounded gas medium. With the help of this relation, we plotted the isolines L_p/λ = const (solid lines). The dashed line 6 and dash-dot line 7 indicate restrictions on the asymptotic model. From the left of line 6 the parameters satisfy the restrictions: Kn<0.5 in low-frequency range, Kn$|\Lambda|<0.5$ in high-frequency range. The line 7 corresponds to the restrictions Kn<1 and Kn$|\Lambda|<1$ correspondingly. This diagram allows us to estimate the wavelength (and frequency) range in which the theory is applicable. Say the molecular mean free path is $\lambda = 0.6\times10^{-5}$ cm, which is typical for air at normal ambient conditions in accordance with a model of hard spheres.[23] For the pore cross-sectional size $L_p=3\times10^{-5}$ cm, the Knudsen number is Kn$=0.2$. Drawing the vertical line Kn$=0.2$ up to the intersection, for example, with the boundary 6 one finds that the dimensionless parameter $|\Lambda|$ should not exceed 2.6. This corresponds to the isoline $L_p/\lambda \approx 1/7$ on which $\lambda \approx 2$ μm is treated as a minimal allowable wavelength. For air temperature $T_0 \approx 273$ K, the

corresponding maximal frequency is $f \sim 10^8$ Hz. Since this frequency is far beyond the ultrasonic range, the theory is applicable to any practical range of acoustic disturbances.

The boundary conditions (3) cannot be satisfied for a polygonal cross section, since the direction of the surface normal N jumps at the polygon apices. This may cause sudden changes of the tangential viscous stress and the normal heat flux on the pore surface. To avoid this unphysical behavior, additional restrictions must be imposed, namely, continuity of the shear stresses and heat fluxes acting on the fracture lines of the pore surface. Analysis of the solutions[10,11,13] for rectangular and triangular pores shows that theoretical values of the tangential viscous stresses and the normal heat flux vanish at the polygonal vertices. Obviously, solutions considered herein should also possess this property for Kn$\to$0. Accordingly, the dominant approximation gives

$$\left(\frac{\partial F}{\partial N}\right)_{(x_w,y_w)\to(x_s-0,y_s-0)} = \left(\frac{\partial F}{\partial N}\right)_{(x_w,y_w)\to(x_s+0,y_s+0)},$$

$$\left(\frac{\partial F}{\partial N}\right)_{w(x_w,y_w)\to(x_s\pm0,y_s\pm0)} \xrightarrow{\quad} O(\Lambda^2)\times\text{Kn} \qquad (4)$$

where subscript "s" denotes the sth salient point of the boundary and F stands for the function u or T'.

III. SOLUTION OF THE PROBLEM

At first, we consider the cases of slit, circular, and triangular pores. The solution for rectangular pores will be obtained later in a different manner. We perform the following substitutions in (1):

$$\tilde{u}(x,y,z) = -\frac{1}{i\omega\rho_0}\frac{d\tilde{p}}{dz}[1-F(x,y,B_u,\Lambda)], \qquad (5)$$

$$\tilde{T}(x,y,z) = \frac{\tilde{p}}{\rho_0 C_p}[1-F(x,y,B_E,\tilde{\Lambda})], \qquad (6)$$

where $\tilde{\Lambda} = \sqrt{\text{Pr}}\Lambda$. In accordance with (1) and (3), the new unknown dimensionless functions $F(x,y,B_u,\Lambda)$ and $F(x,y,B_E,\tilde{\Lambda})$ satisfy the uncoupled Helmholtz equations in two-dimensional space (except the case of slit),

$$(\Delta + \Lambda^2)F(x,y,B_u,\Lambda) = 0, \qquad (7a)$$

$$(\Delta + \tilde{\Lambda}^2)F(x,y,B_E,\tilde{\Lambda}) = 0, \qquad (7b)$$

and the corresponding boundary conditions

$$F(x_w,y_w,B_u,\Lambda) - B_u\left(\frac{\partial F(x,y,B_u,\Lambda)}{\partial N}\right)_w = 1, \qquad (8a)$$

$$F(x_w,y_w,B_E,\tilde{\Lambda}) - B_E\left(\frac{\partial F(x,y,B_E,\tilde{\Lambda})}{\partial N}\right)_w = 1. \qquad (8b)$$

If the boundary contains salient points (the case of pores of triangular cross sections), then the functions F must satisfy the additional conditions (4). Since the problems (7a) and (8a), and (7b) and (8b), are similar, it is sufficient to solve the first one. The solution of the second problem is

obtained by the formal substitutions $B_u \to B_E$ and $\Lambda \to \tilde{\Lambda}$.

In the continuum approximation, the problem for pores of rectangular and triangular cross sections was solved in Refs. 10–13 using Fourier series. However, these series are not differentiable in the vicinity of solid boundaries, because they include decompositions of discontinuous functions. Since the boundary condition (8a) contains the partial derivatives with respect to the space variables, this method cannot be applied to the problem (7a) and (8a). This motivated us to use the appropriate eigensolutions of (7a):

$$F(x,y,B_u,\Lambda) = \begin{cases} A \cos \Lambda y, & \text{slit}; \\ B J_0(\Lambda r), & \text{circle}; \\ \sum_{i=1}^{2} a_i \varphi_i(x,y,\Lambda), & \text{triangle}; \end{cases} \tag{9}$$

where A, B, a_1, and a_2 are constants of integration; $J_0(\Lambda r)$ is Bessel function of the first kind of order zero; $\varphi_1(x,y,\Lambda) = \sin \Lambda \xi_1 + \sin \Lambda \xi_2 - \sin \Lambda \xi_3$ and $\varphi_2(x,y,\Lambda) = \cos \Lambda \xi_1 + \cos \Lambda \xi_2 + \cos \Lambda \xi_3$ are independent eigensolutions of (7a), $\xi_1 = y/2 + \sqrt{3}x/2$, $\xi_2 = y/2 - \sqrt{3}x/2$, $\xi_3 = y$.

In the cases of slit and circular pores, the coefficients A and B are solutions of the algebraic equation resulted from substitution of (9) into the boundary condition (8a):

$$A = \frac{1}{\cos \Lambda \{1 - B_u \Lambda \tan \Lambda\}}, \tag{10}$$

$$B = \frac{1}{J_0(\Lambda)\{1 - 0.5 B_u \Lambda^2 Q(\Lambda)\}}, \tag{11}$$

where $Q(\Lambda) = 2J_1(\Lambda)/\Lambda J_0(\Lambda)$.

Owing to the rotation invariance of the solution for triangular pore, it is sufficient to consider the boundary conditions on one side of the triangle, say $y = -\frac{2}{3}$. Substituting the corresponding expressions into (8a) at $y = -\frac{2}{3}$ and equating to zero the coefficients of similar terms, we obtain the linear algebraic system for a_1 and a_2:

$$a_1 \sin \frac{2\Lambda}{3}\left(1 + \Lambda B_u \cot \frac{2\Lambda}{3}\right) + a_2 \cos \frac{2\Lambda}{3}\left(1 - \Lambda B_u \tan \frac{2\Lambda}{3}\right)$$
$$= 1,$$

$$a_1 \sin \frac{\Lambda}{3}\left(1 + \frac{\Lambda B_u}{2}\cot \frac{\Lambda}{3}\right) - a_2 \cos \frac{\Lambda}{3}\left(1 - \frac{\Lambda B_u}{2}\tan \frac{\Lambda}{3}\right) = 0.$$

Its solution is expressed as

$$a_1 = \cos \frac{\Lambda}{3}\left(1 - \frac{\Lambda}{2}B_u \tan \frac{\Lambda}{3}\right) \Big/ \Delta_u,$$

$$a_2 = \sin \frac{\Lambda}{3}\left(1 + \frac{\Lambda}{2}B_u \cot \frac{\Lambda}{3}\right) \Big/ \Delta_u, \tag{12}$$

where $\Delta_u = [1 + 1.5 \Lambda B_u \cot \Lambda - 0.5(\Lambda B_u)^2]\sin \Lambda$. Direct substitution shows that the solution (9) and (12) satisfies the condition (8a) and the additional conditions (4) at the triangle apices.

Now we consider the case of the rectangular pore. Note that the two-dimensional Fourier expansion

$$\tilde{u}(x,y,z) = \frac{4\Lambda^2}{i\omega\rho_0}\frac{d\tilde{p}}{dz}$$

$$\times \sum_{m=0}^{\infty}\sum_{n=0}^{\infty}\frac{(-1)^{m+n}\cos \alpha_m q_1 x \cos \alpha_n q_2 y}{\alpha_m \alpha_n (\alpha_m^2 q_1^2 + \alpha_n^2 q_2^2 - \Lambda^2)},$$

which was used in Refs. 10 and 11 for continuous media, is reduced to the one-dimensional form using the Fourier series

$$1 - \frac{\cosh(\beta_{2m}q_1 x)}{\cosh \beta_{2m}} = 2\beta_{2m}^2 \sum_{n=0}^{\infty}\frac{(-1)^n \cos \alpha_n q_1 x}{\alpha_n(\alpha_n^2 + \beta_{2m}^2)},$$

$$1 - \frac{\cosh(\beta_{1m}q_2 y)}{\cosh \beta_{1m}} = 2\beta_{1m}^2 \sum_{n=0}^{\infty}\frac{(-1)^n \cos \alpha_n q_2 y}{\alpha_n(\alpha_n^2 + \beta_{1m}^2)},$$

where $(|q_1 x| \le 1, |q_2| \le 1)$. This form is written as

$$\tilde{u}(x,y,z)$$
$$= \frac{\Lambda^2}{i\omega\rho_0}\frac{d\tilde{p}}{dz}\sum_{m=0}^{\infty}\frac{(-1)^m}{\alpha_m}\left\{\frac{1}{q_2^2\beta_{1m}^2}\left(1 - \frac{\cosh(\beta_{1m}q_2 y)}{\cosh \beta_{1m}}\right)\right.$$
$$\times \cos(\alpha_m q_1 x) + \frac{1}{q_1^2\beta_{2m}^2}\left(1 - \frac{\cosh(\beta_{2m}q_1 x)}{\cosh \beta_{2m}}\right)$$
$$\left.\times \cos(\alpha_m q_2 y)\right\}, \tag{13}$$

where $q_1^{-1} = a/L_C$ and $q_2^{-1} = b/L_C$ are dimensionless rectangle sides, $\beta_{1m} = q_2^{-1}\sqrt{\alpha_m^2 q_1^2 - \Lambda^2}$, $\beta_{2m} = q_1^{-1}\sqrt{\alpha_m^2 q_2^2 - \Lambda^2}$, and $\alpha_m = (m + 0.5)\pi$. Note that we use the two independent complete systems of functions to symmetrize (13) with respect to x and y. Now we can modify (13) in order to satisfy the boundary condition (3a). This modification is written as

$$\tilde{u}(x,y,z) = \frac{\Lambda^2}{i\omega\rho_0}\frac{d\tilde{p}}{dz}\sum_{m=0}^{\infty}\sum_{j=1}^{2}\{a_{jm}\Psi_{jm}(x,y,B_u,\Lambda)\},$$

$$\Psi_{1m}(x,y,B_u,\Lambda)$$
$$= \frac{(-1)^m}{q_2^2\gamma_{1m}\beta_{1m}^2}\left(1 - \frac{\cosh(\beta_{1m}q_2 y)}{Q_{1m}\cosh \beta_{1m}}\right)\cos(\gamma_{1m}q_1 x),$$

$$Q_{1m} = 1 + q_2 B_u \beta_{1m} \tanh \beta_{1m},$$

$$\Psi_{2m}(x,y,B_u,\Lambda)$$
$$= \frac{(-1)^m}{q_1^2\gamma_{2m}\beta_{2m}^2}\left(1 - \frac{\cosh(\beta_{2m}q_1 x)}{Q_{2m}\cosh \beta_{2m}}\right)\cos(\gamma_{2m}q_2 y),$$

$$Q_{2m} = 1 + q_1 B_u \beta_{2m} \tanh \beta_{2m}, \tag{14}$$

$$\beta_{1m} = q_2^{-1}\sqrt{\gamma_{1m}^2 q_1^2 - \Lambda^2}, \quad \beta_{2m} = q_1^{-1}\sqrt{\gamma_{2m}^2 q_2^2 - \Lambda^2},$$

where a_{jm} $(j = 1,2)$ are unknown integration constants; the eigenvalues γ_{1m} and γ_{2m} are roots of the equations

$$\cos \gamma_{1m} = q_1 B_u \gamma_{1m} \sin \gamma_{1m}, \tag{15a}$$

$$\cos \gamma_{2m} = q_2 B_u \gamma_{2m} \sin \gamma_{2m}. \tag{15b}$$

In the expansion (14), each function $\Psi_{jm}(x,y,B_u,\Lambda)$ $(j = 1,2)$ satisfies the boundary condition (3a). Hereafter we

4   J. Acoust. Soc. Am., Vol. 117, No. 5, May 2005   Kozlov et al.: Acoustic properties of rarefied gases

PROOF COPY 045505JAS

explain how to find the coefficients a_{jm} in the decomposition (14). Direct substitution shows that (14) satisfies (1a), if $\sum_{m=0}^{\infty}(-1)^m\{a_{1m}\gamma_{1m}^{-1}\cos(\gamma_{1m}q_1x)+a_{2m}\gamma_{2m}^{-1}\cos(\gamma_{2m}q_2y)\}=1$. The left-hand side of this equality may be interpreted as a sum of two series: the first series depends on x and the second on y. The sum of these two terms may be constant if and only if each of them is constant. Thus, taking into account the solution (13) for continuous medium we write

$$\sum_{m=0}^{\infty}(-1)^m a_{1m}\gamma_{1m}^{-1}\cos(\gamma_{1m}q_1x)=\frac{1}{2},$$

$$\sum_{m=0}^{\infty}(-1)^m a_{2m}\gamma_{2m}^{-1}\cos(\gamma_{2m}q_2y)=\frac{1}{2}. \quad (16)$$

This system of linear algebraic equations has a simple solution at $B_u=0$. In this case the system (15) gives $\gamma_{1m}=\gamma_{2m}=\alpha_m=(m+0.5)\pi$. Using Fourier decompositions we obtain the equation $2\sum_{m=0}^{\infty}(-1)^m\alpha_m^{-1}\cos(\alpha_mq_1x)=2\sum_{m=0}^{\infty}(-1)^m\alpha_m^{-1}\cos(\alpha_mq_2y)=1$ ($|q_1x|<1,|q_2y|<1$), which gives $a_{1m}=a_{2m}=1$ ($m=0,1,2,...$). Thus, the solution (14) coincides with (13) in the case of $B_u=0$. Direct verification shows that (14) satisfies the conditions (4) at the angular points of rectangle.

The functions Ψ_{1m} and Ψ_{2m}, which are used in the case of rectangular pore, do not represent an orthogonal system on the rectangle sides. For this reason we cannot immediately solve the system (16). The orthogonalization is performed using the complete trigonometric systems $\{\cos \alpha_nq_1x\}$ and $\{\cos \alpha_nq_2y\}$. Substituting the decompositions

$$\cos(\gamma_{1m}q_1x)-\cos\gamma_{1m}$$
$$=2\gamma_{1m}^2\cos\gamma_{1m}\sum_{n=0}^{\infty}\frac{(-1)^n\cos\alpha_nq_1x}{\alpha_n(\alpha_n^2-\gamma_{1m}^2)} \quad (|q_1x|\leq1),$$

$$\cos(\gamma_{2m}q_2y)-\cos\gamma_{2m}$$
$$=2\gamma_{2m}^2\cos\gamma_{2m}\sum_{n=0}^{\infty}\frac{(-1)^n\cos\alpha_nq_2y}{\alpha_n(\alpha_n^2-\gamma_{2m}^2)} \quad (|q_2y|\leq1)$$

into (16) and using the orthogonal properties of the trigonometric functions we reduce the problem to solving two uncoupled infinite systems of algebraic equations ($j=1,2$):

$$\sum_{n=0}^{\infty}\frac{\cos(\gamma_{jn}-n\pi)}{\gamma_{jn}(\alpha_m^2-\gamma_{jn}^2)}a_{jn}=\frac{1}{2\alpha_m^2}. \quad (17)$$

From (15) we also obtain

$$\cos(\gamma_{jn}-n\pi)=\frac{q_jB_u\gamma_{jn}}{\sqrt{1+(q_jB_u\gamma_{jn})^2}} \quad (j=1,2).$$

Owing to this we can express (17) in the form

$$\sum_{n=0}^{\infty}\frac{a_{jn}}{(\alpha_m^2-\gamma_{jn}^2)\sqrt{1+(q_jB_u\gamma_{jn})^2}}=\frac{1}{2q_jB_u\alpha_m^2}. \quad (18)$$

As discussed above, the solution of (1b) is obtained by the replacement $(B_u,\Lambda)\rightarrow(B_E,\tilde{\Lambda})$ in the solution of (1a). This leads to the amplitude of temperature pulsations

$$\tilde{T}(x,y,z)=-\frac{\tilde{\Lambda}^2\tilde{p}}{\rho_0C_p}\sum_{m=0}^{\infty}\sum_{j=3}^{4}\{a_{jm}\Psi_{jm}(x,y,B_E,\tilde{\Lambda})\},$$
$$(19)$$

where

$$\Psi_{3m}(x,y,B_E,\tilde{\Lambda})$$
$$=\frac{(-1)^m}{q_2^2\gamma_{3m}\beta_{3m}^2}\left(1-\frac{\cosh(\beta_{3m}q_2y)}{Q_{3m}\cosh\beta_{3m}}\right)\cos(\gamma_{3m}q_1x),$$
$$Q_{3m}=1+q_2B_E\beta_{3m}\tanh\beta_{3m},$$

$$\Psi_{4m}(x,y,B_E,\tilde{\Lambda})$$
$$=\frac{(-1)^m}{q_1^2\gamma_{4m}\beta_{4m}^2}\left(1-\frac{\cosh(\beta_{4m}q_1x)}{Q_{4m}\cosh\beta_{4m}}\right)\cos(\gamma_{4m}q_2y),$$
$$Q_{4m}=1+q_1B_E\beta_{4m}\tanh\beta_{4m},$$

$$\beta_{3m}=q_2^{-1}\sqrt{\gamma_{3m}^2q_1^2-\tilde{\Lambda}^2}, \quad \beta_{4m}=q_1^{-1}\sqrt{\gamma_{4m}^2q_2^2-\tilde{\Lambda}^2}.$$

Equations for the eigenvalues γ_{jm} and coefficients a_{jm} of the solutions (14) and (19) may be written in the common form for $j=1, 2, 3, 4$; $m=0,1,2,...$:

$$\cos\gamma_{jm}=h_j\gamma_{jm}\sin\gamma_{jm}, \quad (20)$$

$$\sum_{n=0}^{\infty}\frac{\cos(\gamma_{jn}-n\pi)}{\gamma_{jn}(\alpha_m^2-\gamma_{jn}^2)}a_{jn}=\frac{1}{2\alpha_m^2}, \quad (21)$$

where $h_1=q_1B_u$, $h_2=q_2B_u$, $h_3=q_1B_E$, and $h_4=q_2B_E$.

Approximate solutions of the equations (20) may be obtained as follows. Noting that $m\pi\leq\gamma_{jm}\leq(m+0.5)\pi$ we express the eigenvalues in the form

$$\gamma_{jm}=(m+0.25)\pi+\Delta\gamma_{jm}=\delta_m+\Delta\gamma_{jm},$$

which allows us to rearrange (20) as

$$\Delta\gamma_{jm}=\frac{\pi}{4}-\tan^{-1}(Z_{jm})+\frac{1}{2i}\left\{\ln\left(1-\frac{ih_j\Delta\gamma_{jm}}{1-iZ_{jm}}\right)\right.$$
$$\left.-\ln\left(1+\frac{ih_j\Delta\gamma_{jm}}{1+iZ_{jm}}\right)\right\}$$

$$\approx\frac{\pi}{4}-\tan^{-1}(Z_{jm})-\frac{h_j\Delta\gamma_{jm}}{1+Z_{jm}^2}$$

$$+\frac{Z_{jm}}{(1+Z_{jm}^2)^2}(h_j\Delta\gamma_{jm})^2$$

$$+\frac{1-3Z_{jm}^2}{3(1+Z_{jm}^2)^3}(h_j\Delta\gamma_{jm})^3$$

$$-\frac{Z_{jm}(1-Z_{jm}^2)}{(1+Z_{jm}^2)^4}(h_j\Delta\gamma_{jm})^4-\cdots, \quad Z_{jm}=h_j\delta_m.$$

This equation may be solved in various ways. An approximate solution may be obtained, for example, using the method of successive iterations

$$\Delta\gamma_{jm} \approx \frac{(1+Z_{jm}^2)\tau_{jm}}{1+h_j+Z_{jm}^2}\left\{1+\frac{h_j^2 Z_{jm}\tau_{jm}}{(1+h_j+Z_{jm}^2)^2}+\cdots\right\}, \quad (22)$$

where $\tau_{jm}=\pi/4-\tan^{-1}(Z_{jm})$. Numerical tests showed that the maximal relative deviation of the results obtained with use of (22) from corresponding numerical solutions was less then 10^{-3} at $m=0$ and Kn$=1.0$ ($q_j\leqslant 1$).

Since (20) and (21) do not depend on the parameter Λ (or $\tilde{\Lambda}$), the eigenvalues γ_{jm} and coefficients a_{jm} are determined once (for example, numerically) for particular q_1, q_2, B_u, and B_E. Then these solutions may be used for calculations of the acoustic characteristics at any dimensionless frequency Λ^2.

Since the pressure disturbance in the considered approach does not depend on the transversal variables (x,y), acoustic properties of an isolated pore can be obtained by averaging of the particle velocity and temperature excess over the pore cross-sectional area. In this connection, acoustics of porous media deals with the following parameters:[3,10]

(a) Dynamic density

$$\tilde{\rho}(B_u,\Lambda)=-\frac{1}{i\omega\langle\tilde{u}(z)\rangle}\frac{d\tilde{p}}{dz}. \quad (23)$$

(b) Dynamic compressibility

$$\tilde{C}(B_E,\gamma,\tilde{\Lambda})=\rho_0^{-1}(\langle\tilde{\rho}\rangle/\tilde{p})$$

$$=\frac{1}{p_0}-\frac{\langle\tilde{T}\rangle}{T_0\tilde{p}}=\frac{1}{p_0}\left(1-\frac{\rho_0 R\langle\tilde{T}\rangle}{\tilde{p}}\right), \quad (24)$$

where p_0 is unperturbed ambient pressure and $\langle\ \rangle$ denotes averaging over the cross-sectional area $S\langle\tilde{f}\rangle=(1/S)\oint_S\tilde{f}(x,y)ds$. In turn, the dynamic density and dynamic compressibility are used to calculate the characteristic impedance Z_w and the propagation constant m:

$$Z_w=\sqrt{\tilde{\rho}/\tilde{C}}, \quad (25)$$

$$m=i\omega\sqrt{\tilde{\rho}\tilde{C}}. \quad (26)$$

Using (5) and (6) we obtain

$$\langle\tilde{u}(z)\rangle=-\frac{1}{i\omega\rho_0}\frac{d\tilde{p}}{dz}[1-\langle F(B_u,\Lambda)\rangle], \quad (27)$$

$$\langle\tilde{T}(z)\rangle=\frac{\tilde{p}}{\rho_0 C_p}[1-\langle F(B_E,\tilde{\Lambda})\rangle]. \quad (28)$$

Substituting (27) and (28) into (23) and (24) we express the complex dynamic density $\tilde{\rho}(B_u,\Lambda)$ and the dynamic compressibility $\tilde{C}(B_E,\gamma,\tilde{\Lambda})$ as

$$\tilde{\rho}(B_u,\Lambda)=\rho_0/[1-\langle F(B_u,\Lambda)\rangle], \quad (29)$$

$$\tilde{C}(B_E,\gamma,\tilde{\Lambda})=\frac{1}{\gamma p_0}[1+(\gamma-1)\langle F(B_E,\tilde{\Lambda})\rangle], \quad (30)$$

where

$\langle F(B_u,\Lambda)\rangle$

$$=\begin{cases} \dfrac{\tan\Lambda}{\Lambda[1-B_u\Lambda\tan\Lambda]}, & \text{slit;} \\[4mm] \dfrac{Q(\Lambda)}{1-0.5B_u\Lambda^2 Q(\Lambda)}, & \text{circle;} \\[4mm] 1+\Lambda^2\displaystyle\sum_{m=0}^{\infty}(a_{1m}\langle\Psi_{1m}\rangle+a_{2m}\langle\Psi_{2m}\rangle), & \text{rectangle;} \\[4mm] \dfrac{3(1-\Lambda\cot\Lambda+0.5\Lambda^2 B_u)}{\Lambda^2[1+1.5\Lambda B_u\cot\Lambda-0.5(\Lambda B_u)^2]}, & \text{triangle;} \end{cases}$$

(31)

$\langle F(B_E,\gamma,\tilde{\Lambda})\rangle$

$$=\begin{cases} \dfrac{\tan\tilde{\Lambda}}{\tilde{\Lambda}(1-B_E\tilde{\Lambda}\tan\tilde{\Lambda})}, & \text{slit;} \\[4mm] \dfrac{Q(\tilde{\Lambda})}{1-0.5B_E\tilde{\Lambda}^2 Q(\tilde{\Lambda})}, & \text{circle;} \\[4mm] 1+\tilde{\Lambda}^2\displaystyle\sum_{m=0}^{\infty}(a_{3m}\langle\Psi_{3m}\rangle+a_{4m}\langle\Psi_{4m}\rangle), & \text{rectangle;} \\[4mm] \dfrac{3(1-\tilde{\Lambda}\cot\tilde{\Lambda}+0.5\tilde{\Lambda}^2 B_E)}{\tilde{\Lambda}^2[1+1.5\tilde{\Lambda}B_E\cot\tilde{\Lambda}-0.5(\tilde{\Lambda}B_E)^2]}, & \text{triangle;} \end{cases}$$

(32)

$$\langle\Psi_{jm}\rangle=\frac{\sin(\gamma_{jm}-m\pi)}{D_j\gamma_{jm}^2\beta_{jm}^2}\left(1-\frac{\tanh\beta_{jm}}{\beta_{jm}Q_{jm}}\right);$$

$$D_j=q_2^2 \text{ at } j=1,3 \text{ and } D_j=q_1^2 \text{ at } j=2,4.$$

In the case of triangular pore, the following averages are used:

$$\langle\varphi_1(\Lambda)\rangle=\frac{3}{\Lambda}\left[\frac{1}{2\Lambda}\left(\sin\frac{4\Lambda}{3}+\sin\frac{2\Lambda}{3}\right)-\cos\frac{2\Lambda}{3}\right],$$

$$\langle\varphi_2(\Lambda)\rangle=\frac{3}{\Lambda}\left[\frac{1}{2\Lambda}\left(\cos\frac{2\Lambda}{3}-\cos\frac{4\Lambda}{3}\right)+\sin\frac{2\Lambda}{3}\right].$$

For the Knudsen number Kn$=0$, the formulas (29) and (30) together with (31) and (32) coincide with the corresponding expressions (which are presented, for example, in Ref. 13) for continuum media.

Results of numerical calculations with use of (29)–(32) are presented in Fig. 3 for a circular pore filled with air at Knudsen numbers 0, 0.05, 0.1, and 0.5. In these calculations, we used the approximations $\alpha_u=\alpha_E=0.9$. This assumption is consistent with the data presented in Table II and with data from other literature sources. It is seen that influence of rarefaction effects on acoustical characteristics of air becomes noticeable at Kn~ 0.01 and increases with the Knudsen number.

IV. COMPARISON WITH EXPERIMENT

Unfortunately, we could not find experimental data on sound propagating in uniform channels filled with low-density gases. However, it is known (see, for example, Ref.

6   J. Acoust. Soc. Am., Vol. 117, No. 5, May 2005

Kozlov et al.: Acoustic properties of rarefied gases
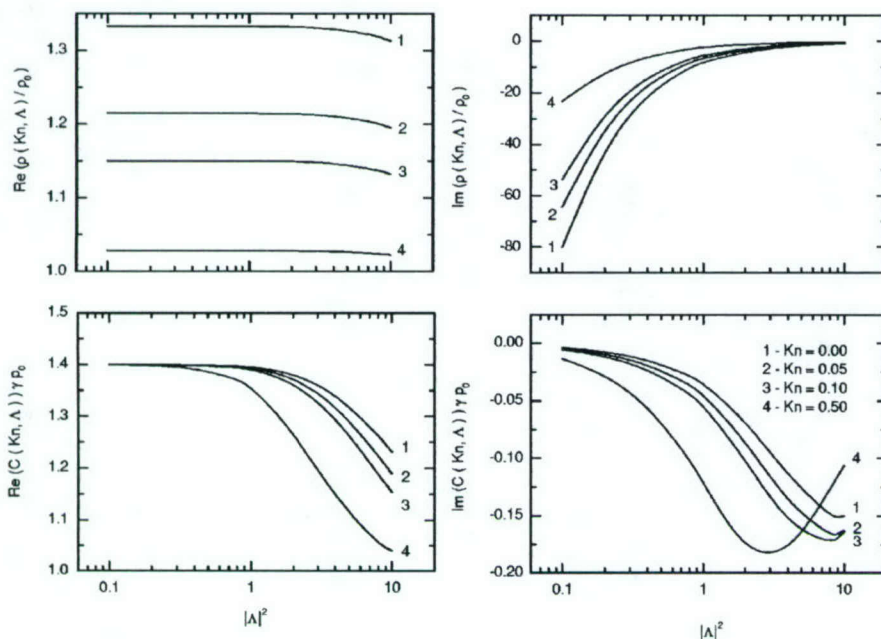
PROOF COPY 045505JAS

FIG. 3. Theoretical dependencies of the dynamic density and dynamic compressibility of air inside an infinitely long cylindrical pore via dimensionless parameters Λ and Kn, $\alpha_u = \alpha_E = 0.9$.

8) that in the low-frequency limit, $|\Lambda| \to 0$, acoustic properties of gas inside pores may be approximately expressed in terms of parameters characterizing steady viscous flows. For the considered above cases, this approximation may be also obtained using expansions of (31) and (32) into power series in Λ. For example, $\langle F(B_u, \Lambda) \rangle \approx 1 + (k_1 + cB_u)\Lambda^2 + \cdots$, where the decomposition coefficients k_1 and c depend on the pore cross-sectional shape: $k_1 = \frac{1}{3}$, $c = 1$ for slit; $k_1 = \frac{1}{8}$ and $c = 1/2$ for circular pores; etc. Substituting this decomposition into the exact formula (29) and using the definition of Λ one finds that $\tilde{\rho}(B_u, \Lambda) \underset{\Lambda \to 0}{\to} \sigma_0/i\omega$, where $\sigma_0 = \eta/(k_1 + cB_u)L_p^2$ is resistivity of slip flow, which coincides with dc flow resistivity in the continuum approach $B_u \to 0$ (see also Ref. 13). Thus, the dynamic density is pure imaginary in the low-frequency limit. It is inversely proportional to frequency with the constant depending on stationary flow characteristics only. Note also that the rarefaction effect on acoustic properties is stronger in the low-frequency band owing to the relatively large imaginary part of the dynamic density, which tends to infinity as $\Lambda^2 \to 0$. This is also confirmed by dependencies shown in Fig. 3. All these arguments allow us to verify the theoretical model by comparisons with numerous experimental data on stationary flows of rarefied gases through long tubes of different cross-sections.

The definition (23) may be written in the form

$$\frac{\tilde{\rho}(B_u, \Lambda)}{\rho_0} = -\frac{1}{i\omega\rho_0\langle\tilde{u}(z)\rangle}\frac{d\tilde{p}}{dz} = -\frac{S}{i\omega G}\frac{d\tilde{p}}{dz}, \quad (33)$$

where $G = \rho_0\langle\tilde{u}(z)\rangle S$ is treated now as the stationary mass flow rate through a pore in the low-frequency limit. Normalizing the mass-flow rate as $\bar{G} = -G\sqrt{2R_gT_0}/SL_p(dp/dz)$, we express the dynamic density in terms of the dimensionless parameters

$$\bar{\rho} = \frac{\tilde{\rho}(B_u, \Lambda)}{\rho_0} = -\frac{\rho_0 L_p\sqrt{2R_gT_0}}{\eta\Lambda^2\bar{G}} = -\frac{\sqrt{\pi}}{\Lambda^2\mathrm{Kn}\bar{G}}. \quad (34)$$

For low frequencies ($|\Lambda| \to 0$), the dynamic compressibility is approximated as

$$\bar{C}(B_E, \gamma, \tilde{\Lambda}) = \gamma p_0\tilde{C}(B_E, \gamma, \tilde{\Lambda}) \approx \gamma + O(B_E, \tilde{\Lambda}^2). \quad (35)$$

Formulas (33)–(35) allow us to evaluate $\tilde{\rho}$ and $\tilde{C}$ using parameters of the stationary flow through pores, and calculate the characteristic impedance Z_w and the propagation constant m using (25) and (26). The experimental data to be used for comparison were reported in forms, which differed from (33) and could not be directly substituted into (34). Hereafter we will derive a suitable modification of (34) for each source of data. All comparisons are performed for the imaginary part of dynamic density at $|\Lambda| = 10^{-1}$. The accommodation coefficient is $\alpha_u = 0.9$, besides the case of a slit for which α_u was measured in experiment. In this case, the relative error of the low-frequency approximation does not exceed 10^{-2}.
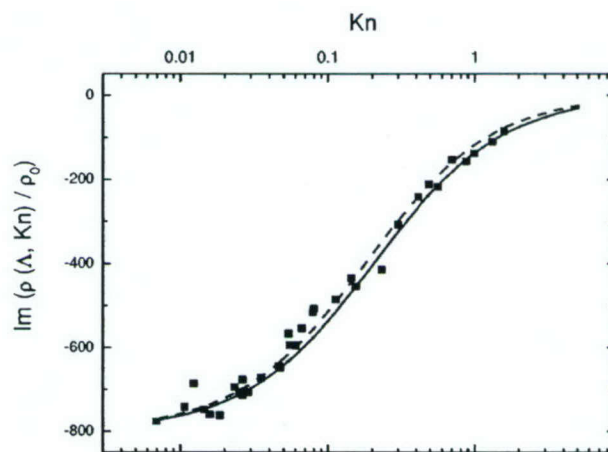

FIG. 4. Comparison of theoretical predictions (solid lines) for the normalized imaginary part of dynamic density at $|\Lambda| = 10^{-1}$, $\alpha_u = 0.9$ with those resulted from Knudsen's interpolation (36) (dashed lines) and experimental data[26] for flows of air in copper pipes of 1.30-cm radius and 332-cm length (squares).

J. Acoust. Soc. Am., Vol. 117, No. 5, May 2005   Kozlov et al.: Acoustic properties of rarefied gases   7
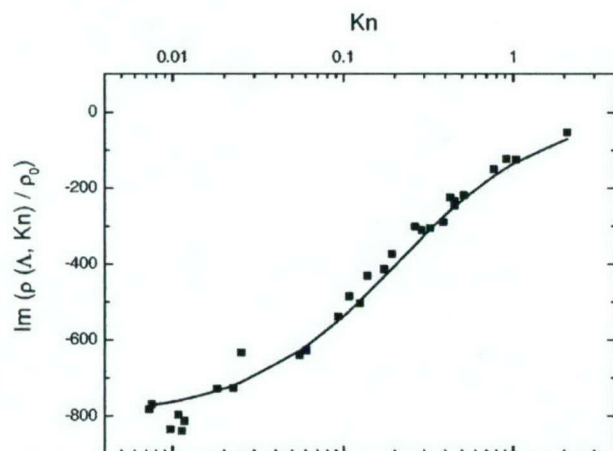
PROOF COPY 045505JAS

FIG. 5. Comparison of theoretical predictions (solid lines) for the normalized imaginary part of dynamic density at $|\Lambda| = 10^{-1}$, $\alpha_u = 0.9$ with those resulted from experimental data[26] for flows of hydrogen in copper pipes of 1.30-cm radius and 332-cm length (squares).

FIG. 6. Comparison of theoretical predictions (solid lines) for the normalized imaginary part of dynamic density at $|\Lambda| = 10^{-1}$, $\alpha_u = 0.9$ with those resulted from experimental data[27] for flow of argon in the square tube of 2.5-mm cross-section side and 305-mm length (squares).

A. Circular pores

The mass-flow rates of stationary flows in circular pipes were evaluated by many researchers, both theoretically and experimentally, for a wide range of Knudsen numbers (see, for example, Ref. 24). Some of the experimental data were approximated analytically. For example, the correlation (in our notation)

$$\bar{G} = \frac{\sqrt{\pi}}{8 \mathrm{Kn}} \left(1 + 8.52 \sqrt{\frac{2}{\pi}} \cdot \mathrm{Kn} \frac{\mathrm{Kn} + \sqrt{2\pi}}{\mathrm{Kn} + 1.235 \sqrt{2\pi}} \right) \qquad (36)$$

is known as Knudsen's formula.[25] Along with (36) we use the data.[26] For comparison with these data, we write (34) in the form

$$\bar{\rho} = -i \frac{\pi}{\Lambda^2 XU} \left(\frac{r_0}{30.48} \right)^3, \qquad (37)$$

where L is the pipe length in cm, r_0 is the pipe radius in cm, U is the gas flow rate per unit pressure drop in micron-cubic foot per second per micron, and $X = (\eta/r_0) p_m (\rho_1 g_c)^{1/2}$ is the dimensionless group of parameters defined in Ref. 26. The theoretical dependences of $\mathrm{Im}\, \tilde{\rho}(B_u, \Lambda)$ were calculated at $|\Lambda| = 10^{-1}$ and compared with the experimental data in Figs. 4 and 5. The theoretical predictions (solid line) agree well with the Knudsen's interpolation (36) (dashed line) and with
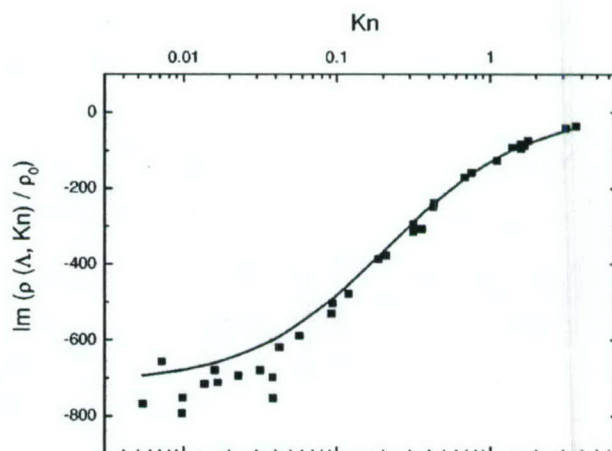
the data on air flow (squares in Fig. 4) and hydrogen flow (squares in Fig. 5) obtained in copper pipes of 1.30-cm radius and 332-cm length. The average relative deviation of the experimental data from the theory does not exceed 6% in the considered range of Knudsen numbers.

B. Square pipes

Data for pipes of square cross section were presented in Ref. 27. For straightforward usage of these data we express the dimensionless dynamic density in the form

$$\bar{\rho} = - \frac{101.325 h^3 \sqrt{2\pi}}{0.76 \Lambda^2 N_K L m_{\mathrm{Ar}} \sqrt{R_{\mathrm{Ar}} T} (\dot{n}/\Delta p)}, \qquad (38)$$

where $h \approx 1.25$ mm is the half-side of square, $L \approx 305$ mm is the tube length, m_{Ar} is the molecular mass of argon, and R_{Ar} is the gas constant per unit mass for argon. The Knudsen number N_K and the molecular flow rate per unit pressure $\dot{n}/\Delta p$ are tabulated in Ref. 27. The factor 101.325/0.76 is used to convert mm Hg to Pa.

The corresponding theoretical dependencies were calculated using (29)–(32) and (20) and (21) at $q_1 = q_2 = 1$. The roots of (20) were determined using the method of bisection. Equations (21) were solved by the Gaussian method. For

TABLE I. Dimensionless flow rate $\bar{G}$ as a function of rarefaction parameter $\delta = 2/\mathrm{Kn}$ (slit 3 in Ref. 28).

H_2		D_2		He		Ne		CO_2	
δ	$\bar{G}$	δ	$\bar{G}$	δ	$\bar{G}$	δ	$\bar{G}$	δ	$\bar{G}$
20.18	7.50	39.45	10.13	27.35	9.66	34.91	11.50	37.15	11.66
9.42	4.79	14.42	6.40	13.55	6.10	17.30	7.08	18.41	6.87
4.95	3.55	7.60	4.21	6.73	4.29	7.83	4.58	7.83	4.37
2.53	3.08	3.55	3.32	3.24	3.39	3.77	3.63	3.44	3.21
1.22	2.89	1.93	3.05	1.60	3.10	2.11	3.26	1.38	2.82
0.624	2.95	1.38	2.95	0.984	3.05	1.11	3.16	0.726	2.84
0.301	3.08	0.489	3.10	0.473	3.24	0.552	3.24	0.318	2.95
0.113	3.45	0.265	3.18	0.301	3.42	0.249	3.39	0.149	3.16
0.0578	3.71	0.113	3.58	0.144	3.60	0.116	3.74	0.0673	3.37

8   J. Acoust. Soc. Am., Vol. 117, No. 5, May 2005   Kozlov et al.: Acoustic properties of rarefied gases

PROOF COPY 045505JAS

TABLE II. Slip constants $\sigma \pm \Delta\sigma$ (slit 3 in Ref. 28 or slit 2 in Ref. 29).

H_2	D_2	He	Ne	CO_2
1.374 ± 0.014	1.407 ± 0.014	1.494 ± 0.010	1.558 ± 0.017	1.235 ± 0.017

each number j of the unknown coefficients, a system of 300 equations was solved. This provided a relative accuracy of the order of 10^{-8}.

Comparisons of the theoretical predictions (solid line) with the experimental data (squares) are shown in Fig. 6. The average relative deviation of experimental values from theoretical results is approximately 10% in the considered range of Knudsen numbers.

C. Narrow slits

The first experimental observations of rarefied gas flows through slits were made by Gaede.[28] However, for comparisons we use the later data,[29,30] which were obtained with accounting for roughness of slit walls and for which the mean accommodation coefficients were determined. Unfortunately, the experimental conditions of the results[29,30] were not well documented. In particular, the pressure gradient $d\tilde{p}/dz$ and the mean pressures inside slits were not specified. This leads to some uncertainty in evaluation of basic parameters such as Knudsen number. The dimensionless dynamic density is approximated using (34). The dimensionless flow rate $\bar{G}$ for different gases is given in Table I as a function of the rarefaction parameter $\delta = 2/Kn$. These data were obtained by scanning of the plots in Fig. 5 of Ref. 29 for slit 3 (see also the data for slit 2 in Ref. 30).

Experimental values of the slip constant σ for various gases are given in Table II. They correspond to the data in Table II of Ref. 29. Since the slip constant is expressed via the molecular tangential impulse accommodation coefficient α_u as $\sigma = (2 - \alpha_u)/\alpha_u$, then $B_u = \sigma Kn$. Data from Table II were used for computations of the theoretical and experimental distributions $\text{Im } \tilde{\rho}(B_u, \Lambda)$.
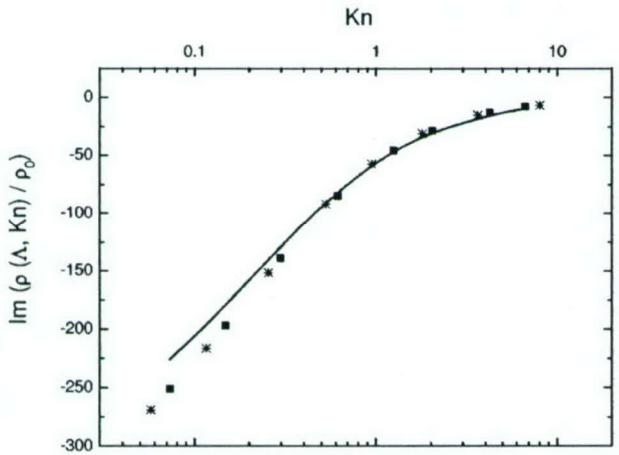
Results of comparison are shown in Figs. 7–9. Since the
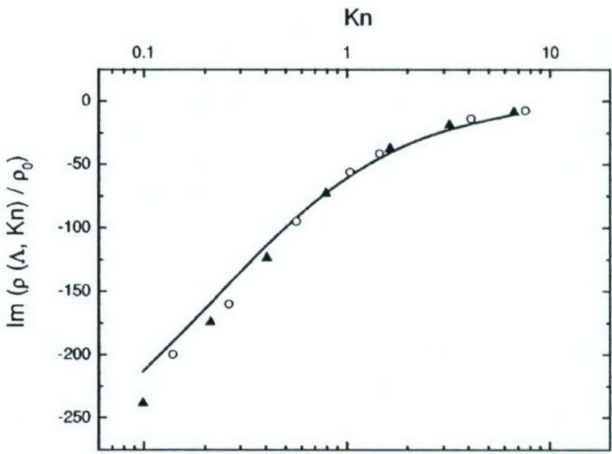

FIG. 8. Comparison of theoretical predictions (solid lines) for the normalized imaginary part of dynamic density at $|\Lambda| = 10^{-1}$ with those resulted from experimental data[29,30] for flows of helium (squares) and neon (asterisks) in flat slits.

dimensionless theoretical distributions weakly depend on Prandtl number and do not depend on other individual gas parameters (besides the specific heat ratio γ), we used the same theoretical curves for deuterium and hydrogen in Fig. 7 and for helium and neon in Fig. 8.

Figures 4–9 show that the normalized imaginary part of the dynamic density predicted by the theory (solid lines) correlates well with the distributions that resulted from experiment (symbols) in the Knudsen number range $0 < Kn < 5$ ($0 < Kn|\Lambda| < 5$) for all considered cases. This indicates remarkable elasticity of the first-order asymptotic model, which was initially elaborated for small Knudsen numbers. Note that a similar feature was observed in the asymptotic theory[31] developed for heat conductivity of highly porous ceramic materials.

Figures 4–9 also show that the gas rarefaction leads to significant reduction of the dynamic density in low-frequency limit. Parametric computations indicate that the gas rarefaction effect decreases with the dimensionless pa-
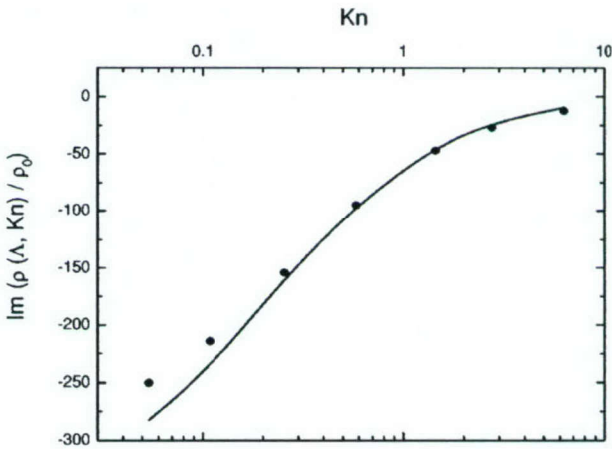

FIG. 7. Comparison of theoretical predictions (solid lines) for the normalized imaginary part of dynamic density at $|\Lambda| = 10^{-1}$ with those resulted from experimental data[29,30] for flows of hydrogen (triangles) and deuterium (circles) in flat slits.

FIG. 9. Comparison of theoretical predictions (solid lines) for the normalized imaginary part of dynamic density at $|\Lambda| = 10^{-1}$ with those resulted from experimental data[29,30] for flows of carbonic gas (rounds) in narrow flat slits.

rameter $|\Lambda|$. This is explained by the reduction of viscous effects on acoustic disturbances of higher frequencies.

Note that the scatter of experimental data presented in Figs. 4–6 increases as the Knudsen number decreases. Reasons for this scatter were not explained in Refs. 26–30. Nevertheless, the rarefaction effect on the dynamic density and other acoustic characteristics diminishes at small Knudsen numbers. Interestingly, the agreement between experiment and theory improves for relatively high Knudsen numbers (Kn~1) in all considered cases.

V. CONCLUSIONS

In this paper, theoretical analysis of monochromatic acoustic waves propagating in long uniform pores of various cross-sectional shapes (circle, rectangular, triangular, and slit) filled with gas of low density (or in pores of microscopic cross-sectional sizes at normal conditions) was performed. The problem was solved using linearized Navier-Stokes equations with the boundary conditions that resulted from the first-order approximation with respect to small Knudsen number. The obtained results allow prediction of the characteristic impedance Z_w, propagation constant m, and other acoustic parameters of isolated pores and perforated panels in wide ranges of pressures and cross-sectional sizes. For the Knudsen number Kn=0, the formulas (29) and (30) along with (31) and (32) coincide with the corresponding expressions for continuum media (see, for example, Ref. 13). In the limiting case of zero frequency, the solutions (5) and (14) describe steady-state isothermal flows (Poiseuille flows) of rarefied gases through long uniform pipes of considered shapes.

The basic theoretical relations were verified by comparisons of the imaginary part of the dynamic density calculated for low frequencies with known experimental data on steady-state flows of rarefied gases through tubes of different cross-sectional shapes. It was shown that theoretical predictions agree well with experiments in the wide range of Knudsen numbers $0 \leqslant Kn < 5$ that considerably exceeds the formal restriction, $Kn \ll 1$, of asymptotic theory.

Parametric calculations also showed that the rarefaction effects are stronger in the low-frequency range and substantially decrease at high frequencies. This is due to the corresponding decrease of viscous effects on the dissipation of acoustic energy at higher frequencies.

The results of this paper may be used in the future as a foundation for the development of theoretical and semi-empirical models predicting acoustic characteristics of randomly porous materials in wide ranges of ambient pressure and pore size.

[1] G. Kirchoff, "Über den Einfluss der Wärmeleitung in einem Gase auf die Schallbewegung," Poggendorfer Ann. **134**, 177–193 (1868).
[2] J. Strutt (Lord Rayleigh), *Theory of Sound*, 2nd ed. (Dover, 1894).
[3] C. Zwikker and C. W. Kosten, *Sound Absorbing Materials* (Elsevier, New York, 1949).
[4] M. A. Biot, "Theory of propagation of elastic waves in a fluid-saturated porous solid. Part I. Low-frequency range," J. Acoust. Soc. Am. **28**, 168–178 (1956).
[5] M. A. Biot, "Theory of propagation of elastic waves in a fluid-saturated porous solid. Part 2. High-frequency range," J. Acoust. Soc. Am. **28**, 179–191 (1956).
[6] M. E. Delany and E. N. Bazley, "Acoustic properties of fibrous absorbent materials," Appl. Acoust. **3**, 105–116 (1970).
[7] K. Attenborough, "On the acoustic slow wave in air-filled granular media," J. Acoust. Soc. Am. **81**, 93–102 (1987).
[8] D. L. Johnson, J. Koplik, and R. Dashen, "Theory of dynamic permeability and tortuosity in fluid saturated porous media," J. Fluid Mech. **176**, 379–402 (1987).
[9] J.-F. Allard and Y. Champoux, "Empirical equations for sound propagation in rigid frame porous materials," J. Acoust. Soc. Am. **91**, 3346–3353 (1992).
[10] M. R. Stinson, "The propagation of plane sound waves in narrow and wide circular tubes and generalization to uniform tubes of arbitrary cross-sectional shape," J. Acoust. Soc. Am. **89**, 550–558 (1991).
[11] H. S. Roh, W. P. Arnott, J. M. Sabatier, and R. Raspet, "Measurement and calculation of acoustic propagation constants in arrays of small air-filled rectangular tubes," J. Acoust. Soc. Am. **89**, 2617–2624 (1991).
[12] M. R. Stinson and Y. Champoux, "Assignment shape factors for porous materials having simple pore geometries," J. Acoust. Soc. Am. **88**, S121 (1990).
[13] M. R. Stinson and Y. Champoux, "Propagation of sound and the assignment of shape factors of model porous materials having simple pore geometries," J. Acoust. Soc. Am. **91**, 685–695 (1992).
[14] A. Fedorov, A. Shiplyuk, A. Maslov, E. Burov, and N. Malmuth, "Stabilization of a Hypersonic Boundary Layer Using an Ultrasonically Absorptive Coating," J. Fluid Mech. **479**, 99–124 (2003).
[15] A. Fedorov, V. Kozlov, A. Shiplyuk, A. Maslov, A. Sidorenko, E. Burov, and N. Malmuth, "Stability of hypersonic boundary layer on porous wall with regular microstructure," AIAA paper no. 2003-4147.
[16] M. Gad-el-Hak, "Use of continuum and molecular approaches in microfluids," AIAA paper no. 2002-2868.
[17] A. Kundt and E. Warburg, "On Friction and Thermal Conductivity in Rarefies Gases," Philos. Mag. **50**, 53 (1875).
[18] J. C. Maxwell, "On Stresses in Rarefied Gases Arising from Inequalities of Temperature," Philos. Trans. R. Soc. London **170**, 231–256 (1879); reprinted in *The Scientific Papers of J. C. Maxwell* (Dover, New York, 1965).
[19] M. V. Smoluchowski, "Über den Temperatursprung bei Wärmeleitung in Gasen," Akad. Wiss. Wien. **107**, 304 (1898); **108**, 5 (1899).
[20] F. O. Goodman and H. Y. Wachman, *Dynamic of Gas-Surface Scattering* (Academic, New York, 1976).
[21] G. N. Patterson, *Molecular Flow of Gases* (Wiley, New York; Chapman and Hall, London, 1956).
[22] V. P. Shidlovski, *Introduction in Dynamics of Rarefied Gas* (Nauka, Moscow, 1965) (in Russian).
[23] S. Chapman and T. G. Cowling, *The Mathematical Theory of Non-Uniform Gases*, 2nd ed. (Cambridge U.P., Cambridge, 1952).
[24] C. Cercignani, *Theory and Application of the Boltzmann Equation* (Scottish Academic, Edinburgh, 1975).
[25] M. Knudsen, "Die Gesetze der Molekularströmung und der inneren Reibungsströmung der Gase durch Rohren," Ann. Phys. **28**, 75–130 (1909).
[26] G. K. Brown, A. DiNardo, G. K. Cheng, and T. K. Sherwood, "The Flow of Gases in Pipes at Low Pressures," J. Appl. Phys. **17**, 802–813 (1946).
[27] M. W. Milligan and H. J. Wilkerson, "Pressure Ratio Effects on Rarefied Flow Through Square Tubes," J. Eng. Ind. **95**, ■–■ (1973).
[28] W. Gaede, "Die äussere Reibung der Gase," Ann. Phys. **41**, 289 (1913).
[29] B. T. Porodnov, P. E. Suetin, and S. F. Borisov, "Gas flows in flat slit in wide range of Knudsen numbers," J. Tech. Phys. **40**, 2383–2391 (1970) (in Russian).
[30] B. T. Porodnov, P. E. Suetin, S. F. Borisov, and V. D. Akinshin, "Experimental investigation of rarefied gas flow in different channels," J. Fluid Mech. **64**, 417–437 (1974).
[31] V. F. Kozlov, "The theoretical model of heat conductivity in high-porous materials," (in Russian), Transactions of First Russian National Conference on Heat Transfer (published by Moscow Power Engineering Institute, Moscow, 1994), vol. X, pt. 2, 3–7.

Proof Corrections of Manuscript ID 045505JAS
V. F. Kozlov, A.V. Fedorov, and N. Malmuth, "Acoustic properties of rarefied gases inside pores of simple geometries"

1. Page 2, Column 2, Line 12: replace "as" by "as:"

2. Page 3, Column 1, Line 12 from the bottom: delete "correspondingly"

3. Page 3, Column 2, Lines 4 and 4: replace "(7a) and (8a), and (7b) and (8b)," by "(7a)-(8a) and (7b)-(8b)"

4. Page 4, Column 2, Line 7: replace "$|q_2| \leq 1$" by "$|q_2 y| \leq 1$"

5. Page 6, Column 1, Line 15 from the bottom: replace "the cross-section area S" by "the cross-sectional area S, "

6. Page 10, Column 1: insert

ACKNOWLEDGMENTS

7. Page 10, Column 1, Line 8 from the top: replace "Kirchoff" by "Kirchhoff"

8. Page 10, Column 1, Line 6 from the top: replace "[2] J. Strutt (Lord Rayleigh) *The Theory of Sound*, 2nd ed. (Dover, 1894)" by "[2] J.W. Rayleigh, *The Theory of Sound*, Dover, New York, 1945."

9. Page 10, Column 2, Line 12 from the bottom: insert page numbers "296-299".